AD-A264 227

AFOSR-TR- 93 0294 ②

DESIGN, SYNTHESIS, AND CHEMICAL PROCESSING OF HIERARCHICAL CERAMIC STRUCTURES FOR AEROSPACE APPLICATIONS

Wendell E. Rhine, Michael J. Cima and H. Kent Bowen
Ceramics Processing Research Laboratory
Massachusetts Institute of Technology
Cambridge, MA 02139

DTIC
ELECTE
MAY 14 1993
S B D

Final Report
Contract No. F49620-89-C-0102
Air Force Office of Scientific Research
Bolling Air Force Base, DC

Report Date
March 30, 1993

93-10665

Period Covered
August 1989 - February 1993

Approved for public release;
distribution unlimited.

93 5 12 101

REPORT DOCUMENTATION PAGE

Form Approved
OMB No. 0704-0188

1a. REPORT SECURITY CLASSIFICATION Unclassified	1b. RESTRICTIVE MARKINGS
2a. SECURITY CLASSIFICATION AUTHORITY	3. DISTRIBUTION/AVAILABILITY OF REPORT Approved for Public release Distribution is unlimited
2b. DECLASSIFICATION/DOWNGRADING SCHEDULE	
4. PERFORMING ORGANIZATION REPORT NUMBER(S) Final Report	5. MONITORING ORGANIZATION REPORT NUMBER(S)
6a. NAME OF PERFORMING ORGANIZATION Massachusetts Institute of Tech	6b. OFFICE SYMBOL (If applicable)
7a. NAME OF MONITORING ORGANIZATION AFOSR/NC	
6c. ADDRESS (City, State, and ZIP Code) Materials Processing Center Cambridge, MA	7b. ADDRESS (City, State, and ZIP Code) Building 410, Bolling AFB, DC 20332-6448
8a. NAME OF FUNDING/SPONSORING ORGANIZATION AFOSR	8b. OFFICE SYMBOL (If applicable) NC
9. PROCUREMENT INSTRUMENT IDENTIFICATION NUMBER F49620-89-C-0102	
8c. ADDRESS (City, State, and ZIP Code) Building 410, Bolling AFB, DC 20332-6448	10. SOURCE OF FUNDING NUMBERS

PROGRAM ELEMENT NO.	PROJECT NO.	TASK NO.	WORK UNIT ACCESSION NO
61102F	2303	A3	

11. TITLE (Include Security Classification)
Design, Synthesis and Chemical Processing of Hierarchical Ceramic Structures for Aerospace Applications

12. PERSONAL AUTHOR(S)
Wendell E. Rhine, Michael J. Cima and H. Kent Bowen

13a. TYPE OF REPORT	13b. TIME COVERED	14. DATE OF REPORT (Year, Month, Day)	15. PAGE COUNT
Final	FROM 8/1/89 TO 2/28/93	93/3/30	213

16. SUPPLEMENTARY NOTATION

17. COSATI CODES		
FIELD	GROUP	SUB-GROUP

18. SUBJECT TERMS (Continue on reverse if necessary and identify by block number)
Ceramic processing, ceramic powders, ceramic composites, nanocomposites, SiC, TiB_2, TiN, TiC, cordierite, Al_2O_3, AlN, synthesis, metal organic precursors,

19. ABSTRACT (Continue on reverse if necessary and identify by block number)

Ceramic materials are beginning to replace conventional materials in high temperature structural applications, but further advances are needed to improve their reliability. To analyze the complex behavior of ceramics, it is useful to consider the structure on four hierarchical levels - namely the molecular-, nano-, micro, and macroscales. Interactions at and between these various levels of structure exert important and often quite specific influences. The research conducted for this effort involved using chemical approaches to synthesize and process ceramic powders to create and control these hierarchical structures in ceramic materials.

With the development of chemical approaches for synthesizing and processing ceramics, it is possible to develop synthetic and processing methods to control the molecular and nanostructure of ceramic powders. This report describes our efforts to synthesize submicron SiC, TiB_2, TiC, and TiN powders, and nanocomposites from preceramic polymers. Efforts to synthesize epitaxial $LiNbO_3$ films from alkoxide precursors are also described.

20. DISTRIBUTION/AVAILABILITY OF ABSTRACT ☒ UNCLASSIFIED/UNLIMITED ☐ SAME AS RPT ☐ DTIC USERS	21. ABSTRACT SECURITY CLASSIFICATION Unclassified	
22a. NAME OF RESPONSIBLE INDIVIDUAL Capt. Thomas Erstfeld	22b. TELEPHONE (Include Area Code) 202-767-4963	22c. OFFICE SYMBOL AFOSR/NC

DD Form 1473, JUN 86

Previous editions are obsolete.

18. (cont.) sol-gel, preceramic polymers, binder thermolysis, non-linear optics, lithium niobate, silicon carbide, titanium carbide, titanium nitride, titanium diboride, alumina, aluminum nitride.

19. (cont.) Understanding polymer chemistry on a molecular or nanostructural level is important in processing ceramics, since these structures affect the behavior of green ceramic bodies. Research on using polymers in sol-gel processing, on improving the dimensional stability of tapes, on binder thermolysis, and on preceramic polymers is also discussed in this report.

It was also demonstrated that nanosized powders can be processed to obtain ceramic composites with ultrafine microstructures and high densities. Nanosized powders of cordierite were prepared and used to prepare cordierite/SiC composites with > 95% TD.

...CTED 5

Accession For
NTIS GRA&I ☑
DTIC TAB ☐
Unannounced ☐
Justification
By
Distribution
Availability Codes
Avail and/or
Dist Special
A-1

CONTENTS

EXECUTIVE SUMMARY 1

RESEARCH SUMMARIES 3

1. An Overview of Chemical and Physical Routes to Advanced Ceramic Powders 3
2. Control of Ceramic Powder Composition by Precipitation Techniques 14
3. Precipitation of Oxalates from Homogeneous Solution: Synthesis of $BaTiO(C_2O_4)_2$ and Ba, Y, Cu Oxalates 23
4. Synthesis and Crystal Structure of Barium Titanyl Oxalate, $BaTi(O)(C_2O_4)_2 \cdot 5H_2O$: A Molecular Precursor for $BaTiO_3$ 29
5. Preparation and Characterization of $Y_3Al_5O_{12}$ (YAG) from Alkoxide Derived Polymers 41
6. Preparation of Zircon and Mullite-Zircon Powders by Sol-Gel Techniques 49
7. Preparation and Characterization of SiC from Alkoxide-Derived Polymeric Precursors 54
8. Preparation and Properties of Silicon Carbide from Polymeric Precursors 59
9. Preparation of Titanium Diboride from Titanium Alkoxides and Boron Powder 71
10. Preparation of Titanium Diboride from Borothermic Reduction of TiO_2 $TiO_x(OH)_y$, or $Ti(O\text{-}n\text{-}Bu)_4$-Derived Polymers 75
11. Preparation of TiN and TiC from a Polymeric Precursor 84
12. In-Situ Preparation of TiC/Al_2O_3, TiN/Al_2O_3 and TiN/AlN Composites From Alkoxide-Derived Precursors 93
13. Synthesis and Pyrolysis of Novel Precursors To TiC/Al_2O_3, TiN/Al_2O_3 and TiN/AlN Nanocomposites 97

14. Preparation of Nanophase SiC/Si_3N_4, SiC/B_4C and Stoichiometric SiC from Mixtures of a Vinylic Polysilane and Metal Powders.................... 106

15. Epitaxial $LiNbO_3$ Thin Films Prepared by a Sol-Gel Process................ 111

16. Structure and Optical Properties of Polycrystalline and Epitaxial $LiNbO_3$ Thin Films Derived by a Sol-Gel Method................ 116

17. Microstructural Evolution of Epitaxial $LiNbO_3$ Thin Films Derived from Metal Alkoxide Solutions.. 124

18. Microstructure of Sol-Gel Derived Epitaxial $LiNbO_3$ Thin Films Observed by Transmission Electron Microscopy.......................... 129

19. Preparation of Porous Oxide Beads Using Polymeric Beads To Control Bead Size and Shape... 136

20. Superabsorbent Polymers as Templates in Forming Oxide Ceramics...... 141

21. A Comparison of Aqueous and non-Aqueous Slurries for Tape-Casting and Dimensional Stability in Green Tapes................ 145

22. Prediction and Explanation of Aging Shrinkage in Tape-Cast Ceramic Green Sheets... 152

23. Effect of Pressure Fluctuation on Removal of Carbon Residue Part I. Theoretical Analysis... 161

24. Effect of Pressure Fluctuation on Removal of Carbon Residue: Part II. Experimental Verification.. 171

25. Direct Observation of Preceramic Binder Decomposition in 2-D Model Microstructures... 181

26. Preceramic Binders in Ceramic Powder Processing............................ 193

27. Preparation of SiC-Cordierite Composites.. 202

28. Preparation of SiC/Cordierite Composites by Pressureless Viscous Sintering... 207

EXECUTIVE SUMMARY

The new structural materials required by the aerospace industry must have high strength, toughness, and thermal stability as well as stability in harsh environments. Other applications require materials with unique optical, electrochemical, or electromagnetic properties. Ceramic materials and ceramic-ceramic composites have many of the desired properties for these advanced materials.

The synthesis, processing, and sintering of simple ceramic systems has been the subject of recent intense investigations. With the development of chemical approaches for synthesizing ceramics comes the possibility of developing processing methods that will lead to control of microstructure and properties. In addition, we believe it is time to begin extending these processing concepts and to reach further into the array of structures which can be designed into components and devices made from ceramic materials. Extending the possible range of compositions and configuration of phases which can be designed into ceramic materials requires establishing the science of synthesizing materials by manipulating and controlling the hierarchical structures of multiphase ceramic materials.

Previous research has demonstrated that there is a strong interdependence of all processing steps, and that very subtle changes can have significant effects on properties. Under certain conditions, the particle size, size distribution, morphology, chemistry, and packing of single-phase ceramic particles can be controlled. This research effort builds on past efforts to create the hierarchical structures needed for advanced ceramic materials, and techniques to extend these processes to multi-cation and multiphase systems are being developed. Therefore, the objectives of this research are: (1) to use chemical approaches to extend the range of compositions and configuration of phases available, (2) to prepare ceramic materials with the homogeneity and properties required for demanding applications, and (3) to investigate the important issues in powder processing to control the hierarchical structures and properties of high-performance ceramics in a reliable and reproducible manner.

Chemical processing routes, which begin with high-purity powders and remove inhomogeneities, lead to improved microstructure and properties. For example, it is widely accepted that unreliable structural behavior of ceramic components is related to large variations in flaw types and sizes. Many flaw types are related to inhomogeneities introduced during the different processing steps: powder manufacture, green body fabrication, consolidation, sintering, and subsequent machining. The average size, size distribution, and types of inhomogeneities introduced during each processing step determine the average strength and strength distribution of the sintered ceramic component. Therefore, chemical processing approaches to remove flaws and inhomogeneities are considered to be the key to improving the properties of ceramic materials.

The research program used model ceramic systems (oxides-carbides-nitride-borides) which allowed us to investigate and test generic principles for synthesizing and improving the performance of ceramic materials. Included in the materials that were investigated are oxide, non-oxide, and composite materials that allowed examination of processing-property relationships.

This report is divided into 28 sections. The first section gives an overview of methods used to synthesize and manufacture ceramic powders. The second and third sections discuss precipitation methods and using molecular complexes to control the stoichiometry of ceramic powders. Perhaps the most studied molecular complex is the barium titanyl oxalate used as a precursor for $BaTiO_3$. Some controversy has developed as to whether this compound is stoichiometric or a solid solution of variable composition. We isolated crystals of barium titanyl oxalate, determined its single crystal X-ray structure (Section 4), and showed that this compound is indeed stoichiometric with a Ba:Ti ratio of 1:1.

The next 10 sections report our progress using sol-gel techniques to synthesize both oxide and non-oxide ceramic materials. Sol-gel approaches for the synthesis of non-oxide materials provide a less expensive route than organometallic preceramic polymers, and the stoichiometry of the product can be more easily controlled. Sections 5-15 cover our efforts to synthesize YAG (section 5), zircon (section 6), SiC (sections 7 and 8), TiB_2 (sections 9 and 10), and TiN and TiC (section 11). Sections 12-14 discuss our approaches for synthesizing nanophase composites from alkoxide-derived polymers.

Epitaxial thin films can also be fabricated using sol-gel techniques, and sections 15-18 report on our efforts to form epitaxial films of $LiNbO_3$ on sapphire substrates. When no water was added to the alkoxide precursors and hydrolysis was conducted after film formation, a heteroepitaxial film with single-crystal nature was obtained by a sol-gel process.

Polymers have many applications in ceramics processing. Sections 19-26 discuss our research on using polymers in ceramics processing. The first two papers discuss using polymers combined with sol-gel processing methods to control the shape of ceramic materials. In the paper in section 19, we impregnated polymeric beads with silica sols to prepare large (>>10 μm) silica spheres with controlled porosity. Section 20 discusses using superabsorbent polymers to control the shape of ceramic bodies.

The papers in sections 21 and 22 compare non-aqueous tape casting with an aqueous tape casting method. The aqueous system employed an acrylic emulsion binder, while the organic system contained the same acrylic polymer dissolved in toluene. Samples cast from the aqueous formulation exhibited lower linear shrinkage than those from the organic system after aging for 35 days under controlled-ambient conditions. The green tapes were given various treatments to stabilize the tapes and reduce dimensional changes. A treatment which involved a 24-h exposure to 80 °C water-saturated air yielded solvent-based green tapes which exhibited the lowest shrinkage and anisotropy after aging and after firing.

Papers in Sections 23 and 24 report the results of an effort to improve the removal of carbon from ceramic bodies during firing. We demonstrated that pressure fluctuation could accelerate the oxidation of carbon in porous ceramic green bodies by overcoming both the internal and external mass transfer resistance. The carbon removal rate was found to depend on temperature, oxygen flow rate, pore size, carbon concentration, sample size, and both the frequency and amplitude of the pressure oscillation.

The new preceramic polymers offer the opportunity to synthesize new composite materials with unique properties. Preceramic polymers have also been used to form net-shape and -size ceramic materials. Since these polymers produce ceramic residues upon pyrolysis, very little or no shrinkage occurs when these polymers are used as binders. Sections 25 and 26 report the results of an effort to determine the properties of preceramic polymers during pyrolysis. Diffuse reflectance Fourier transform infrared spectroscopy was used to study the chemical changes that occur during the thermal decomposition of polycarbosilane (Nicalon) and polyvinylic silane. By using an optical microscope we were able to observe when cracks and bubbles began to form. We believe that this research will allow us to select preceramic polymers with desirable properties and improve the processing methods for forming composites of non-oxide powders and preceramic polymers.

Sections 27 and 28 discuss our efforts to process amorphous ceramic powders. Chemically derived cordierite, which has been reported to densify in the amorphous state, was used to make cordierite-SiC composites. Cordierite powders were synthesized and dispersed with SiC whiskers and powders. These composites densified at 850-900 °C to give a glass-SiC composite. Upon heating at higher temperatures, the glass crystallized to cordierite to give a ceramic-ceramic composite.

AN OVERVIEW OF CHEMICAL AND PHYSICAL ROUTES TO ADVANCED CERAMIC POWDERS

Wendell E. Rhine and H. Kent Bowen

Published in Ceram. Int. 17 (1991) 143-152.

ABSTRACT

To produce ceramic components with reliable and reproducible properties, it is important to use powders with controlled properties. Until recently, ceramic powders were prepared by methods which were difficult to control and did not lead directly to powders with the desired physical properties. Improved powder production methods and new chemical methods have been developed for producing powders with controlled morphologies, purities, and particle size distributions. These chemical methods include solution and gas phase techniques. An overview of these approaches and others currently used to produce advanced ceramic powders is discussed.

INTRODUCTION

Over a decade ago a major effort was initiated to develop techniques for synthesizing submicrometer ceramic powders with controlled and reproducible chemical and physical properties. This effort developed because properties of ceramic materials depend to a great extent on the size, shape, and chemical composition of the initial powders. Rhodes [1] and Barringer et al. [2] have shown that small, unagglomerated powders yield dense, uniform microstructures at relatively low sintering temperatures. Therefore, these types of powders also lead to better control of sintered microstructures and give materials with improved mechanical properties.

Researchers are focusing on two main approaches to improve the quality of ceramic powders: (1) modifying existing processes to improve and control the quality of ceramic powders and (2) developing novel powder preparation techniques based on vapor phase and solution reactions to produce high-purity, chemically derived ceramic powders.

This paper will present a brief overview of chemical and physical routes to ceramic powders and will compare what is possible to prepare in the laboratory with what can be obtained from commercial sources. The methods used to produce commercial powders are often proprietary, so only limited information is available concerning these processes.

BACKGROUND

The production of high-purity ceramic powders with controlled and reproducible properties requires an understanding of the various preparation techniques and their effect on the chemical and physical properties of the ceramic particles. Many chemical approaches for preparing unagglomerated powders have been investigated and recently reviewed [3, 4]. In view of the importance of preparing high-purity ceramic powders with controlled properties, the general requirements for preparing powders by solution, gas phase, and physical techniques will be discussed briefly.

Powders from Solution Methods

Precipitation from homogeneous solutions: Precipitation from homogeneous solutions refers to the formation of a precipitate by a chemical change in a solution which contains metal salts or complexes. For example, precipitation may occur by slowly changing the pH or by hydrolyzing alkoxides to precipitate hydrous oxides. For example, submicrometer TiO_2 [5], SiO_2 [6], and ZrO_2 [7] powders have been prepared by hydrolyzing alkoxides, and Matijevic [8] has developed approaches for synthesizing powders by: (1) forced hydrolysis, (2) thermal decomposition of complex solutes, and (3) phase transformations. The conditions for forming monodispersed particles from homogeneous solutions was explained by LeMer and Barnes [9] and has been reviewed recently

[10-13].

Precipitation from direct mixing of reagents: In "simultaneous precipitation," all substances whose solubilities are exceeded precipitate together. Precipitation is a very viable manufacturing method and is being used to produce $BaTiO_3$ [14]. The simultaneous precipitation of copper, barium, and yttrium oxalates is another example which many research groups are studying. The materials community usually refers to this method as coprecipitation, but the term "coprecipitation" (as defined by chemists) refers to the contamination of the precipitate by unwanted cations. These coprecipitated substances are normally soluble under the conditions for the precipitation. Direct precipitation can produce very small, amorphous particles which are difficult to filter. Hydrous oxides, for example, are often precipitated in an amorphous form or as exceedingly small crystallites that absorb enormous amounts of water [15].

Vapor Phase Methods

Evaporative decomposition of solutions: The evaporative decomposition of solutions (EDS) has been investigated as an approach for preparing oxide and nonoxide powders [16-23]. For example, spray pyrolysis is one of the few methods that has given nonagglomerated submicrometer particles of high T_c ceramic superconductors [21], and recently aerosols containing preceramic polymers have been thermally decomposed to obtain nonoxide particles [22]. The progress in understanding the chemistry and morphology development of powders produced by EDS methods has been reviewed recently [23].

Plasma and laser induced reactions: Preparing powders by thermally induced gas phase reactions requires volatile precursors which are vaporized and thermally decomposed in tube reactors, in plasmas, or by lasers. The range of materials that can be synthesized by gas phase methods is very broad, and methods similar to those used to make CVD coatings are being applied to the production of powders. Wachtmann and Haber have recently reviewed the various methods for making coatings by CVD techniques [24], and papers reviewing mechanisms of particle formation [25] and modeling vapor phase reactions [26] have also appeared. These gas phase techniques have most often been used to produce non-oxide powders such as silicon, silicon nitride, and silicon carbide.

Physical Methods

Carbothermic reduction and nitridation: Improvements in carbothermic reduction methods are being published. Many of the approaches combine sol-gel chemistry with conventional techniques. Aluminum nitride, for example, has been prepared from a pseudoboehmite sol that was processed with furfuryl alcohol as the carbon source. Upon heating, the furfuryl alcohol polymerizes forming a polymeric product containing alumina and a carbon precursor. Heating the mixture to 1575°C in a nitrogen atmosphere produced an aluminum nitride/carbon composite. Excess carbon was removed by heating the sample to 625°C, and crystalline AlN was the only product that remained [27].

OXIDE POWDERS

Alumina

Developing methods for producing high-purity alumina has been a major area of investigation, because impurities in alumina affect its optical and sintering properties. Generally, alumina whose purity is higher than 99.99% must be used to fabricate translucent alumina ceramics. In addition, during sintering some of the impurities accumulate at the grain boundaries. This results in different grain growth at each grain, producing a nonuniform sintered microstructure that consists of large and small grains. In this case, porosity is difficult to remove and the product does not sinter to full density.

Controlling the morphology of α-alumina particles is also difficult because there are many types of aluminum oxides and hydroxides. Each has several different crystal forms and, therefore, different properties. The paths to α-alumina depend on the starting material, and the firing temperature and atmosphere affect the temperature where phase changes occur. The transition from intermediate aluminas to $\alpha\text{-}Al_2O_3$ is accompanied by large density changes. Consequently, spherical AlO(OH) does not retain its shape when transformed to $\alpha\text{-}Al_2O_3$ [28].

Bayer process: Most of the alumina consumed worldwide is produced by the Bayer process since it continues to be the most economical method. Bayer's process was based on the fact that concentrated sodium hydroxide solutions dissolve alumina, whereas the iron, titanium, and silicon compounds are only partially soluble, if not insoluble. The chemical reactions for extracting alumina from Bauxite are:

$$Al(OH)_3 + NaOH \rightarrow NaAl(OH)_4$$

$$AlOOH + NaOH + H_2O \rightarrow NaAl(OH)_4$$

The dissolution reactions are endothermic and, therefore, an increase in temperature increases the solubility.

Alumina produced by the Bayer process contains high levels of impurities. The impurities are mainly Fe, Si, Ga, and the alkali metals. For example, the Na content

Table 1. Inductively Coupled Plasma Emission Spectrometric Analysis of the Impurities in Two Different Al_2O_3 Powders.

Element	Conc. in Sumitomo* (ppm)	Conc. in Reynolds† (ppm)	Element	Conc. in Sumitomo* (ppm)	Conc. in Reynolds† (ppm)
B	2	3	Mn	<1	6
Ba	3	4	Na	<5	26
Be	<1	<1	Ni	<3	4
Ca	3	47	Si	23	220
Cr	3	4	Sn	<5	<5
Cu	3	1	Sr	<1	1
Fe	9	84	Ti	2	8
Ga	<2	92	Zn	6	14
Mg	3	8	Zr	38	4

*Sumitomo Chemical Co. AKP-HP.

†Reynolds Metal Co. RC-172 DBM without MgO classified powder (0.3-0.5 μm).

can be as high as 1%. To produce ceramics-grade alumina, the Bayer process has been modified to reduce the major impurities; however, new synthetic routes must be developed to obtain higher purity alumina (99.999%).

Alum process: Until recently, high-purity alumina was prepared only by the alum process, which was developed to prepare high-purity powder for sapphire production. Alum is synthesized by the following reaction:

$$Al_2(SO_4)_3 + (NH_4)_2SO_4 + 24H_2O \rightarrow 2NH_4Al(SO_4)_2 \cdot 12H_2O$$

By keeping the pH less than 1 during the synthesis, 70-80% of the Fe and Ti impurities can be removed. Almost all of the remaining impurities are removed during recrystallization.

Alum melts at 80°C and gives a viscous liquid which foams during the evolution of volatile decomposition products and produces a low density product which can easily be ground into a fine powder. The alumina powder produced has a low density, few agglomerates, and a fine particle size [29].

Organoaluminum precursors: Organoaluminum compounds are easily hydrolyzed to aluminum hydroxides and then calcined to obtain α-alumina:

$$AlR_3 + 3H_2O \rightarrow Al(OH)_3 + 3RH$$

$$Al(OR)_3 + 3H_2O \rightarrow Al(OH)_3 + 3ROH$$

Preparing alumina from triethylalane is one of the oldest reported uses of organometallic precursors for ceramics [30, 31]. The use of aluminum alkoxide followed and has been studied extensively over the past 15 years. More recently, researchers at DuPont have reinvestigated the purity of alumina from triethylalane and have recommended it as a good precursor for high-purity alumina [32].

Sumitomo Chemical Co. has developed a manufacturing process based on the hydrolysis of an organoaluminum compound which can produce purer and cheaper high purity alumina than the alum process. Sumitomo has constructed a plant for the production of alumina which has a capacity of 250 tons per year [33, 34].

According to Kadokura and Hama [34], purification is achieved by a distillation step. In order to achieve a final purity of 99.99-99.999%, the purity of the organoaluminum compound has to be greater than that value. Table 1 compares the purity of Sumitomo AKP-HP with a Bayer-derived alumina powder. The levels of trace elements determined in our laboratory are a little higher than reported by Sumitomo, but the Bayer-derived powder has significantly higher concentrations of trace impurities. Sumitomo's AKP-HP is one of the highest purity aluminas commercially available.

Titania

Titanium dioxide (rutile pigment) is currently manufactured mainly by two processes: the classical sulfate process and the chloride process. In the sulfate process, ilmenite ore is treated with sulfuric acid, and titania is produced by hydrolyzing the resulting solution by heating to near its boiling point. The chloride process involves the gas phase oxidation of $TiCl_4$.

Sulfate process: The hydrolysis of titanyl sulfate has recently been investigated by Santacesaria et al. [35].

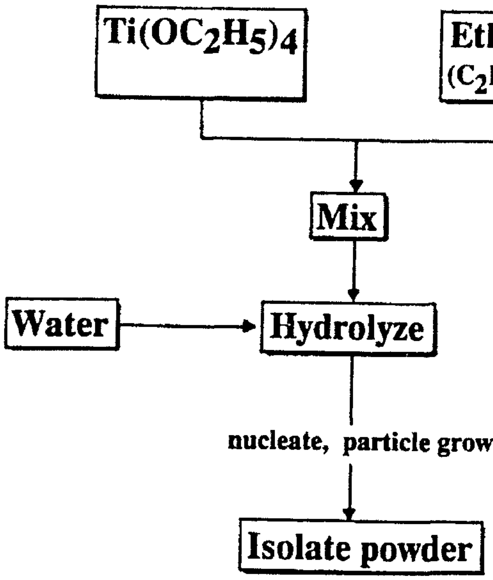

Fig. 1. Preparation of titania from the alkoxides.

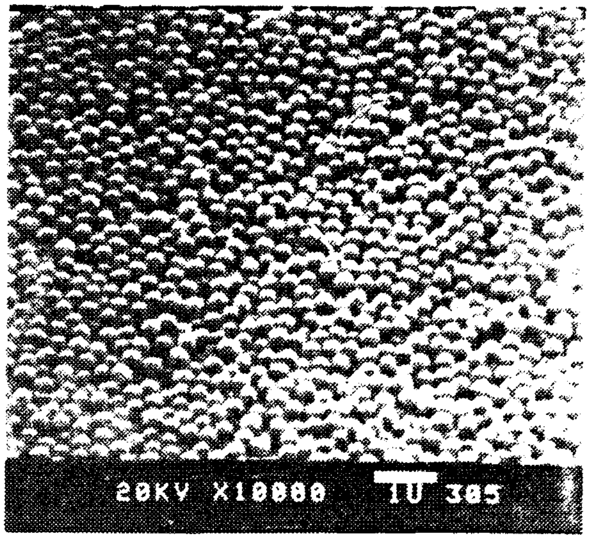

Fig. 2. Powders obtained from alkoxides.

Matijevic [36] has also studied the effect of sulfate ions on the formation of monodispersed TiO_2 particles. When the hydrolysis reaction is carried out carefully, spherical particles are obtained. According to Santacersaria et al., the formation of particles occurs by a nucleation step followed by aggregation of the nuclei. A similar mechanism has been proposed for the formation of monodisperse SiO_2 particles from hydrolysis of tetraethylorthosilicate (TEOS) [37]. The size of the agglomerates was 0.2-0.5 μm as determined by scanning electron microscopy, while that of the elementary particles was 60-90 Å as determined by surface area measurements.

Chloride process: DuPont introduced the chloride process commercially in 1958, and it has seen rapid growth since 1970. Its advantages include continuous operation and the formation of a purer product through purification of the $TiCl_4$ by distillation. This process has been optimized to produce rutile particles for the pigment industry, but anatase can be obtained if the oxidation temperature is below 900°C [38].

Hydrolysis of alkoxides: A method for obtaining very high-purity titania powders, which has been investigated extensively over the past eight years, is the hydrolysis of the alkoxides. A schematic diagram of the alkoxide process for producing TiO_2 is shown in Figure 1. This process produces spherical, unagglomerated powders with a very narrow size distribution [39] as illustrated in Figure 2. The alkoxides rapidly hydrolyze in moist air or water giving a series of condensed titanoxanes, but quantitative cleavage of all the alkoxy groups is difficult to achieve and some alkoxide groups always remain. In contrast to the mechanism proposed for particle formation in the sulfate process, Jean and Ring found that particles produced by hydrolysis of titanium alkoxides are formed by a nucleation and growth mechanism [40].

Zirconia

The raw material for the industrial production of zirconia is zircon, $ZrSiO_4$. In one current method, milled zircon and coke are chlorinated in fluidized beds using chlorine as the fluidizing medium [41, 42]:

$$ZrSiO_4 + 4C + 4Cl_2 \rightarrow ZrCl_4 + SiCl_4 + 4CO$$

The $ZrCl_4$ and $SiCl_4$ can be separated and used as sources for other zirconium and silicon compounds. Wide use of this process has resulted in an abundance of $SiCl_4$ which can be used as an inexpensive precursor for Si ceramics. The $ZrCl_4$ can be oxidized to obtain ZrO_2.

Another starting material for zirconia ceramics is $ZrOCl_2$. To produce $ZrOCl_2$, finely ground zircon is fused with NaOH to obtain sodium silicate [43], sodium zirconate, and some sodium silicozirconate, as shown in Figure 3. Water dissolves most of the sodium silicate, leaving a sodium zirconate which is soluble in most mineral acids. If it is dissolved in hot hydrochloric acid, the $ZrOCl_2{\cdot}8H_2O$ is recovered from solution by crystallization. A commercial process used by Tosoh Corp. [44] to manufacture partially stabilized ZrO_2 involves the hydrolysis of zirconium oxychloride to produce particles of zirconium hydrous oxides, as shown in Figure 4. The zirconium hydrous-oxide precipitate is converted to ZrO_2 thermally and begins to sinter at 1400°C.

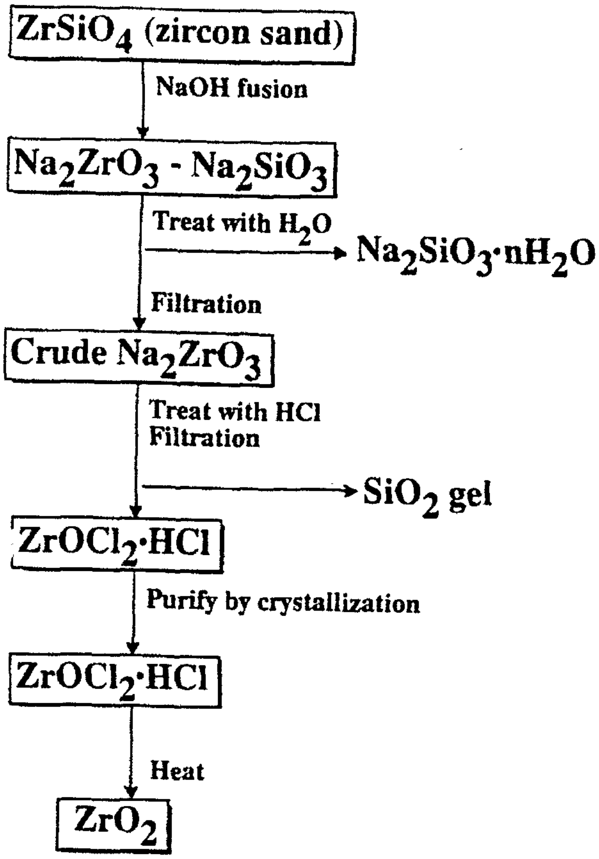

Fig. 3. Preparation of ZrO_2 *from zircon sands.*

The highest purity zirconia is produced in the laboratory by the hydrolysis of zirconium alkoxides. This approach allows excellent control of particle size and size distribution. Zirconium tetrachloride reacts with alcohols in the presence of a base to give the alkoxides. Hydrolysis of the alkoxides gives monodispersed zirconia. This powder can be colloidally processed to give uniform green bodies which sinter to 98% of theoretical density at 1160°C [7]

Multicomponent Systems

The preparation of multicomponent oxide powders from the alkoxides is difficult, because each alkoxide hydrolyzes at a different rate and products are generally segregated or incompletely precipitated and off-stoichiometry. One approach many groups have investigated is to use double alkoxides to control stoichiometry and hydrolysis rates. We have used the the double alkoxide, $SrTi(OR)_6$, to synthesize strontium titanate [45]. Hydrolysis of the SrTi double alkoxide could not be controlled in alcohol solvents to obtain homogeneous nucleation and growth of spherical particles. In this case carboxyalkoxides were prepared and hydrolyzed, giving spherical $SrTiO_3$ particles [46].

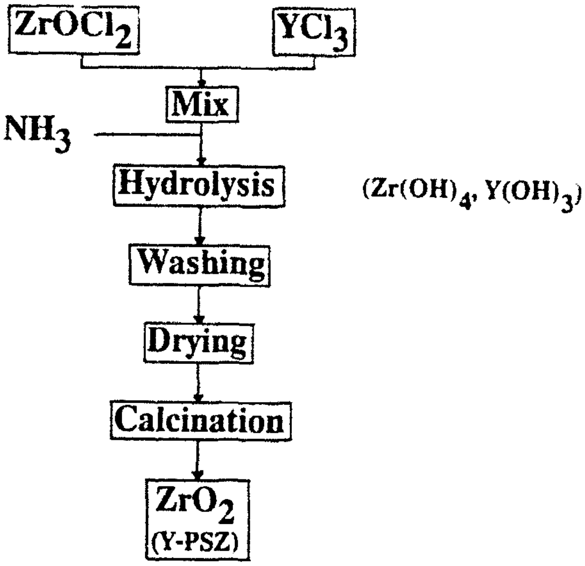

Fig. 4. Preparation of partially stabilized zirconia from zirconium oxychloride.

Powders with controlled morphology and composition for three-component systems are particularly difficult to prepare. We used the $MgAl_2(OR)_8$ double alkoxide to prepare a trimetallic alkoxide containing Mg, Al, and Si for preparing cordierite [46], but obtained only gelatinous precipitates upon hydrolysis. Researchers at the Colloid Research Institute (Japan) have been able to hydrolyze a mixture of TEOS and $MgAl_2(OR)$ and obtain stoichiometric cordierite by carrying out the precipitation at pHs above 11 [47].

Direct precipitation of the elements is one of the oldest and most widely used methods to prepare multicomponent oxides. In certain cases a stoichiometric compound can be precipitated such as $BaTiO(C_2O_4)_2{\cdot}4H_2O$ which decomposes to form $BaTiO_3$. In the first reported use of this barium titanyl oxalate, it was produced at low pH using a mixture of $TiCl_4$ and $BaCl_2$ as the starting solution [48]. When oxalic acid was added, a precipitate of barium titanyl oxalate formed. Clabaugh et al. [48] stated that the presence of ammonium, sodium, or potassium ions interfered with precipitation of stoichiometric precipitates. In our recent work [49], we used ammonium titanyl oxalate, which is stable and readily soluble in water, as the starting material. After adjusting the pH to 1-1.5 with nitric acid, a solution of $Ba(NO_3)_2$ was added to precipitate the barium titanyl oxalate which converted to $BaTiO_3$ at 600°C. Material precipitated when hydrochloric acid was used to adjust the pH required a higher

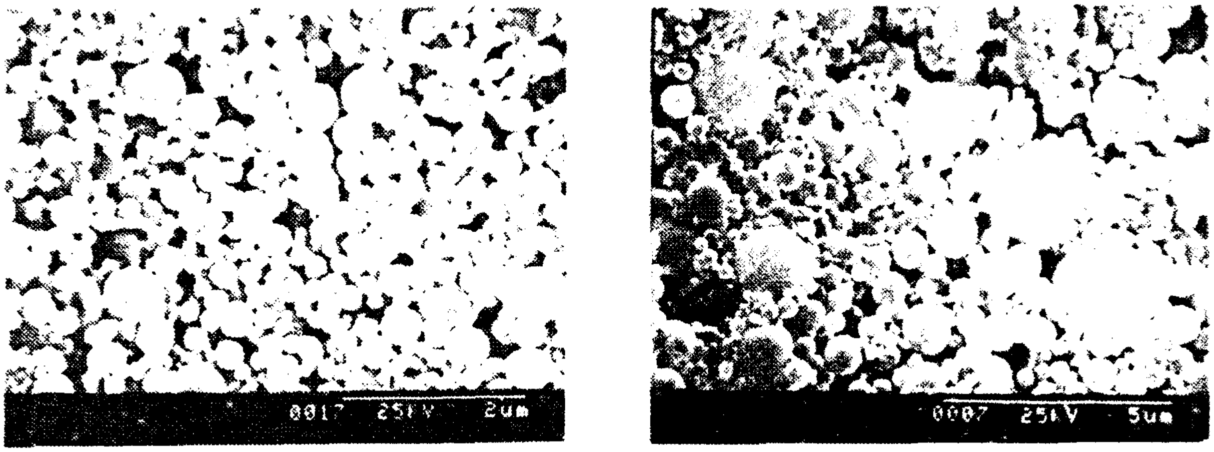

(a) (b)

Fig. 5. Powders prepared by an emulsion technique: (a) alumina and (b) alumina:titania.

calcination temperature (800-900°C) to obtain $BaTiO_3$.

Emulsion Techniques

Emulsion techniques are another method for controlling the morphology of multicomponent ceramic oxides [50-52]. In our laboratory, we have investigated an alkoxide-organic solvent-emulsion technique as a means for synthesizing submicrometer, unagglomerated alumina and aluminum titanate powders. The alkoxides were emulsified in propylene carbonate and ethylene carbonate [53]. The types of powders prepared by this method are illustrated in Figure 5

NON-OXIDE POWDERS

There has been tremendous interest in the preparation of high-purity non-oxide ceramic powders, fibers, and films. Most of the research has focused on the preparation of SiC and Si_3N_4, with comparatively little work being done toward preparing non-oxide powders from solutions by precipitation methods. Most of the approaches investigated for non-oxide powders involve solid state reactions or gas phase processes.

Silicon Carbide

Silicon carbide was first produced in 1891 by passing a strong electric current through a mixture of clay and coke in what has become known as the Acheson process. Silicon carbide is commercially produced by this process using high grade silica sand and carbon in an electric resistance furnace. The overall reaction is:

$$SiO_2 + 3C \rightarrow SiC + 2CO_2$$

Although the Acheson process is cost effective in producing SiC from inexpensive raw materials, it relies on comminution to produce powders of limited fineness: subsequent milling of these powders adds impurities and increases costs. This process produces α-SiC due to the high temperatures involved. With improvements in comminution methods, sinterable α-SiC powders are available which are derived from the Acheson process.

Sinterable silicon carbide powders can be obtained from the self-propagating, high-temperature synthesis of Si and C mixtures. This rapid and efficient method has been used to synthesize stoichiometric α-SiC powders with a relatively uniform size of 0.2-0.5 μm [54].

Laser pyrolysis of SiH_4 and CH_4 or CH_2CH_2 has also been investigated extensively [55] as have plasma methods [56]. Boron-doped powders can be prepared by these approaches [57]. These doped powders simplify processing and also sinter at lower temperatures than conventionally processed powders.

Silicon Nitride

Silicon nitride is produced primarily by the direct nitridation of silicon or by carbothermic reduction and nitridation of silica. Nitrided powders require pulverizing and classifying which increases the production cost and adds impurities. In the synthesis of silicon nitride by carbothermic reduction, seeding is important in controlling the α/β ratios and leads to much better control of particle morphology [58]. The reaction of SiH_4 and NH_3 gases can lead to stoichiometric difficulties [59].

The purest powders available are produced by the reaction of ammonia with silicon tetrachloride. Early synthesis of silicon nitride from these starting materials

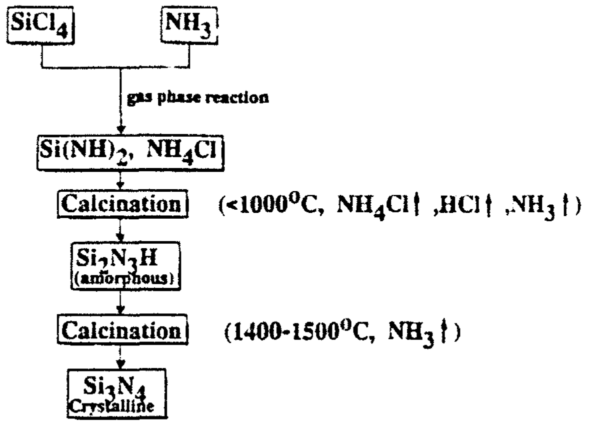
SiCl4
NH3
gas phase reaction
Si(NH)2, NH4Cl
Calcination
(<1000°C, NH4Cl↑ ,HCl↑ ,NH3↑)
Si2N3H (amorphous)
Calcination
(1400-1500°C, NH3↑)
Si3N4 Crystalline

Fig. 6. Gas phase process for producing silicon nitride.

used the gas phase reactions. A little later the reaction of $SiCl_4$ and liquid ammonia was tried [60-63]. However, chlorine retention has been a problem. Later work determined that long term extraction with liquid ammonia was necessary to completely remove chlorine [64].

Reactions between $SiCl_4$ and NH_3 in the gas phase (Fig. 6) and by solution methods (Fig. 7) are being used commercially by Tosoh Corp. and Ube Industries, respectively. In Ube's process the reaction between $SiCl_4$ and liquid ammonia takes place at the interface between an organic solvent (hydrocarbon) and liquid ammonia [64]. A schematic of the reactor is shown in Figure 8. The $SiCl_4$ is introduced via a tube into the organic solvent where it reacts with the ammonia which is in the upper layer. By using this process the NH_4Cl, which forms when $SiCl_4$ is added to NH_3, does not plug the reactor. After the reaction is complete, the product is transferred to a calcination tube and washed with ammonia before it is calcined. The calcination temperature is important: calcination at 1420°C produces an equiaxed α-Si_3N_4 powder, while calcination at temperatures higher than 1460°C produces β-Si_3N_4 whiskers [65].

Aluminum Nitride

A key issue in selecting synthetic routes for AlN has been the ability to generate high purity material. Of the various methods reported [66-71], all require heating to several hundred degrees celsius in order to produce the aluminum imide which is finally converted to AlN. Using metallo-organic precursors, we have developed solution methods which involve direct precipitation of the aluminum imide precursor [72, 73]. This method involves the reaction between H_2AlNMe_2 and ammonia. The powders produced convert to high-purity aluminum nitride upon calcination to 1000°C. These powders have particle sizes of 0.1-0.2 µm and, if processed under nitrogen, have less than 0.5 wt% oxygen. These powders have high reactivities and sinter to >95% density at 1700-1750°C

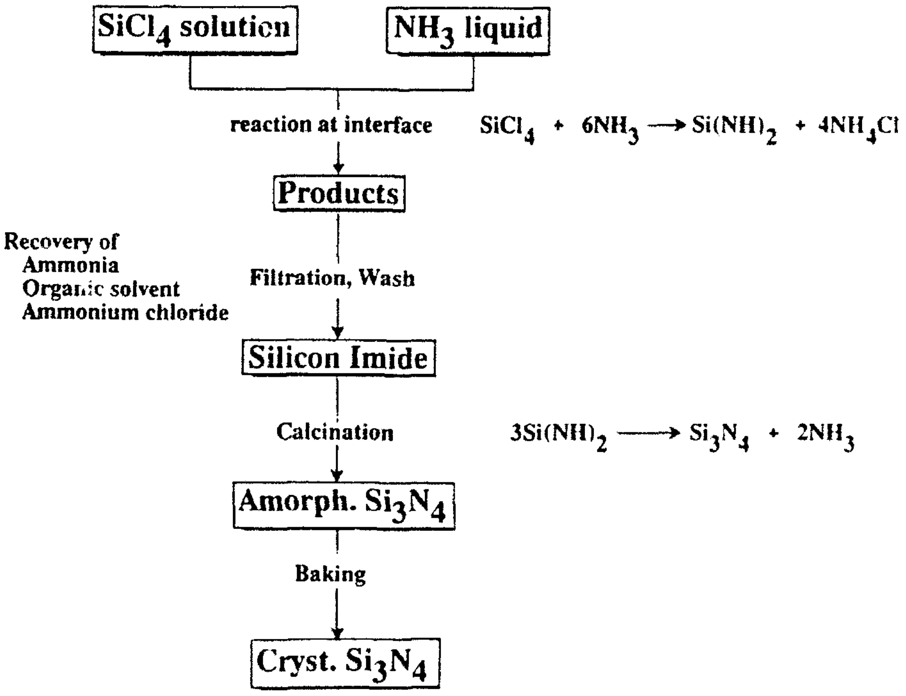
SiCl4 solution
NH3 liquid
reaction at interface
SiCl4 + 6NH3 → Si(NH)2 + 4NH4Cl
Products
Recovery of
Ammonia
Organic solvent
Ammonium chloride
Filtration, Wash
Silicon Imide
Calcination
3Si(NH)2 → Si3N4 + 2NH3
Amorph. Si3N4
Baking
Cryst. Si3N4

Fig. 7. Solution process for producing silicon nitride.

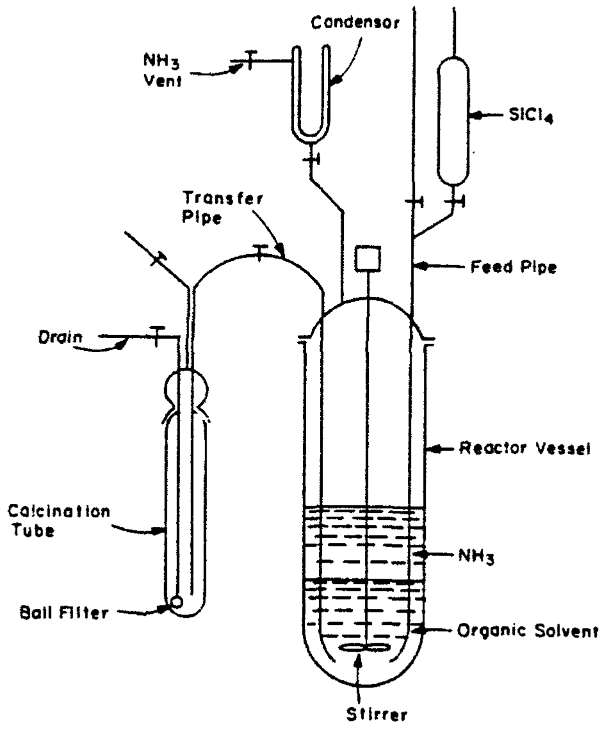

Fig. 8. Reactor used for solution preparation of Si_3N_4.

without the addition of sintering aids.

Metal Diborides

Zirconium and hafnium diboride are currently prepared by the carbothermic reduction of the oxides or by reacting boron carbide with a metal oxide. The reduction of metal and boron halides by hydrogen in a hot tube or plasma has been the subject of most recent research on TiB_2 powder synthesis.

In our studies [74], powders of titanium, zirconium, and hafnium diborides were prepared by a solution technique involving the thermal decomposition of the corresponding metal borohydrides. The metal borohydrides, which are very soluble in aromatic and aliphatic hydrocarbons, decompose to the corresponding metal diborides upon heating. The reaction, which is complete in 2 h in refluxing xylenes, proceeds as follows:

$$2Ti(BH_4)_3 \rightarrow 2TiB_2 + B_2H_6 + 9H_2$$

$$Zr(BH_4)_4 \rightarrow ZrB_2 + B_2H_6 + 5H_2$$

$$Hf(BH_4)_4 \rightarrow HfB_2 + B_2H_6 + 5H_2$$

Electron diffraction studies indicated the powders were amorphous when formed but began to crystallize at temperatures as low as 800°C. After heating the samples to 1500°C, the samples were well crystallized and sharp diffraction lines were observed. In all cases, only lines corresponding to the metal diboride phase were observed.

CONCLUSIONS

During the last five years higher purity and more reproducible ceramic powders have become commercially available. Academic and industrial researchers are continually developing new approaches as well as investigating approaches to scale up laboratory procedures to produce high-quality powders economically. In the future, the cost of these chemically derived powders should decrease as the market for these powders gradually increases.

ACKNOWLEDGMENTS

The authors would like to thank the Air Force Office of Scientific Research for their financial support (contract Nos. F49620-84-C-0097 and F49620-89C-0102DEF).

REFERENCES

1. W.H. Rhodes, "Agglomerates and Particle Size Effect on Sintering Yttria-Stabilized Zirconia," *J. Am. Ceram. Soc.*, **64** 19-22 (1981).
2. E.A. Barringer, R. Brook, and H.K. Bowen, "The Sintering of Monosized TiO_2 Powders"; pp. 1-21 in Sintering and Heterogeneous Catalysts. Edited by G.C. Kuczynski, A.E. Miller, and G.A. Sargent. Plenum Press, New York, NY, 1984.
3. E. Rothman, J. Stitt, and H.K. Bowen, "A Look at Ceramic Powder Production Processes–Old and New," *Ceram. Ind.*, **124** 24 (1985).
4. D.W. Johnson, "Innovations in Ceramic Powder Preparation"; p. 3 in Advanced Ceramics, Vol. 21. Edited by G. Messing, K.S. Mazdiyasni, J.W McCauly, and R.A. Haber. American Ceramic Society, Westerville, OH, 1986.
5. E.A. Barringer and H.K. Bowen, "Formation, Packing, and Sintering of Monodisperse TiO_2 Powders," *J. Am. Ceram. Soc.*, **65** C199 (1982).
6. Stober and A. Fink, "Controlled Growth of Monodisperse Silica Spheres in Micron Size Range," *J. Colloid Interface Sci.*, **26** 62 (1968).
7. B. Fegley, P. White, and H.K. Bowen, "Processing and Characterization of ZrO_2 and Y-Doped ZrO_2 Powders," *Am. Ceram. Soc. Bull.*, **64** 1115 (1985).
8. E. Matijevic, "Monodispersed Metal (Hydrous) Oxides"–A Fascinating Field of Colloid Science,"

Acc. Chem. Res., **14** 22 (1981).

9. V.K. LeMer and M.D. Barnes, "Monodispersed Hydrophobic Colloidal Dispersions and Light Scattering Properties. I. Preparation and Light Scattering Properties of Monodispersed Colloidal Sulfur," *J. Colloid Sci.*, **1** 71 (1946).
10. T. Sugimoto, "Preparation of Monodispersed Colloidal Particles," *Adv. Colloid Interface Sci.*, **28** 65 (1987).
11. E. Matijevic, "Monodispersed Colloidal Metal Oxides, Sulfides, and Phosphates"; pp. 334-52 in Ultrastructure Processing of Ceramics, Glasses, and Composites. Edited by L.L. Hench and D.R. Ulrich. Wiley and Sons, New York, NY, 1984.
12. E. Matijevic, "Production of Monodispersed Colloidal Particles," *Ann. Rev. Mater. Sci.*, **15** 483 (1985).
13. E. Matijevic, "Monodispersed Colloids: Art and Science," *Langmuir*, **2** 12 (1986).
14. J.M. Bind, T. Dupin, J. Schafer, and M. Titeux, "Industrial Synthesis of Coprecitated $BaTiO_3$ Powders," *J. Met.* **Aug. 1987** 60.
15. H.B. Weiser and W.O. Milligan, "The Constitution of Colloidal Systems of the Hydrous Oxides," *Chem. Rev.*, **25** 1 (1939).
16. T.P. O'Holleran, R.R. Neurgaonkar, D.M. Roy, and R. Roy, "EDS for the Preparation of α-Fe_2O_3," *Am. Ceram. Soc. Bull.*, **57** 459 (1978).
17. T.J. Gardner and G.L. Messing, "Preparation of MgO Powder by Evaporative Decomposition of Solution," *Am. Ceram. Soc. Bull.*, **63** 1498 (1984).
18. D.M. Roy, R.R. Neurgaonkar, T.P. O'Holleran, and R. Roy, "Preparation of Fine Oxide Powder by Evaporative Decomposition of Solutions," *Am. Ceram. Soc. Bull.*, **56** 1023 (1977).
19. Y. Suyama and A. Kato, "Characterization and Sintering of Mg-Al Spinel Prepared by Spray-Pyrolysis Technique," *Ceramurgia Int.*, **8** 17 (1982).
20. G.A. Rosetti, Jr., J.L. Burger, and R.D. Sisson, Jr., "Characterization of Mixed Cobalt-Molybdenum Oxides Prepared by Evaporative Decomposition of Solutions," *J. Am. Ceram. Soc.*, **72** 1811 (1989).
21. T.T. Todas, "Generation of Complex Metal Oxides by Aerosol Processes: Superconducting Ceramic Particles and Films," *Angew. Chem. Adv. Mater.*, **101** 814 (1989).
22. T.Q. Liu, O. Sakurai, N. Kieda, M. Kato, and N. Mizutani, "Preparation of Spherical Silicon Nitride Particles from Polysilazane by Ultrasonic Spray Pyrolysis Technique," *Nippon Seramikkusu Kyokai Gakujutsu Ronbunshi*, **97** 1321 (1989).
23. D.W. Sproson and G. L. Messing, "Ceramic Powder Synthesis by Thermal Reaction of Atomized Solutions"; pp. 99-108 in in Advanced Ceramics, Vol. 21, Ceramic Powder Science. Edited by G.L. Messing, K.S. Mazdiyasni, J.W. McCauley, and R. A. Haber. American Ceramic Society, Westerville, OH, 1987.
24. J.B. Wachtmann, Jr. and R.A. Haber, "Ceramic Films and Coatings," *Chem. Eng. Prog.*, 39 46 (1986).
25. R.C. Flagan, "Aerosol Routes for Powder Synthesis"; p. 229 in Ceramic Transactions, Vol. 1A. Edited by Messing, E. Fuller, Jr., and H. Hausner. American Ceramic Society, Westerville, OH, 1988.
26. J.H. Flint and J.S. Haggerty, "Models for Synthesis of Ceramic Powders by Vapor Phase Reaction"; p. 244 in Ceramic Transactions, Vol. 1A. Edited by G. Messing, E. Fuller, Jr., and H. Hausner. American Ceramic Society, Westerville, OH 1988.
27. L.D. Silverman, "Carbothermal Synthesis of Aluminum Nitride," *Adv. Ceram. Mat.*, **3** 418 (1988).
28. J.E. Blendell, H.K. Bowen, and R.L. Coble, "High-Purity Alumina by Controlled Precipitation from Aluminum Sulfate Solutions," *Am. Ceram. Soc. Bull.*, **63** 797-802 (1984).
29. J. Henry and H.J. Kelly, "Preparation and Properties of Ultrafine High-Purity Alumina," *J. Am. Ceram. Soc.*, **48** 217 (1965).
30. P.A. Thiessen and K.L. Thater, "Pure Aluminum Ortho-hydroxide in Gellatinous and Powder Form," *Z. Anorg. Allg. Chem.*, **181** 417 (1929).
31. K.-H. Thiele, W. Schwartz, and Dietmann, "Preparation of High-Purity, Finely Divided Aluminum Oxide from Triethyl Aluminum," *Z. Anorg. Allg. Chem.*, **349** 324 (1967).
32. F. Tebbe, P.A. Morris, R.H. French, U. Chowdhry, and R.L. Coble, "Purity of Aluminum Hydroxide Derived from Triethylaluminum," *J. Am. Ceram. Soc.*, **71** C204 (1988).

33. S. Horikiri, "Production Process and Characteristics of High Purity Alumina"; p. 23 in Fine Ceramics Annual Report 1986. Japan Fine Ceramics Association, Tokyo, Japan, 1986.

34. H. Kadokura and M. Hama, "High Purity Alumina from Organometallic Compound," *New Materials and New Processes*, **3** 335 (1985).

35. E. Santacesaria, M. Tonello G. Storti, R.C. Pace, and S. Carra, "Kinetics of Titanium Dioxide Precipitation by Thermal Hydrolysis," *J. Colloid Interface Sci.*, **111** 44 (1986).

36. E. Matijevic, M. Budnik, and L. Meites, "Preparation and Mechanism of Titanium Dioxide Hydrosol of Narrow Size Distribution," *J. Colloid Interface Sci.*, **61** 302 (1977).

37. G.H. Bogush and C.F. Zukoski, IV, "The Colloidal Chemistry of Growing Silica Spheres"; p. 475 in Material Science Research, Vol. 21, Ceramic Microstructures '86. Edited by J.A. Pask and A.G. Evans. Plenum Press, New York, NY, 1987.

38. Y. Suyama, K. Ito, and A. Kato, "Mechanism of Rutile Formation in Vapor Phase Oxidation of $TiCl_4$ by Oxygen," *J. Inorg. Nucl. Chem.*, **37** 1883-88 (1975).

39. E.A. Barringer and H.K. Bowen, "High-Purity Monodisperse TiO_2 Powders by Hydrolysis of Titanium Tetraethoxide. 1. Synthesis and Physical Properties," *Langmuir*, **1** 414 (1985).

40. J.H. Jean and T.A. Ring, "Nucleation and Growth of Monosized TiO_2 Powders from Alcohol Solution," *Langmuir*, **2** 251-55 (1986).

41. A.A. Manieh and D.R. Spink, "Chlorination of Zircon Sand," *Can. Met. Quart.*, **12** 331 (1973).

42. A.A. Maneih, D.S. Scott, and D.R. Spink, "Electrothermal Fluidized Bed Chlorination of Zircon," *Can. J. Chem. Eng.*, **52** 507 (1974).

43. H.S. Choi, "Preparation of Pure Zirconyl Compounds from Zircon Caustic Frit," *Can. Min. Metall. Bull.*, **68** 193 (1965).

44. Tosoh Corp. Technical Bulletin No. Z-051.

45. A.B. Hardy, G. Gowda, T.J. McMahon, R.E. Riman, W.E. Rhine, and H.K. Bowen, "Synthesis of Oxide Powders"; pp. 407-28 in Ultrastructure Processing of Advanced Ceramics. Edited by J.D. Mackenzie and D.R. Ulrich. John Wiley and Sons, New York, NY, 1988.

46. R.E. Riman, R.R. Landham, and H.K. Bowen, "Synthesis of Uniform Titanium and 1:1 Strontium-Titanium Carboxyhydrosols by Controlled Hydrolysis of Alkoxymetal Carboxylate Precursors," *J. Am. Ceram. Soc.*, **72** 821 (1989).

47. T. Fukui, C. Sakurai, M. Okuyama, and Y. Nomiya, "Preparation of Cordierite Ceramics Through Alkoxide Routes," presented at the 91st Annual Meeting of the American Ceramic Society, Indianapolis, IN, 1989.

48. W.S. Clabaugh, E.M. Swiggard, and R. Gilchrist, "Preparation of Barium Titanyl Oxalate Tetrahydrate for Conversion to Barium Titanate of High Purity," *J. Res. Natl. Bur. Stand.*, **56** 289 (1956).

49. W.E. Rhine, K. Saegusa, R.B. Hallock, and M.J. Cima, "Control of Ceramic Powder Composition by Precipitation Techniques"; in Ceramic Powder Processing Science III. Edited by G.L. Messing. American Ceramic Society, Westerville, OH, 1990, in press.

50. P. Reynen, H. Bastius, and M. Fiedler, "The Use of Emulsions in the Preparation of Ceramic Powders"; p. 499 in Ceramic Powders. Edited by P. Vincenzini. Elsevier, Amsterdam, 1983.

51. M. Akinc and K. Richardson, "Preparation of Ceramic Powders from Emulsion"; p. 99 in Better Ceramics Through Chemistry, Vol. 73, Mat. Res. Soc. Symp. Proc. Edited by C.J. Brinker, D.E. Clark, and D.R. Ulrich. Materials Research Society, Pittsburgh, PA, 1986.

52. T. Kanai, W.E. Rhine, and H.K. Bowen, Preparation of $2ZrO_2 \cdot Yb_2O_3$ Powder by Emulsion Techniques"; pp. 119-26 in Ceramic Transactions, Vol. 1. Edited by G. Messing, E. Fuller, Jr., and H. Hausner. American Ceramic Society, Westerville, OH, 1988.

53. A.B. Hardy, "Preparation of Submicrometer, Unagglomerated Oxide Particles by Reaction of Emulsion Droplets"; PhD Thesis. Dept. Mat. Sci. Eng., MIT, September 1988.

54. R. Pampuch, L. Stobierski, and J. Lis, "Synthesis of Sinterable α-SiC Powders by a Solid Combustion Method," *J. Am. Ceram. Soc.*, **72** 1434 (1989).

55. J.S. Haggerty, "Growth of Precisely Controlled Powders from Laser Heated Gases"; p. 353 in Ultrastructure Processing of Ceramic Glasses and Composites. Edited by D.L. Hench and D. Ulrich. Wiley and Sons, New York, NY, 1984.

56. C.M. Hollabaugh, D.E. Hull, L.R. Newkirk, and J.J. Petrovic, "RF Plasma Synthesis of Ultrafine, Ultrapure Silicon Carbide Powder"; p. 367 in Ultrastrucure Processing of Ceramic Glasses and Composites. Edited by L.L. Hench and D. Ulrich. Wiley and Sons, New York, NY, 1984.

57. J. Kondo and G. Saiki, "Synthesis and Sintering of Boron Doped SiC Powders by Plasma Arc Method"; p. 285 in Ceramic Transactions, Vol. 1. Edited by G. Messing, E. Fuller, Jr., and H. Hausner. American Ceramic Society, Westerville, OH, 1988.

58. H. Inoue, K. Komeya, and A. Tsuge, "Synthesis of Silicon Nitride Powder from Silica Reduction," *J. Am. Ceram. Soc.*, **65** C205 (1982).

59. S. Prochazka and C. Greskovich, "Synthesis and Characterization of a Pure Silicon Nitride Powder," *J. Am. Ceram. Soc.*, **57** 579 (1978).

60. K.S. Mazdiyasni and C.M. Cooke, "Synthesis, Characterization, and Consolidation of Si_3N_4 Obtained from Ammonolysis of $SiCl_4$," *J. Am. Ceram. Soc.*, **56** 629 (1973).

61. O. Glemser and P. Naumann, "Thermal Decomposition of Silicon Diimide, $Si(NH)_2$," *Z. Anorg. Allg, Chem.*, **298** 134 (1958).

62. M. Billy, "Preparation and Characterization of S-Ilicon Nitride," *Ann. Chim.*, **1** 745 (1956).

63. P.E.D. Morgan, "Production and Formation of Si_3N_4 from Precursor Materials," Annual Report AC3316 March 1973, prepared for the Office of Naval Research by the Franklin Research Institute Laboratories, Philadelphia, PA

64. T. Iwai, T. Kawakito, and T. Yamada, "Process for Producing Metallic Nitride Powder," U.S. Pat. No. 4 196 178, April 1, 1980.

65. T. Yamada, T. Kawahito, and T. Iwai, "Crystallization of Amorphous Si_3N_4 Prepared by Thermal Decomposition of $Si(NH)_2$," *J. Mater. Sci. Lett.*, **2** 275 (1983).

66. M. Morita, N. Uesugi, S. Isogai, K. Tsubouchi, and N. Mikoshiba, "Epitaxial Growth of Aluminum Nitride on Sapphire Using Metallorganic Chemical Vapor Deposition," *Jap. J. Appl. Phys.*, **20** 17 (1981).

67. L. Interrante, G.A. Sigel, M. Garbauskas, C. Hejna, and G.A. Slack, "Organomettalic Precursors to AlN: Synthesis and Crystal Structures of $[(CH_3)_2AlNH_2]_3$ and the Planar Species $[(t\text{-}C_4H_9)_2AlNH_2]_3$," *Inorg. Chem.*, **28** 252 (1989).

68. J.F. Janik, E.N. Dueser, and R.T. Paine, "Reactions of Tris(trimethylsilyl)aluminum and Ammonia. Formation, Structure, and Thermal Decomposition of $[(Me_3Si)_2AlNH_2]_2$," *Inorg. Chem.*, **26** 4341 (1987).

69. R.T. Baker, J.D.Bolt, G.S. Reddy, D.C. Roe, R.H. Staley, F.N. Tebbe, and A.J. Vega, "Studies on Organoaluminum Precursors of Aluminum Nitride Fibers"; p. 272 in Better Ceramics Through Chemistry III, Vol. 121, Mat. Res. Soc. Symp. Proc. Edited by C.J. Brinker, D.E. Clark, and D.R. Ulrich, Materials Research Society, Pittsburgh, PA, 1988.

70. D.C. Boyd, R.T. Haasch, D.R. Mantell, R.K. Schulze, J.F. Evans, and W.L. Gladfelter, "Organometallic Azides as Precursors for Aluminum Nitride Thin Films," *Chemistry of Materials*, **1** 119 (1989).

71. M. Seibold and C. Russel, "A Novel Route To Aluminum Nitride Ceramics Using A Polyaminoalane Precursor"; p. 477 in Better Ceramics Through Chemistry III, Vol 121, Mat. Res. Soc. Symp. Proc. Edited by C.J. Brinker, D.E. Clark, and D.R. Ulrich. Materials Research Society, Pittsburgh, PA, 1988.

72. A. Ochi, H.K. Bowen, and W.E. Rhine, "Synthesis of Aluminum Nitride from Aluminum Hydride"; p. 663 in Better Ceramics Through Chemistry III, Vol. 121, Mat. Res. Soc. Symp. Proc. Edited by C.J. Brinker, D.E. Clark, and D.R. Ulrich. Materials Research Society, Pittsburgh, PA 1988.

73. W.E. Rhine, M. Einarsrud, and M.J. Cima, "Synthesis of AlN from Aminoalanes," presented at the 91st Annual Meeting of The American Ceramic Society, Indianapolis, IN, 1989.

74. M.K. Gallagher, W.E. Rhine, and H.K. Bowen, "Low Temperature Route to High-Purity Titanium, Zirconium, and Hafnium Diboride Powders and Films"; p. 901-06 in Ultrastructure Processing of Advanced Ceramics. Edited by J.D. Mackenzie and D.R. Ulrich. John Wiley and Sons, New York, NY, 1988.

SECTION 2

CONTROL OF CERAMIC POWDER COMPOSITION BY PRECIPITATION TECHNIQUES

Wendell E. Rhine, Kunio Saegusa, Robert B. Hallock, and Michael J. Cima

Published in Ceramic Powder Processing Science III, Ceramic Transactions, 12, 107 (1990).

ABSTRACT

Precipitation of metal salts of polyfunctional carboxylates is being investigated in our laboratory as a generic method for synthesizing ceramic powders with controlled compositions. The composition of powders can be controlled by synthesizing complexes such as barium titanyl oxalate where the Ba:Ti ratio is known to be 1:1. To prepare barium titanyl oxalate, we have investigated the reaction of titanyl ammonium oxalate with barium nitrate and barium acetate using hydrochloric and nitric acids to control the pH of the reaction. Similarly, the reaction between ammonium copper oxalate and barium salts produces $BaCu(C_2O_4)\cdot 6H_2O$, a complex copper salt which could form during the precipitation of Ba, Y, and Cu oxalates. We also demonstrated that other polycarboxylic acids can be used to quantitatively precipitate precursors for ceramic powders, and we prepared barium yttrium cuprate from the precipitate obtained by reacting tartaric acid with a solution of the barium, yttrium, and copper acetates.

INTRODUCTION

About ten years ago a major effort was initiated to develop techniques for synthesizing submicrometer ceramic powders with controlled and reproducible chemical and physical properties. So far, however, the experimental conditions for preparing powders with the desired morphology and composition must be determined empirically and cannot be predicted. There are two basic precipitation methods which are being used to synthesize ceramic powders: precipitation from homogeneous solutions and the simultaneous precipitation of metals by direct mixing of reagents.

Precipitation from homogeneous solutions: Precipitation from homogeneous solution refers to the formation of a precipitate by some chemical change in a solution which contains salts or complexes of the metals. For example, precipitation may occur by producing a slow change in pH or by hydrolyzing alkoxides to homogeneously nucleate and grow monodispersed hydrous oxides. Another method is the chemical production of a reagent that forms an insoluble complex which precipitates as it is produced. The formation of monodispersed particles from homogeneous solutions has been reviewed recently [1, 2].

Precipitation from direct mixing of reagents: In simultaneous precipitation, all substances whose solubilities are exceeded precipitate together as the reagents are mixed. The materials community usually refers to this type of precipitation as coprecipitation. However, in the chemical literature, the term "coprecipitation" refers to the contamination of the precipitate by unwanted cations which are normally soluble under the precipitation conditions.

Analytical chemists have established that large, crystalline particles have the best opportunity to form when precipitates are formed (1) in dilute solution, (2) with good stirring, (3) with slow addition of reagents, and (4) at high temperatures. Each of these four measures is neither always effective nor always convenient, but they constitute the standard technique for forming high-purity crystalline precipitates. Therefore, it seems logical that the opposite approach may produce submicrometer particles.

In our research on powder synthesis we started by preparing monodisperse particles of single-component systems. The chemistry for producing such powders from metal alkoxides is now fairly well developed. The preparation of TiO_2 [3], SiO_2 [4], and ZrO_2 [5] by homogeneous nucleation and growth techniques has appeared in the literature. This paper will discuss some of our recent experiences in preparing multicomponent powders with controlled composition and morphology by precipitation techniques. Specifically, we report our results on the synthesis and characterization of $BaTiO(C_2O_4)_2$ and $BaCu(C_2O_4)_2 \cdot 6H_2O$ and our results using various polycarboxylic acids as precipitants for Ba, Y, and Cu.

EXPERIMENTAL PROCEDURE

Preparation of titanyl ammonium oxalate: Titanyl ammonium oxalate was prepared from tetraethoxy titanium (68.4 g, 0.3 mol, Dynamit Nobel Chemical, Rockleigh, NJ) by dissolving it in 10 mL i-PrOH and adding it to a stirred solution of oxalic acid (0.3 mol) and ammonium oxalate (0.3 mol) which had been dissolved in 200 mL hot water. The product crystallized after concentrating the solution, and the colorless crystals were collected by filtration. An elemental analysis confirmed the compound was $(NH_4)_2TiO(C_2O_4)_2 \cdot H_2O$. The only impurity detected was Si (21 ppm).

Precipitation by mixing of reagents: A solution of barium acetate or nitrate (pH adjusted with HCl or HNO_3) was added slowly to a solution of the titanyl ammonium oxalate (pH adjusted with HCl or HNO_3) while stirring at ambient temperature. The barium titanyl oxalate was recovered by filtration and redispersed in water to eliminate excess barium salt. The effect of pH on the stoichiometry of barium titanate was studied by adjusting the pH to between 0.5 and 5.9 while keeping the concentrations of reagents at 0.07 M (after mixing).

Preparation of ammonium copper oxalate: A solution of $CuCl_2 \cdot 2H_2O$ was added to a hot (80°C) saturated solution of ammonium oxalate (25% excess). As the solution cooled, dark blue crystals formed which were collected by filtration before the solution cooled to room temperature.

Preparation of BaCu oxalate: A solution of $BaCl_2 \cdot 2H_2O$ (5.24 g, 21.4 mmol) in 300 mL deionized (DI) water was added slowly at room temperature to a solution of $(NH_4)_2Cu(C_2O_4)_2 \cdot 4H_2O$ (8.22 g; 23.6 mmol) in 1.75 L DI water. After about one half of the $BaCl_2$ solution had been added, blue crystals began to precipitate. The crystals (9.86 g, 20.3 mmol, 94.8% yield) were isolated by filtration and air-dried at room temperature. The product was characterized by Fourier transform infrared (FTIR), thermal gravimetric (TGA), and elemental analysis, and was found to be $BaCu(C_2O_4) \cdot 6H_2O$.

Precipitation of Ba, Y, and Cu with tartaric acid: A: Saturated Solution: Barium acetate (7.67 mmol), yttrium acetate (3.83 mmol), and copper acetate (11.5 mmol) were dissolved in a mixture of 125 mL ethanol and 30 mL water at the boiling point. A solution of 24.9 mmol tartaric acid in 25 mL ethanol was added to the hot acetate solution and a blue precipitate formed immediately. The precipitate was isolated by filtration and dried overnight in a vacuum oven at 80°C.

B: Dilute Solution: Barium acetate (7.67 mmol), yttrium acetate (3.83 mmol), and copper acetate (11.5 mmol) were dissolved in a mixture of 400 mL ethanol and 200 mL water at room temperature. The tartaric acid was dissolved in 600 mL ethanol. The acetate solution was added rapidly (30 s) to the tartaric acid solution. A blue voluminous precipitate formed on mixing and was isolated by filtration and dried at 45°C overnight.

RESULTS AND DISCUSSION

The precipitation of powders using polycarboxylic acids is a generic approach for precipitating metals from solutions. Of the various polycarboxylic acids, oxalic and citric acid have been the most studied. For example, barium titanyl oxalate [6-9] and barium titanyl citrate [10] have been prepared and used to synthesize $BaTiO_3$. A recent patent [11, 12] describes using polyacrylic acid as a precipitant for metals and has been used to prepare reactive Y_2O_3 powders. Also, precipitation of yttrium, barium, and copper oxalates is a viable approach for preparing $Ba_2YCu_3O_{6.9}$ powders [13]. In fact, the first U.S. patent for preparing superconducting powders was based on an oxalate precipitation of the basic Ba, Y, and Cu oxalates under basic conditions [14].

Oxalates can also be precipitated from homogeneous solution [15-17], but this approach has not been used for the preparation of multicomponent ceramic powders. It is interesting to note that the precipitation of oxalates from homogeneous solution was developed to obtain larger particles than could be obtained by direct mixing of the reagents.

Synthesis of Barium Titanate

The objective of this research was to establish the optimum preparation conditions for high-purity, stoichiometric, fine particle-sized barium titanate powders with controlled morphology. Of the various methods for preparing submicrometer sized barium titanate, the oxalate method is known to give stoichiometric material [6-9, 18, 19]. We investigated the reaction between titanyl ammonium oxalate and a barium salt to obtain barium titanyl oxalate.

A TGA plot for the amorphous precipitate obtained when using HCl to adjust the pH and IR spectra obtained for barium titanyl oxalates are shown in Figures 1 and 2, respectively; TGA indicates the formula of the barium titanyl oxalate is $BaTiO(C_2O_4)_2 \cdot 2H_2O$. According to Gallagher and Schrey [8], there should be four waters of hydration. Our precipitates were dried at 70°C for 2-5 days, but when left in an ambient atmosphere, they ab-

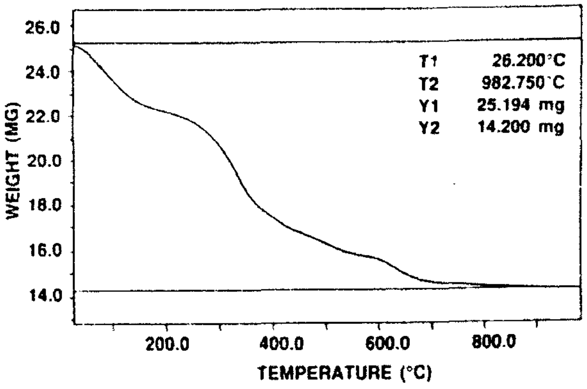

Fig. 1. TGA of barium titanyl oxalate (pH=5.1; HCl).

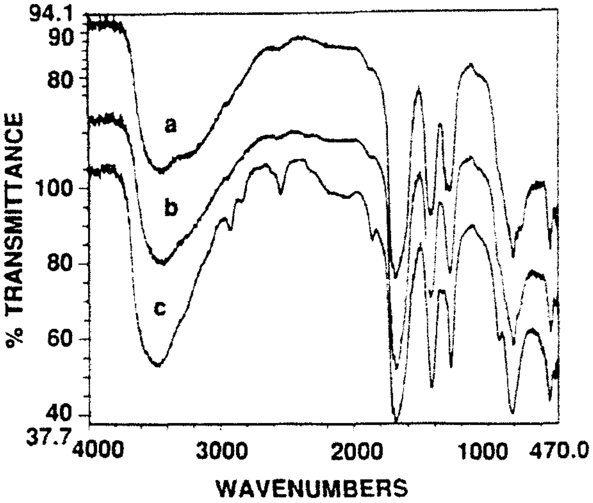

Fig. 2. FTIR of barium titanyl oxalate: (a) amorphous (HCl), (b) amorphous (HNO_3), and (c) crystalline (HNO_3).

sorbed water to give the tetrahydrate. The IR spectra of crystalline and amorphous precipitates are slightly different and are shown in Figure 2.

The results for preparing powders under various conditions are shown in Table 1. The effect of pH on the reaction is not clear. Single phase stoichiometric barium titanate was obtained for pH values from 0.5 to 5.9, but the barium titanyl oxalate obtained using hydrochloric acid (pH 5.1) had to be calcined at 900°C to become single phase, while the precipitates obtained using nitric acid (pH<1.5) only had to be calcined at 600°C to obtain the same result [18]. Other investigators have noted the same difficulties when hydrochloric acid is used [19].

Aging time after precipitation had a significant effect on the preparation of single-phase barium titanate and on the yield. Reaction times of less than 1 h gave an amorphous precipitate, but resulted in better-dispersed, equiaxed, fine particles that were impossible to obtain with the longer reaction times (Fig. 3). After aging, the precipitate crystallized and gave the diffraction pattern reported by Kudaka [20] (Fig. 4). In addition, agglomeration was significant with longer reaction times. Single-phase $BaTiO_3$ powder could be obtained from the crystalline precipitates at a lower calcination temperature (600°C). Aging the precipitate is evidently important to obtain crystalline precipitates; metastable amorphous compounds precipitate first and become crystalline after aging for about 1 h. The change in morphology after the 1 h aging time is dramatic.

Evidently it is not unusual for oxalate precipitates to form initially in a metastable form and then gradually

Table 1. Effect of pH and Reaction Time on the Formation of $BaTiO_3$ at 600℃.

Synthesis Conditions						Characterization	
Conc. (M)	Time (h)	pH	Acid	Ba	ppt	Spec. surf. area (m^2/g)	Phases 600℃
0.45	0.4	5.1	HCl	OAc	amor	17.0 ± 0.11	$BaTiO_3$+$BaCO_3$
0.07	44	5.9	HNO_3	OAc	amor	17.5 ± 0.14	$BaTiO_3$+?
0.07	0.3	1.5	HNO_3	OAc	amor	21.6 ± 0.4	$BaTiO_3$+?
0.07	0.3	0.5	HNO_3	NO3	amor	12.8 ± 0.38	$BaTiO_3$+?
0.07	1.3	1.5	HNO_3	OAc	crys	17.4 ± 0.13	$BaTiO_3$
0.07	3.6	0.7	HNO_3	OAc	crys	13.3 ± 0.1	$BaTiO_3$
0.07	4.0	0.5	HNO_3	NO3	crys	12.7 ± 0.1	$BaTiO_3$
0.13	17	1.2	HNO_3	OAc	crys	12.7 ± 0.41	$BaTiO_3$
0.23	19	0.5	HNO_3	NO3	crys	10.2 ± 0.41	$BaTiO_3$

OAc=$Ba(OAc)_2$; NO_3=$Ba(NO_3)_2$; amor=amorphous; crys=crystalline

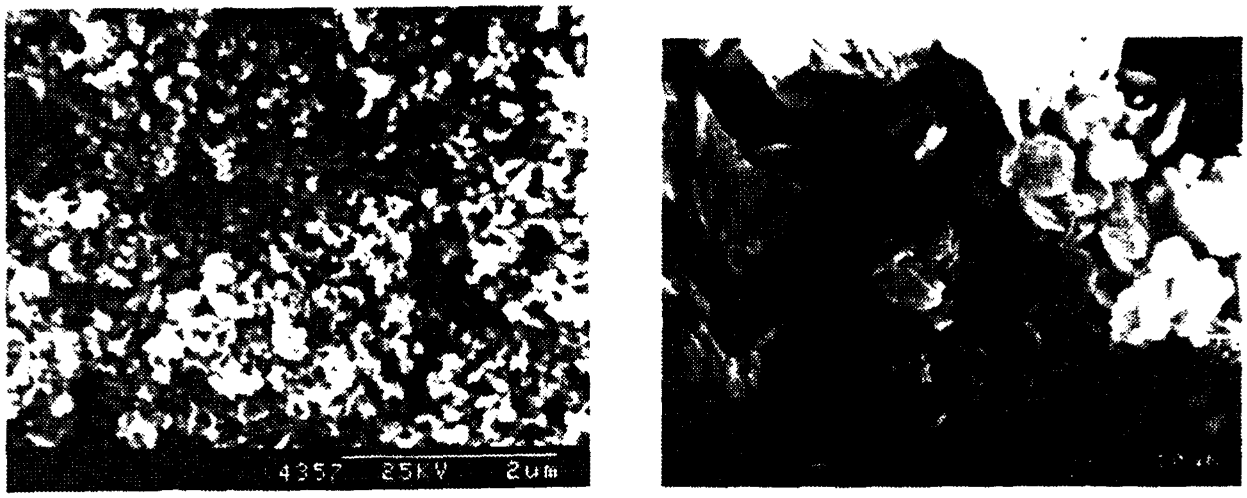

(a) (b)

Fig. 3. Scanning electron micrographs of precipitated $BaTiO(C_2O_4)_2$ particles: (a) amorphous and (b) crystalline.

revert to a stable form on standing. Calcium oxalate precipitated at room temperature, for example, forms as a mixture of di- and trihydrates which are metastable with respect to the monohydrate [21].

The morphology of the $BaTiO_3$ particles after firing was always similar to the unfired morphology. Firing times at temperatures below 900°C were not a critical factor affecting particle size as determined from scanning electron microscopy (SEM) photomicrographs and by measuring the BET surface area versus firing temperature. The effect of firing temperature is very critical; the higher the firing temperature the larger the particle size (Fig. 5). This tendency becomes pronounced above 900°C.

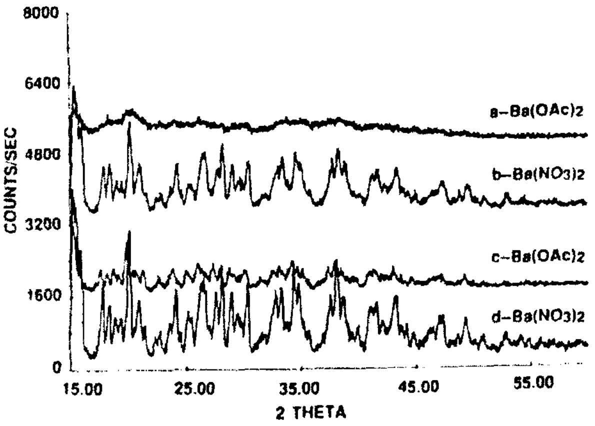

Fig. 4. X-ray diffraction patterns for $BaTiO(C_2O_4)_2{\cdot}4H_2O$ prepared from $Ba(NO_3)_2$ and $Ba(OAc)_2$ at aging times of (a) 3.7 h, (b) 4.0 h, (c) 17 h, and (d) 19 h.

Overall, changes in pH or concentration seemed to have little effect on the formation of single-phase barium titanate, although the precipitates prepared at low pH, low concentration, and using $Ba(NO_3)_2$ appeared to give the best results and gave stoichiometric barium titanate at 600°C.

Synthesis of Cuprates

Research on oxalate precursors for ceramic superconductors has focused on precipitating the three individual oxalates. In addition to the single cation oxalates, $Y_2(C_2O_4)_3{\cdot}9H_2O$, $Ba(C_2O_4){\cdot}0.5H_2O$, and $Cu(C_2O_4){\cdot}0.5H_2O$ [22] complex oxalates have been reported. The ammonium, lithium, sodium, and potassium dihydrates of $[Cu(C_2O_4)_2]^{-2}$ are described in the the early chemical literature [23]. More recently, the magnetic properties of these compounds have been of interest, and the structures of the sodium [24, 25], potassium, and ammonium [26] compounds have been determined by X-ray diffraction studies. Similarly, the complex yttrium oxalates, $(NH_4)Y(C_2O_4)_2$ [27] and $K_8[Y_2(C_2O_4)_7]$ [28], have been prepared and characterized by single-crystal X-ray diffraction studies. Rare earth (Tb and Eu)-copper oxalates have also been reported [29, 30].

To our knowledge no one has considered the possible existence of complex oxalates which would affect the design of any precipitation experiments. The mixed metal oxalate between barium and copper has been reported previously [31] and was prepared by adding oxalic acid or ammonium oxalate to solutions of barium and copper nitrates or formates. $ZnCu(C_2O_4)_2$ has been suggested as the product from the precipitation of zinc and

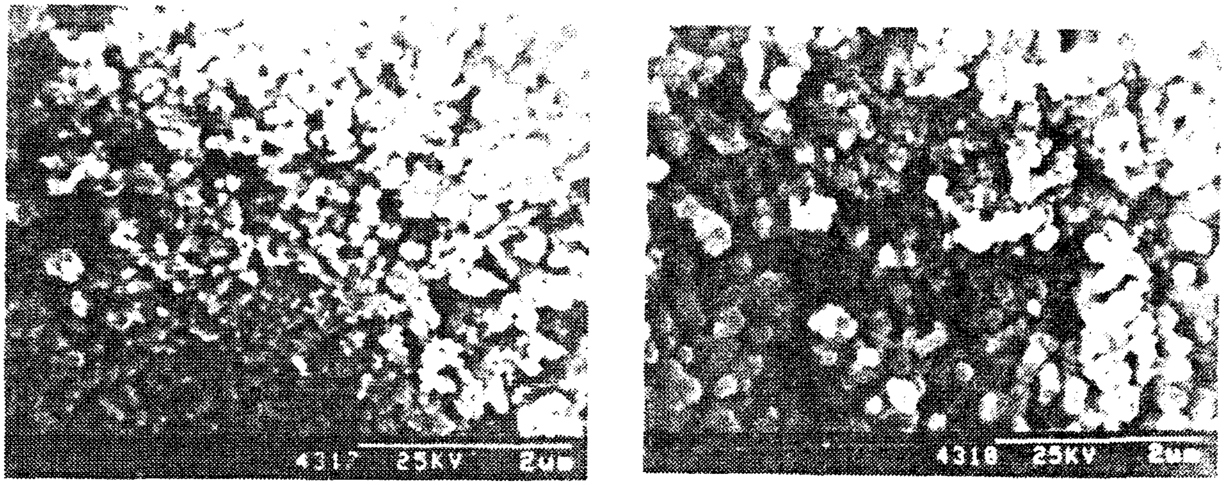

(a) (b)

Fig. 5. Effect of calcining temperature on the $BaTiO_3$ particle size: (a) 800°C and (b) 900°.

copper oxalates [32]. In this section we report our results on the preparation of $BaCu(C_2O_4)_2$, and the precipitation of barium, yttrium, and copper tartrates.

Preparation of $BaCu(C_2O_4)_2$: The compound $BaCu(C_2O_4)_2$ was first reported by Langenbeck [31]. According to our research, the compound crystallizes with six waters of hydration and is appreciably soluble in water with a solubility of 7±2 x 10^{-4} M. This compound readily forms supersaturated solutions and approaches equilibrium slowly.

Crystals of $BaCu(C_2O_4)_2{\bullet}6H_2O$ were grown from dilute solution and isolated for determination of the single crystal X-ray structure. The compound crystallizes in the crystal system P1 [33] (Fig. 6). The structure can be considered as an infinite network of $[Ba{\bullet}5H_2O]^{+2}$ and $[Cu(C_2O_4)_2{\bullet}H_2O]^{-2}$ ions. The geometry around the barium and copper atoms is shown in Figure. 7. In this compound the shortest barium and copper interatomic distance is 4.6 Å. Therefore, the barium and copper can be considered homogeneously mixed on the molecular scale. The IR spectrum (Fig. 8) for this compound was similar to that obtained for the barium titanyl oxalate (Fig. 2).

A TGA plot for the decomposition of BaCu oxalate is shown in Figure 9. Decomposition proceeds in several steps: (1) loss of water, (2) formation of CuO and $BaCO_3$, and (3) decomposition of $BaCO_3$ to form $BaCuO_2$. The TGA shows that steps (1) and (2) were complete by 350 C and occur at lower temperatures than observed for a simple mixture of barium and copper oxalates (Fig. 9). However, decomposition of $BaCO_3$ to form the $BaCuO_2$ is very slow due to the formation of liquid phases which

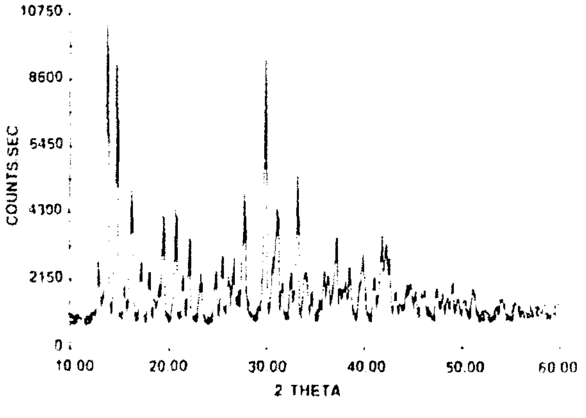

Fig. 6. X-ray diffraction pattern of $BaCu(C_2O_4)_2{\bullet}6H_2O$.

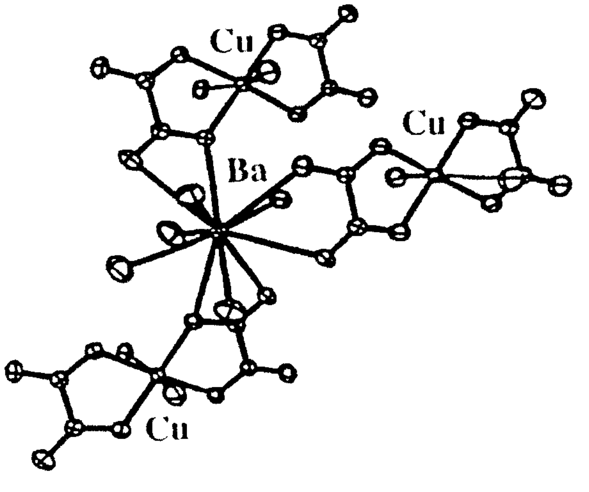

Fig. 7. Structure of $BaCu(C_2O_4)_2{\bullet}6H_2O$ around Ba and Cu atoms.

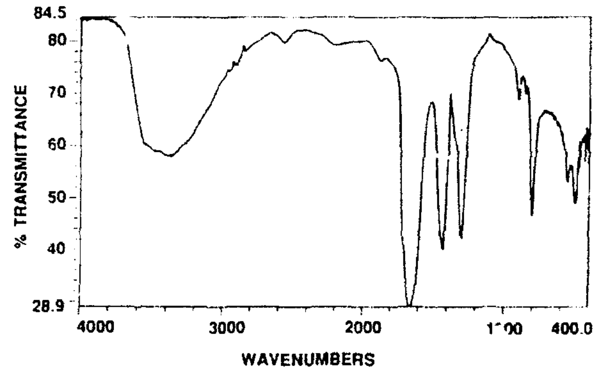

Fig. 8. FTIR of $BaCu(C_2O_4)_2 \cdot 6H_2O$.

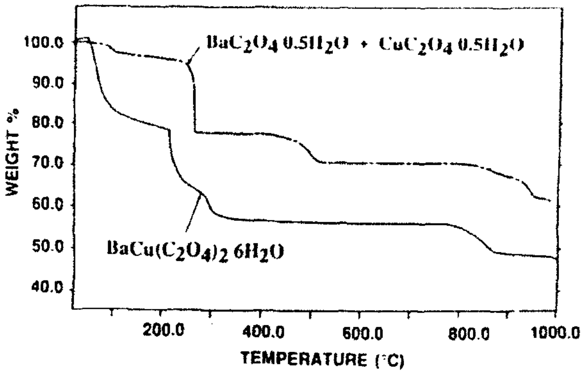

Fig. 9. TGA of Ba Cu oxalates.

allow the particles to densify prior to decomposition of the carbonate. After the particles become dense, decomposition of the $BaCO_3$ becomes very slow.

Preparation of $Ba_2YCu_3O_{6.9}$ from the tartrates: The solubilities of several barium, yttrium, and copper polycarboxylates were determined at pH 4-4.5. The tartaric acid derivatives were the least soluble and had the most promising morphologies. In order to reduce the solubility further and achieve quantitative precipitation of all three metals, mixed ethanol/water solvents were investigated. Reducing the solubility has the added advantage of decreasing the particle size as the solubility decreases.

Initially, the reaction was run at saturated conditions using a 4:1 mixture of ethanol and water as the solvent. Inductively coupled plasma analysis (ICP) showed that quantitative precipitation occurred and only trace amounts of barium (1 ppm), yttrium (<1 ppm), and copper (5 ppm) were detected. However, the precipitate (A) from hot, concentrated solutions was not homogeneous and consisted of particles with two morphologies (Fig. 10). Since the tartrates are essentially insoluble in the ethanol-water mixture, the reaction was repeated at more dilute conditions, and the order of addition was reversed to achieve a more uniform morphology. The precipitate (B) formed under these conditions was agglomerated but had an equiaxed morphology, and the primary particle size was <0.1 µm according to SEM micrographs (Fig. 11). X-ray diffraction showed that the precipitated powder was amorphous.

A TGA for the tartrate powders is shown in Figure 12 and shows that the barium carbonate formed decomposes between 800 and 900°C. The $Ba_2YCu_3O_{7-\delta}$ formed was characterized by X-ray diffraction and carbon analysis to determine the concentration of residual $BaCO_3$. Firing the precipitate isolated from the saturated solution at 810°C for 8 h followed by 1 h at 920°C resulted in formation of a nonsuperconducting tetragonal phase [34], and $BaCO_3$ was observed in the X-ray diffraction pattern

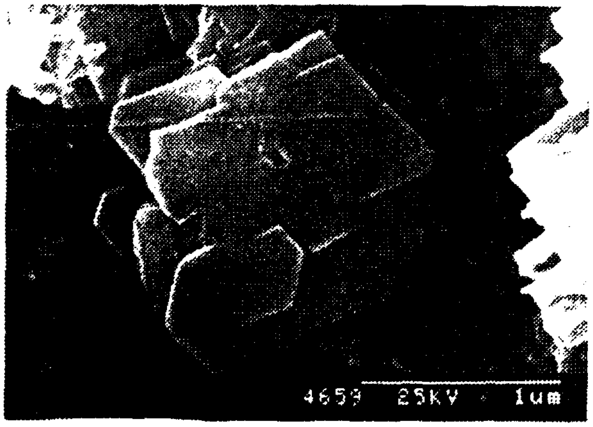

Fig. 10. Tartrate particles obtained from concentrated solutions.

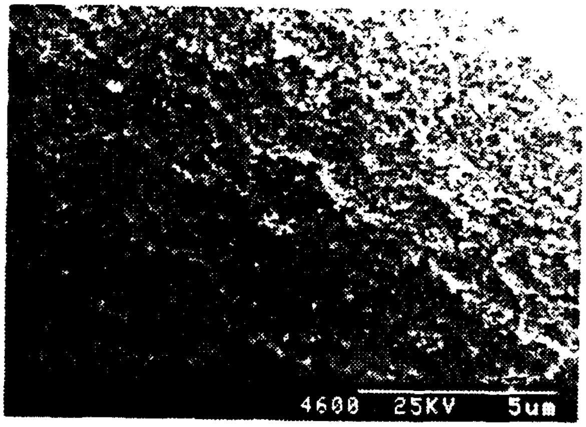

Fig. 11. Tartrate particles obtained from dilute solutions.

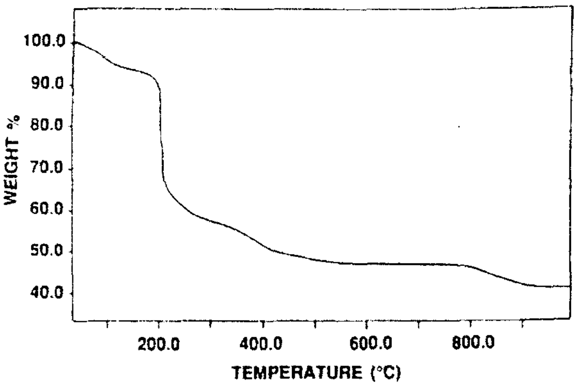

Fig. 12. TGA for decomposition of BaYCu tartrates.

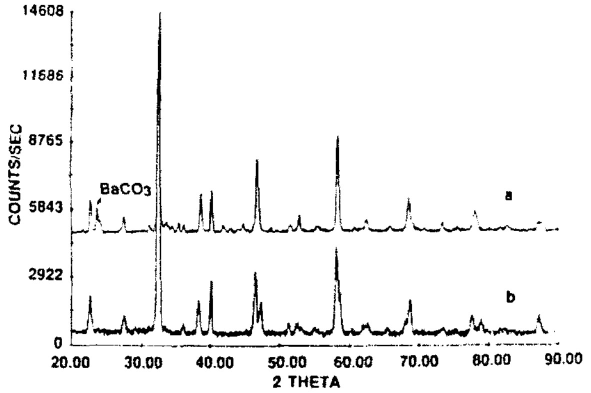

Fig. 13. X-ray diffraction pattern after heating (a) precipitate A to 920°C and (b) precipitate B to 900°C.

(Fig. 13). The carbon content of this phase was 0.49% which, if present as carbonate, would correspond to a stoichiometry of $Ba_2YCu_3(CO_3)_{0.3}O_x$. A sample calcined for 8 h at 940°C was converted to the orthorhombic phase but retained 0.115% carbon.

In contrast, the powder obtained from dilute solution was fully converted to single phase orthorhombic BYC with low carbon content (0.019%) after firing at 850°C for 16 h followed by 1 h at 900°C. The precipitate from dilute solution had a uniform rather than multiphase morphology and therefore converted more readily to BYC.

CONCLUSIONS

Barium titanate can be prepared at 600°C from the precipitate obtained by reacting titanyl ammonium oxalate with barium acetate or barium nitrate and adjusting the pH with nitric acid. Precipitates produced using hydrochloric acid had to be heated to 900°C to obtain single-phase barium titanate.

The complex oxalate, $BaCu(C_2C_4)_2{\cdot}6H_2O$, has been isolated as one of the oxalate complexes that forms during the precipitation of the Ba, Y, and Cu oxalates. Most likely other bimetallic oxalates can be synthesized and used to control the stoichiometry of ceramic powders.

The precipitation of powders using polycarboxy organic acids can be considered as a general method for preparing ceramic powders. We demonstrated that this technique produces submicrometer precipitates. High-purity BYC powders were synthesized by precipitating the barium, yttrium, and copper tartrates.

ACKNOWLEDGMENTS

The research reported in this paper was supported by DARPA under contract number MDA972-88K-0006 and by AFOSR under contract number F49620-89C-0102DEF. The authors also acknowledge the contributions of Simon Bott and Jerry Atwood at the University of Alabama for solving the single crystal X-ray structure of $BaCu(C_2O_4)_2{\cdot}6H_2O$. We also thank Peter Rexer and Mohanjit Jolly for assisting in the experiments to prepare the tartrates.

REFERENCES

1. T. Sugimoto, "Preparation of Monodispersed Colloidal Particles," *Adv. Colloid Interface Sci.*, **28** 65 (1987).
2. E. Matijevic, "Monodispersed Colloids: Art and Science," *Langmuir*, **2** 12 (1986).
3. E.A. Barringer and H.K. Bowen, "Formation, Packing, and Sintering of Monodisperse TiO_2 Powders," *J. Am. Ceram. Soc.*, **65** C199-201 (1982).
4. W. Stober and A. Fink, "Controlled Growth of Monodisperse Silica Spheres in Micron Size Range," *J. Coll. Interface Sci.*, **26** 62-69 (1968).
5. B. Fegley, P. White, and H.K. Bowen, "Processing and Characterization of ZrO_2 and Y-Doped ZrO_2 Powders," *Am. Ceram. Soc. Bull.*, **64** 1115-20 (1985).
6. W. Stanley Clabaugh, E.M. Swiggard, and R. Gilchrist, "Preparation of Barium Titanyl Oxalate Tetrahydrate for Conversion to Barium Titanate of High Purity," *J. Res. Natl. Bur. Std.*, **56** 289 (1956).
7. K. Kiss, J. Magder, M.S. Vukasovich, and R. Lockhart, "Ferroelectrics of Ultrafine Particle Size: I, Synthesis of Titanate Powders of Ultrafine Particle

Size," *J. Am. Ceram. Soc.*, **49** 291 (1966).

8. P.K. Gallagher and F. Schrey, "Thermal Decomposition of Some Substituted Barium Titanyl Oxalate and Its Effect on the Semiconducting Properties of the Doped Materials," *J. Am. Ceram. Soc.*, **46** 567 (1963).
9. P.K. Gallagher, F. Schrey and F.V. DiMarcello, "Preparation of Semiconducting Titanates by Chemical Methods," *J. Am. Ceram. Soc.*, **46** 359 (1963).
10. D. Hennings and W. Mayer, "Thermal Decomposition of BaTi Citrates into Barium Titanate," *J. Sol. State. Chem.*, **26** 329-38 (1978).
11. A.L. Micheli, "Formation of Fine Particle Sinterable Ceramic Powders," U.S. Pat. No. 4 627 966, December 9, 1986.
12. A.L. Micheli, "Synthesis of Reactive Yttria Powders using an Aqueous Organic Polymer Precursor," p. 102 in Ceramic Transactions, Vol. 1. Edited by G. Messing, E. Fuller, Jr. and H. Hausner. American Ceramic Society, Westerville, OH, 1988.
13. F. Callaud, J-F. Baumard, and A. Smith, "A Model for the Preparation of $YBa_2Cu_3O_{7-\delta}$," *Mat. Res. Bull.*, **23** 1273 (1988).
14. F.G. Shrif, "Alkaline Oxalate Precipitation Process for Forming Metal Oxide Superconductors," U.S. Pat. No. 4 804 649, February 14, 1989.
15. L. Gordon and E.R. Caley, "Precipitation of Oxalates from Homogeneous Solution," *Anal. Chem.*, **20** 560 (1948).
16. L. Gordon and A.F. Wroczynski, "Precipitation of Calcium from Homogeneous Solution with Methyl Oxalate," *Anal. Chem.*, **24** 896 (1952).
17. V.K. Rao, I.C. Pius, M. Subbarao, A. Chinnusamy, and P.R. Natarajan, "Precipitation of Plutonium Oxalate from Homogeneous Solutions," *J. Radioanal. Nucl. Chem.*, **100** 129-34 (1986).
18. T.-T. Fang and H.-B. Lin, "Factors Affecting the Preparation of Barium Titanyl Oxalate Tetrahydrate," *J. Am. Ceram. Soc.*, **72** 1899-906 (1989).
19. H. Yamamura, A. Watanabe, S. Shirasaki, Y. Moriyoshi, and M Tanada, "Preparation of Barium Titanate by Oxalate Method in Ethanol Solution," *Ceram. Int.*, **11** 17-22 (1985).
20. K. Kudaka, K. Iizumi, and K. Sasaki, "Preparation of Stoichiometric Barium Titanyl Tetrahydrate," *Am. Ceram. Bull.*, **61** 1236 (1982).
21. E.B. Sandell and I.M. Kolthoff, "Studies in Coprecipitation. III. The Water Content of Calcium Oxalate Monohydrates," *J. Phys. Chem.*, **37** 153 (1933).
22. P. Peshev, G. Gyurov, I. Khristova, K. Petrov, D. Kovacheva, Ya Mimitriev, N. Nencheva, and E. Vlakhov, "Comparative Study of Some Methods of Synthesis of the High-T_c Superconductor Yttrium Barium Copper Oxide," *Mater. Res. Bull.*, **23** 1659 (1987).
23. Gemlin Handbook, 60B, Part 2, 728-38 (1961).
24. A. Gleizes, F. Maury, and J. Galy, "Crystal Structure and Magnetism of Sodium Bis(oxalato)cuprate(II) dihydrate $Na_2(C_2O_4)_2{\cdot}2H_2O$. A Deductive Proposal for the Structure of Copper Oxalate, $Cu(C_2O_4){\cdot}xH_2O$," *Inorg. Chem.*, **19** 2074-78 (1980).
25. P. Chananont, P.E. Nixon, J.M. Waters, and N. Waters, "The Structure of Disodium Caten-bis-(oxalato) Cuprate(II) Dihydrate," *Acta Cryst.*, **B36** 2145-47 (1980).
26. M.A. Viswamitra, "Crystal Structure of Copper Ammonium Oxylate Dihydrate, $Cu(NH_4)_2(C_2O_4)_2{\cdot}2H_2O$," *J. Chem. Phys.*, **37** 1408-14 (1962).
27. T.R.R. McDonald and J.M. Spink, "The Crystal Structure of a Double Oxalate of Yttrium and Ammonium, $NH_4Y(C_2O_4)_2{\cdot}H_2O$," *Acta Cryst.*, **23** 944-49 (1967).
28. I.A. Kahawa, F.R. Fronczek, and J. Selbin, "The Crystal and Molecular Structures of Potassium-oxalato-di[trisoxalato-lanthium(III)-14-hydrates $K_8[Ox_3LnOxLnOx_3]{\cdot}14H_2O$," *Inorg. Chim. Acta*, **82** 167-72 (1984).
29. M.E. Modebadze and Davitashvili, "Composition and Thermal Study of Coprecipitated Europium and Copper Oxalates," *Izv. Akad. Nauk Gruz. SSR, Ser. Kim.*, **11** 252 (1985).
30. M.E. Modebadze and Davitashvili, "Simultaneous Formation of Terbium Copper Oxalates," *Soobshch. Akad. Nauk Gruz. SSR*, **108** 73 (1982).
31. W. Langenbeck, "Uber Mischsalz-kontakte und Ihre Anwendungen," *Angew. Chem.*, **68** 453-57 (1956).
32. B.D. Dalvi and A.M. Chavan, "Thermal Decomposition of Mixed Oxalates," *J. Thermal Anal.*, **14** 331-34 (1978).

33. R.B. Hallock, W.E. Rhine, M.J. Cima, S.G. Bott and J.L. Atwood, "Synthesis and X-ray Crystal Structure of $BaCu(C_2O_4)_2 \cdot 6H_2O$, A Mixed-Metal Oxalate of Barium and Copper"; in Superconductivity and Ceramic Superconductors. Edited by K.M. Nair. The American Ceramic Society, Westerville, OH, 1990, in press.

34. Y. Nakazawa, M. Ishikawa, T. Takabatake, K. Koga, and K. Terakura, "Characterization of Metamorphoric Phases of $Ba_2YCu_3O_{9-\delta}$," *Jpn. J. Appl. Phys.*, **26** L796-98 (1987).

SECTION 3

PRECIPITATION OF OXALATES FROM HOMOGENEOUS SOLUTION: SYNTHESIS OF $BaTi(C_2O_4)_2$ AND Ba, Y, AND Cu OXALATES

Wendell E. Rhine, Robert B. Hallock, William M. Davis, and Michael J. Cima

Published in Forming Science and Technology for Ceramics, Ceramic Transactions, vol 26, 8 (1992)

ABSTRACT

Precipitation from homogeneous solution is one approach being investigated to control the chemical and physical properties of ceramic powders. The degree of supersaturation directly affects the particle nucleation processes and can be used to control the crystal size and particle morphology. Low degrees of supersaturation lead to a low number of nuclei, and regular crystal growth predominates and results in large crystals. High degrees of supersaturation lead to a large number of nuclei, resulting in monodispersed, submicrometer particles in ideal cases. This paper discusses two examples, $BaTiO_3$ and $YBa_2Cu_3O_{7-x}$, both important electronic materials which will illustrate the versatility of precipitation from homogeneous solution.

INTRODUCTION

Precipitation from homogeneous solution is one of the best methods for controlling the particle size, size distribution, stoichiometry, and crystal habit or morphology of ceramic powders. Numerous oxide particles that are uniform in size, shape, and composition can be prepared by homogeneous precipitation methods, and these reactions can be carried out in a variety of ways, as reviewed by Sugimoto [1] and Matijevic [2].

The first step in precipitation is the formation of primary nuclei, which may be only a few ion pairs in size. The formation rate of primary nuclei is negligible until a considerable degree of supersaturation is reached. Thereafter, the formation rate of nuclei increases very quickly and is directly related to the degree of supersaturation. Supersaturated solutions of the solute are required because the supersaturated state is unstable and reverts to the stable state by precipitating the excess solute from the solution. Once formed, the primary nuclei act as seeds and grow larger to become colloidal particles (0.001-0.1 µm). After colloidal particles have formed, the particle growth process may take one of two directions: colloidal particles may be stable and remain small, or they may grow to fine crystals. If given enough time, the stable colloid may agglomerate or the fine crystals may grow to larger ones.

Nucleation is the predominant process at high degrees of supersaturation, whereas regular crystal growth predominates at low degrees of supersaturation. Therefore, if large, well-formed crystals are desired, it is necessary to keep the degree of supersaturation low. Conversely, if small crystals are desired, a large number of nuclei, and consequently a high degree of supersaturation, are required. However, if the degree of supersaturation is very high, extremely small, gel-like precipitates may form and be very difficult to isolate.

Barium titanate and high T_c superconductors are two widely investigated electronic materials which can be prepared from the oxalates. In this paper we report on two different precipitation methods: one involving low degrees of supersaturation to obtain large crystals of barium titanyl oxalate (BTO) and another using high degrees of supersaturation to obtain small crystals of barium, yttrium, and copper oxalates.

EXPERIMENTAL PROCEDURE

Single crystals of BTO: Ammonium titanyl oxalate (0.45 g, 1.5 mmol) was dissolved in 250 mL water, and the pH was adjusted to 1 with nitric acid. The ammonium titanyl oxalate was added to a solution of barium nitrate (0.38 g, 1.5 mmol in 250 mL water adjusted to pH 1 with HNO_3), and a clear solution was obtained. The water was allowed to evaporate slowly from an open Erlenmeyer

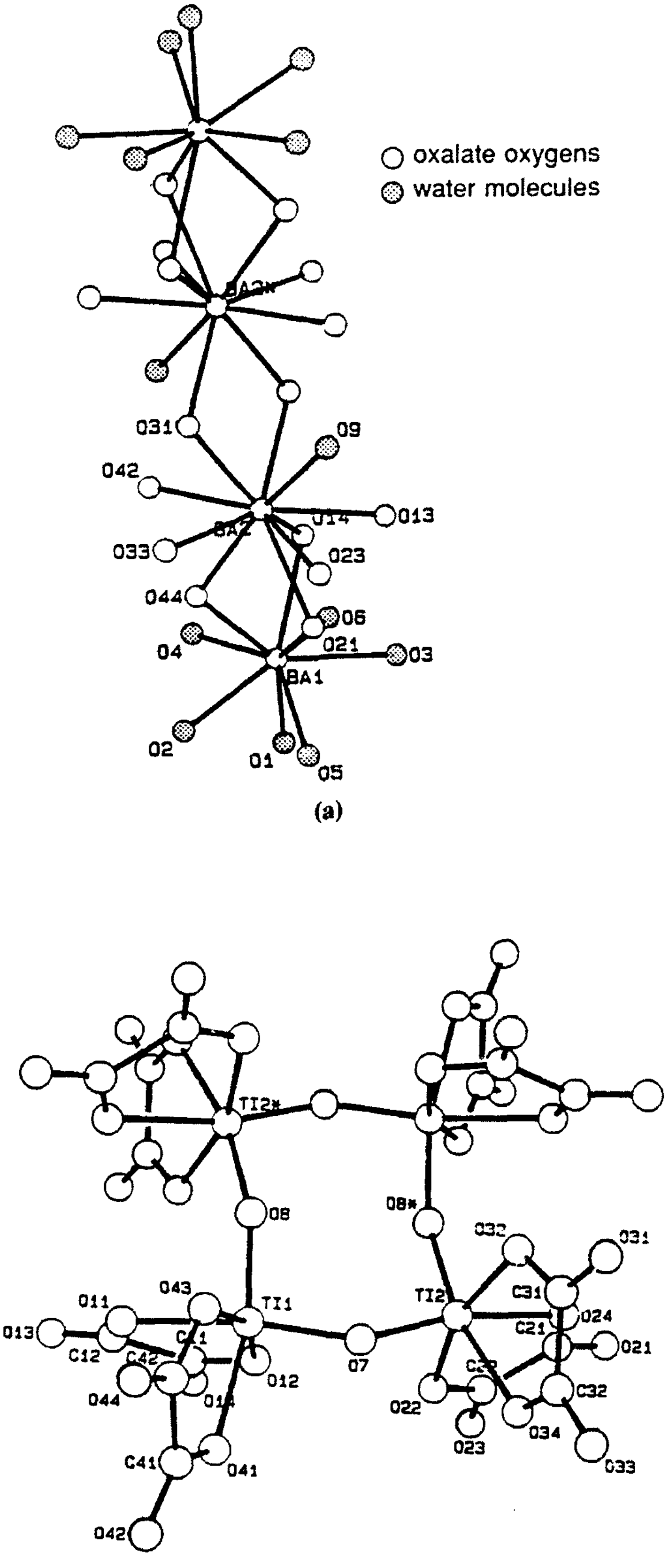
oxalate oxygens
water molecules
BA2*
O31
O9
O42
O13
O14
BA2
O33
O23
O44
O6
O4
O21
O3
BA1
O2
O1
O5
TI2*
O8
O8*
O32
O31
O11
O43
TI1
TI2
C31
O24
O13
C11
C21
O21
C12
C42
O12
O7
C22
O22
C32
O44
O14
O34
O23
C41
O41
O33
O42

(a)

(b)

Fig. 1. Molecular geometry of BTO around the (a) Ti atoms and (b) Ba atoms.

flask, and after several months crystals of $BaTiO(C_2O_4)_2 \cdot 5H_2O$ nucleated and grew. After six months, the crystals were isolated by filtration and air-dried at room temperature.

Homogeneous precipitation of Y, Ba, and Cu oxalates: Aqueous solutions of Cu, Ba, and Y acetates were prepared and diluted with *n*-propanol to give solutions which contained greater than 4:1 alcohol:water ratios. Acetic acid was added as the acid to catalyze the decomposition of diethyloxalate. These solutions were heated to 80-85°C and then diethyloxalate was added. After the reaction was complete, the particles were isolated by filtration.

RESULTS AND DISCUSSION

Synthesis of Barium Titanyl Oxalate

Precipitation of BTO has been investigated extensively as an approach for preparing barium titanate ($BaTiO_3$) powders with controlled stoichiometry. When the reaction is controlled properly, the Ba:Ti ratio of the barium titanate produced is exactly 1:1 [3]. Although BTO has been the subject of more than 40 publications, it has never been structurally characterized, and its existence as a thermodynamically stable compound is the subject of debate in the current literature [4-6].

Barium titanyl oxalate was synthesized by reacting $(NH_4)_2TiO(C_2O_4)_2 \cdot H_2O$ with barium nitrate in dilute solution. By slowly evaporating the water from these dilute solutions, the concentration of BTO gradually increased. This method maintained low degrees of supersaturation and only a small number of nuclei formed. As expected, large, well-defined crystals of BTO were isolated. X-Ray crystallography and elemental analysis indicated the BTO contained five water molecules instead of the four usually reported.

A single crystal X-ray diffraction structural determination was carried out on one of the crystals, and the compound was found to crystallize in the monoclinic space group $P2_1/n$, with cell parameters of a = 13.367(1) Å, b = 13.852(1) Å, c = 14.023(1) Å, and β = 91.61(2)°. The unit cell contains four $Ba_2Ti_2O_2(C_2O_4)_4 \cdot 10H_2O$ asymmetric units. The overall structure of BTO is rather complex and consists of hydrated Ba cations coordinated to $[TiO(C_2O_4)_2]_4$-8 anions. The $[TiO(C_2O_4)_2]_4$-8 groups (Fig. 1a) are eight membered rings consisting of alternating Ti-O bonds. Similar anions are found in the starting material, $(NH_4)_2TiO(C_2O_4)_2 \cdot H_2O$ [7], and other titanyl complexes [8-11].

The two non-equivalent Ba atoms [Ba(1) and Ba(2)] are connected by three bridging oxalate oxygens, and the two equivalent Ba(2) atoms are connected by two bridging oxalate oxygens, as shown in Figure 1b. In addition to the three oxalate oxygens, there are six water molecules associated with Ba(1), making it nine-coordinate. Two of these waters (O5 and O6) have shorter Ba(1)-O bond distances than the other coordinated waters, making them more difficult to remove during thermal decomposition. Barium(2) is coordinated to one water and nine oxalate oxygens making Ba(2) ten-coordinate. The shortest Ba-Ti distance is 5.841(2) Å between Ba(1) and Ti(1). The other three water molecules are waters of crystallization. As expected, these waters of crystallization are easily lost at room temperature.

Precipitation of Ba, Y, and Cu Oxalates

Synthesis of YBCO powders from the oxalates has been investigated by many different groups [12-14]. For most investigators, obtaining complete precipitation of the oxalates in aqueous solution has proven difficult because of the precise control of concentration and pH required. Irrespective of the precautions taken, the ratios of the metals in the precipitated oxalates always differ from those of the initial solutions of metal salts. To overcome this problem, Yamamoto et al. [14] and Awano et al. [15] improved the recovery of oxalates by using alcohol solvents. Use of alcohol solvents reduces the solubility of the oxalates and has a tendency to increase the number of nuclei formed, producing many very small particles. These small particles undergo some sintering during the conversion to YBCO and result in large, vermicular particles which are milled to obtain submicrometer particles (see Fig. 2)

We have successfully precipitated yttrium, barium, and copper oxalates from homogeneous solution by controlling the degree of supersaturation so that it is not too high throughout the process, thus avoiding the formation of gel-like precipitates. This insures formation of larger particles that are more easily isolated than with direct precipitation methods. In the method used here, oxalic acid was generated *in situ* by saponifying oxalic acid esters according to the equation

$$2H_2O + ROCOCOOR + H^+ \rightarrow H_2C_2O_4 + 2ROH.$$

The number of nuclei in this process is controlled by the rate of the reaction generating the precipitant which, in turn, is dependent on the concentration, catalyst, and temperature used for the reaction. Since the saponification of oxalic esters proceeds slowly at room temperature, the reactions were carried out at elevated temperatures (~80°C). Particles nucleated within 1 h when stoichiometric amounts of diethyl oxalate were added and within 5 s when large excess amounts of diethyloxalate were used.

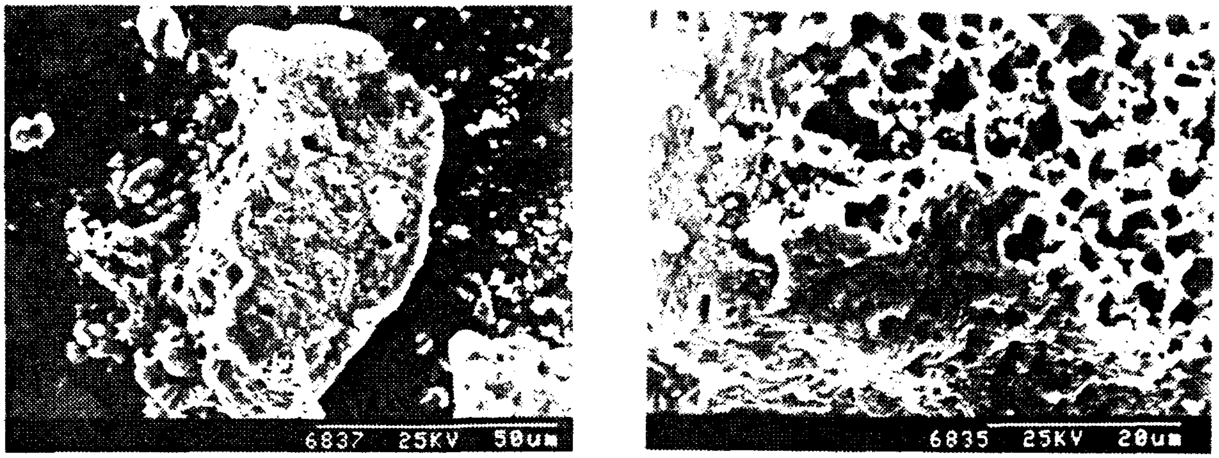

(a) (b)

Fig. 2. Particles obtained after calcining the directly precipitated oxalates at 900°C.

Table 1. Reaction Conditions for Precipitating Ba, Y, and Cu Oxalates from Homogeneous Solution.

	Reaction					
Reagent (mol/L)	1	2	3	4	5	6
$Y(OAc)_3$	0.01	0.01	0.01	0.005	0.0025	0.0025
$Ba(OAc)_2$	0.02	0.02	0.02	0.01	0.005	0.005
$Cu(OAc)_2$	0.03	0.03	0.03	0.015	0.0075	0.0075
$Et_2C_2O_4$	0.07	0.14	0.27	0.27	0.27	0.54
solvent	HOAc	*i*-PrOH	*n*-PrOH	*n*-PrOH	*n*-PrOH	*n*-PrOH
water (mL)	200	200	200	150	100	100
HOAc		20	20	20	20	20
temp (°C)	90	68	65	75	80	80
nucleation	40 min	30 min	1 min	15 s	10 s	5 s
dispersant					HPC	HPC

HPC = hydroxypropyl cellulose (MW = 100,000).

The precipitation of Ba, Y, and Cu oxalates from homogeneous solution was carried out using various amounts of diethyloxalate, as shown in Table 1. During the precipitation process, each metal oxalate precipitated as its solubility product was exceeded, thus producing complete segregation. Since the yttrium oxalate was the least soluble, it precipitated first. Then the copper oxalate precipitated and finally the barium oxalate formed. When less than fourfold excess diethyloxalate was used, the products were deficient in barium, and barium oxalate was observed to precipitate over a period of days. When greater than fourfold excess amounts of diethyloxalate were used, the reaction appeared to be complete within 3-4 h at 80°C.

The morphologies of the Ba, Y and Cu oxalates were different. In separate experiments we showed that the spherical particles observed in Figure 3a are copper oxalate. As the amount of diethyloxalate was increased, the particle size of the precipitated oxalates decreased and, when 16–32-fold excess of diethyl oxalate was used, the particle sizes were ~1 µm (Fig. 3b). What is interesting is that during the thermal decomposition of the oxalates, the particles tended to maintain their morphology. After conversion to YBCO, the morphology of the original particles precipitated from reactions using twofold excess amounts of diethyloxalate could still be seen. However, the particles became porous and had the same type of morphology as the particles obtained from calcining the directly precipitated oxalates. The advantage of direct precipitation from the oxalates lies in the reduced size of the particles, which are only 2-15 µm (Fig. 4) instead of 20-50 µm in diameter (Fig. 2). Particles precipitated from

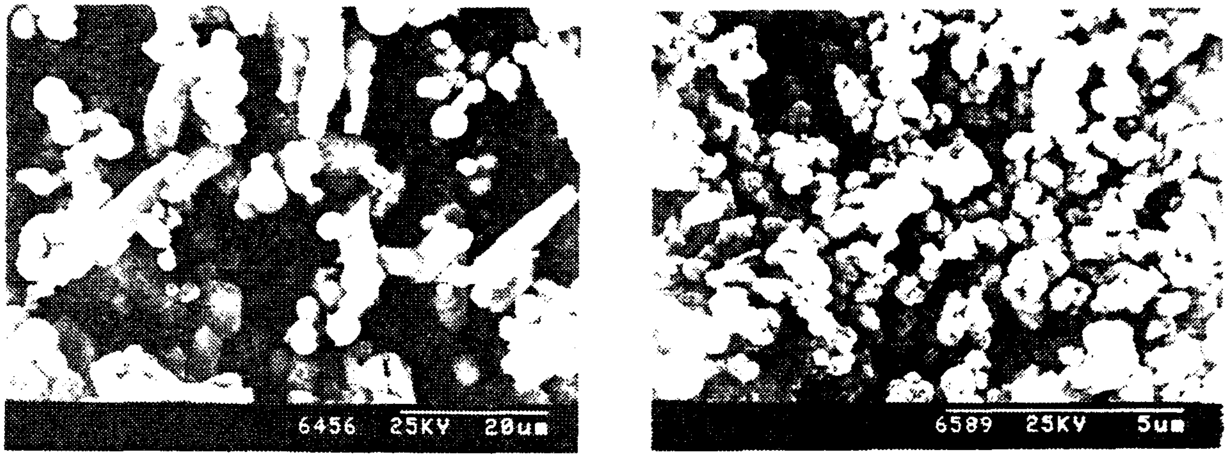

(a) (b)

Fig. 3. Particles obtained using (a) twofold excess and (b) 16-fold excess diethyloxalate.

reactions using 16–32-fold excess amounts of diethyloxalate decomposed to give micrometer sized particles of YBCO.

ACKNOWLEDGMENTS

The authors wish to thank AFOSR (Contract No. F49620-89-C-0102) and DARPA (Contract No. MDA972-88-K-006) for financial support.

REFERENCES

1. T. Sugimoto, "Preparation of Monodispersed Colloidal Particles," *Adv. Colloid Interface Sci.*, **28**, 65-108 (1987).
2. E. Matijevic, "Monodispersed Colloids: Art and Science," *Langmuir*, **2**, 12-20 (1986).
3. W.S. Clabaugh, E.M. Swiggard, and R.J. Gilchrist, "Preparation of Barium Titanyl Oxalate Tetrahydrate for Conversion to Barium Titanate of High Purity," *J. Res. Nat. Bur. Stand.*, **56**, 289 (1956).
4. T.T. Fang and H.B. Lin, "Factors Affecting the Preparation of Barium Titanyl Oxalate Tetrahydrate," *J. Am. Ceram. Soc.*, **72**, 1899 (1989).
5. T.T. Fang, H.B. Lin, and J. B. Hwang, "Thermal Analysis of Precursors of Barium Titanate Prepared by Coprecipitation," *J. Am. Ceram. Soc.*, **73**, 3363 (1990).
6. K. Osseo-Asare, F.J. Arriagada, and J.H. Adair, "Solubility Relationships in the Coprecipitation Synthesis of Barium Titanate: Heterogeneous Equilibria in the Ba-Ti-C_2O_4-H_2O System"; p. 47 in Ceramic Transactions, Vol. 1. Edited by G. Messing, E. Fuller, Jr., and H. Hausner. American Ceramic Society, Westerville, OH, 1988.
7. G.M.H. Van de Velde, S. Harkema, and P.J. Gellings, "The Crystal and Molecular Structure of Ammonium Titanyl Oxalate," *Inorg. Chim. Acta*, **11**, 243 (1974).
8. M. Haddad and F. Brisse, "The Alkali Metal Complexes of Titanium (IV) Oxalates," *Can. Mineralogist.*, **16**, 379 (1978).
9. A.C. Skapski and P.G.H. Troughton, "The Crystal and Molecular Structure of Cyclotetra[μ-oxo-chloro-π-cyclopentadienyl-titanium(IV)]," *Acta Cryst.* **B26**, 716 (1970).
10. J.L. Petersen, "Polynuclear Oxo-Bridged Cyclopentadienyl Transition-Metal Complexes. Formation and Structural Characterization of the Titanoxane Tetramer, $[(\eta^5\text{-}C_5H_4CH_3)TiCl(\mu\text{-}O)]_4$," *Inorg. Chem.*, **19**, 181 (1980).
11. K. Wieghardt, U. Quilitzsch, J. Weiss, and B. Nuber, "Kinetics and Mechanism of Some Reactions of Chelated Complexes of Titanium (IV) with Hydrogen Peroxide. Synthesis and Crystal Structure of Cesium Teta-μ-oxo-tetrakis[(nitrilotriacetato)titanate(IV)] Hexahydrate," *Inorg. Chem.*, **19**, 2514 (1980).
12. F.G. Sherif, Alkaline Oxalate Precipitation Process for Forming Metal Oxide Superconductors, U.S. Pat. No. 4 804 649, February 14, 1989.

13. F. Caliaud, J-F. Baumard, and A. Smith, "A Model for the Preparation of $YBa_2C_3O_{7-\delta}$," *Mat. Res. Bull.*, **23**, 1273 (1988).

14. T. Yamamoto, T. Furusawa, H. Seto, K. Park, T. Hasegawa, K. Kishio, K. Kitazawa, and K. Fueki, "Processing and Microstructure of Highly Dense Barium Lanthanide Copper Oxide ($Ba_2LnCu_3O_7$) Prepared from Co-precipitated Oxalate Powder," *Supercond. Sci. Technol.*, *1*, 153 (1988).

15. M. Awano, M. Tanigawa, H. Takagi, Y. Torii, A. Tsuzuko, N. Murayama and E. Ishii, "Synthesis of Superconducting Y-Ba-Cu-O Powder by Spray Drying Method," *J. Ceram. Soc. Jpn. Inter. Ed.*, **96**, 417 (1988).

SECTION 4

SYNTHESIS AND CRYSTAL STRUCTURE OF BARIUM TITANYL OXALATE, $BaTi(O)(C_2O_4)_2 \cdot 5H_2O$: A MOLECULAR PRECURSOR FOR $BaTiO_3$

Wendell E. Rhine and Robert B. Hallock
Ceramics Processing Research Laboratory
Massachusetts Institute of Technology, Cambrige, MA 02139

William M. Davis
Department of Chemistry, M.I.T., Cambridge, MA 02139

and Winnie Wong-Ng
National Institute of Standards and Technology
Gaithersburg, MD 20899

Published in Chem. Mater. 1992 4, 1208-1216

ABSTRACT

Single crystals of barium titanyl oxalate (BTO), $BaTi(O)(C_2O_4)_2 \cdot 5H_2O$, were grown by slowly evaporating water from a dilute solution of barium nitrate and ammonium titanyl oxalate, $(NH_4)_2Ti(O)(C_2O_4)_2 \cdot H_2O$, at pH 1. The molecular structure of BTO was determined by single crystal X-ray crystallography. The chemical formula is more accurately described as $Ba_2Ti_2O_2(C_2O_4)_4 \cdot 10H_2O$ in order to account for the number of unique atoms in the structure. Seven of the ten water molecules are associated with barium atoms, and the remaining three waters occupy interstitial sites in the structure and are not coordinated to either titanium or barium atoms. The compound readily loses water beginning at room temperature, depending on drying conditions and/or relative humidity; hence in the past the compound has been referred to most often as the tetrahydrate, $BaTi(O)(C_2O_4)_2 \cdot 4H_2O$. *Crystal data:* $C_8H_{20}Ba_2O_{28}Ti_2$, M = 934.65, monoclinic, space group $P2_1/n$ (#14), a = 13.367 (1) Å, b = 13.852(1) Å, c = 14.023(1) Å, β = 91.61(2)°, V = 2595.6 Å^3, Z = 4, D_{calc} = 2.392 g/cm^3, R = 0.064 and R_w = 0.069.

INTRODUCTION

Barium titanate, $BaTiO_3$, is a major component of high dielectric constant ceramics for capacitor manufacture. The microstructure and, consequently, dielectric properties of barium titanate are very dependent on stoichiometry with regard to the Ba/Ti ratio.[1] One of the most studied methods for controlling the stoichiometry of barium titanate is to use a molecular precursor such as barium titanyl oxalate (BTO).

Barium titanyl oxalate was first reported by Pechard[2] in 1893 as a crystalline compound of the formulation $2(C_2O_4H_2).BaO.TiO_2$ (i.e., the tetrahydrate), and it was isolated as the product of the reaction between potassium titanyl oxalate and barium chloride. Rosenheim and Schutte[3] reported the dihydrate as the product of the same reaction. Barium titanyl oxalate was not further investigated until after the emergence of $BaTiO_3$ as an important dielectric material during World War II.

In 1956, Clabaugh *et al.*[4] realized the potential for conversion of BTO to stoichiometric $BaTiO_3$; however, they reported that Pechard's[2] method for the synthesis of BTO resulted in incomplete substitution of Ba for K and resulted in a barium-deficient product. The Ba:Ti stoichiometry in BTO and in the resulting $BaTiO_3$ were found to be very dependent on reaction conditions, and an optimized synthesis was developed which involved the addition of barium chloride (0.675 mol/3 L = 0.225 M) and titanium tetrachloride (0.668 mol/3 L = 0.223 M), with barium in 1% excess, to a hot aqueous solution of oxalic acid containing 10% excess of the amount required for the formation of BTO (final volume = 3 L). Under these conditions, barium titanyl oxalate tetrahydrate with a Ba:Ti ratio of unity was reproducibly prepared and converted to high purity stoichiometric $BaTiO_3$ at 900 °C.[4]

Since the report by Clabaugh *et al.*[4] in 1956, the use of BTO to prepare stoichiometric barium titanate has been widely investigated and is the subject of more than forty publications or patents. Most of the reported syntheses are similar to that of Clabaugh *et al.*[4] but differ in the concentrations of reagents or temperatures used.[5-8] Clabaugh *et al.*[4] carried out the precipitation at 80°C, while others have used lower temperatures and obtained similar results.[13,14,16,17] Several investigators have tried using titanyl nitrate instead of titanium tetrachloride as the titanium source,[5,9,10] and some workers have reported varying degrees of success in preparing BTO from ethanolic solutions.[5,9,11,12]

A majority of researchers have reported BTO as the tetrahydrate, in agreement with the original work of Pechard [2]; however, a close examination of the literature shows that the BTO obtained often contained more than 4 mol water. Strishkov's [6,13] analytical and TGA data were consistent with 4.4 mol water, and in a later paper he referred to BTO as $BaTi(O)(C_2O_4)_2{\cdot}4.5H_2O$.[14] Gallager and Schrey [15] reported an "extra few percent of moisture present" in one of their preparations. Gopalakrishnamurthy and coworkers [16] reported that the degree of hydration of BTO varied depending on the relative humidity of the surrounding atmosphere from 4.5 waters at 50% relative humidity to 4.8 waters at 90% relative humidity. Yen et al.[17] recently studied the low temperature decomposition of BTO assuming it was the tetrahydrate. They observed that BTO was still crystalline after losing 2.9 waters of hydration.

A number of different X-ray powder diffraction patterns have been reported for BTO,[5,6,8,9,12,14,17,18] in addition to several reports of amorphous forms of BTO.[5,9,12] One attempt to prepare BTO in ethanol led to the isolation of a product which gave an X-ray diffraction pattern similar to barium nitrate.[9] The exact composition of this product is not known, but the X-ray powder diffraction pattern was reported to be that of BTO, since this precipitate could be thermally decomposed to barium titanate. In a recent paper, Fang and coworkers[5] reported that the products of the reaction between $Ba(NO_3)_2$ and $TiO(NO_3)_2$ in an ethanolic solution of oxalic acid were a mixture of barium nitrate and $Ti(OH)_2(C_2O_4)$.

The most widely accepted X-ray diffraction pattern for BTO is based on the work of Kudaka et al.[8] and is tabulated for the range of 10-30° 2θ on JCPDS card 36-682[19]; however, Yen and coworkers[17] recently calculated unit cell parameters for BTO as a = 14.954 Å, b = 19.332, c = 13.9332, β = 106.43°, and Z = 12, based on the monoclinic system P2/m. Louër et al.[18] recently published another analysis of the high-resolution powder pattern of BTO based on a monoclinic cell, and the calculated unit cell parameters were a = 14.044(2) Å, b = 13.812(2) Å, c = 13.382(2) Å, and β = 91.48(1)°.

Although BTO has been recognized as a crystalline compound for nearly 100 years, it has never been structurally characterized, and its very existence as a discrete compound remains the subject of debate in the current literature.[5,20,21] In order to ascertain the nature of this widely studied compound, we grew single crystals of BTO and determined its crystal structure by X-ray crystallography.

EXPERIMENTAL SECTION

Preparation of $(NH_4)_2Ti(O)(C_2O_4)_2{\cdot}H_2O$: An ethanol solution of titanium ethoxide (109.96 g, 0.482 mol, Dynamit Nobel Chemicals, Rockleigh, NJ) was added slowly with stirring to a solution containing 60.74 g (0.482 mol) oxalic acid dihydrate (Alfa Products, Danvers, MA) and 68.64 g (0.483 mol) ammonium oxalate monohydrate (Mallinckrodt Inc., Paris, KY) in 600 mL water at 80°C. The overall reaction leading to the synthesis of $(NH_4)_2Ti(O)(C_2O_4)_2{\cdot}H_2O$ is:

$$Ti(OEt)_4 + H_2C_2O_4 + (NH_4)_2C_2O_4 + 3H_2O \rightarrow (NH_4)_2Ti(O)(C_2O_4)_2{\cdot}H_2O + 4EtOH$$

The mixture was initially turbid, but a clear solution was usually obtained after stirring at 80°C for 1 h. If the solution was still turbid, a small amount of oxalic acid was added, and the solution turned clear in a few minutes. The resulting solution was filtered to remove trace solids and allowed to cool to room temperature. A volume of *n*-propanol approximately equal to twice the volume of aqueous solution was then added while stirring. When stirring was stopped, the mixture separated into two layers, and the product crystallized from the aqueous layer upon setting. The product was isolated by filtration, and the crystalline precipitate was washed with *n*-propanol. Yield of purified $(NH_4)_2Ti(O)(C_2O_4)_2{\cdot}H_2O$ was greater than 80%. Elemental analysis for $C_4H_{10}N_2O_{10}Ti$: calcd C, 16.34 (found, 16.37); H, 3.34 (3.36); N, 9.53 (9.49).

Preparation of $BaTi(O)(C_2O_4)_2{\cdot}5H_2O$ (BTO): Ammonium titanyl oxalate (0.45 g, 1.5 mmol) was dissolved in 250 mL water, and the pH was adjusted to 1 with nitric acid. In a separate flask, barium nitrate (0.38 g, 1.5 mmol) was dissolved in 250 mL water, and the pH was adjusted to 1 with nitric acid. The ammonium titanyl oxalate solution was added to the barium nitrate solution, and the mixture remained free of precipitate. Water was allowed to evaporate slowly from an open Erlenmeyer flask, and crystals of $BaTi(O)(C_2O_4)_2{\cdot}5H_2O$ nucleated, grew, and became visible after several months. The crystals, which begin to lose water even at room temperature, were isolated by filtration and air-dried at room temperature. Elemental analysis for

$BaTi(O)(C_2O_4)_2{\bullet}4.5H_2O$. $C_8H_{18}Ba_2Ti_2O_{27}Ti_2$: calcd C, 10.48 (found, 10.48); H, 1.98 (1.95); Ba, 29.96 (29.59); Ti, 10.45 (10.28); Ba/Ti mol ratio = 1.003. Samples that were analyzed for water content after shorter drying times contained more water with 5 waters being the upper limit.

X-Ray Diffraction Study: A colorless prism of BTO having approximate dimensions of 0.15 x 0.15 x 0.15 mm was mounted on a glass fiber. All measurements were made on an Enraf-Nonius CAD-4 diffractometer with graphite monochromated Mo Kα radiation. The data were collected at a temperature of 23°C ± 1°C using the ω-2θ scan technique to a maximum 2θ value of 54.9°. Omega scans of several intense reflections, made prior to data collection, had an average width at half-height of 0.26° with a take-off angle of 2.8°. Scans of (0.80 + 0.35 tan θ)° were made at speeds ranging from 0.9 to 8.0°/min (in omega). Moving-crystal, moving-counter background measurements were made by scanning an additional 25% above and below the scan range. The counter aperture consisted of a variable horizontal slit with a width ranging from 3.0 to 3.5 mm and a vertical slit set to 4.0 mm. The diameter of the incident beam collimator was 0.8 mm and the crystal-to-detector distance was 17.3 cm. For intense reflections, an attenuator was automatically inserted in front of the detector.

Of the 6462 reflections collected, 6203 were unique (R_{int} = 0.081); equivalent reflections were merged. The intensities of three representative reflections, which were measured after every 60 min of X-ray exposure time, remained constant throughout data collection, indicating crystal and electronic stability (no decay correction was applied). The linear absorption coefficient of BTO for Mo Kα radiation is 36.9 cm^{-1}. The data were corrected for Lorentz and polarization effects, but azimuthal scans of several reflections indicated no need for an absorption correction. A correction for secondary extinction was applied (coefficient = 0.10047×10^{-7}).

The structure was solved by a combination of the Patterson method and difference Fourier methods.[22] The non-hydrogen atoms were refined anisotropically. The final cycle of full-matrix least-squares refinement[23] was based on 3883 observed reflections [$I > 3.00\sigma(I)$] and 362 variable parameters, and converged (largest parameter shift was 0.00 times its esd) with unweighted and weighted agreement factors of:

$$R = \frac{\Sigma \,||F_o| - |F_c||}{\Sigma \,|F_o|} = 0.064$$

$$R_w = \left[\frac{\Sigma w(|F_o| - |F_c|)^2}{\Sigma w \, F_o^2}\right]^{1/2} = 0.069$$

The standard deviation of an observation of unit weight[24] was 1.66. The weighting scheme was based on counting statistics and included a factor (p = 0.03) to downweight the intense reflections. Plots of $\Sigma w (|F_o| - |F_c|)^2$ vs. $|F_o|$, reflection order in data collection, sin θ/λ, and various classes of indices showed no unusual trends. The maximum and minimum peaks on the final difference Fourier map corresponded to 2.19 and -3.12 $e^-/Å^3$, respectively.

Neutral atom scattering factors were taken from Cromer and Waber.[25] Anomalous dispersion effects were included in F_{calc}[26]; the values for Δf′ and Δf″ were those of Cromer.[27] All calculations were performed using the TEXSAN [20] crystallographic software package from Molecular Structure Corporation.

Calculated Powder Diffraction Pattern of BTO: A simulated powder diffraction pattern was computed based on the single crystal data, using a local Siemen's version of POWD10.[29] All calculations used Cu Kα1 radiation with a wavelength of 1.5405981 Å and Smith's tabulation of the Cromer and Waber atomic scattering factors.[30,31] Intensities (values reported for $I_{cal} > 1$) were referred to peak height values and were derived from a Cauchy profile with a tabulated width at half-height determined at NIST.[29] Anomalous dispersion corrections were applied to the heavy atoms Ba and Ti.

RESULTS AND DISCUSSION

The preparation of BTO has been the subject of a number of papers. Clabaugh et al.[4] state in their original paper that, when a solution of $BaCl_2$ is added to a solution of $TiCl_4$ and oxalic acid at 80 °C, a precipitate forms immediately which dissolves and reprecipitates as BTO. In this effort, we prepared BTO via reactions of $(NH_4)_2Ti(O)(C_2O_4)_2{\bullet}H_2O$ with barium salts under a variety of conditions, but we encountered difficulty obtaining a precipitate with 1.00:1.00 stoichiometry (i.e., BTO free of other by-products).[32] However, by working at room temperature in dilute solution at pH 0-1.5, we were able to achieve slow crystallization of stoichiometric BTO.

In the method used to grow crystals for this work, a clear solution was obtained when a stoichiometric amount of $Ba(NO_3)_3$ was added to a dilute solution ($<10^{-3}$ M) of ammonium titanyl oxalate as long as the pH was less than 1.5. If the pH was not adjusted by adding acid, a precipitate formed immediately and did not redissolve. X-Ray diffraction patterns of precipitates obtained at pHs of 4-5 indicated the precipitates were amorphous [10]. When the *initial pH* was below 0, crystals of $Ba(NO_3)_2$ were isolated instead of BTO.

Recently, aqueous stability diagrams have been calculated for the Ba-Ti-C_2O_4-H_2O system based

Table I. Crystallographic Data for $Ba_2Ti_2(C_2O_4)_4 \cdot 10H_2O$

empirical formula	$C_8H_{20}Ba_2O_{28}Ti_2$
formula weight	934.65
crystal color, habit	colorless, prism
crystal dimensions (mm)	0.150 × 0.150 × 0.150
crystal system	monoclinic
space group	$P2_1/n$ (No. 14)
lattice parameters	a = 13.367 (1) Å b = 13.852 (1) Å c = 14.023 (1) Å β = 91.61 (2)°
unit cell volume	2595.6 $Å^3$
Z	4
D_{calc}	2.392 g/cm^3
no. of reflections	
measured	6462
unique (R_{int} = 0.081)	6203
observed ($I > 3.00\sigma(I)$)	3883
$2\theta_{max}$	54.9°
R	0.064
R_w	0.069
absorption coefficient	36.9 cm^{-1}

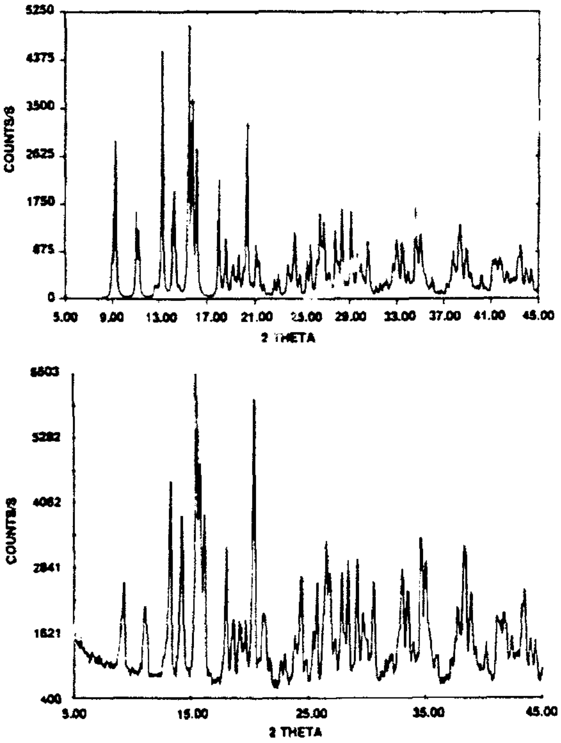

Figure 1. Calculated (a, top) and observed (b, bottom) powder X-ray patterns for BTO.

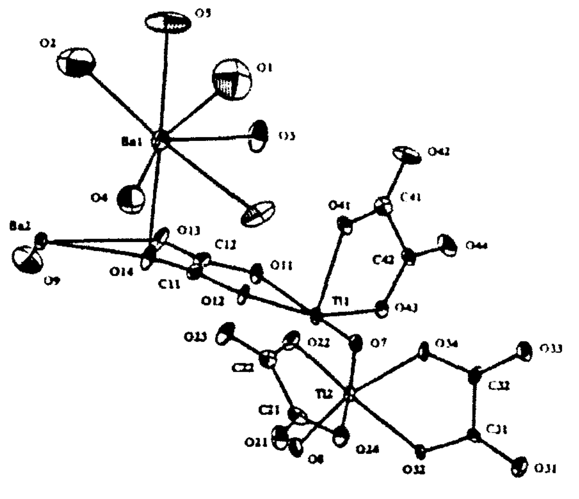

Figure 2. Asymmetric unit of BTO; O(10), O(101), and O(102) occupy intersititial position in the unit cell and are not shown.

on thermodynamic modeling. According to this work, BTO is thermodynamically unstable relative to titanium oxide or hydrous oxide, especially at low ($<10^{-2}$ M) metal ion concentrations; its existence is suggested to be due to complexation with chloride ion or to its precipitation as a metastable phase.[21] The fact that the crystals of BTO grew slowly out of solution over several months suggests that BTO is a thermodynamically stable compound. The results suggest that the precipitate which initially forms, as observed in this work and reported by Clabaugh et al.[4], is the kinetically controlled product and dissolves under acidic conditions (pHs less than 1.5). From our results,[32] the products isolated immediately after combining reagents are titanium-rich. Similar results have been reported by Orlyanski,[7] and most successful preparations use a 1-5% excess of barium in the solutions.[4,8]

Calculated X-Ray Powder Diffraction of BTO: X-Ray diffraction from single crystals showed that BTO crystallizes in the monoclinic space group $P2_1/n$. The crystal data are listed in Table I. The calculated powder diffraction pattern of $BaTi(O)(C_2O_4)_2 \cdot 5H_2O$ for $5° < 2\theta < 40°$, based on the single crystal data (Table I), is shown in Figure 1, along with the observed pattern for crushed crystals of $BaTi(O)(C_2O_4)_2 \cdot 4.5H_2O$ dispersed on silicon grease. The calculated diffraction pattern is in excellent agreement with the observed pattern, and it is quite similar to patterns published by Kudaka et al.[8] and Louër et al.,[18] although some differences in relative intensities are noted, perhaps due to slight deviations from stoichiometry or to varying degrees of hydration between samples prepared under different conditions. The calculated and observed data for $BaTi(O)(C_2O_4)_2 \cdot 4.5H_2O$ and the calculated data for $BaTi(O)(C_2O_4)_2 \cdot 5H_2O$, including d spacings, 2θ, intensity, and hkl values, are tabulated for $2\theta < 40°$ in Table II. The cell constants determined from the single crystal X-ray diffraction results and the calculated powder pattern are in good agreement with those reported by Louër *et al.* except for the assignments for the a and c axis which have been reversed. Since Louër *et al.* prepared their sample by Clabaugh *et al.'s* method and our crystals were grown at room temperature, the temperature of the reaction does not appear to affect the cell constants and,

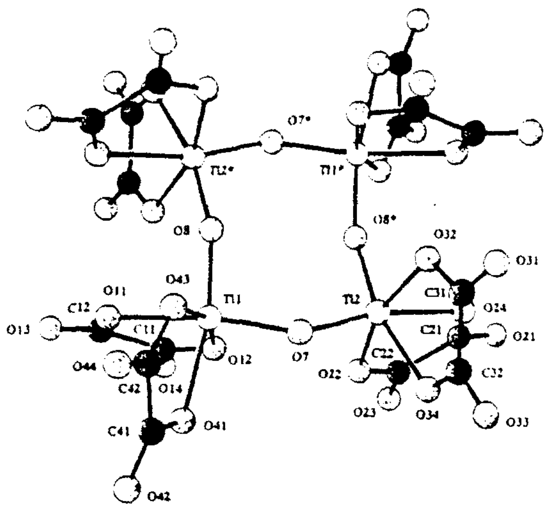

Figure 3. $[Ti(O)(C_2O_4)_2]_4^{8-}$ eight membered ring component of BTO.

therefore, the structure or stoichiometry of the oxalate. Also, no significant effect due to the degree of hydration was observed in the calculated intensities.

Crystal Structure of BTO: Positional and isotropic thermal parameters are given in Table III, and intramolecular bond distances and bond angles are given in Table IV and V, respectively. In order to account for the number of unique atoms in the structure, BTO is formulated as $Ba_2Ti_2O_4(C_2O_4)_4 \cdot 10H_2O$; an ORTEP diagram of the asymmetric unit is shown in Figure 2. The overall structure of BTO is rather complex and not easily viewed in its entirety. The $[Ti(O)(C_2O_4)_2]_4^{-8}$ anions contain eight-membered Ti-O rings composed of two pairs of non-equivalent $Ti(O)(C_2O_4)_2^{-2}$ moieties which are related by an inversion center (Fig. 3).

The Ti-O eight-membered ring observed in BTO is typical of the structures of many titanyl compounds; in fact, very similar $[Ti(O)(C_2O_4)_2]_4^{-8}$ anions are found in the closely related compounds $(NH_4)_2Ti(O)(C_2O_4)_2 \cdot H_2O$[33] and $K_2Ti(O)(C_2O_4)_2 \cdot 2.25H_2O$.[34] Some other examples of titanyl compounds with Ti-O ring structures include $[TiO(acac)_2]_2$,[35] $Cs_4[Ti_4O_4(C_6H_6NO_6)_4] \cdot 6H_2O$ ($C_6H_6NO_6$ = nitrilotriacetic acid),[36] and $[CpTiOCl]_4$.[37] The compounds $[CpTiOCl]_4$ and $Cs_4[Ti_4O_4(C_6H_6NO_6)_4] \cdot 6H_2O$ are tetrameric titanyl compounds with eight-membered Ti-O rings similar to those found in BTO. All of the tetramers except $[CpTiOCl]_4$ have C_i symmetry and exist in the chair form. The $[CpTiOCl]_4$ complex, on the other hand, has D_2 symmetry and exists in a form that the authors describe as two butterfly wings, which could be referred to as the boat form of the eight-membered ring (all four Ti atoms lie on the same side of the plane defined by the four oxygen atoms). $[TiO(acac)_2]_2$ is a dimer with octahedral coordination about the Ti atoms and four-membered Ti-O rings composed of edge-shared octahedra.[37]

The rings in these compounds consist of alternating long and short Ti-O bonds and are presumably the result of oligomerization of Ti=O bonds to form compounds with Ti=O→Ti bonds. In BTO the differences between the long and short distances are less than observed for the ammonium, potassium, and cesium compounds (Table VI), and they are almost equivalent [i.e., 1.81(1), 1.802(8), 1.809(8), 1.799(9)], which suggests complete delocalization to form Ti—O—Ti bonds rather than unequal Ti=O→Ti bonds. Isolated Ti=O bonds have only been observed in a few sterically hindered compounds;[38,39] the majority of titanyl compounds undergo oligomerization to form species with rings composed of Ti=O→Ti bonds.

The Ti-O bond distances in different titanyl compounds serve as a measure of the degree of delocalization of the Ti=O bonding electrons in the ring compounds. Although Ti=O bond distances of 1.62-1.66 Å are observed for sterically hindered monomeric titanyl compounds,[38,39] X-ray diffraction structures of a number of titanyl complexes containing Ti-O rings indicate that a Ti-O bond distance of approximately 1.8 Å can be considered "normal" for these compounds (Table VI). The Ti-O bond distance in the ring is 0.18 Å longer than that observed for an isolated Ti=O bond. This difference of 0.18 Å is the expected value, assuming that a Ti=O bond has a bond order of twice a Ti-O bond.[40,41] The Ti-O bond, however, is still shorter than expected for a single Ti-O bond and, as proposed by van de Velde *et al.*,[33] a significant amount of dπ-pπ bonding may be involved in these bonds. All of the tetrameric titanyl compounds are isoelectronic and have 12 bonding electrons.

As van de Velde *et al.* discussed in their paper on the structure of ammonium titanyl oxalate,[33] the bond angles around O7 and O8 help to define the structure of the eight-membered ring in BTO. It can be described as existing in a chair conformation due to the Ti-O-Ti angles of 142.1(5)° around O7 and 156.4(5)° around O8. The four oxygen atoms form a diamond with sides of 2.74 Å and 2.77 Å and angles of 68.8° and 111.1°. The titanium atoms Ti(2) and Ti(2*) lie within this plane of oxygen atoms. As in the ammonium titanyl oxalate,[33] the Ti atoms nearly form a square with sides of 3.415(3)Å and 3.532(3) and angles of 88.7(5)° and 91.2(5)°.

The non-bonding distances listed in Table VII give a good description of the eight-membered rings in various titanyl compounds, and the distances between opposite oxygen or titanium atoms help to illustrate the geometry of the rings. The distances between oxygen atoms in the Cs compound are 3.90 and 4.04 and are the closest to being identical among

Table II. Calculated and Observed *d* Spacings for BTO

2θ(cal)	2θ(obs)	*d*(cal)	*d*(obs)	*I*(cal)[a]	*I*(cal)[b]	*I*(obs)	*hkl*
8.97	8.80	9.853	10.040	16	17	6	0 1 1
9.26	9.30	9.539	9.502	58	63	30	1 0 1
11.04	11.10	8.006	7.964	32	29	23	-1 1 1
11.25	11.35	7.856	7.790	25	25	12	1 1 1
12.62	12.65	7.009	6.992	5	6	6	0 0 2
12.77		6.926		5	5		0 2 0
13.24	13.30	6.681	6.652	91	90	67	2 0 0
14.25	14.30	6.209	6.189	39	41	50	0 2 1
14.71	14.80	6.018	5.981	5	5	4	2 1 0
15.48	15.50	5.719	5.712	100	100	100	-1 1 2
15.78	15.85	5.610	5.587	73	65	73	1 1 2, 1 2 1
16.16	16.20	5.480	5.467	55	54	56	2 1 1
17.99	18.05	4.926	4.911	44	42	44	0 2 2
18.59	18.65	4.769	4.754	22	2[illegible]	20	2 0 2
19.18	19.15	4.624	4.631	13	12	17	-2 1 2
19.38		4.577		8	6		-2 2 1
19.62	19.65	4.520	5.514	16	14	19	2 2 1
19.94		4.427		11	10		-1 0 3
20.04	20.35	4.364	4.361	64	58	94	0 1 3, 1 0 3
20.74	20.80	4.280	4.267	6	5	6	-3 0 1
21.08	21.10	4.211	4.207	20	15	20	3 0 1
21.29	21.30	4.170	4.168	14	12	20	1 1 3, -1 3 1
21.72	21.75	4.089	4.083	5	4	3	-3 1 1
22.19		4.003		2	1		-2 2 2
22.62	22.65	3.928	3.923	7	6	7	2 2 2
22.94	23.00	3.873	3.864	9	8	10	0 2 3
23.40	23.40	3.798	3.798	1	1	2	2 3 0
23.73	23.80	3.746	3.736	13	11	15	3 2 0, -1 2 3
23.90		3.720		9	8		-1 3 2
24.36	24.40	3.652	3.645	24	22	35	2 3 1, 2 1 3
24.81	24.80	3.586	3.587	9	7	7	3 1 2
25.40	25.40	3.504	3.504	14	13	17	0 0 4
25.70	25.75	3.463	3.457	20	18	33	0 4 0
26.30	26.20	3.385	3.399	14	13	16	2 2 3
26.49	26.50	3.362	3.361	31	29	45	0 4 1, -1 3 2
26.85	26.85	3.318	3.318	28	25	35	2 2 3, 2 3 2
27.29	27.30	3.266	3.264	9	8	13	-1 4 1, -3 0 2
27.82	27.85	3.202	3.201	25	21	35	-1 3 3, 3 3 0
28.04		3.180		14	12		3 0 3, 1 3 3
28.35	28.40	3.145	3.140	33	30	38	4 1 1, -2 0 4
28.79	28.75	3.099	3.103	6	5	2	3 1 3
29.14	29.15	3.062	3.061	32	29	39	-1 2 4, -2 1 4
29.64	29.65	3.011	3.011	17	14	19	-2 4 1
29.99	30.05	2.978	2.971	13	12	11	-4 1 2
30.20		2.957		8	7		-3 2 3
30.63	30.60	2.916	2.919	21	19	28	4 1 2
31.25		2.860		4	4		-2 2 4
31.60	31.65	2.829	2.825	6	5	3	-2 4 2
31.91		2.802		5	5		2 4 2, 2 2 4
32.15	32.15	2.782	2.782	7	6	3	0 4 3
32.69	32.65	2.737	2.740	13	12	9	-3 1 4, 4 2 2
32.99	33.00	2.713	2.712	22	21	31	1 5 0, 1 4 3
33.45	33.45	2.677	2.677	21	19	23	1 1 5
33.95	33.95	2.639	2.639	10	9	6	-5 0 1
34.31		2.612		6	6		5 0 1
34.61	34.65	2.590	2.587	35	32	42	-3 2 4, -5 1 1
35.00	35.05	2.562	2.558	26	25	35	-3 4 2, -4 2 3
35.38	35.45	2.535	2.530	9	8	9	-1 5 2
35.99	36.00	2.493	2.493	7	7	5	5 2 0
36.41		2.466		2	2		-5 2 1
36.75		2.444		3	2		5 2 1
37.22	37.20	2.414	2.415	5	5	6	1 4 4
37.81	37.70	2.378	2.384	18	15	25	-4 4 1
38.44	38.40	2.340	2.313	27	25	45	1 5 3, 3 4 3
38.88	38.90	2.314	2.313	19	17	30	3 5 1, -5 1 3
39.27	39.30	2.292	2.290	9	8	11	5 0 3, -5 3 1
39.62	39.55	2.273	2.277	4	3	4	5 3 1

[a] Calculated intensities for $BaTi(O)(C_2O_4)_2\cdot 5H_2O$. [b] Calculated intensities for $BaTi(O)(C_2O_4)_2\cdot 4.5H_2O$.

Table III. Positional and Isotropic Thermal Parameters for BTO

atom	x	y	z	B(eq)
Ba(1)	0.03349 (6)	0.06976 (6)	0.23622 (6)	1.97 (3)
Ba(2)	-0.03464 (6)	0.33780 (6)	0.04450 (5)	1.42 (3)
Ti(1)	-0.1273 (2)	0.3772 (2)	0.4723 (1)	1.22 (9)
Ti(2)	0.0820 (2)	0.3889 (2)	0.6171 (1)	1.24 (9)
O(1)	0.078 (1)	-0.090 (1)	0.351 (1)	8.0 (1)
O(2)	0.116 (1)	-0.063 (1)	0.109	8.0 (1)
O(3)	-0.1474 (7)	0.1064 (9)	0.3291 (7)	3.3 (5)
O(4)	0.2452 (9)	0.082 (1)	0.2744 (8)	4.3 (6)
O(5)	-0.0922 (9)	-0.072 (1)	0.178 (1)	6.3 (8)
O(6)	0.064 (1)	0.134 (1)	0.4196 (9)	4.9 (7)
O(7)	-0.0434 (6)	0.3609 (6)	0.5738 (5)	1.3 (3)
O(8)	0.1061 (6)	0.4956 (7)	0.5482 (6)	1.8 (4)
O(9)	-0.1965 (8)	0.4585 (8)	-0.0263 (9)	4.0 (6)
O(10)	0.673 (1)	0.073 (1)	0.829 (1)	8.0 (1)
O(11)	-0.2058 (6)	0.3730 (6)	0.3399 (6)	1.7 (4)
O(12)	-0.0255 (6)	0.3255 (7)	0.3842 (5)	1.5 (3)
O(13)	-0.1847 (6)	0.3507 (8)	0.1837 (6)	2.3 (4)
O(14)	0.0099 (7)	0.2887 (7)	0.2355 (6)	2.3 (4)
O(21)	0.3854 (6)	0.3479 (7)	0.6141 (6)	2.3 (4)
O(22)	0.1432 (6)	0.2957 (7)	0.5299 (6)	1.8 (4)
O(23)	0.2878 (7)	0.2424 (7)	0.4713 (6)	2.1 (4)
O(24)	0.2330 (6)	0.3907 (7)	0.6626 (6)	1.9 (4)
O(31)	0.0127 (7)	0.4664 (7)	0.8867 (6)	2.4 (4)
O(32)	0.0511 (6)	0.4698 (6)	0.7333 (6)	1.5 (4)
O(33)	0.0157 (8)	0.2626 (7)	0.8699 (6)	2.7 (5)
O(34)	0.0685 (7)	0.2858 (6)	0.7231 (6)	1.6 (4)
O(41)	-0.185[illegible] (6)	0.2343 (7)	0.4799 (6)	1.7 (4)
O(42)	-0.324[illegible] (7)	0.1540 (8)	0.5165 (8)	3.1 (5)
O(43)	-0.2585 (6)	0.3975 (6)	0.5343 (6)	1.7 (4)
O(44)	-0.4009 (6)	0.3274 (8)	0.5779 (7)	2.5 (4)
O(101)	0.637 (1)	0.425 (1)	0.091 (1)	7.0 (1)
O(102)	0.787 (2)	0.222 (1)	0.735 (1)	10.0 (1)
C(11)	-0.0482 (9)	0.320 (1)	0.2946 (9)	1.6 (5)
C(12)	-0.1552 (8)	0.35[illegible] (1)	0.2677 (9)	1.5 (5)
C(21)	0.2934 (9)	0.348 (1)	0.608 (1)	1.7 (5)
C(22)	0.240 (1)	0.291 (1)	0.5285 (9)	1.6 (5)
C(31)	0.0328 (9)	0.4245 (9)	0.8112 (8)	1.3 (5)
C(32)	0.040 (1)	0.317 (1)	0.8027 (8)	1.7 (5)
C(41)	-0.273 (1)	0.227 (1)	0.5094 (9)	1.7 (5)
C(42)	-0.3168 (8)	0.324 (1)	0.5458 (8)	1.5 (5)

Table IV. Bond Distances (Å) between Non-Hydrogen Atoms in BTO

atom	atom	dist	atom	atom	dist
Ba(1)	O(1)	2.79 (2)	Ti(2)	O(8)	1.799 (9)
Ba(1)	O(2)	2.80 (1)	Ti(2)	O(22)	1.971 (9)
Ba(1)	O(3)	2.824 (9)	Ti(2)	O(24)	2.101 (9)
Ba(1)	O(4)	2.87 (1)	Ti(2)	O(32)	2.030 (8)
Ba(1)	O(5)	2.69 (1)	Ti(2)	O(34)	2.073 (8)
Ba(1)	O(6)	2.74 (1)	O(11)	C(12)	1.27 (1)
Ba(1)	O(14)	3.05 (1)	O(12)	C(11)	1.29 (1)
Ba(1)	O(21)	2.822 (9)	O(13)	C(12)	1.23 (1)
Ba(1)	O(44)	2.80 (1)	O(14)	C(11)	1.23 (1)
Ba(2)	O(9)	2.89 (1)	O(21)	C(21)	1.23 (1)
Ba(2)	O(13)	2.844 (8)	O(22)	C(22)	1.30 (1)
Ba(2)	O(14)	2.811 (9)	O(23)	C(22)	1.24 (1)
Ba(2)	O(21)	2.96 (1)	O(24)	C(21)	1.28 (1)
Ba(2)	O(23)	2.790 (9)	O(31)	C(31)	1.24 (1)
Ba(2)	O(31)	2.923 (9)	O(32)	C(31)	1.29 (1)
Ba(2)	O(31)	2.891 (9)	O(33)	C(32)	1.25 (1)
Ba(2)	O(33)	2.761 (9)	O(34)	C(32)	1.27 (1)
Ba(2)	O(42)	2.85 (1)	O(41)	C(41)	1.27 (1)
Ba(2)	O(44)	2.93 (1)	O(42)	C(41)	1.23 (2)
Ti(1)	O(7)	1.802 (8)	O(43)	C(42)	1.30 (1)
Ti(1)	O(8)	1.81 (1)	O(44)	C(42)	1.22 (1)
Ti(1)	O(11)	2.107 (9)	C(11)	C(12)	1.53 (2)
Ti(1)	O(12)	1.997 (8)	C(21)	C(22)	1.53 (2)
Ti(1)	O(41)	2.131 (9)	C(31)	C(32)	1.50 (2)
Ti(1)	O(43)	1.999 (8)	C(41)	C(42)	1.56 (2)
Ti(2)	O(7)	1.809 (8)			

Table V. Bond Angles around Ti(1), Ti(2), O(7), and O(8)[a]

atom	atom	atom	angle
O(7)	Ti(1)	O(8)	98.7 (4)
O(7)	Ti(1)	O(11)	167.4 (4)
O(7)	Ti(1)	O(12)	91.3 (3)
O(7)	Ti(1)	O(41)	93.7 (4)
O(7)	Ti(1)	O(43)	102.0 (4)
O(8)	Ti(1)	O(11)	87.9 (4)
O(8)	Ti(1)	O(12)	98.0 (4)
O(8)	Ti(1)	O(41)	166.4 (4)
O(8)	Ti(1)	O(43)	94.3 (4)
O(11)	Ti(1)	O(12)	77.0 (3)
O(11)	Ti(1)	O(41)	81.1 (3)
O(11)	Ti(1)	O(43)	88.1 (3)
O(12)	Ti(1)	O(41)	87.3 (4)
O(12)	Ti(1)	O(43)	160.3 (4)
O(41)	Ti(1)	O(43)	77.5 (3)
O(7)	Ti(2)	O(8)	100.0 (4)
O(7)	Ti(2)	O(22)	92.7 (4)
O(7)	Ti(2)	O(24)	168.1 (4)
O(7)	Ti(2)	O(32)	100.4 (4)
O(7)	Ti(2)	O(34)	89.7 (4)
O(8)	Ti(2)	O(22)	97.0 (4)
O(8)	Ti(2)	O(24)	88.2 (4)
O(8)	Ti(2)	O(32)	91.2 (4)
O(8)	Ti(2)	O(34)	166.2 (4)
O(22)	Ti(2)	O(24)	77.6 (3)
O(22)	Ti(2)	O(32)	163.1 (4)
O(22)	Ti(2)	O(34)	92.3 (4)
O(24)	Ti(2)	O(32)	88.0 (3)
O(24)	Ti(2)	O(34)	83.8 (4)
O(32)	Ti(2)	O(34)	77.3 (3)
Ti(1)	O(7)	Ti(2)	142.1 (5)
Ti(1)	O(8)	Ti(2)	156.4 (5)

[a] Angles are in degrees. Estimated standard deviations in the least significant figure are given in parentheses.

the known tetrameric titanyl compounds. It is interesting that the Ti-O distances in this Cs complex are the most unequal (1.74 and 1.91) [36]. The O1-O1* and O2-O2* distances in BTO are the most dissimilar, being 4.54 and 3.11, and the Ti-O distances are the closest to being the same in this titanyl oxalate. The differences in bond distances between complexes indicate that the eight-membered ring is easily distorted and is flexible enough to accommodate various cations.

The octahedral coordination around the Ti atoms in BTO is distorted, and it is similar to the geometry observed for the ammonium and potassium titanyl oxalates.[33,34] The O-Ti-O angles range from 77° to 100°, and Ti(1) is most coplanar with oxygen atoms O12, O11, O7, and O43 (the sum of equatorial angles is 358.4°). Ti(2) is most coplanar with oxygen atoms O22, O32, O24 and O7 (the sum of equatorial angles is 358.7°). As in the other structures which have a Ti-O eight-membered ring, the Ti-O bond lengths exhibit the *trans* effect. The Ti-O bonds *trans* to the titanyl-O bond are always longer [2.107(9), 2.101(9), 2.073(8), and 2.131(9) Å] than the other Ti-O bonds [1.971(9), 1.997(8), 2.030(8), and 1.997(8) Å]. The average Ti-O oxalate distance is 2.050(9) Å. The average Ti-O bond *trans* to the titanyl oxygen is 2.103(9), and the average Ti-O bond length *cis* to the titanyl oxygens is 1.998(8). However, the average Ti-O bond distance for Ti(1) is

Table VI. Ti-O Bond Distances and Ti-O-Ti Bond Angles in Titanyl Complexes

	Ti–O bond distances				bond angles			
					TiOTi	OTiO	TiOTi	OTiO
$(NH_4)_2TiO(Ox)_2$[33]	1.840 (7)	1.788 (8)	1.855 (6)	1.785 (7)	152.1 (5)	96.4 (3)	139.2 (4)	96.8 (3)
$K_2TiO(Ox)_2$[34]	1.820	1.788	1.839	1.790	165.5	98	148.4	98.5
CsTiO(NTA)[36]	1.88 (1)	1.78 (1)	1.91 (1)	1.76 (1)	169.8 (6)	100.1 (6)	148.8 (6)	100.1 (6)
CsTiO(NTA)[36]	1.91 (1)	1.74 (1)	1.90 (1)	1.74 (1)	168.5 (6)	101.3 (6)	161.9 (6)	100.7 (6)
$BaTiO(Ox)_2$	1.81 (1)	1.802 (8)	1.809 (8)	1.799 (9)	156.4 (5)	98.7 (5)	142.1 (5)	100.0 (5)
CpTiO(Cl)[37]	1.797 (1)	1.801 (3)	1.792 (3)	1.800 (1)	169.1 (4)	104.1 (4)	158.2 (2)	102.9 (1)

Table VII

bond	$BaTi(Ox)_2$	$(NH_4)_2Ti(Ox)_2$[33]	$K_2Ti(Ox)_2$[34]	CsTiO(NTA)[36]	CsTiO(NTA)[36]	CpClTiO[37]
Distances between Nonbonding Atoms in Titanyl Complexes						
O1–O2	2.73	2.712 (9)	2.753	2.79	2.79	2.837 (4)
O1–O2*	2.76	2.717 (9)	2.762	2.82	2.82	2.854 (4)
Ti1–Ti2	3.415 (3)	3.411 (2)	3.473	3.63	3.59	3.529 (1)
Ti1–Ti2*	3.532 (3)	3.521 (2)	3.545	3.53	3.63	3.577 (1)
O1–O1*	4.54	4.353 (9)	4.31	4.30	4.04	4.226 (5)
O2–O2*	3.11	3.243 (9)	3.44	3.61	3.90	3.811 (5)
Ti1–Ti1*	4.860 (5)	4.717 (2)	4.83	5.03	5.09	4.959 (1)
Ti2–Ti2*	4.966 (4)	5.080 (2)	5.09	5.11	5.13	4.959 (1)
Bond Angles						
O1–O2–O1*	111.1	106.6 (4)	102.8	100.1	92.0	95.9
O2–O1–O2	68.8	73.4 (3)	77.3	80.0	88.0	83.8
Ti1–O2–Ti2*	156.4 (5)	152.1 (5)	165.5	168.5	169.9	169.1 (1)
Ti1–O1–Ti2	142.1 (5)	139.2 (4)	148.4	148.8	161.9	157.2 (2)

1.974(9) and for Ti(2) is 1.964(9), which are similar to the average Ti-O distance of 1.96 Å found in TiO_2.[42]

The bonding and structure of the eight-membered ring in ammonium titanyl oxalate has been discussed by van de Velde *et al.*[33] who have suggested that in addition to a sigma bond there is dπ-pπ bonding via a two-electron, three-center bond. Petersen[43] and Prout et al.[44] have considered molecular orbital arguments and show that, for compounds such as $[Cp_2L]_2MO$ (M = Ti or Zr), one unfilled hybridized orbital is available to accept electron density from oxygen lone pairs. Consequently, to form the tetramer, each titanium atom must have two empty orbitals available for bonding with two oxo oxygens. Of the nine hybrid orbitals on each Ti atom, [illegible] are involved in sigma bonding with the four oxalate ions and the two bridging oxo groups. Thus, three metal orbitals remain per Ti atom to accept π electron density.

Degree of Hydration of BTO: The crystal structure of BTO reveals that it crystallizes initially as the pentahydrate at room temperature; therefore, our results support the conclusions of Gopalakrishnamurthy and coworkers[16] who reported that the degree of hydration of BTO prepared by Clabaugh's *et al.*[4] method (precipitated at 80°C) varies, depending on the relative humidity of the surrounding atmosphere from 4.5 waters at 50% relative humidity to 4.8 waters at 90% relative humidity. The crystals of BTO used in our study were air dried on a frit at room temperature, and the crystals used for the X-ray structure and the sample submitted for elemental analysis contained nine waters of hydration, reflecting the loss of water at room temperature. Therefore, in the crystal used for the X-ray structure determination, the results indicated the interstitial water sites were only partially occupied. Based on research by Yen *et al.*,[43] removing the waters of crystallization as well as those coordinated to the Ba atoms has very little affect on the diffraction intensities, and since our cell constants are similar to those reported by Louër *et al.*, there is currently no published evidence that the cell constants are affected by water content. In this effort, the effect of water content on the observed cell constants or calculated intensities was not investigated. In addition, the effect of water content on the calculated intensities (Table II) was considered as insignificant.

In the BTO molecule, seven of the ten waters are coordinated to the two barium atoms. As shown in Figure 4, the two non-equivalent Ba atoms, Ba(1) and Ba(2), are bridged by three oxalate oxygens, and the two equivalent Ba(2) atoms are bridged by two oxalate oxygens. Ba(1) is coordinated to six oxygen atoms from water molecules, in addition to three oxalate oxygens, making it nine-coordinate. Ba(2) is ten-coordinate and is associated with one water and nine oxalate oxygens. The average Ba-O bond distances of 2.82(1) Å for Ba(1) and 2.87(1) Å for Ba(2) agree well with the sum of the ionic radii for oxygen and nine- and ten-coordinate barium ions, respectively.[45] The remaining three water molecules per unit cell are defined by oxygen atoms O(10), O(101), and O(102), which are located at interstitial sites in the structure and are not closely associated with the barium or titanium atoms. These interstitial waters are not shown in the ORTEP diagrams. The shortest Ba-Ti distance is 5.841(2) Å, between Ba(1) and Ti(1).

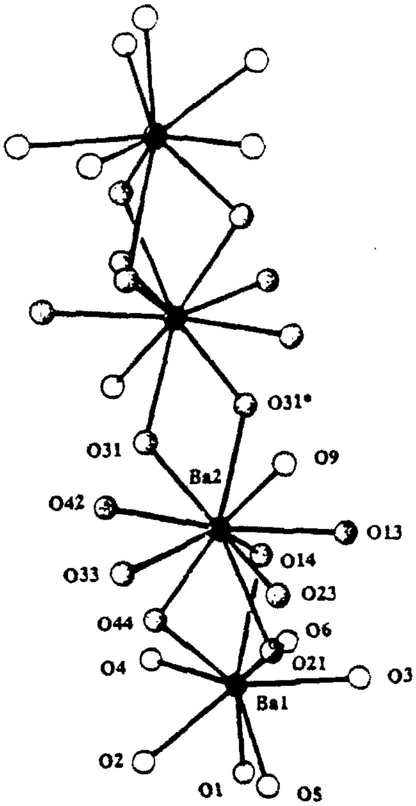

Figure 4. Coordination around the barium atoms in BTO.

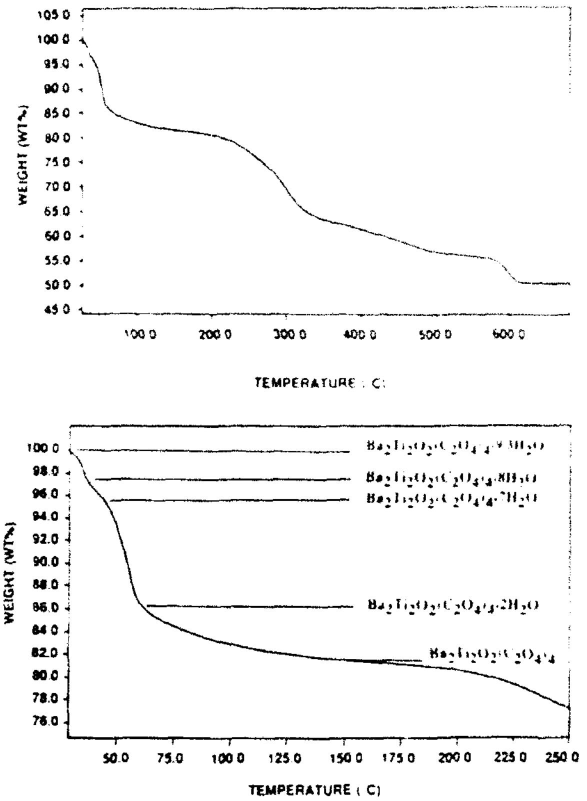

Figure 5. TGA of BTO in air at 0.5 °C/min (a, top) to 650 °C and (b, bottom) to 250 °C.

TGA data on different samples of BTO prepared by the same method in our laboratory usually show between ten and nine waters of hydration at room temperature. Based on the crystal structure data, we would expect the interstitial waters to be the most readily lost. The TGA data in Figure 5 show that 0.7 waters were lost during drying at room temperature, and water loss continued as the temperature was raised above room temperature. At slow heating rates, an additional 1.3 waters were lost below 40 °C and the third water of crystallization was lost by 45 °C. Another five waters were lost by 60 °C, while the two remaining molecules of water were not completely lost until about 150 °C. According to the structure, two of the waters (O5 and O6) bonded to Ba(1) have shorter Ba-O bond distances [2.69(1) and 2.74(1)] than the other coordinated waters [ave. = 2.82(1)]. We assume that these two waters are more strongly bonded and are therefore difficult to remove. Also, Yen et al.[43] have shown that BTO is still crystalline when all the waters but these last two have been removed.

IR Spectra: The IR spectra of BTO agree with the crystal structure and show that it does not contain isolated Ti=O bonds. Titanyl compounds possess a Ti=O stretching frequency in the range of 1050-950 cm^{-1}. This absorption band has been observed for the monomeric compound, (octaethylporphorin)Ti=O,[38] but is not observed in BTO. The IR spectra of ammonium oxalate, ammonium titanyl oxalate (ATO) and BTO are shown in Figure 6. The vibrational frequencies of BTO were observed at

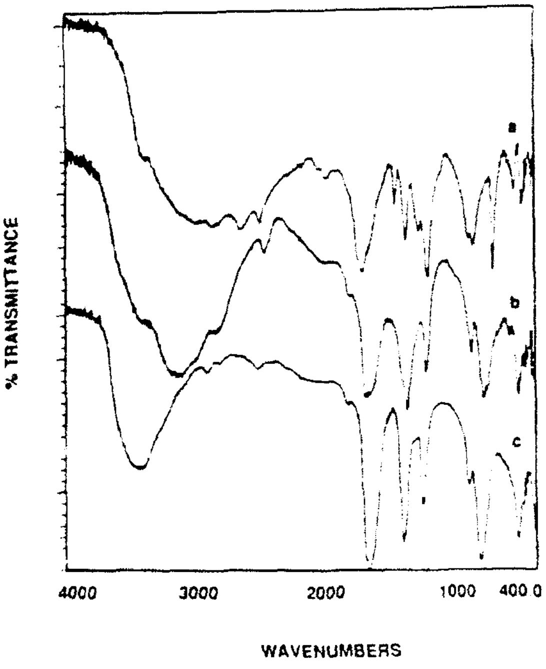

Figure 6. Diffuse reflectance FTIR spectra of (a) ammonium oxalate, (b) ammonium titanyl oxalate, and (c) barium titanyl oxalate.

1705, υ_{as} (C=O); 1424, υ_s (C-O, C-C); 1279, υ_s (C-O) + δ (O-C=O); 910, υ_s (C-O) + δ (O-C=O); and 824 cm^{-1}, δ (O-C=O) + υ (M-O). The IR spectra of the ammonium titanyl oxalate is also shown in Figure 6, and the vibrational frequencies of ammonium titanyl oxalate were observed at 1690, υ_{as} (C=O); 1401, υ_s (C-O, C-C); 1244, υ_s (C-O) + δ (O-C=O); 896, υ_s (C-O) + δ (C-C=O); 880, 778 cm^{-1}, δ (O-C=O) + υ (M-O). The assignments for the IR vibrations are those of Brisse and Haddad.[46] The absorption bands for BTO occur at lower frequencies than the same bands for the ammonium titanyl oxalate. Structurally there is no significant difference in the bond lengths observed for the oxalate groups in BTO and ATO, and the reason for the shift in vibrational frequencies is not clear.

Thermal Decomposition of BTO: The decomposition of BTO has been extensively studied by many different research groups, and the various proposed decomposition schemes have been reviewed.[47] According to the work of Swilam and Gadalla,[48] conversion of BTO to $BaTiO_3$ requires heating 6 h at 600 °C, 1 h at 700 °C and less than 0.5 h at 800-900 °C. Essentially, our results agree with theirs. Although the TGA indicates that decomposition is complete by 700°C at a heating rate of 10 °C/min, we have observed that the decomposition products obtained after heating BTO to 850 °C at 10 °C/min (no hold) contain both phase pure $BaTiO_3$ and a small amount of amorphous material as shown by the broad peak between 15 and 35° in the X-ray diffraction pattern shown in Figure 7. Heating to 900 °C at 10 °C/min (no hold) resulted in complete conversion to barium titanate. TEM micrographs of the products also showed that some amorphous particles were present in the product heated to 850 °C, but only crystalline particles were observed in the product heated to 900 °C.

Gopalakrishnamurthy *et al.*[16] have proposed that the decomposition of BTO proceeds through the following intermediates:

$$Ba_2Ti_2(O)_2(C_2O_4)_4 \rightarrow Ba_2Ti_2(O)_2(C_2O_4)_3CO_3 + CO$$

$$Ba_2Ti_2(O)_2(C_2O_4)_3CO_3 \rightarrow Ba_2Ti_2(O)_5CO_3(CO_2) + 2CO_2 + 3CO$$

$$Ba_2Ti_2(O)_5CO_3(CO_2) \rightarrow Ba_2Ti_2(O)_5CO_3 + CO_2$$

$$Ba_2Ti_2(O)_5CO_3 \rightarrow 2BaTiO_3 + CO_2$$

This proposed mechanism suggests that nonequivalent barium atoms are present in the intermediates. Since the X-ray structure showed that BTO contains two nonequivalent barium atoms, it supports the above mechanism. In the structure of BTO, Ba(1) is 5.84 Å from Ti(1) and 6.95 Å from Ti(2), while Ba(2) is almost equidistant from Ti(1) and Ti(2*), 6.18 and 6.12 Å, respectively. Since the barium atoms are different, it is reasonable that any intermediates would retain the basic structure and that the two Ba atoms may interact with CO_2 differently to form the intermediate carbonates. Therefore, $Ba_2Ti_2O_5CO_3$ is a reasonable composition for the decomposition product responsible for the plateau in the TGA between 500 °C at 570 °C. Yen *et al.*[17] have observed broad X-ray diffraction peaks for products heated to 500 °C, indicating some weakly crystalline intermediates, but there is currently no conclusive evidence that complete segregation occurs to form crystalline $BaCO_3$, $BaTi_2O_5$, or TiO_2 during decomposition of BTO, and $BaTiO_3$ is the only crystalline phase observed upon decomposition as indicated by Figure 7.

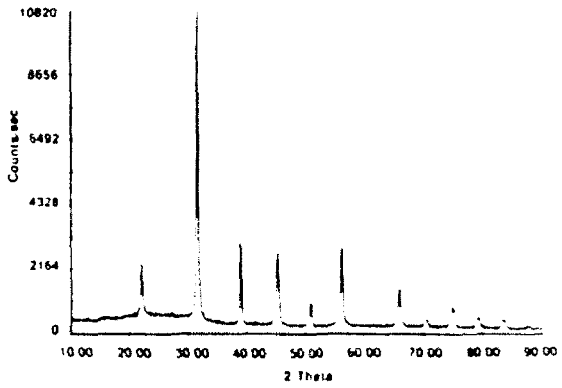

Figure 7. X-ray diffraction pattern of barium titanate obtained for BTO at 850 °C.

Acknowledgements: This work was supported by the Air Force Office of Scientific Research under contract no. F49620-89-C-0102.

REFERENCES

1. See for example: (a) Uchino, K.; Sadanaga, E.; Hirose, T. *J. Am. Ceram. Soc.* 1989, *72*, 1555-1559; (b) Kulcsar, F. *J. Am. Ceram. Soc.* **1956**, *39*, 13-17; (c) Hu, Y.H.; Harmer, M.P. and Smyth, D.M. *J. Am. Ceram. Soc.* **1985**, 372-376; (d) Beauger, A.; Mutin, J.C. and Niepce, J.C. *J. Mater. Sci.* **1984**, *19*, 195-201 and references therein.

2. Pechard, M.E. *Compt. Rend.* **1893**, *116*, 1513-1516.

3. Rosenheim, A. and Schutte, O. *Z. Anorg. Chem.* **1901**, *26*, 239-257.

4. Clabaugh, W.S.; Swiggard, E.M. and Gilchrist, R. *J. Res. Nat. Bur. Stand.* **1956**, *56*, 289-291.

5. Fang, T.-T.; Lin, H.-B. *J. Am. Ceram. Soc.* **1989**, *72*, 1899-1906.

6. Strishkov, B.V.; Lapitskii, A.V. and Vlasov, L.G. *J. Appl. Chem. USSR (Engl. Trans.)* **1960**, *33*, 1986-1990; **1961**, *34*, 646-648; *Zh. Prikl. Khim.* **1960**, *33*, 2009-2014; **1961**, *34*, 673-674.

7. Orlyanskii, Yu.N. *J. Appl. Chem. USSR* **1968**, 44, 1752-1755; *Zh. Prik. Khim.* **1968**, *44*, 1730-1734.

8. Kudaka, K.; Iizumi, K. and Sasaki, K. *Am. Ceram. Soc. Bull.* **1982**, *72*, 1236.

9. Yamamura, H.; Watanabe, A.; Shirasaki, S.; Moriyoshi, Y. and Tanada, M. *Ceram. Int.* **1985**, *11*, 17-22.

10. Rhine, W.E., Saegusa, K., Hallock, R.B., Cima, M.J., "Control of Ceramic Powder Composition by Precipitation Techniques," in *Ceramic Powder Science III Ceramic Transactions*, **1990**, *12*, 107 edited by G.L. Messing, S. Hirano, and H. Hausner, Am. Ceram. Soc. 1990.

11. Pfaff, G.; Schmidt, F.; Ludwig, W. and Feltz, A. *J. Thermal Anal.* **1988**, 771-779.

12. Bhattacharjee, S., Paria, M.K., and Maiti, H.S. *Ceramics Int.* **1990**, *16*, 211-214.

13. Strishkov, B.V.; Lapitskii, A.V.; Vlasov, L.G. and Tsvetkov, A.I. *Dokl. Akad. Nauk SSSR (Engl. Trans.)* **1960**, *133*, 973-975; Russ. orig. 133, 1347-1349.

14. Strizhkov, B.V.; Lapitskii, A.V.; Simanov, Yu.P. and Vlaskov, L.V. *Russ. J. Inorg. Chem.* **1962**, *7*, 1128-1130.

15. Gallager, P.K. and Schrey, F. *J. Am. Ceram. Soc.* **1963**, *46*, 567-573.

16. Gopalakrishnamurthy, H.S.; Subba Rao, M. and Narayanan Kutty, T.R. *J. Inorg. Nucl. Chem.* **1975**, *37*, 891-898; 1875-1878.

17. Yen, F.-U., Chang, C.T., Chang, Y.-H. *J. Am. Ceram. Soc.* **1990**, *73* [11], 3422-27.

18. Louër, D, Boultif, A, Gotor, F.J., and Criado, J.M. *Powder Diffraction* **1990**, 5, 162.

19. Joint Committee on Powder Diffraction Standards, Set 36-682, Philadelphia, PA.

20. Fang, T.-T., Lin, H.-B., and Hwang, J.-B. *J. Am. Ceram. Soc.* **1990**, *73* [11], 3363-3367.

21. Osseo-Asare, K.; Arriagada, F.J. and Adair, J.H. in *Ceramic Trans.* **1988**, *Vol. 1*, 47 Edited by Messing, G.L., Fuller, E. Jr., Hausner, H.; American Ceramic Society: Westerville, OH.

22. Structure solution methods: (a). Calbrese, J.C.; PHASE - Patterson Heavy Atom Solution Extractor. Univ. of Wisconsin-Madison, Ph.D. Thesis (1972). (b). Beurskens, P.T.; DIRDIF: Direct Methods for Difference Structures - an automatic procedure for phase extension and refinement of difference structure factors. Technical Report 1984/1 Crystallography Laboratory, Toernooiveld, 6525 Ed Nijmegen, Netherlands.

23. Least squares function minimized: $\Sigma w (|F_o| - |F_c|)^2$ where $\Sigma w = 4F_o^2 / \sigma^2 (F_o^2)$; $\sigma^2 (F_o^2) = [S^2(C + R^2B) + (pF_o^2)^2] / Lp^2$; S = scan rate; C = total integrated peak count; *R* = ratio of scan time to background counting time; B = total background count; Lp = Lorentz-polarization factor; p = p-factor.

24. Standard deviation of an observation of unit weight: $[\Sigma w(|F_o| - |F_c|)^2 / (N_o - N_v)]^{1/2}$; where N_o = number of observations; N_v = number of variables.

25. Cromer, D.T. and Waber, J.T.; International Tables for X-ray Crystallography, Vol. IV, The Kynoch Press, Birmingham, England, Table 2.2 A (1974).

26. Ibers, J.A. and Hamilton, W.C. *Acta. Cryst.* **1964**, *17*, 781.

27. Cromer, D.T. and Waber, J.T.; International Tables for X-ray Crystallography, Vol. IV, The Kynoch Press, Birmingham, England, Table 2.3.1 (1974).

28. TEXSAN - TEXRAY Structure Analysis Package, Molecular Structure Corporation (1985).

29. Smith, D.K., Nichols, M.C., and Zolensky, M.E. "A Fortran IV Program for Calculating X-ray Powder Diffraction Pattern, Version 10," College of Earth and Mineral Sciences, Pennsylvania State University (1983).

30. Cromer, D.T. and Mann, J.B. *Acta Cryst.* **1968**, *A24*, 321.

31. Cromer, D.T. and Mann, J.B., Los Alamos Scientific Laboratory, LA4403 (1970).

32. Rhine, W.E., Hallock, R.B., Cima, M.J. *Ceramic Transactions* **1992**, *vol. 26*, 8; Edited by Cima, M.J., American Ceramic Society, OH.

33. Van de Velde, G.M.H.; Harkema, S. and Gellings, P.J. *Inorg. Chim. Acta* **1974**, *11*, 243-252.

34. Haddad, M. and Brisse, F. *Can. Mineral.* **1978**, *16*, 379-385.

35. Smith D., Caughlan, C.N., Campbell, J.A. *Inorganic Chem.* **1972**, *11*, 2989.

36. Wieghardt, K., Quiltltzsch, U., Weiss, J., and Nuber, B. *Inorganic Chem.* **1980**, *19*, 2514-2519.

37. Petersen, J.L. *Inorganic Chem.* **1980**, *19*, 181.

38. (a) Guilard R. and Lecomte, C. *Coordination Chemistry Reviews* **1985**, *65*, 87-113; (b) Hill, J., Fanwick, P.E., and Rothwell, I.P. *Inorganic Chem.*, **1989**, *19*, 2514-19.

39. Meyer, J.M. *Inorganic Chem.* **1988**, *27*, 3901 (1988).

40. Pauling, L. *The Nature of the Chemical Bond*, p 228, 240, 256, 3rd Edition, Cornell University Press, Ithaca, NY 1960.

41. Schomaker, V. and Stevenson, D.P. *J. Am. Chem. Soc.* **1941** *63*, 37.

42. Cromer, D.T. and Harrington, K. *J. Am. Chem. Soc.* **1955**, *77*, 4708.

43. Petersen, J.L. *J. Organomet. Chem.*, **1979**, *166*, 179.

44. Prout, K., Cameron, T.S., Critchley, R.A., Denton, B., Rees, G.V. *Acta Crystallogr. Sect. B* **1974**, *30*, 2290.

45. Huheey, J.E. *Inorganic Chemistry*, pp 74, Harper and Roe, NY 1972; Shannon, R.D., and Prewitt, C.T. *Acta Cryst.* **1970**, *B26*, 1076.

46. Brisse, F., and Haddad, M. *Inorganica Chimica Acta*, **1977**, *24*, 173.

47. Sharma, A.K., and Kaushik, N.K., *Thermochemica Acta* **1985**, *83*, 347.

48. Swilam, M.N., and Gadalla, A.M., *Trans. J. Br. Ceram. Soc.* **1975**, *75 [5]*, 159.

SECTION 5

PREPARATION AND CHARACTERIZATION of $Y_3Al_5O_{12}$ (YAG) FROM ALKOXIDE DERIVED POLYMERS

Zhiping Jiang and Wendell E. Rhine
Ceramics Processing Research Laboratory

Presented in part at the 1992 Fall Materials Research Society Meeting, Boston, MA

Abstract

The controlled hydrolysis of Al(O-*sec*-Bu)$_3$ and Y(O-*iso*-Pr)$_3$ or the reaction of Y(OOCCH)$_3$ with partially hydrolyzed Al(O-*sec*-Bu)$_3$ [(HO)$_{0.1}$AlO$_{0.65}$(O-*sec*-Bu)$_{1.6}$] resulted in the formation of soluble polymeric materials. Pyrolysis of these materials under a flow of oxygen led to the formation of yttrium aluminum garnet (YAG) at 650-1500 °C. YAG was the only crystalline phase observed during pyrolysis, and the Al/Y ratio of the pyrolysis products and the starting material were identical. However, infrared spectroscopy indicated that carbonate groups and entrained CO_2 existed in the products at temperatures up to 1250 °C. The pyrolysis chemistry of the precursors and the microstructure of the products were studied by FT-IR, TGA, XRD, SEM and elemental analyses.

Introduction

Yttrium aluminum garnet ($Y_3Al_5O_{12}$, YAG) has interesting structural, electronic and optical properties. Doped single crystals of YAG are widely used in solid-state lasers;[1] doped YAG powders are used as phosphors,[2] and polycrystalline YAG has potential as a high temperature structural ceramic material.[3-5]

An important factor limiting the commercial success of YAG as an engineering material is the availability of pure YAG in various forms (powders, thin films, fibers, etc.) at low processing temperature. Phase-pure YAG has been prepared by hydrothermal[2] or glycothermal[6] reactions at relatively low temperatures (<600 °C) but high pressure conditions. Synthesis of YAG powder by the reaction of mixed aluminum and yttrium oxide powders normally requires temperatures higher than 1600 °C;[7] below that temperature, Al_2O_3 and $YAlO_3$ impurities are present in the products. Chemical methods, such as precipitation of hydroxides from Y and Al alkoxides or Y and Al salts, have led to the formation of YAG powders at 800-1100 °C.[8-11] However, it is still difficult to control the phase purity with these methods, presumably due to the incomplete precipitation of Y and Al components caused by the difference in solubilities of the hydroxides or hydrolysis rates of yttrium and aluminum alkoxides.

Based on the above discussion, it is obvious that the formation of pure YAG at low temperatures requires a precursor with homogeneously mixed Y and Al components. In the present paper, we report the preparation and pyrolysis of two soluble YAG precursors. One of them is derived from the condensation reaction between partially hydrolyzed Al(O-*sec*-Bu)$_3$ [(HO)$_{0.1}$AlO$_{0.65}$(O-*sec*-Bu)$_{1.6}$] and Y(OOCCH$_3$)$_3$ in xylene, and the other one, from the controlled hydrolysis of Al(O-*sec*-Bu)$_3$ and Y(O-*sec*-Pr)$_3$ in toluene. Complete hydrolysis of the former precursor also resulted in a precursor for YAG powder. The pyrolysis chemistry of these precursors and the morphology of the pyrolysis products were studied by FTIR, TGA, XRD, SEM, and elemental analyses.

Experimental Section

General Methods. All the syntheses and manipulations were carried out in a N_2-filled glove box or in Schlenk glassware under N_2, because Al(O-*sec*-Bu)$_3$ and its derivatives are moisture-sensitive. Anhydrous Y(OOCCH$_3$)$_3$ was obtained by heating Y(OOCCH$_3$)$_3$.xH_2O in an oven at 125 °C for 4 h. Al(O-*sec*-Bu)$_3$, Y(O-*iso*-Pr)$_3$, toluene, isopropanol, THF and xylene (AR grade) were used as-received.

Synthesis of a YAG precursor from Y(OOCCH$_3$)$_3$ and Al(O-sec-Bu)$_3$. A solution of 0.165 g of H_2O in 15 mL of THF was slowly dropped into a solution containing 3 g of Al(O-*sec*-Bu)$_3$ and 30 mL of THF (Al:H_2O=1:0.75) at -30 °C, resulting in a colorless solution. The volatile components of the solution were removed at 100 °C under vacuum, leaving a white solid (1.89 g). This solid was redissolved in 120 mL of xylene and mixed with

1.95 g of $Y(OOCCH_3)_3$ (Y:Al=3:5), leaving a white suspension. This suspension, after refluxing under dry N_2 for 3 days, became a clear, light yellow solution. After the volatile components were removed at 140 °C under vacuum, a light yellow solid (**precursor I**) (2.77 g) was obtained.

Synthesis of YAG Powder. The above clear solution (YAG precursor in xylene) was quickly mixed with a solution containing 4 g of H_2O and 20 ml of C_2H_5OH under vigorous stirring (Al:H_2O=1:18), resulting in an instant white precipitate. The suspension was stirred for 0.5 h at room temperature, then the white precipitate was separated by filtration, washed with 25 mL of ethanol and dried at 100 °C for 2 h under reduced pressure, leaving a white powder.

Synthesis of a YAG precursor from Al(O-sec-Bu)$_3$ and Y(O-iso-Pr)$_3$. A solution of 0.447 g of H_2O in 10 mL of isopropanol was slowly dropped into a solution containing 70 mL of toluene, 2.29 g of Y(O-*iso*-Pr)$_3$ and 3.53 g of Al(O-*sec*-Bu)$_3$ at -30 °C (H_2O:Y:Al=8.66:3:5), resulting in a clear, colorless solution. The volatile components of this solution were distilled at 125 °C under vacuum, leaving a light-yellow solid (4.10 g) (**Precursor II**).

Pyrolysis of the YAG Precursors. The pyrolysis experiments were carried out by placing the precursor (0.3-0.6 g) in an alumina boat and loading the boat into a quartz tube (or an alumina tube in the case that the pyrolysis temperature is over 1000 °C) in the glove box. The tube was heated in a furnace under a flow of oxygen or argon (ultra-high purity) at a flow rate of 250 mL/min. The temperature was increased at a heating rate of 200 °C/h, and held at the desired temperature for a period of time (0.5-6 h), and then cooled to room temperature.

Characterization. Diffuse reflectance infrared Fourier transform spectroscopy (DRIFTS) studies were carried out with a Nicolet PC/IR (Model 44) infrared spectrometer. The IR samples for the precursors were prepared by mixing the precursor with dry KBr in glove box. The ground mixture was loaded into the sample cell in the glove box, then it was quickly transferred to the sample chamber of the spectrometer which had been flushed with N_2 for a minimum of 20 min. The IR samples for the pyrolysis products were prepared by a similar procedure except that the grinding and loading were performed in air. Thermal gravimetric analysis of the precursor was performed in a Perkin-Elmer TGA7 thermal analysis system at a heating rate of 10 °C/min. The TGA atmosphere was high-purity air at a flow rate of 250 mL/min. X-Ray powder diffraction (XRD) patterns were measured with a Rigaku 300 diffractometer employing Cu/Kα radiation and a Ni filter at a scanning rate of 10°/min. The X-ray peak assignments were carried out with the JCPDS peak indexing program. The morphology of the pyrolysis products were measured with a Hitachi S-530 scanning electron microscope (SEM). Elemental analyses were obtained from E+R Microanalytical Laboratory, Inc.

Results and Discussion

1. Studies of Precursor I

It is known that metal alkoxides can react with metal acetates by a condensation reaction involving formation of organic esters. This reaction has been used to prepare bimetallic oxide precursors;[14,15] the major advantage of this approach is that the mixing between the two metal components can be controlled at the molecular level. Furthermore, the precursors obtained from this reaction are soluble in common organic solvents, indicating that they have potential for forming coatings, fibers, etc.

The reaction between $Y(OOCCH_3)_3$ and Al(O-*sec*-Bu)$_3$ in hydrocarbon solvent was slow; therefore, a high boiling-point solvent such as xylene was used to increase the reaction rate. The precursor prepared by reacting $Y(OOCCH_3)_3$ with Al(O-*sec*-Bu)$_3$ resulted in an Al-deficient (8.5%) YAG product after pyrolysis, based on the elemental analyses; which was presumably due to the vaporization of unreacted Al(O-sec-Bu)$_3$. To eliminate the loss of Al, we used partially-hydrolyzed Al(O-*sec*-Bu)$_3$ as the starting material for the reaction with $Y(OOCCH_3)_3$, which ensured that no volatile aluminum species remained.

The partially-hydrolyzed aluminum butoxide was prepared by careful hydrolysis of Al(O-*sec*-Bu)$_3$ since it is well known[16] that Al(O-*sec*-Bu)$_3$ is readily hydrolyzed to form a product with a formula of AlO_x(O-*sec*-Bu)$_{3-2x}$, where x is the amount of H_2O (relative to Al) used for the hydrolysis, assuming that the hydrolysis and subsequent condensation reactions are complete. Therefore, the hydrolysis product derived from Al(O-*sec*-Bu)$_3$ and H_2O (Al:H_2O=1:0.75) in the present study should have a formula of $AlO_{0.75}$(O-*sec*-Bu)$_{1.5}$, corresponding to a expected weight loss of 39.6% due to the loss of *sec*-BuOH, which is higher than our observed value of 37.0% indicating that the condensation reactions were not complete and the composition is closer to $(HO)_{0.1}AlO_{0.65}$(O-*sec*-Bu)$_{1.6}$.

This proposed composition agrees with the IR spectrum shown in Figure 1b. The broad absorption band at 3600 cm^{-1} is attributed to the -OH stretching vibrations. The presence of OH groups confirms that the condensation reaction between Al-OH groups during the hydrolysis of Al(O-*sec*-Bu)$_3$ was not complete and supports the suggested compostion for the hydrolysis product.

The reaction between $Y(OOCCH_3)_3$ and $(HO)_{0.1}AlO_{0.65}$(O-*sec*-Bu)$_{1.6}$ resulted in a soluble product after refluxing in xylene for 3 days. Figure 1c shows the IR spectrum of the as-synthesized precursor I, which indicates that both Y-$OOCCH_3$ and Al-O-*sec*-Bu groups remain in the precursor. The acetate groups are represented by the two strong absorption peaks at 1589 and 1452 cm^{-1} (asymmetrical and symmetrical stretching bands of $-COO^{-1}$ groups); the butoxide groups are represented by the absorptions at 2879, 2935 and 2969 cm^{-1} (C-H vibration of O-*sec*-C_4H_9). These assignments are supported by the IR spectra of $Y(OOCCH_3)_3$ (Figure 1a) and $(HO)_{0.1}AlO_{0.65}(O\text{-}sec\text{-}Bu)_{1.6}$ (Figure 1b). The broad absorption bands around 830 and 670 cm^{-1} were attributed to the Al-O-Al and/or Y-O-Al.

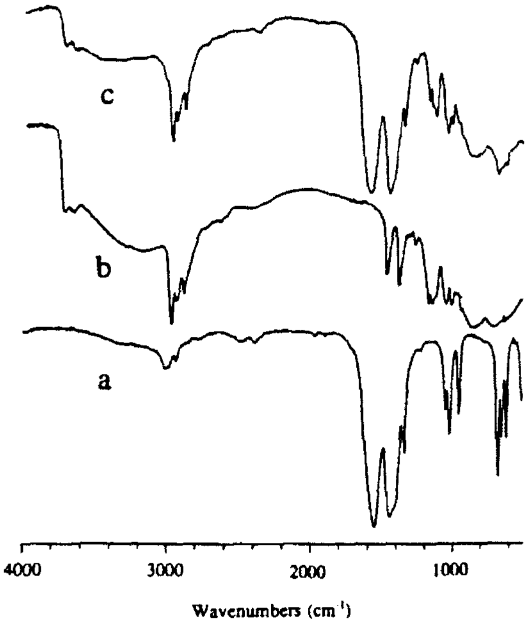

Figure 1. FT-IR spectra of (a) $Y(OOCCH_3)_3$, (b) $(HO)_{0.1}AlO_{0.65}(O\text{-}sec\text{-}Bu)_{1.5}$, and (c) the as-synthesized precursor I.

The condensation of Al-O-*sec*-Bu with Y-$OOCCH_3$ to form Al-O-Y bonds and *sec*-$BuOOCCH_3$ is expected to be the major reaction involved in the above process; therefore, the resulting product should have a formula of $[(HO)_{0.1}AlO_{0.65}(O\text{-}sec\text{-}Bu)_{1.6\text{-}0.6y}]_5[YO_y\,(OOCCH_3)_{3\text{-}y}]_3$, where, y is the amount of reacted $-OOCCH_3$ groups from each mole of $Y(OOCCH_3)_3$. Assuming that 3 equivalents of $Y(OOCCH_3)_3$ were used there are potentially 9y equivalents of *sec*-$BuOOCCH_3$ formed during the condensation reaction. After the condensation reaction and subsequent removal of volatile components, we observed that the product weighed 1.07 g less than the starting materials (based on the starting materials of 1.89 g of $AlO_{0.75}(O\text{-}sec\text{-}Bu)_{1.5}$ and 1.95 g of $Y(OOCCH_3)_3$), that led to a y value of 1.26 and the resulting precursor molecular formula of $[(HO)_{0.1}AlO_{0.65}(O\text{-}sec\text{-}Bu)_{0.84}]_5[YO_{1.26}(OOCCH_3)_{1.74}]_3$ (precursor I). Based on this assumed formula, this precursor should give a pyrolysis yield of 52.1 % when transformed to pure YAG, which is a little higher than the actual pyrolysis yield of 50.1% (Table 1).

Table 1 Pyrolysis Yields obtained from YAG Precursor I[a]

T (°C)	650	780	1000	1250	1500
Yield (%)	53.06	51.83	50.30	50.19	50.10

[a] The precursor was heated in oxygen for 6 h.

The TGA curve (Figure 2) of the as-synthesized precursor I under a flow of air shows a major weight loss around 160-230 °C and 280-410 °C, respectively. The former is attributed to the decomposition of *sec*-BuO- groups and the latter to the decomposition of $-OOCCH_3$ groups; these assignments were confirmed by comparing this TGA curve with those of $Y(OOCCH_3)_3$ and $(HO)_{0.1}AlO_{0.65}(O\text{-}sec\text{-}Bu)_{1.6}$.

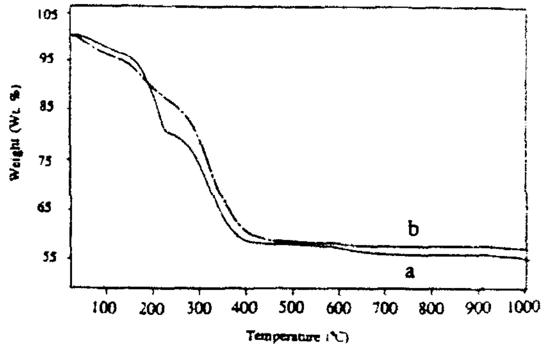

Figure 2. TGA curve of (a) the precursor I under a flow of air and (b) the YAG precursor (II) under a flow of air.

The FT-IR spectrum (Figure 3a) of precursor I heated at 250 °C indicates that the C-H absorptions attributed to the C-H vibration of O-*sec*-Bu groups have almost disappeared. However, the absorption bands due to acetate groups are still evident in the pyrolysis product. After the precursor was heated at 450 °C for 0.5 h, the IR spectrum (Figure 3b) indicated that the acetate groups had decomposed and the major absorption bands observed in the spectrum were attributed to the -OH stretching vibration (the broad band at 3600 cm^{-1}), Al-O-Al and/or Al-O-Y stretching vibrations (the broad peak below 1000 cm^{-1}); as for the strong doublet at 1528 and 1402 cm^{-1}, it was tentatively assigned to the carbonate group since the doublet was in the same region as the absorptions observed for CO_3^{2-} group of $Y_2(CO_3)_3$. These results, which are consistent with the TGA analysis, indicate that most organics in the precursor have disappeared by 450 °C.

The product obtained from heating precursor I to 650 °C in oxygen was a black solid, indicating that carbon was still present in the product. The IR spectrum (Figure 3c) of this product showed strong absorptions around 1527 and 1402 cm^{-1}, which were attributed to the carbonate vibrations; furthermore, a strong, sharp absorption band was observed at 2344 cm^{-1}, which was attributed to the absorption of CO_2 entrained in the solid. Gopalakrishnamurthy *et al.*[17] also observed CO_2 absortion bands in the IR spectra of intermediate decomposition products obtained when $BaTiO(C_2O_4)_2$ was thermally decomposed. They proposed that the retained CO_2 was held in the solid as in clathrates. In this case, CO_2 is probably traped in pores and not in the YAG lattice. The XRD pattern (Figure 4a) of this product showed that the YAG phase had started to crystallize, even though some amorphous material still remained in the product.

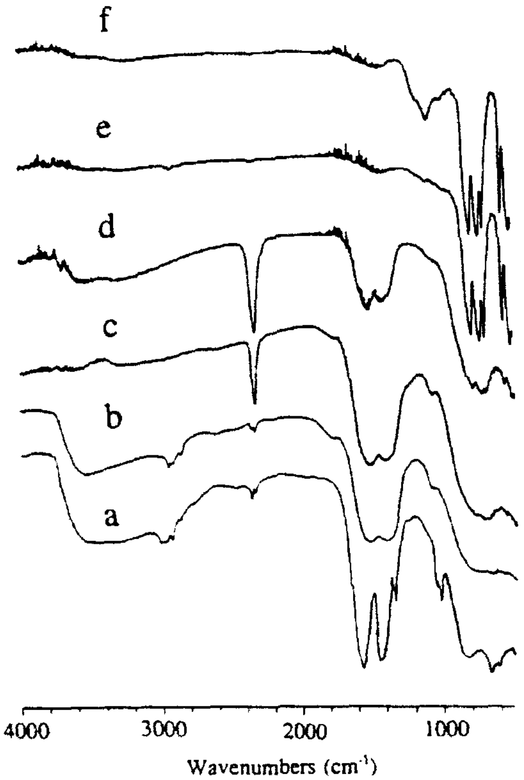

Figure 3. FT-IR spectra of the YAG precursor I heated in oxygen at (a) 250 °C, 0.5 h; (b) 450 °C, 0.5 h; (c) 650 °C, 6 h; (d) 780 °C, 6 h; (e) 1250 °C, 6 h; and (f) 1500 °C, 6 h.

Further heating precursor I in oxygen to 780 °C resulted in the formation of a white solid, indicating that the carbon residue was oxidized between 650 and 780 °C. Oxidation of carbon could be partly responsible for the weight loss observed in the TGA curve at 550-720 °C. The XRD pattern (Figure 4b) of this solid indicated that YAG was the only crystalline phase; however, the IR analysis (Figure 3d) indicated that both carbonate and the CO_2 still remained in the product. This carbonate was thermally stable and still existed in the product after heating to 1000 °C based on the IR analysis. The carbonate absorptions eventually disappeared after the precursor was heated in oxygen at 1250 °C, along with the absortions assigned to entrained CO_2 (Figure 3e).

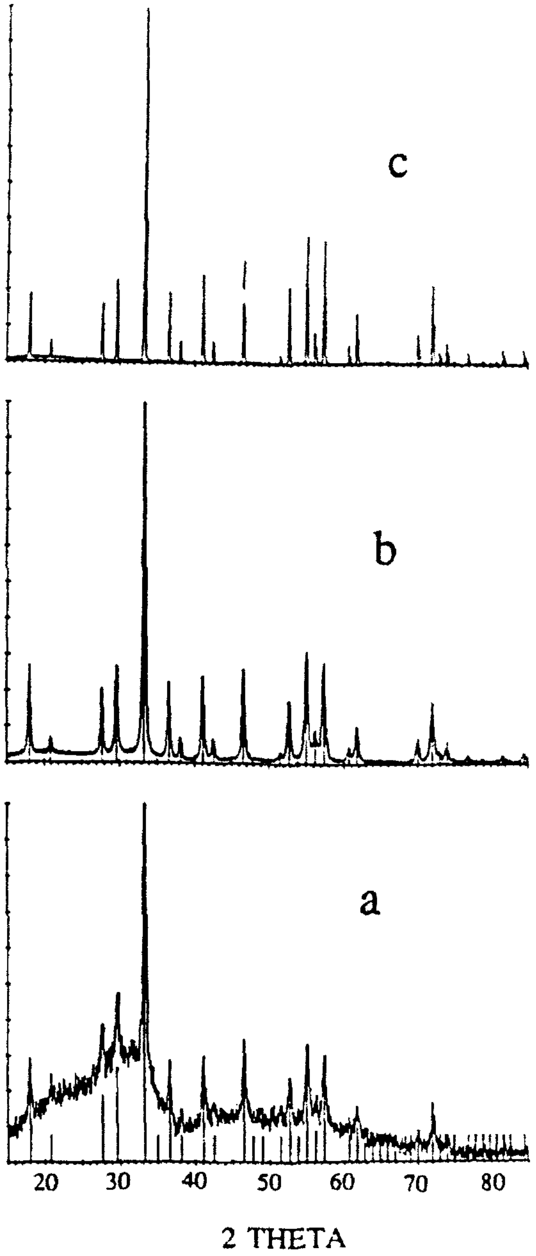

Figure 4. XRD pattern of the YAG precursor I heated in oxygen at (a) 650 °C, 6 h; (b) 780 °C, 6 h; and (c) 1500 °C, 6 h.

We obtained black products after pyrolysis of precursor I under a flow of argon between 650-1000 °C. XRD analyses indicated that YAG was the

Table 2 Elemental Analyses of the Pyrolysis Products#

Precursor	T (℃)	Y	Al	C	H	Y/Al
I	780	42.69	21.97	1.79	0.33	0.590
I	1000	45.21	23.04	0.29	0.12	0.596
I	1500	45.42	23.16	0.19	0.05	0.596
I*	1000	45.93	21.81	0.45	0.10	0.64
I*	1500	45.13	22.82	<0.10	0	0.60
II	1000	44.59	22.60	0.13	0.04	0.599

* Hydrolyzed precursor I

All the pyrolysis products were heated in oxygen for 6 h.

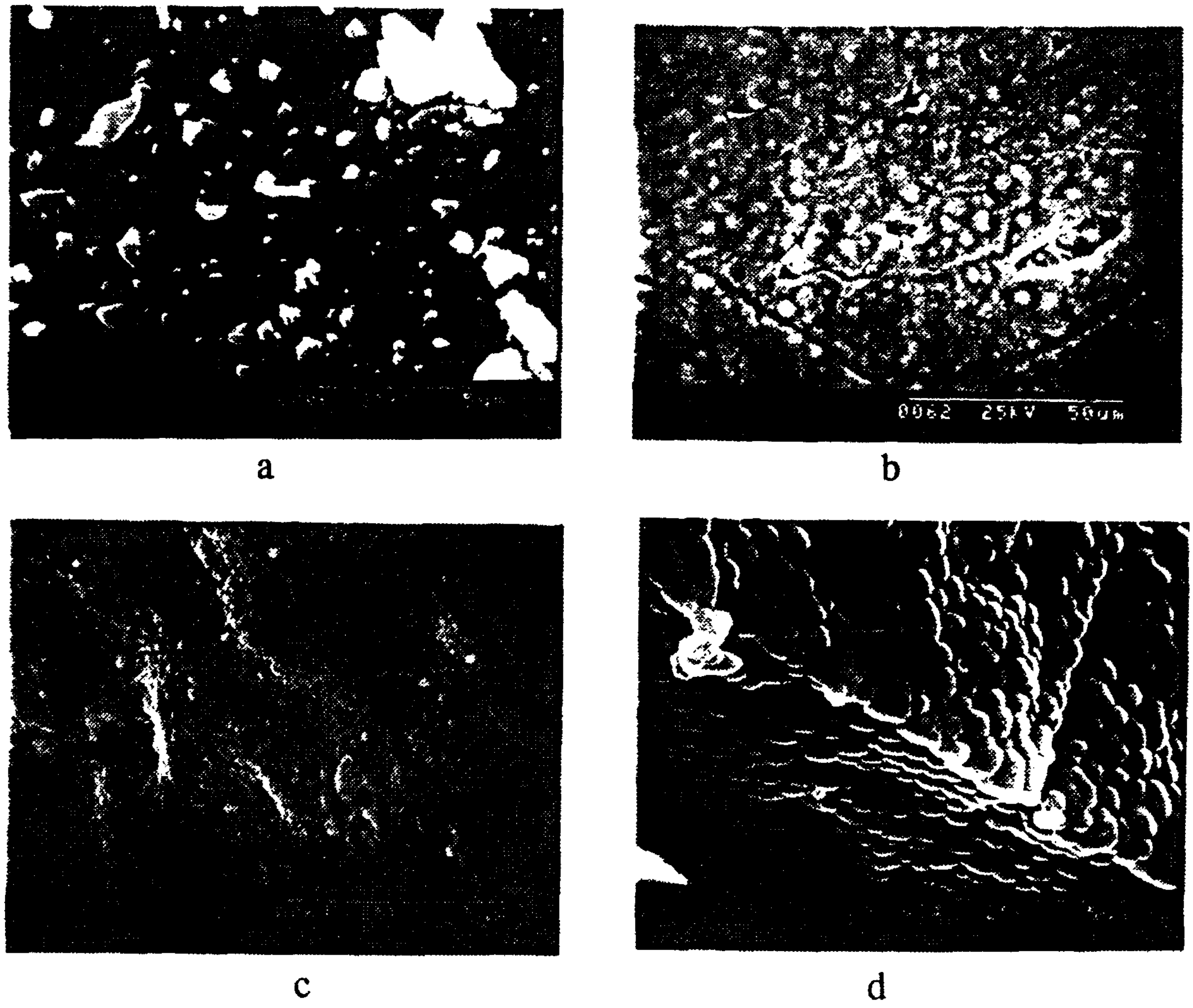

Figure 5. SEM micrograph of the YAG precursor I heated at (a) 1000 ℃, 6 h; (b) polished cross section of the same product at (a); (c) 1250 ℃, 6 h; and (d) 1500 ℃, 6 h.

only crystalline phase in these products. The IR spectra of these products did not indicate the presence of CO_2. The relative intensity of carbonate vibrations in the IR spectra was smaller than for products heated under a flow of oxygen, and in fact, no carbonate absorption bands were observed in the spectrum of the product obtained at 1000 ℃. However, when these products were reheated in oxygen to 1000 ℃ and held for 6 h, a white product (with small amount of black particles) was obtained, and the IR spectra of these products indicated the presence of CO_2 and carbonate.

The above results suggest that the entrained CO_2 is formed by the oxidation of residual carbon in the pyrolysis products. Oxidation probably started above 450 °C since no CO_2 was observed in the IR spectra of products heated in oxygen below that temperature. In addition, one of the formation routes for the carbonate is through the reaction of CO_2 with the oxide. We noticed that both CO_2 and carbonate in the YAG product were thermally stable compared with other Y and Al carbonates; for example, the carbonate present in the Y_2O_3 derived from organometallic complexes disappeared below 700 °C in air.[18] However, it should be pointed out that previous research has not detected the presence of CO_2 in YAG powders which were prepared by precipitation or sol-gel methods and fired in air.[8-13] The presence of CO_2 in the samples prepared for this effort is not completely understood but could be related to firing them in an oxygen atmosphere.

The IR spectrum (Figure 3e) of the product obtained at 1250 °C shows several sharp absorption bands (515, 568, 699, 731 and 792 cm^{-1}) which correspond to the YAG phase.[5] However, the IR spectrum (Figure 3f) of the product obtained at 1500 °C shows a broad absorption band at 1100 cm^{-1} besides the YAG absorptions, even though the XRD pattern of this product indicates that YAG is the only crystalline phase. The reason for the existence of such an extra absorption peak is unknown at present.

Table 1 shows the pyrolysis yields obtained from YAG precursor I, and also indicates there was a weight loss of 2.76% between 650 and 1000 °C but only a 0.2% weight loss between 1000 and 1500 °C. The elemental analyses (Table 2) indicated that there was 1.79% of carbon residue remaining in the product obtained from 780 °C, which decreased to 0.29 and 0.19% at 1000 and 1500 °C, respectively. The Y:Al ratios in all the three products were close to 3:5, indicating that there was no loss of metal components during the pyrolysis.

The products obtained above 780 °C consisted of white, irregular-shaped pieces with a wide range of size distribution (10-400 µm). The SEM micrograph of the particle surfaces after heating at 1000 °C indicates a smooth, dense morphology. However, an SEM micrograph (Figure 5b) of the polished cross section shows that some cracks are present within the particles and some spherical crystallites with sizes of 2-3 µm are dispersed in an apparently amorphous matrix phase. Further heating the precursor to 1250 °C led to porous crystalline particles with grain sizes of 0.2-0.4 µm (Figure 5c). After heating to 1500 °C for 6 h, the particles appear dense and the grain sizes increased to 0.3-1 µm (Figure 5d). Since the spherical particles in figure 5b were 2-3 µm in diameter and are much larger than the grains observed for the products obtained at 1250 and 1500 °C, these spherical particles were probably aggregates of small YAG crystallites. Evidently, YAG completely crystallized and densified while heating to 1250 °C.

*2. **Hydrolysis of Precursor I***

YAG powder was obtained by hydrolyzing precursor I with excess H_2O at room temperature. Figure 6a shows the IR spectrum of the as-synthesized powder, which indicates that nearly all the *sec*-O-C_4H_9 groups have been hydrolyzed; instead, the -OH groups (represented by the broad absorption at 3400 cm^{-1}) are present in the product along with the $OOCCH_3$ groups. Therefore, the precipitate can be described as $Al_5Y_3O_x(OH)_y(OOCCH_3)_z$, where $2x + y + z = 16$.

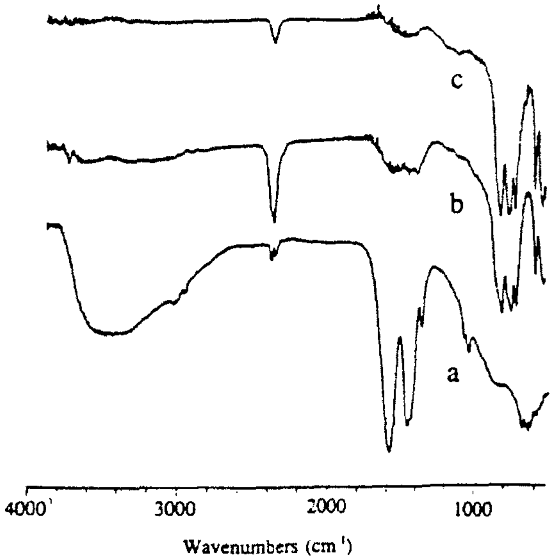

Figure 6. FTIR spectra of the YAG powder precursor II (a) as-synthesized, (b) heated at 1000 °C in oxygen for 6 h, and (c) heated at 1500 °C in oxygen for 6 h.

The SEM micrograph (Figure 7a) of this powder consisted of agglomerated small particles (<0.1 µm). The TGA curve (Figure 2b) of this powder in air shows that the decomposition of all the organic groups was complete by 420 °C and the pyrolysis yield was 57.0% at 1000 °C. Pyrolysis of this precursor at 1000 or 1500 °C in oxygen resulted in a white powder, and the XRD analyses indicated YAG was the only crystalline phase present. However, the IR analyses (Figure 6b and 6c) indicated that the entrained CO_2 was still present after heating to 1500 °C. Furthermore, the carbonate bands were observed in the IR spectra of the product heated to 1000 °C, but absent after heating to 1500 °C. The SEM micrograph (Figure 7b) indicated that the product heated to 1000 °C had a similar morphology to the uncalcined powder (Figure 7a). Further heating to 1500 °C resulted in well-crystallized particles with sizes of 0.3-1 µm (figure 7c), similar to the grain sizes observed in Figure 5c; however, necking between particles is evident. The elemental analyses (Table 2) indicated the products obtained at 1000 and 1500 °C contained 0.45% and 0.10% C, respectively.

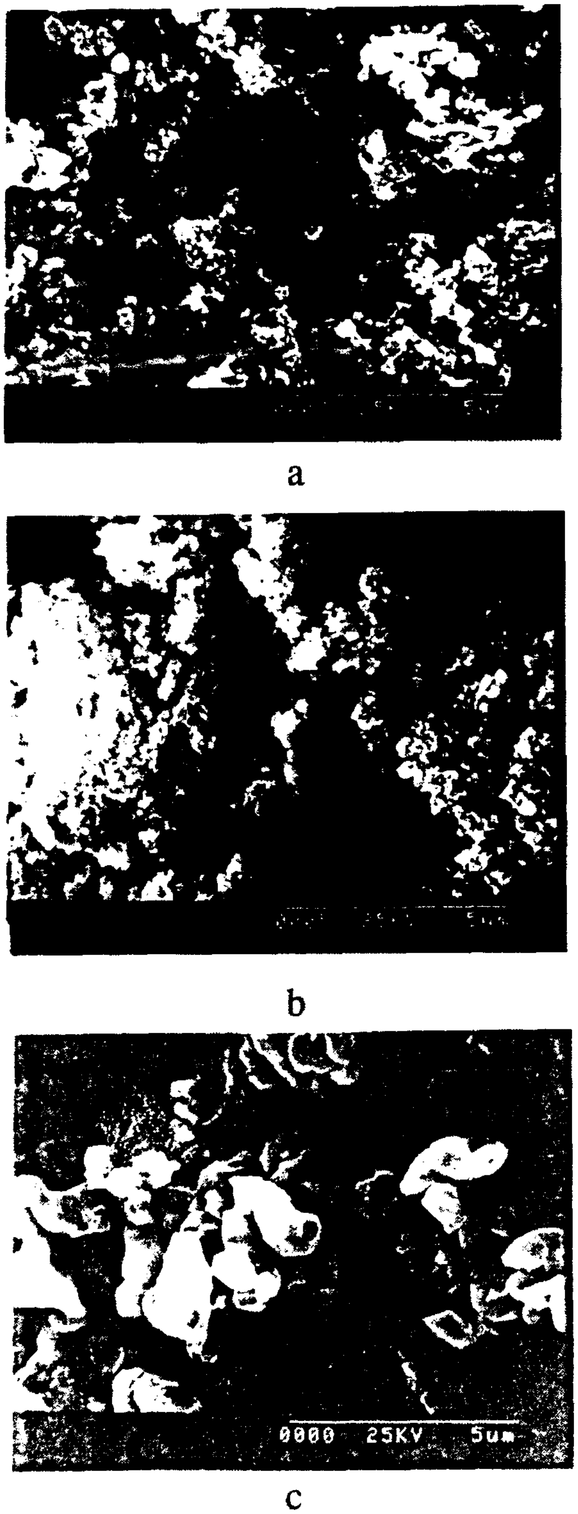

Figure 7. SEM micrograph of the YAG powder (a) the as-synthesized, (b) heated at 1000 °C for 6 h; and (c) heated at 1500 °C for 6 h.

3. Studies of Precursor II

The partial hydrolysis of $Al(O\text{-}sec\text{-}Bu)_3$ and $Y(O\text{-}iso\text{-}Pr)_3$ resulted in a soluble polymeric solid (precursor II). Similar to the $Y(OOCCH_3)_3/(HO)_{0.1}AlO_{0.65}(O\text{-}sec\text{-}Bu)_{1.6}$ system, XRD studies indicated that YAG was the only crystalline phase in the pyrolysis products obtained at 650-1500 °C; furthermore, the elemental analysis (Table 2) of the pyrolysis product heated to 1000 °C in oxygen shows the Y:Al ratio is close to 0.6, which suggested that the controlled partial hydrolysis of $Al(O\text{-}sec\text{-}Bu)_3$ and $Y(O\text{-}iso\text{-}Pr)_3$ has ensured the homogeneity of Al and Y components, as well as eliminated any loss of Al or Y during pyrolysis. The product obtained from heating the precursor in oxygen at 650 °C for 6 h was still black, which indicated that carbon was present in the product. Furthermore, the IR spectrum of this product showed strong absorption bands for carbonate and entrained CO_2, and these bands were also present in the IR spectrum of the product heating to 1000 °C.

In summary, the condensation reaction between $Y(OOCCH_3)_3$ and $(HO)_{0.1}AlO_{0.65}(O\text{-}sec\text{-}Bu)_{1.6}$, or controlled hydrolysis of $Al(O\text{-}sec\text{-}Bu)_3$ and $Y(O\text{-}iso\text{-}Pr)_3$, led to soluble precursors for YAG. The precursors are mixed at the molecular level and have resulted in formation of crystalline of YAG between 650 and 1500 °C. The soluble nature of these precursors in aromatic solvents might be used to prepare YAG coatings by means of solution methods (spin-coating, dip-coating, etc.). However, the high thermal stability of carbonate residue in the products has imposed a challenging issue to obtain carbon-free YAG at low processing temperatures from these precursors.

Acknowledgements

Financial support for this work was provided by the Air Force Office of Scientific Research (AFOSR) under Contract No. F49620-89-C-0102.

Reference

1. K. Washio, *Materials Chemistry and Physics*, 31, 57-66 (1992).

2. T. Takeshi and L.D. David, *Am. Ceram. Soc. Bull.* **65**, 1282-86 (1986).

3. B. Cockayne, *J. Less-Comm. Metal*, **114**, 199-206 (1985).

4. H. Haneda, A. Watanabe, S. Matsuda, T. Sakai, S. Shirasaki and H. Yamamura, " Sintering of Yttrium Aluminum Garnet," p 318 in Sintering 87, Symposium M. Eds. Shimada, M. Yoshimura and R. Watanabe, Elsevier Science Publishers Ltd. Essex, England, 1988.

5. G. de With and H.J.A. van Dijk, *Mat. Res. Bull.*, **19**, 1669-1674 (1984).

6. M. Inoue, H. Otsu, H. Kominami and T. Inui, *J. Am. Cram. Soc.* **77**, 1452-54 (1991).

7. D.R. Messier and G.E. Gazza, *Am. Ceram. Soc. Bull.* **51**, 692 (1972).

8. P. Apte, H. Burke and H. Pickup, *J. Mater. Res.*, **7**, 706-711 (1992).

9. O. Yamaguchi, K. Takeoka and A. Hayashida, *J. Mater. Sci. Lett.*, 101-103 (1991).

10. J. McKittrick, K. Kinsman, S. Connell, K. Sluzky and K. Hesse, "Alkoxide Synthesis of Al_2O_3 and $Y_3Al_5O_{12}$ Powders," Ceramic Transaction Vol 26, M.J. Cima eds., pp. 17-23 (1991).

11. J.W.G.A. Vrolijk, J.W.M.M. Willems and R. Metselaar, *J. Euro. Ceram. Soc.* **6**, 47-51 (1990).

12. G. Gowda, *Mater. Sci. Let.* **5**, 1029 (1986).

13. A. Hardy, G. Gowda, T. McMahon, R. Riman, W.E. Rhine, and H.K. Bowen, p 407 in Ultrastruture Processing of Advanced Ceramics, Eds. J.D. Mackenzie and D.R. Ulrich, John Wiley and Sons, NY, 1988.

14. S.R. Gurkovich and J.B. Blum, p 152-160 in "Ultrastructure Processing of Ceramics, Glass, and Composites" Eds by L.L. Hench and D.R. Ulrich; John Wiley and Sons, NY, 1984.

15. F.G. Sherif, Materials Science and Engineering, **B10**, 59-65 (1991).

16. B.E. Yoldas, *J. Non-Crystalline Solids*, 38, 81 (1980).

17. H.S. Gopalakrishnamurthy, M. Subba Rao and T.R. Narayanan Kutty, *Inorg. Nucl. Chem.* **37**, 891-898 (1975).

18. B. Djuricic, D. Kolar and M. Memic, *J. Euro. Ceram. Soc.* **9**, 75-82 (1992).

SECTION 6

PREPARATION OF ZIRCON AND MULLITE-ZIRCON POWDERS BY SOL-GEL TECHNIQUES

Anne B. Hardy and Wendell E. Rhine

Published in Chemical Processing of Advanced Ceramics, p. 577, Eds. L.L. Hench and J. West, John Wiley and Sons, NY, 1992.

INTRODUCTION

Zircon ($ZrSiO_4$) and mullite ($3Al_2O_3{\cdot}2SiO_2$) are known for their chemical and thermal stability, and both are used extensively in the refractories industry. Mullite is also an important ceramic structural material because of good toughness and strength which are retained at high temperatures. We have begun a study on how the mechanical properties of zircon can be improved. As one approach, we wish to study the properties of high-purity, high-density zircon and, as a second approach, we are interested in investigating the effect of addition of mullite on the mechanical properties of zircon. In preliminary work, we have investigated several chemical methods for preparing zircon, mullite, and zircon/mullite materials.

Both zircon and mullite have been synthesized by sol-gel techniques including both colloidal and polymeric approaches [e.g., 1-14]. Colloidal or diphasic gels are prepared by mixing sols of the individual oxides. Polymeric or single phase gels are typically prepared by gelling a mixture of metal alkoxides or salts and are assumed to be homogeneous, or single phase gels, since the precursors are mixed on the molecular level. Changing the scale of mixing by using colloidal or polymeric gels has been shown to have strong effects on processing conditions, including crystallization temperatures and the sintering behavior. In this paper we compare the densification and crystallization behavior of mullite, zircon, and an equimolar mixture of zircon and mullite ($ZrSiO_4{\cdot}\ 3Al_2O_3{\cdot}\ 2SiO_2$) prepared both colloidally and polymerically.

EXPERIMENTAL PROCEDURE

Mullite, zircon, and mullite-zircon powders were prepared by both colloidal and polymeric routes. Zircon powders were prepared using a polymeric route by dissolving tetraethylorthosilicate (TEOS, Aldrich Chem. Co, Milwaukee, WI) in ethanol (TEOS:ethanol = 1:25 by volume). $ZrOCl_2{\cdot}4H_2O$ (Alfa Products, Danvers, MA) dissolved in ethanol was added to the TEOS solution. The clear solution was stirred for 12 h, and then added dropwise into saturated NH_4OH; a white precipitate formed immediately. Colloidal zircon precursor powders were prepared by mixing stoichiometric amounts of a ZrO_2 sol (ZrO_2 150/20, Nyacol Products Inc., Ashland, MA) and a SiO_2 sol (SiO_2 5050, Nyacol Products Inc., Ashland, MA). An acetone/hexane solution was added to the sol mixtures and the sol rapidly flocced and settled. The powder was recovered by vacuum filtration.

Mullite powders were prepared using a polymeric route by adding TEOS to an ethanol solution containing aqueous HCl (6M; H_2O:TEOS = 1:4 molar). The TEOS solution was refluxed at 60-65°C under N_2 for 1 h, and a solution of aluminum-sec-butoxide in dry isopropanol was then added. Refluxing was continued for 4 h and the clear solution was then added dropwise into concentrated NH_4OH where a white precipitate formed immediately. Colloidal precursor powders were prepared by mixing a boehmite sol (Al20, Nyacol Products Inc., Ashland, MA) and a silica sol (SiO_2 2030, Nyacol Products Inc., Ashland, MA) and floccing the sols by adding acetone. The powder was recovered by filtration.

Equimolar mixtures of mullite and zircon powders were prepared using a polymeric route by dissolving TEOS in ethanol containing aqueous HCl (6M; H_2O: TEOS = 1:4) and refluxing for 1-2 h at 60-65°C. Aluminum-sec-butoxide dissolved in dry isopropanol was added to the partially hydrolyzed TEOS and refluxing continued for 4 h. The solution was then cooled to less than 40°C, and $ZrOCl_2{\cdot}4H_2O$ dissolved in ethanol was added. The clear solution was added to concentrated NH_4OH; a white precipitate formed immediately. Mullite-zircon powders were also prepared by mixing colloidally derived mullite powders and polymerically derived zircon powders with a mortar and pestle.

All powders were calcined at 650°C and then ballmilled for 12 h in isopropanol using ZrO_2 ballmilling media. Pellets were dry pressed at 20.4 ksi and then isostatically pressed at 40 ksi. Samples were heated in air at 10°C/min and held at the final temperature for 2 h. Sintered densities were measured using the Archimedes method. Differential thermal analysis (DTA) and thermal gravimetric analysis (TGA) were performed at a heating rate of 10°C/min (Netzsch, Inc., Exton, PA). X-ray diffraction patterns were measured using a rotating Cu anode (Rigaku RU300, Danvers, MA).

Table 1. Crystalline Composition as a Function of Temperature.

Temperature (°C)	Crystalline Phases
zircon (polymeric)	
1100	tetragonal ZrO_2
1200	zircon (major), cristobalite and ZrO_2 (minor)
1300	zircon
1400	zircon
zircon (colloidal)	
1100	tetragonal ZrO_2
1200	zircon, ZrO_2, cristobalite
1300	zircon, ZrO_2, cristobalite
1400	zircon (major), ZrO_2 and cristobalite (minor)
mullite (polymeric)	
1100	spinel
1350	mullite
mullite (colloidal)	
1200	mullite, cristobalite, and δ-alumina
1300	mullite (major) and cristobalite and α-Al_2O_3
1400	mullite
zircon-mullite (polymeric)	
1100	tetragonal ZrO_2 (major), spinel (minor)
1350	zircon, mullite
1500	zircon, mullite
zircon-mullite (colloidal)	
1100	tetragonal ZrO_2
1200	zircon and mullite (major), cristobalite and ZrO_2 (minor)
1300	zircon, mullite
1400	zircon, mullite

RESULTS AND DISCUSSION

Crystallization behavior of mullite, zircon, and equimolar mixtures of mullite and zircon were determined using DTA and X-ray diffraction. DTA analysis of the polymeric zircon powders (previously calcined to 650°C) showed a single exothermic peak at 980°C. X-ray diffraction results are listed in Table 1 and show that tetragonal zirconia formed first, followed by the formation of zircon between 1100°C and 1200°C. The zircon presumably forms by the reaction of amorphous silica and zirconia. The 980°C exothermic peak was thus attributed to the formation of zirconia. Zircon crystallization apparently does not show a strong DTA peak; this agrees with results reported by Vilmin et al. [1] who found that zircon crystallization cannot be observed by DTA.

Figure 1 compares the X-ray diffraction peaks for the polymerically derived zircon heated to 1200°C and the colloidally derived zircon heated to 1400°C and shows the polymerically derived powder transformed to zircon at a lower temperature than colloidally derived zircon. As shown in Figure 1a, zircon was the major phase at 1200°C for the colloidally derived zircon, but there was still a significant amount of ZrO_2 and cristobalite (SiO_2) present after heating the colloidally derived zircon to 1400°C.

These crystallization results for the polymerically and colloidally derived zircon present an interesting contrast to crystallization results reported by others [1-4]. Table 2 summarizes previously reported zircon crystallization temperatures. Vilmin et al. [1] found that colloidally derived zircon crystallized at lower temperatures than did polymerically derived zircon and attributed it to metastable energy released from the reaction of discrete phases of zirconia and silica. However, we found that in both polymerically and colloidally derived powders, crystalline zircon had formed by 1200°C, and that, in contrast to the work reported by Vilmin et al. [1], the complete transformation to zircon occurred at lower temperatures for the polymerically derived powders. In this work, powders were rapidly precipitated in concentrated NH_4OH. In previous studies, gels were formed by the slow gelation of a precursor sol. It is possible that with slow gelation the zirconia and silica form at different rates and actually segregate within the gel, whereas the rapid precipitation technique we employed gave a more homogeneous mixture of zirconia and silica.

Mullite was also derived from both colloidal and polymeric precursors. DTA analysis for the polymerically derived powder showed two exothermic peaks above 600°C: a peak at 980°C and a peak at 1250°C. Similar DTA results are reported in the literature [8]. When two peaks are present, the 980°C peak is usually attributed to the formation of an aluminum-silicon spinel phase and the 1250°C peak to the crystallization of mullite

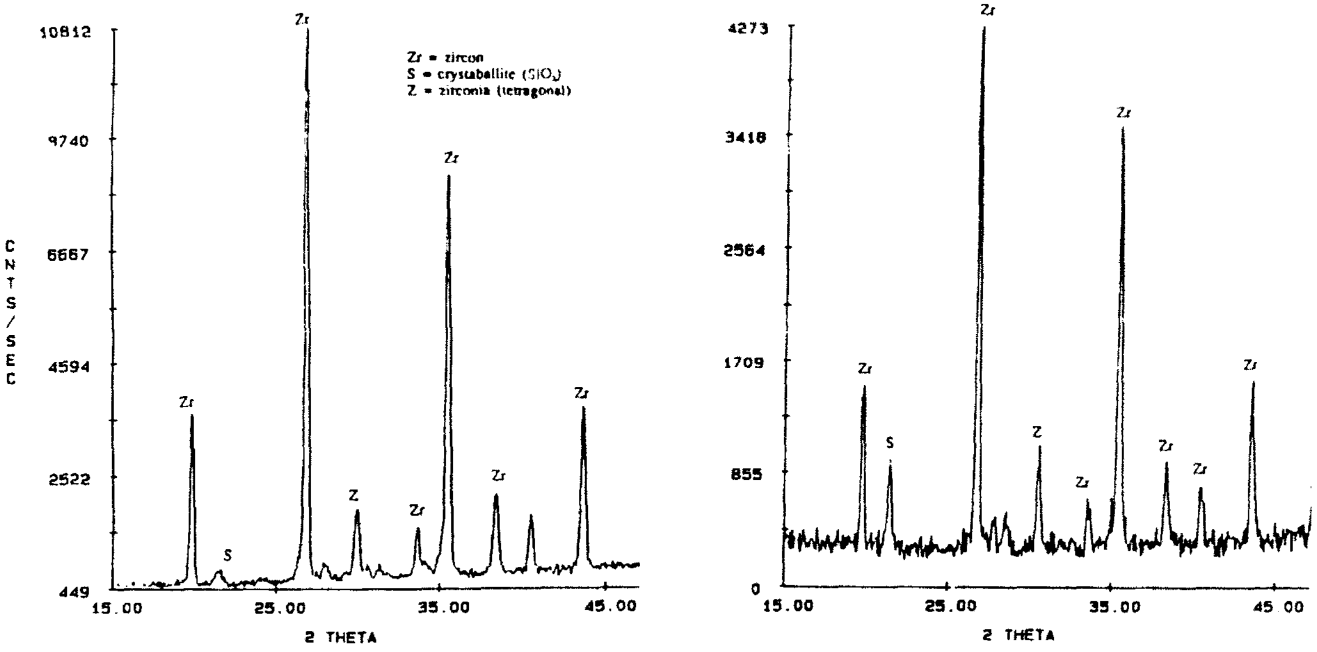

(a) (b)

Fig. 1. X-ray diffraction results for (a) polymerically derived zircon heated to 1200°C and (b) colloidally derived zircon heated to 1400°C.

Table 2. Previously Reported Zircon Crystallization Temperatures.

Precursor	Crystallization Temperature (°C)
SiO_2 and ZrO_2 (sols) [1, 2]	1200
TEOS, $ZrOCl_2$ [1, 2]	1325
TEOS, $ZrOCl_2$ [3]	1425
TEOS, zirconium *n*-propoxide [4]	1600

[8]. DTA analysis of the colloidally derived powder showed only one peak above 600°C, a small exothermic peak at 1340°C. Huling and Messing [12] report a similar single small peak at 1365°C for colloidally derived mullite. The lower crystallization temperatures of polymerically derived powders are assumed to reflect their greater homogeneity although the formation of the spinel phase implies that the powder was not molecularly homogeneous [13]. X-ray diffraction results are summarized in Table 1 and show that crystalline mullite had begun to form after heating colloidally derived samples to 1200°C. Wei and Halloran [10] report formation of mullite (prepared colloidally) at 1200°C, although Huling and Messing [12] did not observe mullite formation until after heating to 1250°C.

Crystallization behavior of colloidally and polymerically derived composite powders was also studied, and both DTA and X-ray diffraction results show that the presence of additional phases did not affect the crystallization sequences or temperatures. Table 1 also summarizes the X-ray diffraction results for the composite materials.

Figure 2 shows the densification behavior of the polymerically and colloidally derived mullite and zircon, and also the densification of the mixed mullite-zircon powders. These results show that both colloidally and polymerically derived zircon, colloidally derived mullite, and the mixture of colloidally derived mullite and polymerically derived zircon densified between 1100°C and 1200°C. The polymerically derived mullite and the polymerically derived mullite-zircon showed little densification even after heating to 1400°C. It has been shown that mullite formed by colloidal methods densifies at ~1100°C by the viscous flow of amorphous silica [14]. Crystalline mullite is then formed by heating to higher temperatures. When mullite is formed from polymeric precursors, crystallization temperatures are lowered such that the material crystallizes at temperatures below the viscous sintering temperature of silica [5-8]. Previous work has shown that in the absence of viscous sintering the mullite must be

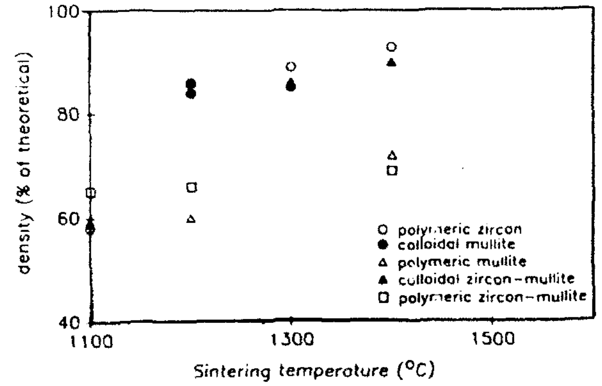

Fig. 2. Density as a function of temperature for polymerically and colloidally derived zircon, mullite and zircon/mullite materials.

heated to temperatures >1600°C or hot pressed to prepare dense materials [6, 7].

Zircon densified by viscous sintering because, even in the polymerically derived zircon, crystallization apparently occurred after the viscous sintering of the amorphous silica. For the polymerically derived zircon-mullite material, the amount of silica remaining after the spinel phase crystallized (980°C) was not enough to promote viscous sintering. To viscous-sinter the composite material it was necessary to use the colloidal mullite precursor combined with the polymeric zircon precursor. This material began to densify between 1100°C and 1200°C and had completely transformed to crystalline zircon and mullite by 1300°C.

Although materials that densified by viscous sintering densified by 1200°C, the final densities of mullite, zircon and the mullite-zircon material were all around 90% of theoretical. The change in density on reacting crystalline ZrO_2 and amorphous silica would give rise to less than 1% porosity; in forming mullite from Al_2O_3 and silica the change in density would account for only about 3% porosity. Scanning electron micrographs confirm that there is still significant internal porosity remaining, as shown in Figure 3.

CONCLUSIONS

Mullite, zircon, and equimolar mixtures of mullite and zircon powders were formed using both polymeric and colloidal routes. We found that, in contrast to previous reports, polymerically derived zircon crystallized at lower temperatures than zircon formed by colloidal routes. Polymerically derived mullite-zircon powders followed the densification behavior of polymerically derived mullite powders and still contained appreciable porosity after heating to 1400°C. Equimolar mixtures of mullite and zircon formed by mixing colloidally derived mullite and polymerically derived zircon densified by viscous flow between 1100°C and 1200°C and formed a mixture of crystalline mullite and zircon by 1300°C.

ACKNOWLEDGMENTS

We wish to acknowledge the generous support of the AFOSR (Contract No. F49620-89-C-0102) in funding this work.

REFERENCES

1. G. Vilmin, S. Komarneni, and R. Roy, "Lowering Crystallization Temperature of Zircon by Nano-heterogeneous Sol-Gel Processing," *J. Mater. Sci.*, **22**, 3556-60 (1987).
2. R. Roy, S. Komarneni, and W. Yarbrough, "Some New Advances with SSG-Derived Nanocomposites"; pp. 571-88 in Ultrastructure Processing of Advanced Ceramics. Edited by J.D. Mackenzie and D.R. Ulrich. J. Wiley and Sons, New York, NY, 1988.
3. R.F. Haaker and R.C. Ewing, "Solution-Gelation Method for Preparing Polycrystalline Zircon," *J. Am. Ceram. Soc.*, **64** [8] C149 (1981).
4. J. Campaniello, E.M. Rabinovich, P. Berthet, A. Revcolevschi, and N.A. Kopylov, "Phase Transformations in ZrO_2-SiO_2 Gels"; pp. 541-46 in Better Ceramics Through Chemistry IV. Edited by C.J. Brinker, D.E. Clark, and D.R. Ulrich, and B.J.J. Zelinski. Materials Research Society, Pittsburgh, PA, 1990.
5. J.C. Pouxviel, J.P. Boilot, A. Dauger, and L. Huber, "Chemical Route to Aluminosilicate Gels, Glasses and Ceramics"; pp. 269-74 in Better Ceramics Through Chemistry II. Edited by C.J. Brinker, D.E. Clark, and D.R. Ulrich. Elsevier Science Publishers, New York, NY, 1986.
6. M.G.M.U. Ismail, Z. Nakai, H. Ohira and S. Somiya, "Preparation and Characterization of Mullite Containing Materials"; pp. 1108-14 in Ceramic Transactions, Ceramic Powder Science II. Edited by G.L. Messing, E.R. Fuller, and H. Hausner. American Ceramic Society, Westerville, OH, 1987.
7. B.E. Yoldas and D.P. Partlow, "Formation of Mullite and Other Alumina-Based Ceramics via Hydrolytic Polycondensation of Alkoxides and Resultant Ultra- and Micro-Structural Effects," *J. Mater. Sci.*,

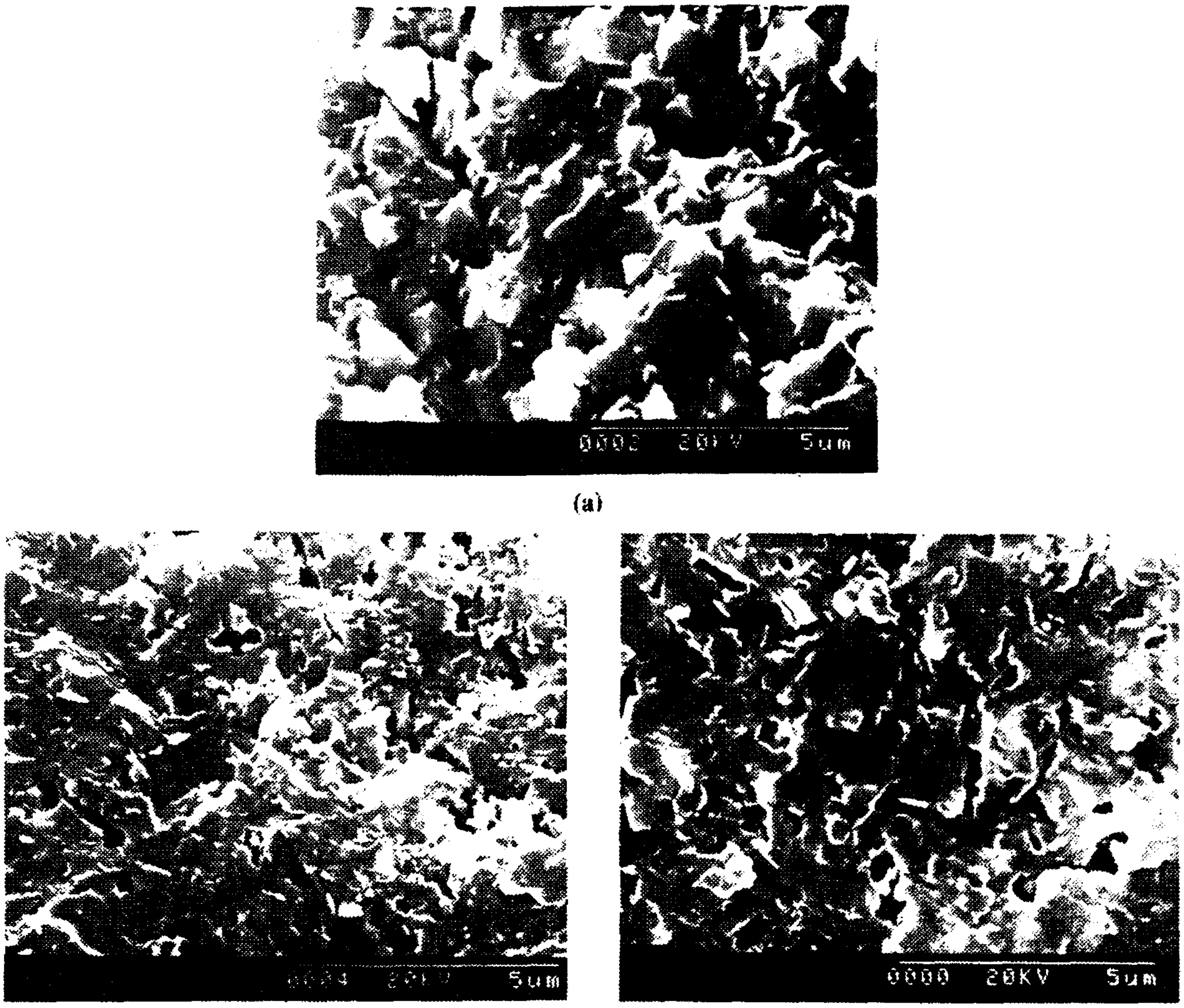

(a)

(b)

(c)

Fig. 3. Fracture surfaces of (a) polymerically derived zircon (b) colloidally derived mullite and (c) mixture of colloidally derived mullite and colloidally derived zircon. All samples were heated to 1400°C.

23 1895-1900 (1988).

8. A.K. Chakraborty and D.K. Ghosh, "Synthesis and 980°C Phase Development of Some Mullite Gels," *J. Am. Ceram. Soc.*, **71** [11] 978-87 (1988).
9. D.W. Hoffman, R. Roy, and S. Kamarneni, "Diphasic Xerogels, A New Class of Materials: Phases in the System Al_2O_3-SiO_2," *J. Am. Ceram. Soc.*, **67** [7] 468-71 (1984).
10. W-C. Wei and J.W. Halloran, "Phase Transformation of Diphasic Aluminosilicate Gels," *J. Am. Ceram. Soc.*, **71** [3] 166-72 (1988).
11. W-C. Wei and J.W. Halloran, "Transformation Kinetics of Diphasic Aluminosilicate Gels," *J. Am. Ceram. Soc.*, **71** [7] 581-87 (1988).
12. J.C. Hulling and G.L. Messing, "Hybrid Gels for Homoepitactic Nucleation of Mullite," *J. Am. Ceram. Soc.*, **72** [9] 1725-29 (1989).
13. K. Okada and N. Otsuka, "Characterization of the Spinel Phase from SiO_2-Al_2O_3 Xerogels and the Formation Process of Mullite," *J. Am. Ceram. Soc.*, **69** [9] 652-56 (1986).
14. J.C. Huling and G.L Messing "Hybrid Gels Designed for Mullite Nucleation and Crystallization Control"; pp. 515-26 in Better Ceramics Through Chemistry IV. Edited by C.J. Brinker, D.E. Clark, D.R. Ulrich, and B.J.J. Zelinski. Materials Research Society, Pittsburgh, PA, 1990.

SECTION 7

PREPARATION AND CHARACTERIZATION OF SiC FROM ALKOXIDE-DERIVED POLYMERIC PRECURSORS

Zhiping Jiang and Wendell E. Rhine
Ceramics Processing Research Laboratory

Published in Synthesis and Processing of Ceramics: Scientific Issues, Mat. Res. Soc. Symp. Proc. vol 249, 25 (1992)

ABSTRACT

Crystalline SiC was prepared by carbothermic reduction of alkoxide-derived polymeric precursors under a flow of argon at 1400-1600°C. The pyrolysis products from the precursors with a molecular source of carbon, i.e., $(R_1)_x(R_2)_ySiO_{1.5}$ (R_1=phenyl; R_2=propyl, vinyl), showed different morphologies from those of the precursors derived from TEOS and a polymeric source of carbon (polyfurfuryl alcohol). Furthermore, the pyrolysis chemistry of theses precursors and the microstructure of their corresponding pyrolysis products were studied by means of FTIR, TGA, XRD, SEM, BET, elemental analyses, etc.

INTRODUCTION

SiC can be prepared by the carbothermic reduction of alkoxide-derived polymers. These polymers are usually prepared by hydrolysis of silicon alkoxides or their derivatives. The carbon source for the reduction is either an external polymeric material, such as polyfurfuryl alcohol [1], polyacrylonitrile [2] and phenolic resin [3-4], or an internal organic group attached to Si, such as alkyl, vinyl, allyl and phenyl groups [5-9]. Here, we report the pyrolysis study of alkoxide-derived precursors with various carbon sources such as furfuryl alcohol (I), polyphenylpropylsilsesquioxane (II), or polyphenylvinylsilsesquioxane (III). The purpose of this study is to compare the pyrolysis chemistry of these polymers and the effect of carbon source on the morphology of the pyrolysis product.

EXPERIMENTAL PROCEDURE

Polyphenylpropylsilsesquioxane (phenyl:propyl = 7:3) (II) and polyphenylvinylsilsesquioxane (phenyl: vinyl = 9:1) (III) were used as-received (Huls Petrarch Systems). $Si(OC_2H_5)_4$ and furfuryl alcohol (FuOH) were purified by distillation. Pyrolyses were carried out in a carbon furnace under argon with a heating rate of 200°C/h. Oxidation or ammonolysis of the ceramic products was performed in either a box furnace under air or a tube furnace under a flow of ammonia.

Precursor (I) was prepared by mixing $Si(OC_2H_5)_4$, H_2O and furfuryl alcohol in a molar ratio of 1:1.2:0.75 using H_2SO_4 as the acid catalyst in THF solvent. The resulting solution was refluxed under nitrogen for 2 h, leaving a deep brown solution. The product, after removal of solvent under vacuum at 120°C, was a dark solid which was slightly soluble in hydrocarbon solvents. Based on a similar procedure, precursors with a Si:FuOH ratio of 1:0.85, 1:1 and 1:1.25 were prepared.

RESULTS AND DISCUSSION

Pyrolyses of Precursor (I)

It is well known that both TEOS/H_2O [10] and FuOH [11] will undergo polymerization under acid catalysis. Furthermore, FTIR studies of the precursor (I) indicated the existence of OC_2H_5, SiO-H, and C=C groups in the structure. Therefore, the as-synthesized polymer can be represented as a mixture of $SiO_x(OC_2H_5)_y(OH)_z$ and polyfurfuryl alcohol.

TGA studies showed that pyrolysis of precursor (I) under argon below 1200°C resulted in two decomposition processes: one at 100-300°C, the second at 300-550°C. The first weight loss was attributed to the volatilization of H_2O, which was formed during the condensation of SiO-H groups to Si-O-Si units. The second one was caused by the decomposition of OC_2H_5 groups and furan rings of polyfurfuryl alcohol into carbon. The IR spectrum of the same precursor (I) heated at 600°C for 1 h suggested that no organics remained in the precursor, and the only detectable absorption bands (1092 and 806 cm^{-1}) were due to Si-O bonds.

Further heating the precursor to 1000°C did not change the product's IR spectrum. The IR spectrum of the pyrolysis product heated at 1200°C for 6 h under argon indicated that the intensity of the absorption band at 1090 cm^{-1} (Si-O) had greatly decreased; relative to the intensity of peak at 820 cm^{-1}. Further heating the precursor to 1300°C for 6 h caused the band at 820 cm^{-1} to increase further. Finally, the absorption band around at 1090 cm^{-1} has completely disappeared for the IR spectrum of the precursor heated at 1400 °C for 6 h. The new band at 820 cm^{-1} is attributed to the Si-C bond.

Based on the IR study, it appears that carbothermic reduction begins between 1200 and 1300°C. The pyrolysis product heated at 1200°C for 6 h consisted of large (>50 μm), dark, shiny, and irregularly shaped pieces. The SEM micrograph (Figure 1a) revealed a smooth surface devoid of visible pores, which is consistent with its low specific surface area (2.5 m^2/g). The pyrolysis product at 1300°C was a dark powdery solid with small amounts of large irregularly shaped particles. The SEM micrograph (Figure 1b) of this product showed a mass of small agglomerated particles; furthermore, a high specific surface area (58.9 m^2/g) was observed for this product. Both XRD and elemental analyses indicated the carbothermic reduction was complete after heating at 1400°C for 6 h. The XRD pattern (2 Theta: 35.73, 41.50, 60.07, 71.85 and 75.57°) of this product indicated that ß-SiC was the only crystalline phase except a small amount of α-SiC, represented by the shoulder on the 100% intensity peak of ß-SiC.

The product obtained at 1400°C is a yellow powdery solid; SEM micrographs (Figure 1c) indicated that these ß-SiC particles have small particle sizes, but some growth of particles was observed. Further heating this product to 1600°C resulted in more particle growth. An average particle diameter of 0.48 and 0.85 μm was determined for the products obtained at 1400 and 1600°C, respectively, based on the centrifugal sedimentation measurements. The elemental analyses of the product heated at 1400°C for 6 h indicated a 1:1.12 ratio of Si:C and 2.3 wt% oxygen content in the product by difference.

We also noticed that the SiC powder was produced at a low yield (77 %) based on the conversion of $Si(OC_2H_5)_4$ to SiC. This low yield of SiC from similar processes has been attributed to the SiO volatilization during the carbothermic reduction [2-4].

When the ratio of Si:FuOH is less than 1:0.75, the pyrolysis products after 1400 or 1600°C was either dark-grey or black solid, suggesting that there was excess C in the products, even though the XRD patterns of these products indicated that highly crystalline ß-SiC was the major phase besides a small amount of α-SiC. The TGA curves of these products in air showed that the excess C was oxidized between 550-720 °C.

The SEM micrographs of these pyrolysis products (with excess C) heated in argon indicated that the surface morphology of these pyrolysis products varied with the relative amount of carbon in the products; that is, with more carbon in the products, a denser surface morphology was observed. In addition, the surface morphology of these products consists of two kind of particles based on their sizes. For instance in Figure 1d, the smaller particles (0.05-0.10 μm) stay together with some pores between them. The bigger particles (>0.25 μm) are randomly dispersed in the mass of smaller particles.

After the product obtained at 1600°C was oxidized at 650°C for various times, the SEM micrographs of these products indicated the small particles were "etched out" first; then the bigger particles were gradually broken; finally, when the pyrolysis product was heated in air for 0.4 h, the SEM micrograph indicated that the SiC particles with a particle size of approximately 0.2-0.4 μm were obtained.

Based on the above results, it is proposed that the small particles in Figure 1d are carbon particles, which are oxidized first, presumably due to their high surface area. The pores between these C particles are formed by the evolution of gaseous products during carbothermic reduction. Furthermore, it is clear that the SiC particles are included in the larger particles. Since these C-SiC composite particles have lower surface area than the smaller carbon particles, they are oxidized slower.

Based on the above discussion, it is obvious that SiC particles in the products before oxidation are not uniformly distributed in the carbon medium. Furthermore, the excess C is divided into two categories, that is the small carbon particles and the carbon in the large C-SiC particles. The average sizes of SiC particles for these three products (Si:FuOH = 1:0.85, 1:1.0 and 1:1.25) after oxidation are 0.41, 0.29 and 0.25 μm, respectively, based on the centrifugal sedimentation measurements. It illustrates that all of them are much smaller than the size (0.85 μm) of the product obtained using a 1:0.75 ratio of Si:FuOH.

The excess carbon in the pyrolysis products in

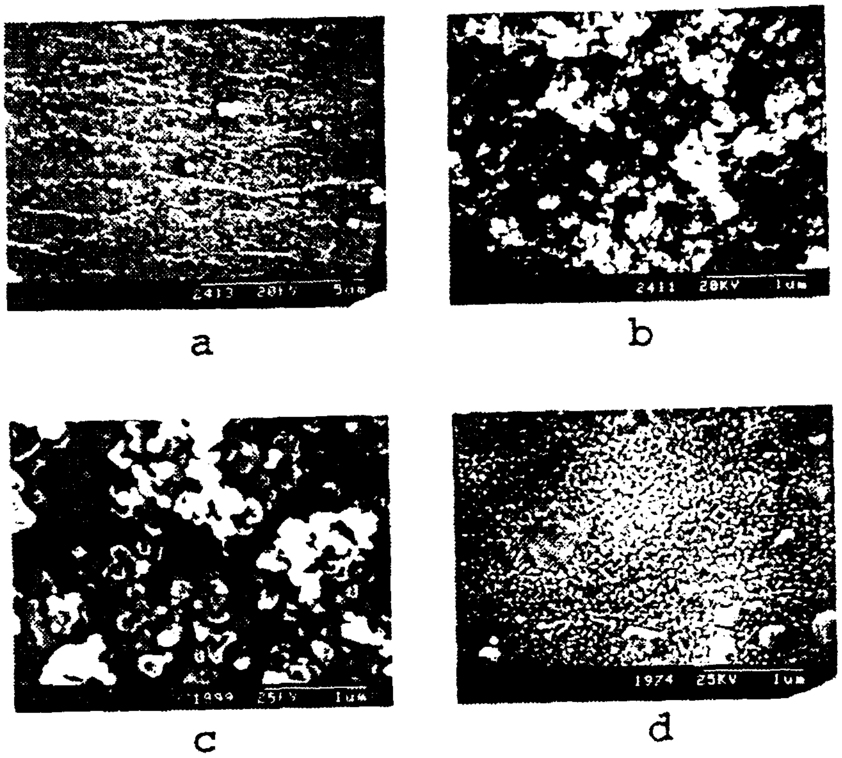

Figure 1 SEM micrographs of the precursor (I) with a Si:FuOH ratio of 1:0.75 heated in argon at (a) 1200°C for 6 h; (b) 1300°C for 6 h; (c) 1400°C for 6 h. (d) the SEM micrograph of the precursor (I) with a ratio of 1:1 heated at 1600°C for 3 h.

argon also can be removed by NH_3. Based on the elemental analysis, 75% of excess C in the pyrolysis product with a 1:1 ratio of Si:FuOH was removed after the product was heated under ammonia at 1000°C for 12 h. The SEM micrograph of this resulting product indicated that some dense SiC-C particles were still left in the product. It is assumed that this carbon residue can be removed when the product is treated in ammonia at higher temperature or/and for longer time. This carbon-removing effect by ammonia was also observed in other ceramic systems, presumably due to the formation of HCN and H_2 [12].

Pyrolyses of Precursor (II) and Precursor (III)

The IR spectra of both precursor (II) and (III) indicated the existence of SiO-H in the structures besides the Si-O and Si-R groups. It was observed that the former precursor has much stronger Si-OH absorption than the latter. Pyrolysis of these precursor under argon resulted in a weight loss around 250°C (SiO-H condensation) and 520°C (decomposition of Si-R), respectively.

The XRD and IR studies of the pyrolysis products of these precursors revealed that the carbothermic reduction started above 1200°C, similar to the precursor (I). When the precursors were heated at 1400-1600°C, XRD patterns of the pyrolysis products of precursor showed that crystalline ß-SiC is the major phase besides a minor α-SiC impurity.

As compared with precursor (I), both precursor (II) and (III) possess a molecular carbon source. Therefore, it is of interest to know how the microstructures of pyrolysis products from these two precursors differ from that of the precursor (I). The pyrolysis products of precursor (II) and (III) heated at 1200°C for 6 h were porous, monolithic pieces with a black, shiny appearance. Their SEM micrographs indicated smooth, dense appearance, just like that of the pyrolysis product from precursor (I) heated at the same condition (Figure 1a). On further heating the precursor to 1600°C, these products have become a black solid with irregularly shaped particles. The SEM micrographs (Figure 2a and 2b) of these products at high magnification shows that these large particles are composed of small particles. As shown by White et al [5-6], the amount of C provided by the molecular source in precursor (II) and (III) will be 3.1 and 3.8 moles for each mole of Si, respectively, which is more than the amount (C/Si=2.5) needed for complete reduction of the SiO_2. Therefore, excess carbon will be left in the pyrolysis products.

Since more C was left in the pyrolysis product of precursor (III), a denser microstructure was observed as shown in Figure 2b. However, BET measurements indicated that the specific surface area (340.0 m^2/g) of the product III at 1600°C is slightly larger than that (299.5 m^2/g) of the product II at 1600°C, suggesting that the former product possesses finer pore sizes. When the pyrolysis product at stage 2a was oxidized in air at 650°C for 0.4 h, a yellow powdery product with an average particle size of 0.38 μm was obtained, suggesting that all the excess C was removed under such a treatment. The SEM micrograph (Figure 2c) of this resulting product indicates that oxidation removed all the carbon between SiC particles. It is noticed that, unlike the pyrolysis products with excess amount of C from precursor (I), the SiC particles formed from precursor (II) appear to be uniformly dispersed in the C matrix, which subsequently yields a homogeneous C-SiC ceramic composite. Similar phenomena were also observed in the oxidation of the product of (III) at 1600°C. The formation of this uniform composite is probably because the C produced from the molecular source will be mixed with the SiO_2 more intimately than that in the biphasic precursor (I)-derived products, which subsequently results in a homogeneous C-SiC distribution after the carbothermic reduction.

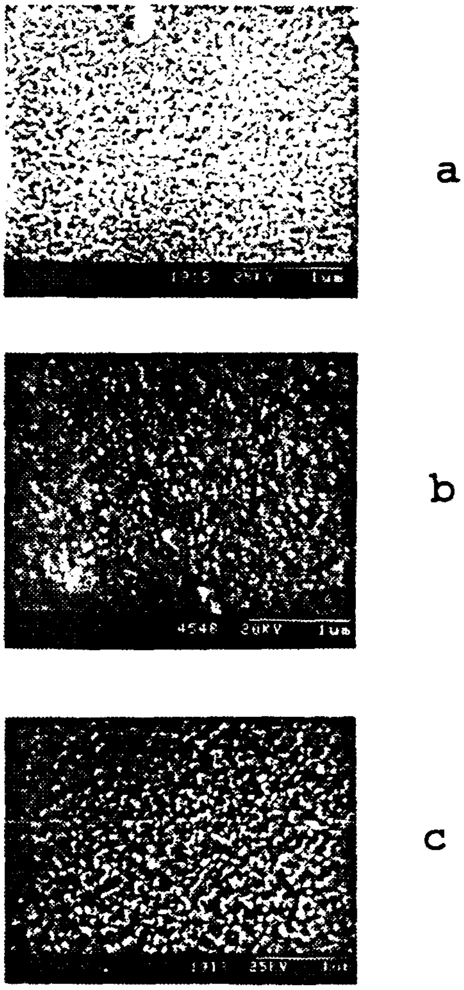

Figure 2 SEM micrographs of (a) the precursor (II) heated in argon at 1600°C for 3 h; (b) precursor (III) heated in argon at 1600°C for 3 h; (c) the product at (a) heated in air at 650°C for 0.4 h.

The elemental analyses of both products revealed a 6-10 wt% oxygen content, therefore, the pyrolysis product of precursor (II) and (III) heated at 1600°C for 3 h in argon can be best described as a mixture of C, SiO_2 and SiC.

ACKNOWLEDGEMENTS

Financial support for this work was provided by the Air Force Office of Scientific Research (AFOSR) under Contract No. F49620-89-C-0102.

REFERENCES

1. J.D. Birchall, M.J. Mockford, D.R. Stanley, P.M.L. Asher and W. R. McCarthy, Eur. Pat. Appl. EP 284235 (1988).
2. Y. Sugahara, Y. Takeda, K. Kuroda, and C. Kato, J. Mater. Sci. Lett. 8, 944 (1989).
3. H. Tanaka and Y. Kurachi, Ceram. International 14, 109 (1988).
4. G.C. Wei, C.R. Kennedy, and L.A. Harris, Am. Ceram. Soc. Bull. 63, 1054 (1984).
5. D.A. White, S.M. Oleff, R.D. Boyer, P.A. Budinger, and J.R. Fox, Adv. Ceram. Mater. 2, 45 (1987).
6. D.A. White, S.M. Oleff, and J.R. Fox, Adv. Ceram. Mater. 2, 53 (1987).
7. F. Hatakeyama, J. Am. Ceram. Soc. 73, 2107 (1990).
8. F.I. Hurwitz, L. Hyatt, J. Gorecki, and L. D'Amore, Ceram. Eng. Sci. Proc. 8, 732 (1987).
9. F.I. Hurwitz, J.Z. Gyekenyesi, and P.J. Conroy, Ceram. Eng. Sci. Proc. 10, 750 (1989).
10. B.E. Yoldas, J. Non-Crystalline Solids 38, 81 (1980).

11. H.F. Mark, N.M. Bikales, C.G. Overberger and G. Menges Eds., Encyclopedia of Polymer Science and Engineering V(7), (John Wiley & Sons Inc., New York, 1987), P. 457.

12. F.K. van Dijen and Pluijmakers, J. Eur. Ceram. Soc. 5, 385 (1989).

SECTION 8

PREPARATION AND PROPERTIES OF SILICON CARBIDE FROM POLYMERIC PRECURSORS

Zhiping Jiang and Wendell E. Rhine
Ceramics Processing Research Laboratory
Massachusetts Institute of Technology, Cambridge, MA 02139

ABSTRACT

The decomposition of polymeric SiC precursors, which were prepared by the polymerization of trialkoxy silanes or silicon alkoxides and pyrolyzed under a flow of argon, proceeded with the loss of water at 200-300 °C, the decomposition of alkoxide groups at 350-700 °C, the carbothermic reduction at 1200-1300 °C, and the crystallization of SiC above 1400 °C. The pyrolysis products from alkyl or aryl polysilsesquioxanes, i.e., $(R_1)_x(R_2)_ySiO_{1.5}$, (R_1=phenyl, R_2=propyl or vinyl where x + y = 1), where the carbon source is an intrinsic component of the polysilsesquioxane, exhibited different morphologies than the pyrolysis products obtained from the precursors derived from tetraethylortosilicate (TEOS) and a polymeric source of carbon (polyfurfuryl alcohol). The pyrolysis chemistry of these oxygen containing precursors and the morphologies of the pyrolysis products were compared with those from a vinylic polysilane (VPS).

INTRODUCTION

Following the pioneering work of Yajima,[1] the preparation of silicon carbide via pyrolysis of polymeric precursors has been widely investigated. The main advantages of polymeric routes over conventional methods include the production of ceramic materials in desirable forms (i.e. fibers, coatings, powders, etc.), improved control over microstructure and homogeneity, and the potential of using polymer processing methods for forming ceramic materials.[2]

In general, polymeric precursors for SiC can be divided into three categories based on the type of structural units bonded to Si in the precursors. In the first one, the polymer backbone is composed of Si-C bonds, and this type of polymer is represented by polycarbosilanes.[3-5] In the second one, the polymer backbone is composed of Si-Si bonds as in polysilanes.[6-8] Pyrolysis of these polymers usually results in the formation of amorphous SiC at low temperatures (below 1000 °C); further heating the precursors to higher temperatures leads to crystalline SiC. In the third category, the basic structural backbone of the polymer consists of Si-O bonds and includes the polymers derived from polymerization of trialkoxy silanes or silicon alkoxides.[9-17] Pyrolysis of these polymers will form SiO_2 and C at low temperatures; SiC is formed at high temperatures (>1200 °C) by the carbothermic reduction of SiO_2. The source of carbon for the carbothermic reduction can be an external source, such as carbon black, or a polymer which produces carbon upon pyrolysis. The source of carbon can also be an internal one. In this case, the carbon is produced during the decomposition of the precursor and is an intrinsic property of the precursor.

The pyrolysis chemistry of these precursors has been extensively studied in recent years,[13,14,18] but how the precursor chemistry, carbon source, product composition, etc. affects the morphology of the pyrolysis products is not well understood even though it is an important issue in practice.

Here we report the results of the pyrolysis of several types of polymeric SiC precursors, as well as the morphologies of their corresponding pyrolysis products. The first one is a polymer derived from the $Si(OC_2H_5)_4$/furfuryl alcohol/H_2O system; the second and third precursors are polyphenylpropylsilsesquioxane (PPPS) and polyphenylvinylsilsesquioxane (PPVS), $[(R_1)_x(R_2)_ySiO_{1.5}$, (R_1=phenyl; R_2=propyl or vinyl; X + Y = 1)]. The fourth one is a vinylic polysilane (VPS). The difference between the first precursor and the last three is that the former system contains an external polymeric source of carbon, while the carbon source in the latter systems is internal and the carbon is produced upon decomposition of the precursor.

These polymers represent the three types of precursors used for SiC in the literature. Furthermore, these polymers have different structures, pyrolysis chemistry, carbon source and product composition. Therefore, studying these systems will be beneficial to designing precursors which will produce stoichiometric SiC with a desirable morphology.

EXPERIMENTAL PROCEDURE

Materials

The $Si(OC_2H_5)_4$ and furfuryl alcohol (FuOH) used to prepare precursors were purified by distillation before being used. The polyphenylpropylsilsesquioxane (phenyl:propyl=7:3), the polyphenylvinylsilsesquioxane (phenyl:vinyl=9:1) (both from Huls Petrarch Systems), and the vinyl polysilane (Y12044, Union Carbide Corporation) were used as-received.

Syntheses of Precursors from TEOS and Furfuryl Alcohol

A solution of 0.52 g of 1 N H_2SO_4 in 20 mL THF was added to 40 mL of a THF solution containing 5 g of $Si(OC_2H_5)_4$ and 2.36 g of furfuryl alcohol (the $Si:FuOH:H_2O$ stoichiometry in the starting material corresponds to 1:1:1.2). The resulting solution was refluxed under nitrogen for 2 h, leaving a clear, deep brown solution. The product, after removal of solvent under 120°C, was a dark solid (3.95 g) which was slightly soluble in hydrocarbon solvents. This procedure was used to prepare precursors with Si:FuOH ratios of 1:0.75, 1:0.85, or 1:1.25.

Pyrolyses of Precursors

Samples of precursors (0.3 - 1 g) were placed in a carbon crucible and pyrolyzed in a carbon furnace under a flow of argon (ultra-high purity grade) at a flow rate of 300 mL/min. The temperature was increased from room temperature to 1600°C at a heating rate of 200°C/h, held at the desirable temperature for a period of time, and then cooled to room temperature. The excess free carbon was removed by heating the products in an alumina tube under a flow of anhydrous ammonia, or in a box furnace under a flow of air.

Characterization

Diffuse reflectance infrared Fourier transform spectroscopy (DRIFTS) studies were performed with a Nicolet PC/IR-44 infrared spectrometer. Samples were prepared by mixing the precursor or pyrolysis product with dry KBr in air. The ground mixture was transferred into the sample holder in air, which was subsequently transferred to the sample chamber flushed with N_2 for a minimum of 10 min before data collection. Thermal gravimetric analysis (TGA) of the compounds was carried out with a Perkin-Elmer thermal analysis system (TGA7) at a heating rate of 10°C/min. The TGA atmosphere was either argon that had been passed through a BTS catalyst (BASF Co.) and a molecular sieve column to remove O_2 and H_2O, respectively, or electronic grade ammonia. X-ray diffraction (XRD) patterns were measured with a Rigaku 300 diffractometer employing Cu/Kα radiation and a Ni filter at a scanning rate of 10°/min. The X-ray peak assignments were determined using a Rigaku Software JCPDS peak indexing program. Elemental analyses were obtained from E+R Microanalytical Laboratory, Inc. The morphologies of the pyrolysis products were observed using scanning electron microscopy (SEM). The particle size distribution of the pyrolysis products was determined using a centrifugal particle analyzer (Horiba, CAPA 500). The samples were dispersed in iso-proponal using an ultrasonic bath before measurement. The specific surface area of the products was measured by single point BET.

RESULTS AND DISCUSSION

Pyrolysis of Mixtures of TEOS and Furfuryl Alcohol

It is well known that the acid catalyzed hydrolysis of 1 mole of $Si(OC_2H_5)_4$ with less than 2 moles of H_2O will produce a polymer which can be represented as $SiO_x(OC_2H_5)_y(OH)_z$[19] (2x + y + z = 4). Furthermore, acid catalysis of furfuryl alcohol (FuOH) produces a polymeric resin by the following dehydration reaction:[20]

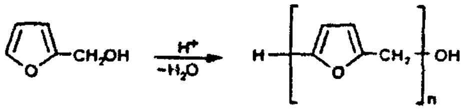

(1)

Therefore, the polymers synthesized from TEOS and FuOH can be represented as a mixture of polymeric $SiO_x(OC_2H_5)_y(OH)_z$ and polyfurfuryl alcohol.

Figure 1b shows the FT-IR spectrum of the silica gel which was produced by hydrolyzing $Si(OC_2H_5)_4$ with $2H_2O$ by the same procedure used to prepare the TEOS:FuOH polymers. This spectrum shows the presence of both OC_2H_5 and OH groups. The ethoxy groups are represented by the C-H stretching absorptions at 2977, 2942 and 2898 cm^{-1} and the C-H bending vibration band at 1394 cm^{-1} (refer to the spectrum of $Si(OC_2H_5)_4$, Figure 1a). The broad O-H stretching vibration centered at 3400 cm^{-1} indicates the presence of hydroxy groups. Figure 1c shows the IR spectrum of the precursor synthesized from a mixture of $Si(OC_2H_5)_4/0.75FuOH/1.2H_2O$, which shows absorption bands similar to those observed in hydrolyzed TEOS (Figure 1b) except for the additional absorptions at 1710, 1607 and 1558 cm^{-1}. These new absorption bands are attributed to the C=C stretching vibrations of polyfurfuryl alcohol.

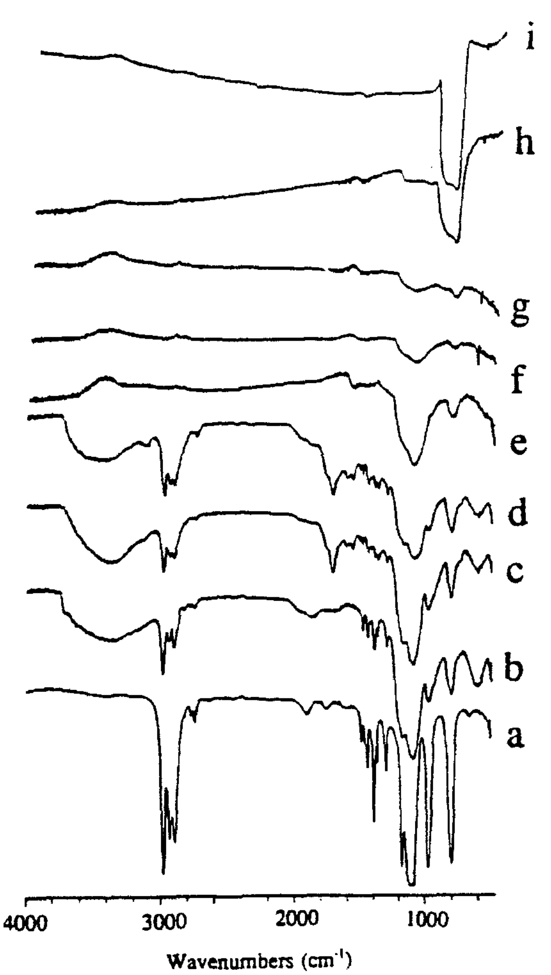

Figure 1. FT-IR spectra of (a) $Si(OC_2H_5)_4$; (b) the hydrolysis product of $Si(OC_2H_5)_4/2H_2O$; (c) as-synthesized TEOS:FuOH with a Si:FuOH ratio of 1:0.75; this precursor was heated at (d) 300 °C for 1 h; (e) 600 °C for 1 h; (f) 1000 °C for 1 h; (g) 1200 °C for 6 h; (h) 1300 °C for 1 h; and (i) 1400 °C for 6 h.

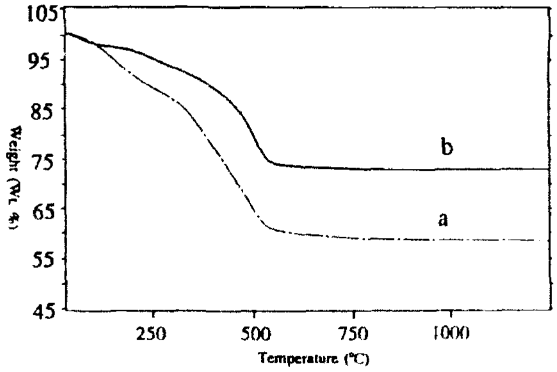

Figure 2. TGA curves in argon for (a) the as-synthesized TEOS:FuOH with a Si:FuOH ratio of 1:0.75 and (b) the hydrolysis product of $Si(OC_2H_5)_4/2H_2O$.

Figure 2a shows the TGA curve obtained under an argon atmosphere from 40-1200 °C of the precursor synthesized from $Si(OC_2H_5)_4/0.75FuOH/1.2H_2O$. This TGA indicates that the precursor undergoes two decomposition processes: one at 100-300°C and the second at 300-550°C. The first one is attributed to the elimination of H_2O which is formed during the condensation of SiO-H groups to Si-O-Si units. This assignment is supported by the fact that the IR spectrum (Figure 1d) of this precursor heated at 300°C for 1 h indicates that the relative intensity of SiO-H (the broad absorption at 3400 cm^{-1}) has decreased (compare Figure 1d with Figure 1c), but the relative intensities of absorption bands of the OC_2H_5 and poly(FuOH) have not changed at all. Moreover, we noticed that the absorption band (1080 cm^{-1}) attributed to the Si-O bonds has become broader.

The TGA curve (Figure 2b) of the gel obtained from hydrolysis of $Si(OC_2H_5)_4/2H_2O$ indicates that the major weight loss occurs at 450-550°C, a loss caused by the decomposition of OC_2H_5. Furthermore, it is known[21] from our previous work that the decomposition of furan rings of poly(FuOH) into carbon occurs at 270-480°C. Therefore, the second weight loss in Figure 2a is assigned as the decomposition of OC_2H_5 groups and poly(FuOH) in the precursor. Figure 1e shows the IR spectrum of this precursor heated at 600°C for 1 h. This spectrum suggests that no organics are left in the precursor after heating to 600 °C, and the only detectable absorption bands (1092 and 806 cm^{-1}) are due to Si-O bonds. The IR spectra are consistent with the TGA (Figure 2a) results and indicate that the decomposition of both OC_2H_5 and furfuryl groups is complete by 600°C. At this stage, SiO_2 and C are the expected products.

Further heating the precursor to 1000°C does not change the product's IR spectrum (Figure 1f). This result is consistent with the TGA which shows that no weight loss occurs between 600 - 1000 °C. The IR spectrum (Figure 1g) of the pyrolysis product heated at 1200°C for 6 h indicates that the relative intensity of the absorption band at 1090 cm^{-1} (Si-O) has greatly decreased relative to the intensity of the band at 820 cm^{-1}. Further heating the precursor to 1300°C for 6 h caused the band at 820 cm^{-1} to become significantly stronger (Figure 1h). Finally, the absorption band at 1090 cm^{-1} completely disappeared from the IR spectrum (Figure 1i) of the precursor heated at 1400 °C for 6 h. The new band at 820 cm^{-1} is attributed to the Si-C bonds, formed from the following carbothermic reduction:

$$SiO_2 + 3C = SiC + 2CO \quad (2)$$

Table 1. Weight Losses (wt%) of Precursors Heated at Various Temperatures in Argon

	TGA$^{@}$	1200°C (6 h)	1300°C (6 h)	1400°C (6 h)	1600°C (3 h)
TEOS:FuOH*	41.4	46.1	53.0	82.5	82.6
TEOS:FuOH$^{\#}$	-	-	-	78.5	78.9
PPPS	23.4	35.7	41.2	52.5	59.7
PPVS	21.6	21.8	35.5	39.2	52.0
VPS	-	43.4	-	-	45.9

* Si:FuOH = 1:0.75, $^{\#}$ Si:FuOH = 1:1, $^{@}$ the weight losses at 1200°C on the TGA curves.

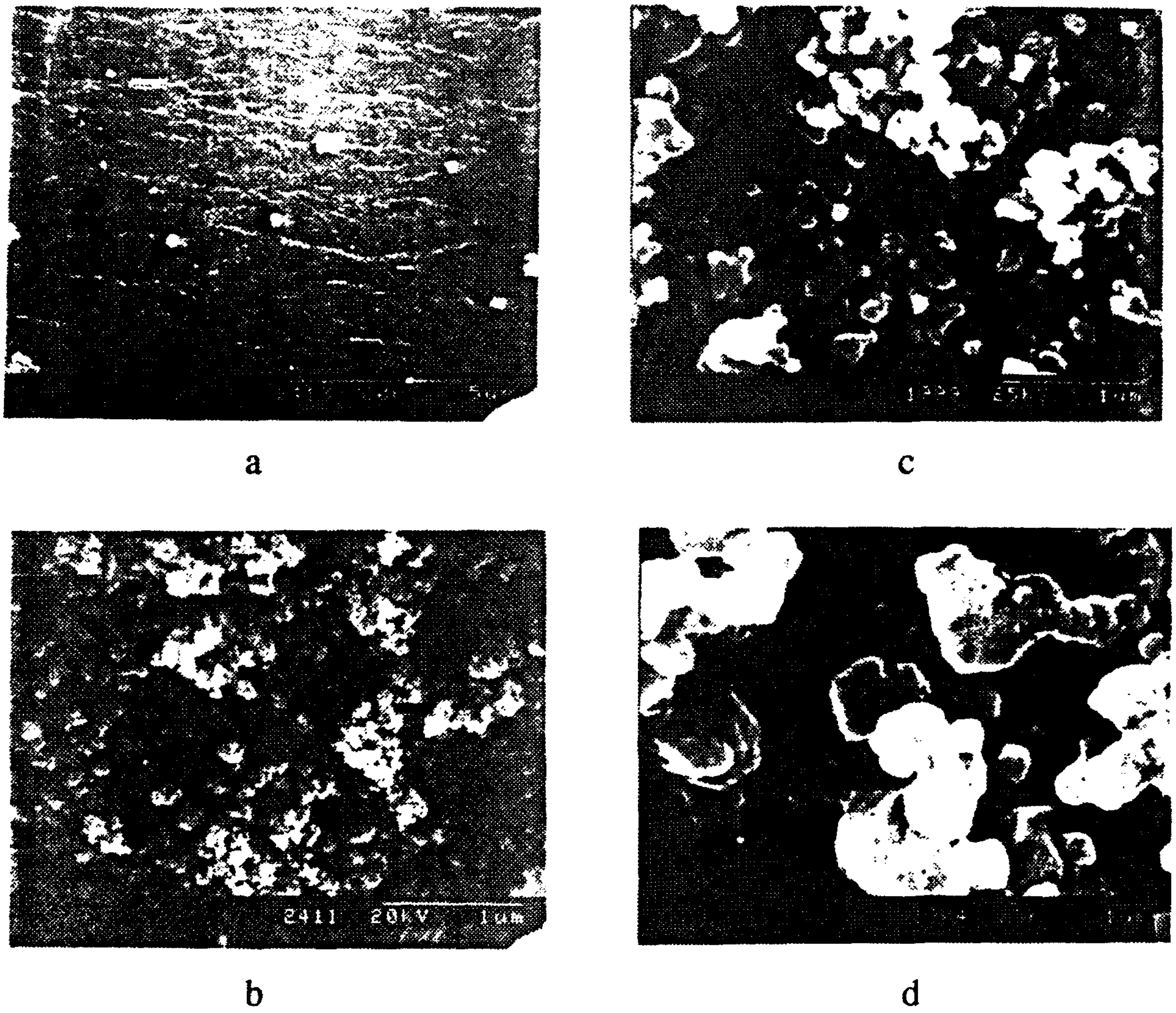

Figure 3. SEM micrographs of the TEOS:FuOH with a Si:FuOH ratio of 1:0.75 heated at (a) 1200 °C for 6 h; (b) 1300 °C for 6 h; (c) 1400 °C for 6 h; and (d) 1600 °C for 3 h.

Even though the TGA curve (Figure 2a) of the precursor showed a 41.4% weight loss at 750 °C and that no further weight loss occurred between 750-1200°C, a weight loss of 46.1% was observed for the same precursor heated at 1200 °C for 6 h (Table 1) in a furnace, indicating that some carbothermic reduction occurred at 1200 °C.

The pyrolysis product after heating at 1200 °C for 6 h consisted of large (>50 μm), dark, shiny, and irregularly shaped pieces. The SEM micrograph

(Figure 3a) of these pieces revealed a smooth surface devoid of visible pores. This product had a low specific surface area (2.50 m^2/g) based on the BET analysis. The pyrolysis product at 1300 °C was a dark, powdery solid with a few large irregularly shaped particles. The SEM micrograph (Figure 3b) of this product showed a mass of small agglomerated particles; furthermore, this product had a high specific surface area (58.90 m^2/g). XRD measurements of both products at 1200 and 1300 °C indicated they were still amorphous.

Crystalline β-SiC emerged as a major phase when the precursor was heated at 1400 °C for 1 h, in addition to the poorly crystalline cristobalite. Further heating of the precursor at 1400° for 6 h gave an XRD pattern (Figure 4) in which β-SiC was the major phase in addition to a small amount of α-SiC polytype, represented by the shoulder on the 100% intensity peak of β-SiC. The pyrolysis product obtained at 1600 °C showed a XRD pattern similar to that of Figure 4 except that these β-SiC peaks were a little sharper due to the growth of β-SiC crystallites.

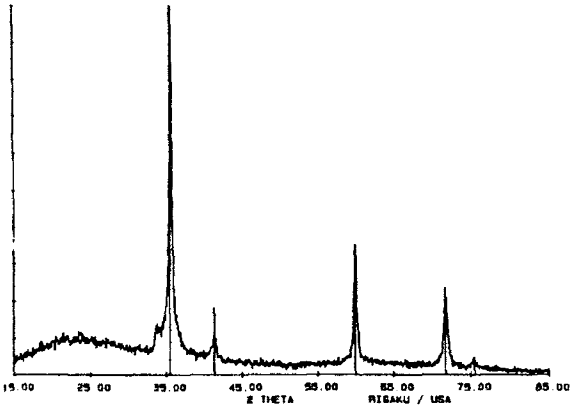

Figure 4. XRD patterns of the TEOS:FuOH with a Si:FuOH ratio of 1:0.75 heated in argon at 1400 °C for 6h.

Both products obtained at 1400°C and 1600°C were yellow powders; furthermore, almost the same pyrolysis yield for both products was observed (Table 1), indicating that the carbothermic reduction was nearly complete at 1400°C. The SEM micrographs (Figure 3c and Figure 3d) of these products show that these β-SiC powders have small grain sizes, but some coarsening of particles was observed for both products, especially for the latter. An average particle diameter of 0.48 and 0.85 μm was determined for the products obtained at 1400 and 1600°C, respectively, based on the centrifugal sedimentation measurements. The elemental analyses (Table 2) of the product heated at 1400°C for 6 h indicates a 1:1.12 ratio of Si:C and 2.3 wt% oxygen content. The oxygen content was estimated by difference assuming that the analysis are accurate and should total 100%.

We determined that the SiC powder was produced in a 77 % yield based on $Si(OC_2H_5)_4$. Similar low yields were also observed and discussed in previous studies[9,12] on the preparation of SiC from gel-derived precursors. We observed in the present system that only a small fraction of Si (4.4%) was lost between 25 and 1000 °C, based on the elemental analyses; this Si loss was presumably due to the vaporization of some Si species during the decomposition of SiO_2 gel. This result illustrated that most of the Si loss occurred above 1000 °C, presumably during carbothermic reduction. Previous studies[9,12] indicate that the carbothermic reduction (2) can be viewed in the following steps:

$$SiO_2 + C = SiO + CO \quad (3)$$

$$CO + SiO_2 = SiO + CO_2 \quad (4)$$

$$CO_2 + C = 2CO \quad (5)$$

$$SiO + 2C = SiC + CO \quad (6)$$

Among them, reactions 3 and/or 4 are important steps in the overall carbothermic reduction. Therefore, the major Si loss in the present work could be attributed to the SiO volatilization.

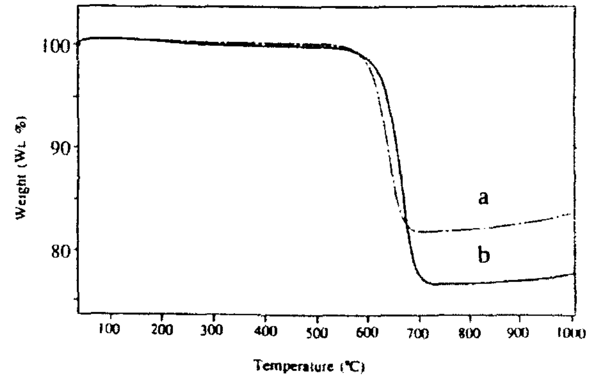

Figure 5. TGA curves (in air) of TEOS:FuOH heated at 1600 °C for 3 h in argon with a ratio of (a) 1:0.85 and (b) 1:1.

When more than 0.75 eq of FuOH was added, the pyrolysis product after 1400 or 1600°C was either a dark-grey or a black solid, indicating that there was excess C in the products, even though the XRD patterns of these products indicated highly crystalline β-SiC was the major phase besides a small amount of α-SiC. In addition, the elemental analyses (Table 2) of the products obtained by pyrolyzing the

Table 2. Elemental Analyses (wt%) of Pyrolysis Products under Argon

	T(℃)	Si	C	H	N
TEOS:FuOH[*]	1400 (6 h)	65.61	31.51	0.55	-
TEOS:FuOH[$]	1600 (3 h)	53.02	42.53	0.63	-
TEOS:FuOH[#]	1600 (3 h)	47.79	46.12	0.29	-
TEOS:FuOH[#]	650[@] (2 h)	66.24	23.98	0.30	-
TEOS:FuOH[#]	1000[$] (12 h)	63.11	29.58	0.29	0.46
PPPS	1600 (3 h)	43.89	45.32	0.12	-
PPVS	1600 (3 h)	40.13	53.27	0.64	-
PPVS	650[@] (2 h)	62.11	22.85	0.15	-
PPVS	1000[$] (12 h)	61.83	27.38	0.12	1.68

[*] Si:FuOH= 1:0.75, [$] Si:FuOH = 1:0.85, [#] Si:FuOH = 1:1. [@] The precursor was heated at 1600 °C for 3 h under argon, then treated under air at 650 °C for 2 h. [$] The precursor was heated at 1600 °C for 3 h under argon, then treated under ammonia at 1000 °C for 12 h.

precursors with a ratio of 1:0.85 and 1:1.0 of Si:FuOH at 1600℃ indicated that they contained almost 6% oxygen content. The TGA curves (Figure 5) of these products in air indicate that the excess C is oxidized between 550-720 ℃, resulting in a weight loss (excess C) of 18.1% and 23.2%, respectively.

The SEM micrographs (Figure 6) of the pyrolysis products with a Si:FuOH ratio of 1:0.85, 1:1 and 1:1.25 heated at 1600 ℃ in argon indicate that the surface morphology of these pyrolysis products varies with the relative amount of carbon in the products; that is, with more carbon in the products, a denser surface morphology is observed. In addition, the surface morphology in each of these three micrographs consists of two kinds of particles based on their sizes. For instance in Figure 6b, the smaller particles (0.05-0.10 µm) stay together with some pores between them; the bigger particles (>0.25 µm) are randomly dispersed in the mass of smaller particles.

When the product with Si:FuOH = 1:1.1 (Figure 6b) was oxidized at 650 ℃ in air, the SEM micrographs (Figure 7a and 7b) of these intermediates indicated the amount of small particles began to decrease after heating for 0.1-0.2 h, but the large particles still remained in the product. After the pyrolysis product was heated in air for 0.4 h, the SEM micrograph (Figure 7c) indicated that the SiC particles with a grain size of approximately 0.1-0.2 µm were obtained.

Based on the above results, it is proposed that the small particles in Figure 6b are carbon particles which are oxidized first. The voids between these C particles are formed by the evolution of gaseous products during carbothermic reduction. Furthermore, it is clear that the larger particles contain both SiC and C. Since these large C-SiC composite particles have lower surface area than the smaller carbon particles, they are oxidized more slowly. In addition, it is obvious that the SiC particles in the products were not uniformly distributed in the carbon matrix.

The average particle sizes of SiC products (with a Si:FuOH=1:0.85, 1:1 and 1:1.25) obtained after oxidation at 650 ℃ for 0.4 h were 0.41, 0.29 and 0.25 µm, respectively, based on the centrifugal sedimentation measurements. These measurements illustrated that all of the these precursors gave products with average particle sizes which were much smaller than the size (0.85 µm) of the product obtained from the precursor using a Si:FuOH ratio of 1:0.75. This decrease in average particle size is because the SiO_2 gel network is essentually being diluted in a carbon matrix as the amount of FuOH increases. Assuming a nucleation and growth model, the lower concentration of SiO_2 in the system results in smaller SiC particles.

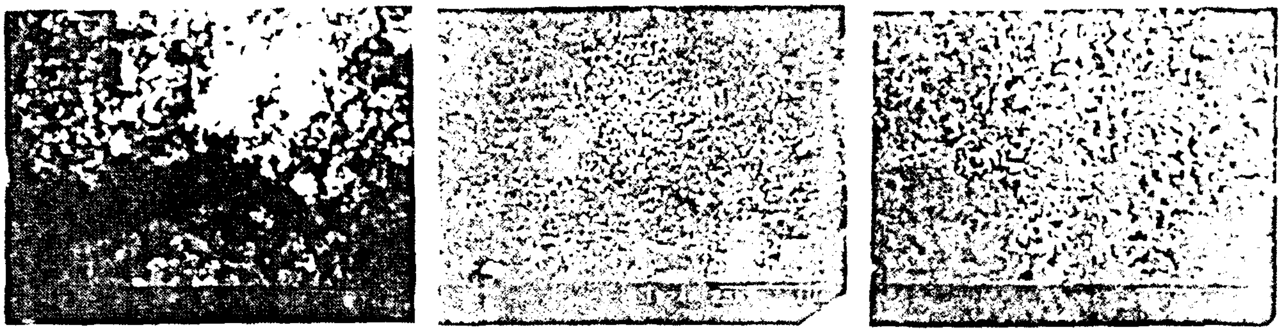

a b c

Figure 6. SEM micrographs of TEOS:FuOH heated at 1600 °C for 3 h in argon with a Si:FuOH ratio of (a) 1:0.85; (b) 1:1; and (c) 1:1.25.

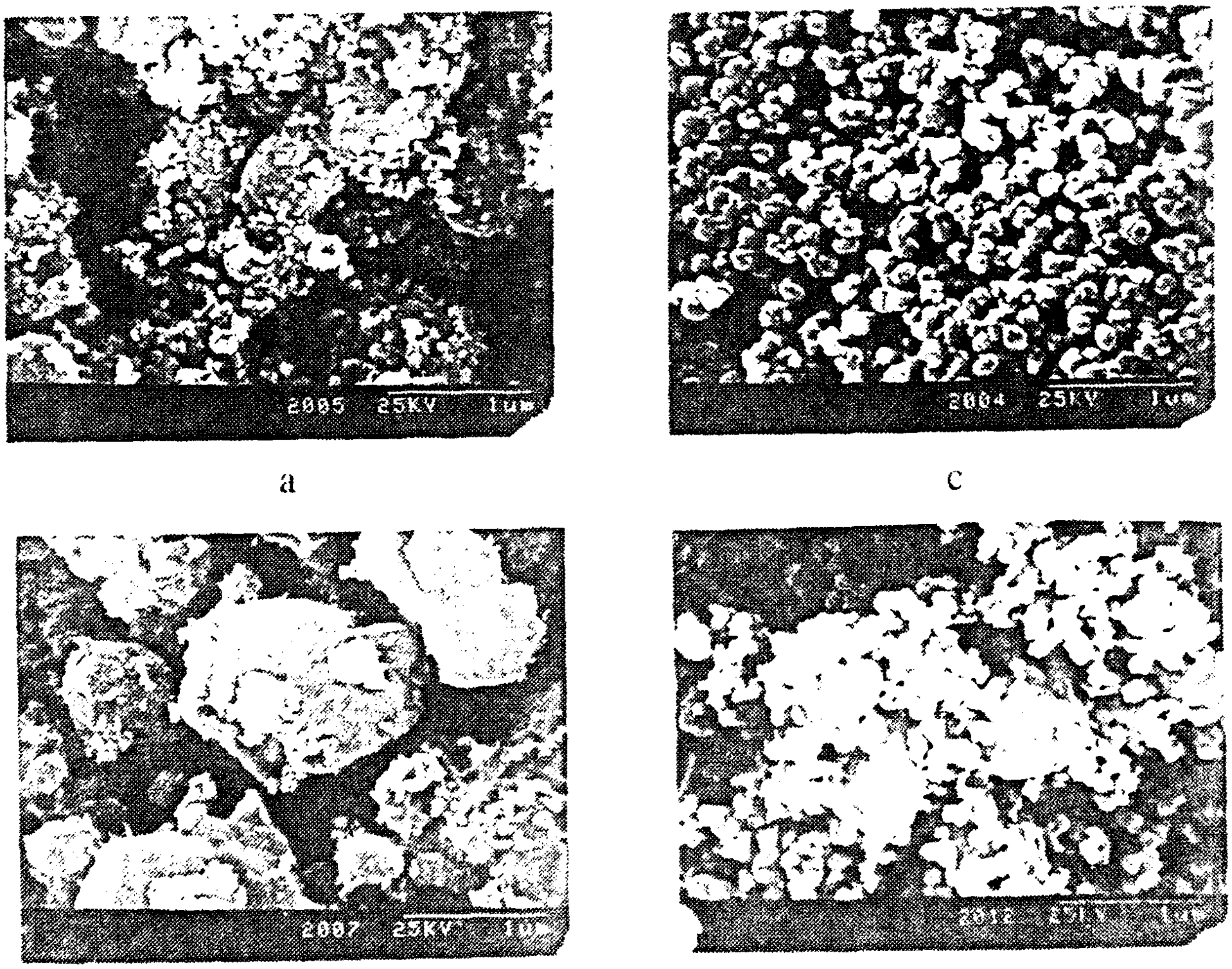
2005 25KV 1um
2004 25KV 1um
2007 25KV 1um
2012 25KV 1um

a c

b d

Figure 7. SEM micrographs of the pyrolysis product (the same product in Figure 6b) heated in air at 650 °C for (a) 0.1 h; (b) 0.2 h; (c) 0.4 h; and (d) the same product in Figure 6b heated at 1000 °C in ammonia for 12 h.

The excess carbon in the pyrolysis products in argon also can be partially removed by NH_3 since it is known[22] that ammonia reacts with carbon to presumably form HCN and H_2 and results in removing carbon from ceramics under non-oxdizing conditions. Based on the elemental analysis (Table 2), 75% of excess C in the pyrolysis product with a 1:1 ratio of Si:FuOH was removed after the product was heated under ammonia at 1000 °C for 12 h. The SEM micrograph (Figure 7d) of this resulting product indicates that some dense SiC-C particles are still left in the product.

Pyrolysis of PPPS and PPVS

Figure 8 shows the FT-IR spectra of the polyphenylpropylsilsesquioxane (PPPS) and its pyrolysis products in argon. The presence of two strong absorption bands at 3300 and 890 cm^{-1} (Figure 8a) revealed that PPPS contains SiO-H groups. The relative intensities of these two bands considerably decreased (Figure 8b) after the precursor was heated at 350°C for 1 h due to the condensation of SiO-H groups into Si-O-Si units. In contrast, the relative intensities of the absorption bands attributed to the C_3H_7 groups (2960, 2986 and 2874 cm^{-1}, C-H stretching; 1430 cm^{-1}, C-H bending) and C_6H_5 groups (3075 and 3053 cm^{-1}, C-H stretching; 1595 cm^{-1}, C=C stretching; 891 and 739 cm^{-1}, out-of-plane C-H bending) do not change at all, indicating that no decomposition of propyl or phenyl groups occurs below 350 °C. Further heating PPPS to 650°C removed most organic groups (Figure 8c); however, some unreacted C_6H_5 groups, represented by the broad peaks at 3050 and 1589 cm^{-1}, are still left in the product.

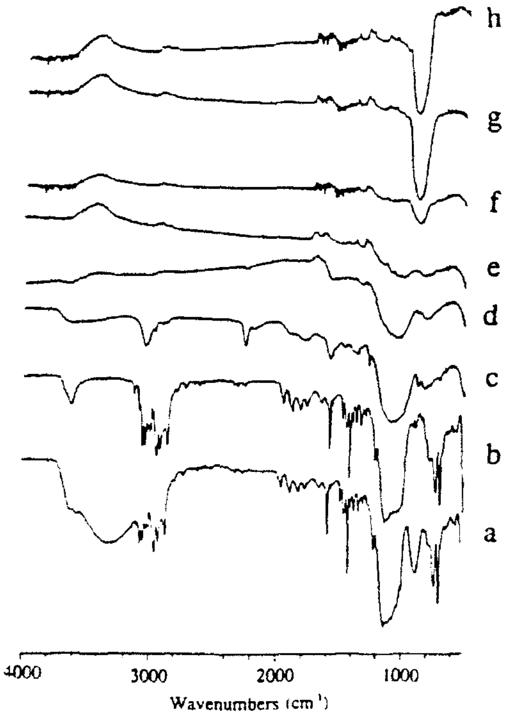

Figure 8. FT-IR spectra of PPPS (a) as-received; (b) heated in argon at (b) 350 °C for 1 h; (c) 650 °C for 1 h; (d) 1000 °C for 1 h; (e) 1200 °C for 6 h; (f) 1300 °C for 6 h; (g) 1400 °C for 6 h; and (h) 1600 °C for 3 h.

The TGA curve (Figure 9a) of PPPS in argon from 40-1200°C shows that two major decomposition processes occur around 250 and 500°C, respectively, which correspond to the SiO-H condensation, and the decomposition of C_3H_7 as well as C_6H_5, respectively, as indicated from the IR studies.

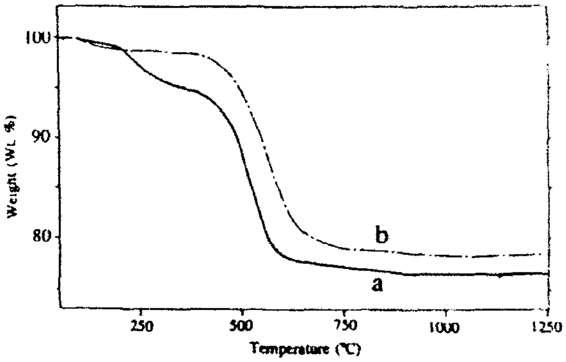

Figure 9. TGA curves (in argon) of (a) PPPS and (b) PPVS.

Heating PPPS to 1000°C caused the typical Si-O and Si-C absorption bands at 1090 and 807 cm^{-1} to appear (Figure 8d). Moreover, the relative intensity of the latter band increased when PPPS was heated at 1200°C for 6 h (Figure 8e) due to the formation of Si-C bonds in the product, which usually appear at 800-900 cm^{-1}. The IR spectra (Figure 8f-8h) of the precursor heated at 1300°C or higher show a strong Si-C stretching band, suggesting that the carbothermic reduction has begun and significant amounts of SiC form above 1300°C. The above results are also consistent with the pyrolysis weight losses presented in Table 1. That is, the thermal reduction appears to start at 1200 °C, since more weight loss (35.7 wt%) at 1200 °C is observed than indicated by the TGA curve (23.4 wt%) shown in Figure 9a. XRD patterns of the pyrolysis products of TEOS:FuOH indicate that a crystalline β-SiC phase emerges at 1300°C; above 1400°C, the major crystalline phase is β-SiC with a minor α-SiC impurity.

In addition, approximately a 10 % Si loss was observed for PPPS between 25 and 1600 °C based on the the elemental analyses; however, unlike the TEOS:FuOH polymers, all of the Si loss for PPPS

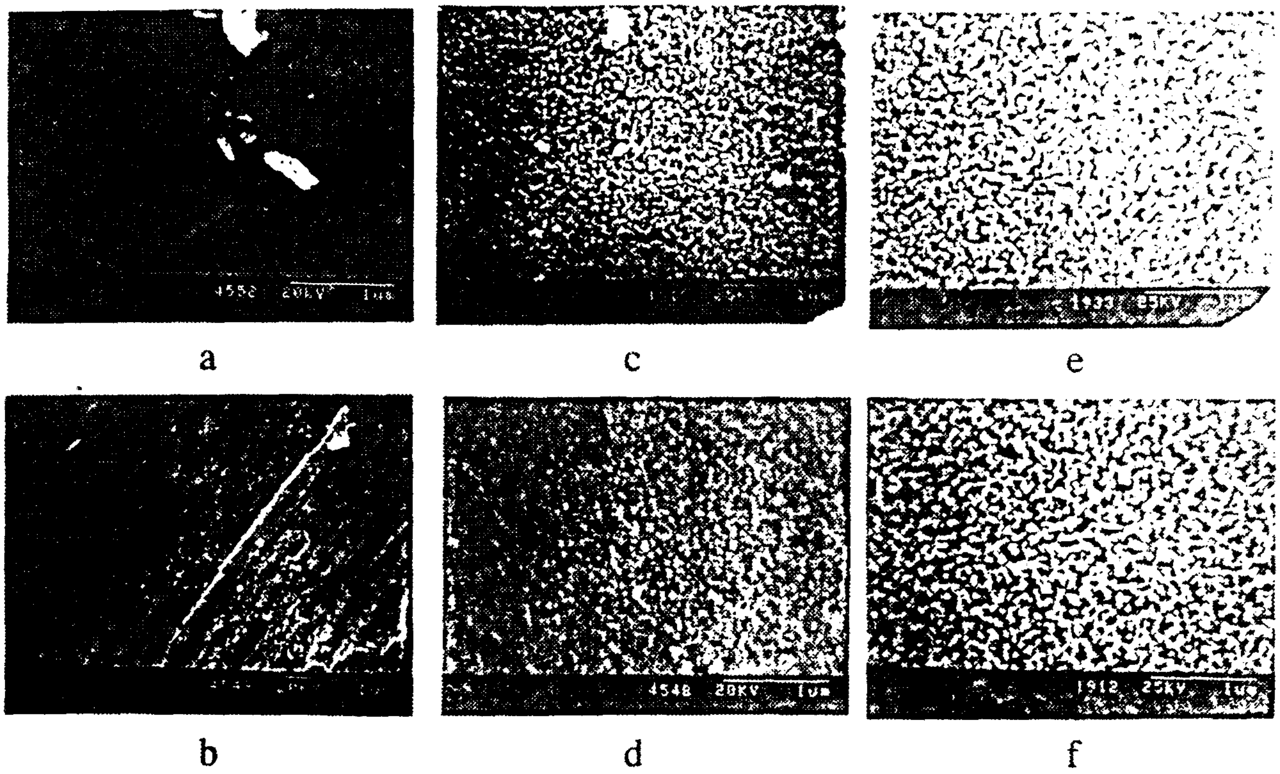

Figure 10. SEM micrographs of the pyrolysis products heated in argon for (a) PPPS, 1200 °C for 6 h; (b) PPVS, 1200 °C for 6 h; (c) PPPS for 1600 °C for 3 h; (d) PPVS, 1600 °C for 3 h; (e) the same product at (c) heated in air at 650 °C for 2 h; and (f) the same product at (d) heated in air at 650 °C for 2 h.

occurred above 1000 °C, presumably during the carbothermic reduction of SiO_2.

Polyphenylvinylsilsesquioxane (PPVS) showed a similar decomposition chemistry. The 2 wt% weight loss below 350°C and 19 wt% weight loss around 550°C in the TGA (Figure 9b) are attributed to the SiO-H condensation and the decomposition of C_6H_5 as well as $CH=CH_2$ groups, respectively. This interpretation is consistent with the FT-IR results of the pyrolysis products. The pyrolysis results (Table 1) indicate that the weight loss (21.8%) after heating the precursor at 1200°C for 6 h was almost the same (21.6%) as that observed in the TGA at the same temperature, suggesting that carbothermic reduction had not started at this temperature. Both XRD and FTIR results indicate crystalline ß-SiC phase is formed above 1400 °C.

Based on the discussion above, it appears that both PPPS and PPVS follow a pyrolysis chemistry similar to that of TEOS:FuOH. That is, the condensation of SiO-H groups in polysilsesquioxanes occurs at 200-300 °C followed by the decomposition of alkyl and aryl groups at 350-700 °C. The carbothermic reduction begins above 1200 °C and is followed by the crystallization of SiC above 1400 °C.

Unlike the TEOS:FuOH precursors, both PPPS and PPVS possess an intrinsic molecular carbon source (phenyl, propyl and vinyl groups). Therefore, it is of interest to know how the microstructure of pyrolysis products from these two precursors differs from that of TEOS:FuOH. The pyrolysis products from PPPS and PPVS heated at 1200°C for 6 h is a porous, monolithic piece with a black, shiny appearance. The surface morphologies of these products (Figure 10a and 10b) possess a smooth, dense appearance, similar to those observed for the pyrolysis products from TEOS:FuOH heated at the same conditions (Figure 3a). However, the BET measurements indicate that the products from PPPS and PPVS have a specific surface area of 47.66 and 33.60 m^2/g, respectively, which is much higher than that observed for the product from TEOS:FuOH.

On further heating the precursors to 1600°C, the products became black irregularly shaped particles. Their SEM micrographs (Figure 10c and 10d) show a flat surface, which is composed of small particles loosely connected with each other. As shown by White *et al.*'s work,[13-14] the amount of C provided by PPPS and PPVS will be 3.1 and 3.8 moles from each mole of Si, which is more than the amount of carbon (C/Si=2.5) needed for the complete carbothermic reduction. Therefore, excess carbon is expected to remain in the pyrolysis products. In fact, a TGA curve (in air) similar to Figure 5 was observed for both pyrolysis products (heated under 1600°C for 3 h in argon) from PPPS and PPVS, which reveals that 24.2 wt% and 35.0 wt% of carbon remains in the products, respectively.

We observed from the SEM micrographs (Figure 10) that the product from PPVS obtained at 1600 °C had a denser surface morphology than the product formed by PPPS, presumably because there is more C in the former system. In addition, both products have shown a high specific surface area (299.45 and 340.01 m^2/g for the pyrolysis products PPPS and PPVS, respectively), revealing that both pyrolysis products are very porous. Furthermore, the elemental analyses of both products (Table 2) reveal a 7-10.5 wt% oxygen content; therefore, the pyrolysis product of PPPS and PPVS heated at 1600°C for 3 h in argon can be best described as a mixture of C, SiO_2 and SiC.

After the pyrolysis products obtained by heating at 1600°C for 3 h in argon from both PPPS and PPVS were oxidized in air at 650°C for 2 h, yellow powdery products were obtained, suggesting that all the excess C in both products was removed under such a treatment. The SEM micrographs (Figure 10e and 10f) of the resulting products indicate that the oxidation has removed all the carbon between SiC particles. At the same time, the specific surface area of the products has decreased greatly after oxidation; for example, the oxidized product from PPVS has shown a specific surface area of 29.70 m^2/g.

We also noticed that, unlike the pyrolysis products with excess amounts of C from TEOS:FuOH, the SiC particles formed from PPPS or PPVS appear to be uniformly dispersed in the C matrix, which subsequently yields a homogeneous C-SiC ceramic composite. This uniform composite is probably formed because the C produced by the precursor is mixed with the SiO_2 more intimately than that in the biphasic TEOS:FuOH-derived products, which subsequently results in a homogeneous C-SiC distribution after the carbothermic reduction.

Pyrolysis of VPS

Recent work by Schmidt et al.[18] has indicated that the pyrolysis of vinylic polysilane (VPS) resulted in: cross-linking by vinyl polymerization with some hydrosilation at low temperatures (200-300 °C); extensive Si-Si, C-H and Si-H bond cleavage with radical formation and methylene insertion at intermediate temperatures (400-750 °C); and the consolidation of the SiC network along with the free carbon and partial crystallization of ceramic product at high temperatures. Unlike the precursors discussed above, there is no major weight loss above 750°C for the VPS, a circumstance that should make the morphologies and surface areas of the pyrolysis products differ from those derived from TEOS:FuOH, PPPS or PPVS.

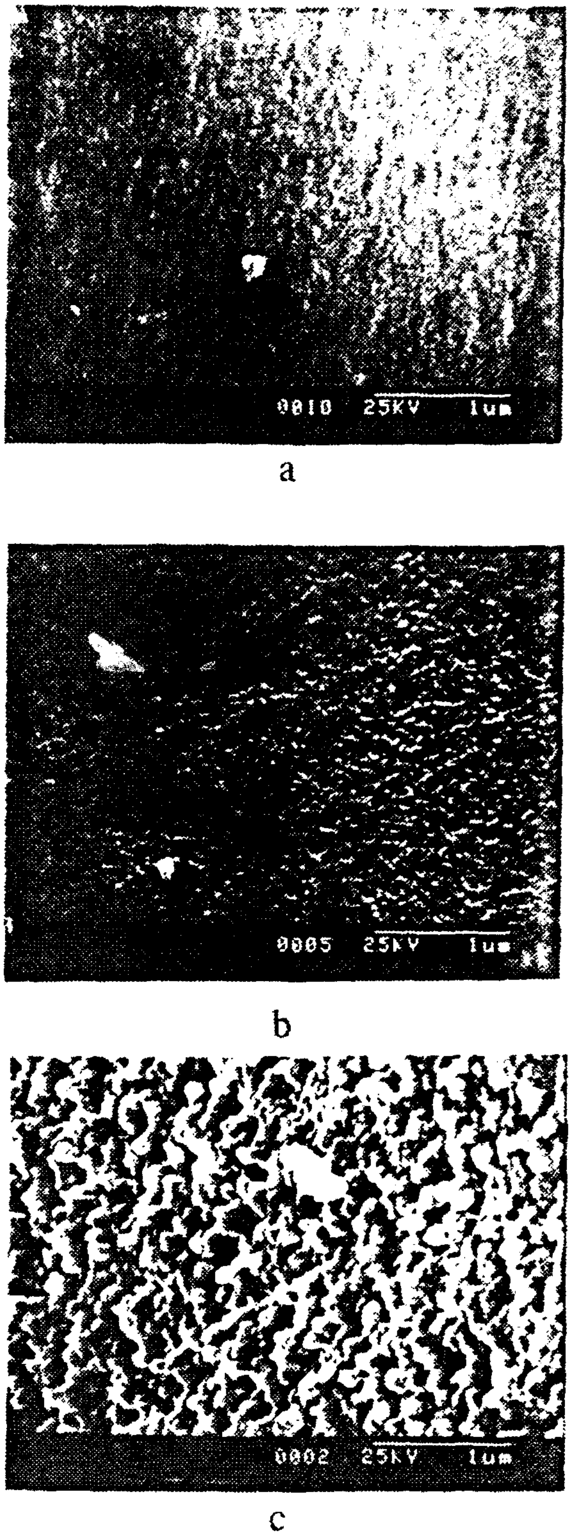

Figure 11. SEM micrographs of the pyrolysis products from VPS heated in argon at (a) 1200 °C for 6 h; (b) 1600 °C for 3 h; and (c) the oxidized residue (in air) of the product at (b).

The pyrolysis product of VPS obtained from heating at 1200 °C for 6 h consisted of a dark, shiny solid. The SEM micrograph (Figure 11a) of this product shows a smooth surface devoid of pores, just like the products from TEOS:FuOH, PPPS and PPVS. However, the XRD pattern of this product indicates that a significant of amount of β-SiC is present in the system. Actually, it has been reported[18] that crystalline β-SiC emerges at 1000 °C in this system. Further heating the product to 1600 °C led to a product giving sharper β-SiC peaks in the XRD pattern; furthermore, the SEM micrograph (Figure 11b) of this product indicated a porous surface. We observed that there was a 2.5% weight loss from 1200 °C (43.4%) to 1600 °C (45.9%); therefore, the porous surface in the latter case could be formed during the volatilization of gaseous product.

We noticed that the products obtained at 1200 and 1600 °C had much lower specific surface areas (0.18 and 2.59 m^2/g, respectively) than the products from TEOS:FuOH, PPPS or PPVS, presumably due to the fact that no gaseous products were generated during the decomposition of VPS above 1000 °C. These low specific surface areas had a significant effect on their oxidation resistance. For example, the TGA curve (Figure 12) for the product obtained at 1200 °C (relatively dense) showed that no oxidation occurs up to 1000 °C. The product obtained from 1600 °C (more porous) began to oxidize from 650 °C and ended at 950 °C, resulting in a 16% weight loss which is close to the amount of excess C predicted based on the elemental analysis.[18] Both products have better oxidation resistance than the products from TEOS:FuOH, PPPS or PPVS.

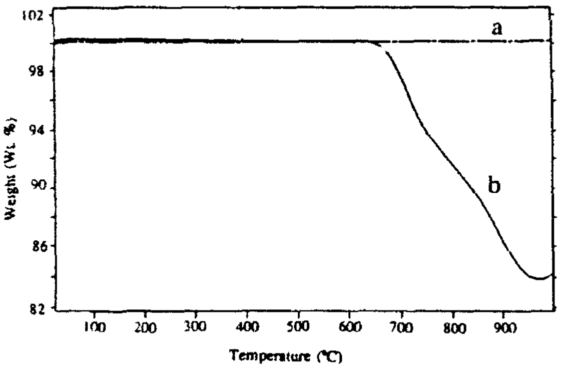

Figure 11. TGA curves (in air) of the pyrolysis products from VPS heated at (a) 1200 °C for 6 h and (b) 1600 °C for 3 h.

The TGA residue (in air) of the product obtained at 1600 °C is a yellow powder. The SEM micrograph (Figure 11c) of this product revealed that the SiC grain sizes are in the range of 50-100 nm and are uniformly distributed in the C matrix due to the internal molecular source of C, just as with PPPS and PPVS.

SUMMARY AND CONCLUSIONS

It is clear that heating TEOS:FuOH, PPPS and PPVS to 650°C resulted in the decomposition of all the organics, yielding a mixture of SiO_2 and C. This C/SiO_2 mixture, which possessed a glassy nature with a dense microstructure, was thermally stable in argon up to 1200°C where carbothermic reduction began. The gases evolved during the carbothermic reduction broke the dense glass into either porous or powdery SiC ceramics, depending on the C content and the extent of carbothermic reduction. Even though the carbothermic reduction had began between 1200-1300°C, the amorphous nature of the pyrolysis products revealed that SiC nucleation could be the major reaction in this temperature range. The abrupt increase in the crystallinity in the SiC phase above 1400°C suggested that crystallite growth is the major reaction above that temperature.

This work illustrates that, if the ratio of TEOS:FuOH in the starting material is carefully controlled, pure and submicron SiC powder can be directly synthesized from the $Si(OC_2H_5)_4$/FuOH/H_2O system under the proper pyrolysis conditions. Having control over the composition of the product is obviously the advantage of using a polymeric carbon precursor as an external C source since the ratio of C:SiO_2 can be easily adjusted. This system appears not to be suitable for the production of SiC coatings, fibers, or monoliths, since the precursor lacks the solubility and processibility unless proper modifications can be implemented.

We noticed that both PPPS and PPVS are soluble in hydrocarbon solvents and possess thermal processibility. Furthermore, their properties can be easily modified by blending with other polysilsesquioxanes. These advantages make them useful as precursors for ceramic fibers, monoliths or composite matrices.[16-17] However, the carbothermic reduction reactions involved in forming SiC may limit the applications for these precursors, because the high temperature (1600 °C) products for both precursors showed high porosity, making the products susceptible to oxidation around 600-700°C.

The formation of SiC from VPS begins at much lower temperatures than those needed for TEOS:FuOH, PPPS or PPVS. The low-temperature pyrolysis product shows superior oxidation resistance, and the processibility of this polymer has made it potentially useful as a composite matrix. In addition, the pyrolysis products from this precursor have much lower specific surface area than those of oxygen-containing precursors, making the products more oxidation-resistant.

ACKNOWLEDGEMENT

Financial support for this work was provided by the Air Force Office of Scientific Research (AFOSR) under Contract No. F49620-89-C-0102.

REFERENCES

1. S. Yajima, T. Shishido, and H. Kayano, "Development of High Tensile Strength Silicon Carbide Fibre Using an Organosilicon Polymer," *Nature (London)* **273**, 525
2. K. J. Wynne and R. W. Rice, "Ceramic via Polymeric Pyrolysis," *Ann. Rev. Mater. Sci.* **14**, 297-334 (1984).
3. H. J. Wu and L. V. Interrante, "Preparation of a Polymeric Precursor to Silicon Carbide via Ring-Opening Polymerization: Synthesis of Poly-[(Methylchlorosilane)-methylene] and Poly-(Silapropylene)," *Chem. Mater.* **1**, 564 (1989).
4. C.K. Whitmarsh and L.V. Interrante, *Organometallics* **10**, 1336 (1991).
5. D. Seyferth and H. Lang, "Preparation of Preceramic Polymers via the Metalation of Poly(dimethylsilene)," *Organometallics* **10**, 551-558 (1991).
6. R. West, L. D. David, P. I. Djurovich, H. Yu, and R. Sinclair,"Polysilastyrene: Phenylmethylsilane-Dimethylsilane Copolymers as Precursors to Silicon Carbide," *Am. Ceram. Soc. Bull.*, **62**, 899-903 (1983).
7. C. L. Schilling, "Polymer Precursor for Silicon Carbide Vinylic Polysilane Y-12044" in Union Carbide Technical Information Bulletin. U.S. Pat. No. 4783516, 1988
8. Z. F. Zhang, F. Babonneau, R. M. Laine, Y. Mu, J. F. Harrod, and J. A. Rahn, "Poly[methylsilane)-A High Yield Precursor to Silicon Carbide," *J Am. Ceram. Soc.*, **74[3]**, 670-73 (1991).
9. G. C. Wei, C. R. Kennedy, and L. A. Harris, "Synthesis of Sinterable SiC Powders by Carbothermic Reduction of Gel-Derived Precursors and Pyrolysis of Polycarbosilane," *Am. Ceram. Soc. Bull.* **63**, 1054-1061 (1984).
10. J. D. Birchall, M. J. Mockford, D. R. Stanley, P. M. L. Asher, and W. R. McCarthy, "Preparation of Polymeric Ceramic Precursors, and Ceramics Obtained by This Process," Eur. Pat. Appl. EP 284235 (1988).
11. Y. Sugahara, Y. Takeda, K. Kuroda, and C. Kato, "Carbothermal Reduction Process of Precursors Derived from Alkoxides for Synthesis of Boron-doped SiC Powder," J. *Mater. Sci. Lett.*, **8**, 944-946 (1989).
12. H. Tanaka and Y. Kurachi, "Synthesis of β-SiC Powder from Organic Precursor and its Sinterability," *Ceram. International*, **14**, 109-115 (1988).
13. D. A. White, S. M. Oleff, R. D. Boyer, P. A. Budinger, and J. R. Fox, "Preparation of Silicon Carbide from Organosilicon Gels: I, Synthesis and Characterization of Precursor Gels," *Adv. Ceram. Mater.*, **2[1]**, 45-52 (1987).
14. D. A. White, S. M. Oleff, and J. R. Fox, "Preparation of Silicon Carbide from Organosilicon Gels: II, Gel Pyrolysis and SiC Characterization," *Adv. Ceram. Mater.*, **2[1]**, 53-59 (1987).
15. F. Hatakeyama, "Synthesis of Monodispersed Spherical-Silicon Carbide Powder by a Sol-Gel Process," *J. Am. Ceram. Soc.*, **73[7]**, 2107-10 (1990).
16. F. I. Hurwitz, L. Hyatt, J. Gorecki, and L. D. Amore, "Silsesquioxanes as Precursors to Ceramic Composites," *Ceram. Eng. Sci. Proc.*, **8[7-8]**, 732-743 (1987).
17. F. I. Hurwitz, J. Z. Gyekenyesi, and P. J. Conroy, "Polymer Derived Nicalon/Si-C-O Composites: Processing and Mechanical Behavior," *Ceram. Eng. Sci. Proc.* **10[7-8]**, 750-763(1989).
18. W. R. Schmidt, L. V. Interrante, R. H. Doremus, T. K. Trout, P. S. Marchetti and G. E. Maciel, *Chem. Mater.* **3**, 257 (1991).
19. B. E. Yoldas, *J. Non-Crystalline Solids* **38**, 81 (1980).
20. H. F. Mark, N. M. Bikales, C. G. Overberger and G. Menges Eds., p 457 in Encyclopedia of Polymer Science and Engineering V(7), John Wiley & Sons Inc., New York, 1987.
21. Z. Jiang and W. E. Rhine, *Chem. Mater* **3**, 1132 (1991).
22. F. K. van Dijen and J. Pluijmakers, *J. Eur. Ceram. Soc.* **5**, 385 (1989).

SECTION 9

PREPARATION OF TITANIUM DIBORIDE FROM TITAINUM ALKOXIDES AND BORON POWDER

Zhiping Jiang and Wendell E. Rhine

Published in Chem. Mater., 4, 497 (1992)

The high chemical and thermal stability of TiB_2, along with its low electrical resistivity and high thermal conductivity, has made it a very interesting engineering ceramic material.[1] An important element controlling the commercial success of TiB_2 as an engineered ceramic material is the availability of pure, submicron TiB_2 powders at low processing temperatures. The methods most often used for preparing TiB_2 powders include either the direct reaction between Ti and B,[2] or the reduction of TiO_2 and B_2O_3 (or B_4C) by carbon.[3-4] These methods generally require high temperatures (around 2000 °C) and yield TiB_2 powders with low purity and large particle sizes (5 - 30 μm). High-purity TiB_2 powders have been prepared by a gas-phase reaction[5] or from organometallic precursors.[6-7]

This communication reports our results on the preparation of highly crystalline TiB_2 powders with small particle sizes (0.3 - 0.4 μm), by pyrolyzing mixtures of boron and a polymeric precursor. It is well known that thermal decomposition of furfuryl alcohol (FuOH) and hydrolysis of $Ti(OBu)_4$ produces carbon[8] and TiO_2,[9] respectively. Therefore, heating a mixture of boron, titanium butoxide and furfuyl alcohol should result in the generation of carbon and titanium oxide. As the temperature is increased the carbon causes the reduction of TiO_2, forming TiB_2 as the final product as indicated by reaction 1:

$$2C + 2B + TiO_2 = TiB_2 + 2CO \qquad (1)$$

The amorphous boron powder used in the present study had an average size of 0.22 μm, based on a centrifugal particle size analysis and SEM micrograph (Figure 1a). The elemental analysis of the powder indicated that it contained 94.06% B; oxygen was assumed to be the major impurity due to surface oxidation. The precursor with a nominal composition of $2.1B/[(FuO)_{0.63}(BuO)_{0.37}TiO_{1.5}]$ was prepared by hydrolyzing titanium butoxide and subsequently mixing it with boron powder.[10] The solid precursor obtained consisted of large (30 -

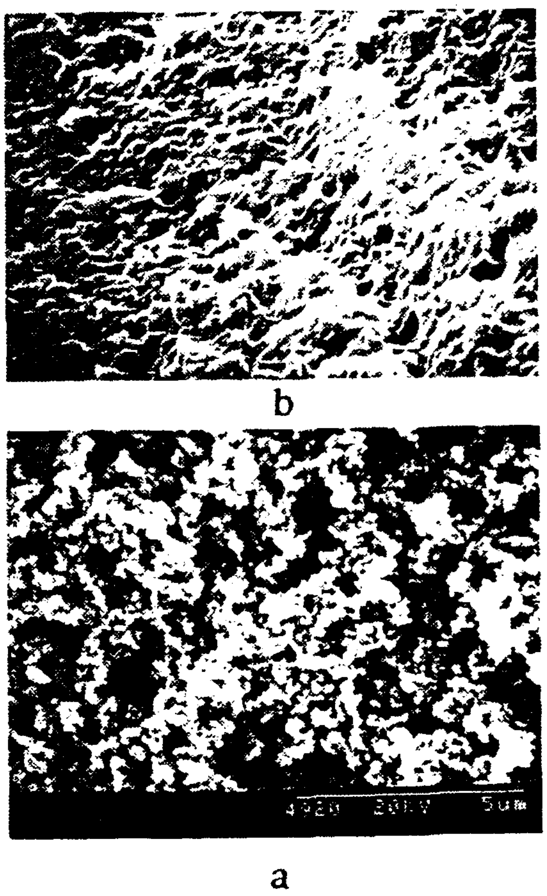

Figure 1. SEM micrograph of (a) boron powder and (b) the as-synthesized precursor.

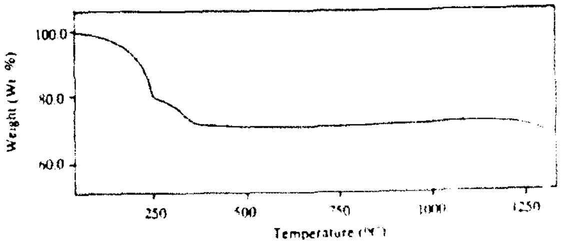

Figure 2. TGA curve of the precursor under a flow of argon.

200 μm), dark and irregularly shaped pieces. An SEM micrograph (Figure 1b) of the pieces revealed that the boron particles were well dispersed in the polymer, and the pieces were devoid of visible pores.

The FT-IR spectrum of the as-synthesized precursor is similar to the spectra previously reported[11] and indicates the existence of both furfuryl alcohol groups (3118 cm^{-1}, C-H stretching vibration of the olefinic H on the furan rings; 1718 and 1596 cm^{-1}, C=C stretching vibrations of the furan rings) and -OBu groups (2960, 2929 and 2870 cm^{-1}, C-H stretching; 1461 and 1375 cm^{-1}, C-H bending). In addition, two broad bands (one below 900 cm^{-1} and the other around at 3500 cm^{-1}) are observed in the spectrum, and they are attributed to the polymeric Ti-O units and the OH stretching vibration, respectively.

Figure 2 shows the TGA curve obtained for the precursor when heated under a flow of argon. The TGA curve indicates that decomposition occurs in three steps between 50-1320 °C. The first weight loss occurs between 120-260 °C and was attributed to the decomposition of -OBu groups; the second one occurs between 260-450 °C and corresponds to the decomposition of -OFu groups and polyfurfuryl alcohol, which will lead to the formation of carbon. All the organics are removed by 450 °C, and no additional weight loss is observed until 1200 °C where the third weight loss begins, which was attributed to the beginning of the carbothermic reduction reactions.

Table I. Weight Losses of the Precursor with a B:Ti Ratio of 2.1:1.0 Heated at Various Temperatures

temp, °C	700[a]	900[a]	900[b]	1100[a]	1300[a]	1500[a]
time, h	6	6		6	6	6
wt loss, wt %	30.70	30.98	29.50	37.23	53.77	66.60

[a] Based on weight loss of sample heated in furnace. [b] The weight loss at 900 °C on the TGA curve.

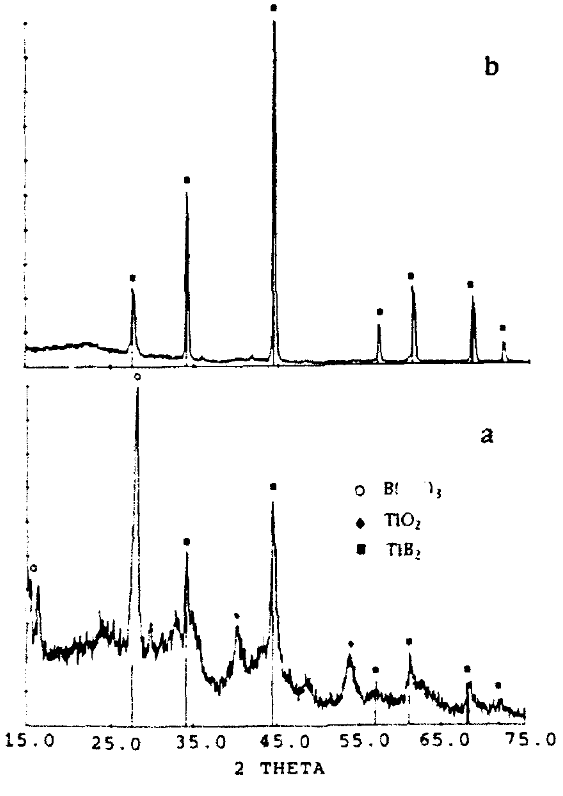

Figure 3. XRD patterns of the precursor heated in a flow of argon at (a) 700 °C and (b) 1300 °C for 6 h.

Weight losses were also determined by weighing samples after heating them in a carbon furnace, with a heating rate of 3.3 °C/min under a flow of argon. Table I shows the weight losses of the precursor between 700 and 1500 °C; these weight losses agree with those observed in the TGA at 900 °C (29.50%). When the precursor is heated at 1100 °C for 6 h, a 37.27% weight loss is observed, suggesting that carbothermic reduction has begun. Further heating the precursor to 1300 °C resulted in more weight loss, and an additional 12.7% weight loss occurred between 1300 and 1500 °C.

The evolution of crystalline phases during the decomposition of $2.1B/[(FuO)_{0.63}(BuO)_{0.37}TiO_{1.5}]_n$ was determined from the XRD patterns of the pyrolysis intermediates. Figure 3a shows the XRD pattern of the pyrolysis product heated at 700 °C for 6 h. The peaks marked with ■ are attributed to TiB_2; the peak at 44° (labeled as O) is assigned to TiO_2. The peaks labeled as ◆ match very well with the XRD pattern of boric acid, $(B(OH)_3)$; however, the IR spectra of this product indicates that B_2O_3 is the actual intermediate. The boric acid detected by XRD probably was produced by the hydrolysis of B_2O_3 during the XRD experiment.[12] After the precursor was heated at 900 °C for 6 h, the XRD pattern of the resulting product showed a similar X-ray diffraction pattern to that of the sample heated to 700 °C, except that the relative intensity of the TiO_2 peak had greatly decreased relative to the TiB_2 peaks. Based on the above observations, B_2O_3 is one of the products, and since no weight loss was observed below 900°C by TGA, carbon is not involved in the formation of TiB_2 below this temperature. Evidently, at these temperatures TiB_2 is formed by the borothermic reduction of TiO_2 through the following reaction:

$$10B + 3TiO_2 = 3TiB_2 + 2B_2O_3 \quad (2)$$

The borothermic reduction of TiO_2 is known and has been studied as a method for preparing TiB_2.[13,14,15] Barton et al.[14] studied the reaction between boron and TiO_2 under vacuum; their study indicated that B_2O_2, rather than B_2O_3, was one of the products:

$$TiO_2 + 4B = TiB_2 + B_2O_2 \quad (3)$$

However, they found that B_2O_2 decomposed to B and B_2O_3 above 450 °C in a nitrogen atmosphere through the following disproportionation reaction:

$$3B_2O_2 = 2B + 2B_2O_3 \quad (4)$$

Therefore, under the present experimental conditions, TiB_2 is assumed to form through reaction (2) which is the combination of reactions (3) and (4). Walker[15] has also reported the formation of TiB_2 at similar temperatures and with no weight loss, when he used B_4C as the boron source.

Heating the precursor to 1100 °C results in additional weight loss and, according to the XRD pattern, leads to the formation of TiC in addition to TiB_2 and B_2O_3. The TiC is presumably formed by the following reaction:[11]

$$TiO_2 + 3C = TiC + 2CO \quad (5)$$

The weight loss observed in the samples heated to 1100 °C in the furnace (Table I) and in the TGA beginning at 1200 °C (Figure II) is attributed to the evolution of CO and is evidence that the carbothermic reduction reaction begins above 1000 °C. The XRD pattern (Figure 3b) of the precursor heated at 1300 °C for 6 h shows that crystalline TiC and B_2O_3 phases have disappeared, and TiB_2 is the only crystalline phase remaining. This fact suggests that TiB_2 may also be formed between 1100 °C and 1300 °C, as illustrated by the following reaction:

$$TiC + B_2O_3 + 2C = TiB_2 + 3CO \quad (6)$$

The XRD pattern of the precursor heated to 1500 °C is similar to the XRD obtained after heating the precursor to 1300 °C (Figure 3b), except that the diffraction peaks are sharper.

Figure 4a shows the SEM micrograph of the pyrolysis product heated at 1300 °C for 6 h, and it indicates that some liquid phase was present in the product, which is presumably B_2O_3. Based on the results in Table I, we know that the carbothermic reduction (6) was not complete by 1300 °C. Evidently, the particles obtained at 1300 °C still contain B_2O_3, C, and/or TiC, which continue to react to form the final TiB_2 particles. An SEM micrograph (Figure 4b) of the product heated to 1500 °C shows that these TiB_2 particles are smaller than the powder obtained at 1300 °C. The particle size distribution measurement (with centrifugal technique) indicates that the particle sizes are between 0.05 and 1 μm. The average particle size based on the above distribution was 0.30 μm.

Table II. Elemental Analyses (wt %) of the Precursor and Pyrolysis Products under Argon

B/Ti[a]	*T*, °C	Ti	B	C	H	B/Ti[b]
2.1/1	as prepared	26.69	12.58	26.59	4.55	2.08
2.1/1	1500 (6 h)	70.67	27.49	0.37	0.22	1.77
2.3/1	1500 (6 h)	65.27	30.58	2.57	1.00	2.08

[a] Molar ratio as prepared. [b] Molar ratio analyzed.

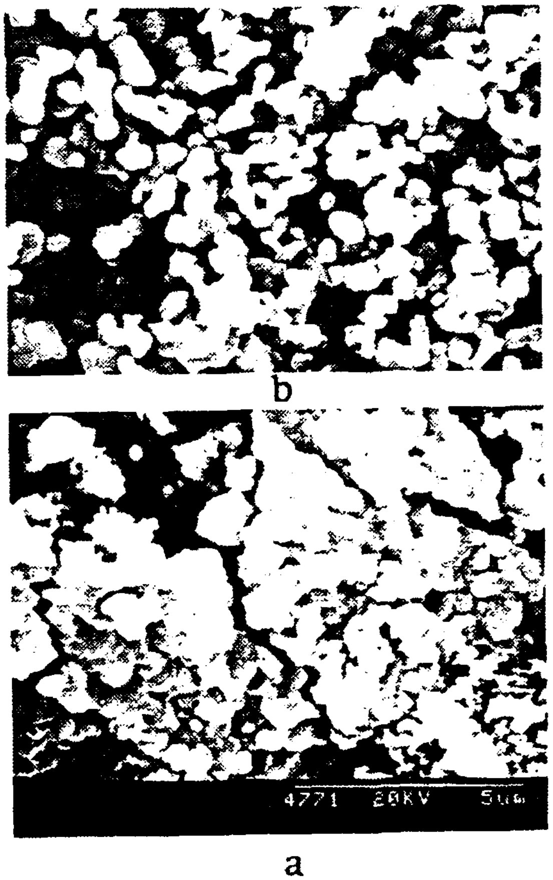

Figure 4. SEM micrographs of the precursor heated in a flow of argon at (a) 1300 °C for 6 h and (b) 1500 °C for 6 h.

The elemental analyses of the precursor and the pyrolysis product at 1500 °C (Table II) indicates that some boron was lost during the heat treatment, which subsequently led to a Ti:B ratio of 1:1.78 in the final product. This loss of boron is not surprising, since boron oxide is known to be volatile above 1300 °C. In addition, this B_2O_3 loss could be partially responsible for the weight loss between 1300 to 1500 °C. The pyrolytic yield (weigth of residue) of product after heating to 1500 °C was 33.40% and is 92.3% of the amonunt expected based on $Ti(O\text{-}nBu)_4$.

To prepare TiB_2 with a 1:2 Ti/B ratio in the final product, a precursor was synthesized which contained more boron and carbon and had a nominal composition of $2.3B/[(BuO)_{0.31}(FuO)_{0.69}TiO_{1.5}]_n$. After pyrolysis at 1500 °C for 6 h, the elemental analyses (Table II) of the resulting pyrolysis product indicated that it had a Ti:B ratio of 1:2.08 but still contained 2.57% C and 1.00% H. The oxygen content in this product was estimated to be less than 0.6%, based on the combined percentages (99.42 %) of Ti, B, C, and H. The average particle size of the product was found to be 0.38 µm. The low oxygen content of this product indicates that the carbothermic reduction of B_2O_3 is nearly complete at 1500 °C, a condition also observed in the borothermic/carbothermic reduction of TiO_2 with B_4C.[14]

Based on the above observations, pure TiB_2 powders with submicron sizes can be prepared with this procedure at 1500 °C if the quantities of the starting materials are carefully controlled. Furthermore, we found that the pyrolysis process did not follow reaction 1, but proceeded by a combination of borothermic and carbothermic reduction reactions in agreement with the results obtained by Walker.[14] However, reaction 1 still can be used to describe the overall reaction, since it is obtained by combining reactions 3, 4, 5 and 6.

Acknowledgements

Financial support for this work was provided by the Air Force Office of Scientific Research (AFOSR) under Contract No. F49620-89-C-0102.

References

1. (a) Kim, J. J.; McMurtry, C. H., *Ceram. Eng. Sci. Proc.* **1985**, 6, 1313. (b) Greenwood, N. N. in Comprehensive Inorganic Chemistry; Edited by Bailar, Jr., J.C., Emeleus, H. J.; Nyholm, R.; Trotman-Dickenson, A. F., Vol(1), Pergamon Press, Oxford, **1973**, p. 697. (c) Funk, R.; Lux, B.; Schachner, H.; Tannenberger, H., **Fr. Patent 2144823, 1973**; Chemical Abstract **1973**, 79, 107206. (d) Murata, Y.; Miccioli, B. R., *Amer. Ceram. Soc. Bull.* **1971**, 50, 182. (e) Janney, M. A., *Amer. Ceram. Soc. Bull.* **1987**, 66, 322. (f) McMurtry, C. H.; Boecker, W. D. G.; Seshadri, S. G.; Zanghi, J. S.; Garnier, J. E., *Amer. Ceram. Soc. Bull.* **1987**, 66, 325. (g) Watanabe, T., *J. Ceram. Soc. Japan* **1991**, 99, 146.

2. Palty, A. E.; Margolin, H.; Nielsen, J. P., *Trans. Am. Soc. Metals* **1954**, 46, 312.

3. Thompson, R., In Progress in Boron Chemistry, Pergamon: New York **1975**; 195.

4. Greenwood, N. N.; Parish, R. V.; Thornton, P., *Quarterly Rev.* **1966**, 20, 444.

5. Baumgartner, H.R.; Steiger, R. A., *J. Am. Ceram. Soc.* **1984**, 67, 207.

6. Gallagher, M. K.; Rhine, W. E.; Bowen, H. K., Ultra-Structure Processing of Advanced Ceramics, Mackenzie, J. D. and Ulrich, D. R. Eds., John Wiley & Sons Inc.: New York, **1988**, p. 901.

7. Su, K.; Sneddon, L. G., *Chem. Mater.* **1991**, 3, 10.

8. Mark, H. F.; Bikales, N, M.; Overberger, C. G.; Menges, G., Eds. Encyclopedia of Polymer Science and Engineering Vol (7); John Wiley & Sons Inc.; New York, **1987**.

9. Bradley, D. C.; Mehrotra, R. C.; Gaup, D. P., Metal Alkoxides, Academic Press: New York, **1978**.

10. A solution of 0.32 g of 1 N H_2SO_4 in 20 mL THF was added dropwise to 30 mL of a THF solution containing 4.00 g titanium butoxide and 0.73 g furfuryl alcohol, under vigorous stirring. The resulting yellow solution was then mixed with 0.284 g of boron powder, yielding a dark suspension of boron powder in the THF solution of furfuryl alcohol-$(BuO)TiO_{1.5}$ (the $B:Ti:FuOH:H_2O$ molar ratio in the starting material is 2.1:1.0:0.63:1.5). After this suspension was stirred at room temperature for 2 h, the volatile components (THF and n-butanol) were removed by distillation at 150 °C under vacuum, leaving a dark solid (2.2 g) which was insoluble in hydrocarbon solvents. This precursor has a nominal composition of $2.1B/[(FuO)_{0.63}(BuO)_{0.37}TiO_{1.5}]_n$.

11. Jiang, Z.; Rhine, W. E., *Chemistry of Materials* **1991**, 3, 1132.

12. The XRD sample for Figure 3a was prepared by grinding the sample in air, dispersing the fine powder on a piece of glass slide with colloidion and drying the slide in oven. The samples prepared in this way experienced severe hydrolysis. For example, commercial B_2O_3 showed a XRD spectrum similar to that of $B(OH)_3$ based on this procedure. The IR sample of the pyrolysis product obatined at 700 °C was prepared by mixing the pyrolysis product with dry KBr in a drybox. The ground mixture was transferred into the IR sample cell in a glove box and quickly transferred to the IR spectrometer's sample chamber, which was flushed with N2 for a minimum 10 min before data collection. In this way, the hydrolysis of B_2O_3 can be avoided as indicated by the absence of the BO-H absorptions (3200 and 1200 cm^{-1}) in the IR spectrum. However, when the IR sample was ground in air, the BO-H absorptions were observed in the IR spectrum.

13. Barton, L.; Nicholls, D., *J. Inorg. Nucl. Chem.* **1966**, 28, 1367.

14. Walker, J. k., *Adv. Ceram. Mater.* **1988**, 3, 601.

15. Peshev, R., and Bliznakov, G., *J. Less-Common Met.* **1968**, 14, 23

SECTION 10

PREPARATION OF TITANIUM DIBORIDE FROM BOROTHERMIC REDUCTION OF TiO_2, $TiO_x(OH)_y$, or $Ti(O\text{-}n\text{-}Bu)_4$-DERIVED POLYMERS

Zhiping Jiang and Wendell E. Rhine
Ceramics Processing Research Laboratory
Massachusetts Institute of Technology, Cambridge, MA 02139

Accepted for publication in J. Eur. Ceram. Soc.

ABSTRACT

The reaction between amorphous boron powder and TiO_2, $TiO_x(OH)_y$ or titanium-alkoxide derived polymers (B:Ti=4:1) was studied at 25 - 1500 °C in a flow of argon. The borothermic reduction of TiO_2 resulted in formation of Ti_2O_3 and $TiBO_3$ at 600 °C; TiB_2 was formed by further borothermic reduction of Ti_2O_3 and $TiBO_3$ above 700 °C; the overall reaction was found to be complete at 1300 °C. The particle sizes of TiB_2 powders obtained were directly related to the starting material used as the titania source. The largest particles were obtained when TiO_2 powder was used as the starting material. The particles were smaller when $TiO_x(OH)_y$ powder was used, and the smallest particles were obtained when the partially-hydrolyzed Ti polymer, $[BuOTiO_{1.5}]_n$, was used as the titanium source. The pyrolysis chemistry of these precursors as well as the morphology of the pyrolysis products were studied by FT-IR, TGA, SEM, XRD, BET, elemental analyses and particle size analyses.

INTRODUCTION

Titanium diboride (TiB_2) is a hard refractory material, which possesses a high melting point, low electrical resistivity and high thermal conductivity.[1] In addition, sintered TiB_2 is resistant to oxidation to 1100 °C and chemically stable in many harsh, corrosive environments.[2] TiB_2 also has low solubility and is wetted by most molten metals up to 1000 °C. The combination of these properties makes TiB_2 a very interesting engineering ceramic material which can be used as ballistic armor, coatings for cutting tools,[3] crucibles and electrodes in metal-refining equipment such as aluminum reduction cells.[4] Furthermore, previous studies indicated that TiB_2 is an excellent component of high-temperature composite materials such as TiB_2/SiC,[5-6] and TiC/TiB_2,[7].

An important element controlling commercial success of TiB_2 as an engineered ceramic material is the availability of pure TiB_2 in various forms (powder, whiskers, fibers, etc.) for fabricating materials at low processing temperatures. There are currently four principle methods for preparing TiB_2 powders: synthesis from the elements (Ti and B) at over 2000 °C,[8] reduction of TiO_2 and B_2O_3 by carbon at 2000 °C,[9] reduction of TiO_2 by boron carbide and carbon at 2000 °C,[1,10] and reduction of the titanium and boron halides by hydrogen at 1200 °C.[11] These methods, except the last one, require high temperatures; furthermore, the powders generated from these methods, in general, have large particle sizes (5 - 30 µm); therefore, extensive milling is required before the material can be processed. Titanium diboride powders prepared by carbothermic reduction methods are usually contaminated by carbon and oxygen which adversely affect the mechanical properties of TiB_2.[1,12] Therefore, improved methods are needed.

In a recent communication[13] we reported that the reaction between B, C and TiO_2 proceeded by a combination of borothermic and carbothermic reduction reactions. Since the borothermic reduction of TiO_2 proceeded at low temperatures we decided to examine this approach in more detail. One of the advantages of this method is that the carbon impurity, which usually exists in the TiB_2 products generated from the carbothermic reduction of oxides, can be avoided. However, details about the reaction mechanism, intermediate phases and morphologies of the intermediates for the borothermic reduction of TiO_2, as well as the effect of the Ti source on these factors, are unresolved issues. Our intention was to begin addressing some of these issues of borothermic reduction by reacting boron powder with TiO_2, $TiO_x(OH)_y$, or a $Ti(O\text{-}n\text{-}Bu)_4$-derived polymer.

EXPERIMENTAL

Titanium diboride was prepared from boron powder and three different titanium oxide sources, TiO_2, $TiO_x(OH)_y$, and $[BuOTiO_{1.5}]_n$. The methods used to prepare the mixtures of boron powder and the Ti source are described below.

Preparation of Mixtures from Boron and TiO_2: A mixture of boron powder (Gallery Chemical Company, Gallery, PA) and TiO_2 powder (Fluka AG, Buchs, West Germany) in a molar ratio of 4:1 was prepared by adding the powders to a round bottom flask and dispersing them in tetrahydrofuran (THF). After the resulting suspension was stirred at room temperature for 2 h, the solvent was removed under vacuum at 100 °C, leaving a grayish powder.

To study the mechanism for the reaction between boron and TiO_2, mixtures of boron and other oxides were prepared. The same procedure as described above was used to prepare these mixtures of boron with Ti_2O_3, B_2O_3, and $TiBO_3$. The ratios of boron to the oxide in these samples were 7B:Ti_2O_3, 3TiO_2:B, 3TiO_2:B_2O_3:B and $TiBO_3$:4B.

Synthesis of TiB_2 Precursor from Boron and $TiO_y(OH)_x$: The starting material, $TiO_y(OH)_x$, for preparation of TiB_2 was synthesized by hydrolyzing titanium butoxide with 5 equivalents of water (containing ammonium hydroxide) in THF solvent under vigorous stirring. The B:Ti:H_2O ratio of the starting material is 4:1:5; NH_4OH was used as the hydrolysis catalyst. Adding the ammonium hydroxide (NH_4OH) to the $Ti(O\text{-}n\text{-}Bu)_4$ solution in THF resulted in the immediate formation of a white precipitate. After stirring the suspension for 0.5 h, the boron powder was added into the system. After the resulting dark suspension was stirred for 0.5 h, the volatile components were removed under vacuum at 150 °C, leaving a dark powder. This precursor had a nominal composition of $4B/TiO_x(OH)_y$ $(2x+y=4)$.

Synthesis of TiB_2 Precursor from $[BuOTiO]_{1.5}$: A polymeric titanium precursor was also prepared by partially hydrolyzing titanium butoxide ($Ti(O\text{-}n\text{-}Bu)_4$) with 1.5 equivalents of H_2O in THF solvent under vigorous stirring. The resulting yellow solution was then mixed with boron powder, yielding a dark suspension (the B:Ti:H_2O ratio in the starting material is 4:1:1.5). After this suspension was stirred at room temperature for 2 h, the volatile components were removed by distillation at 150 °C under vacuum, leaving a dark solid, which was insoluble in hydrocarbon solvents. This precursor has a nominal composition of $4B/(BuO)TiO_{1.5}$.

Pyrolysis of Precursors and Powder Mixtures: Samples of the above mixtures (0.3 - 1 g) were placed in carbon crucibles and pyrolyzed in a carbon furnace under a flow of argon (ultra-high purity grade) at a flow rate of 300 mL/min. The temperature was increased from room temperature to 1500 °C at a heating rate of 200 °C/h, held at the desirable temperature for 6 hours, and then cooled to room temperature.

The B_2O_2 by-product was removed by washing the pyrolysis product (0.3 g) in hot water (85 °C, 50 mL) for 20 min, and the TiB_2 product was isolated by filtering. The product was dried at 100 °C under vacuum.

Characterization: Diffuse reflectance infrared Fourier transform spectroscopy (DRIFTS) studies were performed with a infrared spectrometer (Nicolet PC/IR-44, Nicolet Analytical Instruments, Madison, WI). Samples were prepared by mixing the starting material or the pyrolysis product with dry KBr in a drybox. The ground mixture was transferred into the IR sample cell in the drybox and quickly transferred to the IR spectrometer's sample chamber which was flushed with N_2 for a minimum 10 min before data collection. Thermal decomposition of the starting materials was studied with TGA (TGA7, The Perkin-Elmer Corporation, Norwalk, CT). X-Ray powder diffraction (XRD) patterns were measured with a X-ray diffractometer (Rigaku 300, Rigaku Corporation, Japan) employing Cu Kα radiation and a Ni filter at a scanning rate of 10°/min. The X-ray peak assignments were carried out using Rigaku software JCPDS peak indexing program. The preparation of the samples for the XRD measurements was performed by grinding the sample in the glove box and putting the resulting fine powder on a piece of greased glass slide to minimize the oxidation and hydrolysis of the samples. When the XRD samples were prepared by grinding the sample in air, dispersing the fine powder in collodion on a glass slide, and drying the slide in an oven, severe hydrolysis and oxidation of boron suboxides were observed. The particle-size distribution (by area) of the pyrolysis products was measured by a centrifugal analysis method (Capa-500, Horiba Inst. Inc., Irving, CA) using samples dispersed in isopropanol with an ultrasonic bath. The specific surface area of the product was measured by single-point BET (Quantasorb, Quantachrome Corp., Syosset, NY). The morphologies of the starting materials and the pyrolysis products were observed using a scanning electron microscope (SEM Model S-530; Hitachi Inst. Inc., Mountain View, CA). Elemental analyses were obtained from E+R Microanalytical Laboratory, Inc. (Corona, NY).

RESULTS AND DISCUSSION

The borothermic reduction of metal oxides is well known,[9-10,14-17] and Peshev and Blinzakov[15] have studied the reaction between boron and TiO_2. Based on these previous studies, we expected the borothermic reduction to proceed according to the following reaction:

$$4B + TiO_2 \rightarrow TiB_2 + B_2O_2 \quad (1)$$

The B_2O_2 produced by this reaction is reported to be an amorphous solid.[17] To investigate the properties of the titanium diboride obtained by the above reaction, boron was reacted with TiO_2, $TiO_x(OH)_y$, or partially hydrolyzed titanium butoxide at 500 - 1500 °C. The boron source used in this study was an amorphous powder, which was composed of submicron particles (the average size of the boron particles dispersed in isopropanol was 0.22 µm based on the centrifugal particle size measurement; the specific surface area was 20.41 m^2/g from BET measurements). The elemental analysis of this powder indicated a 94.06% boron content; oxygen was assumed to be the major impurity due to surface oxidation. The TiO_2 sources were crystalline (anatase) TiO_2 powder with an average particle size of 0.63 µm and a specific surface area of 2.94 m^2/g, an amorphous titanium hydrous oxide ($TiO_x(OH)_y$), or the titainum butoxide-derived ($[BuOTiO_{1.5}]_n$) polymer.

Synthesis of TiB_2 from Boron and TiO_2

Based on the XRD studies, the reaction between TiO_2 and boron began at 600 °C. The product obtained from TiO_2 and boron powders (B:Ti=4:1) after heating to 600 °C for 6 h was a dark powdery solid. The XRD pattern of the product dispersed in grease indicated that crystalline TiO_2 (anatase), $TiBO_3$ and Ti_2O_3 were present. After heating the mixture to 700 °C the XRD pattern indicated that the TiO_2 crystalline phase disappeared and TiB_2 appeared (Figure 1a) and was now present in addition to Ti_2O_3 and $TiBO_3$. Furthermore, the XRD pattern of the product dispersed in collodion (Figure 1b) showed that the same product also contained crystalline $B(OH)_3$ in addition to TiB_2, Ti_2O_3, and $TiBO_3$ as indicated by the large diffraction peak at $2\theta = 27.8°$. The small peak at $2\theta = 27.8°$ in Figure 1a is due to either TiB_2 or to a small amount of $B(OH)_3$ that formed during sample preparation. Either the solvents used for or the hydorphilic properties of collodion causes the B_2O_2 in the sample to oxidize and hydrolyze forming $B(OH)_3$.[17] The oxidation and hydrolysis of B_2O_2 does not occur or is very slow for samples dispersed in a hydrocarbon grease (Figure 1a).

After the mixture of TiO_2 and boron was heated at 900 °C, the XRD pattern (in grease) of the resulting product indicated that TiB_2 was the only crystalline phase. As indicated in Table 1, no weight

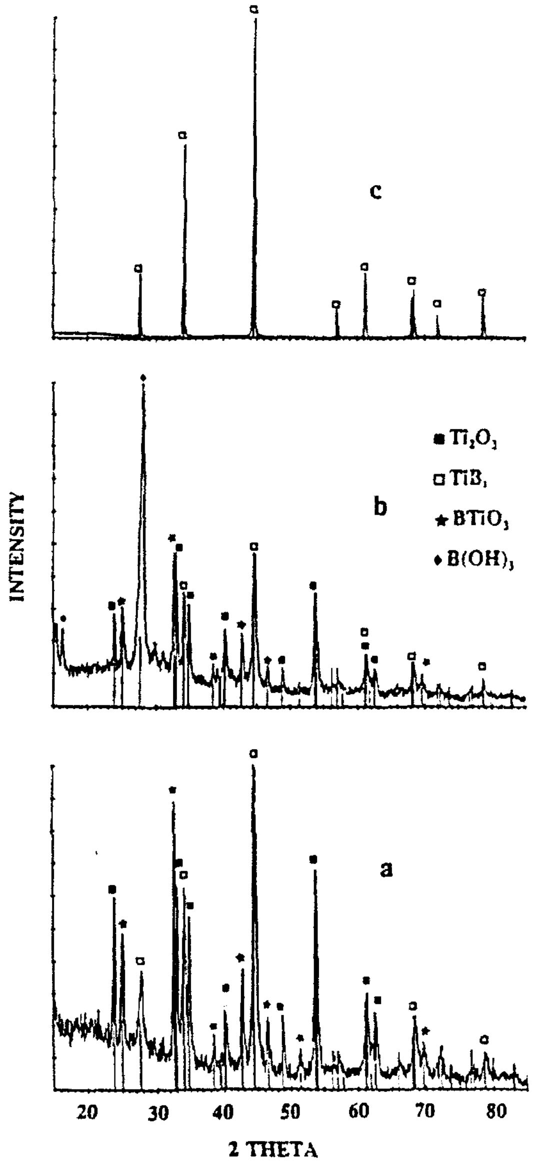

Figure 1. XRD patterns of the pyrolysis product obtained from a mixture of TiO_2 and boron heated at (a) 700 °C, 6 h (in grease), (b) 700 °C, 6 h (in collodion), and (c) 1300 °C, 6 h (in grease).

Table 1 Pyrolysis Residues (Wt%) for the Mixtures

Ti source	Temperature 700°C[a] (6 h)	 900°C (20h)	 1300°C (6 h)	 1500°C (6 h)
TiO_2	100	100	76.2	51.2
$TiO_x(OH)_y$	95.1	94.9	76.5	46.1
$[BuOTiO_{1.5}]_n$	61.1	59.0	32.8	28.3

a: heating time in parenthesis.

Table 2 Elemental Analyses (Wt%) of the Products Obtained by Heating the Precursors under Argon for 6 h.

Ti source	T(°C)	Ti	B	C	H	Ba/Ti
TiO_2	1300[a]	69.21	30.78	-	-	1.97
	1500[b]	69.47	30.38	-	-	1.94
$TiO_x(OH)_y$	1300[a]	68.34	31.50	0.50	-	2.04
	1500[b]	68.74	31.38	-	-	2.02
$[BuOTiO_{1.5}]_n$	1300[a]	69.17	30.38	0.52	0.55	1.95
	1500[b]	69.84	30.21	0.35	0.10	1.92

[a] after washing with hot water. [b] as-pyrolyzed.

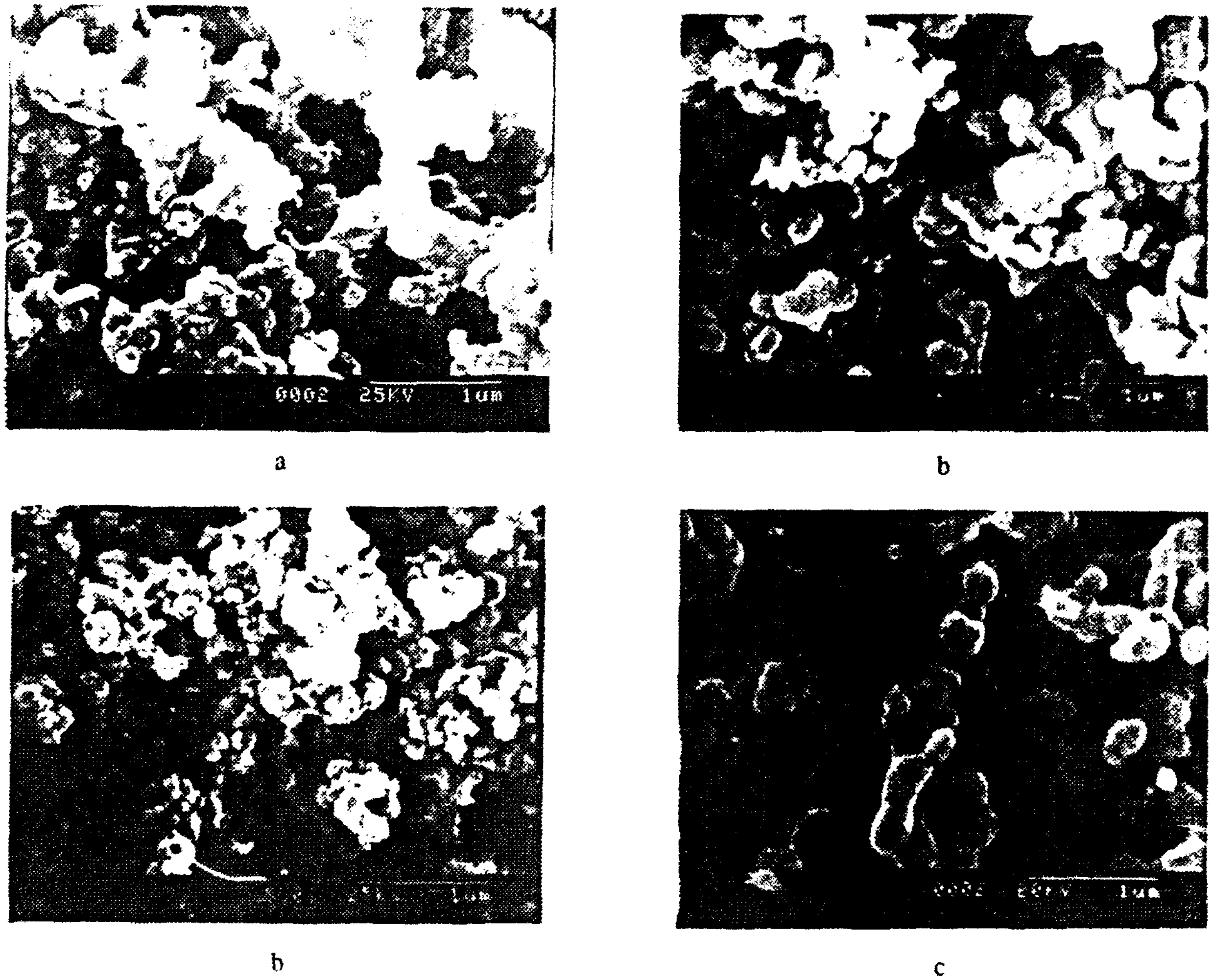

Figure 2. SEM micrographs of product obtained from a mixture of TiO_2 and boron heated at (a) 900 °C for 6 h. (b) the same product as (a) after washing with H_2O, (c) 1300 °C for 6 h, after washing, and (d) 1500 °C for 6 h, as-synthesized.

loss was observed after firing a mixture of boron and TiO_2 under argon up to 900 °C, which indicated that all the B_2O_3 by-product still remained in the product at 900 °C. The SEM micrograph of the product heated at 900 °C (Figure 2a) indicated that the product contained particles and a glassy phase; the latter phase was presumably B_2O_3. After this product was washed with hot water to remove the boron oxide, the XRD pattern of the resulting product illustrated that TiB_2 was the only crystalline phase, and the SEM micrograph (Figure 2b) indicated that the product consisted of small agglomerated particles (surface area = 8.57 m^2/g).

The elemental analyses of the product heated to 900 °C indicated that it contained approximately 10 wt % oxygen, suggesting that the reaction between boron and TiO_2 was not complete at 900 °C. Further heating the mixture to 1300 °C resulted in a grayish powder. The XRD analysis (in grease) illustrated that TiB_2 was the only crystalline phase (Figure 1c). We determined (Table 1) that a significant weight loss occurred at 1300 °C due to the vaporization of boron oxide. However, both SEM and XRD analysis (on collodion) of this product revealed that some boron oxide still remained in the product. The SEM micrograph of the product (Figure 2c) indicated the particle sizes had increased relative to that of the product obtained at 900 °C. The average particle size of the product dispersed in isopropanol was 0.74 μm (surface area = 6.65 m^2/g). Furthermore, elemental analyses (Table 2) indicated that the product contained a low oxygen content (by difference) and had a stoichiometry close to TiB_2, confirming that the reaction was complete after heating at 1300 °C for 6 h.

Heating the mixture to 1500 °C resulted in further weight loss (Table 1) due to the vaporization of boron oxide, and the elemental analyses of the as-fired product showed a stoichiometry close to that of the product obtained at 1300 °C (after washing). This result suggested that all the boron oxide by-product was vaporized at 1500 °C. However, the SEM micrograph (Figure 2d) of this product illustrated that the TiB_2 particles started to coarsen.

Our results were slightly different than Peshev and Bliznakov's[14]. First, in their work, the crystalline TiO_2 (either anatase or rutile) phase remained in the product up to 1500 °C; in addition, they did not observe Ti_2O_3 and $TiBO_3$ as intermediates. Secondly, our results indicated that the borothermic reduction was complete after heating to 1300 °C for 6 h, which was a lower temperature, but longer time than that reported in Peshev and Bliznakov's work (1700 °C for 1 h).

The presence of Ti_2O_3 and $TiBO_3$ as intermediate products suggested that the borothermic reduction of TiO_2 is more complicated than depicted by reaction 1. Based on our XRD results it appears that boron reacts with TiO_2 to form Ti_2O_3 and $TiBO_3$, and then these two phases disappear at 900 °C, presumably reacting with boron to form TiB_2. Therefore, we propose that the following reactions are involved in the borothermic reduction of TiO_2:

$$4TiO_2 + 2B \rightarrow 2Ti_2O_3 + B_2O_2 \qquad (2)$$

$$B_2O_2 + 2TiO_2 \rightarrow 2TiBO_3 \qquad (3)$$

$$3TiO_2 + B \rightarrow TiBO_3 + Ti_2O_3 \qquad (4)$$

$$2Ti_2O_3 + 14B \rightarrow 4TiB_2 + 3B_2O_2 \qquad (5)$$

$$2TiBO_3 + 8B \rightarrow 2TiB_2 + 3B_2O_2 \qquad (6)$$

Here, reaction 4 is the combination of reaction 2 and 3.

To confirm reaction 4, a mixture of TiO_2 and boron (3:1 ratio as indicated by reaction 4) was fired at 900 °C for 6 h under a flow of argon; Ti_2O_3 and $TiBO_3$ were the only crystalline phases in the product. Furthermore, since B_2O_2 can be formed from reaction 7,[17] reaction 3 was confirmed by preparing a sample of $TiBO_3$ by reaction 8.

$$2B + 2B_2O_3 \rightarrow 3B_2O_2 \qquad (7)$$

$$3TiO_2 + B_2O_3 + B \rightarrow 3TiBO_3 \qquad (8)$$

Heating a mixture of TiO_2, B_2O_3, and B in an argon atmosphere for 9.5 h at 700°C resulted in the formation of TiO_2 (rutile) and $TiBO_3$. The conversion of anatase to rutile is expected since Pavlikov et al.[18] reported that rutile crystallizes from a mixture of B_2O_3 and TiO_2 if heated above 680°C. After heating the mixture at 900 °C for 7 h, $TiBO_3$ was obtained. The product had the same X-ray diffraction pattern (Figure 3) as reported by Schmid[19] and no other phases were observed. Titanium borate was also prepared by reacting B_2O_3 with Ti_2O_3, but the reaction proceeded slowly and the yield was low. Although $TiBO_3$ could be prepared by reacting B_2O_3 with Ti_2O_3, B_2O_3 is not expected to be a product in these reactions. These results imply that reaction 2 proceeds to produce B_2O_2 which subsequently reacts with TiO_2 to produce $TiBO_3$ as indicated by reaction 3.

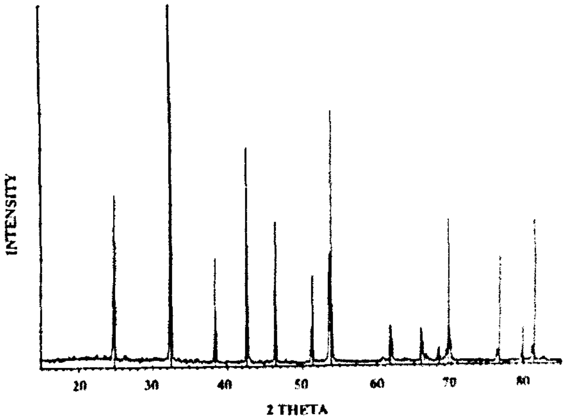

Figure 3. X-ray diffraction pattern observed for $TiBO_3$.

Reaction 5 was confirmed by heating a mixture of boron and Ti_2O_3 ($7B:Ti_2O_3$) in an argon atmosphere at 900 °C for 20 h; the XRD pattern of the resulting product indicated that TiB_2 was the major phase present and a small amount of unreacted Ti_2O_3 still remained. Reaction 6 was confirmed by heating a mixture of $TiBO_3$ and B at 900 °C for 13 h, and TiB_2 was the only product obtained.

Synthesis of TiB_2 from Boron and $TiO_x(OH)_y$

The TiB_2 particles obtained from the mixture of boron and $TiO_x(OH)_y$ powders were similar to those obtained from the mixture of TiO_2 and boron, but there was a significant difference in the particle sizes obtained. Pyrolyzing this mixture in an argon atmosphere at 900°C for 6 h resulted in small particles of TiB_2 (surface area = 20.34 m^2/g). After heating at 1300 °C for 6 h the small particles of TiB_2 increased in size (Figure 4a) (0.2-0.7 μm; surface area = 8.11 m^2/g), and heating the mixture to 1500 °C increased the particle sizes further (Figure 4b). Although the product obtained at 900°C had a high surface area, SEM micrographs of the products obtained at 1300 and 1500 °C indicated that individual particles were larger than those obtained from TiO_2. Furthermore, a small weight loss was observed for the mixture at 700-900 °C (Table 1); the weight loss below 900 °C for the mixture of $TiO_x(OH)_y$ and boron was attributed to the condensation of Ti-OH groups and subsequent evolution of H_2O. In addition, the elemental analyses (Table 2) of products at 1300 and 1500 °C indicated a B/Ti ratio of 2.02 and low carbon contents.

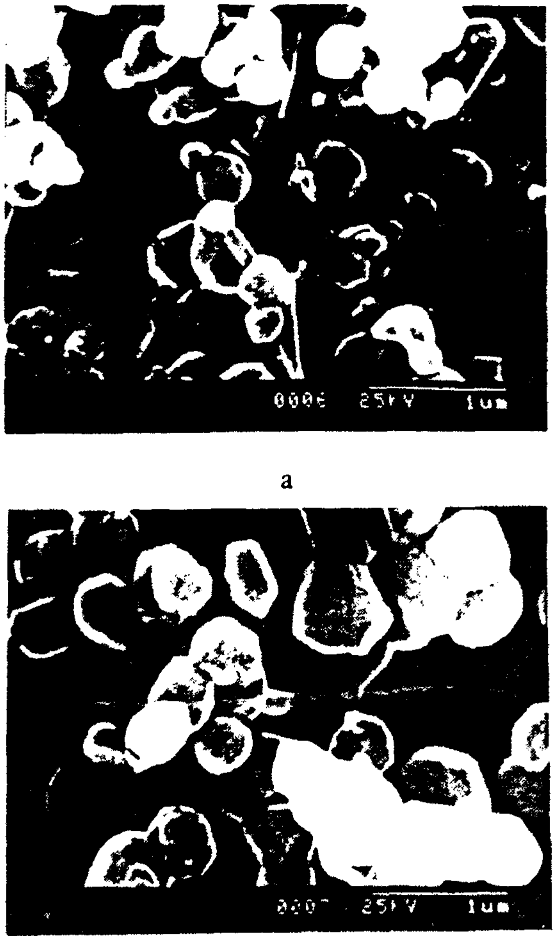

a

b

Figure 4. SEM micrographs of the product obtained from a mixture of $TiO_x(OH)_y$ and boron (a) heated at 1300 °C for 6 h, after washing, and (b) heated at 1500 °C for 6 h, as-synthesized.

Synthesis of TiB_2 from Boron and $Ti(O\text{-}n\text{-}Bu)_4$-Derived Polymers

The mixture of boron and $[BuOTiO_{1.5}]_n$ was synthesized by partially hydrolyzing the Ti butoxide and mixing the resulting Ti polymer with boron powder. The FT-IR spectrum of the as-synthesized mixture of boron and $[BuOTiO_{1.5}]_n$ (Figure 5a) is similar to the spectrum reported previously[20] and indicated the existence of the -OBu groups; they are represented by the strong C-H stretching (2960, 2929 and 2870 cm^{-1}) and C-H bending (1461 and 1375 cm^{-1}) vibrations. In addition, the broad band below 900 cm^{-1} in the IR spectrum is attributed to the polymeric Ti-O units in the precursor. The broad absorption band around 3300 cm^{-1} is assigned as the TiO-H stretching vibration; these OH groups could be due to the hydrolysis of Ti-OBu units during the IR measurement.

Pyrolysis of this mixture of boron and $[BuOTiO_{1.5}]_n$ in argon resulted in the decomposition of -OBu groups and condensation of Ti-OH groups. By 300 °C, no organics were left in the product based on the IR spectra (Figure 5b). Table 1 lists the weight of the pyrolysis residues obtained between 700 and 1500 °C and reveals that there is almost a 40 % weight loss by 700 °C. The XRD pattern of the 600 °C as-pyrolyzed product dispersed in grease indicated that $TiBO_3$ was the only crystalline phase; at 700 °C, TiB_2 was observed in addition to $TiBO_3$. Heating the precursor to 900 °C increased the crystallinity of TiB_2, and the XRD peaks corresponding to $TiBO_3$ disappeared. We noticed, based on the XRD results, that no crystalline titanium oxides formed during the pyrolysis between 600 and 900 °C, which indicates that any reduced titanium oxides are present in the amorphous state.

After the product obtained at 900 °C was washed with hot water, the resulting product, consisted of large (30-100 μm), irregularly shaped agglomerates which could easily be milled into fine particles. An SEM micrograph (Figure 6a) revealed that these agglomerates were loosely connected and consisted of fine particles. BET studies indicated that this product possessed a specific surface area of 24.23 m^2/g, which is 3 times higher than that (8.57 m^2/g) for the product obtained from TiO_2 powder under the same conditions. The calculated equivalent spherical

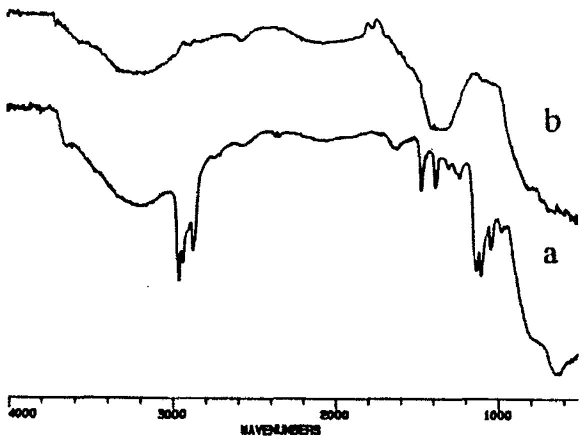

Figure 5. Infrared spectra of the mixture of boron and $[BuOTiO_{1.5}]_n$ (a) as prepared and (b) after heating to 300 °C.

particle size for the TiB_2 powders were 0.055 and 0.156 µm, respectively. The differences in particle sizes and surface areas between the products generated from the mixture of boron and TiO_2 and the mixture of boron and $[BuOTiO_{1.5}]_n$ could arise because the latter method provides more intimate mixing between reactants than does mixing boron and TiO_2 powders. Therefore, upon decomposition and subsequent borothermic reduction, the mixture of boron and partially hydrolyzed titanium butoxide, $[BuOTiO_{1.5}]_n$, yielded smaller particles and a highly agglomerated structure.

It is also possible that the observed particle size differences are related to the particle size of the Ti source material, because when boron and $TiO_x(OH)_y$ powders were mixed, the surface area of the product obtained at 900°C was also high (20.34 m^2/g). The surface areas for the products are summarized in Table 3. The particle sizes of the TiB_2 are directly proportional to the expected particle research would be needed to determine whether the particle size of the titania source or the level of mixing is more important.

After the mixture of boron and $[BuOTiO_{1.5}]_n$ was heated at 1300 °C for 6 h, the XRD pattern (on collodion) indicated sharp TiB_2 peaks; furthermore, the elemental analyses of this product revealed that the borothermic reduction was complete. An SEM micrograph (Figure 6b) illustrated that the TiB_2 particles coarsened slightly, but the surface area determination indicated that the surface area decreased only slightly (18.99 m^2/g). Further heating the precursor to 1500 °C removed the remaining B_2O_2 by-product. SEM micrographs indicated that the particles have increased in size and appear partially sintered (Figure 6c). The surface area decreased to 1.27 m^2/g after heating at 1500°C for 6 h.

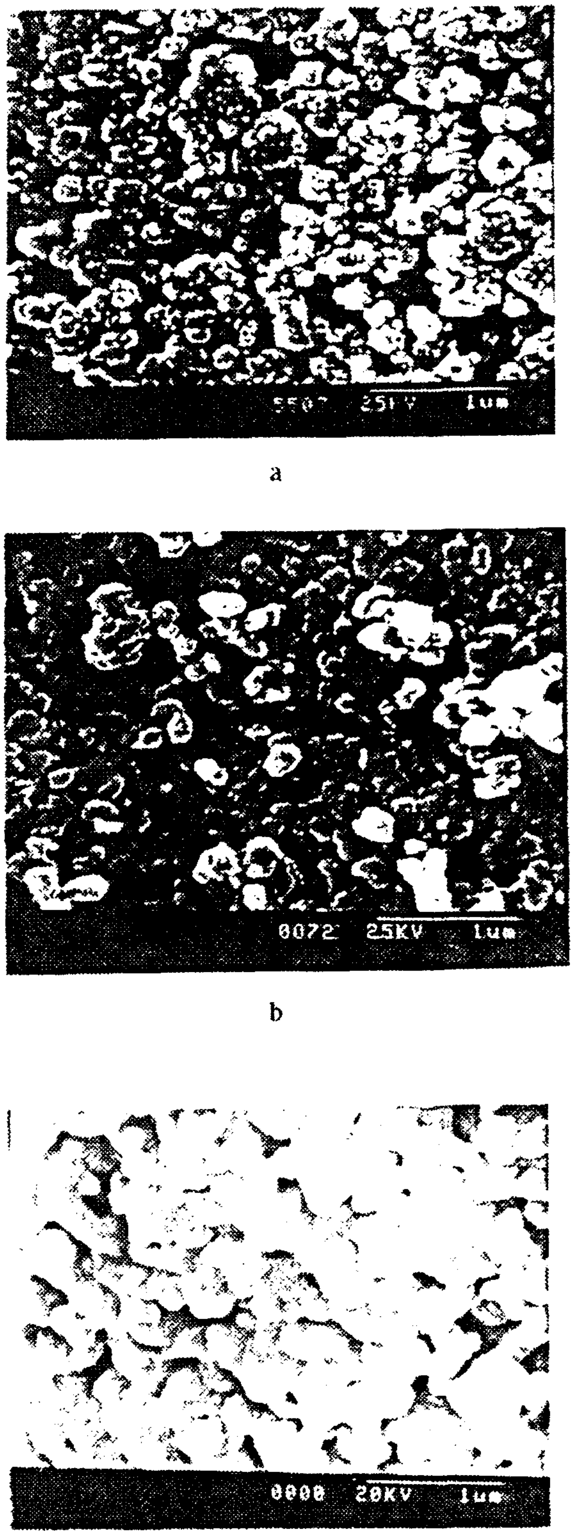

a

b

c

Figure 6. SEM micrographs of the product obtained from a mixture of $[BuOTiO_{1.5}]_n$ and boron (a) heated at 900 °C for 6 h, after washing, (b) heated at 1300 °C for 6 h, after washing, and (c) heated at 1500 °C for 6 h, as-synthesized.

Table 3. Surface Areas (m^2/g) for Residues Heated Under Agron for 6 h.

Ti source	Temperature 900°C	 1300°C	 1500°C
TiO_2	8.57	6.65	-
$TiO_x(OH)_y$	20.34	8.11	-
$[BuOTiO_{1.5}]_n$	23.42	18.99	1.27

In summary, TiB_2 powders with submicron sizes can be prepared by the borothermic reduction of TiO_2 or $TiO_x(OH)_y$ powders or $[BuOTiO_{1.5}]_n$ at 1300 °C for 6 h. The borothermic reduction of TiO_2 began with the formation of Ti_2O_3 and $TiBO_3$ which subsequently reacted with boron to form TiB_2. The particle size and mixing of the precursors had an effect on the particle size of the TiB_2 products, and the surface area of the TiB_2 product appeared to depend on the titanium starting material. As the mixing between boron and titanium became more intimate, the surafce area of the product (at any given temperature) increased. For example, when the partially-hydrolyzed Ti butoxide-derived polymer was used as the Ti source, very small TiB_2 particles were obtained and at 1500 °C the particles appeared to be partially sintered.

ACKNOWLEDGEMENTS

Supported by the Air Force Office of Scientific Research (AFOSR) under Contract No. F49620-89-C-0102.

References

1. J.J. Kim and C.H. McMurtry, "TiB_2 Powder Production for Engineered Ceramics," Ceram. Eng. Sci. Proc. **6** [9-10], 1313-1320 (1985).

2. N.N Greenwood, in Comprehensive Inorganic Chemistry (Vol 1), p. 697. Edited by J.C Bailar, Jr., H.J. Emeleus, R. Nyholm and A.F. Trotman-Dickenson, Pergamon Press, Oxford, 1973.

3. Funk, R.; Lux, B.; Schachner, H.; Tannenberger, H., Increasing The Wear Resistance of Surface Hard Metal Part," **Fr. Patent 2144823, 1973**; Chemical Abstract **1973**, 79, 107206.

4. Murata, Y.; Miccioli, B. R., "Inhibition of Grain Growth In Niobium Diboride," Amer. Ceram. Soc. Bull. **50**, 182-185 (1971).

5. M.A. Janney, "Mechanical Properties and Oxidation Behavior of a Hot-Pressed SiC 15 Vol% TiB_2 Compoiste," Amer. Ceram. Soc. Bull. **66** [2], 322-324 (1987).

6. C.H. McMurtry, W.D.G. Boecker, S.G. Seshadri, J.S. Zanghi and J.E. Garnier, "Microstructure and Material Properties of SiC-TiB_2 Particlate Composite," Amer. Ceram. Soc. Bull. **66** [2], 325-329 (1987).

7. T. Watanabe, "Effects of Carbide Addition on the Mechanical Properties of the $Ti(C_{0.5},N_{0.5})$-30 wt% TiB_2 -Crbide Sintered Compacts," J. Ceram. Soc. Japan **99** [2], 146-149 (1991).

8. A.E. Palty, H. Margolin,and J.P. Nielsen, "Titanium-nitrogen and Titanium-Boron Systems," Trans. Am. Soc. Metals **46**, 312-328 (1954).

9. R. Thompson, in Progress in Boron Chemistry (Vol 2), p. 195. Pergamon Press, New York, 1975.

10. N.N. Greenwood, R.V. Parish and P. Thornton, Quarterly Rev. **20**, 444-445 (1966).

11. R.E. Gannon, R.C. Folweiler and T. Vasilos, "Pyrolitic Synthesis of Titanium Diboride," J. Am. Ceram. Soc. **46** [10], 496-499 (1963).

12. J.K. Walker, "Synthesis of TiB_2 by Borothermic/Carbothermic Reduction of $TiO_2$with B_4C," Adv. Ceram. Mat. **3** [6], 601-604 (1988).

13. Z. Jiang and W.E. Rhine, "Preparation of Titanium Diboride from Titanium Alkoxide and Boron Powder," Chem. Mater. **4**, 497 (1992).

14. P. Peshev and G. Bliznakov, "On The Borothermic Preparation of Titanium Alkoxide and Boron Powder," J. Less-Common Metals **14**, 23-32 (1968).

15. P. Peshev, L. Leyarovska, and G. Bliznakov, "On the Borothermic Preparation of Vandium, Niobium, and Tantalum Borides," J. Less-Common Metals **15**, 259-67 (1968).

16. P. Peshev, G. Bliznakov, and L. Leyarovska, "On the Preparation of some Chromium, Molybdenum, and Tungsten Borides," J. Less-Common Metals **13**, 241-47 (1967).

17. L. Barton and D. Nicholls, "The Hydrogenation of Mono-oxide to Diboride and The Reaction of Boron and Boron Carbide with Titanium and

Zirconium Diboride," J. Inorg. Nucl. Chem. **28**, 1367-1372 (1966).

18. V.N. Pavlikov, V.A. Yurchenko, and S.G. Tresvyatskii, "The B_2O_3-TiO_2 System," Zh. Neorg. Khim. **21**, 233 (1976); Russ. J. Inorg. Chem. **21**, 126 (1976).

19. H. Schmid, "X-ray Evidence for $CrBO_3$, VBO_3, and $TIBO_3$ with Calcite Structure," Acta Cryst. **17**, 1080 (1964).

20. Z. Jiang and W.E. Rhine, "Preparation of TiN and TiC from a Polymeric Precursor," Chem. Mater. **3**, 1132 (1991).

SECTION 11

PREPARATION OF TiN AND TiC FROM A POLYMERIC PRECURSOR

Zhiping Jiang and Wemdell E. Rhine

Published in Chem. Mater. 3 1132 (1991)

ABSTRACT

Hydrolysis of the $Ti(O\text{-}n\text{-}Bu)_4$/furfuryl alcohol mixture resulted in the formation of a polymeric solid. Pyrolysis of the polymer at 1150°C under argon yielded metallic, grey-colored TiC. When the pyrolysis was carried out in an atmosphere of anhydrous ammonia, pure TiN containing less than 0.8 wt% carbon was obtained at 1000°C. The structure and pyrolysis chemistry of the precursor were studied by Fourier transform infrared spectroscopy (FT-IR), thermal gravimetric analysis (TGA), gas chromatography (GC), elemental analyses, and X-ray diffraction (XRD).

INTRODUCTION

Titanium nitride and titanium carbide have many desirable properties such as high melting point, extreme hardness, and strength at high temperatures [1, 2]. At present, both TiN and TiC are used predominantly as cutting materials, although TiN layers also can be used as conductors for electronic applications. Previous studies indicated the addition of TiC to SiC [3, 4] and TiN to BN [5] resulted in improvements in toughness, sinterability, and other specific properties, implying that both materials have excellent potential for use as components of high-temperature composite materials.

Current commercial methods for producing TiC powders include direct reaction of Ti metal with carbon and the carbothermic reduction of TiO_2 [1]. TiN powders are produced by direct nitridation of metallic titanium, by carbothermic reduction and nitridation of TiO_2, or by the reaction of titanium halides or hydrides with anhydrous ammonia or nitrogen/hydrogen mixtures [1, 6]. The above methods generally require high temperatures and cannot be used to prepare TiN or TiC thin films or fibers.

Recently, metalorganic Ti compounds have been used as precursors to TiC or TiN in various final forms. In general, these precursors can be divided into two categories based on the type of structural units bonded to Ti. The first one, which possesses Ti-N or Ti-C bonds, is either a dialkylamide of titanium [7, 8], $Ti(NR_2)_4$, and electrochemically formed polymeric imides of titanium [9], $Ti[(NR)_2]_x$, or tetraalkyl-titanium [10, 11], TiR_4. TiN (thin films and powders) and TiC (thin films) have been produced from these precursors by pyrolysis at temperatures below 1100°C. The second category, which possesses Ti-O bonds, is made either by transesterification of common titanium alkoxides with bifunctional acetates [12] or by alcohol exchange reactions between $Ti(OR)_4$ and organic compounds containing one to three hydroxyl groups [13, 14]. These oxygen-containing precursors yield TiN or TiC, with a considerable amount of carbon and/or oxygen contamination, at higher temperatures than those required to produce TiN or TiC by pyrolyzing the Ti-N or Ti-C metalorganic compounds (especially for the latter where the temperature exceeds 1300°C).

It is well known that acid catalysis of furfuryl alcohol (FuOH) forms a polymeric resin by the following dehydration reaction [15]:

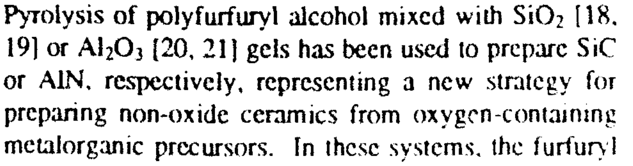

(1)

Furthermore, pyrolysis of this polymeric resin under inert atmosphere leads to the formation of carbon [16, 17]. Pyrolysis of polyfurfuryl alcohol mixed with SiO_2 [18, 19] or Al_2O_3 [20, 21] gels has been used to prepare SiC or AlN, respectively, representing a new strategy for preparing non-oxide ceramics from oxygen-containing metalorganic precursors. In these systems, the furfuryl alcohol group (-OFu) decomposes to carbon to provide a carbon source for the carbothermic reduction of the metal oxide and for the formation of metal carbides upon pyrolysis [13].

In the present study, TiN and TiC were prepared at low temperatures by pyrolysis of a polymeric precursor formed by hydrolysis of a $Ti(O\text{-}n\text{-}C_4H_9)_4$/furfuryl alcohol mixture. Furthermore, the pyrolysis processes involved in the formation of TiN and TiC were studied by various methods, resulting in a better understanding of the chemistry of the above precursor system.

EXPERIMENTAL SECTION

General Methods

All of the syntheses and manipulations were carried out in a N_2-filled drybox or in Schlenk glassware under N_2, because titanium butoxide $Ti(O\text{-}n\text{-}C_4H_9)_4$ and its derivatives are moisture-sensitive. Titanium butoxide and furfuryl alcohol (FuOH) were purified by vacuum distillation. THF (AR grade) was used as-received. Polyfurfuryl alcohol was obtained from Polysciences, Inc.

Diffuse reflectance infrared Fourier transform spectroscopy (DRIFTS) studies were performed with a Nicolet PC/IR (Model 44) infrared spectrometer. Samples were prepared by mixing the precursor or pyrolysis products with dry KBr in a drybox. The ground mixture was quickly transferred into the sample holder in air and immediately transferred to the sample chamber which was flushed with N_2 for a minimum of 10 min before data collection. Gas chromatography (GC) measurements were performed on a Hewlett Packard 5890 gas chromatograph with a 6-ft Carbopack B column using He carrier gas at a flow rate of 25 mL/min. Thermal gravimetric analysis (TGA) of the compounds was carried out with a Perkin-Elmer TGA7 thermal analysis system at a heating rate of 10°C/min. The TGA atmosphere was either argon that had been passed through a BTS catalyst (BASF Co.) and a molecular sieve column to remove O_2 and H_2O, respectively, or electronic grade ammonia. X-ray powder diffraction (XRD) patterns were measured with a Rigaku 300 diffractometer employing Cu Kα radiation and a Ni filter at a scanning rate of 10°/min. The X-ray peak assignments were carried out using the Rigaku Software JCPDS peak indexing program. Elemental analyses were obtained from E+R Microanalytical Laboratory, Inc.

Synthesis of Precursors

A solution of 0.54 g of 1 N H_2SO_4 (corresponding to 0.03 mol H_2O if the amount of H_2SO_4 is neglected) in 20 mL THF was added dropwise to 30 mL of a THF solution containing 6.8 g (0.02 mol) titanium butoxide and 1.96 g (0.02 mol) furfuryl alcohol under vigorous stirring. The resulting light brown solution was refluxed under nitrogen for 12 h, leaving a deep brown solution. The product, after removal of solvent under vacuum at 100°C, was a reddish-brown solid (3.28 g) which was slightly soluble in hydrocarbon solvents. Based on a similar procedure, precursors with a Ti:FuOH ratios of 1:1.3, 1:0.75, 1:0.6, 1:0.5, and 1:0.25 were prepared.

When the hydrolysis was carried out using less than 2 equivalents (relative to Ti) of pure water (no sulfuric acid), the products obtained were either polymeric viscous liquids or solids depending on the ratio of Ti:H_2O; all of them were soluble in hydrocarbon solvents after removal of solvent by vacuum distillation. After hydrolysis, the solvent was removed by distillation and the distillate was analyzed by GC to determine the ratio of butanol and furfuryl alcohol present. The sensitivity of the flame ionization detector was determined by analyzing solutions containing known amounts of butanol and furfuryl alcohol.

Pyrolysis of Precursors

Samples of the isolated precursors were broken into pieces, placed into alumina boats, and transferred to a tube furnace. The tube furnace was fitted with an alumina tube with gas-tight fittings on each end. The samples were pyrolyzed in the tube furnace (Pt heating element) under a flow of either argon (ultra-high purity grade) or anhydrous ammonia at a flow rate of 300 mL/min at atmospheric pressure. The temperature was increased from room temperature to 1300°C at a heating rate of 200°C/h, held at the desired temperature for a period of time (3-12 h), and then cooled to room temperature. The ceramic residues obtained under ammonia were cooled in a flow of argon gas.

RESULTS AND DISCUSSION

Preparation of Precursors

Furfuryl alcohol derivatives of titanium alkoxides were prepared by adding furfuryl alcohol to $Ti(O\text{-}n\text{-}Bu)_4$ at room temperature. As furfuryl alcohol was added to $Ti(O\text{-}n\text{-}Bu)_4$, the light-yellow titanium butoxide turned to a dark yellow-colored liquid, indicating the following alcohol exchange reaction had occurred:

$$\begin{aligned} \mathrm{FuOH} + \mathrm{Ti(O\text{-}n\text{-}Bu)_4} &\rightarrow \mathrm{TiOFu(O\text{-}n\text{-}Bu)_3} \\ &+ \mathrm{HO\text{-}n\text{-}Bu} \end{aligned} \tag{2}$$

Any unreacted FuOH and the n-BuOH produced were transferred to a cold trap by vacuum distillation at 50°C [any unreacted $Ti(O\text{-}n\text{-}Bu)_4$ and the $TiOFu(O\text{-}n\text{-}Bu)_3$ are not volatile enough to be distilled under the above condition]. GC analysis of the distillate indicated the ratio of

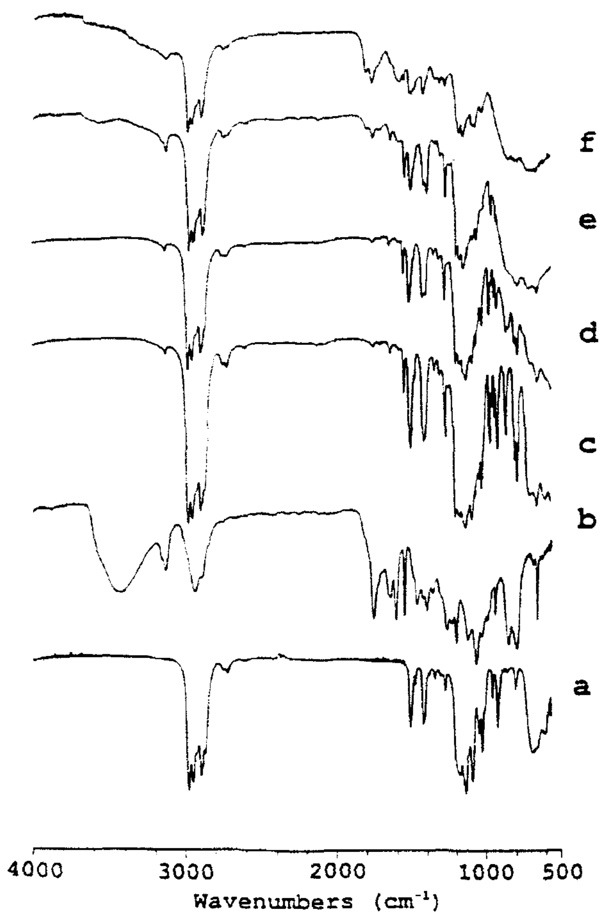

Fig. 1. FI-IR spectra of (a) Ti(O-n-Bu)$_4$, (b) polyfurfuryl alcohol, (c) TiOFu(O-n-Bu)$_3$, (d) hydrolysis product of TiOFu(O-n-Bu)$_3$ with 0.5 mol H_2O, (e) with 1.5 mol H_2O, and (f) with 1.5 mol H_2O and acid catalyst.

butanol to furfuryl alcohol was 100:2.8, indicating reaction (2) is almost quantitative.

Figure 1c shows the IR spectrum of the product from reaction (2). The absence of -OH absorption bands in this spectrum agrees with the GC analysis of the distillate and indicates approximately all (>97%) of the furfuryl alcohol molecules reacted with Ti(O-n-Bu)$_4$ to form TiOFu(O-n-Bu)$_3$. The existence of the furfuryl alcohol groups in the product is indicated by the small peak at 3112 cm^{-1}, which is assigned to the C-H stretching vibration of the olefinic H on the furan rings; the sharp absorption bands at 1597 and 1504 cm^{-1} are assigned to the C=C stretching vibrations, and the absorption band at 1223 cm^{-1} is assigned to the C-O stretching vibrations on the furan rings [22]. As for the n-Bu groups, they are represented by the strong C-H stretching region (2958, 2932, and 2872 cm^{-1}) and C-H bending vibrations [1464 and 1371 cm^{-1}; refer to the spectrum of Ti(O-n-Bu)$_4$, Fig. 1a].

Hydrolysis of TiOFu(O-n-Bu)$_3$ in THF with less than 2 mol H_2O (relative to Ti) produces a soluble Ti-OR polymer. It is well known that as more H_2O is added, more hydrolysis occurs, followed by condensation reactions which result in the subsequent formation of a polymer. Furthermore, some furfuryl alcohol molecules also can be produced through hydrolysis of Ti-OFu groups, even though Ti-OFu is more resistant to hydrolysis than is Ti-O-n-Bu. GC analysis of the distillate from the hydrolysis reactions with 0.5, 1.0, and 1.5 mol H_2O (relative to Ti) indicated the ratios of butanol to furfuryl alcohol in these three distillates were 100:4.6, 100:9, and 100:22.5, respectively.

In order to prevent the loss of FuOH, a catalytic amount of H_2SO_4 was added to catalyze the hydrolysis of TiO-n-Bu groups and the polymerization of any FuOH molecules produced from the hydrolysis of TiOFu groups. GC analysis showed that the ratio of butanol to furfuryl alcohol in the distillate in the case where 1.5 mol H_2O (with acid catalyst) was used was 100:3, indicating the addition of acid is effective in preventing the loss of FuOH. After hydrolysis, we assume that the precursor consists of some polyfurfuryl alcohol plus a molecular precursor with the approximate formula $O_{1.5}Ti(OFu)_{1-x}(O\text{-}n\text{-}Bu)_x$.

The IR spectra of the products after hydrolysis with H_2O (Figs. 1d and e) are similar to that of the starting material, TiOFu(O-n-Bu)$_3$, (Fig. 1c), except that the sharp bands below 900 cm^{-1} in the starting material become broader after hydrolysis, indicating Ti-O-Ti units formed upon hydrolysis. Figure 1f shows the IR spectrum of the product obtained after hydrolyzing TiOFu(O-n-Bu)$_3$ with 1.5 mol H_2O (with acid catalyst). Compared with the IR spectrum of the hydrolysis product without acid (Fig. 1e), most absorption bands in Figure 1f are broader, indicating the structure of the product was more polymeric in nature. Furthermore, the sharp bands corresponding to the furfuryl alcohol groups have almost disappeared; instead, two bands are observed at 1762 and 1718 cm^{-1} which are attributed to the polyfurfuryl alcohol (refer to the spectrum of polyfurfuryl alcohol, Fig. 1b) formed by the acid-catalyzed condensation polymerization of furfuryl alcohol. In addition, this spectrum also indicates the relative concentration of butanol groups decreased considerably compared with that in the uncatalyzed hydrolysis product (Fig. 1e). This decrease in butanol groups occurred because the addition of acid during hydrolysis also catalyzed hydrolysis of Ti-OBu groups, resulting in more butanol molecules produced from the hydrolysis reaction.

We observed that the addition of acid greatly de-

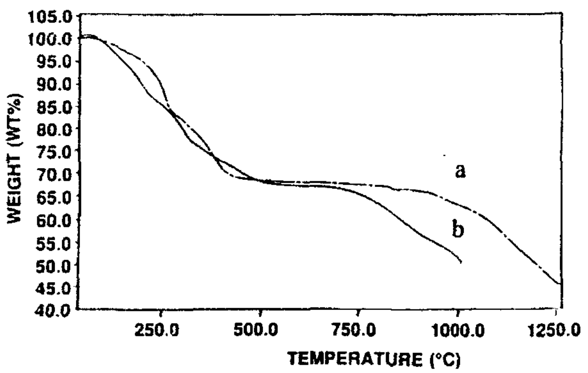

Fig. 2. Thermal gravimetric analysis of the hydrolysis product of $TiOFu(O\text{-}n\text{-}Bu)_3$ *with 1.5 mol* H_2O *and acid catalyst* $[O_{1.5}Ti(OFu)_{1-x}(OBu)_x]$ *under (a) argon and (b) ammonia.*

creased the solubility of the product, making the further structural characterization of the product difficult. The elemental analyses of the hydrolysis product with 1.5 mol H_2O and acid catalyst indicated C, 36.50%; H, 4.67%; and Ti, 27.86, corresponding to an empirical formula of $TiC_{5.4}H_{8.1}O_{3.6}$. The elemental analysis, GC analysis of the distillate, an IR spectrum, and a NMR spectrum indicated hydrolysis was not quantitative and some O-n-Bu groups remained in the product.

Thermal Decomposition of Precursors

Figure 2a shows the TGA curve of the 1:1 Ti:FuOH precursor with nominal composition $[O_{1.5}Ti(OFu)_{1-x}(O\text{-}n\text{-}Bu)_x]_n$ (product obtained after hydrolysis with 1.5 mol H_2O and with acid catalyst) under argon from 40-1260°C. The data indicate the precursor underwent three weight-loss processes: one at 150-270°C, the second at 270-480°C, and the third at 760-1250°C. The first one is attributed to the condensation polymerization of furfuryl groups and the decomposition of O-n-Bu groups attached to Ti atoms. The second weight-loss step presumably corresponds to the decomposition of furan rings. These assignments are supported by the fact that similar decomposition temperatures have been observed for polyfurfuryl alcohol and polymeric $TiO_x(O\text{-}n\text{-}Bu)_y$ [23]. However, unlike the O-n-Bu groups, the decomposition of furan rings results in the formation of carbon. The weight loss starting at around 760°C and ending at 1250°C is assigned to the carbothermic reduction of TiO_2, which is consistent with the previous results obtained for the thermal decomposition of organotitanium compounds [12].

The TGA curve (Fig. 2b) of $[O_{1.5}Ti(OFu)_{1-x}(O\text{-}n\text{-}Bu)_x]_n$ when heated under a flow of ammonia shows a different curve shape than it does when heated under argon, indicating different pyrolysis mechanisms are involved for this precursor under the two atmospheres. The weight loss below 520°C in Figure 2b is attributed to reaction (3), possibly accompanied by the decomposition processes previously discussed concerning the TGA obtained under argon (Fig. 2a).

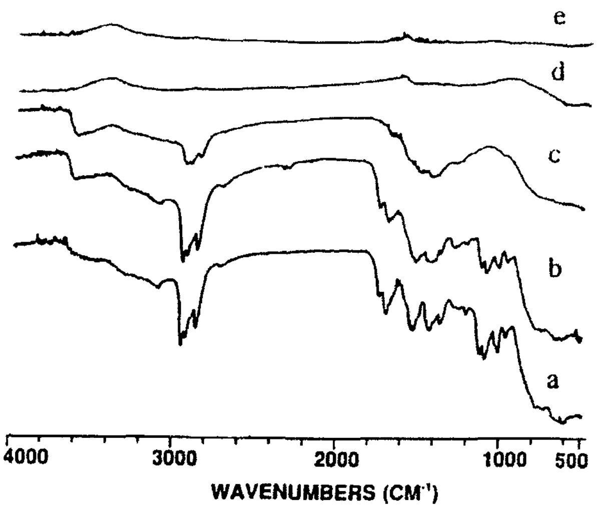

Fig. 3. FT-IR spectra of pyrolysis products of the same precursor in Figure 2 at (a) room temperature and heated under argon at (b) 200°C for 3 h, (c) 300°C for 3 h, (d) 600°C for 3 h, and (e) 800°C for 3 h.

$$TiOR + NH_3 \rightarrow TiNH_2 + ROH \qquad (3)$$

This type of reaction is known to occur for organosilicon compounds [25] and also in reactions of metal alkoxides with amine groups [26]. The weight loss around 680-1000°C is attributed to the following reaction [1, 27]:

$$TiO_2 + C + NH_3 \rightarrow CO + TiN + H_2O + 0.5H_2 \qquad (4)$$

Further investigation into the pyrolysis process under argon and ammonia was carried out with infrared spectroscopy. The IR spectrum for the precursor heated at 200°C for 3 h under argon (Fig. 3b) indicates the absorption peaks attributed to the furan rings are unchanged and the relative intensities of the absorption peaks contributed from the O-n-Bu groups have decreased, presumably due to the decomposition of some O-n-Bu groups into volatile organics during the heat treatment. These observations are consistent with the TGA results. That is, the O-n-Bu groups begin to decompose at 200°C, but the furan rings are still stable at this temperature.

Figures 3c, d, and e show the IR spectra of precursors heated at 300°C, 600°C, and 800°C for 3 h under argon,

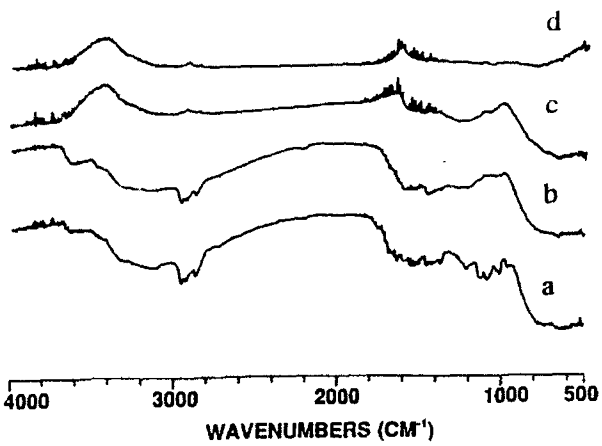

Fig. 4. FT-IR spectra of $O_{1.5}Ti(OFu)_{1-x}(OBu)_x$ heated under ammonia for 3 h at (a) 200°C, (b) 300°C, (c) 600°C, and (d) 800°C.

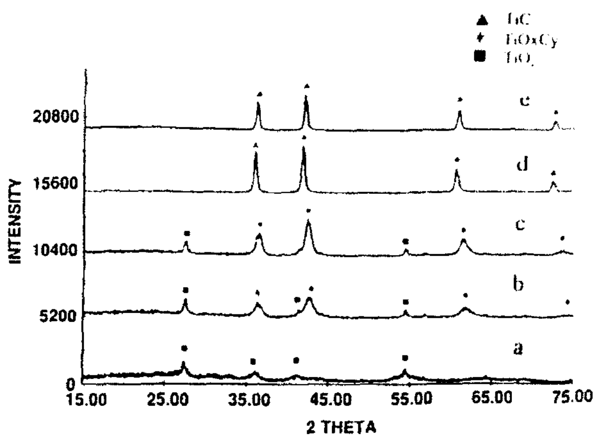

Fig. 5. X-ray diffraction patterns for $O_{1.5}Ti(OFu)_{1-x}(OBu)_x$ after heating under argon for 12 h at (a) 800°C, (b) 900°C, (c) 1000°C, (d) 1150°C, and (e) 1300°C.

respectively. After heating to 600°C (Fig. 3d), the only detectable absorption bands (1000-500 cm^{-1}) in the spectrum are due to Ti-O units, even though carbon remains in the precursor at this stage. The IR spectrum illustrated in Figure 3e indicates the Ti-O absorption disappeared after heating at 800°C, presumably due to the carbothermic reduction of Ti-O units (TGA indicates the reduction starts at 760°C). However, both TGA and XRD (vide infra) results indicate some oxygen remains in the product, since the carbothermic reduction is not complete at 800°C.

The pyrolysis of the precursor under ammonia was also studied by FT-IR. The IR spectrum (Fig. 4a) for the precursor heated at 200°C under ammonia shows two broad bands around 3200 and 1600 cm^{-1}, which are attributed to the NH_2 stretching and bending vibrations, respectively [28]; these NH_2 groups are presumably generated from reaction (3). Furthermore, the IR spectrum indicates the relative absorption intensities contributed by the O-n-Bu groups (C-O and C-H stretching vibrations) are much less than is observed when the same precursor is heated under argon (compare Fig. 4a with Fig. 3b), which is expected if reaction (3) is involved during the pyrolysis. The IR spectrum obtained after heating to 300°C under NH_3 (Fig. 4b) is similar to the one obtained after heating to 300°C under argon (Fig. 3c) except for the extra NH_2 absorption bands. The IR spectrum in Figure 4c indicates some organics (represented by the broad band around 1220 cm^{-1}) remain after heating the precursor at 600°C in ammonia. The Ti-O stretching vibrations which are still present at 600°C (Fig. 4c) disappear after the precursor is heated at 800°C under ammonia (Fig. 4d).

Formation of TiC under Argon

XRD analysis of the pyrolysis products in argon (Fig. 5a) shows that TiO_2 is the only crystalline phase which remains after the precursor is heated at 800°C for 12 h, even though both TGA and IR studies suggest that carbothermic reduction has already started at this temperature. At 900°C, some new peaks (36.40°, 42.55°, 61.75°, and 73.85°, labeled as ✦) emerge in addition to the TiO_2 peaks (Fig. 5b), and the relative intensities of these new peaks increase with heating of the precursor at 1000°C (Fig. 5c, 36.36°, 42.35°, 61.45°, and 73.56°, labeled with ✦). Figure 5d shows that the TiO_2 phase disappears and only four peaks (35.92°, 41.72°, 60.52°, and 72.40°, labeled with ▲) are observed after heating the precursor at 1150°C for 12 h under argon. Further heating of the precursor at 1300°C gives a similar XRD pattern (Fig. 5e, 36.00°, 41.84°, 60.60°, and 72.48°, labeled with ▲), except that these four peaks are a little sharper. Both products at 1150°C and 1300°C are shiny, grey-colored solids.

Table 1 shows the elemental analyses of precursors with various Ti:FuOH ratios heated under argon for 12 h. (Note: these results indicate some nitrogen contamination in all the products even though the pyrolyses were performed under argon of ultra-high purity grade; the reason is explained in reference 24.) Based on these results and the assumption that all the titanium in the starting material transforms into TiN and TiC around 1300°C and that no furfuryl alcohol molecules added to the reaction were lost in the distillation step, we determined the total amount of carbon contributed by the furfuryl alcohol in each system, which includes the carbon consumed by reactions (5) and

Table 1. Elemental Analyses of Pyrolysis Products Heated under Argon for 12 h.

Ti:FuOH	T (°C)	No.	wt% Ti	wt% C	wt% H	wt% N
1.3	1300	1	57.94	39.60	0.00	0.69
1.0	1300	2	69.25	28.74	0.00	0.88
1.0	1150	3	69.72	28.24	0.00	1.25
0.75	1300	4	78.03	17.62	0.00	2.73
TiC (calcd.)			79.95	20.05		

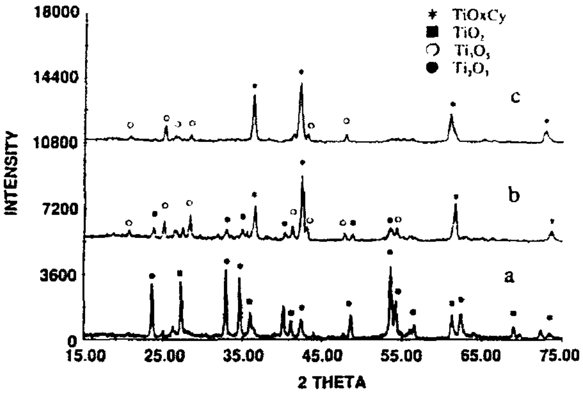

Fig. 6. X-ray diffraction patterns for the hydrolysis products heated at 1250°C for 12 h under argon with Ti:FuOH ratios of (a) 1:0.25, (b) 1:0.5, and (c) 1:0.6.

(6), and the excess carbon represented by xC in reaction (5) in the final product. In this way, the yield of carbon from each furfuryl alcohol molecule was obtained. The calculation from analyses 1, 2, and 4 in Table 1 indicates a carbon yield of 44.6 wt%, 44.8 wt%, and 46.5 wt%, respectively. Therefore, the theoretical Ti:FuOH ratio for the formation of pure TiC through reaction (5) is proposed to be approximately 1:0.80.

$$TiO_2 + 3C + xC \rightarrow TiC + 2CO + xC \quad (5)$$

$$TiO_2 + NH_3 + 2C \rightarrow TiN + 2CO + 0.5H_2 \quad (6)$$

The elemental analyses in Table 1 indicate 0.8-1.8 wt% oxygen remains in the products if we assume that the rest of the weight belongs to residual oxygen due to incomplete carbothermic reduction. Preparing pure titanium carbide is extremely difficult, and Konopicky [2] has reported that titanium carbide made from a thermal reduction process at 2100°C contained at least 2 wt% oxygen. Therefore, even with these levels of nitrogen and oxygen contamination, the TiC prepared in this study is purer than that obtained with other metalorganic precursors [12, 13] or by conventional carbothermic processes.

After comparing the XRD pattern (36.00°, 41.84°, 60.56°, and 72.50°) of pure commercial TiC with those in Figures 5d and e, it is clear that TiC is the only crystalline phase obtained above 1150°C. Furthermore, the elemental analyses indicate the products obtained at 1150°C and 1300°C have almost the same composition, suggesting that the carbothermic reduction is complete by 1150°C. We observe that TiO_2 is present at 800°C and an intermediate phase appears at 900°C, labeled with ▲ in both Figures 5b and c, and the diffraction peaks for this phase tend to shift to lower 2θ angles with increasing temperature until they reach the positions of TiC, as shown in Figure 5d.

It is well known that TiO is soluble in TiC over a wide range of concentrations to form a solid solution of TiO_xC_y, due to the similar cubic structures of TiC and TiO, which have lattice constants of 0.433 and 0.417 nm, respectively. Therefore, the X-ray diffraction peaks obtained after pyrolysis at 900°C (Fig. 5b) and 1000°C (Fig. 5c) are attributed to titanium oxycarbide. Judging by the diffraction peak positions, the solid solution phase obtained at 900°C has higher oxygen and lower carbon content than the product obtained at 1000°C.

To study the reduction process in more detail, precursors with Ti:FuOH ratios of 1:0.25, 1:0.5 and 1:0.6 were heated at 1250°C for 12 h under argon. These X-ray diffraction patterns (Fig. 6) indicate no pure TiC phase forms in the three systems, and that the only crystalline phases observed are TiO_2, Ti_2O_3, Ti_3O_5, and TiO_xC_y, as expected from the previous experiments. Figures 6b and c indicate the relative intensities of the TiO_xC_y phase peaks increase with increasing amounts of FuOH in the system; moreover, the TiO_xC_y phase (36.08°, 41.92°, 60.78°, and 72.80°, Fig. 6c) obtained using 0.6 FuOH has a higher carbon content and a lower oxygen content than the product obtained using 0.5 FuOH, based on their X-ray diffraction peak positions (36.40°, 42.32°, 61.44°, and 73.66°, Fig. 6b)

Formation of TiN under Ammonia

X-Ray diffraction studies (Fig. 7) of the pyrolysis products of the precursor with a Ti:FuOH ratio of 1:0.75

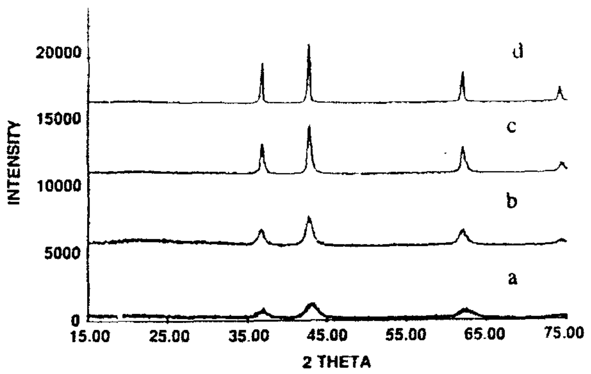

Fig. 7. X-ray diffraction patterns for the hydrolysis product with a Ti:FuOH ratio of 1:0.75 after heating under ammonia at (a) 700°C for 5 h, (b) 800°C for 5 h, (c) 900°C for 5 h, and (d) 1000°C for 12 h.

under ammonia indicate a crystalline phase emerges at 700°C; moreover, the peaks of this phase shift to lower angles and become sharper with increasing calcination temperature, as shown in Figure 5 for TiO_xC_y. Based on the peak positions of the products, these phases in the X-ray diffraction patterns in Figures 7a-c are attributed to titanium oxynitride solid solutions (TiO_xN_y).

The elemental analysis of the precursor heated at 800°C under ammonia for 5 h (Table 2) shows that about 10 wt% oxygen (determined by difference) still remains in the product. The pyrolysis product obtained at 1000°C is a gold-colored solid, typical of TiN, and it contains 0.76 wt% carbon (Table 2). Furthermore, based on the combined percentages (100.68 wt%) of Ti, N, and C, the oxygen content of this product necessarily must be quite low. Finally, it is clear that ammonia can function as a nitrogen source for the pyrolysis product under both low and high temperature through reaction (3) and reaction (4), respectively.

It is important to know how much nitrogen is contributed by reactions (3) and (4) to the final product in order to better understand the pyrolysis chemistry of the precursors in ammonia. The elemental analysis of the 1:1 Ti:FuOH precursor heated at 600°C for 3 h under ammonia and then heated to 1300°C for 12 h under argon shows that the product has low nitrogen content (4.27 wt%) and high carbon content (23.52 wt%) (No. 5, Table 2), indicating reaction (3) is of minor importance and most of the butanol and furfuryl groups survive this reaction. Based on the XRD peak positions of this product (36.08°, 41.90°, 60.80°, and 72.78°), the crystalline phase of the product is TiN_xC_y solid solution. On the other hand, the elemental analysis of the 1:0.75 Ti:FuOH precursor heated at 600°C for 3 h under argon (at this stage all the furfuryl alcohol has converted to carbon) and then heated to 1000°C for 12 h under ammonia (No. 3, Table 2), indicates pure TiN forms containing only 0.55 wt% carbon.

This result confirms that reaction (3) is not an important source of nitrogen, and pure TiN still can be obtained through reaction (4). However, only one equivalent of carbon is consumed in reaction (4) rather than three equivalents of carbon as in reaction (5). Pyrolysis of the 1.0:0.75 Ti:FuOH precursor under argon gave a product with the empirical formula $TiC_{0.9}N_{0.1}$, indicating 0.75 equivalents FuOH should yield approximately 2.9 equivalents carbon. Therefore, if reaction (4) is the only reaction involved in removing carbon, there should be a large excess (~1.9 equivalents) of carbon left in the product. Evidently, the excess carbon reacts with ammonia at high temperatures to form volatile compounds. The above proposal is also supported by the fact that no residue was left when 0.1 g of the polyfurfuryl alcohol was pyrolyzed at 600°C for 3 h under argon and then

Table 2. Elemental Analyses of Pyrolysis Products Heated under Ammonia.

Ti:FuOH	T (°C)	No.	wt% Ti	wt% N	wt% C	wt% H
0.75^a	1000 (12 h)	1	77.64	22.28	0.76	0.00
0.75^a	800 (5 h)	2	64.74	18.64	6.87	0.23
0.75^b	1000 (12 h)	3	77.81	21.98	0.55	0.00
TiN (calcd.)			77.38	22.62		
1.0^c	600 (3 h	4	70.67	4.27	23.52	0.00

[a] Heated under NH_3 to T (°C).

[b] The precursor was heated at 600°C for 3 h under argon, then further heated to 100°C under ammonia and held for 12 h at that temperature.

[c] The precursor was heated at 600°C for 3 h under ammonia, then further heated to 1300°C under argon and held for 12 h at that temperature.

1000°C for 12 h under ammonia. Furthermore, the reaction between carbon and ammonia was also observed in Maya's recent work [29]. However, the detailed reaction mechanism between ammonia and carbon is unknown at present.

CONCLUSIONS

Furfuryl alcohol derivatives of titanium n-butoxide were prepared and then hydrolyzed to obtain polymers $[O_{1.5}Ti(OFu)_{1-x}(OBu)_x]$ which were characterized by elemental analysis and spectroscopic methods. The value of x depends on the relative hydrolytic stability of the OR groups and was estimated to be less than 0.3 based on the analytical results. To improve the hydrolysis reactions and decrease the loss of furfuryl alcohol from the system, trace amounts of sulfuric acid were added to catalyze the hydrolysis of the titanium alkoxide and the polymerization of furfuryl alcohol.

Since furfuryl alcohol is known to be a good precursor for glassy carbon, these titanium polymers could be thermally converted to an intimate mixture of titanium oxides and carbon. When the polymer was pyrolyzed under ammonia, we observed that the oxynitride, TiO_xN_y, began to form at temperatures as low as 700°C and that TiN was completely formed by 1000°C. Ammonia also removed carbon from the system and almost pure TiN was obtained. When the polymer was pyrolyzed under argon, TiO_xC_y was observed to form at 900°C and TiC was completely formed by 1150°C. The temperatures observed for the formation of TiN and TiC in this research are lower than those reported for the formation of TiN and TiC by the conventional carbothermic reduction method.

ACKNOWLEDGMENTS

Financial support for this work was provided by the Air Force Office of Scientific Research (AFOSR) under Contract No. F49620-89-C-0102.

REFERENCES

1. L. Toth, Transition Metal Carbides and Nitrides. Academic Press, New York, 1971.
2. E.K. Storms, The Refractory Carbides. Academic Press, New York, 1967.
3. S. Yajima, T. Iwai, T. Yamamura, K. Okamura, and Y. Hasegawa, "Synthesis of a Polytitanocarbosilane and its Conversion into Inorganic Compounds," *J. Mater. Sci.*, **16**, 1349-55 (1981).
4. Y. Song, C. Feng, Z. Tan, and Y. Lu, "Structure and Properties of Polytitanocarbosilanes as the Precursor of SiC-TiC Fibre," *J. Mater. Sci. Lett.*, **9**, 1310-13 (1990).
5. H. Shimoda, "Sintered Hard Alloys of Cutting Tools," *Jpn. Kokai Tokko Koho* JP 61,179,847.
6. C.F. Powell, J.H. Oxley, and E.M. Blocker, Vapor Depositions. Wiley Press, New York, 1966.
7. K. Sugiyama, S. Pac, Y. Takahashi, and S. Motojima, "Low Temperature Deposition of Metal Nitrides By Thermal Decomposition of Organometallic Compounds," *J. Electrochem. Soc.*, **122**, 1545-49 (1975).
8. G.M. Brown and L. Maya, "Ammonolysis Products of the Dialkylamides of Titanium, Zirconium and Niobium as Precursors to Metal Nitrides," *J. Am. Ceram. Soc.*, **71**, 78-82 (1988).
9. C. Russel, "Preparation and Pyrolysis of a Polymeric Precursor for the Formation of TiN-TiC Solid Solutions," *Chem. Mater.*, **2**, 241-44 (1990).
10. G.S. Girolami, J.A. Jensen, G.M. Pollina, W.S. Williams, A.E. Kaloyeros, and C.M. Allocca, "Organometallic Route to the Chemical Vapor Deposition of Titanium Carbide Films at Exceptionally Low Temperature," *J. Am. Chem. Soc.*, **109**, 1579-80 (1987).
11. A.E. Kaloyeros, W.S. Williams, C.M. Allocca, G.S. Pollina, and G.S. Girolami, "Amorphous Titanium Carbide Films Produced by Low-Temperature Organometallic CVD," *Adv. Ceram. Mater.*, **2**, 257-63 (1987).
12. S.J. Ting, C.J. Chu, E. Limatta, J.D. Mackenzie, M. Getman, and M.F. Hawthorne, "The Formation of Thin Films and Fibers of TiC from a Polymeric Titanate Precursor"; pp. 457-60 in Better Ceramics Through Chemistry IV, Mat. Res. Soc. Symp. Proc., Vol. 180. Edited by C.J. Brinker, D.E. Clark, D.R. Ulrich, and B.J.J. Zelinsky. Materials Research Society, Pittsburgh, PA, 1990.
13. T. Gallo, F. Cambria, C. Greco, B. Simms, and R. Valluzzi, "Metal Carbides from Alkoxides and Modified Alkoxides"; p. 444 in Final Program and Abstracts, 1990 MRS Meeting.
14. K. Kuruda, Y. Tanaka, Y. Sugahara, and C. Kato, "Preparation of Titanium Nitride (TiN1-x-yCxOy) from Ti(OPr)4-Triethanlamine Condensation Product by Pyrolysis"; pp. 575-79 in Better Ceramics Through Chemistry III, Mat. Res. Soc. Symp. Proc., Vol. 121. Edited by C.J. Brinker, D.E. Clark, and

D.R. Ulrich. Materials Research Society, Pittsburgh, PA, 1988.

15. H.F. Mark, N.M. Bikales, C.G. Overberger, and G. Menges, Eds. Encyclopedia of Polymer Science and Engineering, Vol. 7. John Wiley & Sons Inc., New York, 1987.

16. E. Fitzer, W. Schaefer, and S. Yamada, "The Formation of Glasslike Carbon by Pyrolysis of Polyfurfuryl Alcohol and Phenolic Resin," *Carbon*, **7**, 643-48 (1969).

17. E. Fitzer and W. Schafer, "The Effect of crosslinking on the Formation of Glasslike Carbons from Thermosetting Resins," *Carbon*, **8**, 353-64 (1970).

18. S.Y. Parker and B.I. Lee, "Reaction Sintering of Gel Derived Ceramic Composites" *J. Non-Cryst. Solids*, **100**, 345-51 (1988).

19. J.D. Bircell, M.J. Mockford, D.R. Stanley, P.M. Asher, M. Lawford, and W. Richard, Preparation of Polymeric Ceramic Precursors, and Ceramics Obtained by This Process, Eur. Pat. Appl. No. EP284 235.

20. L.D. Silverman, "Carbothermal Synthesis of Aluminum Nitride," *Adv. Ceram. Mater.*, 3, 418-19 (1988).

21. B.I. Lee and M.A. Einarsrud, "Low-Temperature Synthesis of Aluminum Nitride via Liquid-Liquid Mix Carbothermal Reduction," *J. Mater. Sci. Lett.*, **9**, 1389-91 (1990).

22. A.K. Solanki and A.M. Bhandari, "Furfuroxides of Lanthanum, Praseodymium, Neodymium and Samarium," *Z. Anorg. Allg. Chem.*, **453**, 185-89 (1979).

23. Z. Jiang and W.E. Rhine, unpublished data, CPRL, MIT (1991).

24. The same alumina tube was used in this work, when pyrolyses under both argon and ammonia were performed. In the latter case, AlN layer could be formed on the ceramic tube, which released N_2 at high temperature when the pyrolyses were carried out under argon. The contamination of the products with nitrogen presumably resulted from the following reaction:

$$0.5N_2 + TiO_2 + 2C \rightarrow TiN + 2CO$$

2. V. Bazant, V. Chvalovsky, and J. Rathousky, Organosilicon Compounds. Academic Press, New York, 1965.

26. D.C. Bradley, R.C. Mehrotra, and D.P. Gaup, Metal Alkoxides. Academic Press, New York, 1978.

27. C.J. Brinker and D.M. Haaland, "Oxynitride Glass Formation from Gels," *J. Am. Ceram. Soc.*, **66**, 758-65 (1983).

28. R.M. Silverstein, G.C. Bassler, and T. Morrill, Spectrometric Identification of Organic Compounds, 4th Ed. John Wiley & Sons Inc., New York, 1981.

29. L. Maya and H.L. Richards, "Polymeric Cyanoborane, (CNBH2)n: Single Source for Chemical Vapor Deposition of Boron Nitride Films," *J. Am. Ceram. Soc.*, **74**, 406-09 (1991).

SECTION 12

IN-SITU PREPARATION OF TiC/Al_2O_3, TiN/Al_2O_3 AND TiN/AlN COMPOSITES FROM ALKOXIDE-DERIVED PRECURSORS

Zhiping Jiang and Wendell E. Rhine
Ceramics Processing Research Laboratory

Published in Synthesis and Processing of Ceramics: Scientific Issues, Mat. Res. Soc. Symp. Proc., **vol 249**, *45 (1992)*

ABSTRACT

The reaction between furfuryl alcohol (FuOH) and the hydrolysis product of a mixture of $Ti(O\text{-}n\text{-}Bu)_4$ and $Al(O\text{-}sec\text{-}Bu)_3$ (Al:Ti=1:1) resulted in the formation of soluble polymeric solids. Pyrolysis of these polymers in argon yielded TiC/Al_2O_3 composite at 1250°C. When there polymers were pyrolyzed in ammonia, TiN/Al_2O_3 or TiN/AlN composite was formed. All these composites showed fine microstructure and excellent homogeneity. Furthermore, the structure and pyrolysis chemistry of these polymeric precursors as well as the microstructure of the pyrolysis products were studied by means of FTIR, TGA, XRD, SEM, TEM, STEM, Auger, elemental analyses etc.

INTRODUCTION

Al_2O_3, TiN, TiC and AlN are hard refractory ceramic materials. TiC/Al_2O_3 and TiN/AlN composites ceramics have exhibited superior mechanical property and potential applications as cutting tools or wear-resisting parts.[1-3] Preparation of these composites is usually achieved by using ceramic powders as starting materials with typical solid-state processing procedures, including milling, drying and subsequent sintering at elevated temperature, often under hot-pressing condition.

Here, we report the preparation of TiC/Al_2O_3, TiN/Al_2O_3 and TiN/AlN composites from alkoxide-derived organometallic polymers. We expect that the Ti and Al polymers form interpenetrating networks. Therefore, pyrolysis of these precursors will produce composites with fine microstructures and better homogeneity than those prepared from the conventional ceramic processing methods. Furthermore, the high solubility of these polymers makes them potentially useful as precursors to make composite coatings by means of spin-coating or dip-coating techniques.

EXPERIMENTAL PROCEDURES

The precursors were prepared by adding a solution of H_2O in THF dropwise to a solution containing $Ti(O\text{-}n\text{-}Bu)_4$ and $Al(O\text{-}sec\text{-}Bu)_3$ in THF solvent under vigorous stirring at -30°C ($Al:Ti:H_2O=1:1:2.5$), which yielded a colorless solution. Then a furfuryl alcohol solution in THF was added dropwise to the above solution, resulting in a yellow solution. After this solution was refluxed for 1 h, the THF solvent was removed at 120°C under vacuum leaving a yellow or brown solid.

Pyrolysis of the precursors was performed in a carbon furnace in argon or a tube furnace under ammonia. In the latter case, the precursors were heated in argon to 600°C, then further heated to higher temperature under ammonia. A heating rate of 200°C/h was used for all the pyrolysis experiments.

RESULTS AND DISCUSSION

It is known[4,5] that furfuryl alcohol groups connected to metals will decompose into carbon. Furthermore, both $Ti(O\text{-}n\text{-}Bu)_4$ and $Al(O\text{-}sec\text{-}Bu)_3$ hydrolyse easily and their hydrolysis products will transform into TiO_2 and Al_2O_3, respectively, under pyrolysis. Therefore, in the present systems, if the precursor has suitable ratio of furfuryl alcohol to metal alkoxides, TiC/Al_2O_3, TiN/Al_2O_3 or TiN/AlN can be formed from the following reactions:

$$TiO_2 + Al_2O_3 + C \rightarrow Al_2O_3/TiC + CO \quad (1)$$

$$TiO_2 + Al_2O_3 + C + NH_3 \rightarrow Al_2O_3/TiN + CO + H_2O + H_2 \quad (2)$$

$$TiO_2 + Al_2O_3 + C + NH_3 \rightarrow AlN/TiN + H_2O + CO + H_2 \quad (3)$$

The precursor had a yellow or brown color depending on the relative concentration of furfuryl alcohol in the starting material. It was known[5] from our previous study that furfuryl alcohol replaced Ti-O-*n*-Bu group easily; furthermore, in the present work, it was observed that a white solid material was formed instantly by mixing Al(O-*sec*-Bu)$_3$ with furfuryl alcohol, which was presumably an Al furfuryl complex formed by exchange of O-*sec*-Bu groups. Therefore, the precursors in the present study could be described as a polymer of $Ti(O\text{-}n\text{-}Bu)_xAl(O\text{-}sec\text{-}Bu)_y(FuO)_zO_{2.5}(x + y + z = 2)$ assuming that the hydrolysis reaction and the FuOH exchange reaction were complete. However, in reality, it is more complex. For instance, when the ratio of FuOH:Ti (or Al) was larger than 2:1, IR spectra of the polymers indicated that O-*n*-Bu and O-*sec*-Bu groups were still present, which suggested that the FuOH exchange reaction was not complete. In addition, the IR spectra of all the investigated precursors (with a FuOH:Ti ratio from 0.75:1 to 3:1) showed that presence of OH^{-1} groups, indicating that the condensation reaction was also not complete. Therefore, based on the above discussion, the precursors with a small FuOH:Ti ratio (less than 2:1) can be described as a polymer of $Ti(O\text{-}n\text{-}Bu)_xAl(O\text{-}sec\text{-}Bu)_yO_a(OFu)_z(OH)_b$ (the ratio of x and y depends on the relative exchange rates for Ti and Al alkoxides and z is the amount of furfuryl alcohol added; a=2.5-0.5b), which had a yellow color. The precursors with large FuOH:Ti ratio (more than 2) probably also contain polyfurfuryl alcohol since the furfuryl alcohol readily polymerizes.

The TGA studies of the precursor with a FuOH:Ti ratio of 0.75:1 in argon and the FTIR spectra of its pyrolysis products showed that both O-*n*-Bu and O-*sec*-Bu groups decomposed below 300°C, presumably forming some volatile organics; the FuO groups decomposed between 300-450°C, yielding C. By 500°C no organics remained in the precursor. The carbothermic reduction for the pyrolysis product began at 850°C, as indicated by the weight loss between 850-1170°C.

The XRD spectra indicated that the product obtained after heating the precursor (with a FuOH:Ti ratio of 1.5:1) to 800°C for 6 h in argon was amorphous; after heating to 1000°C, crystalline α-Al_2O_3 and TiO_xC_y were observed. The XRD pattern (Figure 1a) of the same precursor heated at 1250°C for 12 h in argon indicated that TiC and α-Al_2O_3 were the only crystalline phases. However, the elemental analyses of this product indicated that there was excess of C in the product.

In order to find the precursor with suitable amounts of C for the carbothermic reduction of TiO_2 precursors with the FuOH:Ti ratio of 0.75:1, 1.0:1 or 1.25:1 were also pyrolyzed at 1250°C for 12 h in argon. XRD studies of these pyrolysis products indicated that the precursor with a FuOH:Ti ratio of 0.75:1 gave a product containing three crystalline phases (Ti_2O_3, α-Al_2O_3 and TiO_xC_y); the pyrolysis product from the precursor with a FuOH:Ti ratio of 1:1 had two crystalline phases (α-Al_2O_3 and TiO_xC_y). The precursor with a FuOH:Ti ratio of 1.25:1 yielded a pyrolysis product possessing a XRD pattern similar to that of Figure 1a, that is, TiC and α-Al_2O_3 are the only crystalline phases. The elemental analyses of this product indicated a stoichiometry close to TiC/Al_2O_3 with a small amount of excess C. Therefore, it appears that the precursor with a FuOH:Ti ratio of 0.75:1 or 1:1 does not have enough C for the carbothermic reduction of TiO_2; a pyrolysis product with a stoichiometry close to TiC/Al_2O_3 will result from the precursor with a FuOH:Ti ratio between 1:1 and 1.25:1.

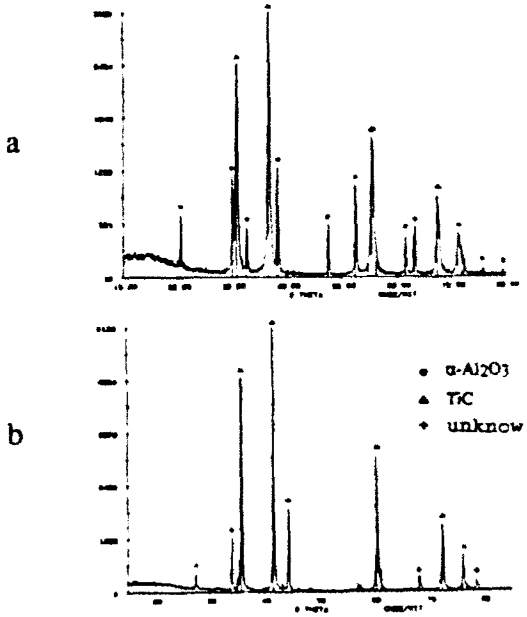

Figure 1. XRD pattern of the precursor (with a FuOH:Ti ratio of 1.5:1) heated in argon at a) 1250 °C for 12 h and b) 1500 °C for 6 h.

The pyrolysis products obtained at 1250°C consisted of large (100-1000 μm), metallic-gray and irregularly shaped pieces. The SEM micrograph of the pyrolysis product from the precursor with a FuOH:Ti ratio of 1.25:1 (Figure 2a) showed a morphology consisting of two phases; that is, one phase consisting of large grains with a size of 0.7-1 μm and the other consisting of small grains (0.05-0.1 μm) between these large grains. Auger analyses indicated that the large grains contained only Al and O elements; Ti and C were the major components of these small grains with small amount of Al, which suggested the large and small grains belonged to α-Al_2O_3 and TiC, respectively. In addition, the SEM micrograph indicated the α-Al_2O_3 grains were dispersed well in the TiC phase. It was also observed that the excess carbon in the product has an effect on the morphology of the pyrolysis product. For instance, in the SEM micrograph of the product from the precursor with a FuOH:Ti ratio of 1.5:1, excess C had obscured the grains of both Al_2O_3 and TiC, which resulted in a flat, featureless morphology.

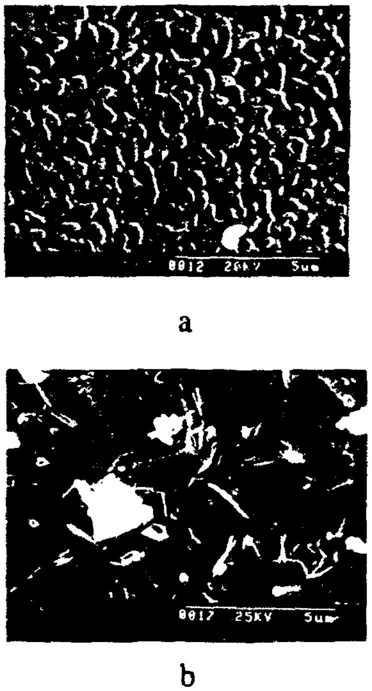

Figure 2. SEM micrographs of the precursor with a FuOH:Ti ratio of 1:1.25 heated in argon at a) 1250 °C for 12 h and b) 1500 °C for 6 h.

Based on the XRD patterns of the pyrolysis products heated at 1250°C, it appeared that these products still contained some amorphous materials which should crystallize at higher temperature. The XRD patterns of the precursors heated at 1500°C under argon indicated the XRD peaks are much sharper than those of pyrolysis products obtained at 1250°C. The SEM micrographs of the products indicated that the products crystallized very well (Figure 2b). In addition, a new crystalline phase was observed in these XRD patterns besides the phases (α-Al_2O_3, TiC, TiO_xC_y) we observed before; the relative concentration of this new phase increased with increasing the furfuryl alcohol content. This new phase was also formed at the expense of teh α-Al_2O_3. For instance, the XRD pattern (Figure 1b) of the product with a FuOH:Ti ratio of 1.5:1 indicated that also most all the crystalline α-Al_2O_3 had disappeared; instead TiC and this new phase were the only crystalline compounds present. The identification of this phase is under way.

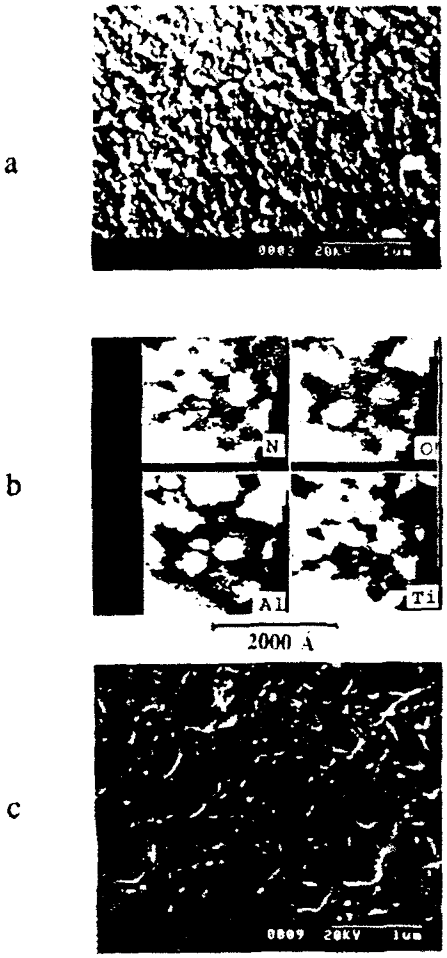

Figure 3. The SEM micrographs of the precursor with a FuOH:Ti ratio of 0.75:1 heated in ammonia a) at 1250 °C for 12 h; b) the STEM for the sam product; c) the SEM micrograph of the same product at a) further heated at 1500 °C under N_2 for 6 h.

The formation of TiN/Al_2O_3 was achieved by the pyrolysis of the precursors in argon at 600°C and then heated to 1250°C in NH_3. The XRD pattern of the pyrolysis product from the precursor with the FuOH:Ti ratio of 0.75:1 indicated α-Al_2O_3 and TiN were the only crystalline phases. The SEM micrograph (Figure 3a) of this product shows a microstructure consisting of grains which are 150-400 Å in size according to TEM measurements. The elemental analyses of this product agree with stoichiometry close to TiN/Al_2O_3. Furthermore, the STEM micrograph (Figure 4\3b) indicated that the TiN and Al_2O_3 components were dispersed very well. Further heating of the product (obtained at 1250°C in ammonia) to 1500°C under N_2 increased the crystallinity of both TiN and α-Al_2O_3 based on the XRD study. The SEM micrograph (Figure 3c) of the resulting product indicated the grain sizes of the product had increased significantly; furthermore, two kind of grains appeared in the morphology, judging by the sizes.

It was also observed that TiN could be formed from two different reactions in the present studies. The first one is the carbothermic reduction and nitridation of TiO_2; the second one is the reduction and nitridation of TiO_2 by ammonia.[6,7] For instance, pyrolysis of a precursor prepared from Ti(O-*n*-Bu)$_4$, Al(O-*sec*-Bu)$_3$ and 2.5H_2O at 1250°C for 6 h in ammonia yielded crystalline α-Al_2O_3, TiN and Ti_2O_3. This result indicated the direct nitridation was involved in the formation of TiN, and also demonstrated that the presence of C is necessary for the complete nitridation of TiO_2 in the present system.

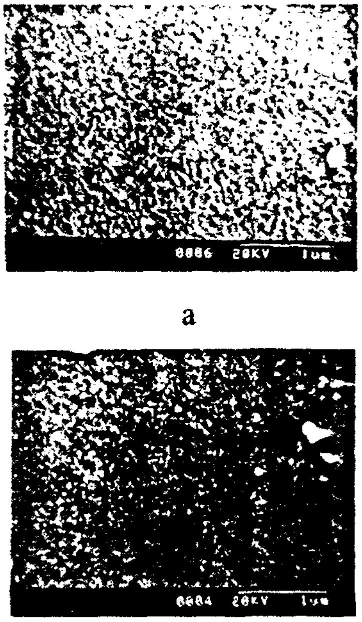

a

b

Figure 4. The SEM micrographs of the precursor with a FuOH:Ti ratio of 3:1 heated at 1250 °C for 12 h; b) the same product at a) heated in N_2 at 1500 °C for 6 h.

The formation of AlN/TiN from the precursor was achieved by heating the precursors with a FuOH:Ti ratio of 2.5:1 or 3:1 to 1250°C in ammonia. The XRD patterns of both pyrolysis products indicated that AlN and TiN were the only crystalline phases. The SEM micrograph (Figure 4a) of the pyrolysis products showed a morphology consisting of small grain sizes (150-400 Å by TEM); furthermore, the STEM revealed that both Al and Ti components were dispersed well in the product. However, a larger amount of oxygen (10-15%) was present in the product based on the elemental analyses, indicating that the nitridation of the oxides was not complete, even though excess C has been supplied from the precursors. This could be because the NH_3 reacts with C forming HCN and removes the C before the carbothermic reduction of Al_2O_3 is complete.[8] This also explained why both products showed a similar elemental analyses results. When the pyrolysis products were further heated at 1500°C in nitrogen the XRD pattern indicated the crystallinity of both TiN and AlN had increased. The SEM micrograph (Figure 4b) of the corresponding product showed that the grains grew to 500-1000 Å. In addition, the elemental analyses indicated almost pure TiN/AlN composite were obtained by such a treatment.

ACKNOWLEDGEMENTS

Financial support for this work provided by the Air Force Office of Scientific Research (AFOSR) under Contract No. F49620-89-C-0102.

REFERENCES

1. J. Mukerji and S.K. Biswas, *J. Am. Ceram. Soc.* **73**, 142 (1990).

2. J.P. Mathers, T.E. Foreser and W.P. Wood, *Ceram. Bull.* **68**, 1330 (1989).

3. T. Nagano, H. Kato, F. Wakai, *J. Am. Ceram. Soc.* **74**, 2258 (199).

4. T. Gallo, F. Cambria, C. Greco, B. Simms and R. Valluzzi, "Metal Carbide from Alkoxides and Modified Alkoxides" Final Program and Abstract, 1990 Fall MRS Meeting, p. 439.

5. Z. Jiang and W.E. Rhine, "Preparation of TiN and TiC from a Polymeric Precursor" to be published in Chem. Mater.

6. K. Kamiya, T. Yoko, M. Bessho, *J. Mater. Sci.* 22, 937 (1987).

7. J.L. Keddie, J. Li, J.W. Mayer and E.P. Giannelis, *J. Am. Ceram. Soc.* **74**, 2937 (1991).

8. F.K. van Dijen and J. Pluijmakers, *J. Eur. Ceram. Soc.* **5**, 385 (1989).

SECTION 13

SYNTHESIS AND PYROLYSIS OF NOVEL POLYMERIC RECURSORS TO TiC/Al_2O_3, TiN/Al_2O_3 AND AlN/TiN NANOCOMPOSITES

Zhiping Jiang and Wendell E. Rhine
Ceramics Processing Research Laboratory
Massachusetts Institute of Technology, Cambridge, MA 02139

Abstract

The reaction between furfuryl alcohol (FuOH) and the products obtained by hydrolyzing a mixture of $Ti(O\text{-}n\text{-}Bu)_4$ and $Al(O\text{-}sec\text{-}Bu)_3$ resulted in the formation of soluble polymeric solids. Pyrolysis of these polymers in argon yielded TiC/Al_2O_3 composites at 1250-1375 °C; further heating the precursors to 1500 °C in argon led to the formation of a new phase due to the reaction between C, Al_2O_3 and TiC. When these polymers were pyrolysed in ammonia or nitrogen, a TiN/Al_2O_3 or TiN/AlN nanocomposite was formed, depending on the concentration of FuOH in the polymers. All these composites exhibited a fine-grained microstructure and excellent homogeneity. Furthermore, the structure and pyrolysis chemistry of these polymeric precursors as well as the microstructure of the pyrolysis products were studied by FTIR, TGA, GC, XRD, SEM, TEM, STEM, Auger electron spectroscopy (AES) and elemental analyses.

Introduction

Ceramic matrix composites offer a method for improving the reliability of structural ceramics and are expected to have a promising future. It is well known that the ceramic composites have exhibited superior mechanical properties and have potential applications as cutting tools or wear-resistant parts.[1-3] Preparation of these composites is usually achieved by typical powder processing procedures, including mixing, milling, drying and subsequent sintering at elevated temperature, often under hot-pressing conditions. However, as performance requirements for advanced ceramics increase, integrating materials synthesis and product design is becoming more important. For example, fabricating composites with controlled composition, nano-sized grains,[4] or with interpenetrating ceramic phases[5] will require developing new synthesis and processing techniques.

Various methods are being investigated to prepare composite powders with better homogeneity than can be otained by mechanical mixing of several ceramic powders. An aluminothermic method has been used to prepare a TiC/Al_2O_3 composite from a mixture of TiO_2, C, and Al.[6] A recent publication described an approach for synthesizing Al_2O_3/SiC composite powders by adding a source of carbon to aluminosilicates.[7] The authors report that the Al_2O_3/SiC composites powders could be hot pressed to obtain composites with > 95% relative densities. Even more versatile approaches are needed to prepare composite coatings, fibers, and films with controlled compositions and microstructures.

Organometallic precursors for ceramics have been used in processing advanced ceramic materials.[8] Key reasons for the interests in these precursors include the potential for improved control over composition, grain size and homogeneity as well as formation of ceramics in desirable forms (i.e., powders, monolithic pieces, fibers, coatings, etc.) at low processing temperature. Processing of ceramic/ceramic composites using organometallic precursors has been reported in systems such as SiC/SiO_2,[9] SiC/TiC,[10] SiC/Al_2O_3,[9] SiC/AlN,[11] Si_3N_4/AlN,[12] and BN/Si_3N_4[13]. These studies have resulted in formation of composites with fine-grained microstructures by pyrolysis of polymeric or molecular precursors. Although organometallic precursors to TiN, TiC and AlN have been reported,[14-17] no studies on the preparation and pyrolysis of organometallic precursors for TiC/Al_2O_3, TiN/Al_2O_3, or TiN/AlN composites have been reported.

The purpose of the present study is to illustrate a flexible method for controlling the composition and microstructure of ceramic composites. The method involves combining alkoxide-derived precursors with a polymeric carbon source and converting the mixture to ceramic composites by pyrolysis. In this paper we report the synthesis of precursors for TiC/Al_2O_3, TiN/Al_2O_3, or TiN/AlN and study their pyrolysis chemistry and the microstructure of the pyrolysis products. These studies indicated that alkoxide-derived polymers can be more versatile than organometallic precursors for preparing homogeneous, non-oxide/oxide, and non-oxide/non-oxide composites.

Experimental Procedure

General

All of the synthesis and manipulations of the precursors were carried in a N_2-filled glove box or in Schlenk glassware under N_2. Titanium butoxide ($Ti(O\text{-}n\text{-}Bu)_4$) and furfuryl alcohol were purified by distillation. Aluminum butoxide ($Al(O\text{-}sec\text{-}Bu)_3$) and THF were used as received.

Synthesis and Pyrolysis of the Precursors

A solution of 0.45 g of H_2O in 10 mL of THF was added dropwise to a 50 mL of THF solution containing 3.40 g of titanium butoxide and 2.46 g of aluminum butoxide under vigorously stirring at -30 °C ($Al:Ti:H_2O$=1:1:2.5), yielding a clear, colorless solution. Then a solution of 0.735 g of furfuryl alcohol in 10 mL of THF was added dropwise to the above solution (Ti:FuOH=1:0.75), resulting in a yellow solution. After this solution was refluxed for 1 h, the volatile components were removed at 120 °C under vacuum leaving a yellow solid. On the basis of a similar procedure, precursors with Ti:FuOH ratios of 1:1, 1:1.25, 1:1.5, 1:2, 1:2.5 and 1:3 were prepared, and all these precursors were soluble in hydrocarbon solvents.

Pyrolysis of the precursors was performed in a carbon furnace in argon (ultra-high purity) or an alumina tube furnace under anhydrous ammonia or nitrogen (ultra-high purity) at a flow rate of 200 mL/Min. When ammonia was used, the precursors were first heated in argon to 600 °C and then heated to higher temperatures under ammonia. A heating rate of 200 °C/h was used for all the pyrolysis experiments.

Characterization

Diffuse reflectance infrared Fourier transform spectroscopy (DRIFTS) studies were performed with a Nicolet PC/IR (Model 44) infrared spectrometer. Samples were prepared by mixing precursors or pyrolysis products with dry KBr in the glovebox. The ground mixture was loaded in the IR sample holder in the glove box and quickly transferred to the sample chamber of the spectrometer, which then was flushed with N_2 for 10 min before data collection. Thermogravimetric analysis (TGA) of the precursor was carried out with a Perkin-Elmer TGA7 thermal analysis system at a heating rate of 10 °C/Min. The TGA atmosphere was argon that had been passed through a BTS catalyst (BASF CO.) and a molecular sieve column to remove O_2 and H_2O, respectively. X-ray powder diffraction patterns were measured with a Rigaku 300 diffractometer employing Cu/Kα radiation and a Ni filter at a scanning rate of 10°/Min. The XRD peak assignments were carried out using the Rigaku Software JCPDS peak indexing programs. Gas chromatography (GC) measurements were performed on a Hewlett-Packard 5890 gas chromatograph with a 6-ft Carbopack B column using He carrier gas at a flow rate of 25 mL/Min. The morphologies of the pyrolysis products were observed using a Hitachi S-530 scanning electron microscope with a beam voltage of 20-25 KV. Transmission electron microscopy (TEM) was performed on a TOPCON EM002B operating at 200 KV accelerating voltage. X-ray fluorescence elemental analyses was performed on a VG HB5 STEM (scanning transmission electron microscope) operating at 100 KV accelerating voltage. Auger analyses was recorded on a Perkin-Elmer 660 scanning Auger microscope with a working voltage of 15 KV. Elemental analyses were obtained from E+R Microanalytical Laboratory (Corona, NY).

Results and Discussion

It is well known that mixed metal alkoxides have provided successful methods for preparing homogeneous metal oxide ceramics, glasses or composites in various forms.[18-19] Therefore, adding an organic carbon source to the Al and Ti alkoxide systems in a suitable concentration should form precursors to TiC/Al_2O_3, TiN/Al_2O_3 or TiN/AlN, since these composites can be formed from the oxides by the following reactions:

$$2TiO_2 + Al_2O_3 + 6C \longrightarrow (2TiC)/Al_2O_3 + 4CO \quad (1)$$

$$2TiO_2 + Al_2O_3 + 2C + 2NH_3 \longrightarrow (2TiN)/Al_2O_3 + 2CO + 2H_2O + H_2 \quad (2)$$

$$2TiO_2 + Al_2O_3 + 4C + 4NH_3 \longrightarrow 2(AlN/TiN) + 4CO + 3H_2O + 3H_2 \quad (3)$$

In the present study, soluble alkoxide-derived polymeric precursors to TiC/Al_2O_3, TiN/Al_2O_3 and TiN/AlN were prepared by paratially hydrolyzing Ti and Al alkoxides.

Synthesis and Characterization of Precursors

It is well known[20-22] that furfuryl alcohol or polyfurfuryl alcohol gives good yields of carbon upon pyrolysis and can serve as a soluble polymeric carbon precursor in the alkoxide-derived polymers. Therefore, if the precursor has the desired ratio of furfuryl alcohol to metal alkoxides, TiC/Al_2O_3, TiN/Al_2O_3 or TiN/AlN can be formed from reaction

Table 1. Elemental Analyses of the Precursor and of Pyrolysis Products Obtained under Argon.

No	FuOH:Ti	T(°C)	Ti	Al	C	H	O[a]
1	1.5:1	RT[b]	18.77	11.11	39.42	5.23	25.4
2	1:1	650 6 h	29.65	16.68	21.70	0.29	31.68
3	1.25:1	1250 6 h	46.52	23.64	12.39	0.1	17.35
4	1.5:1	1250 6 h	47.87	25.20	18.22	0.17	8.54
5	1.5:1	1500 6 h	72.04	5.59	14.82	0	7.55

[a] by difference. [b] the as-synthesized precursor.

1, 2 or 3, respectively.

Experiments in our laboratory have shown that furfuryl alcohol readily replaces the alkoxy groups of metal alkoxides *via* an alcohol exchange reaction. For example, a white solid material formed instantly when Al(O-*sec*-Bu)$_3$ and furfuryl alcohol were mixed at room temperature in THF; the FT-IR spectrum of the isolated solid product derived from the reaction of Al(O-*sec*-Bu)$_3$ and FuOH in a 1:1 molar ratio indicated that almost all the -*sec*-BuO- groups in Al(O-*sec*-Bu)$_3$ were replaced by FuOH groups indicating the solid product was probably Al(FuO)$_3$. Our previous study[20,21] showed that furfuryl alcohol also readily replaces the butoxy groups of Ti butoxide.

Both Ti(O-*n*-Bu)$_4$ and Al(O-*sec*-Bu)$_3$ hydrolyze easily to form oligomeric or polymeric species depending on the amount of H_2O added to the alkoxides.[20] In order to obtain soluble precursors, a low H_2O:M ratio (1.25:1) and a low reaction temperature (-30 °C) were chosen for the hydrolysis reaction. GC analyses of the distilled components after hydrolysis of Ti and Al alkoxides (H_2O:Ti:Al=2.5:1:1) indicated that more *sec*-butyl alcohol than *n*-butyl alcohol was present (the ratio of *sec*-C_4H_9OH:*n*-C_4H_9OH was 1.45:1), suggesting that the hydrolysis of Al(O-*sec*-Bu)$_3$ was greater than that of Ti(O-*n*-Bu)$_4$.

To contol the amount of carbon available for reduction of the oxides, furfuryl alcohol was added to the hydrolyzed alkoxides. When the FuOH:Ti ratio was less than 2, the precursors could be described as a polymer of $[\mathrm{Ti(O\text{-}}n\mathrm{\text{-}Bu)_xAl(O\text{-}}sec\mathrm{\text{-}Bu)_y(FuO)_zO_{2.5}}]_n$ (x + y + z = 2) assuming that the hydrolysis reaction of the alkoxides and subsequent condensation, as well as the FuOH exchange reaction, were complete. Here, z is the amount of furfuryl alcohol added: the ratio of x and y depends on the relative stabilities and exchange rates for Ti and Al alkoxides. Therefore, the precursor with a FuOH:Ti ratio of 1.5:1 should give an empirical formula of $\mathrm{TiAlO_{4.5}C_{9.5}H_{12}}$, which is relatively close to the actual empirical formula of $\mathrm{TiAl_{1.05}O_{4.05}C_{8.36}H_{13.32}}$ obtained from the elemental analyses (No 1, Table 1). The precursors were yellow or brown depending on the relative concentration of furfuryl alcohol in the starting materials.

Figures 1a - 1d show the FTIR spectra of precursors synthesized with various FuOH:Ti ratio. The existence of O-*n*-Bu and O-*sec*-Bu groups are represented by the strong C-H stretching region (2959, 2933 and 2875 cm^{-1}) and C-H bending vibrations (1463 and 1375 cm^{-1}). These assignments were confirmed by comparing these spectra with the FTIR spectrum (Figure 1e) of the hydrolysis product resulting from Ti(O-n-Bu)$_4$-Al(O-sec-Bu)$_4$-2.5H_2O. As for the furfuryl alcohol groups, they are indicated by the absorption band at 3119 cm^{-1}, which is attributed to the C-H stretching vibration of the olefinic H on the furan rings. The sharp absorption bands at 1600 and 1506 cm^{-1} were assigned to the furfuryl alcohol C=C stretching vibrations. As expected, the spectra of Figures 1a - 1d also indicate that the relative intensity of the absorption bands for furfuryl alcohol groups increases as the amount of furfuryl alcohol increases in the precursors. In addition, the strong absorption band at 3630 cm^{-1} was attributed to the OH stretching vibration. The broad bands below 900 cm^{-1} were assigned to the Ti-O-Ti, Al-O-Al and Al-O-Ti units.

From the IR spectra, we noticed that all the investigated precursors (with a FuOH:Ti ratio from 0.75:1 to 3:1) showed the presence of M-OH groups, indicating that the condensation reaction was not complete. Therefore, the precursors can be described as a polymer of $[\mathrm{Ti(O\text{-}}n\mathrm{\text{-}Bu)_xAl(O\text{-}}sec\mathrm{\text{-}Bu)_y(OFu)_zO_a(OH)_b}]_n$, (a=2.5-0.5b). Furthermore, even when the ratio of FuOH:Ti was larger than 2, the IR spectra of the precursors indicated that *n*-BuO and *sec*-BuO groups were still present, which suggested that the FuOH exchange reaction was not complete. The furfuryl alcohol, which did not bond to the Al or Ti atoms, probably polymerized to polyfurfuryl alcohol.

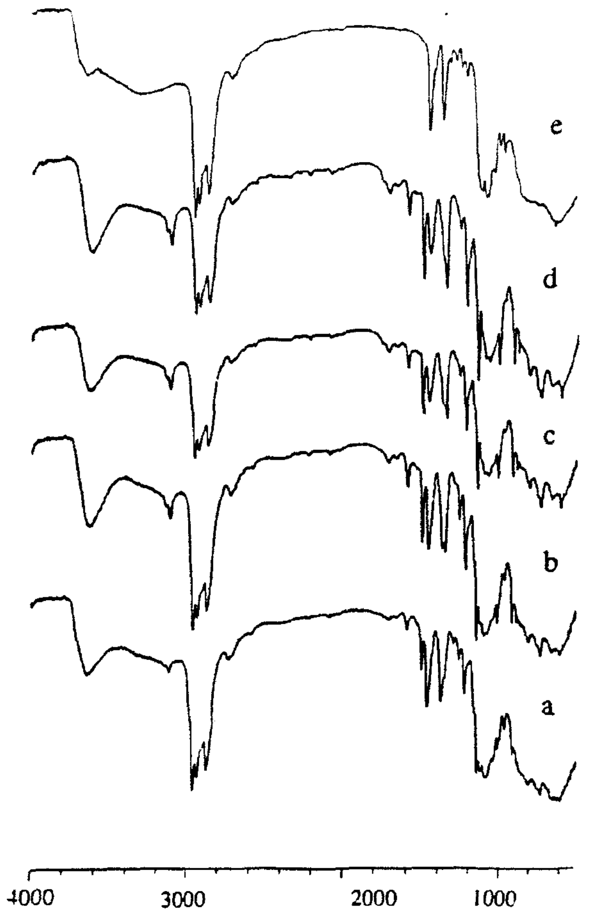

Figure 1 the IR spectra of the as-synthesized precursors with a FuOH:Ti ratio of (a) 0.75:1; (b) 1.5:1; (c) 2:1; (d) 3:1; (e) 0 (no FuOH in the system).

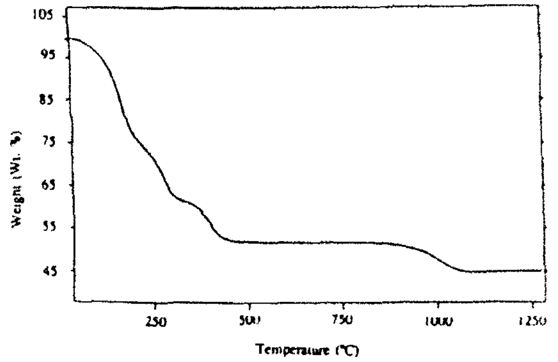

Figure 2 TGA curve (in argon) of the precursor with a FuOH:Ti ratio of 0.75:1.

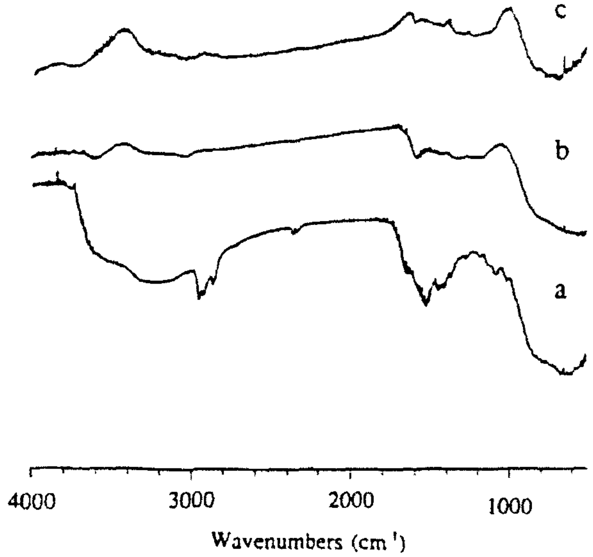

Figure 3 FT-IR spectra of the precursor (FuOH:Ti=1.5:1) heated in argon at (a) 300 °C, 1 h; (b) 600 °C, 1 h; (c) 800 °C, 6 h.

Preparation of TiC/Al_2O_3

The TGA curve (Figure 2) of the precursor with a FuOH:Ti ratio of 0.75:1 in argon indicated several weight-loss steps; the weight loss below 300 °C was attributed to the condensation of M-OH and decomposition of both O-*n*-Bu and O-*sec*-Bu groups, presumably forming H_2O and other volatile organics; the FuO groups decomposed between 300-450 °C, yielding carbon. By 500 °C, no organics remained in the precursors. These assignments were supported by the IR spectra of the pyrolysis product. For example, the IR spectrum (Figure 3a) of the precursor heated at 300 °C for 1 h in argon indicated that the absorption bands corresponding to the OH or butyl groups had decreased compared with those (Figure 1b) of the as-synthesized precursor. In addition, the absence of the C-O stretching vibration around 1200 cm^{-1} and the C-H vibration at 3110 cm^{-1} also suggested that the FuO groups had begun to decompose at 300 °C. In fact, the strong absorption at 1600 cm^{-1} was assigned as the C=C stretching vibrations, which was the major structural unit resulting from the decomposition of polyfurfuryl alcohol to carbon.[23] Further heating the precursor to 600 °C resulted in the disappearance of this C=C absorption band (Figure 3b). The broad absorption band between 500-1000 cm^{-1} observed in the spectrum was attributed to the Ti-O and Al-O stretching vibrations.

The weight loss observed between 850-1170 °C in the TGA was attributed to the carbothermic reduction of TiO_2, which resulted in the formation of TiC. The XRD patterns of the pyrolysis products indicated that the product obtained after heating to 800 °C for 6 h in argon was amorphous. The IR spectrum (Figure 3c) of this product showed the relative intensity of Ti-O absorption band had decreased, which indicated that the carbothermic reduction of TiO$_2$ had begun. Further heating the precursor resulted in the formation of TiO$_x$C$_y$ at 1000 °C, and α-Al$_2$O$_3$ at 1150 °C. The XRD pattern (Figure 4a) of the same precursor heated to 1250 °C for 12 h in argon indicated that TiC and α-Al$_2$O$_3$ were the only crystalline phases. In addition, a weight loss of 48.4%, 59.8% and 63.2% was observed for the precursor heated at 800 °C, 1150 °C and 1250 °C, respectively.

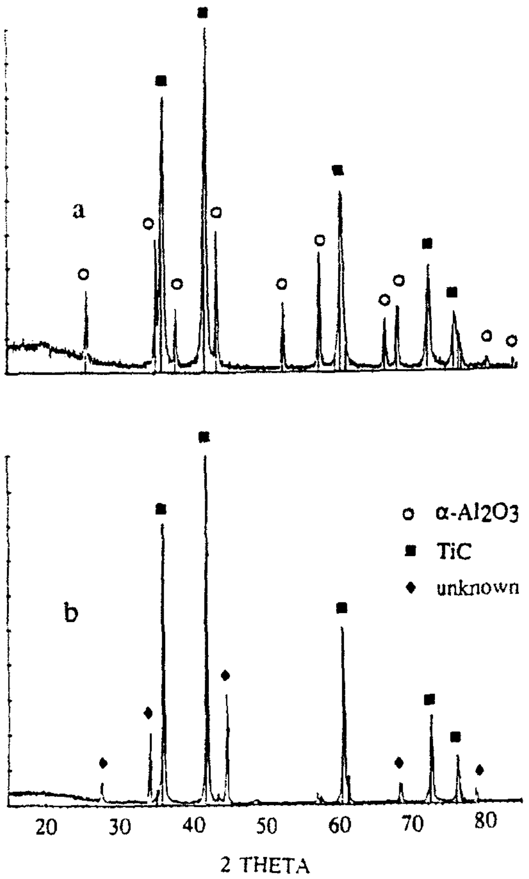

Figure 4 XRD patterns of the precursors heated in argon at (a) 1250 °C for 6 h; (FuOH:Ti=1.5:1) (b) 1500 °C for 6 h; (FuOH:Ti=1.5:1).

In order to determine the appropriate amount of furfruyl alcohol for the carbothermic reduction of TiO$_2$, it is necessary to know how much carbon will be derived from the pyrolysis of each mole of FuOH. The precursor with the FuOH:Ti ratio of 1:1, when pyrolyzed at 650 °C for 6 h in argon, had a composition of TiAlC$_{2.92}$H$_{0.47}$O$_{3.19}$ based on the elemental analyses (No. 2, Table 1), indicating that pyrolysis of each mole of FuOH will lead to 2.92 mole of carbon if we assume that the all the carbon in the product is contributed from furfuryl alcohol.

Based on the above analysis, pure TiC/Al$_2$O$_3$ will result from the precursor with a Ti:FuOH ratio of approximately 1:0.92 according to reaction (1) if the carbothermic reduction is complete.[24] In agreement with this estimate, we observed that the precursors with a FuOH:Ti ratio of 1.25:1 and 1.5:1 gave products (obtained by heating the precursors in argon at 1250 °C for 12 h) containing excess C (No. 3 and 4, Table 1) even though TiC and Al$_2$O$_3$ are observed as the only crystalline phases in the XRD patterns. Under the same condition, the precursor with a FuOH:Ti ratio of 1:1 gave a product containing two crystalline phases (TiC$_x$O$_y$ and Al$_2$O$_3$), which indicated that the carbothermic reduction was not complete at 1250 °C. Further heating the precursor to 1375 °C resulted in the formation of TiC and Al$_2$O$_3$ as the only crystalline phases. As for the precursor with a Ti:FuOH ratio of 0.75:1, it gave a product containing three crystalline phases (Ti$_2$O$_3$, α-Al$_2$O$_3$ and TiO$_x$C$_y$) at 1250 °C, further heating to 1375 °C resulted in Al$_2$O$_3$, TiC and TiO.

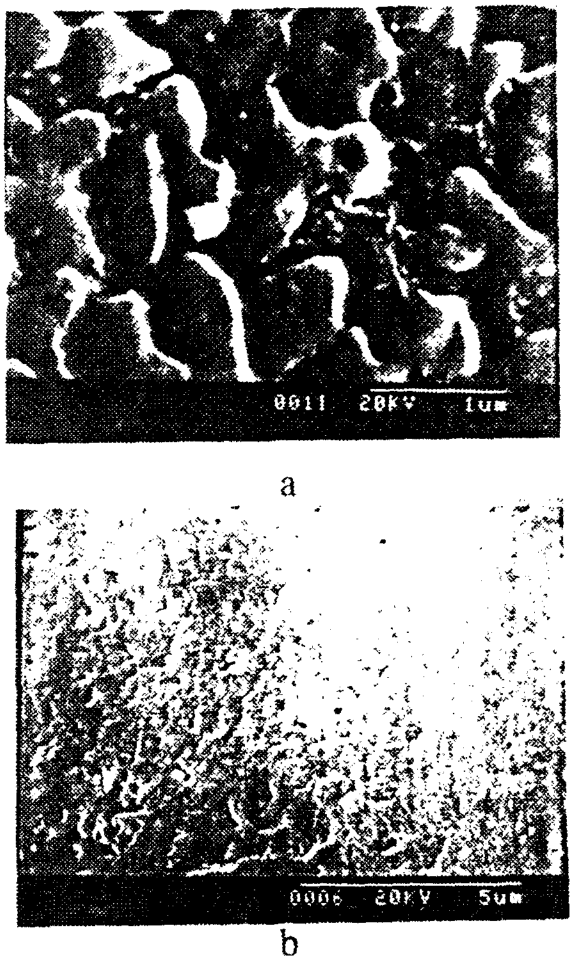

Figure 5 SEM micrographs of the precursor heated in argon at (a) 1250 °C, 6 h; (FuOH:Ti=1.25:1). (b) 1250 °C, 6 h; (FuOH:Ti=1.5:1).

The pyrolysis products from precursors with a FuOH:Ti ratio from 1:1 to 1.5 obtained at 1250 °C were composed of large (100-1000 μm), metallic-gray, irregular shaped pieces. The SEM micrograph of the pyrolysis product from the precursor with a FuOH:Ti ratio of 1.25:1 (Figure 5a) showed a morphology consisting of two phases; that is, one phase consisting of large grains (0.7-1 μm) and the other consisting of small grains (0.05-0.1 μm). Auger analyses indicated that the large grains contained only Al and O elements; Ti and C were the major components of these small grains with small amounts of Al. These results suggested that the large and small grains were to α-Al$_2$O$_3$ and TiC, respectively. In addition, the SEM micrograph indicated that the α-Al$_2$O$_3$ grains were homogeneously distributed in the TiC phase, presumably due to the intimate mixing between Al and Ti components in the precursor. Figure 5b shows the SEM micrograph of the product from the precursor with a FuOH:Ti ratio of 1.5:1, which indicated that excess C obscured the grains of both α-Al$_2$O$_3$ and TiC, which resulted in a flat, featureless surface.

The XRD patterns for all the precursors with a FuOH:Ti ratio of 0.75:1 to 1.5:1 heated to 1500 °C under argon indicated that the XRD peaks were much sharper than those of the pyrolysis products obtained at 1250 °C. Furthermore, a substantial weight loss (5-32 %) was observed upon heating from 1250 to 1500 °C, indicating some material was lost during the treatment. In addition, an unidentified crystalline phase was observed in the XRD patterns of these products in addition to the phases we observed before (α-Al$_2$O$_3$, TiC and TiO$_x$C$_y$).

As this new phase formed, the intensity of α-Al$_2$O$_3$ diffraction peaks decreased. Furthermore, the concentration of this new phase relative to that of α-Al$_2$O$_3$ was dependent on the concentration of carbon; as the concentration of C in the system increased, higher concentrations of this new phase were observed. For example, the XRD pattern of the pyrolysis product with a FuOH:Ti ratio of 1.25:1 indicated that some α-Al$_2$O$_3$ crystalline phase still remained in the product, but the XRD pattern (Figure 4b) of the product with a FuOH:Ti ratio of 1.5:1 indicated that almost all the crystalline α-Al$_2$O$_3$ phase had disappeared; instead, TiC and this new phase were the major crystalline compounds present.

Pyrolysis of the precursor with a FuOH:Ti ratio of 1.5:1 from 1250-1500 °C resulted in a weight loss of 32.5%; the elemental analyses (No. 5, Table 1) of this product indicated the relative content of Al, C and O has significantly decreased as compared with that heated at 1250 °C. We also observed that excess C plays an important role in the formation of this new phase, since this phase was not observed in the product obtained by heating a mixture of TiC and Al$_2$O$_3$ (Ti:Al=1:1) powders at 1650 °C. This reaction resulted in the disappearance of Al$_2$O$_3$ as well as the formation of other unidentified phase. In addition, Ti also appears to be indispensable for the formation this phase since pyrolysis of the precursor derived from Al(O-*sec*-Bu)$_3$-H$_2$O-FuOH only leads to α Al$_2$O$_3$ and Al$_3$C$_4$.

The above results indicate the unidentified phase formed in the present system could be the reaction product of TiC, Al$_2$O$_3$ and C. Kim *et al.*[25] briefly mentioned that an unidentified compound containing Al, Ti, C and O, was present in product of the reaction between Al$_2$O$_3$, TiC and C. However, since no detailed data was given for this unidentified compound in their study, it could not be compared with the new phase in the present system.

Preparation of TiN/Al$_2$O$_3$

The formation of TiN/Al$_2$O$_3$ was achieved by the pyrolysis of the precursor (with a FuOH:Ti ratio of 0.75:1) in argon at 600 °C and then further heating to higher temperature in NH$_3$. The XRD patterns of the pyrolysis products indicated that TiO$_x$N$_y$ was the only crystalline phase at 1000 °C; the crystalline α-Al$_2$O$_3$ phase emerged at 1150 °C. Further heating the precursor to 1250 °C for 12 h resulted in the formation of α-Al$_2$O$_3$ and TiN. The SEM micrograph (Figure 6a) of this product showed a microstructure consisting of fine grains. TEM analyses of the same product revealed the grain sizes were in the range of 150-400 Å. The elemental analyses (No 1, Table 2) of the product agreed closely with the stoichiometry of TiN/Al$_2$O$_3$. Figure 6b showed the STEM micrograph of the product, which indicated that the images of Ti and Al were similar to that of N and O, respectively, suggesting that TiN and α-Al$_2$O$_3$ were the only components in the system, and homogeneously dispersed.

Both XRD and TEM results of the product resulting from 1250 °C indicated the presence of some amorphous material in the system. Further heating of this product to 1500 °C under N$_2$ increased the crystallinity of both TiN and α-Al$_2$O$_3$ based on the XRD study. Furthermore, no weight loss or gain was observed during this treatment, indicating no reaction was involved. The SEM micrograph (Figure 6c) of the resulting product showed that the grain sizes of the product had increased and two sizes of grains were present which corresponded to the α-Al$_2$O$_3$ (the large grains) and TiN (the small grains), respectively.

The formation of the TiN in the present study could result from two different reactions. The first one was the carbothermic reduction of TiO$_2$ and subsequent nitridation, which was proposed in reaction (2); the second one is the direct reduction and nitridation of TiO$_2$ by ammonia. In fact, recent studies[26-27] indicated that TiN fibers and thin films can be made by reacting NH$_3$ with a Ti alkoxide-derived polymer. In our system, pyrolysis of a precursor prepared from $Ti(O\text{-}n\text{-}Bu)_4$, $Al(O\text{-}sec\text{-}Bu)_3$ and H_2O in a molar ratio of 1:1:2.5 (no FuOH) at 1250 °C for 6 h in ammonia yielded crystalline $\alpha\text{-}Al_2O_3$, TiN and Ti_2O_3. This result indicated that both reaction (2) and the direct reaction with NH_3 are involved.

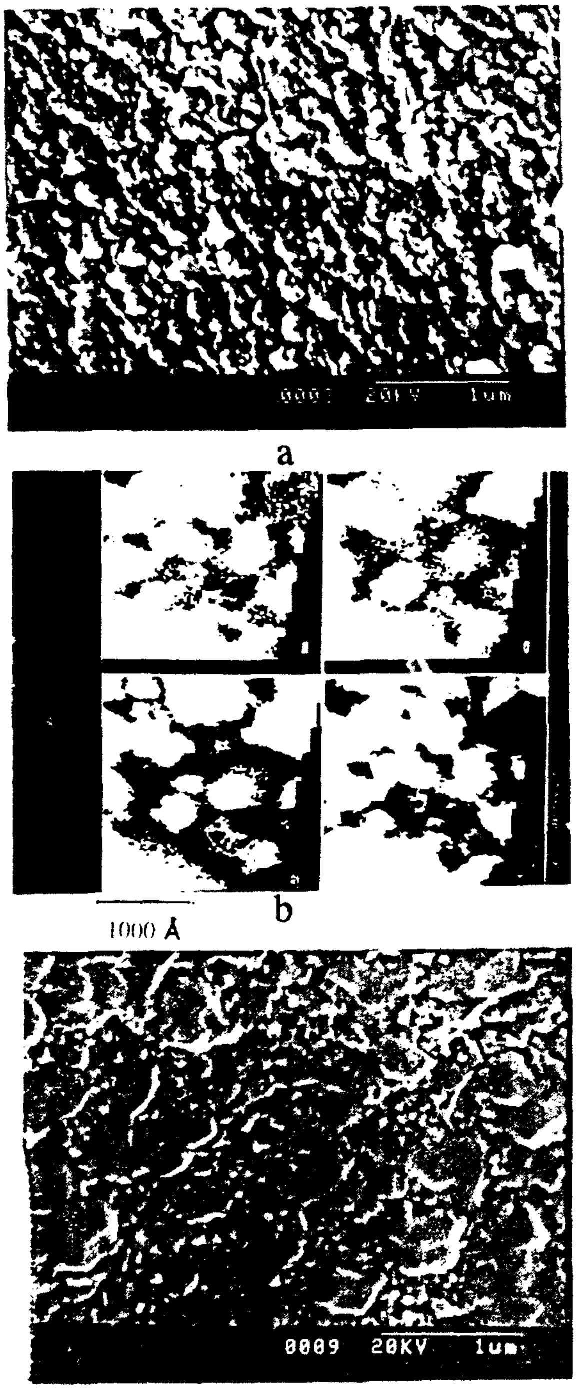

Figure 6 SEM micrographs of the precursor (FuOH:Ti=0.75:1) heated in ammonia at 1250 °C for 6 h; (b) the STEM micrograph for the same product at (a); (c) the SEM micrograph of the same product at (a) further heated at 1500 °C under N_2 for 6 h.

Preparation of AlN/TiN

The formation of AlN/TiN was achieved by heating the precursors with a FuOH:Ti ratio of 2.5:1 or 3:1 in ammonia. The XRD patterns of these pyrolysis products indicated the presence of TiO_xN_y at 1000 °C; AlN and TiO_xN_y at 1150 °C; AlN and TiN at 1250 °C. The SEM micrograph (Figure 7a) of the latter pyrolysis products showed a morphology consisting of small grain sizes (150-400 Å by TEM); furthermore, the STEM study of the products revealed that both Al and Ti components were homogeneously dispersed. However, elemental analyses (No. 2 and 3, Table 2) of the products indicated significant amounts of oxygen were present; furthermore, both products had similar compositions, even though different amount of carbon were provided. This could be because the NH_3 reacted with C forming HCN and removed C before the carbothermic reduction of Al_2O_3 was complete,[28] which subsequently resulted in

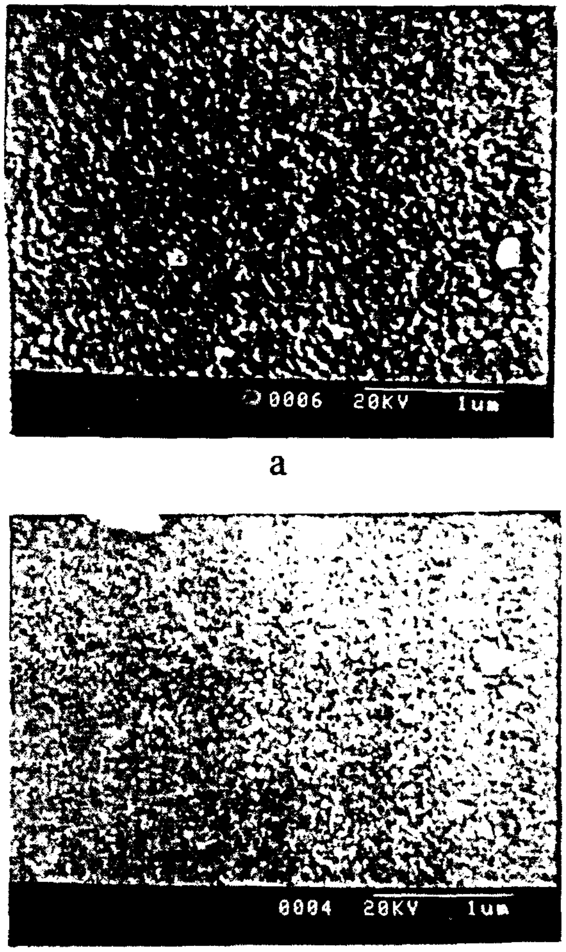

Figure 7 SEM micrographs of the precursor (FuOH:Ti=3:1) heated in ammonia at 1250 °C for 6 h; (b) the same product at (a) heated in nitrogen at 1500 °C for 6 h.

Table 2. Elemental Analyses of Pyrolysis Products Obtained Under Ammonia and Nitrogen

No	FuOH:Ti	T(C)	Ti	Al	C	H	O^a	N
1	0.75:1	1250^b 6 h	41.31	24.83	0.21	0.10	11.25	22.30
2	2.5:1	1250^b 6 h	43.3	26.46	0.42	0.20	12.93	16.69
3	3:1	1250^b 6 h	44.22	26.69	0.95	0.21	11.13	16.80
4	3:1	1500^c 6 h	45.83	27.78	0.40	0.10	-	26.54
5	2:1	1250^d	42.68	27.60	4.42	0.18	5.55	19.67

^{a} by difference. ^{b} pyrolyzed below 600 C in argon, then in ammonia at high temperatures.
^{c} pyrolyzed in nitrogen. ^{d} pyrolyzed in nitrogen at 1500 °C for 6 h, then in ammonia at 1250 °C for 6 h.

a similar composition for both precursors. Furthermore, the results indicate that the direct nitridation of Al_2O_3 was much more difficult than the nitridation of TiO_2.

When the pyrolysis products obtained at 1250 °C were further heated to 1500 °C in nitrogen, a weight loss of 11.1% was observed. The XRD pattern of the resulting product indicated that the crystallinity of both TiN and AlN had increased. Furthermore, the SEM micrograph (Figure 7b) of the corresponding product showed that the grains grew to 500-1000 Å. In addition, the elemental analyses (No. 4, Table 2) revealed that almost pure TiN/AlN composite was obtained by such a treatment, presumably due to the nitridation of Al-O by N_2.

As mentioned earlier, we observed that, even though much more carbon than needed for reaction (3) remained after pyrolysis, the carbothermic reduction was still not complete at 1250 °C presumbaly due to the removal of C by the reaction with ammonia. It appears that one solution to this problem is to pyrolyze the precursors in nitrogen to 1500 °C and then treat the resultant product in ammonia at 1250 °C to remove any residual carbon. In this way, AlN/TiN can be formed with a lower FuOH:Ti ratio since there is no significant reaction between carbon and nitrogen at 1500 °C. However, the XRD pattern of the pyrolysis product obtained by heating the precursor (FuOH:Ti=1.25:1) in nitrogen at 1500 °C for 6 h, indicated that some α-Al_2O_3 still remained in the product besides AlN and TiN, even though enough C was provided for the carbothermic reduction of Al_2O_3 and TiO_2.[29] With more C in the precursor (for example, the precursor with the FuOH:Ti ratio of 2:1), the α-Al_2O_3 phase disappeard after heating at 1500 °C (in nitrogen) for 6 h; however, the XRD result indicated that TiN_xC_y was formed besides AlN, indicating that some of the excess C has combined with TiN. Pyrolysis of the above product in ammonia at 1250 °C for 6 h resulted in a 8.5% weight loss, which was presumably caused by the reaction between amminia and free carbon; however, the elemental analyses (No. 5, Table 2) of this product indicated that 4.42% of carbon still remained in the product, furthermore, the XRD of this product showed the presence of TiN_xC_y besides AlN. Therefore, it appears that the carbon in TiN_xC_y is more difficult to remove than free carbon.

Acknowledgements

Financial support for this work was provided by the Air Office of Scientific Research (AFOSR) under Contract No. F49620-89-C-0102.

References

1. J. Mukerji and S.K. Biswas, J. Am. Ceram. Soc. 73, 142 (1990).

2. J.P. Mathers, T.E. Forester and W.P. Wood, Ceram. Bull. 68, 1330 (1989).

3. T. Nagano, H. Kato and F. Wakai, J. Am. Ceram. Soc. 74, 2258 (1991).

4. I-W. Chen and L. An Xue, *J. Am. Ceram. Soc.*, 73, 2585 (1990)

5. D.R. Clarke, *J. Am. Ceram. Soc.*, 75, 739 (1992)

6. R. Abramovici, Mater. Sci. Eng., 71, 313 (1985).

7. A.C.D. Chaklader, S. Das Gupta, E.C.Y. Lin and B. Gutowski, *J. Am. Ceram. Soc.*, 75, 2283-85 (1992)

8. M. Peuckert, T. Vaahs and M. Bruck, Adv. Mater. 2, 398 (1990)

9. B.I. Lee and L.L. Hench, Am. Ceram. Soc. Bull. 66, 1482 (1987).

10. S. Yajima, T. Iwai, T. Yamamura, K. Okamura and Y. Hasegawa, J. Mater. Sci. 16, 1349 (1981).

11. C.L. Czeckaj, M.L.J. Hackney, W.J. Hurley, Jr., L.V. Interrante, G.A. Sigel, P.J. Shields and G.A. Slack, J. Am. Ceram. Soc. 73, 352 (1990).

12. L.V. Interrante, C.L. Czekaj, M.L.J. Hackney, G.A. Siegel, P.J. Shields and G.A. Slack, Mate. Res. Symp. Proc. 121, 465 (1988).

13. D. Seyferth and H. Plenio, J. Am. Ceram. Soc. 73, 2131 (1990).

14. L.V. Interrante, L.E. Carpenter II, C. Whitmarsh, W. Lee, M. Garbauskas and G. A. Slack, Mat. Res. Soc. Symp. Procc. 73, 359 (1986).

15. A.E. Kaloyeros, W.S. Williams, C. M. Allocca, D.M. Pollina and G.S. Girolami, Adv. Ceram. Mater. 2, 257 (1987).

16. C. Russel, Chem. Mater. 2, 241 (1990).

17. G. M. Brown and L. Maya, J. Am. Ceram. Soc. 71, 78 (1988).

18. B.E. Yoldas, J. Non-Crysatlline Solids 38, 81 (1980).

19. D.S. Tucker, J.S. Sparks and D.C. Esker, Ceramic Bulletin 69, 1971 (1990).

20. Z. Jiang and W.E. Rhine, Materials Research Society Symposium Proceedings Vol(249), 1992, pp. 45-50.

21. Z. Jiang and W.E. Rhine, Chem. Mater. 3, 1133 (1991).

22. T. Gallo, F. Gambria, C. Greco, B. Simms and R. Valluzzi, "Metal Carbides from Alkoxides and Modified Alkoxides" Final Program and Abstract, 1990 MRS Meeting, p. 444.

23. E. Fitzer and W. Schafer, Carbon 8, 353 (1970).

24. since one mole of FuOH will lead to 2.92 mole of C, 0.92 mole of FuOH will result in 2.69 mole of C which is used for the formation of TiC (1 mole) and CO (1.69 mole), the latter is obtained by substrating the total oxygen amount (2.92 mole) from the oxygen needed for the formation of Al_2O_3 (1.5 mole).

25. Y.W. Kim and J.G. Lee, J. Am. Ceram. Soc. 72, 1333 (1989).

26. K. Kamiya, T. Yoko and M. Bessho, J. Mater. Sci. 22, 937 (1987).

27. J.L. Keddie, J.Li, J.W. Mayer and E.P. Giannelis, J. Am. Ceram. Soc. 74, 2937 (1991).

28. F.K. van Dijen and J. Pluijmakers, J. Eur. Ceram. Soc. 5, 385 (1989).

29. Based on the reaction ($TiO_2 + 0.5Al_2O_3 + 3.5C + N_2 = TiN/AlN + 3.5CO$) and the formula of $TiAlC_{2.92}H_{0.47}O_{3.19}$, the complete carbothermic reduction in this system will need 1.09 mole of FuOH.

SECTION 14

PREPARATION OF NANOPHASE SiC/Si_3N_4, SiC/B_4C AND STOICHIOMETRIC SiC FROM MIXTURES OF A VINYLIC POLYSILANE AND METAL POWDERS

Zhiping Jiang and Wendell E. Rhine
Ceramics Processing Research Laboratory

Presented at the 1992 Fall MRS Meeting in Boston, MA, Dec. 1992

ABSTRACT

Pyrolysis of a vinylic polysilane (VPS, Union Carbide Y12044) under argon at 1600 °C resulted in the formation of SiC with 20% residual carbon. The excess carbon was transformed to B_4C or SiC by mixing B or Si powder with VPS and pyrolyzing the mixture under a flow of argon. When excess Si was added and the mixture was pyrolysed under N_2 at 1395 °C, a SiC/ Si_3N_4 composite was obtained. All the products showed a fine-grained microstructure and excellent homogeneity. The precursors and the pyrolysis products were characterized by means of FTIR, TGA, XRD, SEM, STEM, BET, and elemental analysis.

INTRODUCTION

Organometallic ceramic precursors have received increasing attention as processing aids for advanced ceramic materials [1]. Key reasons for the interest in these precursors include the potential for improved control over composition and microstructure as well as the ability to synthesize ceramics in desirable forms (i.e., powders, fibers, monoliths, foams, etc). However, many precursors, especially those for the carbides [2-3], have often produced ceramics with residual carbon and oxygen [4]. Excess carbon has detrimental effects on the oxidation-resistance and mechanical properties of the ceramics. One solution to this problem is to use reactive fillers such as metal powders, which react with the excess carbon to form metal carbides [5-7]. Such an approach can be used to control the stoichiometry of the ceramic obtained from the preceramic polymer or used to prepare new ceramic nanocomposites.

In the present study, a vinylic polysilane (VPS) was blended with B or Si powder in toluene. Pyrolysis of these mixtures in argon resulted in the formation of SiC/B_4C or near stoichiometric SiC. A SiC/Si_3N_4 composite was obtained by pyrolysis of the mixture of Si/VPS in a flow of nitrogen. The pyrolysis chemistry of these mixtures and the microstructure of the pyrolysis products were studied by TGA, XRD, BET, SEM, STEM, and elemental analyses.

EXPERIMENTAL

The polymer was a vinylic polysilane designated by the producer (Union Carbide Corporation) as Y-12044. The amorphous silicon powder was synthesized from CO_2 laser heated SiH_4 gas [8]. The amorphous boron powder was purchased from Gallery Chemical Company. The B and Si powders have an average size of 0.22 and 0.19 μm, respectively, based on centrifugal particle size analyses. The VPS and the silicon powder were stored in a N_2-filled glove box.

Silicon or boron powder (0.2-1.0 g) was mixed with a solution containing VPS (2-3 g) and toluene (50-70 mL), resulting in a dark suspension. After the suspension was stirred at room temperature for 1 h, the solvent was removed at 100 °C under vacuum, forming a viscous powder/polymer blend. The blend was further heated at 150 °C under vacuum until it became a dark- (for the mixture of B/VPS) or light-brown (for the mixture of Si/VPS) solid.

Pyrolysis of the mixtures was performed in a carbon furnace in argon (ultra-high purity) or an alumina tube furnace under nitrogen (ultra-high purity) at a flow rate of 200 mL/min. A heating rate of 200 °C/h was used for all the pyrolysis experiments.

RESULTS AND DISCUSSION

Previous studies [3] have indicated that VPS is a thermoset polymer which cross-links at 140-200

°C by vinyl polymerization with some hydrosilyation. Heating the polymer to higher temperatures results in extensive Si-Si, C-H and Si-H bond cleavage with radical formation and methylene insertion, and finally consolidation of the SiC network with the formation of free carbon at temperatures higher than 1000 °C. The XRD results for the pyrolysis products of VPS in the present study indicated that SiC began to crystallize at 1000 °C. Heating the precursor to higher temperatures resulted in sharper XRD peaks.

The pyrolysis product of VPS obtained at 1600 °C consisted of large (>2000 μm), dark and irregularly-shaped pieces; the XRD pattern of this product indicated that β-SiC was the major phase with a minor amount of α-SiC present. The SEM micrograph (Figure 1a) of this product exhibited a microstructure consisting of equiaxed submicrometer grains. The TGA analysis of this product under a flow of air showed a weight loss of approximately 20% between 700-950 °C due to the oxidation of the residual carbon. The SiC obtained after removing the carbon was a yellowish powder consisting of <0.05 μm particles (Figure 1b). Therefore, the product obtained from the pyrolysis of VPS in argon can be considered as a SiC/C composite in which nanosized SiC particles are uniformly dispersed in a carbon matrix, forming hard particles.

In order to obtain stoichiometric SiC from VPS, VPS was mixed with Si powder which would react with excess C. The as-prepared mixture of the Si/VPS (the weight ratio of Si:VPS is 1:2.72) was a light-brown solid. IR studies indicated that the relative intensity of the asymmetric $=CH_2$ stretch (3050 cm^{-1}) in the mixture had significantly decreased compared to that of the as-received VPS, suggesting that the vinyl polymerization had occurred when the mixture was heated at 150 °C during its preparation. The TGA obtained for this mixture was similar to that of VPS, although VPS lost a little more weight than the mixture of Si/VPS. The TGA for the mixture of the Si/VPS under a flow of argon showed weight loss at 100-150 and 350-750 °C, respectively. The first weight loss was attributed to the solvent or other volatiles trapped in the mixture, and the second one was attributed to the decomposition of VPS. These results suggested that adding Si powder to VPS does not change the pyrolysis chemistry of VPS below 1100 °C.

Based on previous studies [9], we expected that the reaction between Si powder and carbon would occur at 1200-1300 °C. As expected, the XRD peaks of the pyrolysis products obtained from Si/VPS heated between 1200 and 1600 °C were much sharper than those from the pyrolysis product obtained from VPS, implying that the reaction between Si and the residual C in the Si/VPS system led to formation of SiC with larger crystallites.

The ratio of Si:VPS in the mixture was determined empirically based on the elemental analyses of the pyrolysis products. Based on the TGA of Si/VPS to 1180 °C, there was no further weight loss above 800 °C; however, we observed an additional 7% weight loss after heating Si/VPS in the furnace to 1600 °C (Table 2). This weight loss is not completely unexpected since we had to use more Si powder to obtain stoichiometric SiC than that calculated for reacting with the expected amount of

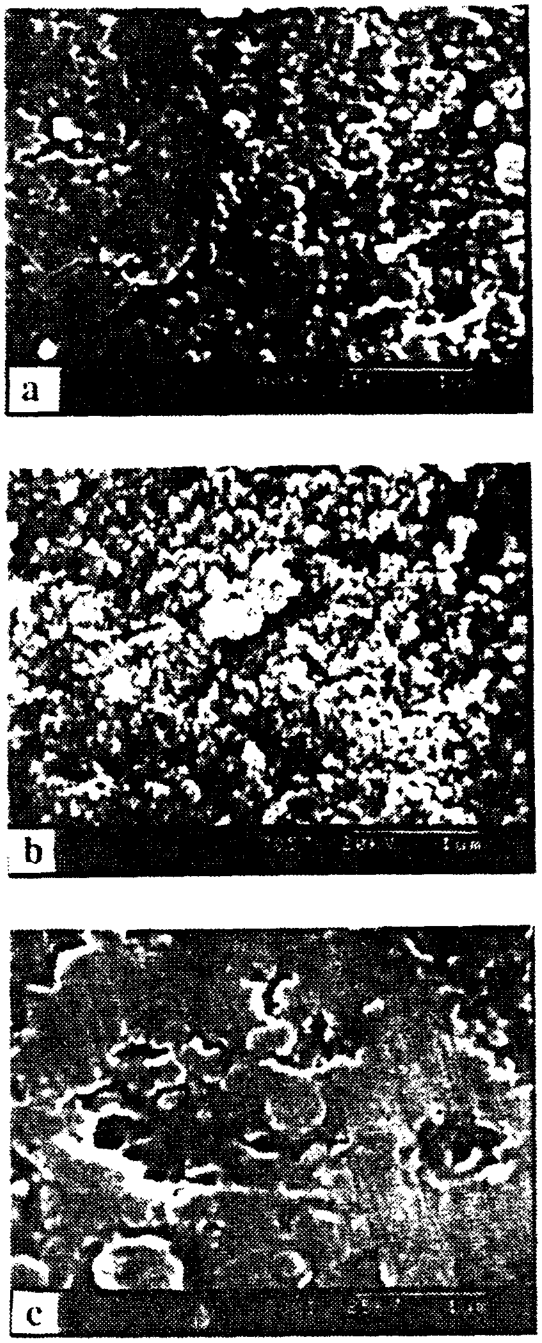

Figure 1. SEM micrograph of (a) VPS heated at 1600 °C for 3 h, (b) the TGA residue of the product at (a) in air, (c) the mixture of the Si/VPS heated at 1600 °C for 3 h.

Table 1 Elemental Analyses (Wt.%) of the Products

	T (°C)	Si	C	B	N	H
SiC	1600 3 h	69.60	30.28	-	-	0
SiC/Si_3N_4	1395 12 h	67.66	22.60	-	9.82	0
SiC/B_4C	1600 3 h	29.80	25.40	44.00	-	0

Table 2 The Weight Loss Observed for the Mixtures Heated in Argon

T(°C)	1100*	1180*	1200	1300	1395	1600
	-	-	6 h	6 h	6 h	3 h
SiC	-	29.5	-	33.3	34.0	36.6
SiC/Si_3N_4	20.5	-	-	-	33.5	-
SiC/B_4C	17.7	-	27.2	-	-	29.6

* The weight loss observed from the TGA curves.

residual carbon (20% based on the TGA). These results indicated that Si species such as Si and/or Si-O were lost during pyrolysis.

The pyrolysis product obtained from heating the Si/VPS mixture to 1600 °C was a yellow solid; the XRD pattern (Figure 2a) of this product showed sharp peaks for ß-SiC; furthermore, the peaks due to the α-SiC phase were negligible. The TGA for this product in a flow of air showed no weight loss from 25-1000 °C, suggesting that very little excess carbon was present in the product. These results were consistent with the elemental analyses (Table 1) of this product, from which an empirical formula of $Si_{1.00}C_{1.02}$ was calculated.

The SEM micrograph of a polished section of the product is shown in Figure 1c and shows that the grain sizes were 0.1-0.2 µm for this product. The BET analysis showed that this product had a specific surface area of 2.50 m^2/g, indicating that the product contained pores and cracks as was observed in the SEM micrographs. This type of microstructure is to be expected from a process which involves a combination of polymer pyrolysis and reaction bonding.

The SiC/B_4C composite was prepared by heating a mixture of VPS and B powder (the weight ratio of B:VPS is 1:2.14) at 900-1600 °C under a flow of argon. The XRD studies indicated that SiC and B_4C crystallized at 1000 °C and 1200 °C, respectively. The XRD pattern (Figure 2b) of the product heated at 1600 °C showed that β-SiC and B_4C were the major phases with some minor unidentified peaks. As with the Si/VPS system, we had to use more B powder than that calculated based on the expected amount of excess carbon produced upon pyrolysis of VPS in order to obtain a product free of residual carbon. As a result we observed that there was almost a 12% weight loss when the mixture of B/VPS was heated under argon between 1100 and 1600 °C (Table 2). We attributed the weight loss at high temperature to the vaporization of Si-O, CO and B-O species. The evaporization of BO species at high temperature was also observed in the B/TiO_2 systems [11].

An SEM micrograph of the product is shown in Figure 3a. The TEM micrograph (Figure 3b) of the product showed that the grain sizes were in the range of 40-60 nm, and the elemental mapping of Si, B and C based on STEM analyses (Figure 3c) suggested that the B_4C and SiC components were uniformly distributed. The BET analysis of this product indicated that its specific surface area was 6.44 m^2/g. The elemental analyses (Table 1) of the product gave a formula of $Si_{1.00}B_{3.82}C_{1.99}$, which was close to a composition of $(SiC)_{1.00}(B_4C)_{1.00}$. The TGA of this product in a flow of air showed a weight gain of 3.5% from 500-1000 °C, presumably due to the oxidation of a small amount of the B_4C.

The precursor for the SiC/Si_3N_4 composite was prepared by mixing VPS with more Si powder than that used in the case of the SiC precursor (the weight ratio of Si:VPS was 1:1.75). The preparation of the composite was carried out by pyrolyzing the mixture in argon at 1395 °C for 6 h and further heating the product in nitrogen at the same temperature for 6 h. It was expected that pyrolysis of the mixture in argon would produce a mixture of SiC and Si, which was confirmed by the XRD pattern. Further heating the product in nitrogen resulted in a 10.5% gain in weight, implying that the nitridation of the Si had occurred. The XRD pattern (Figure 2c) of

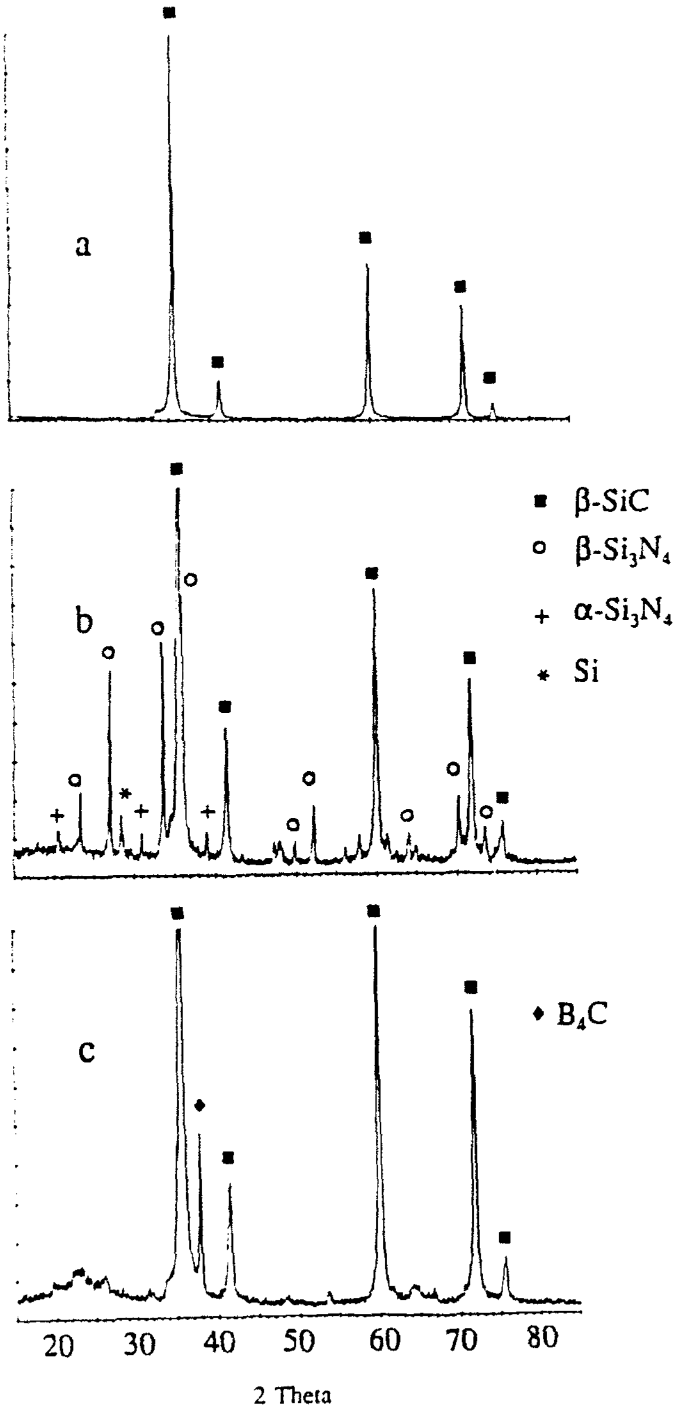

Figure 2. XRD pattern of (a) the mixture of Si/VPS heated at 1600 °C for 3 h, (b) the mixture of the B/VPS heated at 1600 °C for 3 h, (c) the mixture of Si/VPS heated in nitrogen at 1395 °C for 6 h.

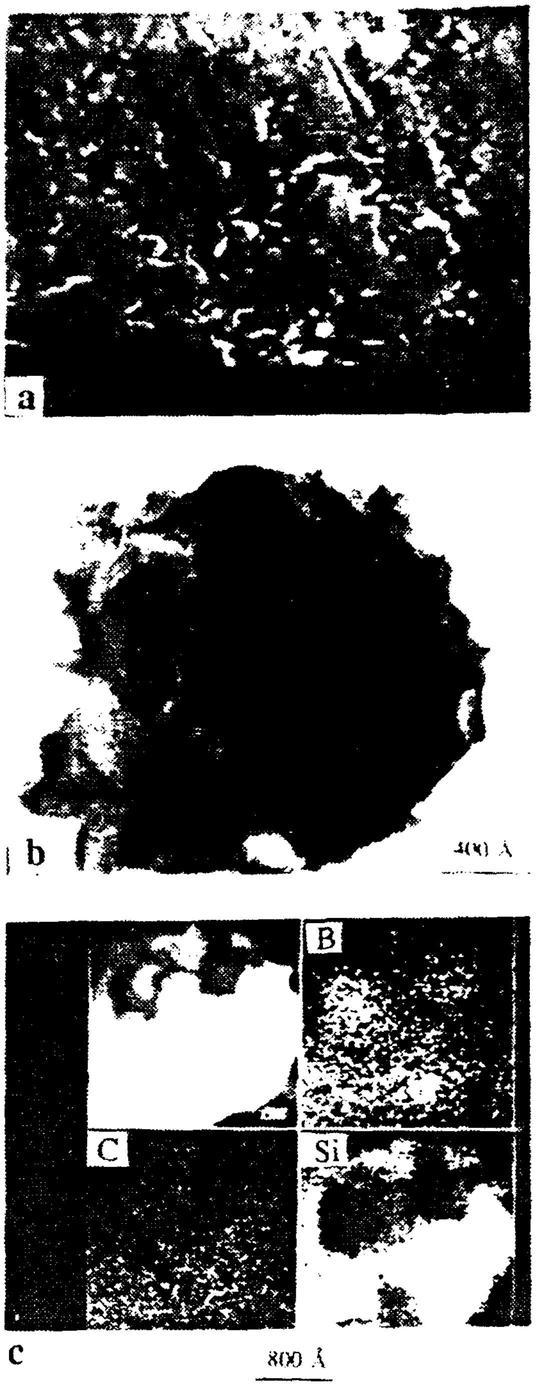

Figure 3. (a) SEM micrograph of the mixture of B/VPS heated at 1600 °C for 3 h, (b) TEM micrograph of the same product at (a), (c) STEM micrograph of the same product at (a).

the nitridation product indicated that β-Si_3N_4 and β-SiC were the major phases with small amounts of α-Si_3N_4 and unreacted Si. The SEM micrograph (Figure 4a) of the product after nitridation showed that the microstructure consisted of small grains (0.1 μm). The STEM micrograph (Figure 4b) of the product indicated that the SiC and Si_3N_4 components were homogeneously dispersed, and BET analysis indicated that this product had a specific surface area of 3.23 m^2/g. The elemental analysis of the nitridation product resulted in an empirical formula of $Si_{3.45}C_{2.69}N_{1.00}$, which approximately corresponded to a SiC/Si_3N_4 ratio of 10.78/1. The TGA of the nitridation product under a flow of air showed that a gain of 0.3% in weight was observed between 25 and 1000 °C, indicating very little oxidation between these temperatures.

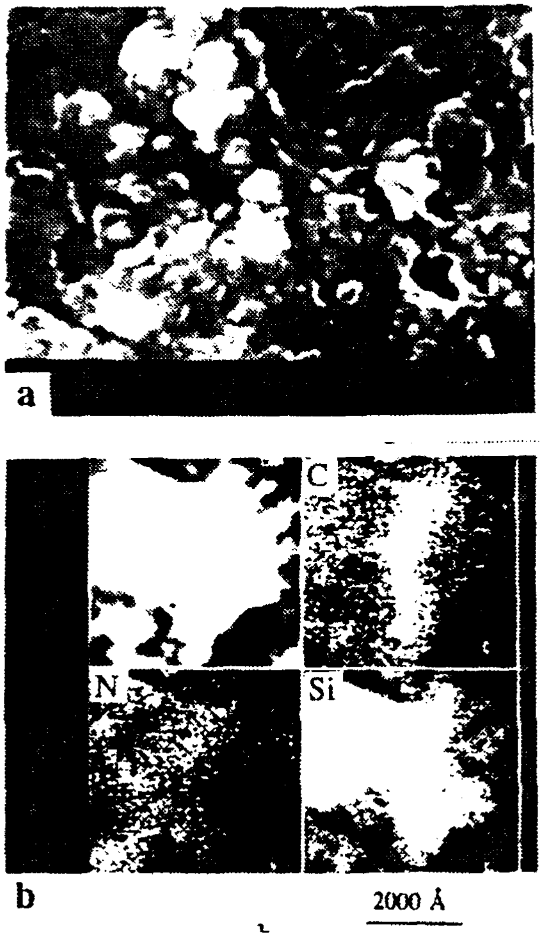

Figure 4. SEM micrograph for the mixture of Si/VPS (a) heated in nitrogen at 1395 °C for 6 h, (b) STEM micrograph of the same product at (a).

SUMMARY

This study indicates that it is possible to prepare pure carbides or carbide/carbide composites by pyrolysis of the mixtures of a metal powder and a polymeric precursor in argon if the ratio of metal powder to precursor is properly adjusted; when the nitridation of metal powders is involved, the complete nitridation appears to be difficult since the metal powders are dispersed in a dense polymer matrix. We observed that all of the products showed a fine-grained microstructure and excellent homogeneity. However, we also observed all the products contained pores and cracks. These pores and cracks are presumably caused by the gas evolution during pyrolysis and the density change between precursor and product. Due to the nature of the mixtures, it is difficult to avoid these defects. The successful application of this process will require efforts to control the pore (and crack) sizes and their distribution so that these mixtures can be used to produce ceramics with the desired properties.

ACKNOWLEDGEMENT

Financial support for this work was supported by the Air Force Office of Scientific Research (AFOSR) under Contract No. F49620-89-C-0102. We are grateful to Dr. John S. Haggerty (CPRL, MIT) for the donation of Si powder.

References

1. K.J. Wynne and R.W. Rice, *Annu. Rev. Mater. Sci.* **14**, 297 (1984).

2. D. Seyferth and H. Lang, *Organometallics* **10**, 551 (1991).

3. W.R. Schmidt, L.V. Interrante, R.H. Doremus, T.K. Trout, P.S. Marchetti and G.E. Maciel, *Chem. Mater.* **3**, 257 (1991).

4. J. Lipowitz, T.A. Rabe, G.A. Zauk, Y. Xu and A. Zangvil, p 767 in "Chemical Processing of Advanced Ceramics," Ed. L.L. Hench and J.K. West, John Wiley and Sons 1992.

5. M. Seibold, B. Ahlers and P. Greil, pp.555 in "Advanced Structural Inorganic Composites" Ed. by P. Vincenzini, Elsevier Science Publishers B.V., 1991.

6. D. Seyferth, H. Lang, C.A. Sobon, J. Borm, H.J. Tracy and N. Bryson, *J. Inorganic and Organometallic Polymers* **2**, 59 (1992).

7. K. Ohara, T. Shizuki, H. Mitamura and M. Sugino, "Process for Preparation of a Metal Carbide-Containing Molded Product" US Patent **4126652**, 1978.

8. W.R. Cannon, S.C. Danforth, J.H. Flint, J.S. Haggerty and R.A. Marra, *J. Am. Ceram. Soc.* **65**, 324 (1982).

9. R. Pampuch, L. Stobierski and J. Lis, *J. Am. Ceram. Soc.* **72**, 1434 (1989).

10. Z. Jiang and W.E. Rhine, MRS Symposium Proceesings, Vol(249), 1992, pp.45-50.

11. Z. Jiang and W.E. Rhine, *Chem. Mater.* **4**, 497 (1992)

SECTION 15

EPITAXIAL $LiNbO_3$ THIN FILMS PREPARED BY A SOL-GEL PROCESS

Keiichi Nashimoto and M.J. Cima

K. Nashimoto and M.J. Cima, "Epitaxial $LiNbO_3$ Thin Films Prepared by a Sol-Gel Process," Mater. Lett., 10 (7,8) 348-54 (1991).

ABSTRACT

$LiNbO_3$ thin films were prepared on sapphire substrates by a sol-gel process using lithium ethoxide and niobium pentaethoxide. Decreasing the amount of water added for hydrolysis of the alkoxides caused the films to show a higher preferred orientation in the same crystal plane as the orientation of the substrate. Without the addition of water to the alkoxides, a heteroepitaxial film with single-crystal nature was obtained. Films of this quality have not been reported previously.

INTRODUCTION

The sol-gel process is an attractive method for synthesizing ceramic or glass thin films because it allows for precise composition control, low temperature processing, and preparation of large area films by spin coating or dipping a substrate with a precursor derived from organometallic substances. For these reasons, polycrystalline $LiNbO_3$ films have been prepared on silicon substrates by a sol-gel process [1]. In addition, the feasibility of epitaxial growth by the sol-gel process was demonstrated by Partlow and Greggi when they observed homoepitaxial growth on $LiNbO_3$ [2]. Subsequently, several studies of chemically derived highly oriented or homoepitaxial thin films such as $LiNbO_3$ [3, 4], $PbTiO_3$ [5], and ZrO_2-Y_2O_3 [6] were reported. However, there have been no reports describing heteroepitaxial growth by a sol-gel process.

Lithium niobate is a leading electro-optical material for active waveguides, modulators, and switches because it has large non-linear optical coefficients, a large birefringence, a high Curie point, a high electro-optic coefficient, a strong piezoelectric effect, and excellent acousto-optic properties [7]. Usually single crystal $LiNbO_3$ has served as the substrate upon which the optical waveguide is fabricated; however, this single crystal device is quite complicated and expensive due to the difficulty in controlling the lithium to niobium ratio of the single crystal. The properties of $LiNbO_3$, such as the Curie point and refractive indices, are very sensitive to fluctuations in its stoichiometry.

The deposition of high quality $LiNbO_3$ thin films is important to the fabrication of integrated electro-optic devices. Therefore, a variety of epitaxial thin film formation techniques have been used to prepare $LiNbO_3$ films: liquid phase epitaxy [8], epitaxial growth by melting [9], chemical vapor deposition [10], rf sputtering [11, 12], and molecular beam epitaxy [13]. None of these methods, however, completely solves the difficulties controlling the chemical composition of $LiNbO_3$. Sapphire is usually used as a substrate for the epitaxial growth of $LiNbO_3$ because the refractive index of sapphire is smaller than that of $LiNbO_3$, and lattice mismatching between $LiNbO_3$ and sapphire is relatively small. The combination of $LiNbO_3$ with a material of lower refractive index can create an effective optical waveguide.

EXPERIMENTAL PROCEDURE

Lithium niobate precursors were prepared from lithium ethoxide (99.9%) and niobium pentaethoxide (99.999%) in a dry nitrogen atmosphere. Equal molar amounts of each alkoxide were dissolved in absolute ethanol to form a 0.05 M solution. The solution was then stirred and refluxed at 78.5°C for 24 h. This procedure is similar to that described by Hirano and Kato [14] and is known to result in the formation of the double alkoxide, $LiNb(OC_2H_5)_6$, although Eichorst, Howard, and Payne discovered evidence of instantaneous formation of the double alkoxide at room temperature [15]. Three types of solutions were prepared for spin coating. A measured amount of 2.5 vol% water in ethanol was added to two of the double alkoxide solutions. Enough water-ethanol solution was added very slowly to the first solution to total 3.0 mol water per mole of double alkoxide, while the second totaled 1.0 mol water per mole double alkoxide. These solutions were stirred and refluxed for an additional 24 h at 78.5°C. The third solution included no added water. All three solutions were concentrated to 0.5 M at room temperature by vacuum distillation. Dry gel powders were prepared from portions of the hydrolyzed solutions by further drying.

The precursors were spin coated onto 15 x 15 mm optically polished sapphire (110) substrates at 2000 rpm in a dry nitrogen environment. Prior to coating, the sapphire substrates were cleaned in an acetone ultrasonic bath, an aqueous 20 vol% HCl solution, and deionized water. The cleaned substrates were oven-dried at 120°C. The coated substrates and/or dry gel powders were heated at a rate of 10°C/min to a specified temperature and held there for 60 min in moist oxygen and for 30 min in dry oxygen according to the procedure used by Hirano and Kato [3]. Water vapor was introduced by bubbling the oxygen through an attached reservoir of deionized water at room temperature prior to flowing through the furnace.

The texture of the prepared films was examined by X-ray powder diffraction (XRD) (Rigaku RU300), by X-ray pole figures (Rigaku RU200), by Schulz reflection method, and by scanning electron microscopy (SEM) (Hitachi S-530).

RESULTS AND DISCUSSION

Figure 1 shows XRD patterns of $LiNbO_3$ films. These films were prepared from the precursor solution with the double alkoxide:water molar ratio of 1:3, that is, a hydrolyzed precursor. Although the powder derived from the same precursor crystallized at 300°C, the film annealed at 300°C was amorphous. It seems that crystallization of the film is more difficult than that of the powder. At temperatures over 400°C, this film shows an XRD pattern identical to that of the powder except for the sapphire (110) peak at $2\theta=37.8°$. The similarity between the two patterns indicates the film has randomly oriented grains. Increasing the annealing temperature does not change the relative intensity of the reflections. On a pole figure measurement, the off-diagonal (012) plane was used since it shows the strongest intensity in powder diffraction. A pole figure of the (012) plane will show only four high intensity spots at 43.3° off-normal to the (110) plane when the lattice parameters listed in Table 1 [11] for lithium niobate are used and when the film is <110> axis-oriented single crystal. In the pole figure generated, the (012) plane was distributed almost randomly, confirming the interpretation of the XRD pattern, although there were several spots, indicating the film has a slightly textured nature.

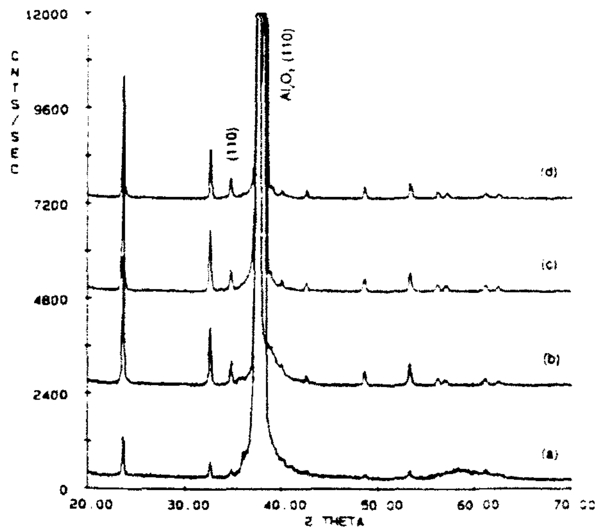

Fig. 1. X-ray diffraction patterns of $LiNbO_3$ films derived from a precursor solution with $LiNb(OEt)_6$:$H_2O=1:3$ and annealed at: (a) 400°C, (b) 500°C, (c) 600°C, and (d) 700°C.

Table 1. Lattice Parameters of $LiNbO_3$ and Sapphire at Room Temperature.

Crystal	Crystal System	a (Å)	c (Å)
$LiNbO_3$	Hexagonal	5.149	13.862
Sapphire	Hexagonal	4.758	12.991

XRD patterns of the films prepared from the precursor solution with a double alkoxide:water molar ratio of 1:1, a partially hydrolyzed precursor, are shown in Figure 2. Although the powder was nearly amorphous at 400°C, the corresponding film annealed at 400°C crystallized well and had a <110> axis preferred orientation. For this precursor, it appears that crystallization in the film occurs more easily than in the bulk powder. Increasing the annealing temperature seems to decrease the <110> texture since the relative (110) reflection intensity decreases. There is a weak unknown diffraction peak at $2\theta=36.1°$. Although an (012) pole figure of the film derived from the above precursor and annealed at 400°C contained two weak spots approximately 30° off-normal to the film surface, there were four intense spots approximately 43° off-normal to the film surface. These spots have the same rotation angle as the (012) diffraction spots of the substrate in the surface plane, and therefore the (110) plane is epitaxial to the substrate.

When a film was derived from the precursor solution containing only double alkoxide, very intense diffraction

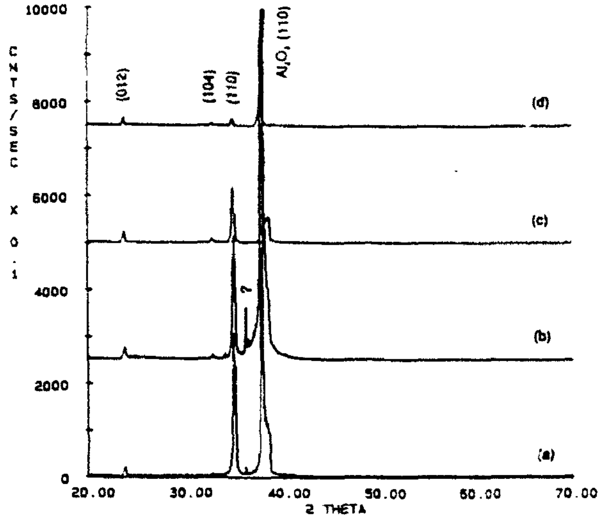

Fig. 2. X-ray diffraction patterns of $LiNbO_3$ films derived from a precursor solution with $LiNb(OEt)_6$: $H_2O=1:1$ and annealed at: (a) 400°C, (b) 500°C, (c) 600°C, and (d) 700°C.

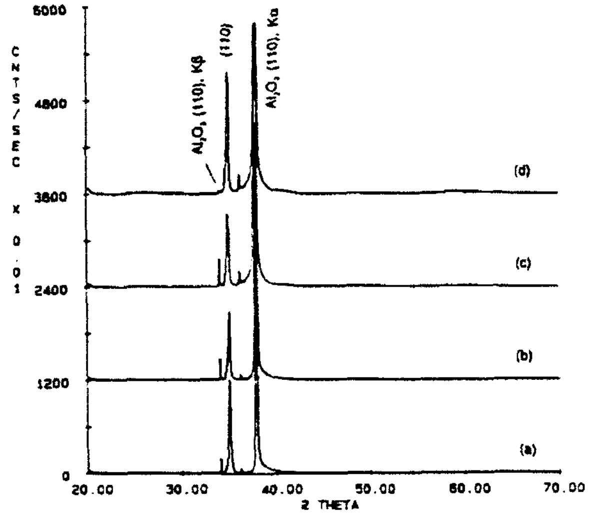

Fig. 3. X-ray diffraction patterns of $LiNbO_3$ films derived from a precursor solution of $LiNb(OEt)_6$ and annealed at: (a) 400°C, (b) 500°C, (c) 600°C, and (d) 700°C.

in the (110) plane was observed, and no other orientations of $LiNbO_3$ were observed, as shown in Figure 3. In contrast with the above result, the intensity of the peak tended to increase with increasing annealing temperature. Also, as in the case above, the powder was almost amorphous at 400°C while the corresponding film annealed at 400°C crystallized well. As shown in Figure 4, a pole figure of the (012) plane shows only four spots approximately 43° off-normal to the film surface, and the rotation

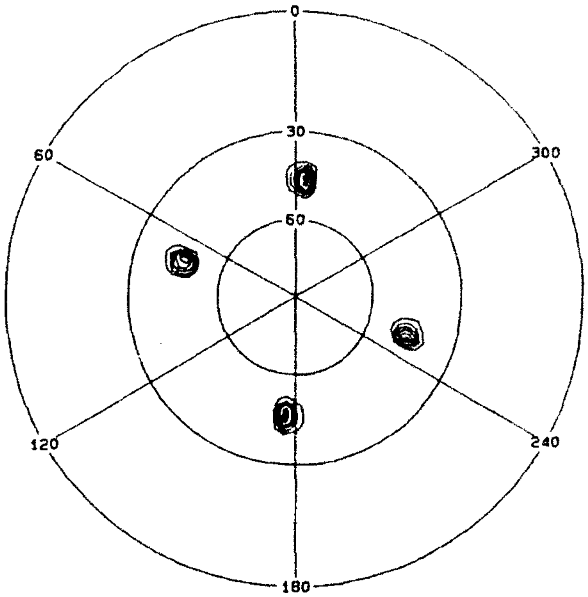

Fig. 4. X-ray diffraction pole figure for the (012) plane of a $LiNbO_3$ film derived from a precursor solution of $LiNb(OEt)_6$ and annealed at 400°C.

angles are the same as those of the (012) diffraction spots of the substrate. These results confirm epitaxial growth of the film with single-crystal nature on the substrate.

By comparing the films derived from the three different precursors, it is clear that the film exhibits greater epitaxy with decreasing hydrolysis prior to spin coating. Hirano and Kato showed that preferred orientation was obtained by partial hydrolysis of the double alkoxide before dip coating [3]; however, we have shown that no prehydrolysis is needed to obtain epitaxial films. A possible explanation may involve homogeneous nucleation in prehydrolyzed films. During crystallization, nucleation may occur homogeneously within the film and/or heterogeneously on the substrate surface. Heterogeneous nucleation will lead to the formation of an epitaxial film. When the double alkoxide is hydrolyzed prior to spin coating, homogeneous nucleation is favored because the sol particles may act as nuclei. When these particles are absent, however, heterogeneous nucleation may have a smaller activation energy than homogeneous nucleation because of the presence of an epitaxial substrate. Consequently, heterogeneous nucleation will begin at lower temperatures than will homogeneous nucleation, followed by the preferred growth of the heterogeneous nuclei which have an epitaxial relationship with the substrate. This mechanism seems to be supported by the differences in crystallization temperatures between films and powders depending on precursor composition. The

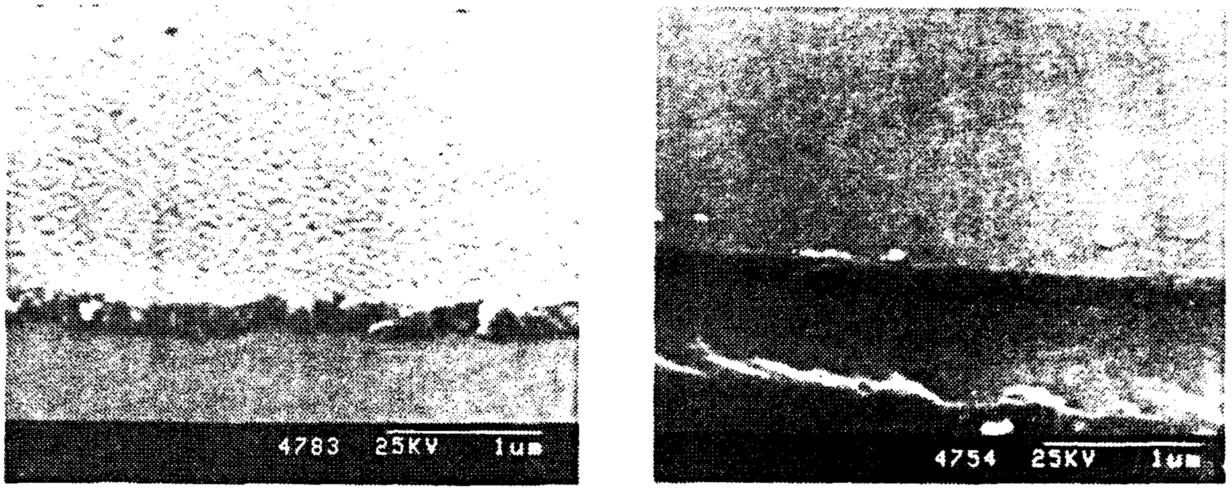

(a) (b)

Fig. 5. Scanning electron micrographs of $LiNbO_3$ *films derived from (a) a precursor solution with* $LiNb(OEt)_6$:H_2O *= 1:3 and (b) a precursor solution of* $LiNb(OEt)_6$, *and annealed at 500°C.*

crystallization temperature of the film derived from the hydrolyzed precursor was higher than that of the powder derived from the same precursor, whereas the crystallization temperature of the film derived from the partially hydrolyzed or non-hydrolyzed precursor was lower than that of the powder derived from the corresponding precursor.

Figure 5 shows the morphology of the films prepared from the 1:3 double alkoxide:water precursor solution and the double alkoxide-only precursor solution, and annealed at 500°C. At annealing at 400°C, these films looked dense and smooth with a thickness of approximately 110 nm and refractive indices from 1.84 to 2.03, depending on the precursors. However, the film derived from the hydrolyzed or partially hydrolyzed precursor began to exhibit grain growth at 500°C, as shown in Figure 5a. The film derived from the double alkoxide-only precursor began to show grain growth at 600°C, although XRD showed this film still maintained epitaxy. The grain growth of the films prepared from the hydrolyzed or partially hydrolyzed precursor began at a lower temperature than that of the film prepared from the non-hydrolyzed precursor. This may result from growth of grains which have smaller surface energies than the (110) plane. The grain growth of the film prepared from the non-hydrolyzed precursor does not possess this growth process because of its single orientation nature.

CONCLUSIONS

The epitaxial growth of $LiNbO_3$ thin films on sapphire substrates was examined in terms of the composition of a precursor solution prepared from lithium ethoxide and niobium pentaethoxide. Films fabricated from solutions that were not prehydrolyzed exhibited epitaxial growth on (110) sapphire substrates. Prehydrolysis favored the development of a random microstructure. The morphology of the films changed with the composition of the precursor and with the annealing temperature, although all of the films displayed smooth surfaces at relatively low annealing temperatures.

ACKNOWLEDGMENTS

This work was supported by Fuji Xerox Co., Ltd., Japan, and by AFOSR under contract F49620-89-C-0102.

REFERENCES

1. D.J. Eichorst and D.A. Payne, "Sol-Gel Processing of Lithium Niobate Thin-Layers on Silicon"; pp. 773-78 in Better Ceramics Through Chemistry III, Mat. Res. Soc. Symp. Proc., Vol. 121. Edited by C.J. Brinker, D.E. Clark, and D.R. Ulrich. Materials Research Society, Pittsburgh, PA, 1988.
2. D.P. Partlow and J. Greggi, "Properties and Microstructure of Thin $LiNbO_3$ Films Prepared by a Sol-Gel Process," *J. Mat. Res.*, **2**, 595-605 (1987).
3. S. Hirano and K. Kato, "Preparation of Crystalline $LiNbO_3$ Films with Preferred Orientation by Hy-

drolysis of Metal Alkoxides," *Adv. Ceram. Mat.*, **3**, 503-06 (1988)

4. S. Hirano and K. Kato, "Processing of Crystalline Li(Nb,Ta)O_3 Films with Preferred Orientation through Metal Alkoxides"; pp. 181-90 in Processing Science of Advanced Ceramics, Mat. Res. Soc. Symp. Proc., Vol. 155. Edited by I.A. Aksay, G.L. McVay, and D.R. Ulrich. Materials Research Society, Pittsburgh, PA, 1989.
5. C. Chen, D.F. Ryder, Jr., and W.A. Spurgeon, "Synthesis and Microstructure of Highly Oriented Lead Titanate Thin Films Prepared by a Sol-Gel Method," *J. Am. Ceram. Soc.*, **72**, 1495-98 (1989).
6. K.T. Miller and F.F. Lange, "Single Crystal Zirconia Thin Films from Liquid Precursors"; pp. 191-97 in Processing Science of Advanced Ceramics, Mat. Res. Soc. Symp. Proc., Vol. 155. Edited by I.A. Aksay, G.L. McVay, and D.R. Ulrich. Materials Research Society, Pittsburgh, PA, 1989.
7. M.M. Abouelleil and F.J. Leonberger, "Waveguides in Lithium Niobate," *J. Am. Ceram. Soc.*, **72**, 1311-21 (1989).
8. S. Kondo, S. Miyazawa, S. Fushimi, and K. Sugii, "Liquid-Phase-Epitaxial Growth on Single-Crystal $LiNbO_3$ Thin Film," *Appl. Phys. Lett.*, **26**, 489-91 (1975).
9. S. Miyazawa, "Growth of $LiNbO_3$ Single-Crystal Film for Optical Waveguides," *Appl. Phys. Lett.*, **23**, 198-200 (1973).
10. S. Fushimi and K. Sugii, "Growth of Lithium Niobate Single Crystal by Sulphur Vapour Transport Technique," *Jap. J. Appl. Phys.*, **13**, 1895-96 (1974).
11. S. Takada, M. Ohnishi, H. Hayakawa, and N. Mikoshiba, "Optical Waveguides of Single-Crystal $LiNbO_3$ Film Deposited by RF Sputtering," *Appl. Phys. Lett.*, **24**, 490-92 (1974).
12. G.H. Hewig, K. Jain, F.O. Sequeda, R. Tom, and P. Wang, "R.F. Sputtering of $LiNbO_3$ Thin Films," *Thin Solid Films*, **88**, 67-74 (1982).
13. R.A. Betts and C.W. Pitt, "Growth of Thin-Film Lithium Niobate by Molecular Beam Epitaxy," *Electron. Lett.*, **21**, 960-62 (1985).
14. S. Hirano and K. Kato, "Synthesis of Lithium Niobate by Hydrolysis of Metal Alkoxides," *Adv. Ceram. Mat.*, **2**, 142-45 (1987).
15. D.J. Eichorst, K.E. Howard, and D.A. Payne, "NMR Investigation of Lithium Niobate Alkoxide Solutions"; in the proceedings of the Fourth International Conference on Ultrastructure Processing of Glasses and Composites. Edited by D.R. Uhlmann, M.C. Weinberg, S.H. Risbud, and D.R. Ulrich. J. Wiley & Sons, New York, NY, in press.

STRUCTURE AND OPTICAL PROPERTIES OF POLYCRYSTALLINE AND EPITAXIAL $LiNbO_3$ THIN FILMS DERIVED BY A SOL-GEL METHOD

Keiichi Nashimoto, M.J. Cima, and W.E. Rhine

Published in Ferroelectric Films, Ceramic Transactions, vol 25, 371 (1992).

ABSTRACT

Microstructural evolution and optical behavior of polycrystalline and epitaxial $LiNbO_3$ thin films derived by a sol-gel process were investigated. Although the films looked dense and smooth after annealing at 400°C, they contained porosity of 10 nm in diameter. The polycrystalline films and the films with preferred orientation prepared from prehydrolyzed precursors exhibited grain growth and developed a porous structure at 700°C, making ellipsometric measurement impossible. The epitaxial films prepared on sapphire substrates with (110) or (001) orientation from non-hydrolyzed precursors showed higher refractive indices than did the polycrystalline films or the films with preferred orientation.

INTRODUCTION

Lithium niobate has been studied as a leading electro-optical material. Actual applications of this material, which include its use in active optical waveguides, light modulators, optical switches and surface acoustic wave devices, are a result of its variety of attractive properties such as large non-linear optical coefficients, a large birefringence, a high electro-optic coefficient, and excellent acousto-optic and piezoelectric properties [1]. For optical waveguide applications, single crystal $LiNbO_3$ usually serves as the substrate upon which the optical waveguide is fabricated. However, because these single crystal devices are quite complicated and expensive, thin film waveguide devices are desirable. In the single crystal growth process, it is difficult to control the lithium to niobium ratio due to a solid-solution range near the stoichiometric composition and the congruent melting composition of 48.45 mol% [2, 3]. The properties of $LiNbO_3$, such as the refractive index, are very sensitive to fluctuations in stoichiometry. Also, in order to prepare typical titanium in-diffusion waveguides at around 1000°C, the concentration of Li_2O must not fluctuate more than 0.02 mol% or the reproducibility of the device performance will deteriorate [4]. In addition, the titanium in-diffusion process presents problems such as out-diffusion of lithium and morphological deterioration of the waveguide surface [4, 5].

Therefore, it would be useful to develop a low temperature processing route to lithium niobate thin films for use in integrated electro-optic devices. Epitaxial growth techniques are important in preparing high quality $LiNbO_3$ because the properties of $LiNbO_3$ depend on the crystallographic orientation. The combination of $LiNbO_3$ with a material of lower refractive index can create an effective optical waveguide. For this reason, sapphire is usually used as a substrate for epitaxial growth of $LiNbO_3$ because the refractive index of sapphire is smaller than that of $LiNbO_3$, and lattice mismatching between the two is relatively small. A number of epitaxial growth methods have been reported for $LiNbO_3$: liquid phase epitaxy [6], epitaxial growth by melting [7], chemical vapor deposition [8], rf sputtering [9], molecular beam epitaxy [10], and ion-plating [11]. However, these methods still present difficulties in controlling the chemical composition of $LiNbO_3$, and they all require relatively high substrate temperatures ranging from 500°C to 1250°C. In addition, optical loss has been attributed to surface or grain boundary scattering.

For the reasons above, a number of polycrystalline [12, 13] and oriented [14-16] $LiNbO_3$ films have been prepared by the sol-gel process, which is attractive because it provides for precise composition control, low temperature processing, and preparation of large-area films by spin or dip coating a substrate with a precursor derived from metalorganic substances. The feasibility of epitaxial growth by the sol-gel process was demonstrated by Partlow and Greggi when they observed homoepitaxial growth of $LiNbO_3$ [17]. Also, chemically derived, polycrystalline ferroelectric thin films such as $BaTiO_3$ [18], $PbTiO_3$ [19], PZT [19, 20], PLZT [19], and $Pb(Fe_{1/2}Nb_{1/2})O_3$ [21] have been reported. We were able to obtain heteroepitaxial $LiNbO_3$ films with single crystallographic orientations on sapphire substrates by a sol-gel process from a non-prehydrolyzed metal alkoxide precursor, while prehydrolysis of the precursor favored the development of a random microstructure in films and decreased the crystallization temperature in $LiNbO_3$ powder synthesis [22, 23]. We refer to polycrystalline films as those that exhibit random orientation of grains as determined by X-ray diffraction (XRD). Highly oriented films are those films that show preferred orientation of certain lattice planes by XRD but also indicate a considerable number of misaligned grains. Epitaxial films, however, are those in which we observe registration of the film lattice with the substrate, as determined by X-ray powder diffraction, X-ray pole figure analysis, and high resolution transmission electron microscopy. In the present study, microstructural evolution and optical behavior of polycrystalline and epitaxial $LiNbO_3$ thin films derived by a sol-gel process were investigated to examine the feasibility of preparing sol-gel derived epitaxial $LiNbO_3$ films for optical applications.

EXPERIMENTAL PROCEDURE

As described previously [22, 23], precursors for lithium niobate were prepared from commercially available lithium ethoxide and niobium pentaethoxide in a dry nitrogen atmosphere. Equal molar amounts of each alkoxide were dissolved in absolute ethanol to form a 0.05 M solution, and the solution was stirred and refluxed at 78.5°C for 24 h in order to form the double alkoxide, $LiNb(OC_2H_5)_6$. The formation of the double alkoxide in solution form was suggested from NMR spectroscopic results [24, 25]. Also, the solid state crystal structure of the double alkoxide prepared from the solution was shown by Eichorst et al. [26]. Three types of solutions were prepared for spin coating. A measured amount of 2.5 vol% water in ethanol was added to two of the double alkoxide solutions to total 1.0 and 3.0 mol water per mole of double alkoxide: A:W=1:1 composition, a partially hydrolyzed precursor, and A:W=1:3 composition, a hydrolyzed precursor. These solutions were stirred and refluxed for an additional 24 h at 78.5°C. The third solution included no added water: A:W=1:0 composition, a non-hydrolyzed precursor. All three solutions were concentrated to 0.5 M at room temperature by vacuum evaporation.

The precursors were spin coated onto 15 x 15 mm^2 optically polished sapphire substrates with (110) or (001) orientation or silicon substrates with (111) or (100) orientation at 2000 rpm in a dry nitrogen environment. Prior to coating, the sapphire substrates were cleaned in an acetone ultrasonic bath, an aqueous 20 vol% HCl solution, and deionized water. Also, the Si substrates were cleaned in the acetone ultrasonic bath and deionized water prior to coating. The cleaned substrates were oven-dried at 120°C. The coated substrates were dried for 30 min at room temperature under dry nitrogen, heated in moist oxygen at a rate of 10°C/min to a specified temperature and held there for 60 min, then held there for another 30 min after switching the atmosphere from moist to dry oxygen, and then cooled to room temperature by shutting the furnace down. Moist oxygen, produced by bubbling the gas through an attached reservoir of deionized water at room temperature at a gas flux rate of 2.0 L/min, was assumed to cause hydrolysis of the films during the course of the heat treatments.

The texture of the prepared films was analyzed by X-ray powder diffraction (Rigaku RU300) and X-ray pole figures (Rigaku RU200) with the Schulz reflection method. Morphology and structure of the films were observed by transmission electron microscopy (TEM, JEOL 200CX) and high resolution transmission electron microscopy (HRTEM, EM002B) with an acceleration voltage of 200 kV, and by scanning electron microscopy (SEM, Hitachi S-530). Planar and cross-sectional view specimens for TEM observation were prepared by a polishing and ion-milling process. Fourier transform infrared spectroscopy (FTIR, Nicolet IR-44) and scanning Auger electron spectroscopy (AES, Perkin Elmer Model 660) were also employed to examine the chemical structure of the films. Refractive indices of the films were measured by ellipsometry with a He-Ne laser.

RESULTS AND DISCUSSION

The XRD patterns of the films prepared on sapphire (110) substrates and annealed at 400°C are shown in Figure 1. The polycrystalline film was prepared from the precursor with A:W=1:3 composition at 400°C (Fig. 1a), while the film obtained from the precursor with A:W=1:1 composition crystallized at 400°C and showed preferred orientation (Fig. 1b). The films prepared from the A:W=1:0 composition precursor on sapphire (110) and (001) substrates epitaxially crystallized at 400°C, with intense single plane reflections, as shown in Figures 1c and d. The intensity of the peaks tended to increase with increasing annealing temperature up to 700°C without any indication of a Li-deficient phase or other orientations of

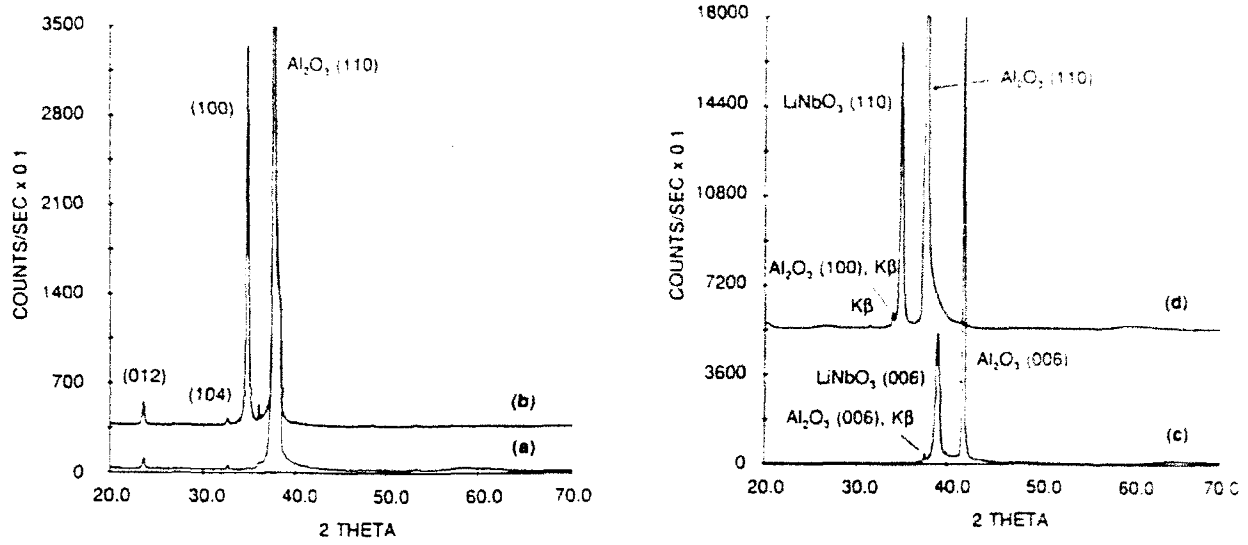

Fig. 1. X-ray diffraction pattern of films on sapphire (110) substrates prepared from (a) A:W=1:3 and (b) A:W=1:1 composition precursors and annealed at 400°C, and on sapphire substrates with (c) (001) plane and (d) (110) plane prepared from a precursor solution with A:W=1:0 composition and annealed at 400°C.

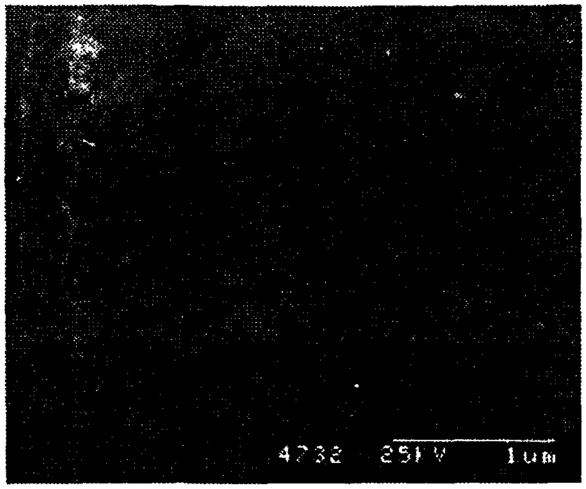

Fig. 2. Scanning electron micrograph of a film prepared on a sapphire (110) substrate from a precursor with A:W=1:0 composition and annealed at 400°C.

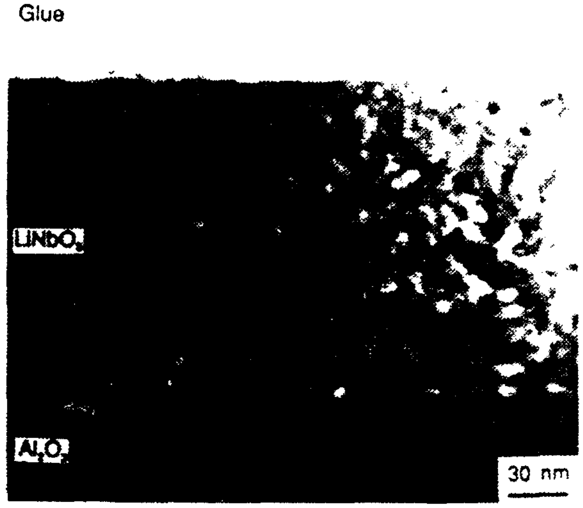

Fig. 3. Cross-sectional TEM photograph of a film prepared on a sapphire (001) substrate from a precursor with A:W=1:0 composition and annealed at 400°C.

$LiNbO_3$. An epitaxial relationship between the films and substrates was confirmed by X-ray pole figure measurement, showing symmetric patterns of spots, and by previous results [22, 23]. When these films prepared on Si (111) substrates were annealed at 400°C, only the film prepared from the A:W=1:3 composition precursor contained a crystalline phase. Films derived from the precursors with A:W=1:1 or A:W=1:0 composition were amorphous at 400°C and crystallized between 400°C and 450°C. No microstructural texture was observed in any of the films formed on Si substrates.

Figure 2 shows an SEM image of an epitaxial film prepared on a sapphire (110) substrate from the A:W=1:0 composition precursor solution and annealed at 400°C. The films prepared from each precursor solution looked dense and had optically smooth surfaces with thickness of approximately 110 nm, like the film shown in Figure 2. However, as shown by the cross-sectional TEM photo-

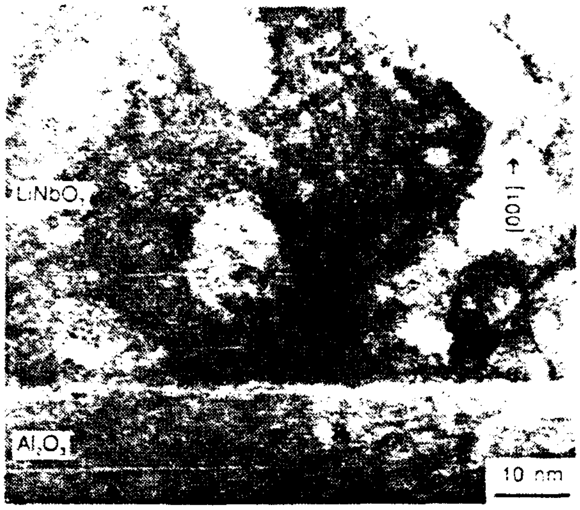

Fig. 4. Cross-sectional HRTEM photograph of a film prepared on a sapphire (001) substrate from a precursor with A:W=1:0 composition and annealed at 400°C.

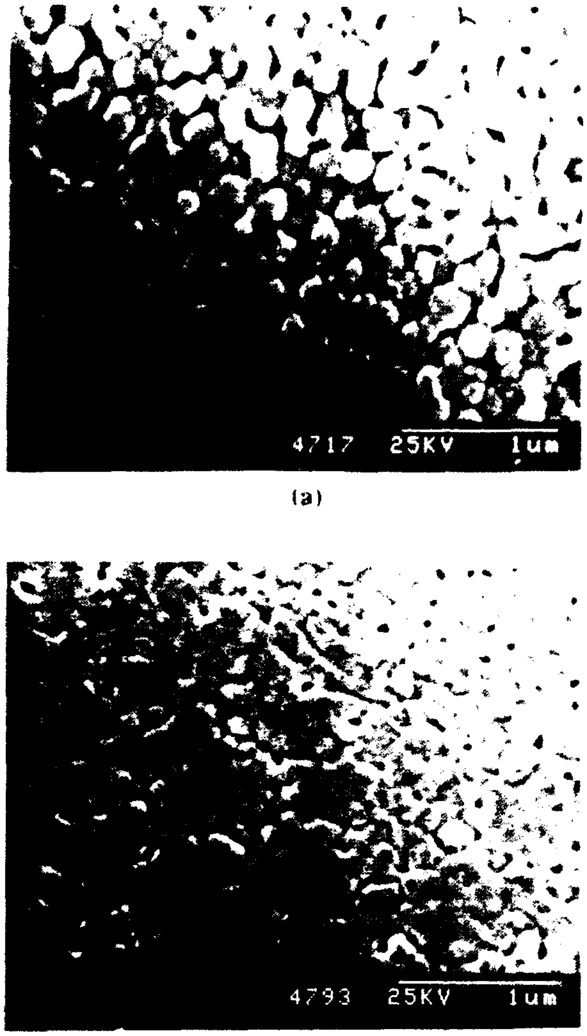

(a)

(b)

Fig. 5. Scanning electron micrographs of films on sapphire (110) substrates prepared from (a) A:W=1:1 and (b) A:W=1:0 composition precursors and annealed at 700°C.

graph of the film prepared on a sapphire (001) substrate in Figure 3, the microstructure of the epitaxial film showed microporosity of 10 nm in diameter, as observed by Partlow and Greggi [17]. The film-substrate interface looked very sharp, and the surface of the film was very smooth as observed by SEM. The cross-sectional HRTEM photograph shown in Figure 4 confirmed the epitaxial growth of the film. The (003) lattice planes of the film and the substrate, which have the same direction and run parallel to each other, are visible. The film seemed to have a single crystal nature since the (003) plane of the film had a single direction regardless of the porous structure.

The films derived from the A:W=1:3 and A:W=1:1 composition precursors began to exhibit SEM-observable grain growth at 500°C. The epitaxial film derived from the precursor with A:W=1:0 composition began to show obvious grain growth at 600°C. Figures 5a and b show films derived from the A:W=1:1 and A:W=1:0 composition precursors on sapphire (110) substrates and annealed at 700°C, respectively. The film with preferred orientation prepared from the precursor with A:W=1:1 composition showed a very porous structure consisting of grains of about 200 nm in diameter. In contrast, the epitaxial film had a denser structure than did the film with preferred orientation and contained abnormally large, single grainlike structures of 1 μm or more in diameter. Also, the single grainlike structure size of the epitaxial film with (001) orientation was larger than that of the epitaxial film with (110) orientation. Figure 6 shows a planar-view TEM photograph of the epitaxial film prepared on a sapphire (001) substrate and annealed at 700°C. The pores were approximately 50 to 100 nm in diameter, and the sub-grains, which were evolving into single grainlike structures, seemed to be about 150 to 200 nm in diameter. A detailed report of the microstructure obtained will appear in a future publication [27].

Figure 7 shows transmission FTIR spectra of the films on Si (100) substrates derived from the precursor with A:W=1:1 composition, as measured in dry air. A film annealed at 300°C showed a Nb-O band at 540 cm^{-1}, a

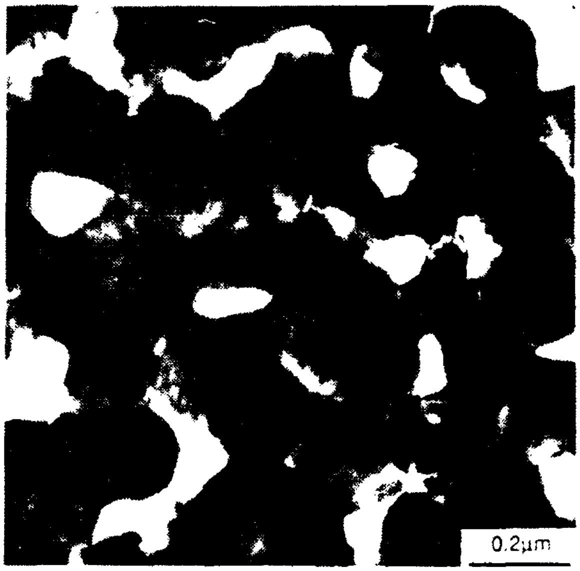

Fig. 6. Planar-view TEM photograph of a film prepared from a precursor with A:W=1:0 composition and annealed at 700°C.

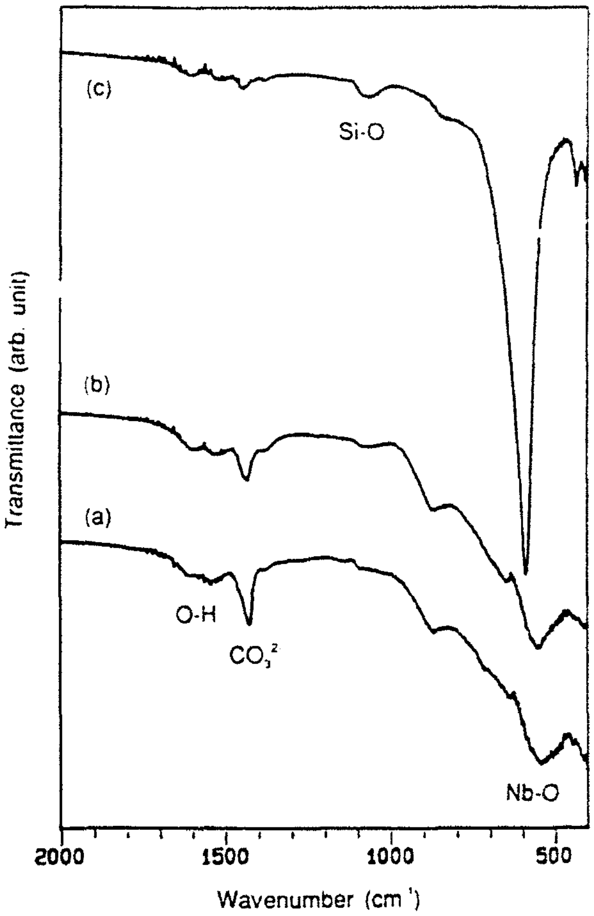

Fig. 7. FTIR spectra of films derived from a precursor with A:W=1:1 composition on a Si (100) substrate and annealed at (a) 300°C, (b) 400°C, and (c) 500°C.

C-O bond of CO$_3^{-2}$ at 1428 cm^{-1} and an O-H band around 1600 cm^{-1}. The origin of this carbonate contamination is the thermal decomposition of the residual alkoxy radical. The carbonate band's intensity decreased upon heating to 400°C. With annealing at 500°C, the Nb-O band shifted to higher frequency and became very intense, indicating the formation of crystalline LiNbO$_3$. There was almost no C-O band observed for CO$_3^{-2}$ at this temperature. The AES depth profile of the film prepared from the A:W=1:1 composition precursor and annealed at 400°C is shown in Figure 8. The distribution of Li, Nb, and O over the depth of the film was uniform. Residual carbon content was barely above background, as also concluded by FTIR.

Figure 9 shows change in refractive index of the films formed on sapphire (110) substrates as a function of annealing temperature. Of the three types of films, the epitaxial films prepared from the precursor with A:W=1:0 composition showed the highest refractive indices at almost all annealing temperatures. The refractive indices of the polycrystalline films prepared from the precursor with A:W=1:3 composition increased with increasing annealing temperature, as reported by Hagberg et al. [28] for the LiNbO$_3$ films with preferred orientation. However, the films prepared from the precursors with A:W=1:1 and A:W=1:0 composition showed complicated changes in refractive indices. Their refractive indices increased between 300°C and 400°C, decreased between 400°C and 500°C, were stable between 500°C and 600°C, and increased between 600°C and 700°C. This behavior may result from competition between physical and chemical structural changes in the films during annealing. Densification will promote an increase in the indices of the films, whereas a decrease in residual carbon in the films, as observed by FTIR and AES, may reduce the refractive indices of the films. The polycrystalline film prepared from A:W=1:3 composition precursor showed the only consistent increase in refractive index with increasing annealing temperature. It was also found to contain the least carbon contamination, as will be described in a future paper [29]. The refractive index and thickness of the films prepared from the precursors with A:W=1:3 and A:W=1:1 composition and annealed at 700°C could not be obtained because the scattering of the laser light was too strong to perform ellipsometric measurement. These were the only films that were not transparent, as can be seen from the SEM photograph in Figure 5a. The films

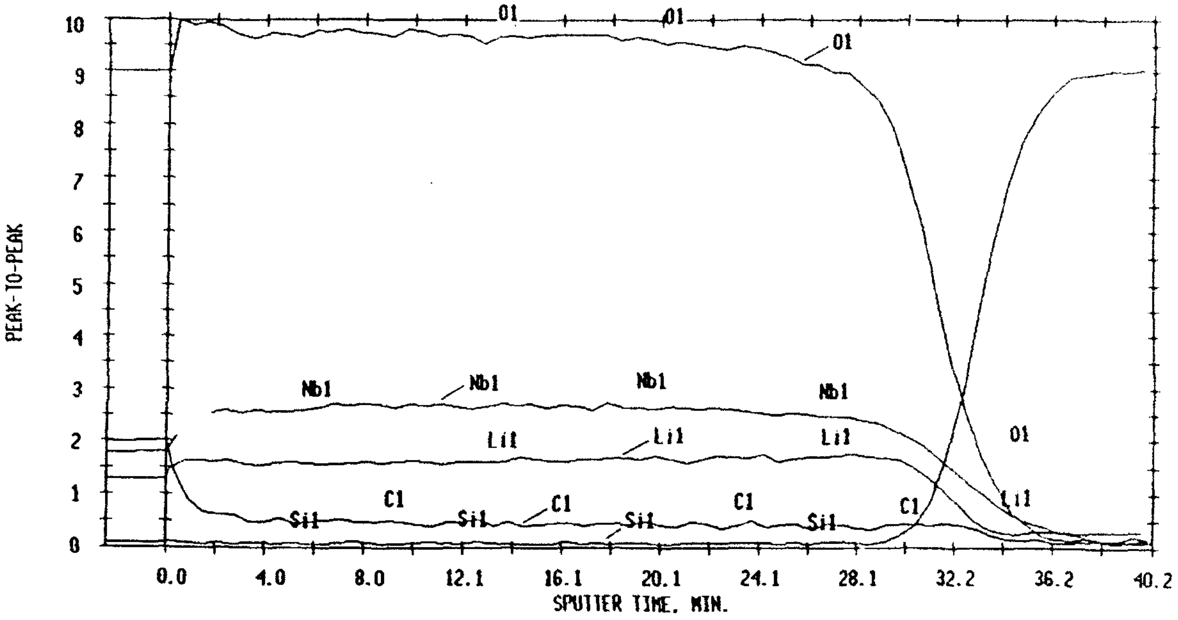

Fig. 8. AES depth profile of a film prepared on a Si (100) substrate from an A:W=1:1 composition precursor and annealed at 400°C.

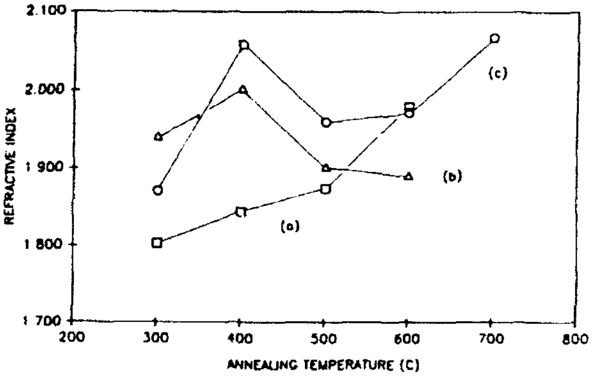

Fig. 9. Change in refractive index of films on sapphire (110) substrates prepared from (a) A:W=1:3, (b) A:W=1:1, and (c) A:W=1:0 composition precursors as a function of annealing temperature.

prepared from these precursors had grain growth comparable in size to the wavelength of He-Ne laser light and also developed very porous structure with annealing at 700°C.

CONCLUSIONS

Thin films were formed by spin coating precursor solutions prepared from lithium ethoxide and niobium pentaethoxide onto substrates. Polycrystalline films were obtained from prehydrolyzed precursors on sapphire substrates. Films prepared from all precursors on silicon substrates were polycrystalline, although films prepared from prehydrolyzed precursors showed lower crystallization temperatures than did those prepared from non-hydrolyzed precursors. Epitaxial films were obtained on sapphire substrates with (110) or (001) orientation from non-hydrolyzed precursors. The films looked dense and smooth after annealing at 400°C, although the films contained porosity of 10 nm in diameter. The polycrystalline films and the films with preferred orientation developed grain growth and porous structure at 700°C, making ellipsometric measurement impossible. The epitaxial films showed relatively dense structure and high refractive indices compared with the polycrystalline or films with preferred orientation.

ACKNOWLEDGMENTS

The authors would like to acknowledge the cooperation of M. Frongillo for the use of the HRTEM equipment and E. Shaw for the use of the AES equipment. This work was supported by Fuji Xerox Co., Ltd., Japan, and by the Air Force Office of Scientific Research under contract F49620-89-C-0102.

REFERENCES

1. M.M. Abouelleil and F.J. Leonberger, "Waveguides in Lithium Niobate," *J. Am. Ceram. Soc.*, **72** 1311-21 (1989).
2. J.R. Carruthers, G.E. Peterson, M. Grasso, and P.M.

Bridenbaugh, "Nonstoichiometry and Crystal Growth of Lithium Niobate," *J. Appl. Phys.*, **42** 1846-51 (1971).

3. H.M. O'Bryan, P.K. Gallagher, and C.D. Brandle, "Congruent Composition and Li-Rich Phase Boundary of $LiNbO_3$," *J. Am. Ceram. Soc.*, **68** 493-96 (1985).
4. T. Nozawa, S. Sudo, and S. Miyazawa, "Optical-Device Applications of $LiNbO_3$ Single Crystals," *Oyo Buturi*, **59** 996-1013 (1990).
5. H. Nishihara, M. Haruna, and T. Suhara, Optical Integrated Circuits. McGraw-Hill, New York, NY, 1989.
6. S. Kondo, S. Miyazawa, S. Fushimi, and K. Sugii, "Liquid-Phase-Epitaxial Growth of Single-Crystal $LiNbO_3$ Thin Film," *Appl. Phys. Lett.*, **26** 489-91 (1975).
7. S. Miyazawa, "Growth of $LiNbO_3$ Single-Crystal Film for Optical Waveguides," *Appl. Phys. Lett.*, **23** 198-200 (1973).
8. S. Fushimi and K. Sugii, "Growth of Lithium Niobate Single Crystal by Sulphur Vapour Transport Technique," *Jpn. J. Appl. Phys.*, **13** 1895-96 (1974).
9. S. Takada, M. Ohnishi, H. Hayakawa, and N. Mikoshiba, "Optical Waveguides of Single-Crystal $LiNbO_3$ Film Deposited by RF Sputtering," *Appl. Phys. Lett.*, **24** 490-92 (1974).
10. R.A. Betts and C.W. Pitt, "Growth of Thin-Film Lithium Niobate by Molecular Beam Epitaxy," *Electron. Lett.*, **21** 960-62 (1985).
11. H. Matsunaga, H. Ohno, Y. Okamoto, and Y. Nakajima, "Heteroepitaxial Growth of $LiNbO_3$ Single Crystal Films by Ion Plating Method," *J. Cryst. Growth*, **99** 630-33 (1990).
12. D.J. Eichorst and D.A. Payne, "Sol-Gel Processing of Lithium Niobate Thin-Layers on Silicon"; pp. 773-78 in Better Ceramics Through Chemistry III, Mat. Res. Soc. Symp. Proc., Vol. 121. Edited by C.J. Brinker, D.E. Clark, and D.R. Ulrich. Materials Research Society, Pittsburgh, PA, 1988.
13. M.I. Yanovskaya, E.P. Turevskaya, A.P. Leonov, S.A. Ivanov, N.V. Kolganova, S.Yu. Stefanovich, N.Ya. Turova, and Yu.N. Venevtsev, "Formation of $LiNbO_3$ Powders and Thin Films by Hydrolysis of Metal Alkoxides," *J. Mater. Sci.*, **23** 395-99 (1988).
14. S. Hirano and K. Kato, "Preparation of Crystalline $LiNbO_3$ Films with Preferred Orientation by Hydrolysis of Metal Alkoxides," *Adv. Ceram. Mater.*, **3** 503-06 (1988).
15. S. Hirano, K. Kikuta, and K. Kato, "Processing of Stoichiometric and Ti Doped $LiNbO_3$ Films with Preferred Orientation from Metal Alkoxides"; pp. 3-11 in Ferroelectric Thin Films, Mat. Res. Soc. Symp. Proc., Vol. 200. Edited by E.R. Myers and A.I. Kingon. Materials Research Society, Pittsburgh, PA, 1990.
16. D.J. Eichorst and D.A. Payne, "Grain-Oriented Lithium Thin Layers by Sol-Gel Methods"; pp. 19-23 in Ferroelectric Thin Films, Mat. Res. Soc. Symp. Proc., Vol. 200. Edited by E.R. Myers and A.I. Kingon. Materials Research Society, Pittsburgh, PA, 1990.
17. D.P. Partlow and J. Greggi, "Properties and Microstructure of Thin $LiNbO_3$ Films Prepared by a Sol-Gel Process," *J. Mater. Res.*, **2** 595-605 (1987).
18. J. Fukushima, K. Kodaira, and T. Matsushita, "Preparation of $BaTiO_3$ Films by Hydrolysis of Organometallic Compounds," *Am. Ceram. Soc. Bull.*, **55** 1064-65 (1976).
19. K.D. Budd, S.K. Dey, and D.A. Payne, "Sol-Gel Processing of $PbTiO_3$, $PbZrO_3$, PZT, and PLZT Thin Films," *Brit. Ceram. Soc. Proc.*, **36** 107-21 (1985).
20. T. Suzuki, M. Matsuki, Y. Matsuda, K. Kobayasi, and Y. Takahasi, "Preparation and Properties of PZT Thin Films by Metal Alkoxides-DEA Method," *J. Ceram. Soc. Jpn.*, **98** 754-58 (1990).
21. H.M. Quek and M.F. Yan, "Sol-Gel Preparation and Dielectric Properties of Lead Iron Niobate Thin Films," *Ferroelectrics*, **74** 95-108 (1987).
22. K. Nashimoto and M.J. Cima, "Epitaxial $LiNbO_3$ Thin Films Prepared by a Sol-Gel Process," *Mater. Lett.*, **10** 348-54 (1991).
23. K. Nashimoto, M.J. Cima, and W.E. Rhine, "Microstructural Evolution of Epitaxial $LiNbO_3$ Thin Films Derived From Metal Alkoxide Solutions"; pp. 439-44 in Evolution of Thin Films and Surface Microstructure, Mat. Res. Soc. Symp. Proc., Vol. 202. Edited by C.V. Thompson, J.Y. Tsao, and D.J. Srolovitz. Materials Research Society, Pittsburgh, PA, 1991.
24. S. Hirano and K. Kato, "Synthesis of $LiNbO_3$ by Hydrolysis of Metal Alkoxides," *Adv. Ceram.*

Mater., **2** 142-45 (1987).

25. D.J. Eichorst, K.E. Howard, and D.A. Payne, "NMR Investigation of Lithium Niobium Alkoxide Solutions," in Proceedings of the Fourth International Conference on Ultrastructure Processing of Glasses and Composites. Edited by D.R. Uhlmann, M.C. Weinberg, S.H. Risbud, and D.R. Ulrich. John Wiley & Sons, New York, NY, in press.

26. D.J. Eichorst, D.A. Payne, S.R. Wilson, and K.E. Howard, "Crystal Structure of $LiNb(OCH_2CH_3)_6$; A Precursor for Lithium Niobate Ceramics," *Inorg. Chem.*, **29** 1458-59 (1990).

27. K. Nashimoto, M.J. Cima, and W.E. Rhine, in preparation.

28. D.S. Hagberg, D.J. Eichorst and D.A. Payne, "Electrical and Optical Properties of Alkoxide-Derived Lithium Niobate Thin Layers"; pp. 466-473 in Sol-Gel Optics, SPIE, Bellingham, WA, 1990

29. K. Nashimoto, M.J. Cima, and W.E. Rhine, in preparation.

MICROSTRUCTURAL EVOLUTION OF EPITAXIAL $LiNbO_3$ THIN FILMS DERIVED FROM METAL ALKOXIDE SOLUTIONS

Keiichi Nashimoto, M.J. Cima, and W.E. Rhine

K. Nashimoto, M.J. Cima, and W.E. Rhine, "Microstructural Evolution of Epitaxial $LiNbO_3$ Thin Films Derived from Metal Alkoxide Solutions"; pp. 439-44 in Evolution of Thin-Film and Surface Microstructure, Mat. Res. Soc. Symp. Proc., Vol. 202. Edited by C.V. Thompson, J.Y. Tsao, and D.J. Srolovitz. Materials Research Society, Pittsburgh, PA, 1991.

ABSTRACT

The evolution of the microstructure of sol-gel derived $LiNbO_3$ thin films was investigated to understand the growth of epitaxial films. $LiNbO_3$ films were prepared from a precursor solution of lithium ethoxide and niobium pentaethoxide. Prehydrolysis promoted the development of polycrystalline $LiNbO_3$ films, whereas nonhydrolysis produced solid-state epitaxial growth of $LiNbO_3$ films on sapphire substrates. Although the films looked smooth after annealing at 400°C, the morphology of the films changed, depending on substrates and precursors, due to grain growth at high annealing temperature. Prehydrolysis of the alkoxides caused a decrease in the temperature at which grain growth occurred, whereas the film prepared from the nonhydrolyzed precursor on a sapphire substrate showed denser texture and contained abnormally large domains that appeared to be single phase.

INTRODUCTION

Ferroelectric materials are of great interest for piezoelectric and electro-optic applications. Among these materials, lithium niobate is a leading electro-optical material for active waveguides, modulators, and switches. In order to prepare $LiNbO_3$ thin films for integrated electro-optic devices, a variety of epitaxial thin film formation techniques have been used [1-5], none of which, however, controls the chemical composition of $LiNbO_3$. For optical waveguide applications, the combination of $LiNbO_3$ with a material of lower refractive index, such as sapphire, is necessary. Therefore, sapphire substrates are usually used for epitaxial growth of $LiNbO_3$, since the lattice mismatching between $LiNbO_3$ and sapphire is relatively small.

Preparing ferroelectric films by a sol-gel process allows for precise composition control, low temperature processing, and preparation of large area films by spin coating or dipping a substrate with a precursor derived from organometallic substances. For these reasons, a number of polycrystalline films have been prepared by a sol-gel process: $BaTiO_3$ [6], $PbTiO_3$ [7], PZT [7, 8], PLZT [7], and $LiNbO_3$ [9] films. In addition, the feasibility of epitaxial growth by the sol-gel process was demonstrated by Partlow and Greggi when they observed homoepitaxial growth on $LiNbO_3$ [10]. Several studies of chemically derived highly oriented thin films such as $PbTiO_3$ [11], $Li_2B_4O_7$ [12], and $LiNbO_3$ [13], in addition to homoepitaxial ZrO_2-Y_2O_3 films [14], were also reported. Recently, we obtained heteroepitaxial $LiNbO_3$ films on sapphire substrates by a sol-gel process with a non-prehydrolyzed metal alkoxide precursor [15]. It was observed that this prehydrolysis favored the development of a random microstructure. In the present study, the evolution of the microstructure of the films was investigated in order to understand the solid state epitaxial growth process of $LiNbO_3$ thin films prepared by a sol-gel method.

EXPERIMENTAL PROCEDURE

Precursors for lithium niobate were prepared from lithium ethoxide (99.9%) and niobium pentaethoxide (99.999%) in a dry nitrogen atmosphere. Equal molar amounts of each alkoxide were dissolved in absolute ethanol to form a 0.05 M solution. The solution was then stirred and refluxed at 78.5°C for 24 h to prepare the double alkoxide, $LiNb(OC_2H_5)_6$. A measured amount of 2.5 vol% water in ethanol was added slowly to the solu-

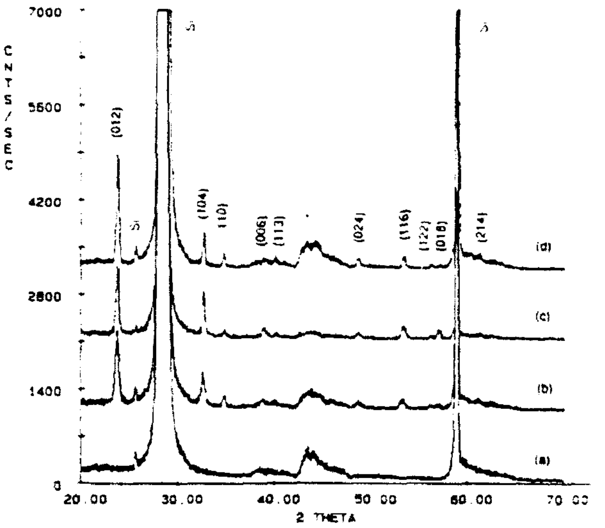

Fig. 1. X-ray diffraction patterns of films on Si (111) substrates prepared from A:W=1:0 composition precursors and annealed at (a) 400°C, (b) 500°C, (c) 600°C, and (d) 700°C.

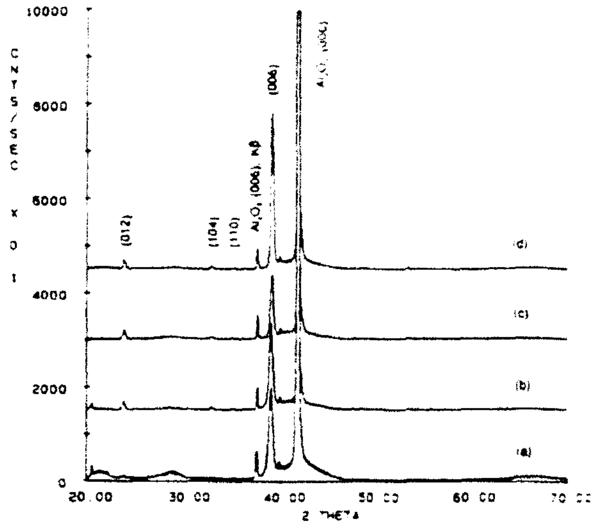

Fig. 2. X-ray diffraction patterns of films on sapphire (001) substrates prepared from A:W=1:1 composition precursor and annealed at (a) 400°C, (b) 500°C, (c) 600°C, and (d) 700°C.

tions to total 1.0 mol water per mole of double alkoxide: A:W=1:1 composition, a partially hydrolyzed precursor. The solution was stirred and refluxed for an additional 24 h at 78.5°C. The other solution included no added water: A:W=1:0 composition, a nonhydrolyzed precursor. These solutions were concentrated to 0.5 M at room temperature by vacuum distillation.

In a dry nitrogen environment, the precursors were spin coated onto 15 x 15 mm optically polished sapphire substrates with (110) or (001) orientation and silicon substrates with (111) orientation at 2000 rpm and then dried for 30 min at room temperature. Prior to coating, the sapphire substrates were cleaned in an acetone ultrasonic bath, an aqueous 20 vol% HCl solution, and deionized water. Also, the Si substrates were cleaned in the acetone ultrasonic bath and deionized water prior to coating. The cleaned substrates were oven dried at 120°C. The coated substrates were heated in moist oxygen at a rate of 10°C/min to a specified temperature, held there for 60 min, and then held there for another 30 min after switching the atmosphere from moist to dry oxygen.

The crystallization of the prepared films was examined by X-ray powder diffraction (XRD) using a Rigaku RU300 with CuK_α radiation. X-ray pole figures were generated (Rigaku RU200), using the Schulz reflection method, to observe the epitaxial relationship between films and substrates. The microstructure of the films was observed using scanning electron microscopy (SEM) (Hitachi S-530).

RESULTS AND DISCUSSION

Figure 1 shows XRD patterns of films prepared from the precursor with A:W=1:0 composition on Si (111) substrates. In this study, silicon substrates were not etched before spin coating. Therefore, the above substrates were assumed to be amorphous, since silicon substrates have a native amorphous silicon oxide layer on the surface of the silicon. These films crystallized between 400°C and 450°C and consisted of a single phase, hexagonal material identical to crystalline $LiNbO_3$ powder. No microstructural texture was indicated by XRD.

The films derived from the precursor with A:W=1:1 composition on sapphire (001) substrates crystallized between 350°C and 400°C, as shown in Figure 2. These films showed (006) preferred orientation. The intensity of the (006) reflection decreased from 400°C to 600°C and increased from 600°C to 700°C. The relative intensity of the (006) reflection remained about the same, although the relative intensity of the (110) reflection of the film prepared from the corresponding precursor on a sapphire (110) substrate decreased with increasing annealing temperature, as reported previously [15].

For the pole figure measurements, the off-diagonal (012) plane was used since it shows the strongest intensity in powder diffraction. A pole figure for the (012) plane of $LiNbO_3$ will show six spots at 57.2° off-normal to the (006) plane with a symmetric 60° rotation angle when the $LiNbO_3$ film is c-axis oriented single crystal. The 2θ

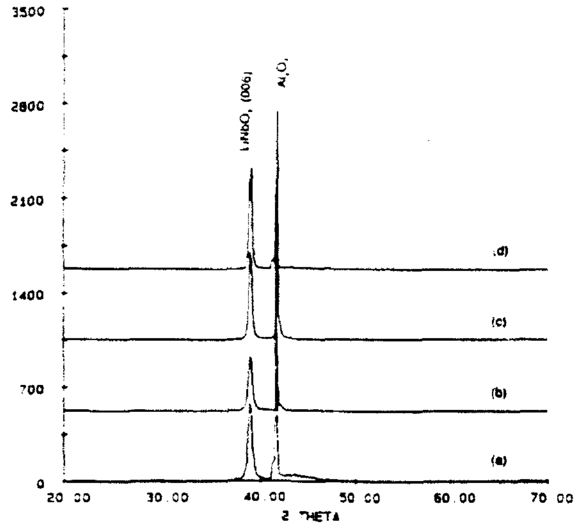

Fig. 3. X-ray diffraction patterns of films on sapphire (001) substrates prepared from A:W=1:0 composition precursor and annealed at (a) 400°C, (b) 500°C, (c) 600°C, and (d) 700°C.

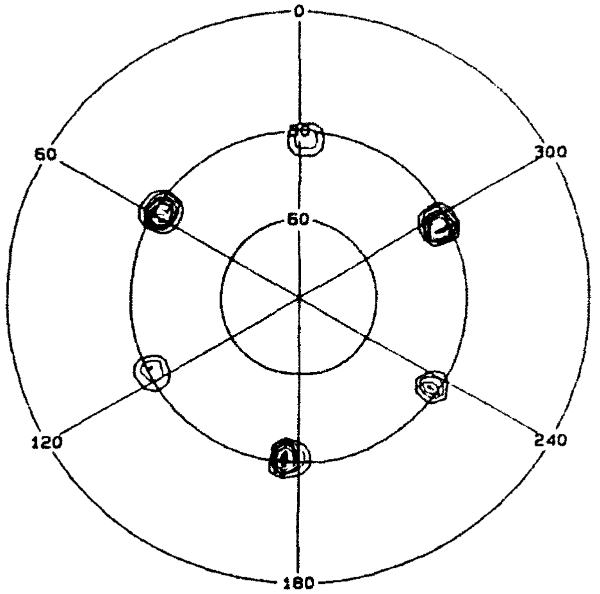

Fig. 4. X-ray diffraction pole figure for the (012) plane of the film prepared from the A:W-1:0 composition precursor on a sapphire (001) substrate and annealed at 700°C.

angle of $LiNbO_3$ (012) is 23.7°, and that of hexagonal Al_2O_3 is 25.6°, according to JCPDS data at CuK_α = 1.541838 Å. These 2θ values were well separated for pole figure measurement; none of the 2θ values overlapped. The (012) plane pole figure of the film derived from the above precursor and annealed at 700°C contained six intense spots approximately 57.2° off-normal to the film surface with weak spots around the center of the pole figure. The pole figure of the film annealed at 400°C had almost the same pole figure pattern with a slight increase in the area of (012) reflection around the center of the pole figure. Therefore, the films prepared on sapphire (001) substrates seemed to show no crystallographic change with increasing annealing temperature. However, the diffraction spot at the center of pole figure increased in intensity at 700°C, indicating the degree of random texture increased over that at 400°C when the film with (110) preferred orientation was prepared from the precursor with A:W=1:1 composition on sapphire (110) substrates. This behavior may result from surface-energy-driven grain growth [16]. That is, the grains which have lower surface energy than the grains with (110) plane surface grow preferentially. Therefore, epitaxial growth of a $LiNbO_3$ film on a sapphire (110) substrate may occur less easily than on a sapphire (001) substrate because of the difference in surface energies. The (001) plane of the film on the sapphire (001) substrate and the (110) plane of the film on the sapphire (110) substrate were epitaxial to the sapphire substrate, as indicated by the spots having the same rotation angle as the (012) diffraction spots of the substrate.

The films derived from the precursor with A:W=1:0 composition on sapphire (001) substrates crystallized between 350°C and 400°C and showed a single intense (006) reflection, as shown in Figure 3. The intensity of the (006) reflection decreased from 400°C to 500°C and increased from 500°C to 700°C. The film on a sapphire (110) substrate also showed a single reflection in the (110) plane of $LiNbO_3$ and demonstrated the same tendency for variation in intensity of the (110) reflection with temperature as the film on sapphire (001).

The pole figure for the (012) plane of the film derived from the corresponding precursor, prepared on a sapphire (001) substrate, and annealed at 700°C contained only six intense spots approximately 57.2° off-normal to the film surface, as shown in Figure 4. These spots had the same rotation angle as the (012) diffraction spots of the substrate. XRD and pole figure results indicate these films are epitaxial to the sapphire substrates, and this in turn shows that the crystallization of films on sapphire seems to be enhanced by the presence of the epitaxial substrates.

Figure 5 shows an SEM image of a film prepared on a sapphire (110) substrate from the A:W=1:0 composition precursor solution and annealed at 400°C. After annealing at 400°C, the films from both precursors looked smooth, with a thickness of approximately 110 nm, re-

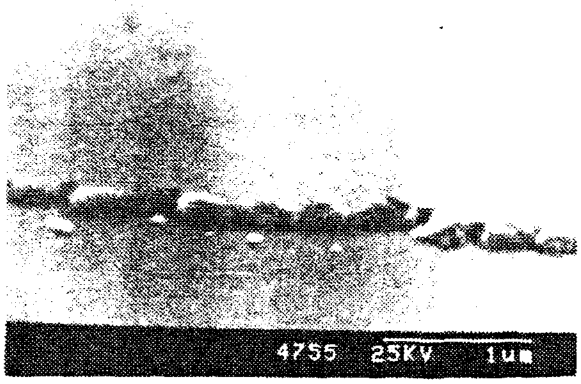

Fig. 5. Scanning electron micrograph of a film prepared from a precursor with A:W=1:0 composition on a sapphire (110) substrate and annealed at 400°C.

gardless of the substrate used. The films derived from the A:W=1:1 composition precursor began to exhibit obvious grain growth at 500°C. The film derived from the non-hydrolyzed precursor with A:W=1:0 composition began to show grain growth at 600°C, although XRD shows this film still maintains epitaxy as described before.

At 700°C, the film prepared from the precursor with A:W=1:1 composition on a sapphire (001) substrate showed a porous structure consisting of grains of about 200 nm in diameter, as shown in Figure 6a. In contrast, as shown in Figure 6b, the film prepared from the precursor with A:W=1:0 composition on a sapphire (001) substrate and annealed at 700°C was smoother than the films prepared from the precursor with A:W=1:1 composition and contained abnormally large areas (diameter > 1 μm) that appeared to be single grain. Also, the size of these areas in the film with the (001) plane was larger than that of the film with (110) plane. Thermal grooving undoubtedly contributes to the lack of surface smoothness when the films are heat treated at high temperatures. This implies that films prepared from precursors with A:W=1:0 composition have larger grains. Films prepared on silicon (111) substrates, however, have the smoothest surface, as shown in Figure 7. One possibility is that surface-energy-driven mass transport, which causes thermal grooving, is modified by contamination from the silicon substrate.

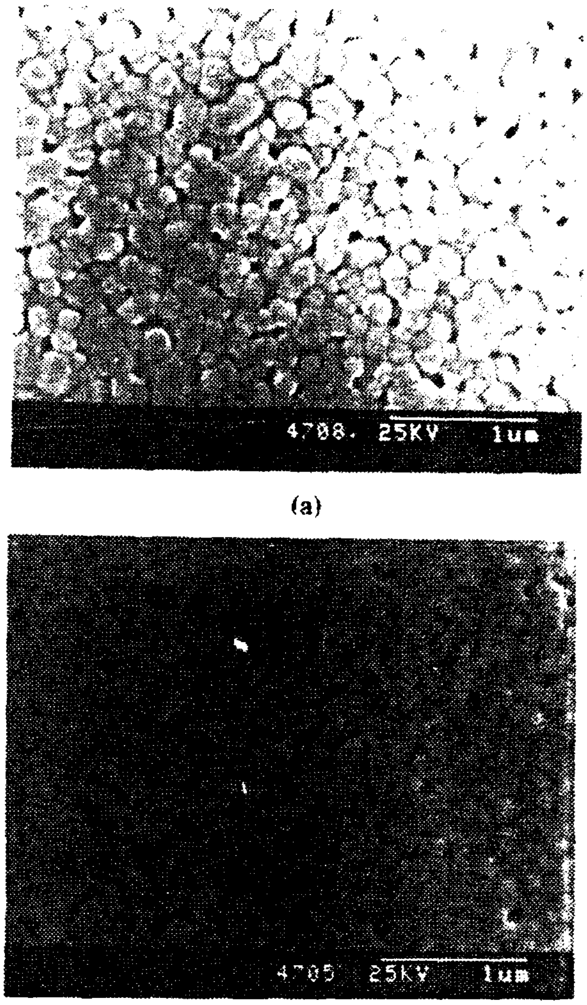

(a)

(b)

Fig. 6. Scanning electron micrographs of films prepared from precursors with (a) A:W=1:1 composition and (b) A:W=1:0 composition on sapphire (001) substrates and annealed at 700°C.

CONCLUSIONS

The relationship between films' microstructural evolution and their preparation conditions was investigated for the purpose of understanding the growth of epitaxial $LiNbO_3$ thin films prepared by a sol-gel method. The $LiNbO_3$ films were prepared from a precursor solution of lithium ethoxide and niobium pentaethoxide. Prehydrolysis of this solution caused the development of thin films with random microstructure on sapphire substrates. Non-prehydrolysis caused epitaxial growth of $LiNbO_3$ films on sapphire substrates. The films crystallized and looked smooth after annealing at 400°C and showed a different grain size and density, depending on the substrates used, when they were observed after annealing at 700°C. Prehydrolysis of the alkoxides caused a decrease

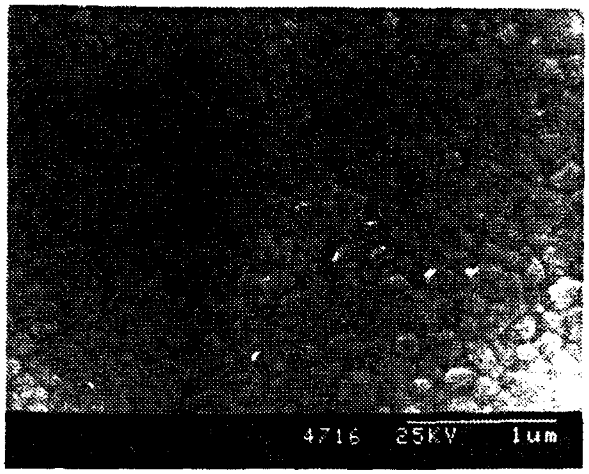

Fig. 7. Scanning electron micrograph of a film prepared from a precursor with A:W=1:1 composition on a silicon (111) substrate and annealed at 700°C.

in the temperature at which grain growth occurred. After annealing at 700°C, the films showed different grain sizes and smoothness, depending on the substrates used. However, the films prepared from the nonhydrolyzed precursor on sapphire substrates contained abnormally large areas that appeared to be single grain.

ACKNOWLEDGMENTS

The authors wish to thank the Air Force Office of Scientific Research for partial support of this work, under contract no. F49620-89-C-0102.

REFERENCES

1. S. Kondo, S. Miyazawa, S. Fushimi, and K. Sugii, "Liquid-Phase-Epitaxial Growth on Single-Crystal LiNbO$_3$ Thin Film," *Appl. Phys. Lett.*, **26**, 489-91 (1975).
2. S. Miyazawa, "Growth of LiNbO$_3$ Single-Crystal Film for Optical Waveguides," *Appl. Phys. Lett.*, **23**, 198-200 (1973).
3. S. Fushimi and K. Sugii, "Growth of Lithium Niobate Single Crystal by Sulphur Vapour Transport Technique," *Jap. J. Appl. Phys.*, **13**, 1895-96 (1974).
4. S. Takada, M. Ohnishi, H. Hayakawa, and N. Mikoshiba, "Optical Waveguides of Single-Crystal LiNbO$_3$ Film Deposited by RF Sputtering," *Appl. Phys. Lett.*, **24**, 490-92 (1974).
5. R.A. Betts and C.W. Pitt, "Growth of Thin-Film Lithium Niobate by Molecular Beam Epitaxy," *Electron. Lett.*, **21**, 960-62 (1985).
6. J. Fukushima, K. Kodaira, and T. Matsushita, "Preparation of BaTiO$_3$ Films by Hydrolysis of Organometallic Compounds," *Am. Ceram. Soc. Bull.*, **55**, 1064-65 (1976).
7. K.D. Budd, S.K. Dey, and D.A. Payne, "Sol-Gel Processing of PbTiO$_3$, PbZrO$_3$, PZT, and PLZT Thin Films," *Brit. Ceram. Soc. Proc.*, **36**, 107-21 (1985).
8. S.K. Dey, K.D. Budd, and D.A. Payne, "Thin-Film Ferroelectrics of PZT by Sol-Gel Processing," *IEEE Trans. Ultrason. Ferroelect. Freq. Contr.* **35**, 80-81 (1988).
9. D.J. Eichorst and D.A. Payne, "Sol-Gel Processing of Lithium Niobate Thin-Layers on Silicon"; pp. 773-78 in Better Ceramics Through Chemistry III, Mat. Res. Soc. Symp. Proc., Vol. 121. Edited by C.J. Brinker, D.E. Clark, and D.R. Ulrich. Materials Research Society, Pittsburgh, PA, 1988.
10. D.P. Partlow and J. Greggi, "Properties and Microstructure of Thin LiNbO$_3$ Films Prepared by a Sol-Gel Process," *J. Mat. Res.*, **2**, 595-605 (1987).
11. C. Chen, D.F. Ryder, Jr., and W.A. Spurgeon, "Synthesis and Microstructure of Highly Oriented Lead Titanate Thin Films Prepared by a Sol-Gel Method," *J. Am. Ceram. Soc.*, **72**, 1495-98 (1989).
12. H. Yamashita, T. Yoko, and S. Sakka, "Preparation of Highly Oriented Li$_2$B$_4$O$_7$ Films by Sol-Gel Method," *J. Ceram. Soc. Jpn.*, **98**, 913-16 (1990).
13. S. Hirano and K. Kato, "Preparation of Crystalline LiNbO$_3$ Films with Preferred Orientation by Hydrolysis of Metal Alkoxides," *Adv. Ceram. Mat.*, **3**, 503-06 (1988).
14. K.T. Miller and F.F. Lange, "Single Crystal Zirconia Thin Films from Liquid Precursors"; pp. 191-97 in Processing Science of Advanced Ceramics, Mat. Res. Soc. Symp. Proc., Vol. 155. Edited by I.A. Aksay, G.L. McVay, and D.R. Ulrich. Materials Research Society, Pittsburgh, PA, 1989.
15. K. Nashimoto and M.J. Cima, "Epitaxial LiNbO$_3$ Thin Films Prepared by a Sol-Gel Process," Mater. Lett., 10 [7,8] 348-54 (1991).
16. C.V. Thompson and H.I. Smith, "Surface-Energy-Driven Secondary Grain Growth in Ultrathin (<100 nm) Films of Silicon," *Appl. Phys. Lett.*, **44**, 603-05 (1984).

SECTION 18

MICROSTRUCTURE OF SOL-GEL DERIVED EPITAXIAL $LiNbO_3$ THIN FILMS OBSERVED BY TRANSMISSION ELECTRON MICROSCOPY

Keiichi Nashimoto*, Michael J. Cima, Paul C. McIntyre, and Wendell E. Rhine

Ceramics Processing Research Laboratory
Massachusetts Institute of Technology
Cambridge, MA 02139

ABSTRACT

The microstructure of epitaxial $LiNbO_3$ thin films prepared on sapphire from lithium ethoxide and niobium pentaethoxide precursor solutions was investigated using SEM and HRTEM. Films of about 100 nm nominal thickness were prepared by spin coating a solution of the alkoxides on sapphire (001) substrates and annealing at 400°C or 700°C. The film annealed at 400°C exhibited single-crystal nature with a coherent $LiNbO_3$-sapphire interface and an epitaxial relationship with the substrate. The subgrains were misorientated a few degrees, and numerous pores of about 10 nm in diameter were observed in these films. After annealing at 700 °C, the film contained larger subgrains and pores. The subgrains were about 150-200 nm in diameter. Differences in orientations between subgrains were much smaller than those observed in the film annealed at 400 °C.

INTRODUCTION

Lithium niobate has been actively investigated for electro-optic and surface acoustic wave applications. The applications include active optical waveguides, optical modulators, optical switches, and SAW devices because of the material's large non-linear optical coefficients, a large birefringence, a high electro-optic coefficient, a high Curie point, a strong piezoelectric effect, and excellent acousto-optic properties [1]. For electro-optic applications, single crystal $LiNbO_3$ is employed as the substrate for fabricating optical waveguides. However, fabrication of single crystal lithium niobate devices is complicated by the following issues: 1) stoichiometric lithium niobate melts incongruently; therefore, single crystals are grown from a non-stoichiometric congruent melt with 48.45 mol% Li_2O composition which can lead to crystals with variable composition; 2) the properties of $LiNbO_3$, such as the Curie point and refractive indices, are very sensitive to fluctuations in its stoichiometry; and 3) fabricating optical waveguides by the usual titanium in-diffusion method requires high temperatures (over 1000°C). Therefore, there is a need for methods which can control the stoichiometry and provide low temperature processing of lithium niobate thin films in order to produce integrated electro-optic devices.

Since the properties of $LiNbO_3$ films depend on the crystallographic orientation, heteroepitaxial growth techniques are important. The combination of $LiNbO_3$ with a material of lower refractive index can create an effective optical waveguide. For these reasons, a number of epitaxial growth methods have been reported; liquid phase epitaxy [2], epitaxial growth by melting [3], chemical vapor deposition [4], rf sputtering [4, 5], molecular beam epitaxy [6], and ion-plating [7]. However, controlling the chemical composition of $LiNbO_3$ by these methods is difficult, and they require relatively high substrate temperatures ranging from 500°C to 1250°C.

The preparation of thin films by sol-gel processing is an attractive method since this wet chemical process allows for precise composition control, low temperature processing, and preparation of large area films by simply coating a substrate with a precursor derived from organometallic compounds. A large number of polycrystalline films have been prepared by the sol-gel process: $BaTiO_3$ [14, 15], $PbTiO_3$ [16], PZT [16, 17], PLZT [16], and $Pb(Fe_{1/2}Nb_{1/2})O_3$ [18], and several studies of chemically derived highly oriented or homoepitaxial thin films such as $PbTiO_3$ [19], ZrO_2-Y_2O_3 [20], $Li_2B_4O_7$ [21] have also been reported. There are many reports about the preparation of $LiNbO_3$

polycrystalline films [8, 9], oriented films [10, 11, 12], and homoepitaxial films [13]. The potential of growing epitaxial $LiNbO_3$ films by the sol-gel process was demonstrated by Partlow and Greggi when they observed homoepitaxial growth [13]. Then, Hirano et. al. reported preparation of $LiNbO_3$ films with preferred orientation on sapphire substrates [10, 11], and we obtained heteroepitaxial $LiNbO_3$ films on sapphire substrates by a sol-gel process using a metal alkoxide precursor [22, 23]. In the present study, the microstructure of the epitaxial $LiNbO_3$ films prepared by a sol-gel method was characterized using high resolution transmission electron microscopy to understand the unique single-crystal nature of the films.

EXPERIMENTAL PROCEDURE

As described in our previous papers [22, 23], precursors for lithium niobate were prepared from lithium ethoxide (99.9%) and niobium pentaethoxide (99.999%) in a glove box containing a dry nitrogen atmosphere. Equal molar amounts of each alkoxide were dissolved in absolute ethanol to obtain a 0.5 M solution. The solution was then stirred and refluxed at 78.5°C for 24 h. This process has been reported to form the double alkoxide, $LiNb(OC_2H_5)_6$ [24]. The double alkoxide has also been reported to form instantaneously at room temperature [25].

Prior to coating the substrates, they were cleaned in an acetone ultrasonic bath, an aqueous 20 vol% HCl solution, and deionized water. The cleaned substrates were oven-dried at 120°C. In a dry nitrogen environment, the precursors were spin coated at 2000 rpm onto 15 x 15 mm optically polished sapphire substrates with (001) orientation and dried for 30 min at room temperature. The coated substrates were heated in moist oxygen at a rate of 10°C/min to a 400 or 700 °C and held there for 60 min. The gas was switched to dry oxygen and then held there for another 30 min. The moist oxygen was obtained by bubbling the oxygen through deionized water held at room temperature prior to introducing it into the furnace. This process was assumed to hydrolyze the alkoxide film during the heat treatments and produced ~130 nm thick films.

The films' microstructures were examined using scanning electron microscopy (SEM, Hitachi S-530) and high resolution transmission electron microscopy (HRTEM, EM002B). Plan and cross-sectional view specimens for HRTEM observation was prepared by using the polisher described by Bennedict et. al. [26]. Samples for plan view electron miroscopy were scribed to approximately 3 mm squares and reduced to about 10 μm thick by grinding and polishing. Samples for cross-sectional observation were scribed along the (110) plane, and two pieces of sample were glued together with film sides face to face. After the glue was cured the samples were reduced to about 10 μm thick by grinding and polishing. Final thinning was accomplished by ion-milling in a GATAN dual ion mill. The plan view samples were thinned from the sapphire substrate side. Initial ion-milling was performed at 6.0 kV with incident angle of 18° and was followed by final ion-milling at 4.0 kV to minimize damage to the samples.

RESULT AND DISCUSSION

Our previous studies on using a sol-gel synthesis approach [22, 23] to prepare $LiNbO_3$ films indicated that the films are amorphous prior to nucleation and growth of crystalline $LiNbO_3$. A carbonaceous intermediate formed during the heat treatment of all the films investigated in these previous studies. The same intermediates were observed in films derived from precursors solutions that were hydrolyzed before spin-on deposition. X-ray diffraction experiments indicated that films prepared on (110) sapphire single crystals from prehydrolyzed double alkoxides were polycrystalline [22]. These results indicated that prehydrolysis of the double alkoxide solution encouraged nucleation of $LiNbO_3$ crystallites that lacked epitaxial registry with the underlying substrate.

Similar results have been reported by several authors. Joshi *et al.* [30] found that sol-gel derived $LiNbO_3$ films became increasingly porous and inhomogeneous with increasing precursor prehydrolysis. Amini and Sacks [31] reported hydrolysis of the sol-gel precursor weakened crystallization of $KNbO_3$, and Chen *et al.* [19] reported loss of crystallographic orientation with increasing solution prehydrolysis in $PbTiO_3$ thin films on MgO single crystal substrates. This behavior is likely caused by the change in structure of the green (as-spun) film that occurs as a function of alkoxide prehydrolysis. Sol particles present in the prehydrolyzed solutions may act as preferred sites for nucleation of $LiNbO_3$ during the subsequent heat treatment. These nucleation sites within the film compete with nucleation sites on the substrate surface, resulting in the formation of polycrystalline films. However, films derived from non-prehydrolyzed alkoxide precursors were epitaxial, with only (110) reflections detected in XRD powder scans and pole figures [22]. The $LiNbO_3$ thin films derived from non-prehydrolyzed precursors evidently nucleate at the film-substrate interface, and therefore, heteroepitaxial growth occurs on the lattice-matched substrate.

In this effort, films were prepared by spin-coating solutions of the Li-Nb double alkoxide and hydrolyzing the alkoxide *in situ* by using a moist oxygen atmosphere. Figure 1 shows an SEM photomicrograph of the epitaxial $LiNbO_3$ film

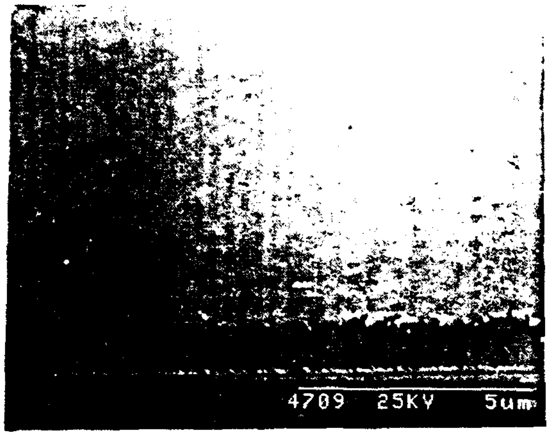

Fig. 1. SEM photomicrograph of epitaxial $LiNbO_3$ film prepared on sapphire (001) substrates grown by annealing at 400°C.

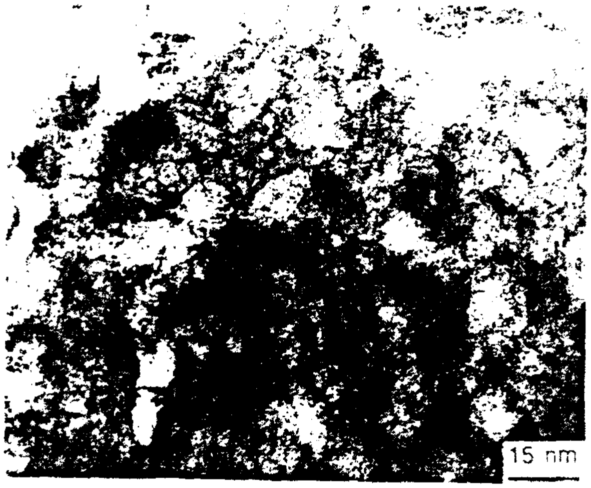

Fig. 2. Plan view TEM photomicrograph of the [001] oriented film annealed at 400°C.

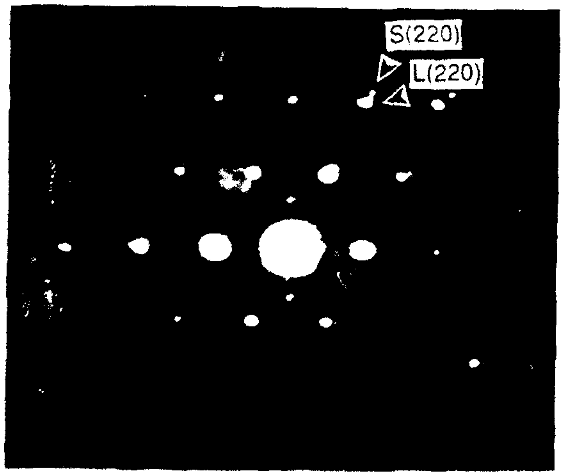

Fig. 3. Electron diffraction pattern of the film. The $LiNbO_3$ pattern is superimposed over the pattern of the sapphire substrate.

prepared on sapphire (001) substrates after annealing at 400°C. In the SEM, the films appeared dense with a very smooth surface. However, when observed in the TEM, the films appeared to have a micro porous spherulitic structure as shown in Figure 2. The pores were approximately 10 nm in diameter and the subgrains were approximately 1-5 nm in diameter. This kind of porous microstructure is usually observed in sol-gel derived films as reported by Partlow et. al. [13] and Hsueh et. al. [27]. The presence of porosity was also reported for sputtered films obtained by Hsueh et. al. [27] and Goral et. al. [28].

Figure 3 shows the electron diffraction pattern obtained from a thicker region of the film. The $LiNbO_3$ pattern is superimposed over that of the

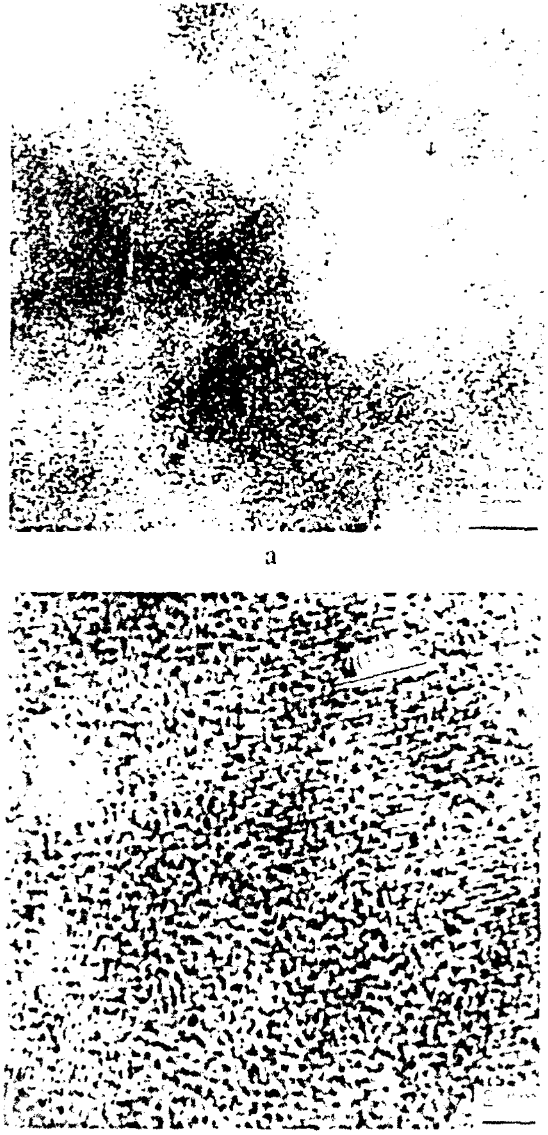
a

b

Fig. 4. (a) HRTEM plan view of the [001] oriented film and (b) HRTEM photomicrograph at higher magnification of the arrowed area in Figure 4 (a) (arrow in Figure 4 (b) shows subgrain boundary).

underlying sapphire substrate. The diffraction pattern shows the expected symmetrical hexagonal pattern for an epitaxial film. The diffraction spots originating from the $LiNbO_3$ film and the weak spots originating from sapphire substrate have the same rotation angle indicating an epitaxial relationship between the film and the substrate. Lattice mismatching along the a-axis obtained from the electron diffraction pattern was 8.1% and that calculated using the reported lattice parameters obtained from single crystals, 5.149Å for $LiNbO_3$ and 4.758Å Al_2O_3 [5], was 8.2 %. These values were in good agreement, suggesting the existence of misfit dislocations in the interface between the film and the substrate.

Figure 4 (a) shows the HRTEM plan view of the (001) oriented film shown in Figure 2. The (110) plane lattices are visible over the photomicrograph regardless of the existence of pores, and all of the subgrains have the same orientation as expected from the electron diffraction pattern. This result indicates the film is eptiaxial. The HRTEM photo-micrograph at higher magnification of the arrowed area in Figure 4 (a) is shown in Figure 4 (b). The arrow in Figure 4 (b) shows a subgrain boundary. At the boundary, the (110) lattice fringes are misoriented by a few degrees.

Figure 5 (a) shows cross-sectional HRTEM image of a (001) oriented film observed along [120] zone axis. Both the (110) and the (113) plane lattices were visible. At the interface, the [001] axis between the $LiNbO_3$ film and the Al_2O_3 substrate the planes are tilted 2 degrees. This tilt misalignment

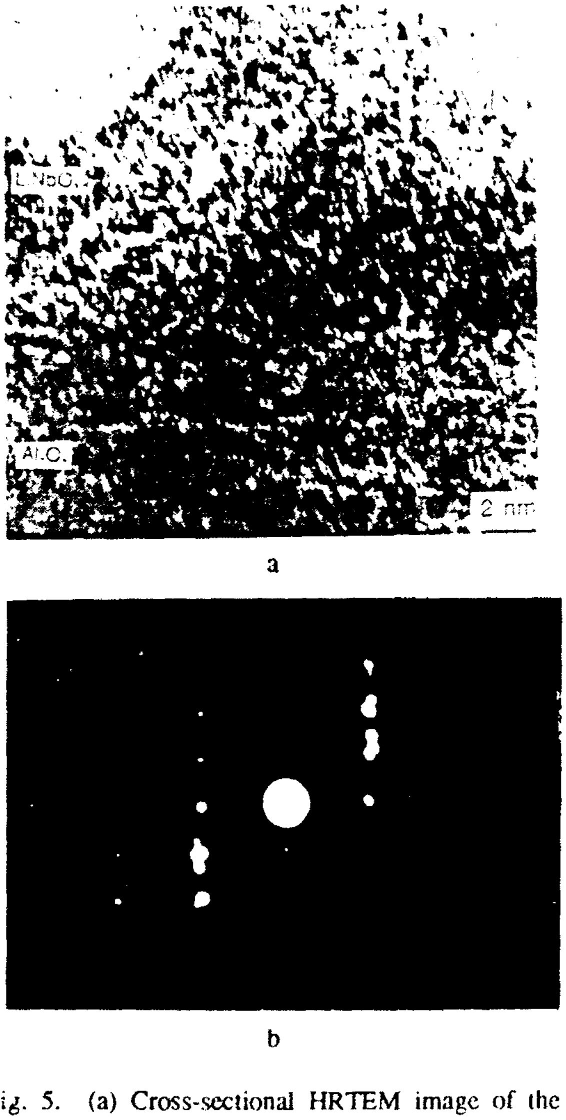

a

b

Fig. 5. (a) Cross-sectional HRTEM image of the [001] oriented film-substrate interface annealed at 400°C and (b) selected area electron diffraction pattern from the interface region (observed along [120] zone axis).

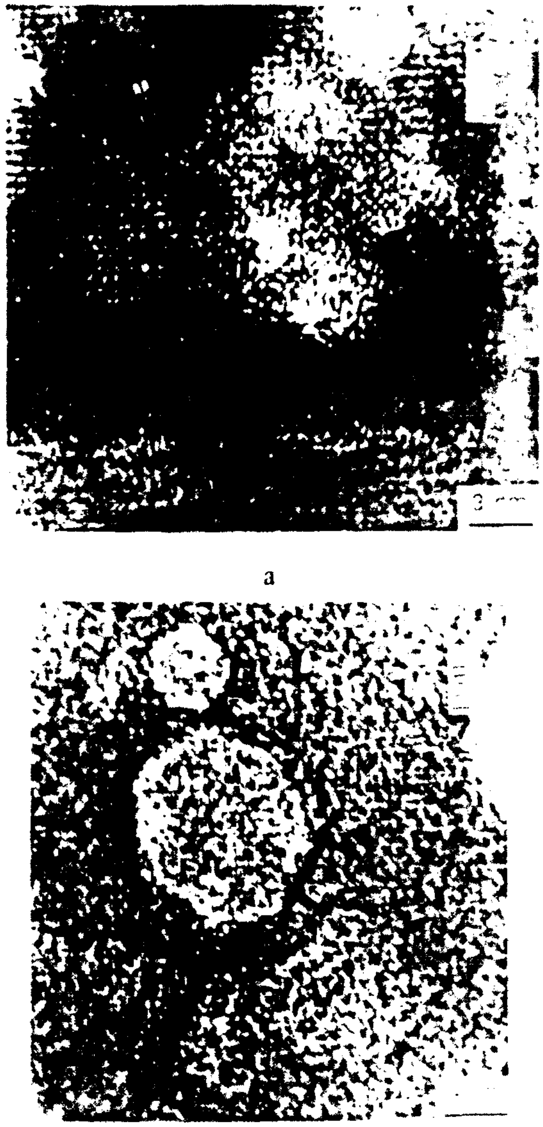

a

b

Fig. 6. (a) Crystal imperfection in the [001] oriented film annealed at 400°C and (b) step feature on the surface of pores in the film.

was probably caused by the large lattice mismatch between the film and the substrate. Misalignment between the film and the substrate was also observed in the electron diffraction pattern from the interface as shown in Figure 5 (b). These observations suggest that the lattice mismatch between the $LiNbO_3$ film and the sapphire substrate causes the misfit dislocations at the interface and the axis tilt misalignment. Such tilt misalignments occur frequently in heteroepitaxial films grown on substrates with large misfits. Improved lattice matching through tilt misalignment of epitaxial $YBa_2Cu_3O_7$ on MgO has been discussed in detail by Norton and Carter [29].

There were other crystal imperfections in the (001) oriented film annealed at 400°C as shown in Figures 6 (a). The arrowed region indicates a subgrain boundary with edge dislocations in the (001) planes resulting from the slight misorientation between adjacent subgrains. Also it is interesting to note that the pores are faceted as indicated at the arrowed areas in Figure 6(b).

The TEM results presented here for the film annealed at 400°C (Fig.'s 2-6) suggest nucleation of epitaxial $LiNbO_3$ occurs at the substrate surface, followed by rapid growth into an amorphous overlayer. The observation of small, faceted pores enclosed in the epitaxial film, suggests that the crystallization front swept through the amorphous intermediate film quickly, trapping pre-existing porosity. Alternatively, the fine porosity forms to accomodate the density difference bewteenthe amorphous precursor an the crystalline product. The porosity that is likely present in the Li-Nb amorphous hydrous oxide [13] may encourage the formation of crystallographic defects such as dislocations and low-angle grain boundaries separating regions with slightly different orientations. The epitaxial growth of these sol-gel derived oxide films may be similar to solid phase epitaxial (SPE) growth [32] of silicon fromamorphous Si films on single crystal Si substrates. In the absence of an interfacial impurity layer that inhibits epitaxial growth, such as an oxide coating on the substrate surface in the case of silicon SPE, the these $LiNbO_3$ films are expected to grow by a layer-by-layer mechanism.

Figure 7 is SEM photomicrograph of epitaxial a $LiNbO_3$ film prepared on sapphire (001) substrates after annealing at 700°C. The small, enclosed voids present at 400°C had coallesced to form larger, pinholes. Substantial growth of the subgrains within the film had also occurred. Figure 8 (a) shows a plan view TEM photomicrograph of the film. The pores were approximately 50 nm to

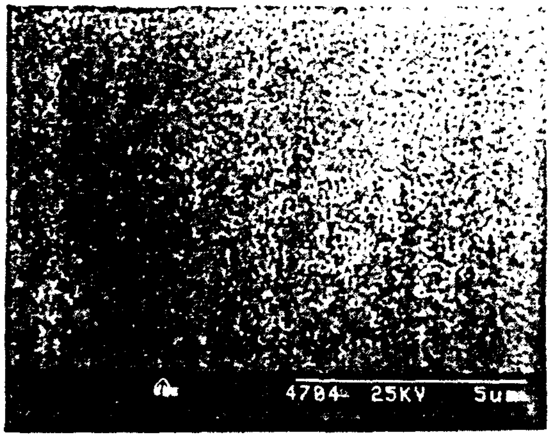

Fig. 7. SEM photomicrograph of epitaxial $LiNbO_3$ film prepared on sapphire (001) substrates grown by annealing at 700°C.

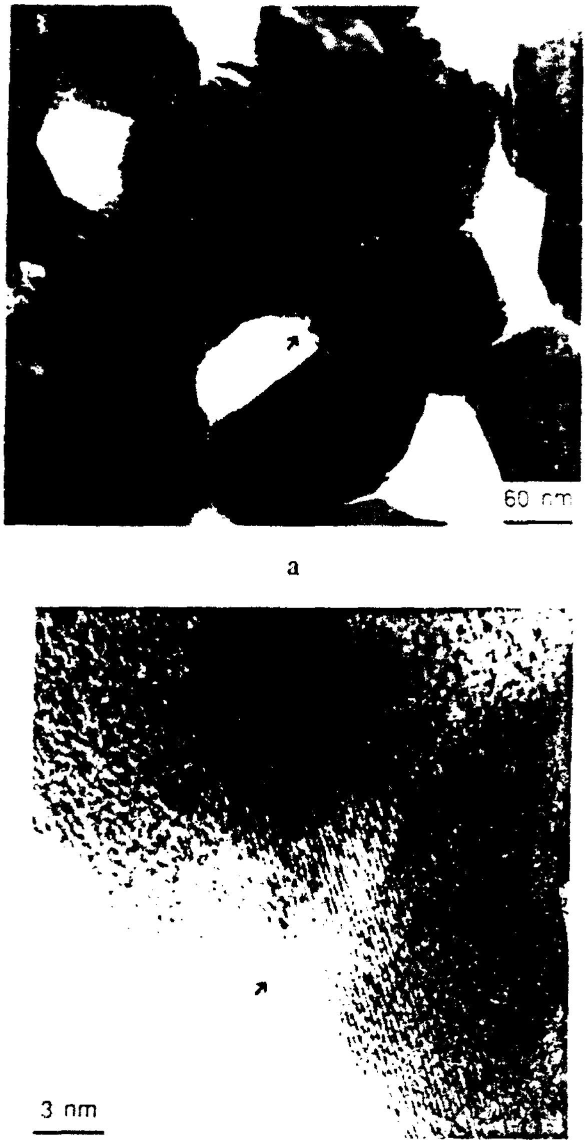

a

b

Fig. 8. (a) Plan view TEM photomicrograph of the [001] oriented film annealed at 700°C and (b) HRTEM image of the arrowed area in Figure 9 (a).

100 nm in diameter, and the subgrains were about 150 nm to 200 nm in diameter. Figure 8 (b) is a HRTEM image of arrowed area in Figure 7 (a). The (110) lattice plane is running throughout the subgrain boundary area, and the contrast at the subgrain boundary seemed to be caused by the thickness changes in the film or due to thermal grooving at the subgrain bourdary. The (110) plane changed its direction just 1 degree at this subgrain boundary. The observation that annealing at higher temperatures reduces the misorientation between adjacent subgrains implies that the grain boundary energy drives the elimination of grains that are significantly (>1°) misoriented relative to the rest of the film. Therefore, the subgrains are almost perfectly oriented, and the film may be thought of as a single crystal film in principle. In contrast, the films we prepared [22, 23] from partially hydrolyzed alkoxides were not epitaxial but did have a preferred orientation. These films when annealed at 700°C had grain sizes around 200 nm in diameter and a very porous structure [22, 23].

CONCLUSIONS

Films of about 130 nm thickness were prepared from lithium ethoxide and niobium pentaethoxide precursor solutions by spin coating the solutions on sapphire (001) substrates and annealing at 400°C or 700°C. The film annealed at 400°C was an epitaxial film according to the HRTEM image and selected area electron diffraction patterns. The subgrains were misorientated only a few degrees, and the film contained many pores about 10 nm in diameter. The film grown by annealing at 700°C had larger subgrains which were about 150-200 nm in diameter. Any misorientation between subgrains was much smaller than that observed in the film annealed at 400°C.

ACKNOWLEDGEMENT

High resolution electron microscopy was performed at MIT's CMSE electron microscopy facility. The authors would like to acknowledge the assistance of M. Frongillo in using the HRTEM. This work was supported by Fuji Xerox Co., Ltd., Japan, and by AFOSR under contract F49620-89-C-0102.

REFERENCES

1. M.M. Abouelleil and F.J. Leonberger, "Waveguides in Lithium Niobate," *J. Am. Ceram. Soc.*, **72** 1311-1321 (1989).

2. S. Kondo, S. Miyazawa, S. Fushimi, and K. Sugii, "Liquid-Phase-Epitaxial Growth of Single-Crystal $LiNbO_3$ Thin Film," *Appl. Phys. Lett.*, **26** 489-491 (1975).

3. S. Miyazawa, "Growth of $LiNbO_3$ Single-Crystal Film for Optical Waveguides," *Appl. Phys. Lett.*, **23** 198-200 (1973).

4. S. Fushimi and K. Sugii, "Growth of Lithium Niobate Single Crystal by Sulphur Vapour Transport Technique," *Japn. J. Appl. Phys.*, **13** 1895-1896 (1974).

5. S. Takada, M. Ohnishi, H. Hayakawa, and N. Mikoshiba, "Optical Waveguides of Single-Crystal $LiNbO_3$ Film Deposited by RF Sputtering," *Appl. Phys. Lett.*, **24** 490-492 (1974).

6. R.A. Betts and C.W. Pitt, "Growth of Thin-Film Lithium Niobate by Molecular Beam Epitaxy," *Electron. Lett.*, **21** 960-962 (1985).

7. H. Matsunaga, H. Ohno, Y. Okamoto and Y. Nakajima, "Heteroepitaxial Growth of $LiNbO_3$ Single Crystal Films by Ion Plating Method," *J. Cryst. Growth*, **99** 630-633 (1990).

8. D.J. Eichorst and D.A. Payne, "Sol-Gel Processing of Lithium Niobate Thin-Layers on Silicon," *Mat. Res. Soc. Symp. Proc.*, **121** 773-778 (1988).

9. M.I. Yanovskaya, E.P. Turevskaya, A.P. Leonov, S.A. Ivanov, N.V. Kolganova, S.Yu. Stefanovich, N.Ya. Turova and Yu.N. Venevtsev, "Formation of $LiNbO_3$ powders and thin films by Hydrolysis of Metal Alkoxides," *J. Mat. Sci.*, **23** 395-399 (1988).

10. S. Hirano and K. Kato, "Preparation of Crystalline $LiNbO_3$ Films with Preferred Orientation by Hydrolysis of Metal Alkoxides," *Adv. Ceram. Mat.*, **3** 503-506 (1988).

11. S. Hirano, K. Kikuta and K. Kato, "Processing of Stoichiometric and Ti Doped $LiNbO_3$ Films with Preferred Orientation from Metal Alkoxides," *Mat. Res. Soc. Symp. Proc.*, **200** 3-11 (1990).

12. D.J. Eichorst and D.A. Payne, "Grain-Oriented Lithium Thin Layers by Sol-Gel Methods," *Mat. Res. Soc. Symp. Proc.*, **200** 19-24 (1990).

13. D. P. Partlow and J. Greggi, "Properties and Microstructure of Thin $LiNbO_3$ Films Prepared by a Sol-Gel Process," *J. Mat. Res.*, **2** 595-605 (1987).

14. J. Fukushima, K. Kodaira and T. Matsushita, "Preparation of $BaTiO_3$ Films by Hydrolysis of Organometallic Compounds," *Am. Ceram. Soc.*

Bull. **55** 1064-1065 (1976)

15. T. Tuchiya, T. Kawano, T. Sei and J. Hatano, "Preparation of Ferroelectric $BaTiO_3$ Films by Sol-Gel Process and Dielectric Properties," *J. Ceram. Soc. Jpn.*, **98** 743-748 (1990).

16. K.D. Budd, S.K. Dey and D.A. Payne, "Sol-Gel Processing of $PbTiO_3$, $PbZrO_3$, PZT, and PLZT Thin Films," *Brit. Ceram. Soc. Proc.*, **36** 107-121 (1985).

17. T. Suzuki, M. Matsuki, Y. Matsuda, K. Kobayasi and Y. Takahasi, "Preparation and Properties of PZT Thin FIlms by Metal Alkoxides-DEA Method," *J. Ceram. Soc. Jpn.*, **98** 754-758 (1990).

18. H. M. Quek and M. F. Yan, "Sol-Gel Preparation and Dielectric Properties of Lead Iron Niobate Thin Films," *Ferroelectrics*, **74** 95-108 (1987).

19. C. Chen, D.F. Ryder, Jr., and W.A. Spurgeon, "Synthesis and Microstructure of Highly Oriented Lead Titanate Thin Films Prepared by a Sol-Gel Method," *J. Am. Ceram. Soc.*, **72** 1495-1498 (1989).

20. K.T. Miller and F.F. Lange, "Single Crystal Zirconia Thin Films From Liquid Precursors," *Mat. Res. Soc. Symp. Proc.*, **155** 191-197 (1989).

21. T. Yoko, H. Yamashita and S. Sakka, "Preparation of $Li_2B_4O_7$ Thin Films by Sol-Gel Method and Their Characterization,"; pp. 416-427 in Sol-Gel Optics. Edited by J.D.Mackenzie and D.R. Ulrich. SPIE, Bellingham, WA, 1990.

22. K. Nashimoto and M. J. Cima, "Epitaxial $LiNbO_3$ Thin Films Prepared by a Sol-Gel Process," *Materials Letters*, **10** 348-354 (1991).

23. K. Nashimoto, M. J. Cima, and W. E. Rhine, "Microstructural Evolution of Epitaxial $LiNbO_3$ Thin Films Derived From Metal Alkoxide Solutions," Evolution of Thin Films and Surface Microstructure, *Mat. Res. Soc. Symp. Proc.* **Vol 202**, 439 (1991).

24. S. Hirano and K. Kato, "Synthesis of $LiNbO_3$ by Hydrolysis of Metal Alkoxides," *Adv. Ceram. Mat.*, **2** 142-145 (1987).

25. D. J. Eichorst, K. E. Howard, and D. A. Payne, "NMR Investigation of Lithium Niobium Alkoxide Solutions," p 87 in *Ultrastructure Processing of Advanced Materials.*, D. R. Uhlmann and D.R Ulrich , Eds., J. Wiley & Sons, New York, 1993.

26. J. P. Bennedict, R. Anderson, S. J. Klepeis and M. Chaker," A Procedure for Cross Sectioning Specific Semiconductor Devices for Both SEM and TEM Analysis,"; pp.189-204 in Specimen Preparation for Transmission ELectron Microscopy of Materials II. Edited by R. Anderson. Materials Research Society, Pittsburgh, PA, 1990.

27. C. Hsueh and M. L. Mecartney, "TEM Analysis of Sol-Gel Derived and Sputtered PZT Thin Films,"; pp.219-224 in Ferroelectric Thin Films. Edited by E. R. Myers and A. I. Kington. Materials Research Society, Pittsburgh, PA, 1990.

28. J. P. Goral, M. Huffman and M. M. Al-Jassim, "TEM Investigation of The Ferroelectric Domain Stracture in Sputtered PZT Thin Films," pp.225-230 in Ferroelectric Thin Films. Edited byE. R. Myers and A. I. Kington. Materials Research Society, Pittsburgh, PA, 1990.

29. M.G. Norton and C.B. Carter, "Growth of $YBa_2Cu_3O_{7-\delta}$ Thin Films - Nucleation, Heteroepitaxy, and Interfaces," *Scanning Microscopy*, **6** 385-98 (1992)

30. V. Joshi, G.K. Goo, and M.L. Mecartney, "Microscopy Studies of Sol-Gel Derived Lithium Niobate," *Mater. Res. Soc. Symp. Proc.*, **249** 459-63 (1992).

31. M. Amini and M.D. Sacks, "Preparation of Single-Phase $KNbO_3$ Using Bimetallic Alkoxides," *Mater. Res. Soc. Symp. Proc.*, **180** 675-83 (1990).

32. M. von Allmen, S.S. Lau, J.W. Mayer, and W.F. Tseng, "Solid-State Epitaxial Growth of Deposited Si Films," *Appl. Phys. Let.*, **35** 280-82 (1979).

PREPARATION OF POROUS OXIDE BEADS USING POLYMERIC BEADS TO CONTROL BEAD SIZE AND SHAPE

Anne B. Hardy, Wendell E. Rhine, and H. Kent Bowen

*Published in Better Ceramics Through Chemistry IV, Mat. Res. Soc. Symp. Proc., **180**, 1009 (1990)*

ABSTRACT

A method was developed for preparing silica gels by silicon alkoxide hydrolysis using water-swellable polymers to control the shape. A variety of polymer beads with different water absorbencies and different bead sizes were used. Silica beads in a wide range of sizes were prepared from polymer beads. The final bead size was dependent on the size and water absorbency of the beads, on the extent of reaction, and on the final density. It was shown that porosity could be formed in two regions. The silica beads contained pores of 3-4 nm that were attributed to the intrinsic gel structure. In addition, when large amounts of polymer were removed, additional porosity on the scale of 20-50 nm was formed. It was also shown that surface areas varied dramatically with calcining. For beads containing only small pores, surface areas varied from 400 m^2/g to less than 0.2 m^2/g as the calcining temperature was increased from 600°C to 1000°C. Beads containing porosity formed by removal of the polymer remained porous even after calcining at 1000°C.

INTRODUCTION

In ceramics applications, control of morphology is often of critical importance. Because ceramics are solids with high melting points, many of the processing approaches used to control morphology in metals or polymers are not feasible. In this paper a method is presented for controlling the shape and porosity of silica gels using water absorbable polymers as a template for the final gel shape. Silicon alkoxide (TEOS) was reacted with water absorbed in the beads to form a silica gel within the polymer. Previous research has shown that acidic water droplets in a water-in-oil emulsion react with TEOS and that the silica gelation appears to take place in the water phase [1]. This method incorporates the processing flexibility of polymers into the preparation of ceramics. Water absorbable polymers are available in a variety of shapes. Polymer beads were used because the regular shape simplified comparison between the original polymer and the silica beads and also because silica gels in spherical bead form are desirable for some applications.

Polymer fibers and other absorbent fibers have been used to prepare oxide fibers. In a typical formulation [2], cellulosic fibers such as Rayon imbibe an aqueous salt solution. The fibers are then heated to remove the polymer and convert the salt to the oxide. The oxide retains the shape of the original fiber. In addition to cellulose derivative fibers, a variety of novel fibers have been used including carbon fibers [3, 4] and intercalated graphite fibers [5]. Typically in these techniques absorption of the oxide precursor solution is relatively low, and when the precursor is converted to the oxide and the polymer is removed, the overall oxide yield is low. By contrast, in the technique presented here, by combining highly water absorbent polymers with silicon alkoxide hydrolysis, it was possible to obtain high oxide-to-polymer yields.

EXPERIMENTAL PROCEDURE

Several water absorbing polymeric beads were used including Dowex® MSC-1 (Dow Chemical Co, Midland, MI), a series of crosslinked dextrans (Sephadex® G-25 and LH-60), and Sephasorb® (Pharmacia Biotechnology Products, Piscataway, NJ) and a superabsorbing polymer, Quat™ (supplied by Bernard Obenski and Co., Berwyn, PA). The Sephadex and Quat were preswelled in deionized water at various pHs. Hydrochloric acid was used as an acid catalyst (pH = 2-4), and either NaOH or NH_4OH was used as a base catalyst (pH = 10-12). The crosslinked dextrans were swelled for 1-3 h; the Quat was swelled for

Table 1. Some Properties of the Polymer Beads.

Polymer	Commercial Use	Physical Structure	Characteristics
Dowex MSC-1	ion exchange resin	sulfonized styrene divinylbenzene copolymer	rigid beads 300-850 μm
Sephadex Sephasorb	gel-filtration medium	crosslinked dextran	range of crosslinking particle size ranges: 10-23 μm 20-50 μm 40-120 μm
Quat	superabsorbent	quaternary ammonium compound monomer: 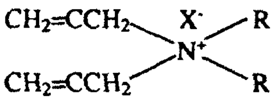	lightly crosslinked 5-100 μm (dry)

Table 2. Amount of Water Absorbed.

Polymer	Absorbency (g water/g dry polymer)
Dowex MSC-1	1.0
Sephadex LH-60	4-5
Sephadex G-25	1-2
Sephasorb	0.4
Quat	50-70

5 min. Excess water was removed by filtering and then rinsing the beads with isoamyl alcohol. The Dowex beads contained 50 wt% water as received and were used without further swelling.

The water-swelled beads were transferred to a TEOS in hexane solution (TEOS:hexane ratio was either 1:1 or 1:2 by volume). Dowex beads were reacted for 5 h; Quat beads were reacted for 6-20 h. Reaction times for the crosslinked dextrans were dependent on the catalyst concentration and ranged from 12 h to 7 days. The reacted beads were recovered by filtering and rinsing with isopropanol to remove unreacted TEOS. They were dried at room temperature overnight before being heated to remove the polymer. A standard heating schedule was as follows: samples were heated at 2°C/min to 400°C with a 2 h isothermal hold and were then heated at 5°C/min to the final temperature followed by a 2 h isothermal hold. Final temperatures ranged from 600°C to 1000°C. Bead morphology was observed by both optical microscopy and scanning electron microscopy (SEM) (Model S-530, Hitachi Ltd, Tokyo, Japan). Shrinkage of individual Quat beads after reaction was followed by optical microscopy using a hot stage attached to an optical microscope. Pore size distributions and densities were measured by mercury porosimetry (Autopore 9220, Micromeretics, Norcross, GA). Pore sizes were also measured by nitrogen adsorption (Quantasorb, Quantachrome, Syosset, NY) using 15 different nitrogen partial pressures. Surface areas were measured by the single point BET method.

RESULTS AND DISCUSSION

Preparation

Several different types of water-absorbing beads were used to provide a range of polymer types, bead sizes, and water absorbencies. Table 1 summarizes some of the physical properties of the polymers which were used. Measured absorbencies are reported in Table 2 and were found to vary by almost two orders of magnitude from the Sephasorb beads (0.4 g water/g dry polymer) to the superabsorbing Quat beads which absorbed up to 70 g water/g dry polymer.

Figures 1-4 show some of the silica beads that were formed and illustrate that it was possible to produce silica beads in a wide range of sizes by using polymer beads with different sizes. The alkoxide reaction was catalyzed by the polymer for the Dowex and Quat polymers which have acidic groups in the polymer structure. For the crosslinked dextrans, both acid- and base-catalyzed hydrolysis was successfully used. Silica yields were very dependent on the pH of the absorbed water as shown in

Figure 5. Weight losses (Table 3) ranged from~20 wt% for the Quat-derived silica beads to 70 wt% for the Dowex beads. Weight losses were attributed to the removal of polymer and unreacted water and the further conversion of unreacted hydroxyl groups and alkoxy groups to the oxide. After heating, the Dowex and crosslinked dextran products were white; the Quat products were either white or translucent. Silica to polymer ratios ranged from ~15-20 g oxide/g polymer for the Quat-derived silica to ~0.1 g oxide/g polymer for the Sephasorb-derived silica beads. Reaction times were limited because long reaction times caused beads to form hard agglomerates.

Quat-derived silica particles rapidly shrank 10-15% (linear shrinkage) while drying; the beads then shrank another 10% as they were heated. For the crosslinked dextran-derived beads, the final bead size was compared to the initial (dry polymer) bead size using SEM micrographs. The final bead size was dependent on the initial absorbency and on the extent of reaction. Ratios of the final silica bead size to the initial polymer size ranged from ~0.5 (Sephasorb) to 1.5 (Sephadex LH-60).

Presumably the reaction either began at the TEOS/water interface or some TEOS was transferred into the water phase (TEOS has a limited solubility in water [6]) where the reaction then began. Intermediate hydrolysis products were water soluble and further reacted within the water phase to form the hydrous oxide. As the reaction progressed, ethanol was produced which is preferentially soluble in the water phase [7]; the alcohol would increase the TEOS solubility in the water phase.

Bead Characteristics

Surface properties and pore sizes are important properties for many applications of silica gels (e.g. see [8, 9]).

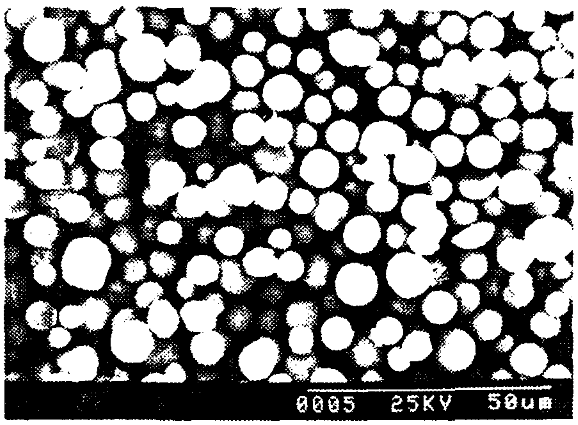

Fig. 1. Silica beads formed from Sephasorb (original bead diamater = 10-23 μm).

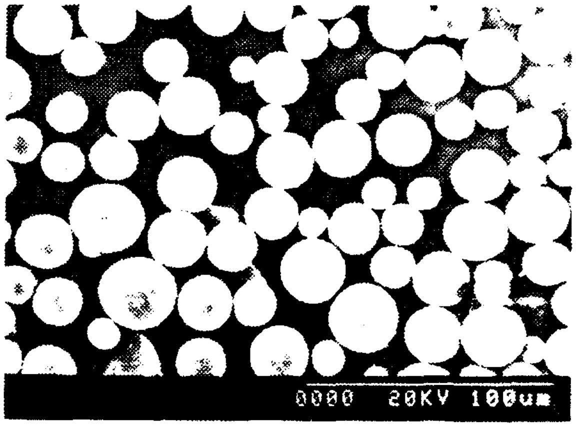

Fig. 2. Silica beads formed from Sephadex G-25 (original bead size = 25-50 μm).

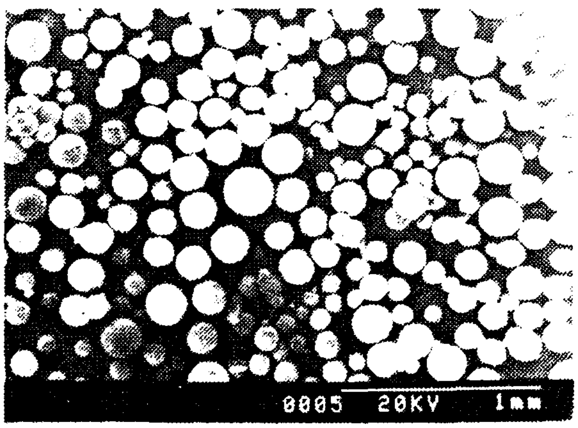

Fig. 3. Silica beads formed from superabsorbing Quat.

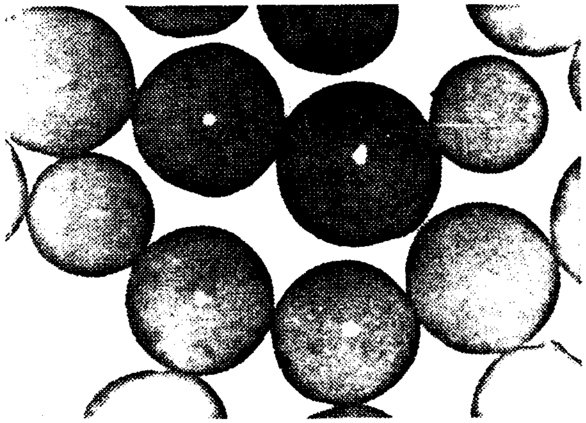

Fig. 4. Silica beads formed from Dowex MSC-1.

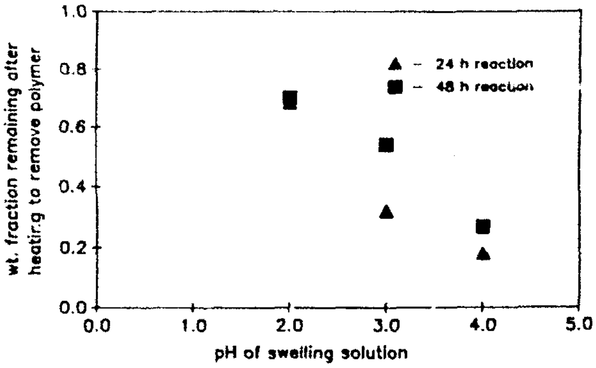

Fig. 5. Silica yield after polymer removal as a function of pH and reaction time.

The surface area and pore sizes of silica beads prepared from Dowex and from Quat were measured to investigate how the pore structure was affected by removing different amounts of polymer. Dowex beads contained relatively little water (1 g/g dry polymer) and this was reflected in the product; the oxide-to-polymer ratio was low, indicating large amounts of polymer were removed on heating. Mercury porosimetry measurements showed that before removing the polymer, the bead had essentially no measurable porosity, which was reflected in the low surface areas for unheated beads (see Table 4). After removing the polymer, pores in the range of 20 to 50 nm formed and the surface areas increased substantially. Upon further heating to 1000°C, the surface area decreased but the pore size range remained about the same (see Fig. 6). The bead density after heating to 1000°C varied but was typically 0.8-0.9 g/cm^3. SEM micrographs (Fig. 7) show that the porosity appears to take the form of interstices between discrete particles (corpuscular type porosity [8]) rather than interconnected channels.

Table 3. Weight Losses and Oxide/Polymer Ratios for Different Silica Beads.

Polymer	Weight Loss (%)	Silica/Original Polymer (g/g)
Dowex MSC-1	70	0.2
Sephasorb (pH=2, 24 h)	90	0.1
Sephadex LH-60 (pH=4, 36 h)	--	8
Quat	20-25	15-20

Table 4. Surface Areas as a Function of Calcination Temperature.

Temperature (°C)	Dowex MSC-1 Surface Area (m^2/g)	Quat Surface Area (m^2/g)
uncalcined	0.6	400-450
600	250-300	410-450
800	180-230	160-250
1000	100-130	0.14-0.15

By contrast, beads formed from the Quat polymer and the Sephadex LH-60 polymers had very high surface areas before polymer removal (Table 4). After heating to 1000°C, the surface area corresponded to essentially non-porous, smooth-surface beads which indicated most of the surface accessible porosity was removed. Mercury porosimetry measurements showed almost no measurable

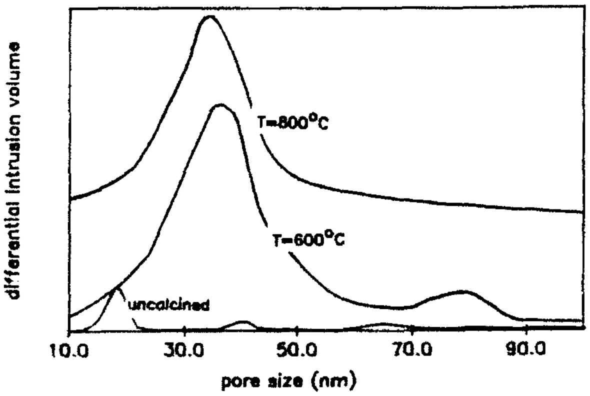

Fig. 6. Pore size for Dowex-derived silica beads as a function of calcination.

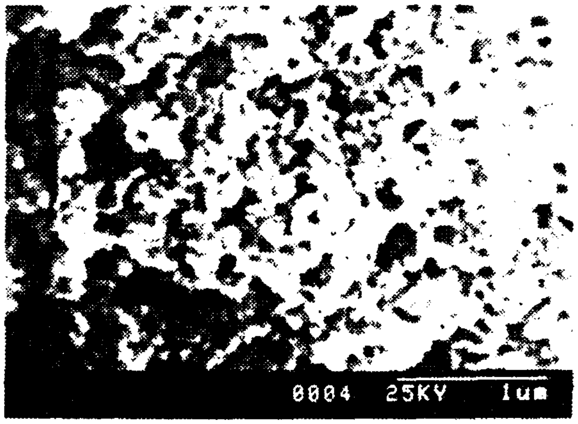

Fig. 7. Interior structure of broken silica bead (Dowex-derived).

porosity (lower measurement limit was 5 nm). Nitrogen adsorption measurements showed sharp pore size distributions around 4-5 nm which are consistent with reported pore diameters for alkoxide-derived silica gels [10].

It was assumed in the Dowex-derived silica beads that the porosity measured by mercury porosimetry was dominated by pores created by the removal of polymer. However, for the Quat-derived silica it appeared that removal of the polymer had little effect on the porosity and that the porosity was intrinsic to the silica gel. The measured pore size and surface area for the Quat and Sephadex beads were within the range of porosity reported for other alkoxide-derived silica gels.

CONCLUSIONS

It was shown that water absorbed within polymer structures could be reacted with TEOS to form silica gels and that the gel retained the shape of the polymer. Silica beads were formed in a range of sizes from 5-10 μm up to ~0.5 mm depending on the size of the initial polymer bead. The oxide to polymer ratio was dependent on the absorbency of the polymer and the extent of reaction and ranged from ~0.1 g silica/g polymer to ~20 g silica/g polymer. It was possible to form pores in two size ranges. When large amounts of polymer were removed (e.g., Dowex MSC-1), 20-50 nm pores were formed, apparently due to the removal of polymer. These beads retained significant porosity on heating to 1000°C. When little polymer was removed (e.g., Quat), the pores were ~3-4 nm and were attributed to the intrinsic gel structure. Surface porosity could be eliminated by heating to 1000°C.

ACKNOWLEDGMENTS

The authors gratefully acknowledge the support of the Air Force Office of Scientific Research, contract number F49620-89C-0102DEF.

REFERENCES

1. A.B. Hardy, "Preparation of Submicrometer, Unagglomerated Oxide Particles by Reaction of Emulsion Droplets"; PhD Thesis. Dept. Mat. Sci. Eng., MIT, September, 1988.
2. B.H. Hamling, Process for Producing Metal Oxide Fibers, Textiles and Shapes, U.S. Patent No. 3 385 915, 1968.
3. R.J. Card, "Preparation of Hollow Ceramic Fibers," *Adv. Cer. Mater.*, 3 [1] 29-31 (1986).
4. R.J. Card and M.P. O'Toole, "Solid Ceramic Fibers via Impregnation of Activated Carbon Fibers," *J. Am. Ceram. Soc.*, **73** [3] 665-68 (1990).
5. B.W. McQuillan and G. Reynolds, "Growth of Alumina Fibers from Intercalated Graphite Precursor Fibers"; pp. 739-45 in Ultrastructure Processing of Advanced Ceramics. Edited by J.D. Mackenzie and D.R. Ulrich. J. Wiley and Sons, New York, NY, 1988.
6. H. Pentinghaus, "Alkoxide Derived Gels as Starting Materials in Experimental Petrology and Solid State Chemistry," *J. Non-Cryst. Sol.*, **63** 193-99 (1984).
7. A. Seidell, Solubility of Organic Compounds, Vol. 2, 3rd ed; p. 148. D. Van Nostrand Co. Inc., New York, NY, 1941.
8. K.K. Unger, Porous Silica, Its Properties and Use as Support in Column Liquid Chromatography; p. 41. Elsevier Science Publishing Co. Inc., New York, NY, 1979.
9. R.K. Iler, The Chemistry of Silica, Solubility, Polymerization, Colloid and Surface Properties, and Biochemistry; pp. 578-99. J. Wiley and Sons, New York, NY, 1979.
10. J.D. Mackenzie, "Applications of Sol-Gel Processing"; in Ultrastructure Processing of Ceramics, Glasses, and Composites. Edited by L.L. Hench and D.R. Ulrich. J. Wiley and Sons, New York, NY, 1984.

SECTION 20

SUPERABSORBENT POLYMERS AS TEMPLATES IN FORMING OXIDE CERAMICS

Anne B. Hardy and Wendell E. Rhine

Published in Forming Science and Technology for Ceramics, Ceramic Transactions, Vol 26, 141 (1992)

ABSTRACT

Superabsorbent polymers, a class of crosslinked polymers which absorb large quantities of water, were used to control the shape of a ceramic product in a modification of the relic process. Three oxide sources were used to impregnate the polymer: alkoxide hydrolysis, metal salts, and oxide sols. The infiltrated polymer was heated to remove the polymer, and the oxide retained the shape of the polymer. Because the polymers are highly absorbent, the amount of polymer necessary to maintain the shape was significantly reduced.

INTRODUCTION

In ceramics processing, control of morphology is often of critical importance. Because ceramics are solids with high melting points, many of the processing approaches used to control morphology in metals or polymers are not feasible. One method for forming ceramic fibers [1-5] or beads [6] is the relic process, where ceramics are formed by infiltrating a polymer with a precursor and then heating it to remove the polymer and convert the precursor to the ceramic form. This method incorporates the processing flexibility of polymers into the production of ceramics. In a standard formulation [1], cellulosic fibers, such as rayon, imbibe an aqueous metal salt solution. The fibers are then heated to remove the polymer and convert the salt to the oxide. The oxide retains the shape of the original fiber. In addition to cellulose derivative fibers, a variety of novel precursor fibers have been used, including activated carbon fibers [2-4] and intercalated graphite fibers [5].

Highly absorbent polymers, called superabsorbent polymers, have been developed which are capable of absorbing upwards of 100 mL H_2O/g polymer: the absorption depends on the polymer type and on the swelling conditions. The polymers are crosslinked and retain an expanded form of the original shape on swelling. After swelling, the polymer network consists primarily of water with the small amount of polymer maintaining the shape. Because many common ceramic processes are based on aqueous systems, superabsorbing polymers appear to be good candidates for use in conjunction with aqueous-based processing to control the shape of the ceramic product. Three different methods were used: alkoxide hydrolysis, metal salt decomposition, and gelation of oxide sols. Two superabsorbing polymers were used: Quat,™ a bead-shaped polymer with diameters ranging from 5 to 100 µm (dry), and Sanwet,® a superabsorbing polymer which was supplied in the shape of ~2.8 cm high animal figures.

EXPERIMENTAL PROCEDURE

Quat™ (Bernard J. Obenski and Co., Berwyn, PA) was obtained commercially, and the following three methods were used to transform the polymeric beads into ceramic beads.

Alkoxide hydrolysis: The Quat polymer was swollen in water (pH 4) for 1 h. It was then filtered and rinsed with isoamyl alcohol to remove excess water from between the beads. The water-swollen beads were reacted for 20 h with tetraethyl orthosilicate (TEOS, Aldrich Chemical Co., Inc., Milwaukee, WI) diluted 1:1 by volume with hexanes. The beads were filtered and rinsed with isopropyl alcohol.

Metal salt decomposition: An aqueous aluminum salt solution was prepared using $Al(NO_3)_3 \cdot 9H_2O$. The pH was raised to 2.5-3 using hexamethylenetetramine. The Al concentration was 3.6 wt%. Quat polymer was swelled in an excess of $Al(NO_3)_3$ solution for >2 h. The beads were isolated by filtering and then added to a stirred NH_4OH solution. The beads were filtered, then stirred in isopropanol, and then filtered again.

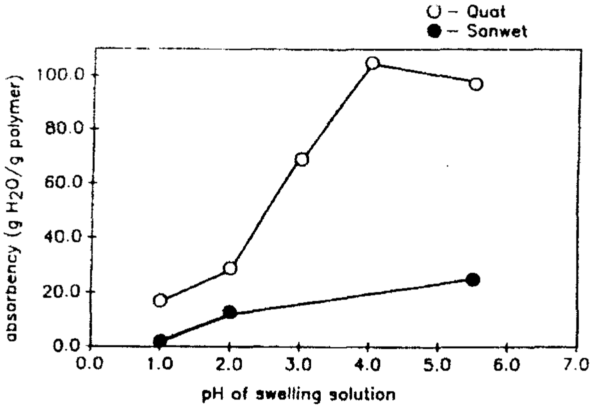

Fig. 1. Absorbency as a function of pH for Quat and Sanwet.

Sol gelation: Quat beads were swollen in three different ZrO_2 sols (Nyacol Products, Ashland, MA): ZrO_2 acetate (diameter = 5-10 nm), ZrO_2 50/20 (diameter = 50 nm) and ZrO_2 150/20 (diameter = 150 nm). The oxide concentration was 20 wt% for all three sols. The beads were left in the sol for >2 h and then separated from the sol by filtration. The ZrO_2 impregnated beads were added to isoamyl alcohol and stirred for 5-10 min. The beads were filtered and rinsed with isopropyl alcohol.

Sanwet® (Hoechst Celanese, Portsmouth, VA), a starch grafted sodium polyacrylate, was supplied as animal shapes measuring approximately 2.8 cm high. The polymer was preswollen in deionized water (>3 days) and then placed in a ZrO_2 sol for 4 days. The ZrO_2-infiltrated polymer was then either placed in NH_4OH or exposed to NH_3 (g) to gel the sol. The polymer was dried under vacuum at 60-80°C for ~10 h before heating.

Both Quat and Sanwet polymers were removed by heating the samples in air at 2°C/min to 500°C followed by heating to 850°C at 5°C/min. Bead morphology was examined using a scanning electron microscope (SEM, model S-530, Hitachi, Ltd., Tokyo, Japan). Bead density was measured with a helium pycnometer (Quantachrome, Syosett, NY). The densities of the pieces formed from Sanwet were measured by the Archimedes method.

RESULTS AND DISCUSSION

The focus of this project was to demonstrate that superabsorbing polymers could be used in conjunction with typical aqueous ceramic processing routes to control the shape of the ceramic product. Because superabsorbing polymers are much more absorbent than other preforms that have been used in the relic process, we also wanted to see if we could significantly reduce the amount of polymer needed to control the shape. Removal of large amounts of polymer is inefficient and can lower the quality of the ceramic product. Quat and Sanwet were used because they showed the effects of different polymer types with different absorbancies, and because they enabled us to change the size scale of the product by several orders of magnitude.

Figure 1 shows that for both Quat and Sanwet, absorbency clearly decreased with decreasing pH, although the polymers still absorbed significant amounts of water above pH 2. Quat was consistently more absorbent than Sanwet. Both Quat and Sanwet are ionic polymers and rely on charge repulsion between ions to aid in swelling. The presence of salts and changes in pH decrease the distance over which the ionic repulsion acts and can inhibit the polymer swelling. In addition, multivalent cations can sometimes crosslink between polymer hydroxyl groups, and this increase in crosslinking can limit the polymer absorbency.

Each of the processing methods used had constraints that determined the pH that was used. Hydrolysis of TEOS required either an acid or base catalyst. The more acidic the solution, the faster the reaction occurred. We chose a pH of 4 because the Quat was highly absorbent, and yet the reaction proceeded fast enough to give good silica yields within 20 h. Aluminum nitrate solutions were very acidic as prepared (pH < 1); however, the pH could be raised to about 4 before the solution began to gel. ZrO_2 sols rely on surface charge to prevent agglomeration of sol particles, and the sols were most stable towards agglomeration at pHs of 3-3.5.

The Sanwet polymer was not compatible with TEOS or with many common organic solvents (e.g., hexane and toluene). On being added to TEOS it often crazed or split rapidly into smaller pieces. Also, due to difficulties drying the aluminum salt solutions in the large Sanwet samples, Sanwet was used primarily with ZrO_2 sols.

Table 1 lists the ratio of the oxide product weight to the original polymer weight for the three methods. For comparison it also lists the product to polymer ratio for alumina fibers formed from rayon. The highest yields were obtained for silica beads, but even for the alumina beads the product yields per weight of polymer were greater than 400% that of the rayon. The low alumina yields compared to silica and zirconia were largely a reflection of the low aluminum concentration in the salt solution. By using superabsorbing polymers it was clearly possible to minimize the amount of polymer used.

ZrO_2 sols with different particle sizes were used to determine how the absorption was affected by particle size. For larger particle size sols (i.e., ZrO_2 50/20 and ZrO_2 150/20), essentially no ZrO_2 was incorporated into

Table 1. Summary of Oxide Properties.

Polymer	Oxide Source	Metal Ion Conc. (wt%)	g Oxide/g Polymer	Density (g/cc)	Oxide Bead Diam./ Polymer Diam.
Quat	TEOS	—	14	2.1	1.9
Quat	$Al(NO_3)_3$	3.6	1.3	3.0	.76
Quat	ZrO_2 acetate	20	6	5.3	1.1
	ZrO_2 50/20	20	<0.1	—	—
	ZrO_2 150/20	20	<0.1	—	—
Sanwet	ZrO_2 acetate	20	0.8	2.7	—
	ZrO_2 50/20	20	—	—	—
	ZrO_2 150/20	20	—	—	—

either the Quat or the Sanwet polymer. The larger sol particles were apparently too large to move through the open porosity in the swelled polymer. We also found with the large Sanwet samples that it was much more efficient to preswell the polymer in deionized water so that the polymer was fully expanded before absorbing the sol particles into the polymer.

The silica beads were translucent, and inspection of the interior of broken particles showed that even large particles were solid. Zirconia bead surfaces were cracked, and broken particles also had cracks in the particle interior. The alumina particles were less spherical in shape, probably in part because of the low oxide yield and hence the greater shrinkage on drying and heating. Representative SEM micrographs of the beads are shown in Figure 2. From these micrographs we estimated that the bead diameters after heating to 850°C ranged from approximately 10 to 300 µm. Because of the wide range in particle sizes it was difficult to estimate the overall change in diameter from polymer to oxide particle, but a ratio of the oxide particle diameter to the polymer particle diameter was calculated from the change in mass and density (we assumed the density of Quat was 1 g/cm^3). Table 1 shows that the calculated ratios of oxide diameter to polymer diameter ranged from 1.9 for silica to 0.75 for the alumina beads.

The Sanwet polymer underwent large volume changes during the process, but overall the linear shrinkage from the original polymer to the oxide form was 5-10% (see Fig. 3). After removing the polymer, the pieces were not very strong, particularly in the interior, which was often very powdery and appeared less dense than the surface. The interior of the oxide pieces always had hollow regions which were due, in part, to hollow regions in the original polymer. However, the hollow regions in the product also appeared to result from the response of the water-swollen polymer to the sol dispersion. When the preswollen polymer was placed in the sol it began to shrink (the polymer absorbency in the sol was lower than in the water in which it was preswollen). As the polymer shrank it apparently reached a point at which the open space in the polymer became too small to admit the sol particles and infiltration was effectively stopped.

CONCLUSIONS

A superabsorbing polymer was used in conjunction with alkoxide hydrolysis, salt decomposition, and gelation of oxide sols to form oxide beads. We showed that Quat, a highly absorbent polymer, could be used with a variety of techniques to significantly reduce the amount of polymer needed to control the shape compared to a traditional polymer such as rayon, and that the morphology was maintained well after heating. Sanwet was less versatile and ceramics formed from the less absorbent Sanwet tended to have hollow regions.

ACKNOWLEDGMENTS

The authors wish to thank AFOSR (Contract No. F49620-89-C-0102) for financial support.

REFERENCES

1. B.H. Hamling, U.S. patent 3,385,915, issued to Union Carbide, 1968.
2. R.J. Card, "Preparation of Hollow Ceramic Fibers," *Adv. Ceram. Mater.*, 3 [1] 29-31 (1988).
3. R.J. Card and M.P. O'Toole, "Solid Ceramic Fibers via Impregnation of Activated Carbon Fibers," *J. Am. Ceram. Soc.*, **73** [3] 665-68 (1990).
4. D.J. Waller, A. Safari, R.J. Card, and M.P. O'Toole, "Lead Zirconate Titanate Fiber/Polymer Composites Prepared by a Replication Process," *J. Am.*

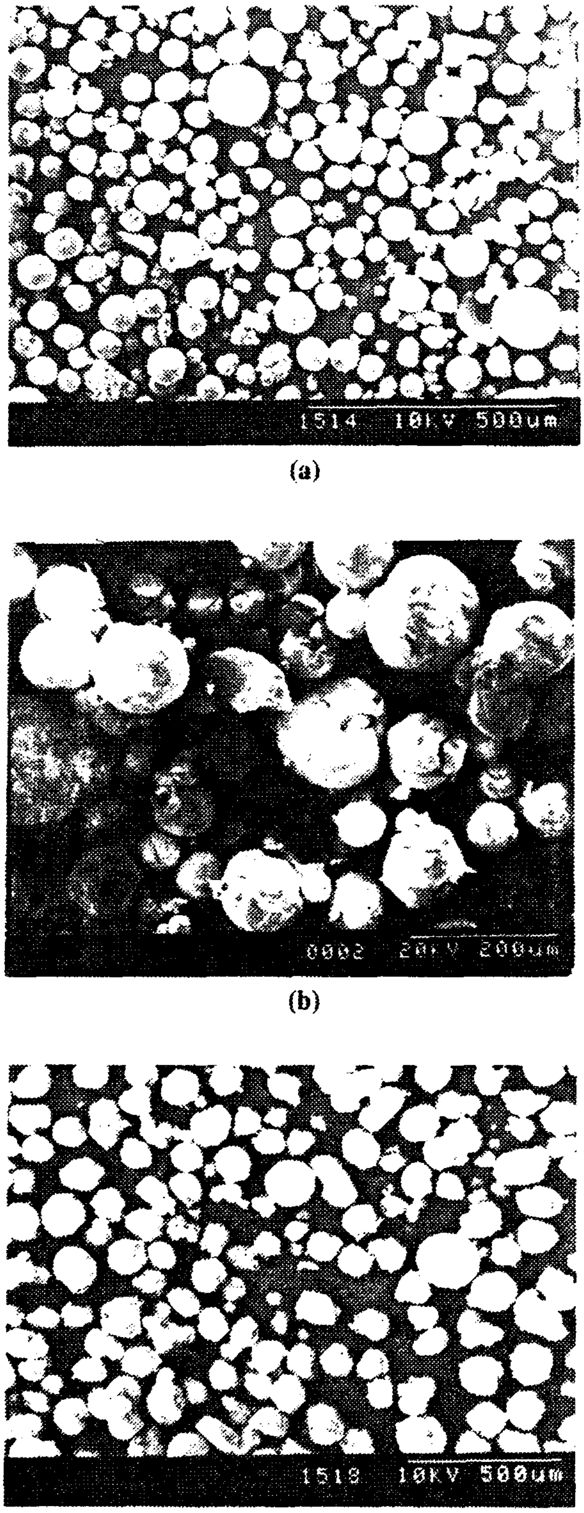

(a)

(b)

(c)

Fig. 2. Scanning electron micrographs of oxide beads after heating to 850°C: (a) SiO_2, (b) ZrO_2, and (c) Al_2O_3.

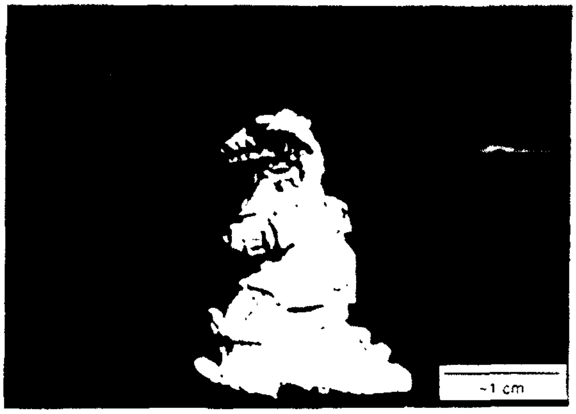

Fig. 3. ZrO_2 ceramic formed from Sanwet polymer infiltrated with ZrO_2 acetate sol (after heating to 850°C).

Ceram. Soc., **73** [11] 3503-506 (1990).

5. B.W. McQuillan and G. Reynolds, "Growth of Alumina Fibers from Intercalated Graphite Precursor Fibers"; pp. 739-45 in Ultrastructure Processing of Advanced Ceramics. Edited by J.D. Mackenzie and D.R. Ulrich. J. Wiley and Sons, New York, NY, 1988.
6. A.B. Hardy, W.E. Rhine, and H.K. Bowen, "Preparation of Porous Oxide Beads using Polymeric Beads to Control Bead Size and Shape"; pp. 1009-14 in Better Ceramics Through Chemsitry IV., Mat. Res. Soc. Symp. Proc. Vol 180. Edited by B.J.J. Zelinski, C.J. Brinker, D.E. Clark, and D.R. Ulrich. Materials Research Society, Pittsburgh, PA, 1990.

SECTION 21

A COMPARISON OF AQUEOUS AND NON-AQUEOUS SLURRIES FOR TAPE-CASTING, AND DIMENSIONAL STABILITY IN GREEN TAPES

Paul Nahass, Wendell E. Rhine, Richard L. Pober, H. Kent Bowen, and William L. Robbins*

Published in Materials and Processes in Microelectronic Systems, Ceramic Transactions, Vol 15, 355 (1990)

ABSTRACT

Aqueous and non-aqueous formulations were developed for tape casting alumina for the purpose of comparison of the resulting green sheets. The aqueous system employed an acrylic emulsion binder while the organic slurry contained the same polymer dissolved in toluene. Green tapes from both systems had similar physical properties. Samples cast from the aqueous formulation exhibited lower linear shrinkage than those from the organic system after aging for 35 days under controlled-ambient conditions. Treatments intended to improve dimensional stability had little effect on aqueous-based green sheets but yielded solvent-based samples which experienced a dimensional change of ~0.15% over 35 days and no difference in shrinkage in the tape casting direction compared to the transverse direction. Solvent-based tapes had greater linear firing shrinkage than aqueous-based samples but lower shrinkage anisotropy on firing. A treatment which involved 24-h exposure to saturated water vapor at 80°C yielded solvent-based green tapes which exhibited the lowest shrinkage and anisotropy after aging and after firing.

INTRODUCTION

Tape-cast ceramic green sheets for multilayer electronics applications are generally punched, screened, stacked, and laminated prior to firing. The punch step usually involves mechanical perforation of *vias* through each layer which are subsequently filled with conductor pastes to interconnect the circuitry between layers. Aside from exhibiting strength and flexibility sufficient for subsequent handling and processing steps, green sheets must exhibit excellent dimensional stability over time to ensure accurate interlayer registration upon lamination [1, 2]. Even slight variations from design tolerances can lead to device rejection. As ceramic components become more densely loaded with circuits, the necessity for maintaining rigid device tolerances becomes of the utmost importance.

The objective of this investigation was to develop formulations for tape-casting alumina using water-based and organic solvent-based slurries and to determine the effect of changing solvent systems on slurry processing and green tape quality. Considerations involve selection of compatible materials to effect a valid comparison and evaluation of processing steps necessary for each system. Green tape comparisons with regard to physical and mechanical properties, dimensional stability upon aging, response to stabilization treatments, and firing shrinkage behavior will be addressed.

Evaluating the effect of changing any one component of a slurry formulation requires maintaining all other components as constant as possible, keeping in mind component interactions which may change an important property such as particle packing, slurry viscosity, or polymer morphology.

MATERIALS AND PROCESS SELECTION

AKP-30 alumina powder (Sumitomo Chemical USA, New York) was chosen for use in this study. AKP-30 showed rheological and dispersion properties superior

---

* C.S. Draper Laboratory, Cambridge, MA

to those of other alumina powders evaluated, including MPA-4 (Ceralox Corporation, Tucson, AZ). AKP-30 has an average particle diameter of 0.3 µm, surface area of 6.4 m^2/g, and purity of 99.99%.

Binders from two general classes were recommended by industrial contacts for use in water-based tape-casting systems: standard water-soluble polymers and stable polymer emulsions dispersed in water. Rhoplex B-60A (Rohm and Haas, Philadelphia, PA), a proprietary emulsion formulation of acrylic polymers, yielded the toughest films with the simplest preparation. The emulsion afforded very high loadings of polymer (nearly 50 wt% solids, as received) at viscosities *2 to 3 orders of magnitude* less than similar concentrations of polymer solutions. This property is especially desirable for tape casting; low solvent content keeps drying times down and can lower the large volume reduction (as high as 70%) encountered on drying, limiting drying cracks.

A potential drawback of using an emulsion for tape casting is film formation. Onions [3] describes the general behavior of these latex films. He indicates emulsions filled with TiO_2 formed uniform films with little or no porosity if the particle concentration was lower than the *critical pigment concentration*, or CPC [4]: the morphology of the film may reflect the emulsion latex particle size. Particle size distribution of Rhoplex B-60A emulsion droplets and AKP-30 powder particles dispersed with Darvan®C (R.T. Vanderbilt, Norwalk, CT), an ammonium salt of poly(methacrylic acid), in water were measured using a Horiba CAPA 500 centrifugal analyzer. The mean diameter of the ceramic particles was ~2.5 times that of the latex, revealing the size of the defects which might be incurred above the CPC.

Chemically, little is known about Rhoplex products. Transmission Fourier transform infrared (FTIR) spectroscopy (IR-44, IBM Instruments) was performed on a dried film of B-60A. The spectrum resembled many acrylate and methacrylate polymers, especially those of poly(ethyl acrylate) and poly(methyl methacrylate). A mixture of these polymers could provide a glass transition temperature near that of B-60A (reported at about 15°C).

B-60A films were dried at 100°C for 24 h. Small amounts of these dried films did not dissolve in either ethanol or isopropanol, but readily dissolved in toluene and toluene/ethanol mixtures. Toluene/ethanol was considered acceptable as a solvent system which could dissolve the dried B-60A acrylic polymer as well as an effective water-soluble dispersant for AKP-30. Toluene alone is responsible for dissolution of B-60A solids in a toluene/ethanol system; similarly ethanol alone might be responsible for dispersant dissolution. A 50/50 mixture of toluene and ethanol (by weight) readily formed a 20 wt% polymer solution and also formed a 10 wt% solution of p-HBA (para-hydroxybenzoic acid, Aldrich Chemical, Milwaukee, WI). Therefore this mixture was chosen as the solvent system to be compared with water for casting tapes.

Darvan®C was found to give stable dispersions of AKP-30 in water with powder settling densities near 50% of theoretical after 30 days. p-HBA also yielded stable dispersions with settling densities near 50% in water; however p-HBA seemed to break down the emulsion in Rhoplex B-60A and therefore could not be used. Results for p-HBA in toluene/ethanol were not as promising, but p-HBA in pure ethanol provided adequate settling densities for comparison. The maximum density for the poorer dispersant (p-HBA) occurred at 2.0 wt% p-HBA (by weight of powder) and was 43% of the theoretical density for alumina. The same settling density was achieved using 0.8% Darvan®C in water, and hence these amounts were used in slurry formulations.

Poly(propylene glycol), or PPG (molecular weight 1200, Fluka Chemical Corp., Hauppage, NY), was used as plasticizer for both aqueous and organic systems. A solution of lecithin (capsules, CVS, Woonsocket, RI) in isopropanol was applied to tempered glass plates as a release agent for the dried green tapes. A fluorocarbon dry release was used for the solvent-based slurries (MS-136, Miller-Stephenson, Danbury, CT).

Cracking was common in many water-based tapes. Garino [5] found the principal factors responsible for cracking in ceramic slurries were binder content, surface tension, solids content, and film thickness. Since desired film thickness and binder content were fixed for this study, cracking was deterred by increasing solids content and reducing surface tension in the slurry. Slurries containing powder, dispersant, and solvent were centrifuged at 3500 rpm for >30 min to remove excess water not necessary for powder dispersion. Usually 60-70% of the water necessary for initial dispersion was decanted after centrifugation while flow properties were maintained.

Surface tensions of solvents and solvent-binder mixtures were measured to uncover slurry differences which might induce cracking in the aqueous system. A Rosano Surface Tensiometer (Biolar Corp., North Grafton, MA), which employs the Wilhelmy Plate principle of surface tension measurement, was used. Pine oil was recommended as a surfactant, by the binder manufacturer, for Rhoplex acrylic latexes for use in pigment-filled films [6]. Significant reduction in surface tension of water was achieved with small additions of pine oil to the emulsion. Additions of nearly 1 wt% pine oil (too much according to Allyn) did not reduce the surface tension of water or

Table 1. Slurry Formulations for Comparison.

Component	Organic System (g)		Aqueous System (g)	
powder	Al_2O_3, AKP-30	55	Al_2O_3, AKP-30	55
solvent	ethanol/toluene[a]	85	deionized water	15
dispersant	p-HBA	1.1	Darvan® C	0.7
binder	dried Rhoplex	10	Rhoplex B-60A	20
plasticizer	PPG-1200	4	PPG-1200	4
surfactant	none		pine oil	0.1
solids content (%)		10-15		44[b]
slurry viscosity (cp)		~5000		700
surface tension (dyne/cm^2)		29		42

[a]Equimass mixture used.

[b]40% of this was due to polymer solids in Rhoplex.

water and binder to near that of the solvent system, but 0.1 wt% seemed to eliminate cracking in tapes.

The slurry formulations used for this study are presented in Table 1. To cast a tape, release agent was applied to a glass plate and allowed to dry. Dispersant was dissolved in the appropriate solvent, which was then added to the powder and stirred until fluid. The mixture was sonicated 3-7 min (until no visibly undispersed ceramic particles remained) using a 400-W Ultrasonic Disperser with a 0.5-in probe (Harvey Scientific, Buffalo, NY) set at 40 W. More solvent was added if the rheological properties were unsuitable for sonication. The mixture was added to the binder-plasticizer mixture (often a small amount of solvent was necessary for miscibility in the aqueous system) and ball-milled for at least 4 h to intimately mix the components. This step enabled tapes with low polymer concentrations to have high strength and toughness; without milling the same slurries formed brittle, cracked tapes. Ball-milling was carried out on a roller mill in porcelain jars filled to slurry height with alumina media. The slurry was filtered through a 400-mesh stainless steel screen to remove large particles and bubbles. The solvent-based slurries often required pressure for efficient filtration. Slurry viscosity was then measured using a Model RVT Synchro-lectric viscometer (Brookfield Inc., Stoughton, MA). Slurries were cast inside a glove box: under flowing air at 23°C and 50% relative humidity (RH) for the aqueous system; in pure N_2 for the solvent system. The casting head had two blades and was driven by magnetic field along rails (Anorail-5, Anorad Corp. Hauppage, NY) at ~2 cm/s. A plastic cover was placed over the cast to slow the drying process. Polymer films were made by manually casting mixtures of solvent and all organic components onto glass.

After casting, slurries were allowed to dry at least 24 h with room conditions 23 ± 2°C and 50 ± 7% RH. Lower drying times enabled by controlled low-humidity atmospheres always caused aqueous-based tapes to crack severely on drying. Drying cracks were observed to occur parallel to the direction of the cast while cracks due to tape brittleness usually occurred normal to the casting direction. Tapes were removed from the glass plates with a wide razor blade and cut into two-inch squares, then punched by an automatic programmable punch (Model SK 5470, Schneider & Marquard, Newton, NJ, with model MD5-5 Berger-Lahr controller) with 0.25-cm measurement holes, and subjected to appropriate storage conditions or treatments. Strips of tape and polymer films ~0.5 cm x ~6 cm were cut parallel and normal to the casting direction for directional property measurements.

Punched tape samples and accompanying strips for both aqueous and organic systems (in duplicate) were subjected to one of several treatments in order to assess dimensional change on aging. Sample treatments included: (1) simple bake (2 h at 120°C in flowing air); (2) thermal cycling (-5°C for 30 min, then 120°C for 30 min, 4 times); (3) solvent exposure [7] (saturated toluene vapor for 1 h at room temperature, then *simple bake*); and (4) humidity [8] (24 h at 100% RH, 80°C, then 24 h at 80°C in flowing air). Control samples were left untreated. All samples were then stored under controlled conditions, 23 ± 2°C and 50 ± 7% RH. Positions of punched holes were measured using an optical comparator with radial viewing template at 20x magnification. Hole positions were measured after punching, immediately after treatments, periodically during aging, and after firing.

Green tapes were sintered for 30 min at 1500°C in air. A porous alumina coverplate was placed on the sample during sintering to ensure flatness of the sample while allowing organics to escape. Fired densities were measured geometrically and by the Archimedes method with t-butanol as the solvent, with some at nearly 99%. Sintering temperature and time were not optimized.

Properties of green tapes were analyzed by several techniques. Weight loss was measured by thermal gravimetric analysis (TGA) on a 7-Series Thermal Analysis System (Perkin Elmer) at a constant heating rate of 10°C/min to 500°C. Thickness was measured mechanically using an Ono Sokki measurement device. Bulk and directional green densities were measured dimensionally. Bulk porosity was calculated from green density measurements and TGA results. Surface finish was analyzed over a 1-cm profile. Glass transition temperatures of tape strips and polymer films were measured by dynamic mechanical analysis on a Rheovibron Direct Reading Dynamic Viscoelastometer (Model DDV-II, Imass, Hingham, MA) over a temperature range of -120°C to 150°C.

RESULTS

Table 2 summarizes the physical properties of green tapes. All data in this study are from individual casts of solvent- and aqueous-based slurries. Overall, physical and compositional consistency was maintained between the aqueous-based and solvent-based tapes. TGA weight loss represents the amount of organics and other components which decompose at temperatures less than 500°C. Green tape thicknesses were averaged from 50 to 75 points over the entire cast (15 x 100 cm), excluding 5 cm from the beginning and end of the cast and 1 cm from the side edges. Standard deviations of thickness were low and green densities were satisfactorily high. The low porosity indicates powder concentrations in green tapes were probably below the CPC for each system, and thus drastic morphological differences should not be present. Green tape samples did not dissolve in toluene or hexane.

Table 2. Physical Properties of Green Tapes for Comparison.

	Organic Slurry	Aqueous Slurry
TGA weight loss (%)	21.8	21.3
average thickness (µm)	239	274
average bulk density (g/cm^3)	2.43	2.46
porosity (%)	0.8	0.6

Dimensional stability results for green tapes are shown in Figure 1; estimated shrinkage error is 0.05% for all data. Untreated solvent-based samples exhibited anisotropic shrinkage on aging, with parallel shrinkage significantly greater than transverse shrinkage. During stabilization treatments, solvent-based tapes experienced up to 3% linear shrinkage, with all samples shrinking more in the casting direction. The baked samples showed significantly lower shrinkage during treatment than all other samples. After completion of treatment, all solvent-based tapes underwent significantly less shrinkage than untreated tapes and showed little or no anisotropy. Samples which underwent the bake shrunk the most after treatment and had the most anisotropy, while samples which underwent the solvent and humidity treatments had less than 0.2% linear shrinkage after 35 days.

Untreated aqueous-based green tapes shrunk less than solvent-based tapes on aging. However, all aqueous-based tapes experienced significantly less shrinkage during stabilization treatments than solvent-based sam-

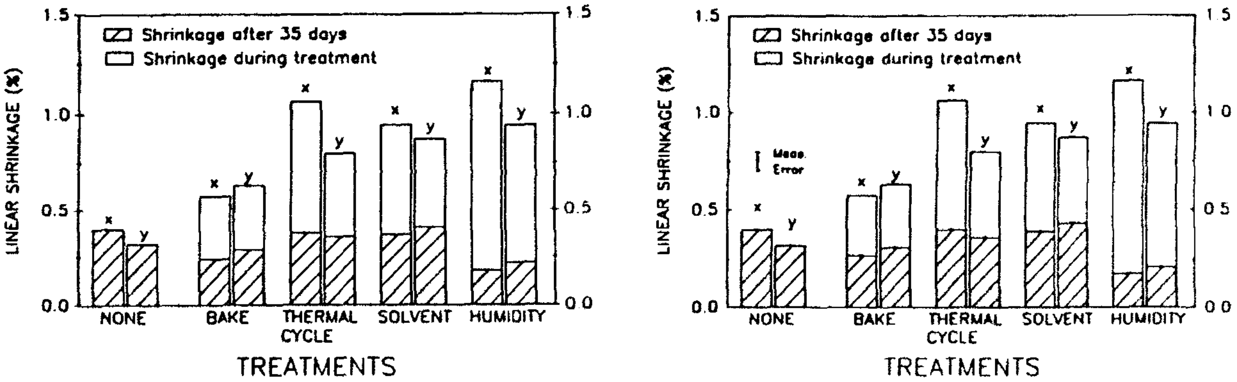

(a)

(b)

Fig. 1. Shrinkage of green tapes after treatments and after aging: (a) water-based and (b) solvent-based.

ples did. After treatment, little change was observed in the magnitude of shrinkage from that of untreated samples, though anisotropy was lowered. As in the solvent system, the humidity treatment caused the most dramatic difference in shrinkage behavior. Reproducibility was assessed by repeating the slurry preparation procedure to form a new batch of green tape. Tape samples were subjected to solvent and humidity treatments and again compared to untreated tape. All data agreed with that from the previous batch within the measurement error.

Green tapes from the two systems did exhibit some similar behavior. Samples within each slurry system showed wide variations in overall shrinkage (combining shrinkage during and after treatments) which were accompanied by corresponding green density changes. No quantitative correlation could be made, however, due to the comparatively low accuracy of density measurement capability. Sample weights did change *during* treatments, but only untreated samples experienced weight changes greater than 0.1% on aging.

Firing Behavior

Directional linear shrinkage incurred during firing of samples is given in Table 3. Each shrinkage value was averaged from two samples, with four data points per sample. Several samples from different slurry batches were fired to check reproducibility of firing shrinkage. All green tapes from the solvent-based slurry had less shrinkage anisotropy on firing, in general. Stabilization treatments performed on solvent-based green tapes reduced the magnitude of firing shrinkage noticeably and consistently except for the humidity treatment, which caused more shrinkage reduction than the other treatments and eliminated anisotropy.

Fired densities were measured for all samples by geometric methods and were consistent for all samples. Archimedes measurements gave artificially high results for all samples. The discrepancy between the results from the measuring techniques was attributed to open porosity in films, which is known to be present in ceramics below 90% of theoretical density. The same samples refired at 1600°C for 1 h sintered to between 99% and 100% of theoretical density (densities were equivalent using both measurement techniques), and therefore samples fired to 1500°C for 30 min can be considered to have been underfired.

The aqueous-based samples shrunk less than the organic, solvent-based samples, in general, and with more shrinkage anisotropy. As in the solvent-based system, treatments lowered the magnitude of firing shrinkage without altering anisotropic behavior. Samples exposed to the humidity treatment underwent the lowest firing shrinkage (as in the solvent-based system), but shrinkage anisotropy remained the same as for all other aqueous samples. Fired densities for aqueous, emulsion-based tapes were again consistent for all samples and were similar to those for solvent-based samples.

Table 3. Linear Firing Shrinkage of Green Tape Layers (%).[a]

Solvent System:	Organic		Aqueous	
Direction:	Parallel	Transverse	Parallel	Transverse
no treatment	19.0	18.7	16.5	17.0
	18.0[b]	17.8	16.5[b]	16.9
	17.6[c]	17.3		
bake	18.6	18.4	16.1	16.7
thermal cycle	18.6	18.4	16.3	16.8
solvent	18.6	18.4	16.2	16.6
humidity	17.4	17.4	15.9	16.5
	17.4[b]	17.5		
average density (% theor.)[d]	87.2		86.5	
standard deviation	0.98		0.86	

[a] All layers were aged 40 days prior to firing unless otherwise noted.

[b] Aged 70 days.

[c] Aged 100 days.

[d] Measured geometrically.

Reproducibility of firing shrinkage was investigated by firing samples which were prepared from different slurry batches. These samples had been aged longer before firing (70 or 100 days) than the two batches used for most of the data collection in this study (40 days). The magnitude of the shrinkage for untreated solvent-based samples decreased with aging time, while the x/y ratio remained constant. The magnitude of the firing shrinkage for the sample which had aged 100 days was nearly identical to that for the humidity-treated sample. The untreated, aqueous-based sample aged 70 days experienced the same shrinkage as tape from a different aqueous slurry batch which had been aged only 40 days. The solvent-based sample which underwent the humidity treatment and 70 days of aging had the same shrinkage (within measurement error) same as the humidity-treated sample which had aged only 40 days.

DISCUSSION

Every effort was made to keep systems as similar as possible in this study, in order to isolate green tape differences due to solvent and those caused by changes in binder states. Processing techniques and formulation compositions needed to be slightly altered for each system to produce samples which would be valid for comparison (see Materials and Process Selection section). While the results presented are for only one cast for each system, they reflect numerous attempts, as both systems had major processing difficulties to overcome. The solvent-based slurry, very much more volatile and irritating to process, was relatively insensitive to perturbations; it produced strong, uniform green tapes nearly every time. The aqueous slurry, without dissolved polymer, was easy and not unpleasant to process but had a smaller tolerance to minor changes in drying conditions, casting composition, or film thickness; it produced crack-free, uniform green tapes only when all variables were controlled extremely well.

The concept of aging of polymers and polymer systems is the subject of an exhaustive work by Struik [9]. Amorphous polymers experience aging only below their glass-transition temperature, where aging is defined by Struik as the process of approaching thermodynamic equilibrium. Glasses, for example, are known to undergo dimensional change on very long time-scales. Polymers in the rubbery state (above T_g) are able to achieve equilibrium very quickly (essentially faster than measurement can detect), and are therefore considered (by Struik) not to age. Semi-crystalline polymers and rubbery polymers filled with carbon black were found to age at temperatures above their T_g. The hypothesis for this phenomenon is that polymeric material near or attached to the surface of the particle or crystallite behaves as part of this rigid matrix while that material further away from particle surfaces behaves as amorphous polymer. The composite system cannot achieve equilibrium rapidly due to the lowered mobility of the attached polymer due to constraint by the rigid filler/attached-polymer matrix and the broadened glass transition of the amorphous phase. The model proposed by Struik was verified by correlations of aging with particle size of the filler.

The driving force, then, for aging in filled polymer systems is internal stress in the system. Stresses are generated when polymer chains are constrained by the matrix, usually due to processing. Therefore, it can be seen that two factors influence aging in these systems: (1) the degree of stress in the system, or how far it is from thermodynamic equilibrium, determines the magnitude of the conformational changes which might occur; and (2) the mobility of the bulk polymer phase in the matrix will influence the time-scale at which equilibrium is approached, or the rate of aging.

The purpose of the stabilization treatments was to determine their effect on limiting dimensional change in ceramic green sheets. All the treatments involved heating, which accelerated the aging (hence shrinkage) process. The bakeout involved heating at 120°C, just above the boiling points of toluene (110.5°C) and water (100°C), and was intended to eliminate nearly all residual solvent that might cause dimensional change on evaporation over time. Thermal cycling provided more resistance to dimensional change than constant temperature treatment for the same total time. Four cycles of 30 min each at -5°C and 120°C were administered to green tapes. The total time at 120°C was equal to the bakeout time, 2 h. Cycling caused volume changes which allowed the system to rearrange and relax. Solvent-vapor saturation is believed to relieve residual stresses in the green tape incurred during constrained drying [7], by swelling the polymer and causing an increase in mobility due to higher free-volume in the swelled state. The humidity treatment was taken from an ASTM test for dimensional testing of plastics after simulated aging conditions [8]. It also causes swelling, which increases mobility and causes shrinkage.

Higgins [10] found by infrared spectroscopy that poly(methyl methacrylate) chemisorbs on alumina surfaces, sometimes displacing other surface species. This phenomenon may have occurred in these systems, with soluble poly(alkyl acrylates and methacrylates) present. A ceramic-polymer interaction like this would contribute to property differences between systems on aging and firing. The presence of toluene (a good solvent for the polymer) in the solvent-based slurry might thermodynamically prevent some polymer from adsorbing, thereby allowing for more polymer mobility and hence more shrinkage over time. This issue is currently being investigated.

Another factor probably affecting shrinkage differences between the two systems and between x and y directions within the same green tape is the physical state of the binder in the slurries. Shear under the doctor-blade during tape-casting causes alignment or deformation in both polymer systems. Soluble polymer chains become *stretched*, or aligned more in the casting direction, and then become frozen in that state by drying; hence more shrinkage occurs in the casting direction. Dispersed latex particles in the emulsion may be dragged along by the doctor-blade, and then in order to form a continuous film, polymer chains must stretch somewhat in the casting direction as the water evaporates, causing anisotropic shrinkage in that system due to the film-formation mechanism. Shrinkage differences between the two slurry systems are most likely affected by the solvent-drying rate combined with the polymer conformation.

REFERENCES

1. B. Schwartz, "Review of Multilayer Ceramics for Microelectronic Packaging," *J. Phys. Chem. of Solids*, 45 [10] 1051 (1984).
2. R.R. Tummala, "Ceramic Packaging"; ch. 7 in Microelectronics Packaging Handbook. Edited by R.R. Tummala and E.J. Rymaszewski. Van Nostrand Reinhold, New York, NY, 1989.
3. A. Onions, "Films from Water-Based Colloidal Dispersions," *Manufacturing Chemist*, March 1986, p. 55; article continued April 1986, p. 66.
4. G.P. Bierwagen, "The Critical Pigment Volume Concentration and Its Effects in Latex Coatings"; in Organic Coatings Science and Technology, Vol. 5. Edited by G. Parfitt and A. Patsis. Marcel Dekker, New York, NY, 1983.
5. T.J. Garino, "Patterning, Drying, and Sintering of Particle Films on Rigid Substrates"; PhD Thesis, Dept. Mat. Sci. Eng., MIT, May 1987.
6. G. Allyn, "Acrylic Ester Emulsions and Water-Soluble Resins"; ch. 1 in Characterization of Coatings: Physical Techniques, Vol. 1, Part 1. Edited by R.R. Myers and J.S. Long. Marcel Dekker, New York, NY, 1976.
7. G.F. Hait and R.W. Nufer, "Process for the Elimination of Dimensional Changes in Ceramic Green Sheets," U.S. Pat. No. 3 953 562, April 27, 1976.
8. "Determination of Weight and Shape Changes of Plastics Under Accelerated Service Conditions," D756-78, Annual Book of ASTM Standards, Vol. 8.01. American Society for Testing of Materials, New York, NY, 1983.
9. L.C.E. Struik, Physical Aging in Amorphous Polymers and Other Materials. Elsevier Scientific Publishing Company, New York, NY, 1978.
10. R.J. Higgins, "The Chemistry of Carbon Retention During Non-Oxidative Binder Removal from Ceramic Greenware"; ScD Thesis, Dept. Mat. Sci. Eng., MIT, January 1990.

SECTION 22

PREDICTION AND EXPLANATION OF AGING SHRINKAGE IN TAPE-CAST CERAMIC GREEN SHEETS

Paul Nahass, Richard L. Pober, Wendell E. Rhine, William L. Robbins, and H. Kent Bowen

Published in J. Am. Ceram. Soc., 75, 2373 (1993)

ABSTRACT

A simple test to predict linear shrinkage of tape-cast green sheets as a function of time was developed. Shrinkage was found to correlate inversely with the amount of organic phase bound to ceramic particle surfaces. The test was developed for alumina green tapes with acrylic binder. The correlation was found to be independent of the medium used for the two slurry systems evaluated, water and toluene/ethanol. Treatments developed to dimensionally stabilize green sheets reduced shrinkage after 35 days of aging to less than 0.15%. Stabilization treatments involved heating and/or polymer swelling which facilitated the binding of organic phase to alumina particles, causing the tape to be in a more relaxed state.

INTRODUCTION

Tape-cast ceramic green sheets for multilayer electronics applications are generally punched, screened, stacked, and laminated prior to firing. The punch step usually involves mechanical perforation of *vias* through each layer which are subsequently filled with conductor pastes to interconnect the circuitry between layers. Aside from exhibiting strength and flexibility sufficient for subsequent handling and processing steps, green sheets must exhibit excellent dimensional stability over time to ensure accurate interlayer registration upon lamination [1]. Even slight variations from design tolerances can lead to device rejection. As ceramic components become more densely loaded with circuits, the necessity for maintaining precise device tolerances becomes of the utmost importance [2].

Ceramic green sheets used immediately after casting and drying are not allowed sufficient opportunity to undergo significant dimensional changes; however, aging for any length of time results in changes in green sheet dimensions that are unacceptable for use in multilayer electronic component applications. The causes for dimensional change are normally thought to be stresses which develop during green sheet formation [3] and evaporation of residual solvent over time. Although these mechanisms are generally accepted in the industry [2] and widely observed in the polymer literature [4-7], they are not directly documented for the ceramic green sheet system. In addition to simple dimensional change over time, the industry often observes anisotropic dimensional changes in green sheets. Anisotropic stresses are thought to develop in green sheets as a result of polymer or ceramic particle orientation due to shear induced by the doctor blade during tape casting. Particle number density can be significantly lower (on a microscopic scale) in the casting direction than in the direction normal to cast. Since volume fraction of each component in a composite is known to be a significant factor in determining the stresses incurred during film formation [8], directional particle number density differences, even on a microscopic (as opposed to bulk) scale, might cause stress variations which could lead to anisotropic dimensional changes in green sheets over time.

A previous investigation documented dimensional changes over time in green tapes [9]. The formulations developed for that study were unique in that they used the same binder in aqueous (dispersed latex form) and nonaqueous (soluble polymer form) slurries, enabling a direct comparison of the different solvent systems. That study determined that subjecting green tapes to various thermal and environmental treatments could reduce aging shrinkage to tolerable levels for many applications. Continuing along this path, the objective of this study was to assess the mechanisms by which these stabilization treatments prevent further aging shrinkage in green tapes and to develop a simple, reliable technique to predict aging shrinkage in either treated or untreated samples.

MATERIALS AND METHODS

The tape-casting formulations used in this study were described in a previous publication [9]. To summarize, the two slurry systems developed used the same acrylic binder in either an aqueous latex form or as a soluble polymer in an organic solvent system. AKP-30 alumina powder (Sumitomo Chemical Company USA, New York) was chosen for use in this study. Rhoplex B-60A aqueous acrylic emulsion (Rohm and Haas, Philadelphia, PA) was used as the binder for the aqueous system. For solvent-based slurries, B-60A films were dried at 100°C for 24 h and dissolved in solvent. An equimass mixture of toluene and ethanol was the solvent system used for the non-aqueous slurry. The dispersants for the aqueous and solvent-based slurries were different. Darvan®C (R.T. Vanderbilt Co., Norwalk, CT) was an effective dispersant for AKP-30 in deionized water. In toluene/ethanol, 4-hydroxybenzoic acid (p-HBA, Aldrich Chemical, Milwaukee, WI) was the most effective dispersant for AKP-30. The dispersant amounts were adjusted to yield the same ceramic powder packing density.

Polypropylene glycol (PPG-1200, MW=1200, Fluka Chemical Company, Hauppage, NY), was used as plasticizer for both aqueous and non-aqueous systems. It is a liquid at room temperature and was readily miscible with water and toluene/ethanol. A saturated solution of lecithin (capsules, CVS, Inc., Woonsocket, RI) in isopropanol was applied to tempered glass plates as a release agent for the aqueous-based green tapes. A fluorocarbon dry release agent (MS-136, Miller-Stephenson, Danbury, CT) was used for the solvent-based slurries. Pine oil (Aldrich Chemical, Milwaukee, WI) was added to reduce surface tension and aid in film formation of aqueous slurries, although surface tension in the aqueous system was never quite as low as that in the solvent-based system. Unless stated otherwise, pine oil was always present in polymer films and green tapes cast from the aqueous emulsion system.

The slurry formulations used in this study are presented in Table 1. Each of the materials used came from one product batch to reduce extraneous variables. All materials were received 9-12 months prior to use in this study. A detailed description of the tape-casting process for aqueous and non-aqueous slurries with acrylic emulsion binder was described previously [9].

After casting, slurries were allowed to dry at least 24 h at 23 ± 2°C and 50 ± 7% relative humidity (RH). Tapes were removed from the glass plates with a wide razor blade and cut into 5-cm squares; they were then punched by an automatic programmable punch (model SK 5470, Schneider & Marquard, Newton, NJ, with model MD5-5 Berger-Lahr controller) with 0.25-cm diameter measurement holes and subjected to selected storage conditions or treatments.

Punched tape samples for both aqueous and solvent-based systems (in duplicate) were subjected to one of several treatments. Sample treatments included: (1) a simple bake (2 h at 120°C in flowing air); (2) thermal cycling (-5°C for 30 min, then 120°C for 30 min, 4 times); (3) solvent exposure (saturated toluene vapor for 1 h at room temperature, then *simple bake* [3]); and (4) humidity (24 h at 100% RH, 80°C, then 24 h at 80°C in flowing air [10]). Control samples were left untreated. All samples were then stored under controlled conditions at 23 ± 2°C and 50 ± 7% RH. Positions of punched holes were measured using an optical comparator at 20x magnification with radial viewing template and digital translational readings (to $2.5x10^{-5}$ cm). The template enabled very precise measurement. Hole positions were measured after punching, immediately after treatments, then every

Table 1. Slurry Formulations Used in Tape Casting.

Component	Organic System	(g)	Aqueous System	(g)
powder	Al_2O_3, AKP-30	55	Al_2O_3, AKP-30	55
solvent	ethanol/toluene[a]	85	deionized water	15
dispersant	p-HBA	1.1	Darvan C	0.7
binder	dired Rhoplex B-60A	10	Rhoplex B-60A (emulsion)	20
plasticizer	PPG-1200	4	PPG-1200	4
surfactant	none		pine oil	0.1
solids content (vol%)		10-15		44[b]
slurry viscosity (cp)		~5000		700
surface tension ($dyne/cm^2$)		29		42

[a] Equimass mixture used.

[b] 40% of this was due to polymer solids in Rhoplex.

3 to 5 days during aging and, finally, after firing. Four of the seven holes were used to quantify shrinkage in the casting (x) direction and four were used for the transverse (y) direction, as shown in Figure 1.

Polymer films and green tape samples were immersed in several solvents to determine their chemical resistance to dissolution or disintegration. Toluene and THF were the organic solvents used; triethylamine (Aldrich Chemical Company, Milwaukee, WI), an organic base, was added to these solvents in an effort to enhance sample dissolution; a 20% aqueous sodium hydroxide solution was also used. Samples were observed periodically for one week at room temperature and then heated for 12 h at 95°C.

In a similar experiment, 0.2-0.3-g samples of untreated and treated green tapes were placed in 50 mL toluene at room temperature for 90 min. Upon removal, samples were immersed in 50 mL fresh toluene to remove any remaining soluble organics. Tape samples were removed from the solvent and placed in an oven at 60°C under vacuum for 1 h to remove residual toluene, after which they were weighed. After weighing, tape samples were heated to 500°C for 10 min to remove remaining insoluble organics and then weighed again to determine by difference the amount of insoluble organics in green tapes.

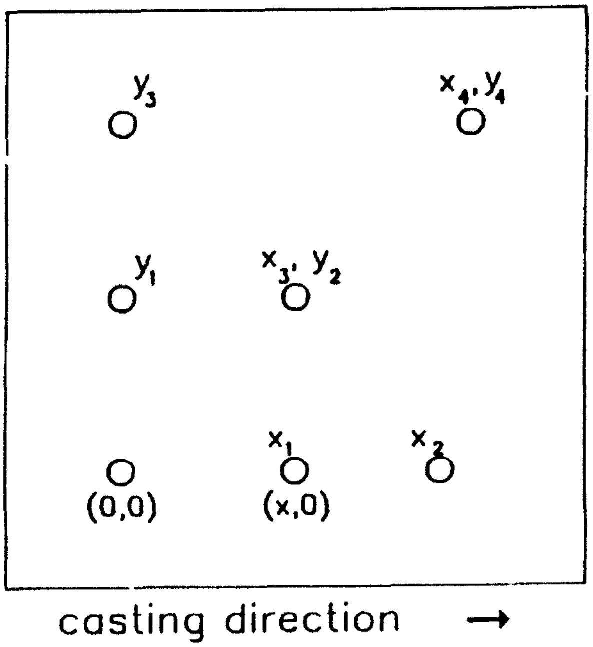

Fig. 1. Punch pattern for green tape shrinkage determination.

Table 2. Physical Properties of Green Tapes.

	Organic Slurry	Aqueous Slurry
TGA weight loss (%, to 500°C)	21.8	21.3
average thickness (μm)	239	274
average bulk density (g/cm^3)	2.43	2.46
porosity (%)	0.8	0.6
yield strength (MPa)		
casting direction	—	0.98
normal to cast	—	1.15

Table 3. Approximate Composition of Green Tapes Used in this Study.

Component	Solvent (wt%)	Aqueous (wt%)
alumina	78.2	78.7
dispersant	1.6	1.0
binder	14.5	14.2
plasticizer	5.8	6.1

RESULTS

Table 2 summarizes the physical properties of green tapes. All data in this section are from individual casts of slurries unless otherwise specified. Overall, physical and compositional consistency was maintained between the aqueous-based and solvent-based tapes. Weight loss, as determined by thermal gravimetric analysis (TGA), represents the amount of organics and other components which decompose at temperatures less than 500°C; there was a slight difference in this value between the two systems due to variations in slurry preparation (TGA values were used to calculate the approximate green tape compositions in Table 3). Green tape thicknesses were averaged from 50 to 75 locations over the entire cast (15 cm x 90 cm long), excluding 5 cm from the beginning and end of the cast and 1 cm from the side edges. Intracast standard deviations of thickness were low (2-10%), and green densities were consistent. The low porosity indicates powder loading in green tapes was probably below the critical pigment volume concentration (CPVC) for each system; hence drastic morphological differences between aqueous and non-aqueous tapes should not be present. There were consistent directional differences in yield strength (which was averaged over several samples), with strength parallel to the casting (or longitudinal) direction lower than that in the normal (or transverse)

Table 4. Summary of Directional Linear Aging Shrinkage of Green Tapes, in Percent.[a]

	Solvent-Based		Aqueous-Based	
Treatment	*x*	*y*	*x*	*y*
untreated	0.92	0.71	0.40	0.31
bake	0.30	0.27	0.28	0.32
thermal cycle	0.25	0.27	0.40	0.36
solvent	0.25	0.27	0.40	0.44
humidity	0.15	0.14	0.17	0.21

[a]After 35 days of aging; measurement error ±0.05%.

direction. Both solvent- and aqueous-based tapes laminated easily top-to-bottom at 120°C for 2 s at very low pressure (<3.5 MPa). Laminated layers held together well after pressureless sintering of samples.

Table 4 summarizes aging shrinkage data for green tapes cast from solvent-based and aqueous-based slurries [9]. As the data shows, aging shrinkage varied significantly for untreated samples *between* systems, as well as between treated and untreated samples *within* a system.

Table 5 describes the response of polymer films and green tapes when placed in various solvents for several days. Toluene and THF are known to be solvents for many acrylic polymers. Films of the binder-plasticizer system used in the tape formulations cast from both the aqueous emulsion and the soluble-polymer system dissolved readily. Dissolution of green tapes was defined as destruction of all integrity of the matrix composite system, usually leaving what appears to be only ceramic powder (small amounts of binder might be attached). Green tapes formulated for this study did not dissolve in the presence of any of the solvents listed in Table 6. There was, however, some interesting behavior shown by samples of untreated green tape and unplasticized green tape (cast from the solvent). These samples broke into small pieces (several millimeters in diameter) after several days in solvent, but they did not disintegrate.

The fact that green tapes made with Rhoplex B-60A binder did not dissolve is quite interesting. It is easier to explain what did not happen in the system than to isolate exactly what did happen, although it is clear that the binder strongly adsorbed to the ceramic particle surfaces. Although chemical crosslinking of the polymer chains in the binder could account for the observed chemical resistance, this is highly unlikely for two reasons: (1) Rhoplex B-60A is designed by the manufacturer to be a non-crosslinking system, and any efforts to cause crosslinking would require addition of specific crosslinking agents (such as dimethacrylates); and (2) the identical polymer system without alumina particles present was readily soluble at room temperature, and there is no reason alumina particle addition should cause chemical crosslinking to occur in the polymer. The fact that green tapes did not lose their integrity in solvents does not automatically imply that none of the polymer phase was dissolved. TGA indicated treated and untreated green tape samples did lose some organics in the system after 2 h in toluene at room temperature. These results are summarized in Table 6. Untreated tapes from the solvent-based formulation had fewer bound organics, but this value increased after these samples were treated; these had the same or more bound species than equivalent samples of aqueous-based tapes.

DISCUSSION

Figure 2 may help to explain the shrinkage mechanism in green tapes over time. It linearly correlates the average of *x* and *y* shrinkage values in green tapes, over the 35-day aging period (values given in Table 4), with the amount of organics remaining in green tapes after

Table 5. Dissolution Behavior of Polymer Films and Green Tapes in the Presence of Various Solvents.

		Solvent			
Film Type	Cast From	Toluene	THF	Tol/TEA	NaOH
B-60A/PPG (polymer film)	aq. emulsion	diss.	diss.	diss.	—
	org. solution	diss.	diss.	diss.	—
untreated tape	aq. emulsion	no diss.	no diss.	no diss.	no diss.
	org. solution	partial diss.	no diss.	no diss.	no diss.
unplastic. tape	org. solution	partial diss.	—	—	—
treated tapes:					
bake	org. solution	no diss.	—	—	—
humid	org. solution	no diss.	—	—	—

Table 6. Organic Content of Green Tapes Before and After Extraction in Toluene.

Green Tape	Solvent-Based (wt%)	Aqueous-Based (wt%)
as-cast	21.9	21.3
after extraction:		
untreated	8.9	13.0
bake	14.1	14.4
humidity	15.3	14.6

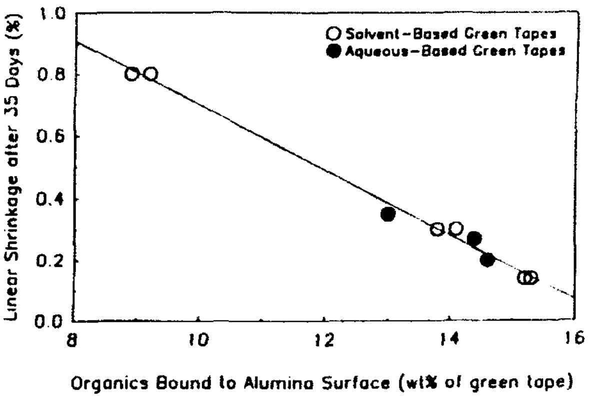

Fig. 2. Correlation of shrinkage in green tapes to amount of organics attached to alumina particle surfaces.

toluene extraction (Table 6). Treated and untreated tapes from aqueous and organic slurries were used for this correlation (including duplicates of three different samples), which had a linear regression coefficient of 0.996. It can be concluded, then, that for the alumina/B-60A/PPG system, *green shrinkage is inversely proportional to* the amount of organics bound to the ceramic phase, regardless of processing history (i.e., solvent used or physical state of the binder).

This relation may hold (in some form) for green tape systems with other binders and possibly other ceramics. It might be used to design tapes with given amounts of shrinkage by precisely controlling processing or post-casting treatments to affect the amount of non-extractable binder. One caution worth mentioning is that tapes without any binder in the bulk phase (i.e., those after extraction) had poor mechanical properties. Attempts to eliminate shrinkage by fabricating tapes with all the polymer chemically adsorbed, or by extracting all the bulk organics, might not be advantageous for further processing steps. Aside from the mechanical flexibility required for punching and machining, bulk polymer may be necessary for layers to adhere during lamination.

Based on infrared spectroscopy and glass-transition analyses, the Rhoplex B-60A probably contains a significant amount of poly(methyl methacrylate) and another, softer acrylic polymer such as ethyl acrylate [11]. Higgins [12] investigated the interaction of PMMA with alumina surfaces. He found that PMMA reacted with basic hydroxyl sites on alumina surfaces to form strong ionic bonds, sometimes displacing other adsorbed species. He calculated (by quantitative FTIR) that the number of sites which functional groups of PMMA occupied at room temperature was 3.4 per 10^{-14} cm^2 (100 Å^2) of alumina surface. Comparing this result with the amount of Rhoplex polymer present in the green tape system (15.6 wt% of the green tape) [11], the average molecular weight of Rhoplex chains (MW = 298,000 g/mol, as determined by gel permeation chromatography), and the surface area of the alumina powder used (6.4 m^2/g), there should be approximately eight bonds to the ceramic surface per polymer chain present. This number would enable most of the polymer chains present in the green tape binder to react with particle surfaces, and explains why green tapes maintained their integrity in solvents that normally dissolve these polymers. The fact that tapes did not dissolve in the presence of solvents even when heated indicates polymer chains were not simply tangled in the web of a few chains bonded to the particle surfaces. Heating might enable chains not attached to particles to have higher mobility and to solubilize. On the other hand, heating might promote the reaction with alumina hydroxyl sites, as Higgins found. It can be concluded that a continuous matrix of ceramic particles exists, connected by polymer chains bound to the alumina particle surfaces.

The high molecular weight of the binder facilitates the existence of such a matrix, requiring that only a few percent of the monomer units present be bound to oxide surfaces to create particle bridging. The root-mean-square end-to-end distance of an amorphous chain of PMMA or a similar acrylic polymer with MW = 300,000 is approximately 8x10^{-16} cm (800 Å). This distance corresponds to the calculated surface separation of alumina particles in dried green tapes, based on the maximum green density achieved in this study (53% of theoretical) [11].

The results of the toluene extraction (Table 6) indicate the amount of insoluble organics in untreated green tapes varies with the casting system used. After green tape treatments (all of which involved heating), the amounts of insoluble organics were similar in samples from the different casting systems. The composition of

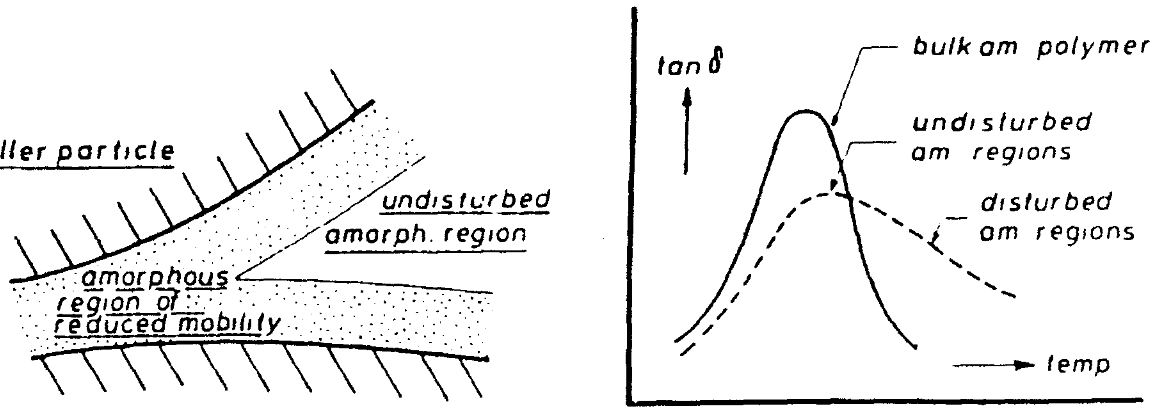

Fig. 3. The broadened glass-transition of filled polymers (am. and amorph. = amorphous). From Struik [7].

the organics remaining in the tape is unknown, although it is safe to assume that nearly all of the plasticizer was probably dissolved [13], leaving only binder and dispersant. Calculations based on this assumption indicate nearly 100% of the binder remained in the treated green tapes after toluene extraction. The binder itself was exactly the same in each solvent system, likely a high molecular weight copolymer of ethyl acrylate and methyl methacrylate [11]. The dispersants were 4-hydroxy benzoic acid (MW = 138) in the organic solvent system and Darvan C (MW = 14,000; 86/functional group), poly-(methacrylic acid) with ammonium ions in place of some of the acid functional groups, in the aqueous emulsion system. The amounts of dispersant used in each system correspond to a molar ratio of about 1.6:1, p-HBA: Darvan C. For p-HBA, this amount equals 74 times one monolayer of alumina surface coverage (based on hydroxyl site surface area of 5.88×10^{-16} cm^2) [12]. Since dispersant amounts in excess of one monolayer cannot be attached to particle surfaces unless dispersant molecules bond to each other, most of the dispersant in the solvent-based system was probably extracted by the toluene. In contrast to p-HBA, if one functional group of a Darvan C molecule bonds to the surface, the molecule is no longer extractable by toluene.

Even considering these expected differences in dispersant extractability, the insoluble organic content in the solvent-based system is lower than that in the aqueous-based system, indicating less binder reacted with the alumina particle surfaces in the solvent-based system. Either the thermodynamics do not favor the reaction between the polymer and the particle surface when the polymer is in solution, or a polar solvent such as water facilitates the reaction between the polymer and the alumina particle surface. The latter argument is the most plausible since the basic hydrolysis of esters is a bimolecular reaction [14] between OH^- ions and ester groups and would be favored in polar solvents. Higgins [12] also observed that water facilitates the reaction of esters with the alumina surface.

A physical basis for correlation of amount of adsorbed polymer with aging shrinkage in this filled-polymer system can be inferred from the work of Struik [7]. The Struik model for aging in filled-polymer systems (shown in Fig. 3) indicates polymeric material near or attached to the surface of the particle behaves as part of the rigid matrix. Mobility is lower in the chemically adsorbed-polymer phase than in the bulk phase. If this is so, it would make physical sense that the system with the highest fraction of its polymer in the bound state would be the most rigid and the least mobile, and would age the least on the time scales observed for this study (assuming constant initial sample composition).

Two issues are of interest with regard to stabilization treatments for green tapes: how do treatments cause shrinkage and how do they facilitate polymer attachment to alumina surfaces? Polymer relaxation and polymer redistribution may not be distinct, independent processes, but thinking of them as such helps to assess why the treatments yield different results.

Table 6 shows that the simple bake and humidity treatments each caused a significant increase in the fraction of organics which were attached to alumina particle surfaces. Untreated, solvent-based tapes had the smallest amount of insoluble organics of all the samples analyzed. Solvent-based slurries contained toluene, which is a good nonpolar solvent for the binder, preventing much of the polymer from attaching to the particle surfaces, since the reaction between the particle surface and PMMA is favored in polar solvents. The treatments simply caused the

Table 7. Linear Green Tape Shrinkage Incurred on Treatment, Broken Down into Mechanistic Causes.

Treatment	Total Shrinkage, % (avg. of x and y)	Estimated Percent of Total Shrinkage Due to: Solvent	Heating	Other
BAKE				
solvent	1.10	25	75	—
aqueous	0.35	30	70	—
THERMAL CYCLE				
solvent	1.80	15	45	40
aqueous	0.60	15	45	40
SOLVENT				
solvent	2.10	15	40	50
aqueous	0.50	20	50	30
HUMIDITY				
solvent	2.70	10	44	45
aqueous	0.85	10	80	5

equilibrium to shift, favoring an increased amount of binder bound to the surface (facilitated by the presence of water and the higher temperatures). These results are consistent with those of Higgins [12], who observed increased and irreversible PMMA bonding to alumina surfaces at higher temperatures.

The results shown in Table 7 point out significant variation of shrinkage caused by stabilization treatments. This variation was present for samples treated differently within the same solvent system as well as for those of different systems subjected to the same treatment. There are certainly different mechanisms acting to induce stress relaxation in green tapes during treatments.

A crude approximation to assess shrinkage mechanisms during treatment can be described from simple kinetic principles. The simplest treatment, simple bake, involved heating for 2 h at 120°C. Assuming that diffusion and chemical kinetic processes approximately double in rate for every 10°C of temperature increase (a generally accepted rule of thumb), the bake process was equivalent to aging 2000 h, or 83 days, at room temperature (20°C). After 83 days of aging, extrapolation of shrinkage curves for untreated solvent-based green tapes [11] indicates an average (based on x and y values) of about 25% less shrinkage than the bake process caused. This indicates another mechanism, in addition to a polymer mobility increase due to heating, operated to cause shrinkage during the bake treatment. The only certain difference between baked and untreated samples is that some residual solvent was still present in untreated samples after 83 days (from sample weight measurements).

The thermal cycle and solvent treatments both consisted of the simple bake treatment plus some other process. Therefore, the amount of shrinkage due to a mechanism other than solvent evolution and increased mobility at high temperature (both of which were accomplished by the bake treatment) may be determined for those treatments by comparing the shrinkage they caused to that of the simple bake treatment. For example, the humidity treatment may be broken down into two parts: (1) heating for 48 h at 80°C, and (2) holding for 24 h at 100% RH. The thermal part correlates to about 250 days of aging at room temperature.

Following extrapolated shrinkage curves for untreated tapes out to 250 days, we estimated the fraction of shrinkage which was *not* due to the thermal part of the humidity treatment, but rather due to the presence of saturated water vapor. This extrapolation, however, probably contains substantial error. The results of this analysis are summarized in Table 7 for solvent-based and aqueous, emulsion-based tapes, using average x and y shrinkage values for comparison. The numbers are not precise by any means but are simply intended to suggest why the treatments work to the extent that they do. The values seem to make more intuitive sense for the solvent-based system, most likely because the shrinkage curves for those samples (which were the baseline for this analysis) leveled off quickly, enabling reliable extrapolation. This was not the case for aqueous-based tapes, resulting in more error in the analysis for these samples.

One purpose of the stabilization treatments was to determine their effect on limiting dimensional changes in ceramic green sheets. The bakeout involved heating at 120°C, just above the boiling points of toluene (110°C) and water (100°C). The bake treatment was intended to eliminate all residual solvent that might cause dimensional change over time due to evaporation, and to allow the tape to relieve internal stresses incurred during drying. Samples which had been exposed to the thermal cycling treatment were more resistant to dimensional change than those exposed to constant temperature treatment for the same total time. Four cycles of 30 min each at -5°C and 120°C were administered alternately to green tapes. The total time at 120°C was equal to the bakeout time, 2 h, but temperature cycling caused the sample volume to change continuously during treatment. This result is consistent with that of McLoughlin [15], who found that rapid heating and cooling increased stress relaxation processes in PMMA. Volume change during thermal cycling facilitated configurational changes in the polymer phase and allowed it to approach a relaxed state. Solvent-vapor saturation is believed to relieve residual stresses by substantial swelling, which increases free volume, thereby enhancing polymer mobility [7]. Since the bake part of the solvent treatment occurred *after* the solvent exposure part, the value for shrinkage attributed to swelling is artificially low because most of the relaxation occurred prior to heating for that sample.

The humidity treatment was taken from an ASTM test [10] for dimensional testing of plastics after simulated aging conditions. Berry [6] found that room temperature exposure of PMMA to 100% RH induced stress relaxation equivalent to that incurred by raising the temperature of the sample by 90°C, and that humidity treatments can be comparable to, or even surpass, heating for effectiveness of altering stresses in thin samples of PMMA. That result is consistent with those of this study, since the amount of shrinkage attributed to humidity alone was approximately equal to that caused by a temperature increase of 60°C. Berry attributes relaxation to swelling of PMMA leading to free volume and mobility increases, similar to the mechanism proposed for the solvent-vapor treatment.

CONCLUSIONS

Linear shrinkage over time in green tapes with acrylic binder correlated extremely well to the amount of the organic phase which was attached to alumina particles. This correlation was independent of the solvent-dispersant system used to prepare green tapes. Relaxation of polymer stresses is the mechanism for shrinkage of green tapes during aging. These stresses are caused by constrained drying and polymer-ceramic interactions. According to this analysis, solvent-based, soluble-polymer green tape slurries dried to a less relaxed state (further from thermodynamic equilibrium) than did aqueous, emulsion-based tapes. This can be attributed to the higher degree of polymer orientation probably caused by doctor-blade shear in the solvent-based system.

Some dimensional stabilization treatments caused green tapes to undergo less than 0.15% linear shrinkage after 35 days of aging at controlled room conditions and experience no shrinkage anisotropy (within measurement limits) after treatment. This result was reproducible. Stabilization treatments increased the amount of polymer bound to alumina surfaces in green tapes, enabling these treated samples to shrink less on aging. The mechanisms for relaxation of green tapes during treatments were increased polymer mobility and polymer free volume due to thermal energy input and swelling of the polymer. Treatments which involved only thermal energy input were less effective than those involving an additional relaxation mechanism.

ACKNOWLEDGMENTS

The authors wish to thank AFOSR (contract no. F49620-89C-0102DEF) and C.S. Draper Laboratory for support of this work.

REFERENCES

1. B. Schwartz, "Review of Multilayer Ceramics for Microelectronic Packaging," *J. Phys. Chem. of Solids*, **45** [10] 1051 (1984).
2. R.R. Tummala, "Ceramic Packaging"; Ch. 7 in Microelectronics Packaging Handbook. Edited by R. R. Tummala and E. J. Rymaszewski. Van Nostrand Reinhold, New York, NY, 1989.
3. G. F. Hait and R. W. Nufer, Process for the Elimination of Dimensional Changes in Ceramic Green Sheets, U.S. Pat. No. 3 953 562, April 27, 1976.
4. B. F. Blumentritt, "Laminated Films with Isotropic In-plane Properties," *IBM J. Res. Develop.*, **23** [1] 66 (1979).
5. L. E. Nielsen, Mechanical Properties of Polymers, Vol. 1. Marcel Dekker, New York, 1974.
6. B. S. Berry and W. C. Pritchet, "Bending-Cantilever Method for the Study of Moisture Swelling in Polymers," *IBM J. Res. Develop.*, **28** [6] 662 1984.
7. L. C. E. Struik, Physical Aging in Amorphous Polymers and Other Materials. Elsevier, New York, 1978.
8. A. M. Borick, J. E. Akin, and C. D. Armeniades, "Setting Stress Distribution in Particle-Reinforced Polymer Composites," *J. Comp. Mater.*, **22** 986 (1988).

9. P. Nahass, W. E. Rhine, R. L. Pober, and H. K. Bowen, "A Comparison of Aqueous and Non-Aqueous Slurries for Tape-Casting, and Dimensional Stability in Green Tapes"; pp. 355-64 in Materials and Processes in Microelectronic Systems, Ceramic Transactions, Vol. 15. Edited by K. M. Nair, R. Pohanka, and R. C. Buchanan. American Ceramic Society, Westerville, OH, 1990.

10. Amer. Soc. Test. Mater., "Determination of Weight and Shape Changes of Plastics Under Accelerated Service Conditions," D756-78, Annual Book of ASTM Standards, Vol. 8.01. American Society for Testing of Materials, New York, 1983.

11. P. R. Nahass, "The Effect of Changes in Chemistry and Ceramic Slurry Processing on Alumina Green Tapes"; PhD Thesis. Dept. of Materials Science and Engineering, Massachusetts Institute of Technology, Cambridge, MA, 1990.

12. R. J. Higgins, "The Chemistry of Carbon Retention During Non-Oxidative Binder Removal from Ceramic Greenware"; ScD Thesis. Dept. of Materials Science and Engineering, Massachusetts Institute of Technology, Cambridge, MA, 1990.

13. J. K. Sears and J. R. Darby, The Technology of Plasticizers. John Wiley and Sons, New York, 1982.

14. E. S. Gould, Mechanism and Structure in Organic Chemistry; p. 315. Holt, Rinehart and Winston, New York, 1959.

15. J. R. McLoughlin and A. V. Tobolsky, "The Viscoelastic Behavior of Polymethyl Methacrylate," *J. Coll. Sci.*, 7 555 (1952).

SECTION 23

EFFECT OF PRESSURE FLUCTUATION ON REMOVAL OF CARBON RESIDUE: PART I. THEORETICAL ANALYSIS

Chun Dong

ABSTRACT

The removal of carbon residue from a ceramic body is expected to accelerate when the total pressure inside the firing chamber oscillates instead of remaining constant, because both internal and external mass transfer may be increased. This technique was analyzed theoretically by numerical calculation of the carbon residue removal rate under both constant and fluctuating pressure conditions. These calculations showed that significant improvement in carbon removal rates could be achieved through pressure fluctuation. For example, an oscillating pressure of 0.5 atm in amplitude and 5 Hz in frequency could improve carbon conversion in air by at least 17% over 50 min. Influencing factors such as the frequency and amplitude of the oscillating pressure were also investigated.

INTRODUCTION

During firing of ceramic compacts, most of the organic binder, which is added to ceramic powders to improve their workability, decomposes within the temperature range from 200°C to 500°C. A small amount of carbonaceous material formed by binder decomposition remains, but this can be removed at higher temperature by oxidation. Removal of this carbon residue must be accomplished before sintering of the solid material commences, or the carbon residue remaining in the ceramic body may alter the desired properties of the final product. Because removal of this final 2% of residue may require an exceedingly long time [1], and because the oxidation rate at high temperatures is totally mass transfer-controlled [1, 2], a method for increasing the mass transfer could greatly improve the efficiency of carbon residue removal processes.

A scheme for oscillating the total pressure inside the firing chamber to increase the rate of mass transfer was therefore proposed. A periodic pressure cycling inside the firing chamber may cause oscillating bulk flows of gas within the porous ceramic structure, purging the product, CO_2, as the pressure drops and charging the fresh reactant, O_2, as the pressure rises. These flows may significantly increase the internal mass transfer. In addition, under conditions of pressure cycling, the gas flow pattern around the exterior surface of the ceramic body becomes turbulent, which may prevent the formation of a stable boundary layer [3]. Thus, external resistance to mass transfer could also be reduced. Furthermore, the convective flow inside pores generated by pressure fluctuation will cause streamwise dispersion of gas, which will result in a much greater effective diffusivity [4].

Many researchers have made theoretical investigations of the influence of pressure oscillations within a fluid upon mass transfer between a solid surface and the fluid. This problem is related to many chemical engineering areas such as drying, desublimation, and chemical reactions where kinetics are determined by mass transfer.

Hamer and Cormack [5] studied gas phase reactions in porous catalysts. They determined that in the mass transfer-controlled temperature region, the effectiveness factor (the ratio of the actual rate of conversion to the maximum attainable rate) could be increased to more than 500% of the steady state value by applying pressure fluctuation. Sohn and Chaubal [6] investigated the gaseous reduction of porous iron oxide and theoretically predicted that reduction could increase by about 25% within 20 min by applying an oscillating pressure of 0.5 atm in amplitude and 0.5 Hz in frequency. Dill and Brenner [4] studied the dispersion of a soluble substance in a porous medium under a periodic flow. They found that in situations where the time-average convective transport is zero, the dispersivity may increase by many orders of magnitude with the application of a zero-mean periodic flow. This enhanced dispersivity is another example of the benefits that an oscillating flow can produce with regard to mass transfer.

While the influence of pressure oscillation within a fluid on mass transfer has been investigated by many researchers with impressive results, the use of this same concept in ceramics processing has not been reported in the literature. The feasibility of applying this method to elimination of carbon residue is still in question and depends on several parameters such as the reaction rate constant of carbon oxidation, the effective gas diffusivity, and the gas permeability of the ceramic body.

The purpose of this study was, therefore, to investigate theoretically the effects of oscillating versus constant pressure inside the firing chamber on the removal rate of carbon residue in a ceramic body. A mathematical calculation was performed to predict the effectiveness of oscillating pressure over that of constant pressure. To carry out the numerical calculations, we made initial assumptions and parameter determinations. Results show that pressure fluctuation can increase oxygen concentration inside a porous ceramic body and thus can accelerate the reaction rate. Influencing factors such as frequency and amplitude were also studied.

ASSUMPTIONS

The mathematical calculations were based on the following assumptions:

1) the effective diffusivity was simply taken to be uniform:

$$\nabla D_e = 0 \tag{1}$$

2) the removal of carbon residue over the temperature range of interest proceeds by the reaction [1, 7]:

$$C + O_2 = CO_2 \tag{2}$$

3) the rate of reaction is first order with regard to both carbon mole fraction and oxygen concentration [8] and can be expressed as:

$$v_{O_2} = K_{rea} C_{O_2} Y_C \tag{3}$$

4) equimolar counter-diffusion occurs inside the porous body, and hence the effective diffusivities are:

$$D_{eO_2} = D_{eCO_2} = D_e \tag{4}$$

5) there is a uniform and constant temperature throughout the body during the oxidation process, and the heating effects caused by the exothermic reaction are neglected;

6) the ordinary molecular diffusion dominates [9];

7) the gas phase conforms to the ideal case:

$$C = \frac{P}{RT} \tag{5}$$

8) the reaction rate constant, K_{rea}, and the effective diffusivity, D_e, for constant pressure are valid for the case of oscillating pressure;

9) the external pressure, P, applied is a sine wave which can be expressed as:

$$P = P_0 [1 + A \sin(2\pi\omega t)] \tag{6}$$

10) a stable boundary layer which surrounds the exterior surface of the pellet is neglected since our main objective in applying pressure fluctuation is to increase the internal mass transfer. Therefore, the oxygen mole fraction at the exterior surface of the ceramic body, X_{O_2}, is the same as that at all other points throughout the bulk of gas in the furnace, X_{O_2b}.

MATHEMATICAL FORMULATIONS

Oxygen Molar Fraction Inside Pores

As shown by Bird, Stewart, and Lightfoot [10], the concentration of oxygen, C_{O_2}, inside a porous pellet for an O_2-CO_2 binary diffusing system can be expressed as:

$$\varepsilon \frac{\partial C_{O_2}}{\partial t} + \nabla(C_{O_2} V) - \nabla(D_{eO_2} C \nabla X_{O_2}) + v_{O_2} = 0 \tag{7}$$

where the first term represents the oxygen concentration inside pores as it changes with time, the second term shows the convective flow of the reactant gas, the third term is the contribution of the diffusive flux, and the last term accounts for the consumption of gaseous reactant by chemical reaction.

A similar expression for carbon dioxide generated inside pores is:

$$\varepsilon \frac{\partial C_{CO_2}}{\partial t} + \nabla(C_{CO_2} V) - \nabla(D_{eCO_2} C \nabla X_{CO_2}) + v_{CO_2} = 0 \tag{8}$$

It can be stated that:

$$v_{O_2} = -v_{CO_2} \tag{9}$$

and:

$$C = C_{O_2} + C_{CO_2} \tag{10}$$

The summation of Equations 7 through 10 gives the overall gas phase continuity equation:

$$\varepsilon\frac{\partial C}{\partial t} + \nabla(CV) = 0 \tag{11}$$

High permeability model

For the case of high permeability, we have:

$$\nabla P = 0 \tag{12}$$

Combining Equation 5 with Equations 11 and 12 gives:

$$\varepsilon\frac{\partial P}{\partial t} + P\nabla V = 0 \tag{13}$$

The convective gas flow velocity inside pores caused by the external pressure cycling can be determined directly by Equation 13 together with the boundary conditions:

$$V = 0 \text{ at } r = 0 \tag{14}$$

Thus, the resulting velocity profile in spherical coordinates is:

$$V = -\frac{\varepsilon r}{P}\frac{\partial P}{\partial t} \tag{15}$$

Incorporating Equations 5 and 12 with the relation $P_{O_2} = PX_{O_2}$, Equation 7 yields:

$$\varepsilon\frac{\partial(PX_{O_2})}{\partial t} = -PV\nabla X_{O_2} - PX_{O_2}\nabla V + PD_e\nabla^2 X_{O_2} - \nu_{O_2}RT \tag{16}$$

In spherical coordinates:

$$\nabla^2 X_{O_2} = \frac{2}{r}\frac{\partial X_{O_2}}{\partial r} + \frac{\partial^2 X_{O_2}}{\partial r^2} \tag{17}$$

Therefore, Equation 3 can be combined with Equations 15 through 17 to give:

$$\frac{\partial X_{O_2}}{\partial t} = \frac{D_e}{\varepsilon}\left(\frac{2}{r}\frac{\partial X_{O_2}}{\partial r} + \frac{\partial^2 X_{O_2}}{\partial r^2}\right) + \frac{r}{P}\frac{\partial P}{\partial t}\frac{\partial X_{O_2}}{\partial r} - \frac{K_{rea}Y_C X_{O_2}}{\varepsilon} \tag{18}$$

with the boundary conditions:

$$\frac{\partial X_{O_2}}{\partial r} = 0 \text{ at } r = 0 \tag{19}$$

and:

$$X_{O_2} = X_{O_2b} \text{ at } r = r_p \tag{20}$$

Equation 18 can be used to determine the oxygen molar fraction, X_{O_2}, inside pores as a function of time, t, and radial position, r_p.

Limited permeability model

For the case of limited permeability, Darcy's law can be used to express the convective gas flow velocity inside pores:

$$V = -\frac{\kappa}{\mu}\nabla P \tag{21}$$

Equation 11 can then be combined with Equations 5 and 21 to give the following equation:

$$\varepsilon\frac{\partial P}{\partial t} + \left(|\nabla P|\nabla P + P\nabla^2 P\right)\left(-\frac{\kappa}{\mu}\right) = 0 \tag{22}$$

In spherical coordinates:

$$\nabla^2 P = \frac{2}{r}\frac{\partial P}{\partial r} + \frac{\partial^2 P}{\partial r^2} \tag{23}$$

Incorporating Equations 22 and 23 gives:

$$\frac{\partial P}{\partial t} = \frac{\kappa}{\varepsilon\mu}\left(\left|\frac{\partial p}{\partial r}\right|\frac{\partial P}{\partial r} + \frac{2P}{r}\frac{\partial P}{\partial r} + P\frac{\partial^2 P}{\partial r^2}\right) \tag{24}$$

Furthermore, using Equations 5, 21, and 24, Equation 7 can be rearranged as:

$$\frac{\partial X_{O_2}}{\partial t} = \frac{1}{\varepsilon P}\left(D_{eO_2}\left(P\frac{\partial^2 X_{O_2}}{\partial r^2} + \frac{2P}{r}\frac{\partial X_{O_2}}{\partial r}\right) + \frac{\kappa}{\mu}P\frac{\partial X_{O_2}}{\partial r}\frac{\partial P}{\partial r} - RT\nu_{O_2}\right) \tag{25}$$

Besides the boundary conditions given in Equations 19 and 20, Equations 24 and 25 are subject to the additional boundary conditions:

$$\frac{\partial P}{\partial r} = 0 \text{ at } r = 0 \tag{26}$$

$$P = P_0\,[1 + A\sin(2\pi\omega t)] \text{ at } r = r_p \tag{27}$$

Carbon Molar Fraction Inside Pores

The molar fraction of carbon inside the porous ceramic body as a function of time can be calculated from the consumption rate of oxygen. Combination of Equations 3, 5, and 9 with the knowledge of the reaction rate, $\nu_{CO_2} = n_C^0\frac{\partial Y_C}{\partial t}$, gives:

$$-n_C^0\frac{\partial Y_C}{\partial t} = \frac{K_{rea}Y_C P X_{O_2}}{RT} \tag{28}$$

where n_C^0 is the initial carbon concentration. Equation 28 can then be integrated with the initial condition:

$$Y_C = 1 \text{ at } t = 0 \tag{29}$$

The mole fraction of carbon inside the body is thus obtained:

$$Y_C = \exp\left(\frac{-K_{rea} P X_{O_2} t}{RT n_C^0}\right) \tag{30}$$

This allows us to view the dynamic nature of the carbon distribution profile inside the porous ceramic body.

Total Conversion

The total conversion of carbon (the weight percentage of carbon removed) can be obtained simply by integrating the local value of the fractional carbon removal through the entire pellet:

$$\phi = \frac{3}{r_p^3}\int_0^{r_p}(1 - Y_C)r^2 dr \tag{31}$$

DETERMINATION OF PARAMETERS

Effective Diffusivity

For diffusion of oxygen and carbon dioxide in bulk gas, the molecular diffusivity can be determined from [10]:

$$D_{CO_2\text{-}O_2} = \frac{0.001858 T^{3/2}\left(\frac{M_{CO_2} + M_{O_2}}{M_{CO_2} M_{O_2}}\right)^{1/2}}{P\sigma^2\Omega_D} \tag{32}$$

where M_i is the molecular weight, and σ and Ω_D were calculated to be 3.704 Å and 0.81, respectively [11]. The effective diffusivities were calculated by using the relationship [11]:

$$D_e = D_{CO_2\text{-}O_2}\frac{\varepsilon}{\tau} \tag{33}$$

where ε is the porosity and τ is the tortuosity, which usually ranges from 2 to 8 [11].

Chemical Reaction Rate Constant

The reaction rate constant was calculated according to:

$$k_{rea} = H \exp\left(\frac{-A_E}{RT}\right) \tag{34}$$

where the frequency factor, H, and the activation energy, A_E, at 600°C were chosen to be 2.9×10^9 cm/sec, and 58 ±4 Kcal/mol, respectively, as obtained by Wicke [12].

To coordinate the units in our theoretical calculations, we used a modified reaction rate constant, K_{rea}, with a unit of s^{-1}, defined as:

$$K_{rea} = k_{rea} S_C^0 \tag{35}$$

where S_C^0 is the initial interstitial area of carbon.

Initial Interstitial Area of Carbon

Initially, carbon residue was assumed to coat uniformly the channel surface of the porous ceramic body, and hence the initial interstitial area of carbon was simply assumed to be equal to the surface area of the porous ceramic structure:

$$S_C^0 = \frac{A_s\rho}{\varepsilon^0} \tag{36}$$

where ρ is the theoretical density of the ceramic powder and was chosen to be 3.97 g/cm^3 for Al_2O_3 powder, A_s is the surface area of the ceramic powder and was taken as 5.4×10^4 cm^2/g, and ε^0 is the initial porosity and was chosen to be 0.42 according to the experimental samples used.

Initial Carbon Concentratior

The initial carbon concentration, n_C^0, used to calculate the mole fraction of carbon as shown in Equation 30 was determined from:

$$n_C^0 = \frac{\rho(1 - \varepsilon^0)\, C_{wt\%}^0}{M_C} \tag{37}$$

where the initial weight percent of carbon inside the porous body, $C_{wt\%}^0$, was 0.17 based on the experimental sample used. The high carbon content of our experimental sample was chosen for ease of visual demonstration.

Porosity

Considering the high carbon content used in our calculation, the porosity of the porous structure was assumed to be a function of conversion:

$$\varepsilon = \varepsilon^0 + n_C^0\psi\phi \tag{38}$$

where ψ is the atomic volume of carbon, which equals 4.58 cm^3/mol, and ϕ is the total conversion.

Gas Permeability

The gas permeability at a specific temperature can be calculated based on following equation [13]:

$$\kappa = 0.00559\varepsilon\left(\frac{\varepsilon d}{1 - \varepsilon}\right)^2 \tag{39}$$

where d is the powder diameter.

Gas Viscosity

The gas viscosity was estimated from:

$$\mu_i = \mu_i^0\sqrt{\frac{T}{293}} \tag{40}$$

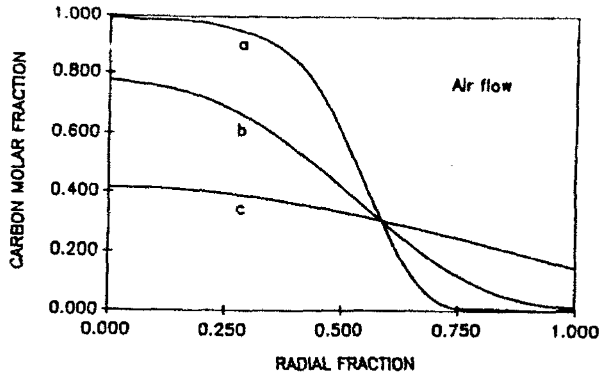

Fig. 1. Theoretical calculation of carbon removal from a porous ceramic body under constant pressure, air flow, and (a) 600°C, 55 min; (b) 570°C, 65 min; and (c) 530°C, 120 min.

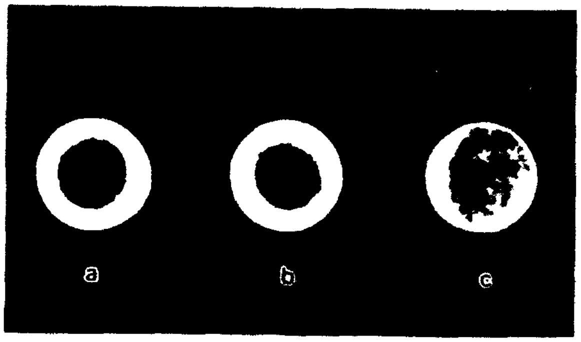

Fig. 2. Cross section of colloid-pressed samples subjected to partial carbon removal at air flow and (a) 600°C, 55 min ("shell progressive reaction"); (b) 570°C, 65 min (transition); and (c) 530°C, 120 min ("intrinsic reaction").

where μ_i^0 is the viscosity of gas species i at a temperature of 20°C and a pressure of 1 atm, and T is the specific temperature.

RESULTS AND DISCUSSION

Since the analytical solutions to Equations 18 and 25 cannot be found, the parabolic partial differential equations were solved by a numerical integration technique [14]. Both implicit and explicit forms were used, and the resulting differences in calculations between the two forms were found to be smaller than 5%. The differential equations were converted into two-dimensional matrices with time in one direction and radius in the other. Computer programs were written in FORTRAN to solve the problems.

To verify the mathematical calculations, the computer program was first run to show the extreme cases, such as intrinsic reaction-controlled oxidation and internal mass transfer-controlled oxidation, by changing the value of the reaction temperature. The plots of carbon molar fraction versus radial fraction after partial carbon removal under constant pressure and air flow were thus obtained. Each calculated curve was then compared with the cross section of a sample tested under corresponding conditions.

Figure 1 shows the calculated results of carbon distribution inside porous samples with tortuosity $\tau = 5$ and containing initially 17 wt% carbon, with the activation energy of carbon oxidation, A_E, equal to 54 Kcal/mol. It indicates the following: 530°C corresponds to the chemical reaction-controlled region with carbon oxidized uniformly throughout the cross-section; 600°C corresponds to the internal mass transfer-controlled region, characterized by a sharp moving boundary between the reacted and unreacted zones (the process is generally termed as "shell model"); and 570°C represents the transition region between the two.

Figure 2 shows the cross sections of three tested samples which were subjected to isothermal partial carbon removal under conditions corresponding to the three calculations made above. The samples were prepared by colloid pressing a mixture of Al_2O_3 powder and carbon powder (carbon content 17 wt%). The resulting structures were cylindrical in geometry and measured 0.12 µm in pore size and 0.39 in porosity.

Comparison of Figures 1 and 2 shows good consistency of results and lends credibility to the numerical calculations. Pressure fluctuation is best applied in the temperature region above 600°C to increase internal mass transfer. It should be pointed out that:

1) by decreasing the tortuosity, τ, the effective diffusivity, D_e, will increase (Eq. 33), and each curve in Figure 1 will become flatter (less diffusion-limited);
2) by decreasing the activation energy, A_E, the reaction rate constant, K_{rea}, for each temperature will increase, and each curve in Figure 1 will become steeper (more diffusion-limited); and
3) by simultaneously increasing or decreasing both τ and A_E, the characteristic carbon removal profiles at the three temperatures may be similar to those shown in Figure 1, while the total carbon removal rate will be changed. Therefore, the chosen values for D_e and K_{rea}, or more specifically, for τ and A_E, are unique values.

In the case of applying pressure fluctuation inside a

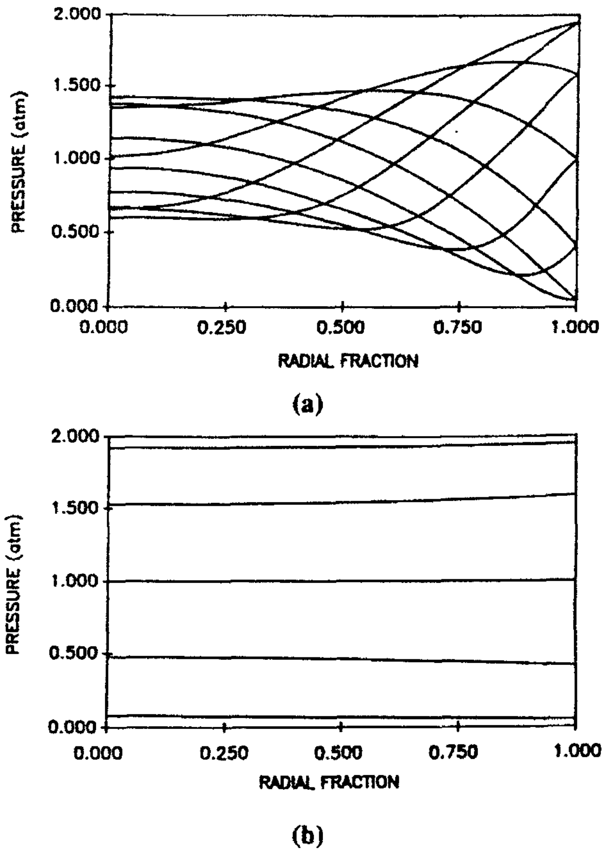

Fig. 3. Pressure distribution in a spherical ceramic body 0.6 cm in diameter and (a) 1 μm in powder size, or 1.23 x 10^{-11} cm^2 in gas permeability and (b) 10 μm in powder size, or 1.23 x 10^{-9} cm^2 in gas permeability. The oscillating pressure assumed is 1 atm in amplitude, 1 Hz in frequency, and at a condition of 600°C, air flow.

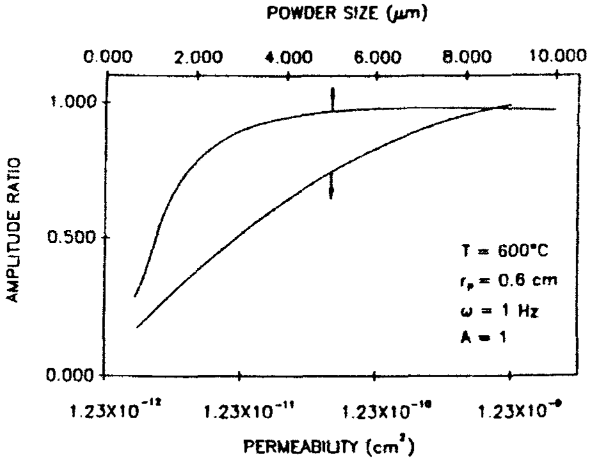

Fig. 4. The effect of gas permeability and powder size on the ratio of pressure oscillation amplitude.

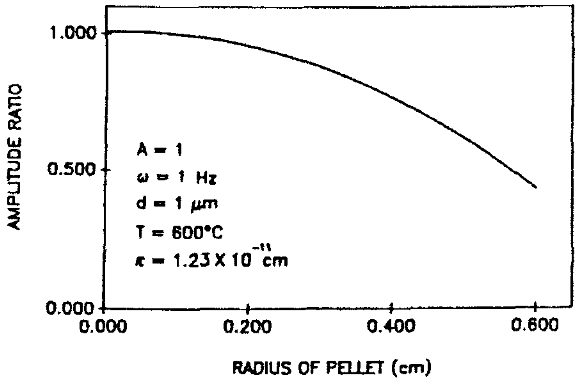

Fig. 5. The effect of sample radius on the ratio of pressure fluctuation amplitude.

firing chamber, pressure distribution within the porous ceramic body as a function of time can be calculated by using the limited permeability model. Figure 3a shows results calculated for the case where the total pressure inside the firing chamber is fluctuated over 1 atm in amplitude and 1 Hz in frequency, the thickness of the sample is 0.6 cm, and the permeability of the gas is about 1.23 x 10^{-11} cm^2, which corresponds to a ceramic powder diameter of 1 μm. The distance from one curve to the next adjacent one corresponds to a time period of 1/10 of an oscillating cycle, and the total of all ten curves represents one entire cycle. From this plot, it can be seen that there exists a significant attenuation and timing delay from the surface to the center of the body, representing the limited gas permeability.

As shown in Equation 39, if the ceramic powder diameter increases by one order, for example from 1 to 10 μm, the gas permeability will increase by two orders, from 1.23 x 10^{-11} cm to 1.23 x 10^{-9} cm (porosities are the same at 0.42). Figure 3b shows that for this higher gas permeability, 1.23 x 10^{-9} cm, the pressure distribution becomes much more uniform and the viscous effect can be neglected. Figure 4 summarizes the effect of gas permeability and powder size on the ratio of pressure fluctuation amplitude (the ratio of amplitude at the center of the body to that at the surface of the body). Furthermore, decreasing the thickness of the ceramic body can also induce a change of the ceramic body from a low permeability solid to a high permeability solid (Fig. 5).

Since for limited permeability solids the benefit of pressure fluctuation on carbon removal cannot be very large, and also since our calculation shows that for a porous ceramic body with a powder size of 1 μm and a radius smaller than 0.3 cm, a high permeability model is

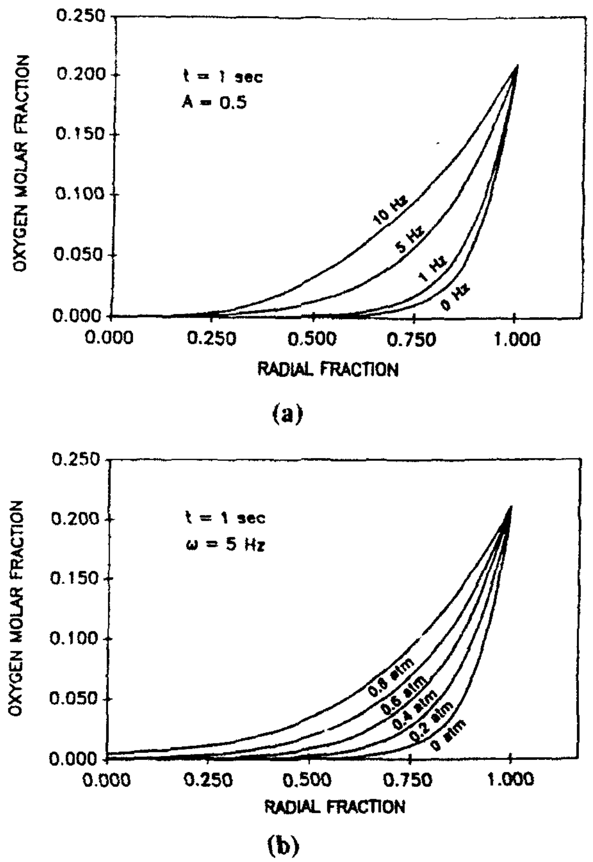

(a)

(b)

Fig. 6. The effect of oscillating (a) frequency and (b) amplitude on oxygen molar fraction inside pores at 600°C, air flow. High permeability model is applied.

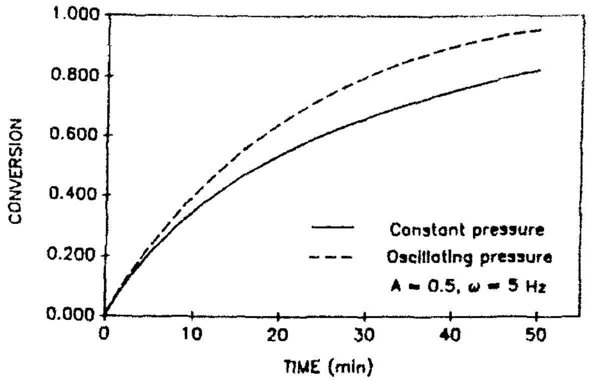

Fig. 7. Conversion vs. time for a ceramic pellet under both constant pressure and oscillating pressure (0.5 amplitude, 5 Hz frequency), at 600°C, air flow. High permeability model is applied.

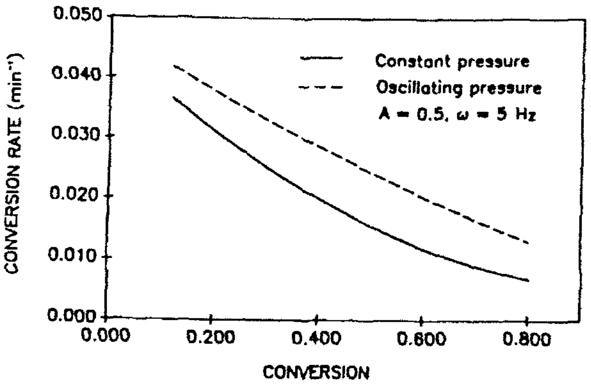

Fig. 8. Relationships between the rate of conversion and the fractional conversion under both constant pressure and pressure fluctuation (0.5 atm amplitude, 5 Hz frequency), at 600°C, air flow. High permeability model is applied.

applicable (Fig. 5), only the high permeability model was considered in the present study.

As the total pressure outside a ceramic body oscillates, an oscillating bulk flow can be generated within the porous structure. The oxygen molar fraction distribution across the radius of the ceramic body will thus be affected by a combination of convection, diffusion, and chemical reaction. Figures 6a and b show the effect of oscillating frequency and amplitude on the oxygen molar fraction inside a porous structure. In Figure 6a, the calculation was based on a time period of 1 s from the start of the reaction, an oscillating amplitude of 0.5 atm (from 0.5 atm to 1.5 atm), and a variation in frequency from 0 Hz (constant pressure) to 10 Hz. It is clear that more frequent pressure cycling accelerates oxygen penetration into the pellet. Similarly, Figure 6b shows the effect of oscillating amplitude. Increasing the oscillating amplitude enhances oxygen penetration due to the larger convective flow inside the porous structure.

To quantitatively study the effect of pressure fluctuation, carbon conversion for both fluctuating and constant pressure conditions as a function of time was plotted in Figure 7. The total pressure was oscillated at an amplitude of 0.5 atm and a frequency of 5 Hz over a time period of about 50 min from the start of the reaction. The extent of conversion under constant pressure was 0.82, while under oscillating pressure it was 0.96: an improvement of about 17%. It should be pointed out that additional improvement could be expected when the reduction of external resistance to mass transfer [3] and the increase of effective gas diffusivity [4] are taken into account..

The rate of conversion was calculated by numerically differentiating the conversion curve. In Figure 8, the rate of conversion calculated from Figure 7 was plotted against time, indicating pressure fluctuation accelerates

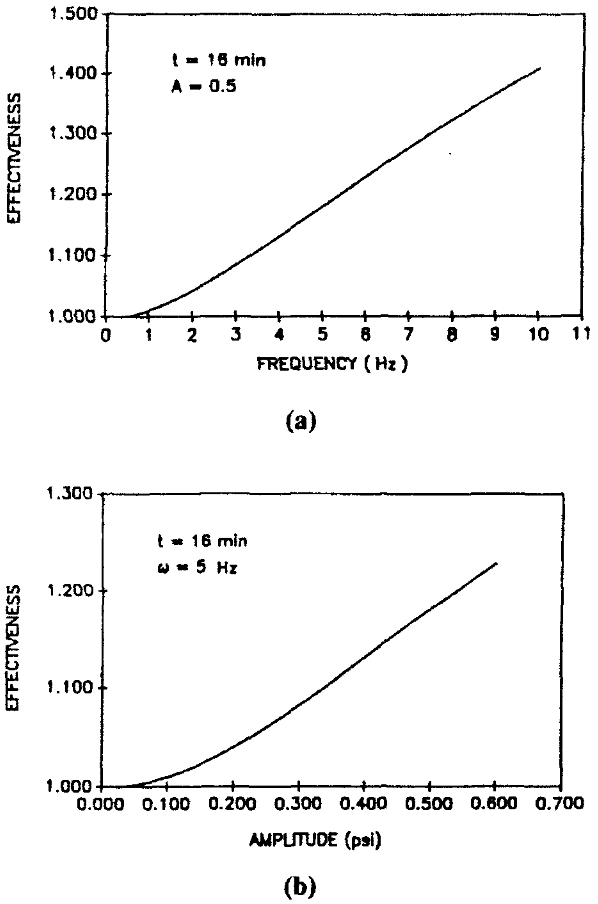

(a)

(b)

Fig 9. The effectiveness on conversion improvement as a function of (a) frequency and (b) amplitude at 600°C, air flow, and 16 min. High permeability model is applied.

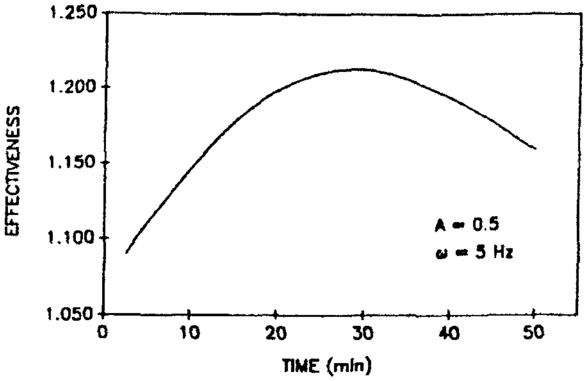

Fig. 10. The relationship between effectiveness of conversion improvement and the reaction time period at 600°C, air flow. High permeability model is applied.

the conversion rate over the entire conversion process.

Figures 9a and b show the effectiveness of pressure fluctuation (the ratio of conversion under pressure fluctuation to that under constant pressure) as a function of frequency (Fig. 9a) and as a function of amplitude (Fig. 9b) at 600°C over a period of about 16 min from the start of the reaction. It can be seen that much greater improvement in conversion can be obtained at higher frequency and amplitude.

In Figure 10, the effectiveness of pressure fluctuation calculated from Figure 7 was plotted against time, indicating that under pressure fluctuation, improvement in conversion can be obtained at all stages of the reaction, with a maximum value after some reaction has taken place. The existence of a maximum effectiveness value is probably due to the fact that as the moving front of the "shell model" shifts toward the center of the ceramic body, the limit on internal mass transfer increases, which results in an enhancement of effectiveness; at the same time, however, the convective gas flow velocity inside pores decreases (convection equals zero at the center of the porous structure), which abates the effect of pressure fluctuation. The combination of these two effects results in a maximum on the effectiveness curve.

CONCLUSIONS

A theoretical analysis of the effect of pressure fluctuation on removal of carbon residue from a porous ceramic body has been conducted. The following results were obtained from this theoretical study:

1) For the case of carbon removal under air flow, the intrinsic reaction dominates when the temperature is below 530°C, and the internal mass transfer dominates when the temperature is above 600°C.
2) A high permeability model is applicable for samples with pellet radius smaller than 0.3 cm and powder size of 1 μm.
3) Pressure fluctuation increases the oxygen penetration within the porous ceramic body. Increasing the frequency and amplitude promotes this effect.
4) A significant improvement in carbon removal can be achieved through pressure fluctuation. For example, an oscillating pressure of 0.5 atm in amplitude and 5 Hz in frequency can improve conversion by at least 17% over 50 min.
5) With increasing oscillating frequency and amplitude, the effectiveness of carbon removal will increase.
6) Under pressure fluctuation, improvements in conversion can be obtained at all stages of the reaction, with a maximum value after some reaction has taken place.

NOTATIONS

A: dimensionless amplitude of oscillation

A_E: activation energy (kcal/mol)

A_s: surface area of the ceramic powder (cm^2/g)

C: total concentration of gaseous species (mol/cm^3)

C_i: concentration of gaseous species i (mol/cm^3)

$C^0_{wt\%}$: initial weight percent of carbon inside the pellet

d: powder diameter (cm)

D_i: molecular diffusivity of species i (cm^2/s)

D_{ei}: effective diffusivity of species i (cm^2/s)

H: frequency factor (cm/s)

k_{rea}: reaction rate constant (cm/s)

K_{rea}: modified reaction rate constant (s^{-1})

M_i: molecular weight of species i (g/mol)

n_i^0: initial concentration of species i (mol/cm^3)

P: total pressure (atm)

P_0: average pressure (atm)

r: radial position (cm)

r_p: radius of pellet (cm)

R: universal gas constant

S_i^0: initial interstitial area of carbon per unit volume of pellet (cm^{-1})

t: time (s)

T: temperature (K)

v_i: rate of consumption of species i (mol/cm^3-s)

V: convective gas flow velocity inside porous body (cm/s)

X_i: mole fraction of gas species i

Y_C: mole fraction of carbon

ε: porosity

ε^0: initial porosity

κ: gas permeability (cm^2)

μ: gas viscosity (atm-s)

ρ: density of ceramic powder (g/cm^3)

σ: Lennard-Jones force constant (Å)

τ: tortuosity

ϕ: conversion

ψ: atomic volume of carbon (cm^3/mol)

ω: frequency of oscillation (Hz)

Ω_D: collision integral

REFERENCES

1. S. Strijbos, "Burning Out of Carbonaceous Residue from a Porous Body," *Chem. Eng. Sci.*, **28** [1] 205-13 (1973).
2. P.B. Weisz and R.D. Goodwin, "Combustion of Carbonaceous Deposits with Porous Catalyst Particles I. Diffusion-controlled Kinetics," *J. Catal.*, **2** [5] 397-404 (1963).
3. M.H.I. Baird, "Some Observations on Pulsed Flow Past a Cylinder," *Chem. Eng. Sci.*, **22** 1056-57 (1967).
4. L.H. Dill and H. Brenner, "Dispersion Resulting from Flow Through Spatially Periodic Media III. Time-periodic Processes," *PCH PhysicoChem., Hydrodyn.*, **4** [3] 279-302 (1983).
5. J.W. Hamer and D.E. Cormack, "Influence of Oscillating External Pressure on Gas-Phase Reaction in Porous Catalysts," *Chem. Eng. Sci.*, **33** 935-44 (1978).
6. H.Y. Sohn and P.C. Chaubal, "Rate Enhancement of the Gaseous Reduction of Iron Oxide Pellets by Pressure Cycling," *Trans. Iron Steel Inst. Jpn.*, **24** 387 (1984).
7. D.R. Gaskell, Introduction to Metallurgical Thermodynamics; p. 287. Hemisphere Publishing Corporation, New York, NY, 1981.
8. H.S. Mickley, J.W. Nestor, J. Gould, and L.A. Gould, "A Kinetic Study of the Regeneration of a Dehydrogenation Catalyst," *Can. J. Chem. Eng.*, April 61-68 (1965).
9. R.M. German, "Theory of Thermal Debinding," *The Int. J. Powder Metall.*, **23** 4 237-45 (1987).
10. R.B. Bird, W.E. Stewart, and E.N. Lightfoot, Transport Phenomena; pp. 511, 557. John Wiley and Sons, Inc., New York, NY, 1960.
11. C.N. Satterfield, Mass Transfer in Heterogeneous Catalysis; pp. 33-40. Robert E. Krieger Publishing Company, Huntington, New York, NY, 1981.

12. E. Wicke, Fifth Symposium on Combustion; pp. 245-52. Reinhold, New York, NY, 1955.

13. J. Szekely, J.W. Evans, and H.Y. Sohn, Gas Solid Reactions; p. 28. Academic Press, New York, NY, 1976.

14. L. Lapidus Digital Computation for Chemical Engineer; pp. 131-77 McGraw-Hill, Book Company, Inc., New York, NY, 1962.

SECTION 24

EFFECT OF PRESSURE FLUCTUATION ON REMOVAL OF CARBON RESIDUE: PART II. EXPERIMENTAL VERIFICATION

Chun Dong

ABSTRACT

In this experimental study of the effect of pressure fluctuation on the removal of carbon residue, colloid-pressed Al_2O_3 samples containing initially 5 to 17 wt% carbon were isothermally oxidized with oxygen under both constant and oscillating pressure. Pressure fluctuation was generated by a piston oscillated in a firing tube and driven by an electric motor. It was demonstrated that pressure fluctuation could indeed accelerate the oxidation rate of carbon in porous ceramic bodies by overcoming both the internal and external mass transfer resistance. As the oxidation progressed, the improvement in carbon conversion usually peaked at a maximum value such as 40% and then started to drop. Most of the experimental results agree well with previous theoretical calculations [1], and the carbon removal rate was found to depend upon temperature, oxygen flow rate, ceramic body pore size, initial carbon concentration, sample thickness, and both the frequency and amplitude of the oscillating pressure.

INTRODUCTION

In our earlier study [1], the enhancing effect of pressure fluctuation on the removal of carbon residue was proven theoretically using a mathematical model. The numerical calculations showed that a much higher carbon removal rate could be obtained by applying pressure fluctuation. These calculations, however, were based on many assumptions and simplifications; a realistic system will be much more complicated than what we specified in the mathematical model. Therefore, as a continuation of the theoretical study, a careful experimental examination was made of the effect of pressure fluctuation on carbon removal.

In the field of reduction of iron ore pellets, several researchers have made experimental studies of the pressure fluctuation method to increase the reduction rate. Schenck and Cloth [2] reported that the overall reduction rate of iron ores could be accelerated significantly by oscillating the total pressure of the gas in the frequency range 0.1 to 430,000 Hz. Taniguchi et al. [3] discovered this same acceleration effect on iron ore reduction by pulsating the flow of hydrogen in the frequency range 3.3 to 43.3 Hz and amplitude range 250 to 300 mmAq (0.36 to 0.44 psi). Similar experimental work was also done by other researchers [4-7], and although they all found that pressure cycling favorably affects mass transfer in porous materials, the following questions still exist:

1) The mechanisms upon which the acceleration effect of pressure fluctuation was based were not fully understood. Although there is no doubt pressure fluctuation can accelerate the mass transfer process in the gas film, the acceleration effect on the internal mass transfer is still a conjecture;

2) The influence of such variables as frequency, amplitude, temperature, and flow rate on the effect of pressure fluctuation was not entirely clear. Taniguchi's results [3] showed that the effect of pressure oscillation tends to decrease when the temperature is increased to 700-800°C. The frequency dependence, however, was not clearly recognized; and

3) The relationship between the effect of pressure fluctuation and the characteristics of the porous structure, such as pore size and porosity, has not been fully studied. In all the papers reviewed, none reported information on the pore size of the tested sample; only the porosity of the sample was stated. The pore size of a porous structure is a very important factor because it directly reflects the permeability of a gas and the diffusion mechanism during the reaction.

The objectives of this study were three-fold. The first was to demonstrate experimentally the acceleration effect

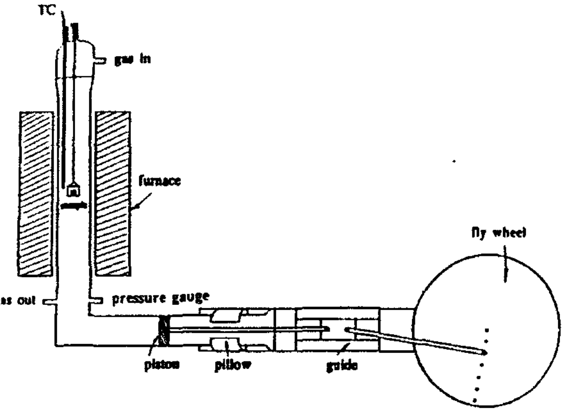

Fig. 1. The experimental setup.

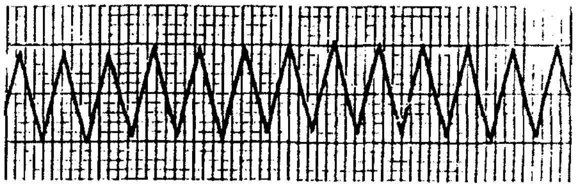

Fig. 2. Characterization of pressure waves (1 Hz frequency, 2 psi amplitude) inside firing tube.

of pressure fluctuation on carbon oxidation in ceramics. Secondly, an attempt was made to investigate the influencing variables on the effect of pressure fluctuation, such as temperature, oxygen flow rate, characteristics of the porous body, and the frequency and amplitude of oscillation. The third objective was to compare the experimental results with the theoretical calculations made previously and explain any differences between the two approaches.

EXPERIMENTAL SETUP

Figure 1 shows the experimental setup. The firing tube was set vertically so that a uniform flow pattern around a cylindrical sample hanging in the tube could be applied during tests. Pressure fluctuation was generated by a motor-driven oscillating piston traveling in the horizontal part of the furnace. Gas flow during the experiment was controlled through the gas inlet and outlet on the vertical part of the furnace under both pressure conditions. To prevent the opposite flow of gas during pressure fluctuation, two check valves allowing only unidirectional gas flow were added on both the gas inlet and gas outlet. Besides the thermocouple used for temperature control, an additional thermocouple was placed close to the sample in order to record the temperature change continuously. The amplitude of the pressure oscillation was adjusted from the connecting point on the fly wheel, and the frequency of the pressure oscillation was varied by a speed controller. The maximum amplitude of pressure oscillation achievable with this setup was about 6 psi; the oscillating frequency was varied from 0 to 5 Hz. The pressure wave pattern inside the furnace was measured by a pressure transducer connected to the furnace and was recorded by a chart recorder. As shown in Figure 2, the pressure wave (1 Hz frequency, 2 psi amplitude) inside the firing tube was like a saw wave. Since the attenuation of the oscillating pressure along the length of the furnace was found to be negligible, the pressure oscillation could be considered uniform throughout the furnace.

EXPERIMENTAL PROCEDURE

To demonstrate more clearly the effect of pressure fluctuation on the burnout of carbon residue, samples containing a significant amount of carbonaceous material are desirable. For the present study, samples were colloid-pressed based on a technique developed by Moffatt [8]: 40 g Al_2O_3 powder (AKP-20, Sumitomo Chemical Co., Ltd., Osaka, Japan) and an amount varying between 2 and 8 g of carbon powder (Sterling R, Cabot Corp., Boston, MA) were added to 400 ml of a 0.333 wt% solution of polyvinyl alcohol in water. The pH was adjusted to 2-3 with concentrated nitric acid. The slurry was then ultrasonically agitated for 8 min and flocculated with 500 ml acetone; the floccs were then filtered and consolidated in a colloidal press. The resulting samples were cylindrical in geometry with a 0.6-cm radius and a 2-cm height. The samples were then dried at 60-80°C and the volatile products were removed by heating at 2°C/min to 600°C under an argon flow. The weight percent of initial carbon left in the sample was measured by thermal gravimetric analysis (TGA), and the pore size and porosity of the ceramic body were determined by mercury porosimetry.

For simplification, the study of the burnout rate of carbon residue was conducted under isothermal temperatures with oxygen flow. Pure oxygen was used instead of air or other gases as the reactant gas to reduce the experimental time period. If carbon removal indeed proceeds more favorably under conditions of oscillating pressure with a pure oxygen flow, this concept could be tested using a gas flow with partial oxygen molar fraction.

The experimental procedure involved hanging the colloid-pressed sample vertically in the testing chamber and subjecting it to a controlled flow of argon while the temperature was increased to the experimental tempera-

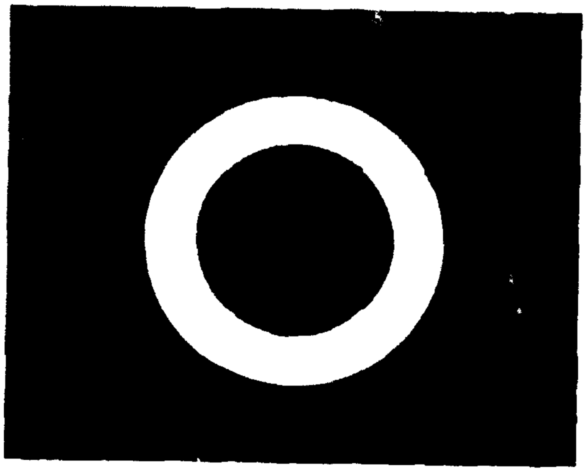

Fig. 3. *Cross section of a colloid-pressed sample subjected to a partial carbon removal at 500°C under oxygen flow ("shell progressive reaction").*

ture. After thermal equilibrium was reached, the argon flow was replaced by an oxygen flow for 1 min to allow oxygen to fill up the entire furnace, and then the system was operated under either oscillating pressure or constant pressure with equivalent mean oxygen flow rate and mean pressure (1 atm). After a specified amount of time, the oxygen flow was replaced by an argon flow, and the furnace was then cooled down from the experimental temperature.

The effect of pressure fluctuation was determined by comparing the carbon conversion rate of two samples, one reacted under pressure fluctuation and the other under constant pressure. The conversion rate can be determined by two different methods: 1) direct observation of a sample cross-section, which must be done carefully because the unsintered sample is not very strong, and 2) measurement of sample weights before and after each run with an electrical balance with a sensitivity of 1.0 mg (<1% of total weight loss). The first method gives a visual basis for qualitative analysis, while the second method provides data for quantitative study; the two methods complement each other.

RESULTS AND DISCUSSION

Internal Mass Transfer-Limited Temperature Region

Since our proposed theory of pressure fluctuation was based on the assumption that internal mass transfer is the controlling step, the temperature region where the internal mass transfer dominates carbon removal was first determined under conditions of constant pressure. The cylindrical samples, which were initially black, were subjected to isothermal partial carbon removal at various

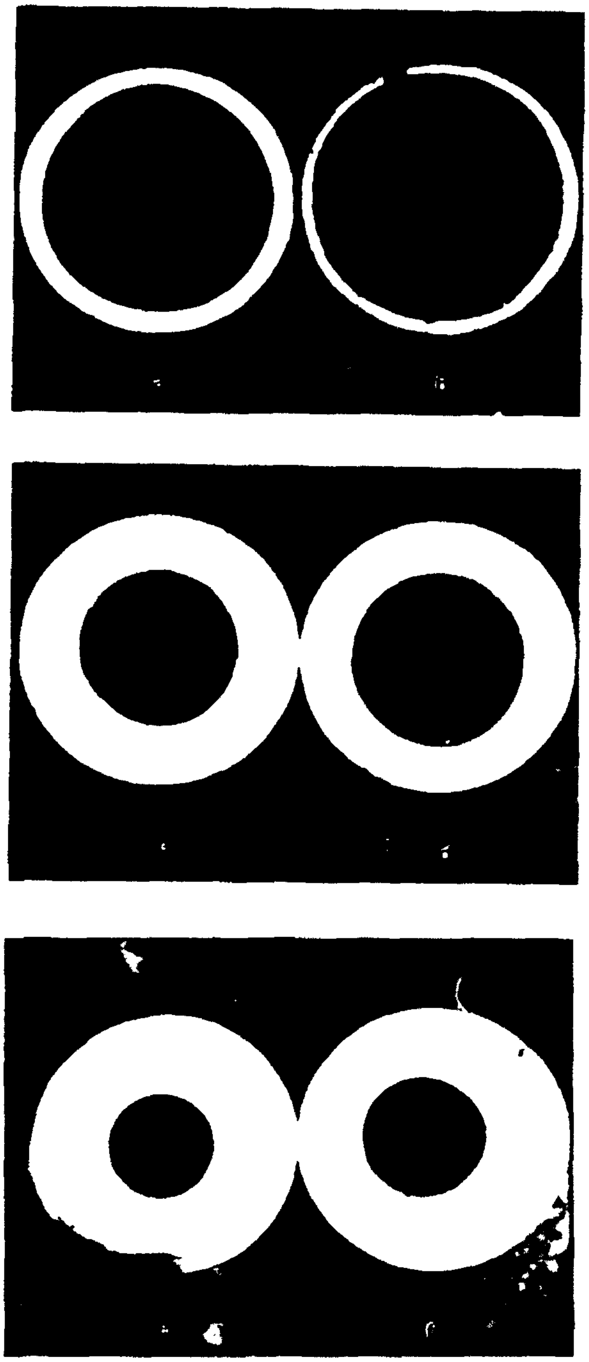

Fig. 4. *Comparison of core shrinking rate of colloid-pressed samples containing initially 17 wt% carbon under both oscillating pressure (2 Hz frequency, 3 psi amplitude) and constant pressure at 600°C and a 3 cfh oxygen flow: (a) oscillating pressure, 4 min; (b) constant pressure, 4 min; (c) oscillating pressure, 7 min; (d) constant pressure, 7 min; (e) oscillating pressure, 10 min; (f) constant pressure, 10 min.*

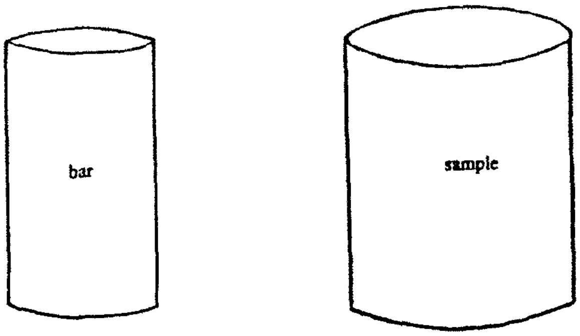

Fig. 5. The cylindrical sample and bar as set vertically near each other (about 0.3 cm separation) inside the furnace with a 3 cf/h oxygen flow (side view).

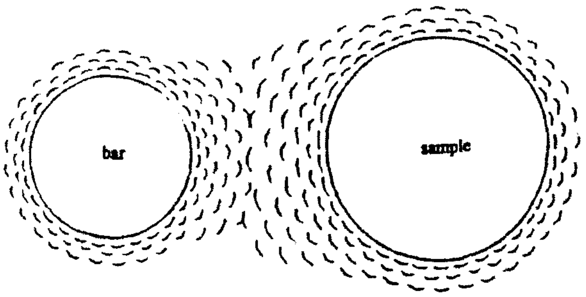

Fig. 6. Gas flow pattern around the sample under constant pressure (top view).

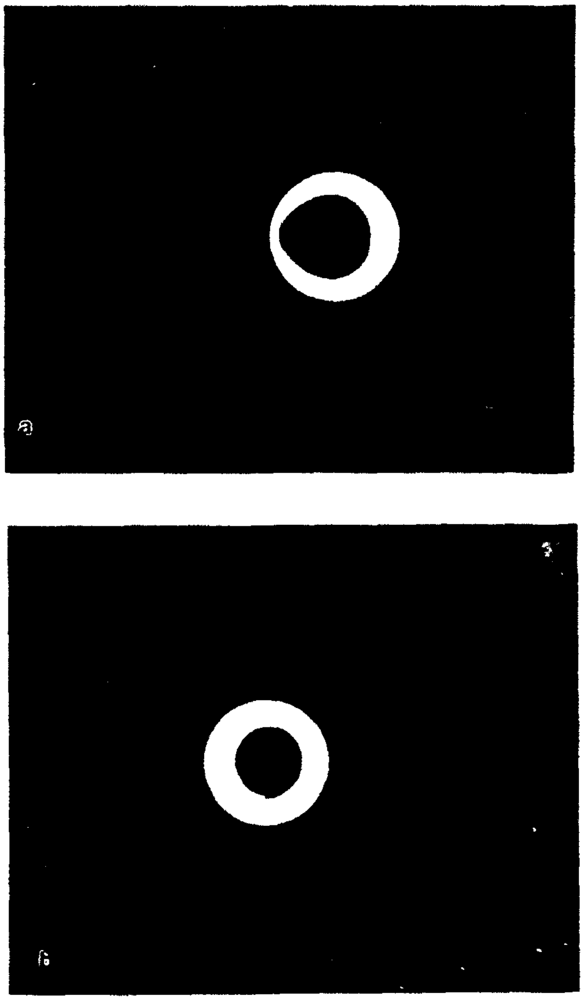

Fig. 7. Cross section of the sample partially oxidized at 600°C under (a) constant pressure and (b) oscillating pressure (2 Hz frequency, 2 psi amplitude).

temperatures with the same oxygen flow rate, and then cut apart to observe the cross sections. Above 500°C, cross sections of samples containing initially 17 wt% carbon showed evidence of a "shell progressive reaction" (Fig. 3) corresponding to the internal mass transfer-limited region; below 450°C, however, the removal of carbon was uniform throughout the entire sample, representing the "intrinsic" region of chemical kinetics. It should be pointed out that this result differs from that of our earlier experiment [1], which was carried out under an air flow. This is probably due to the fact that the reaction order of carbon oxidation is a function of oxygen partial pressure, as predicted by Suuberg et al. [9].

Comparison of Carbon Removal under Two Pressure Conditions

To gain a general impression of the difference in carbon removal rate between the two pressure models, an examination of sample cross sections was first conducted. As shown in Figure 4, samples containing initially 17 wt% carbon were oxidized at 600°C and an oxygen flow of 3 cf/h under the two pressure models. The oscillating pressure model applied was 2 Hz in frequency and 4 psi in amplitude. The photos indicate the acceleration effect of pressure fluctuation on carbon oxidation is significant, especially in the earlier stages of the reaction.

It was expected that pressure fluctuation could overcome such causes of external resistance to mass transfer as a stationary gas film surrounding the sample. The following experiment was performed to test this effect. A cylindrical sample and a bar were set vertically near each other (about 0.3-cm separation) inside the furnace with an oxygen flow of 3 cf/h (Fig. 5). Under constant pressure, the stable boundary layer in the region between the sample and the bar was thicker than in other places (Fig. 6). After partial carbon removal at 600°C, a cross section of the sample showed that the oxidation rate was the slowest

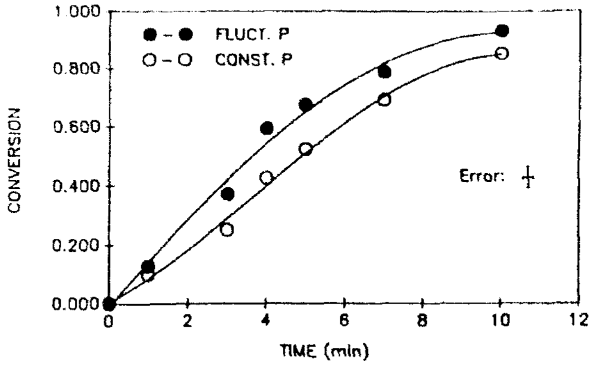

Fig. 8. Comparison of conversion versus time under both constant pressure and oscillating pressure (2 Hz frequency, 4 psi amplitude). The samples, which contained initially 5 wt% carbon, were oxidized at 550°C with a 3 cfh oxygen flow.

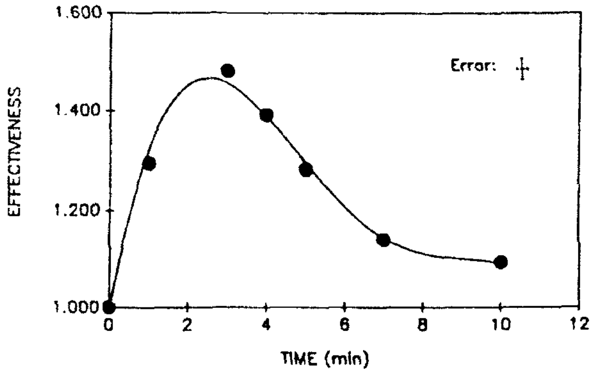

Fig. 9. Effectiveness of conversion improvement versus time calculated from Fig. 8.

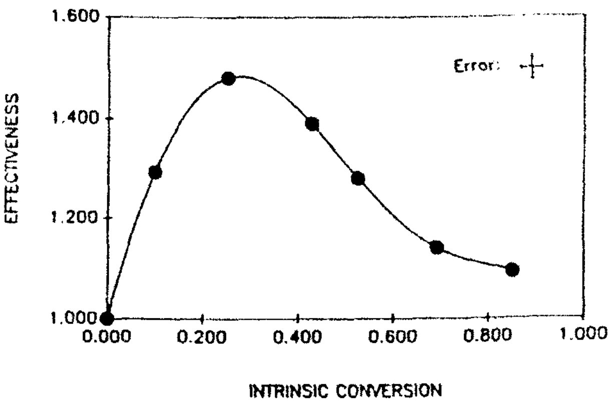

Fig. 10. Effectiveness of conversion improvement versus intrinsic conversion calculated from Fig. 8.

on the side of the sample facing the bar (Fig. 7a). If a pressure fluctuation of 2 Hz in frequency and 2 psi in amplitude was applied instead of constant pressure, however, the cross-section showed a symmetric carbon removal rate (Fig. 7b).

By using the method of weight-loss measurement, the conversion of carbon from a tested sample can be calculated. Figure 8 is a plot of conversion versus time under the two pressure conditions. The samples containing initially 5 wt% carbon were oxidized at 550°C under an oxygen flow of 3 cf/h. The oscillating pressure applied was 2 Hz in frequency and 4 psi in amplitude. Results indicated conversion of carbon under oscillating pressure was always greater than that under constant pressure, which is consistent with the visual observations.

The effectiveness of carbon conversion as a ratio of conversion under pressure fluctuation to that under constant pressure can be calculated from the above results. Figure 9 shows that the effectiveness values are all greater than one over the entire reaction period. Furthermore, as the reaction progresses, the effectiveness peaks at a maximum value and then starts to drop significantly. This behavior agrees with our previous theoretical calculations [1], and can be accounted for by the influence of two opposing phenomena: 1) as the reaction interface moves inward, the resistance to internal mass transfer increases and thus the potential of pressure fluctuation increases; and 2) toward the center of the ceramic body, the convective velocity decreases (the velocity equals zero at the center of the body), and therefore the effect of pressure fluctuation is abated. These phenomena can be demonstrated further by plotting the effectiveness versus the intrinsic conversion (conversion under constant pressure), as shown in Figure 10. It can be seen that the maximum effectiveness corresponds to a conversion level of 0.3. This value is much lower than the theoretically calculated result [1], in which the conversion level was about 0.6. This is probably due to the fact that the experimental samples used were not truly high permeability solids, as assumed in the mathematical model, and pressure fluctuation was thus attenuated with movement away from the surface and toward the interior of the porous structure. As a result, the effect of pressure fluctuation was reduced.

Factors Influencing Carbon Removal

Temperature

As described earlier, the internal mass transfer-limited reaction or "shell progressive reaction" occurs above 500°C under conditions of oxygen flow. To study the effect of temperature on pressure fluctuation, carbon

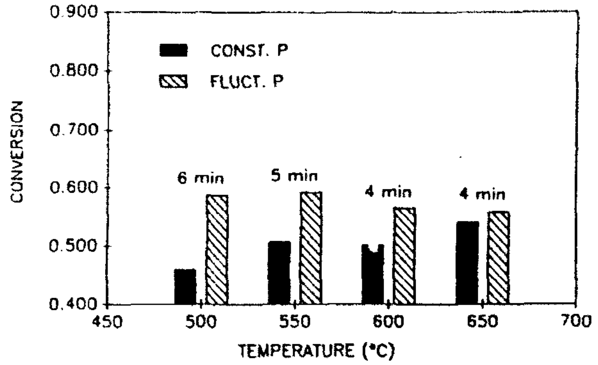

Fig. 11. Conversion under constant pressure and oscillating pressure (2 Hz frequency, 4 psi amplitude). The samples, which contained initially 17 wt% carbon, were oxidized with a 3 cf/h oxygen flow.

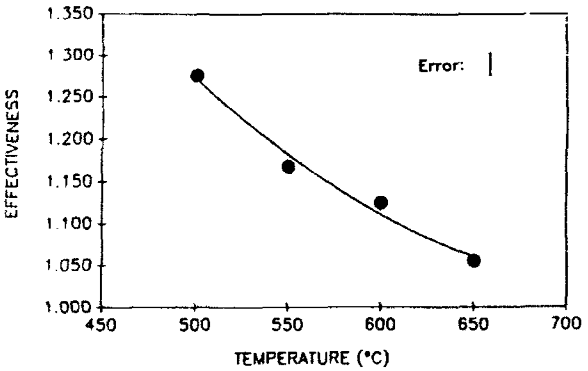

Fig. 12. Effectiveness of conversion improvement as a function of temperature, calculated from Fig, 11.

removal experiments under the two pressure conditions were conducted at different temperatures above 500°C. It was found that for the same applied oscillating frequency and amplitude, the effect of pressure fluctuation decreased with increasing temperature. As shown in Figure 11, carbon conversion under both pressure fluctuation and constant pressure was carried out at four temperatures, keeping conversions under oscillating pressure the same for all testing temperatures by adjusting the reaction time (because conversion rate is a function of conversion). The difference in conversion between the two pressure conditions diminishes as the temperature rises. Therefore, effectiveness as a ratio of the conversion under pressure fluctuation to that under constant pressure follows the same tendency (Fig. 12). For instance, at 500°C the effectiveness is 1.28, while at 650°C it is only 1.03. This result is in agreement with that obtained by Taniguchi et al. [3] and may be explained as follows. Mass transfer under pressure fluctuation is composed of both natural

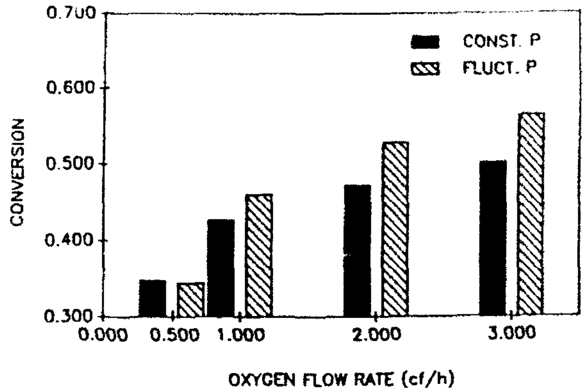

Fig. 13. Conversion under both constant pressure and oscillating pressure (2 Hz frequency, 4 psi amplitude). The samples, which contained initially 17 wt% carbon, were oxidized at 600°C for 4 min.

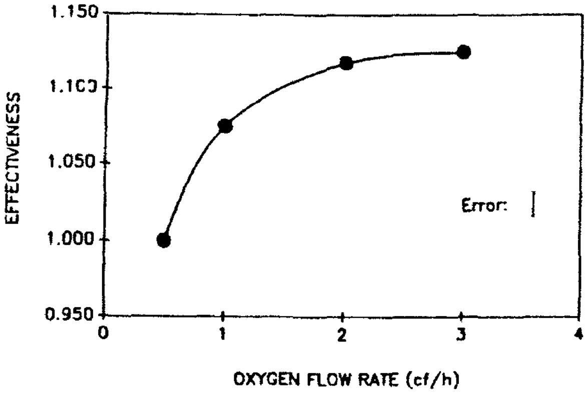

Fig. 14. Effectiveness of conversion improvement as a function of oxygen flow rate, calculated from Fig. 13.

diffusion and pulsating gas flow inside the pores. As the temperature increases, the natural diffusion factor gets larger and closer to that of the pulsating flow, and this in turn reduces the effect of pressure fluctuation.

Oxygen Flow Rate

Another important variable to be examined was the oxygen flow rate. Based on the reaction rate constant determined in the mathematical model [1], a simple calculation shows that at 600°C, the oxygen flow rate necessary to compensate for the consumption due to carbon oxidation is about 2 cf/h. This calculation was verified by the following experiment.

Samples were oxidized for the same amount of time under both oscillating pressure and constant pressure with a varied oxygen flow rate of 0.5 to 4 cf/h. As shown in Figure 13, with increasing flow rate, conversion as well

Table 1. Pore Size and Porosity of Tested Samples.

	Powder Size	Pore Size	Porosity
Group 1	0.5 µm	0.12 µm	0.39
Group 2	<0.3 µm	0.065 µm	0.41

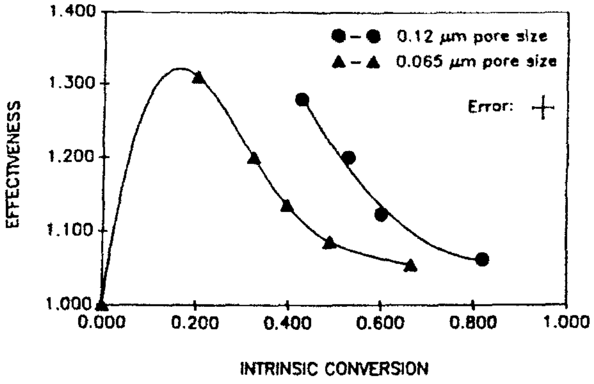

Fig. 15. Comparison of effectiveness versus intrinsic conversion for two groups of samples with pore sizes of 0.12 µm and 0.065 µm which were oxidized at 550°C with a 3 cf/h oxygen flow under both constant pressure and oscillating pressure (2 Hz frequency, 4 psi amplitude).

as the difference in conversion are promoted. The influence of flow rate on the effectiveness of pressure fluctuation is presented in Figure 14. At a lower oxygen flow rate of 0.5 cf/h, the value of the effectiveness is only 1.0. This may be due to the fact that at the lower oxygen flow rate, the reaction is actually limited by external mass supply and thus pressure fluctuation cannot demonstrate any benefit to the carbon conversion. As the oxygen flow rate increases to more than 2 cf/h, the effectiveness reaches a stable maximum value of 1.126. This means that above this point, internal mass transfer is the wholly dominating step in the reaction, and therefore pressure fluctuation achieves its maximum potential. The critical flow rate of 2 cf/h is exactly the same as the calculated value. Similar results were also obtained at higher temperatures with a large critical oxygen flow rate.

Pore Size

The next study was focused on the relationship between the effect of pressure fluctuation and the pore size of the ceramic body. Two groups of samples were prepared for this study. In the first group, the samples were made of Sumitomo alumina with a powder size of 0.5 µm combined with 9 wt% initial carbon (about 0.1 µm in powder size). The samples in the second group, however, were composed of classified alumina with a powder size of less than 0.3 µm combined with the same amount of initial carbon, 9 wt%. Mercury porosimetry measurements were used to determine the corresponding pore size and porosity of the sample (Table 1). These two groups of samples were oxidized at 550°C under both constant pressure and oscillating pressure (2 Hz frequency, 4 psi amplitude) for various time periods. The effectiveness versus intrinsic conversion for both groups of samples was obtained and is plotted in Figure 15. It shows that the group of samples with larger pore size had higher effectiveness values. This is a reasonable conclusion since the viscous effect of gas will be less important for samples having larger pore sizes.

Table 2. Initial Carbon Content of Tested Samples.

	Powder Size	Initial Carbon	Pore Size	Porosity
Group 1	0.5 µm	5 wt%	0.15 µm	0.36
Group 2	0.5 µm	9 wt%	0.12 µm	0.39
Group 3	0.5 µm	17 wt%	0.11 µm	0.39

Initial Carbon Concentration

To study the effect of initial carbon concentration on pressure fluctuation, three groups of samples were prepared with initial carbon concentrations of 5, 9, and 17 wt%, respectively. The corresponding pore size and porosity of the porous structures were measured and are summarized in Table 2. These three groups of samples were subjected to partial carbon removal at 550°C with a 3 cf/h oxygen flow, under both constant pressure and oscillating pressure (2 Hz frequency, 4 psi amplitude). The effectiveness values under each intrinsic conversion level were measured and calculated. Figure 16 compares these values for the three different levels of initial carbon content. Results indicate a higher effectiveness value is associated with samples containing lower amounts of initial carbon. There are two possible explanations for this phenomenon: (1) convective gas flow through pores generated by pressure fluctuation will increase the dispersion of oxygen [10, 11]; this increase in oxygen dispersion will be more beneficial for samples with lower initial carbon, and therefore the effect of pressure fluctuation is more significant and (2) with decreasing initial carbon content, the pore size of the porous structure is enlarged (Table 2), and thus the resistance to convective gas flow through pores will be reduced (the same as pore size effect).

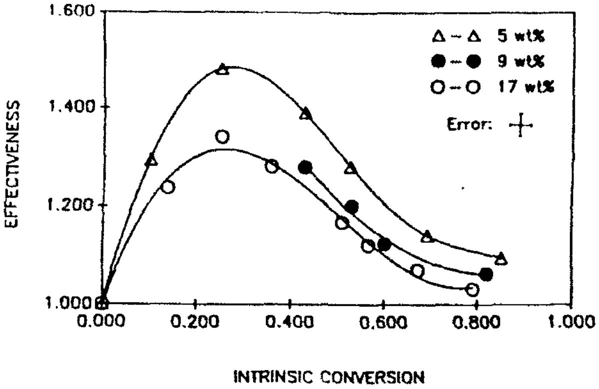

Fig. 16. Comparison of effectiveness versus intrinsic conversion for three groups of samples containing initially 5, 9, and 17 wt% carbon which were oxidized at 550°C under a 3 cf/h oxygen flow under both constant pressure and oscillating pressure (2 Hz frequency, 4 psi amplitude).

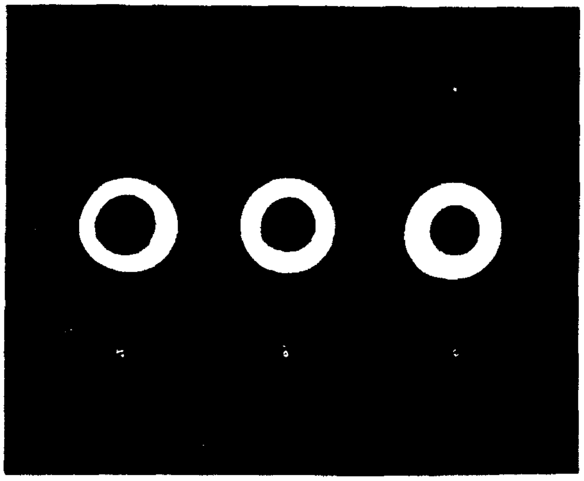

Fig. 17. Comparison of cross sections of colloid-pressed samples tested at 600°C under (a) constant pressure; (b) oscillating pressure of 2 Hz in frequency and 2 psi in amplitude; and (c) oscillating pressure of 3 Hz in frequency and 2 psi in amplitude.

Frequency and Amplitude

The first study of the relationship between the effect of pressure fluctuation and the oscillating frequency was done in a preliminary experiment, which gave a direct observation of the sample cross sections after partial carbon removal under three oscillating frequencies. Results shown in Figure 17 indicate the carbon removal rate indeed increases as the oscillating frequency increases from 0 Hz (constant pressure) to 3 Hz with same oscillating amplitude of 2 psi.

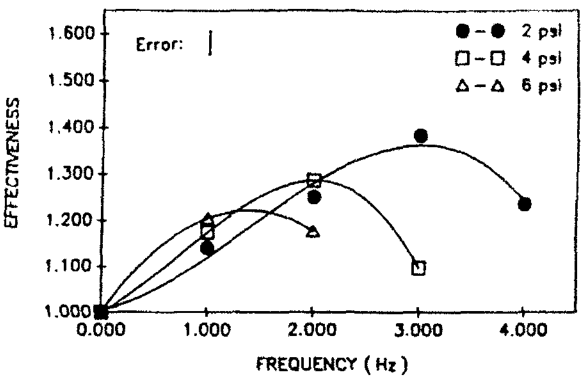

Fig. 18. Comparison of effectiveness versus frequency for amplitudes of 2, 4, and 6 psi. Samples containing initially 17 wt% carbon were oxidized at 500°C under a 3 cf/h oxygen flow for 5 min.

Further study was conducted using weight-loss measurements to investigate the effect of both frequency and amplitude on carbon removal under conditions of pressure fluctuation. Samples containing initially 17 wt% carbon were reacted at 500°C with oxygen flow of 3 cf/h for a time period of 5 min, under both pressure conditions. In the oscillating pressure model, the amplitudes exerted varied from 2 to 6 psi, and the frequencies ranged from 0.5 to 4 Hz. Results of effectiveness versus frequency are summarized in Figure 18. For each amplitude applied, the relationship between effectiveness and frequency is not monotonous, having an optimum frequency corresponding to a maximum effectiveness; the lower the amplitude exerted, the higher this optimum frequency will be. This phenomenon may be explained as follows. At higher frequencies and amplitudes, the finite gas permeability of the ceramic body may limit response to outside pressure oscillations, and the pressure wave inside the porous body may be attenuated. Thus, the effectiveness of pressure fluctuation on carbon conversion tends to decrease. This result does not agree completely with our theoretical calculations, because there we made the assumption that the sample was a high permeability model for all the frequencies applied.

Sample Thickness

For the samples used in our study, the following method was developed to investigate the change from a high permeability model to a low permeability model as the sample thickness increased. As shown in Figure 19, a cylindrical sample (0.12 μm pore size, 0.39 porosity) was installed into an adapter, with one end surface of the sample facing a transducer and the other connected to the firing tube. The circumferential surface of the sample

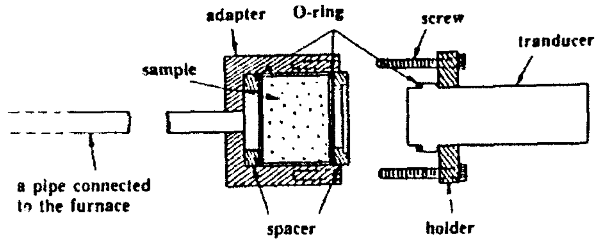

Fig. 19. Cross section of an adapter used to measure the attenuation of pressure fluctuation across the thickness of a colloid-pressed sample.

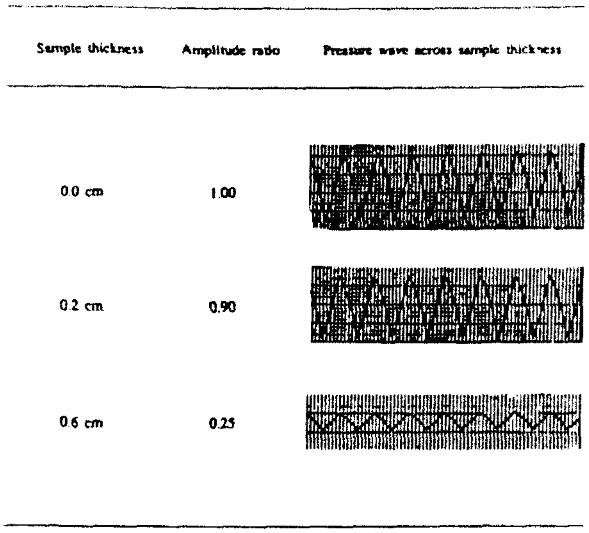

Fig. 20. Attenuation across the sample thickness of a pressure fluctuation of 1 Hz in frequency and 2 psi in amplitude.

facing the interior surface of the adapter was tightly sealed with O-rings. As the pressure fluctuated at one end of the sample, an oscillating gas flow through its porous channels was generated and the pressure transducer connected on the other end of sample recorded the pressure oscillations. The wave pattern measured by the transducer was recorded on a plotter. As shown in Figure 20, the amplitude ratio (the ratio of amplitude at the surface facing the transducer to that at the other surface) of a pressure fluctuation (1 Hz frequency, 2 psi amplitude) for a 0.2 cm-thick sample is about 0.9, and for a 0.6 cm-thick sample it is about 0.25. Therefore, 0.2 cm probably can be taken as the critical half thickness for a sample to be a high permeability solid.

The results from the pressure attenuation measurement indicate the 0.6 cm-radius cylindrical sample used in the experimental study is indeed not a truly high permeability solid. When the reacted shell is less than 0.2 cm thick, the sample can be considered a high permeability model; when the reacted shell increases to above 0.2 cm, however, the viscous effect of gas will attenuate the pressure wave and therefore decrease the effect of pressure fluctuation. This is why our experimental results did not completely agree with those from our theoretical calculations, where a ceramic body with a radius of 0.6 cm was assumed to be a high permeability solid.

CONCLUSIONS

An experimental technique to study the effect of pressure fluctuation on the removal of carbon residue was developed. Pressure fluctuation in a firing tube was generated by an oscillating piston driven by an electric motor. The samples used were colloid-pressed Al_2O_3 powder and carbon powder with initial carbon content varying from 5 to 17 wt%. The experiments were conducted at isothermal temperatures under oxygen flow. Results obtained can be summarized as follows:

1) over the internal mass transfer-controlled temperature region, the oxidation of carbon from the samples indeed proceeds more favorably under conditions of fluctuating pressure;
2) improvements in carbon conversion show a maximum value after some reaction has taken place;
3) pressure fluctuation can successfully overcome the external resistance to mass transfer;
4) the internal mass transfer can also be accelerated by pressure fluctuation, especially in the earlier stages of the reaction;
5) the effect of pressure fluctuation is more significant at lower temperatures;
6) the effect of pressure fluctuation can be increased if the ceramic body has a lower carbon concentration or has a larger pore size;
7) at higher oscillating frequencies and amplitudes, the effect of pressure fluctuation is limited by finite gas permeability through the pores; and
8) the structure can generally be considered a high permeability solid for samples (0.12-μm powder size, 39% porosity) with half thicknesses below 0.2 cm.

REFERENCES

1. C. Dong, M.J. Cima, and H.K. Bowen, "Effect of Pressure Fluctuation on Removal of Carbon Residue: Part I. Theoretical Analysis," to be published.

2. H. Schenck and J. Cloth, "Effect of Oscillating Gas Flow on the Reduction of Iron Oxide," *Stahl u Eisen*, **80** 1453-1457 (1960).
3. S. Taniguchi, M. Ohmi, and M. Yamada, "Accelerated Reduction of an Iron Ore Pellet in a Pulsating Flow of Hydrogen," *Trans. Iron Steel Inst. Jpn.*, **14** 241-246 (1974).
4. K. Kodama, A. Shigemi, and T. Higashi, *Tetsu-to-Hagan*, **48** 379 (1962).
5. Y. Yamada and T. Tsuda, *Tetsu-to-Hagan*, **52** 1370 (1966).
6. A.V. Yavoiskii, A.A. Zhukhovitskii, and V.A. Grigoryan *Izv. Vyssh. Ucheb. Zaved., Chern. Met.*, **9** 13 (1970).
7. K. Kuroda, T. Shimotsuma, K. Sano, T. Hasegawa, and E. Sakamoto, *Tetsu-to-Hagan*, **53** 245 (1976).
8. W.C. Moffatt, "Processing and Properties of Alumina-Zirconia Composite Ceramics"; ScD Thesis. Dept. Mat. Sci. Eng., MIT, Cambridge, MA, June 1987.
9. E.M. Suuberg, M. Wojtowicz, and J.M. Calo, "Reaction Order for Low Temperature Oxidation of Carbons" presented at the Twenty-Second International Symposium on Combustion, 1988.
10. J.W. Hamer and D.E. Cormack, "Influence of Oscillating External Pressure on Gas-Phase Reaction in Porous Catalysts," *Chem. Eng. Sci.* 43 935-944 (1987).
11. L.H. Dill and H. Brenner, "Dispersion Resulting from Flow through Spatially Periodic Porous Media III. Time-Periodic Processes," *PCH PhysicoChem. Hydrodyn.*, **4** [3] 279-302 (1983).

SECTION 25

DIRECT OBSERVATIONS OF PRECERAMIC BINDER DECOMPOSITION IN 2-D MODEL MICROSTRUCTURES

Jennifer A. Lewis

ABSTRACT

Preceramic binder decomposition processes during thermolysis were studied to relate physico-chemical properties of the binder to the microstructure of the ceramic. Examination of binder-filled 2-D microstructures enabled direct observations of changes in porosity and polymer morphology during binder thermolysis. These observations revealed that mass transport processes involved during thermolysis, as well as the developing microstructural features, depend on the properties of the binder system during thermal decomposition. The distribution of polymer in the 2-D network of pores was observed as a function of temperature for two organic polymers, polymethacrylate and a crosslinked polymethacrylate, and two preceramic polymers, polycarbosilane (PCS) and vinylic polysilane (VPS). Diffuse reflectance Fourier transform spectroscopy was used to study the chemical changes that occurred during the decomposition of the preceramic polymers in inert atmosphere.

INTRODUCTION

Application of preceramic polymers (e.g., organosilicon polymers) as binders for ceramics processing has received recent attention [1-5]. Since preceramic polymers decompose to amorphous-covalent ceramics [6], new types of composites can also be prepared from these materials [2, 4, 7]. The strengths of amorphous-covalent ceramic (pyrolyzed preceramic polymer)-ceramic composites were reported by Rogers et al. [2] to be as high as 430 MPa. In addition, numerous advantages such as increased green density, reduced shrinkage, and improved strength of the presintered ceramic part [2, 4, 8-10] have been reported for ceramic bodies containing preceramic binders.

The microstructure which develops during preceramic polymer decomposition determines whether the advantages listed above are realized. The preceramic binder system must meet several requirements: (1) give high yields of ceramic pyrolysis product, (2) decompose to give a uniform distribution of this product, and (3) produce minimal defects during the formation of ceramic product. Many investigators have focused on organosilicon polymer synthesis with the goal of increasing pyrolysis yields; however, relatively little is know about the effects of the binder's physical and chemical properties on the final microstructure of the composite.

Direct examination of fired preceramic polymer-ceramic composites is only partially useful for establishing the relationship between polymer chemistry and final microstructure. The principal difficulty is that microstructural features are difficult to attribute to either the polymer pyrolysis chemistry or to the initial distribution of polymer within the ceramic matrix. The initial distribution of the polymer in the polymer-ceramic composite is difficult to characterize on a micrometer scale. Scanning electron microscopy (SEM), for example, shows little contrast between polymeric binder and ceramic particles [11]. Typically, the binder tends to coat the particles when it is introduced as a solution, or it tends to remain as a separate phase when it is milled together with the ceramic particles. Thus, any inhomogeneous distribution of polymer-derived ceramic within the final component can be attributed either to changes in the microstructure upon pyrolysis or to the method by which the polymer was introduced to the green body.

We report *in situ* observations of binder distribution processes and porosity development by modeling the porous microstructure of ceramic bodies in two dimensions. The model stucture consists of a two dimensional random pattern of binder-filled pores between two pieces of glass. The polymer in the pores can clearly be observed with an optical microscope. This approach has considerable advantages over direct examination of fired bodies, since the initial morphology of the polymer phase can be

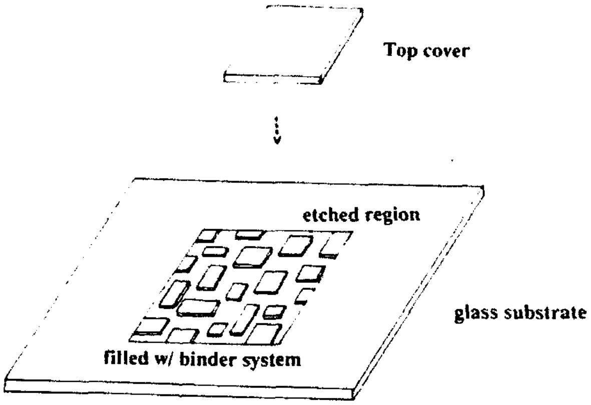

Fig. 1. Fabrication process for binder-filled 2-D model microstructures [11].

followed throughout its thermal decomposition.

A schematic view of the 2-D samples is shown in Figure 1. The channel depth in these 2-D samples was approximately 5 µm, and the channel widths ranged from 20 to 200 µm. These "pore" dimensions are approximately two orders of magnitude greater than the pores present in ceramic green bodies. Another important point is that two dimensional networks of pores do not quantitatively represent the percolative transition of three dimensional networks [12]; nonetheless, it seems reasonable to assume that microstructural features on the scale of particles are adequately represented by this model. The binder is subjected to similar resistance to flow and capillary stress on the scale of the particles for both three and two dimensional networks. Thus, the change in dimensionality and larger absolute pore size must be considered when using these 2-D results to predict the behavior of binders during their removal from ceramic green bodies. Previous results, however, indicate similar distribution processes occur in green bodies containing organic binder systems and in these 2-D samples [13].

Conventional organic binders used for ceramics processing display a range of behaviors that vary from thermoplastic to thermosetting at elevated temperatures. Thus, for comparison with the preceramic polymers, two organic polymers of similar chemical composition were studied. A thermoplastic polymer (PMMA) and a thermosetting polymer (crosslinked PMMA) were chosen for these observations because of their different physical properties during decomposition. PMMA becomes molten ($T_g \approx 105°C$) before it depolymerizes to form methyl methacrylate (MMA), while the crosslinked material is essentially infusible.

Several organosilicon polymers have been developed which form silicon carbide (SiC) or silicon nitride (Si_3N_4) upon decomposition [14-16]. Polycarbosilane (PCS) and vinylic polysilane (VPS) are representative of those preceramic polymers that have been proposed for use as binders. They thermally decompose in an inert atmosphere to form first an amorphous non-oxide (1000°C) and then crystalline SiC (yield ≈ 50-60%).

PCS and VPS, like PMMA and crosslinked PMMA, represent very different types of binders. PCS and VPS lose mass and have associated changes in physical characteristics upon thermal decomposition. These characteristics and weight losses are summarized in Table 1. Several important properties are revealed which may affect their distribution and defect formation processes, as well as the distribution of ceramic pyrolysis products in porous networks. First, at 25°C PCS is a solid, while VPS is a liquid. Secondly, prior to significant weight loss, PCS melts and becomes fluid, while VPS crosslinks [6, 17] and becomes an infusible solid. Thirdly, during the decomposition of these polymers, the majority of their weight is lost between 350°C and 550°C. Finally, above 550°C the conversion from the organic ($\rho \approx 1$ g/cc) to the amorphous phase ($\rho \approx 2.2$ g/cc) begins and results in a significant volume reduction (33% linear shrinkage) [1, 18].

The PCS used in this study had an average molecular weight of 1580 g/mol as measured cryoscopically in benzene [5]. Elemental analysis [5] showed that this polymer contained 49.14% Si, 41.73% C, 7.83% H, and

Table 1. Physical Characteristics of PCS and VPS During Decomposition.

	Temperature (°C)	Wt% Loss	Physical
	30-325	<5%	solid
PCS	325-550	40%	molten
	550-700	≈5%	solid (x-linked)
	30-150	<10%	liquid
VPS	200-300	none	solid (x-linked)
	350-700	30-35%	solid

0.71% O (neutron activation), which is in good agreement with the values reported by Hasegawa et al. [19]. The VPS used in this study had an average molecular weight of 1040 g/mol as measured cryoscopically in benzene [5]. Both preceramic polymers have been characterized by IR and NMR spectroscopy [15, 17, 19, 20], but most of the previous research on characterizing the decomposition of PCS has been on samples which were cured in air to obtain an infusible polymer suitable for conversion to SiC fibers [15, 19]. In this work, however, we studied the decomposition of PCS and VPS by IR spectroscopy under inert atmosphere.

EXPERIMENTAL PROCEDURE

Binders

The PCS (NICALON™ X9-6348, Lot PL-79, Dow Corning Co., Midland, MI, marketed for Nippon Carbon Co., Ltd., Japan) and VPS (Y-12044, Lot 50911030586, Union Carbide Co., Specialty Chemicals Division, Tarrytown, NY) used were obtained from commercial sources, as was the PMMA (Aldrich Chemical Co., Inc., Milwaukee, WI) used. The crosslinked PMMA was prepared *in situ* using a solution consisting of 80% methyl methacrylate, 19% ethylene glycol dimethacrylate, and 1% benzoyl peroxide. The Nicalon™ polycarbosilane was dissolved in toluene to give a solution consisting of 90% PCS and 10% toluene.

Infrared Spectroscopy

Samples for infrared spectroscopy were prepared by weighing about 50 mg of PCS or VPS and placing them in porcelain crucibles. The samples were heated in an argon atmosphere furnace that was evacuated and backfilled with argon [$P(O_2) \sim 10^{-13}$ atm] twice prior to starting the heating schedule. The samples were heated from room temperature to 225°C at a heating rate of 1.3°C/min and from 225°C to T_{max} at a heating rate of 0.3°C/min. The VPS polymer began crosslinking at 140°C and was almost completely crosslinked at temperatures between 200°C and 250°C; consequently, the temperature was held at 225°C for 3 h to cure the VPS polymer. After curing, the VPS polymer was infusible. Approximately 2 mg of the pyrolyzed sample was diluted with 100 mg KBr and ground to a fine powder to obtain samples for IR analysis. Diffuse reflectance infrared Fourier transmission spectroscopy (DRIFTS) was performed on a spectrometer (Nicolet Model 44, Madison, WI) equipped with a dry, CO_2-free air purge (Balston, Inc., Lexington, MA) using a diffuse reflectance attachment (SpectraTech, Stamford, CT). IR spectra were collected (256 scans) at 2 cm^{-1} resolution with a TGS detector. The DRIFTS spectra were plotted as percent reflectance versus wavenumbers [21].

2-D Model Microstructures

There were three steps in the preparation of the 2-D samples: (1) patterning the substrates, (2) filling the channels with binder, and (3) bonding the top glass cover. The substrates used were circular glass cover slides (diameter = 22 mm), and they were processed by a standard photolithography procedure [22] to form etched channels on their surface. An outline of the procedure used is given in Table 2. The resulting channel depth was approximately 5 μm, and the channel widths ranged from 20 to 200 μm.

The channel filling procedure depended on the binder system. To fill the channels with crosslinked PMMA, a syringe was used to place a small droplet of solution onto

Table 2. Procedure for Substrate Fabrication.

Step #	Description
1. Clean	Immerse substrates in a 1:1 solution of sulfuric acid and hydrogen peroxide (≈300 s), then rinse in deionized (DI) water and allow to dry overnight at 120°C.
2. Apply photoresist	Cover top surface of substrate with resist[a] and spin coat at 5000 rpm for 30 s.
3. Prebake	Heat substrates coated with resist at 90°C for 30 min.
4. Expose	Expose prebaked substrates to UV light (contact aligner) for 40 s.
5. Develop	Develop exposed pattern by immersing substrates in a 1:1 solution of DI water and positive resist developer[b] for 120 s, then rinse in DI water.
6. Postbake	Heat patterned substrates at 120°C for 30 min.
7. Etch	Etch postbaked samples for 0.5 h using a buffered oxide etchant, then rinse in DI water.
8. Clean	Remove photoresist with acetone and then clean (refer to Step 1).

[a] Positive photoresist 820 (KTI Chemicals, Inc., Sunnyvale, CA).

[b] Positive photoresist developer (KTI Chemicals).

the etched region of the substrate. The top glass cover was then placed upon the filled channels (see Fig. 1), and the sample was heated above 60°C for 12 h to polymerize the mixture. For the PMMA samples, a small amount of the polymer was placed on top of the etched region of the substrate and heated to a temperature above its softening point (T > 200°C). The top cover was placed upon the filled channels and the sample was allowed to cool to 25°C.

The procedure used for the PCS and VPS samples was similar to that used for the crosslinked PMMA. A droplet of the PCS-toluene solution or VPS was placed onto the etched region of the substrate and a top cover was then placed upon that region. The as-prepared PCS sample contained residual toluene which was removed during the subsequent heat treatment.

Microstructure Characterization

Decomposition of the 2-D samples filled with PMMA and the crosslinked PMMA was observed using hot-stage (Linkam THM 600, United Kingdom) optical microscopy (Olympus, Lake Success, NY). These samples were heated to 300°C at 10°C/min in air, and optical micrographs were taken during the heating cycle. Hot-stage optical microscopy could not be used for the preceramic polymer samples because of their sensitivity to air during decomposition. Therefore, the 2-D samples filled with PCS and VPS were fired in an inert atmosphere furnace that was evacuated and backfilled twice with gettered argon [P(O_2) = 10^{-13} atm] prior to heating. The PCS and VPS 2-D samples were heated using the same heating schedule as described above for the IR samples. After each heat treatment, optical micrographs were taken of the PCS and VPS samples.

RESULTS

Decomposition of Preceramic Polymers

The structural changes associated with the decomposition of preceramic polymers were characterized by infrared spectroscopy. The infrared spectra (DRIFTS) for the polycarbosilane heated in argon are shown in Figure 2. Absorption bands were observed at 3680 cm^{-1} (free O-H stretching); 2953 and 2896 cm^{-1} (C-H stretching); 2095 cm^{-1} (Si-H stretching); 1355 cm^{-1} (C-H bending in Si-CH_2-Si); 1407 cm^{-1} (CH_2 deformation of Si-Me); 1250 cm^{-1} (Si-Me deformation); a band centered at 1020 cm^{-1} (Si-O stretching or Si-CH_2-Si deformation); and a band centered at 830 cm^{-1} with shoulders at 880, 735, 685, and 625 cm^{-1} (Si-H deformation, Si-Me rocking, and Si-C stretching). The presence of the free OH band may be due to a slight reaction with the moisture in the KBr since this band was very weak in the transmission IR spectrum of PCS.

The DRIFTS spectra of VPS at various temperatures during decomposition are shown in Figure 3. The IR spectrum of VPS at 25°C exhibits absorption bands at 3050 cm^{-1} (C=CH_2 stretching); 2998 cm^{-1} (-CH=C stretching); 2959 and 2898 cm^{-1} (C-H stretching); 2082 cm^{-1} (Si-H stretching); 1875(w) cm^{-1} (olefinic overtone); 1584(w) cm^{-1} (C=C stretching); 1400 cm^{-1} (-CH=CH_2 deformation); 1245 cm^{-1} (Si-Me deformation); 1043 cm^{-1} (Si-O stretching or Si-CH_2 deformation); 1004 cm^{-1} (-CH=C deformation); 937 cm^{-1} (=CH_2 out-of-plane deformation); 859, 830, and 770 cm^{-1} (Si-H bending and Si-Me stretching); and 709, 695, and 620 cm^{-1}. The sharp absorption bands at 1004 and 937 cm^{-1} have been assigned to Si-H bending vibrations [17], but we believe that these bands are better assigned to monosubstituted vinyl groups [23, 24]. The olefinic band at 937 cm^{-1} and associated olefinic overtone at 1875 cm^{-1} are both characteristic of vinyl groups.

2-D Model Microstructures

Direct observations of the distribution processes of

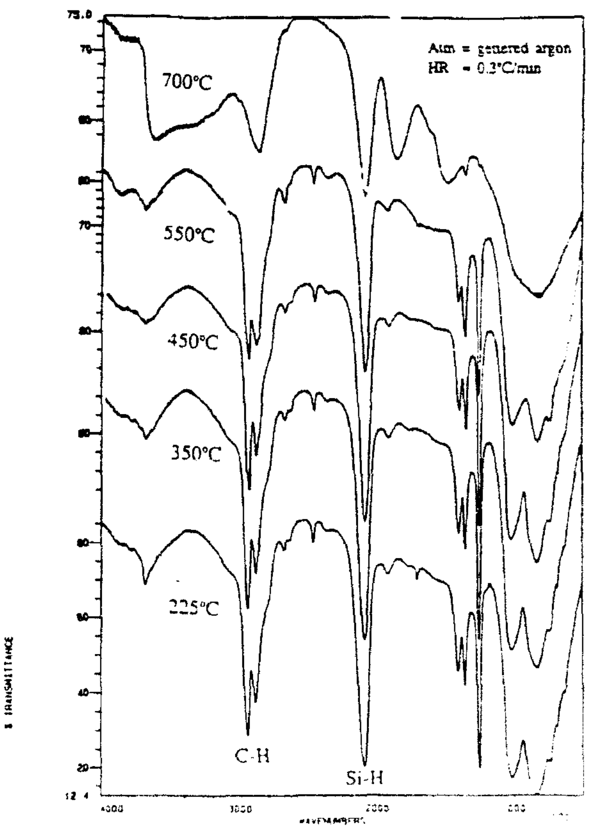

Fig. 2. DRIFTS analysis of polycarbosilane at various temperatures during decomposition

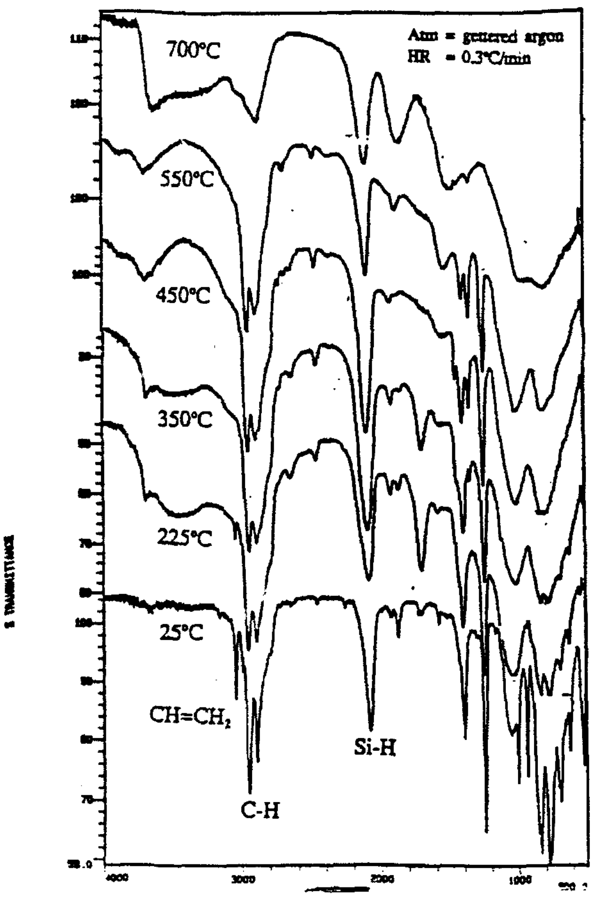

Fig. 3. DRIFTS analysis of vinylic polysilane at various temperatures during decomposition.

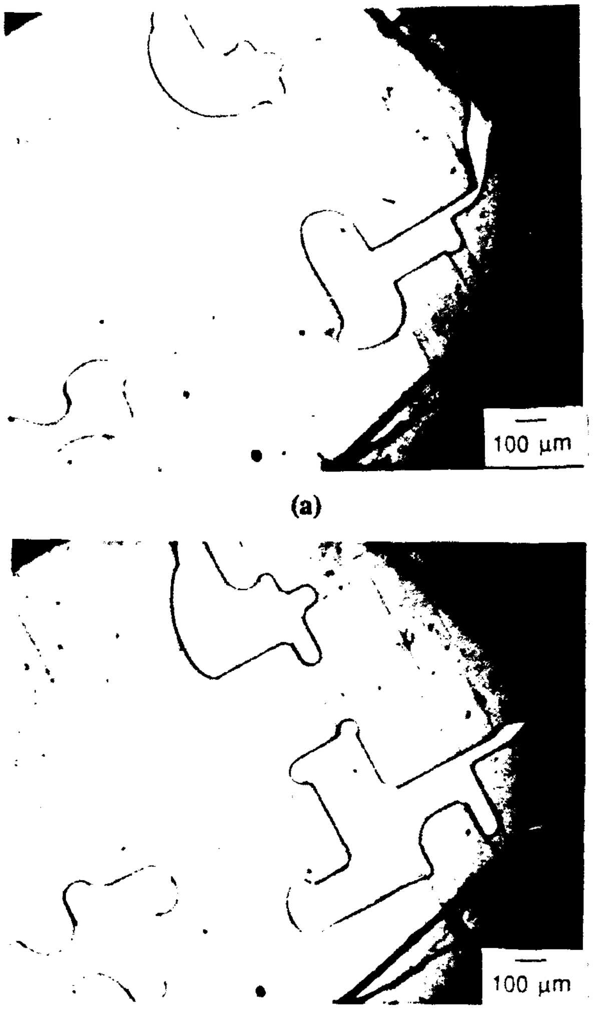

(a)

(b)

Fig. 4. Optical micrographs (mag = 50x) of PMMA-filled 2-D samples heated at 10°C/min in air: (a) T=291°C and (b) T=297°C.

PMMA and the crosslinked PMMA during decomposition were made by hot-stage optical microscopy. Figures 4 and 5 illustrate representative optical micrographs (mag = 50x) as a function of temperature for the 2-D samples filled with PMMA and crosslinked PMMA, respectively. Because PMMA is molten during decomposition, the microstructure observed in Figure 4 resulted from the formation of bubbles. Crosslinked PMMA decomposes without becoming fluid; therefore, no bubbles formed. Instead, as illustrated in Figure 5, cracks formed during decomposition beginning at 250°C. These cracks propagated along the width of the channels and widened as thermolysis progressed until they matched the width of the channels.

Comparison of Figures 6-9 indicates many differences exist in the microstructure that develops during decomposition of these two preceramic binders in the 2-D porous networks. Figures 6 and 7 show optical micrographs (mag = 50x and 200x, respectively) of the 2-D samples filled with PCS and heated to various temperatures. At 25°C, the PCS-filled sample contained residual solvent since it was dissolved in toluene to fill the channels. Pores developed as the residual solvent was removed due to capillary redistribution of the remaining binder solution. Drying cracks formed in the regions around these developing pores. By 300°C, the solvent was completely removed, and regions containing drying cracks, open porosity, and entrapped bubbles were present in the microstructure. The drying cracks healed between 350°C and 550°C as the PCS softened and began to flow as its viscosity decreased. These cracks were no longer observed in the microstructure at 550°C, and the pore development was more extensive due to the elimination of volatile decomposition products. Between 550°C and

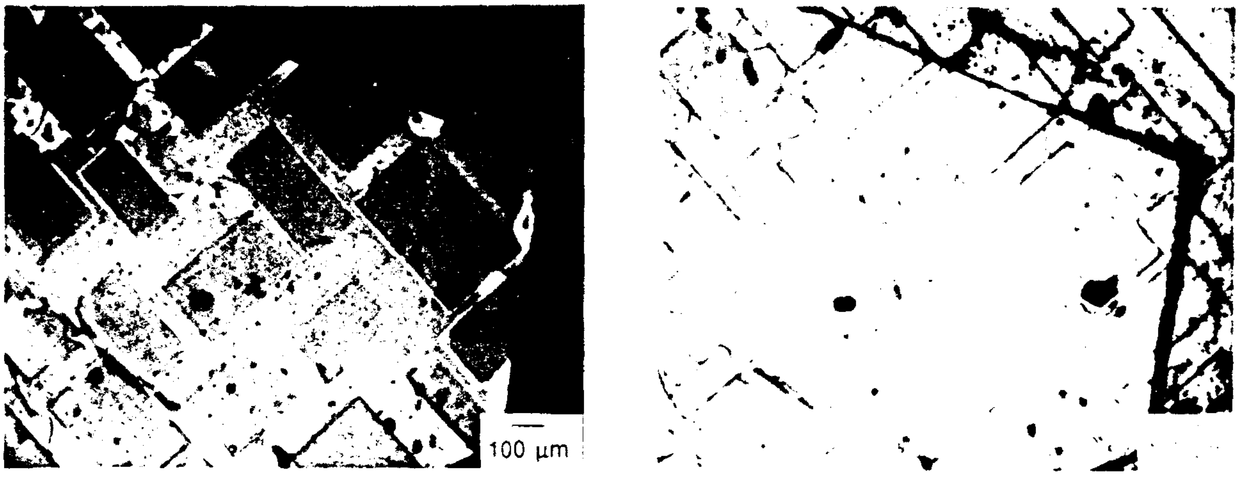

(a) (b)

Fig. 5. Optical micrographs (mag = 50x) of crosslinked PMMA 2-D samples heated at 10°C/min in air: (a) T=264°C and (b) T=278°C.

700°C, crack formation, which occurred throughout the microstructure as the polymer residue solidified, accommodated the reduction in volume associated with the loss of material and the increasing density. The pyrolyzed microstructure at 700°C was clearly inhomogeneous; it contained both empty pores and those filled with the desired pyrolysis product.

Figures 8 and 9 show optical micrographs (mag = 50x and 200x, respectively) of the 2-D samples filled with VPS and heated to various temperatures. At 25°C, VPS was distributed uniformly in these 2-D channels because it was a liquid precursor that flowed at room temperature. The first changes in microstructure were observed between 450°C and 550°C when the binder-filled channels began to darken and microporosity developed. In addition, cracks formed near the edges of the covered region, but they did not propagate into the interior regions. In the temperature range between 550°C and 700°C, crack formation occurred throughout the VPS-filled region to accommodate the reduction in volume associated with the conversion of the polymer to ceramic material. In the pyrolyzed microstructure at 700°C, the pyrolysis product was uniformly distributed within the channels, but cracks and microporosity were present.

DISCUSSION

The micrographs above clearly demonstrate a relationship between the physical and chemical changes which occur during polymer decomposition and the resulting microstructure. Figure 4 shows representative optical micrographs (mag = 50x) as a function of temperature for the 2-D samples filled with PMMA. Because PMMA is molten during decomposition, its distribution can be influenced either by capillary forces or by the formation of bubbles, which then can grow violently to the edge of the top cover (or the free surface). Bubble formation dominates the transport process if the removal rate of volatile products (e.g., MMA) is slower than their generation rate, because the local vapor pressure of MMA can grow to exceed 1 atm [21, 25].

Due to the fast heating rate (10°C/min) and the rapid generation of monomer when PMMA depolymerized, the pore development shown in Figure 4 resulted from the formation of bubbles. Once bubbles ceased to form, the distribution of the remaining PMMA was characterized by liquid retention in the smallest of the pores due to these pores' high capillary pressure. The cessation of bubble generation may be linked to the relatively short diffusion distance in the small amounts of liquid remaining in the small capillaries.

Figure 5 shows representative optical micrographs (mag = 50x) as a function of temperature for the 2-D samples filled with crosslinked PMMA. Crosslinked PMMA decomposes to volatile species without becoming fluid. Therefore, no porosity can develop as a result of capillary redistribution. Instead, cracks formed during decomposition beginning at 250°C. These cracks propagated along the binder-filled channels and widened as thermolysis progressed until they matched the width of the channels. The volume change that occurred upon decomposition was apparently accommodated by fracture of the crosslinked PMMA.

Figures 6-9 illustrate the variety of microstructural

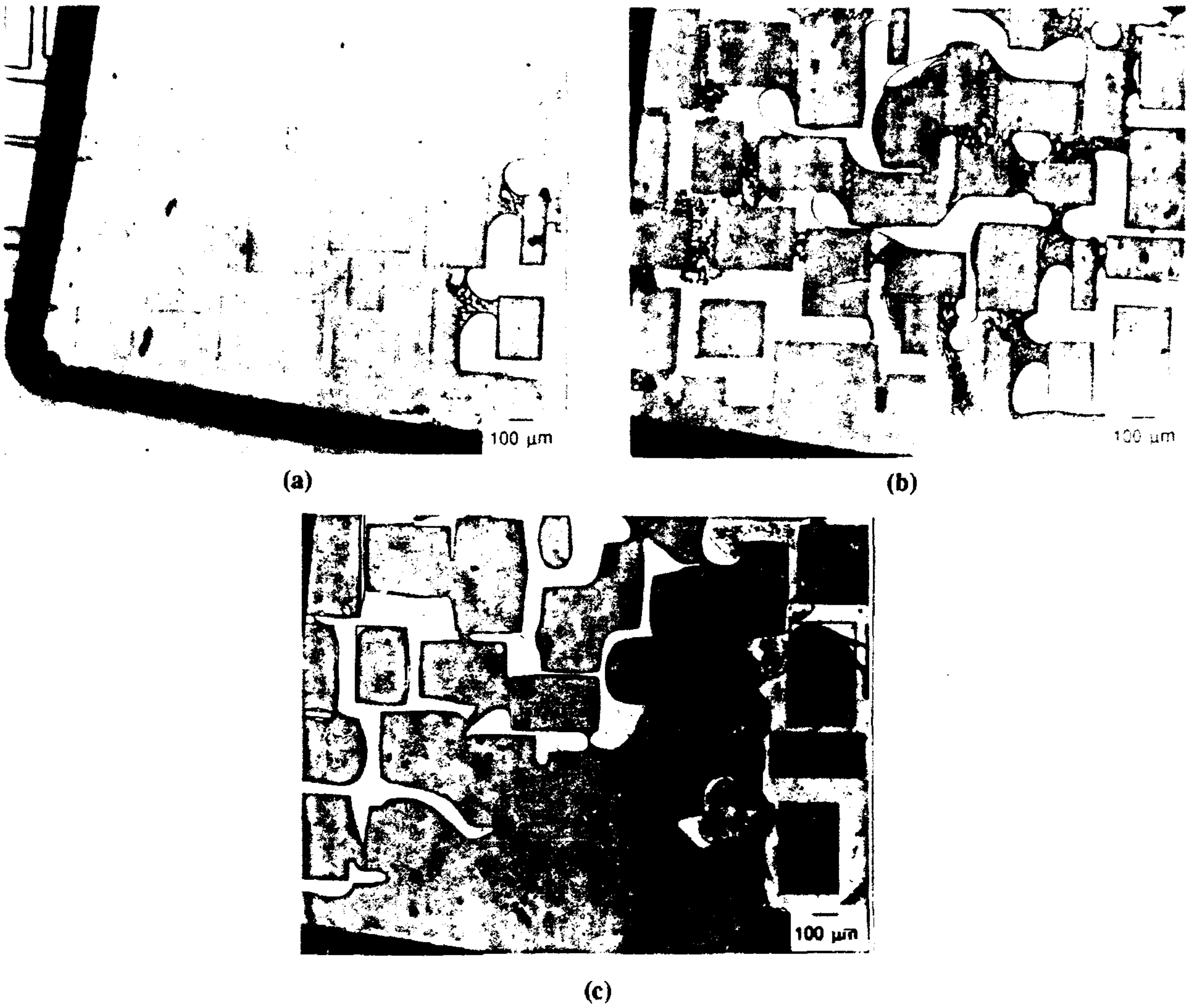

(a) (b) (c)

Fig. 6. Optical micrographs (mag = 50x) of PCS-filled 2-D samples heated in argon: (a) T=25°C, (b) T=300°C, and (c) T=550°C.

changes which occurred during the decomposition of preceramic polymers. Some of the changes observed are related to the chemistry of these preceramic polymers, which was studied in this work by IR spectroscopy. The IR spectra of PCS show that the chemical structure of PCS remained unchanged from 25-550°C. According to Yajima et al. [15, 19, 20], mainly low molecular weight polycarbosilanes are lost between these temperatures and no major structural changes occur. Above 550°C, PCS begins to crosslink via condensation reactions which eliminate hydrogen and methane and eventually lead to the formation of amorphous SiC. When decomposed in argon, there is little change in the O-H and Si-O absorption bands during decomposition; when decomposed in air, these absorption bands increase in intensity [19]. The IR spectra of PCS began to change above 550°C due to the elimination of organic groups, and the intensity of the C-H stretching vibrations decreased substantially by 700°C, as shown in Figure 2.

In comparing the room temperature IR spectra for PCS and VPS, two main differences, indicative of differences in their structures, are apparent: the presence of the olefinic C-H band at 3050 cm^{-1} is characteristic of the vinyl groups, and the absence of the absorption band at 1355 cm^{-1} is due to $SiCH_2Si$ groups in polycarbosilanes such as PCS. Also the Si-H stretching vibration in VPS is about 13 cm^{-1} lower than in PCS. The shift is in the expected direction, since the Si-H stretching frequency has been observed to decrease as the groups bonded to Si become more electropositive [26].

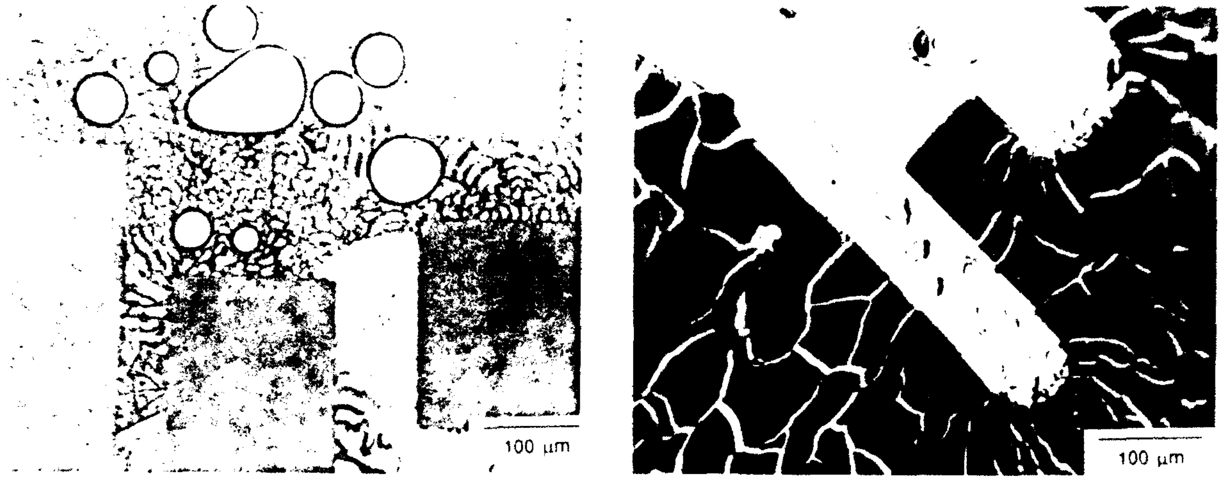

(a) (b)

Fig. 7. Optical micrographs (mag = 200x) of PCS-filled 2-D samples heated in argon: (a) T=300°C and (b) T=700°C.

Upon heating, VPS polymerizes between 140°C and 250°C to form an infusible solid. Schilling [14] reported that the formation of an infusible solid is the result of crosslinking through predominantly hydrosilylation reactions involving the SiH and vinyl groups, and reported that the Si-H stretching vibrations disappeared completely by 300°C. Our work and the results published by Schmidt et al. [17] show that the adsorption bands at 3050 and 2082 cm^{-1} do decrease in intensity with increasing temperature. However, the absorptions due to the vinyl groups completely disappeared by 350°C (by 400°C in ref. 17), but the Si-H absorption band was still present. This result indicates crosslinking occurred through both vinyl polymerization and hydrosilylation reactions, and that polymerization of the vinyl groups predominated, in agreement with results reported recently [17]. The presence of the broad band (the absorption band for $SiCH_2Si$ is usually narrow [23]) at 1020-1100 cm^{-1} (Si-O) and the appearance of the bands at 1710 cm^{-1} (C=O) after heating to 225°C indicate this VPS polymer contains some oxygen or that oxidation occurred during pyrolysis. The VPS sample used contained 1.13% oxygen, as determined by neutron activation [18].

The SiMe groups in polysilanes undergo an insertion reaction between 350°C and 550°C in which the polysilane (=SiMeSiMe=) rearranges to form a polycarbosilane (=$Si(H)CH_2Si(H)$=) [14, 15, 17, 19]. As the temperature increased, a new band appeared near 1355 cm^{-1} and the Si-H band increased in intensity, as previously noted by Schilling [14] and Schmidt et al. [17]. By 450°C the Si-H band had shifted from 2082 to 2099 cm^{-1}, indicating a structural change had occurred, and the Si-H group was now bonded to carbon instead of silicon atoms [26]. The new band at 1355 cm^{-1} corresponded to the C-H deformation associated with $Si\text{-}CH_2\text{-}Si$ groups [23]. Above 550°C, VPS undergoes condensation reactions (similar to PCS) leading to the eventual formation of amorphous SiC. The IR spectrum of VPS at 700°C is nearly identical to that of PCS at this temperature.

The redistribution processes between 350°C and 550°C for PCS and VPS in the 2-D microstructures (Figs. 6-9) are similar to those observed for PMMA and the crosslinked PMMA, respectively. According to the IR spectra, no major structural changes occurred below 550°C that would affect the properties of PCS. Below 550°C, PCS remains fluid (like PMMA), and the observed changes in binder distribution and development of porosity were similar to the PMMA-filled samples. Thus, both capillary forces and the formation of bubbles could have contributed to the pore development observed for the PCS-filled samples. As indicated by the IR spectra and previously published results, VPS could not flow by capillary forces during decomposition due to its crosslinked nature, and thus it behaved similarly to the crosslinked PMMA. The first change in the microstructure was observed at 450°C where the small pores observed in Figure 9a began to appear and, according to the IR spectra, coincided with the rearrangement of the VPS to a polycarbosilane. Between 350°C and 550°C, a large volume of volatile species is generated during PCS and VPS decomposition, and these species must diffuse through polymer-filled regions and empty pore space.

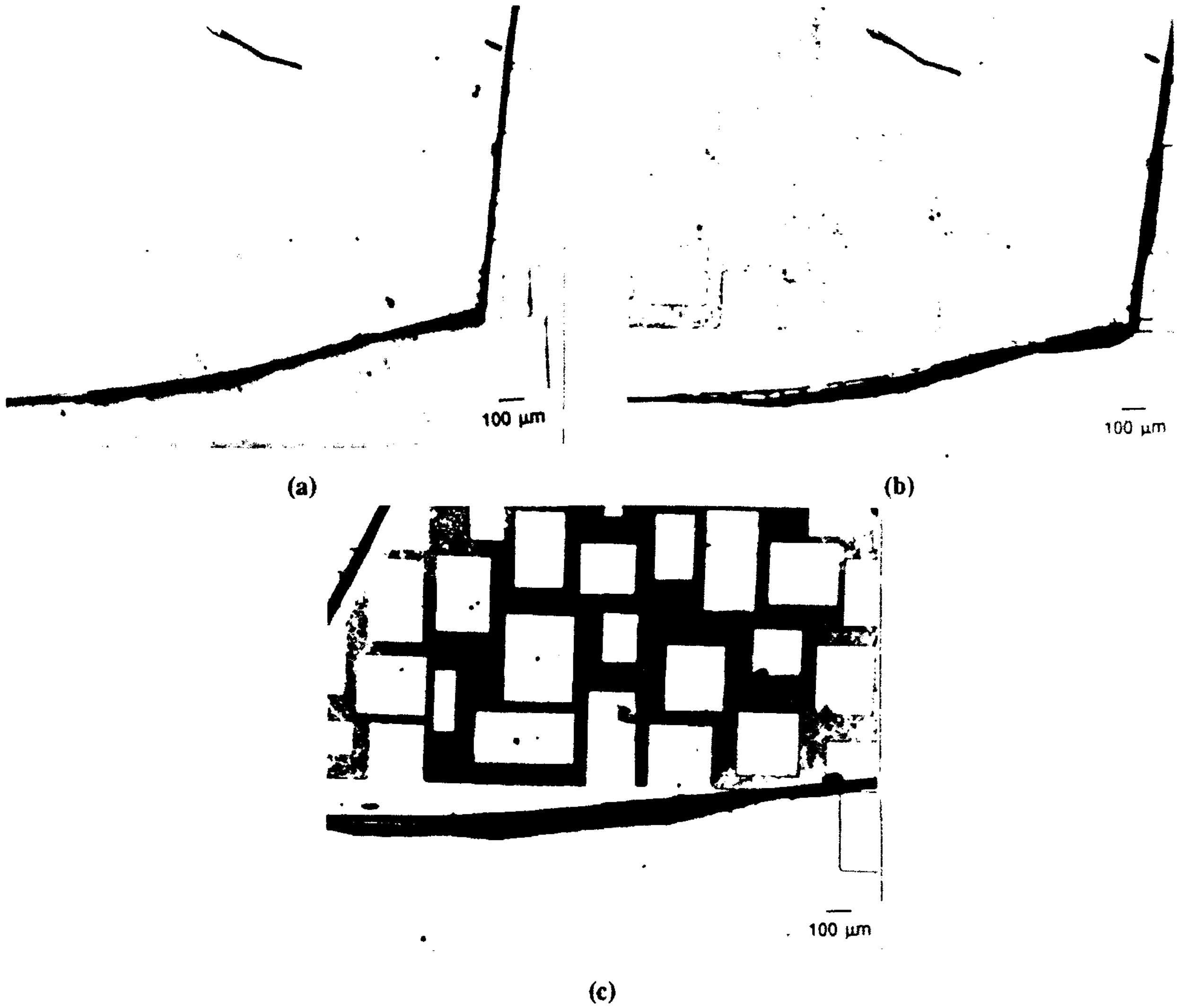

Fig. 8. Optical micrographs (mag = 50x) of VPS-filled 2-D samples heated in argon: (a) T=25°C, (b) T=450°C, and (c) T=550°C.

The defects observed above are of significant concern for those preparing composites from preceramic polymers. Cracks or bubbles produced upon decomposition of the polymer are not necessarily removed during densification. Rather, they may persist and become a strength-limiting flaw in the final component.

Above 550°C, the preceramic polymers are no longer analogous to organic binders, and both PCS and VPS begin to transform to amorphous SiC in this temperature range. A significant volume reduction must occur to produce the necessary density increase associated with this ceramic phase. Thus, this process represents another source of defects. Typically, the densities reported for SiC compacts processed with these preceramic polymers are quite low (<70% of theoretical), due to the internal porosity present in the compact [1, 2, 4, 27]. Based on our observations, compacts processed with each of these binders would be expected to have different distributions of porosity and pyrolysis product.

Spotz [5] examined the pore structure of β-SiC compacts fired to 1000°C that initially contained 42 vol% of either PCS or VPS. His results showed that, in fact, there are differences in the pore development between compacts processed with each of these polymers. Three pore size ranges were observed to exist for these samples: large-scale, >300 nm; intermediate, 50-300 nm; and fine-scale, <20 nm. The presence of large-scale porosity was low (<3% of total intruded volume) for compacts processed with either polymer (uniaxially pressed at 280 MPa). The distribution of porosity in the PCS-based

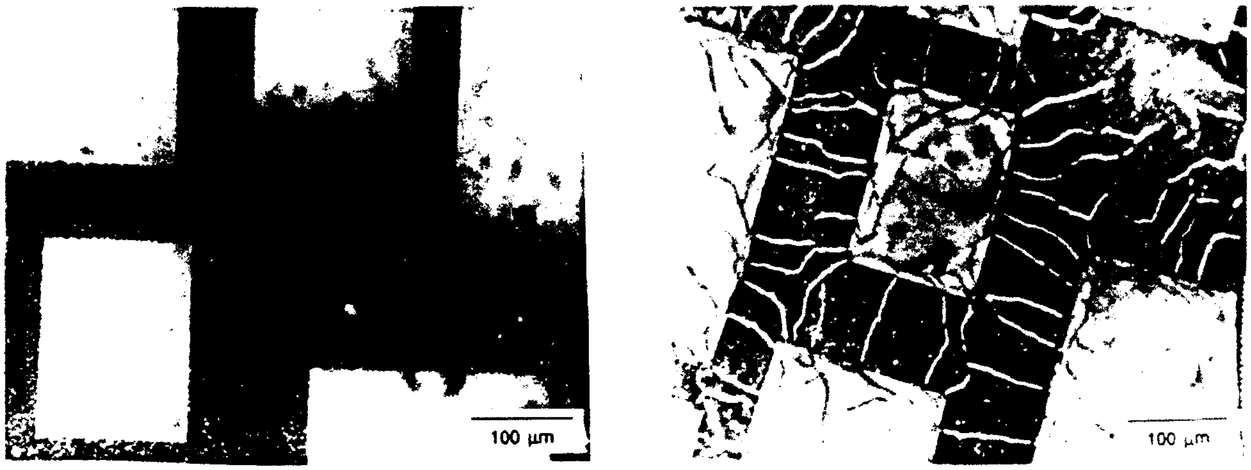

(a) (b)

Fig. 9. Optical micrographs (mag = 200x) of VPS-filled 2-D samples heated in argon: (a) T=550°C and (b) T=700°C.

compacts was exclusively in the intermediate size range, with no fine-scale porosity observed. The distribution of porosity in the VPS-based compacts was predominantly fine-scale porosity with little porosity observed in the intermediate range. These results are in agreement with the 2-D observations described here. By comparison, the pore development for the VPS-filled 2-D samples is clearly on a finer scale than that observed for the PCS-filled samples (refer to Figs. 6-9).

CONCLUSIONS

The decomposition of preceramic polymers was directly observed in 2-D microstructures, and the chemical changes occurring during thermolysis were determined by IR spectroscopy. Several important features were illustrated by the IR spectra of these polymers. The IR spectra of PCS included in this paper were obtained after heating in argon and indicate when PCS is heated in an inert atmosphere, its structure remains essentially unchanged up to 550°C. Above 550°C it begins to crosslink, eventually forming amorphous SiC. According to the changes observed in the vinyl and SiH absorption bands, VPS, on the other hand, crosslinks via a combination of hydrosilylation and vinyl polymerization reactions at temperatures between 140°C and 300°C, forming an infusible polymer. As indicated by a shift in the SiH absorption frequency and the appearance of the $SiCH_2Si$ absorption band, VPS rearranges to form a polycarbosilane at temperatures between 350°C and 550°C. The changes observed in the IR spectra during the decomposition of PCS and VPS in an inert atmosphere agreed with those reported by Hasegawa and Okamura [20] and Schmidt et al. [17].

Our observations indicate the distribution of polymeric binders in ceramic green bodies is dependent on the binders' physico-chemical properties and processing conditions. The distribution of liquid binders in green bodies was very homogeneous, but the distribution of solid polymers depended on the processing conditions used. When the polymer was dissolved in a solvent, for example, drying defects were introduced as the solvent was removed.

Polymers which are fluid during decomposition form bubbles if volatile products are formed too fast, and they also flow by capillary forces. Infusible polymers, on the other hand, do not redistribute during decomposition but instead develop microcracks as volatile material is eliminated. Microstructural changes were also observed to occur during the chemical reactions which occur during thermolysis, and microporosity developed for the VPS polymer between 450°C and 550°C. The chemical reaction occurring during the development of this microporosity was identified by IR spectroscopy as the reaction which converts the polysilane to a polycarbosilane.

Preceramic polymers diverge in behavior from their organic counterparts during the final stage of their decomposition. Instead of being completely removed, preceramic polymers produce a pyrolysis product that must transform to an amorphous covalent ceramic material of significantly higher density. The residue from preceramic polymers crosslinks at high temperatures, and polymers that are fluid at lower temperatures become infusible during pyrolysis. During thermolysis, cracks were observed to form in the residues to accommodate the volume shrinkage associated with the elimination of volatile decomposition products and with the increasing density of the residue as it transformed to ceramic material. The pore morphology that developed in these 2-D samples upon decomposition corresponded to observed pore size distributions in ceramic compacts processed with each of these preceramic polymers.

ACKNOWLEDGMENTS

The authors gratefully acknowledge the Air Force Office of Scientific Research for their sponsorship of this research under contract number F49620-89C-0102DEF. Special thanks are extended to the MIT Technology Research Laboratory for use of their photolithography equipment and to O. Hurtado and Prof. R. Reif.

REFERENCES

1. R.W. Rice, "Ceramics from Polymer Pyrolysis, Opportunities, and Needs--A Materials Perspective," *Am. Ceram. Soc. Bull.*, **62** [8] 889-92 (1983).
2. J.J. Rogers, J. Semen, and D.Y.-F. Yu, "Silicon Carbide and Silicon Nitride Structural Ceramics Derived from a Preceramic Polymer Binder," *Ceram. Eng. Sci. Proc.*, **10** [7-8] 833-36 (1989).
3. K.B. Schwartz, D.J. Rowcliffe, and Y.D. Blum, "Microstructural Development in Si_3N_4/Polysilizane Bodies During Heating," *Adv. Ceram. Mater.*, **3** [4] 320-23 (1988).
4. S. Yajima, T. Shishido, and K. Okamura, "SiC Bodies Sintered with Three-Dimensional Cross-linked Polycarbosilane," *Am. Ceram. Soc. Bull.*, **56** [12] 1060-63 (1977).
5. M.S. Spotz, "Organosilicon Polymers as Preceramic Binders for Silicon Carbide"; PhD Thesis. Dept. Mat. Sci. Eng., MIT, Cambridge, MA, January, 1990.
6. G.D. Soraru, F. Babonneau and J.D. Mackenzie, "Structural Concepts of New Amorphous Covalent Solids," *J. Non-Crystalline Solids*, **106** 256-61 (1988)
7. R.P. Boisvert and R.J. Diefendorf, "Polymeric Precursor SiC Matrix Composites," *Ceram. Eng. Sci. Proc.*, **9**, 873-89 (1988).
8. S. Yajima, "Special Heat-Resisting Materials from Organometallic Polymers," *Am. Ceram. Soc. Bull.*, **62** [8] 893-903 (1983).
9. K.B. Schwartz and D.J. Rowcliffe, "Modeling Density Contributions in Preceramic Polymers/Ceramic Powder Systems," *J. Am. Ceram. Soc.*, **69** [5] C106-08 (1986).
10. B.C. Mutsuddy, "Use of Organometallic Polymer for Making Ceramic Parts by Plastic Forming Techniques," *Ceram. Inter.*, **13**, 41 (1987)
11. M.J. Cima, J.A. Lewis, and A.D. Devoe, "Binder Distribution in Ceramic Greenware During Thermolysis," *J. Am. Ceram. Soc.*, **72** [7] 1192-99 (1989).
12. E.A. Holm and M.J. Cima, "Zero-Shrinkage Whisker Fraction in Ceramic Matrix-Ceramic Whisker Composites"; pp. 319-30 in Processing Science of Advanced Ceramics, Mat. Res. Soc. Symp. Proc., Vol. 155. Edited by I.A. Aksay, G.L. McVay, and D.R. Ulrich. Materials Research Society, Pittsburgh, PA, 1989.
13. J.A. Lewis and M.J. Cima, "Direct Observation of Binder Distribution Processes in 2-D Porous Networks During Thermolysis"; pp. 583-90 in Ceramic Powder Science III. Edited by G.L. Messing, S. Hirano, and H. Hausner. American Ceramic Society, Westerville, OH, 1990.
14. C.L. Schilling, Jr., "Polymeric Routes to Silicon Carbide," *British Polymer Journal*, **18** [6] 355-58 (1986).
15. S. Yajima, Y. Hasegawa, J. Hayashi, and M. Imura, "Synthesis of Continuous Silicon Carbide Fibre with High Tensile Strength and High Young's Modulus, Part 1 Synthesis of Polycarbosilane as Precursor," *J. Mater. Sci.*, **13** 2569-76 (1978).
16. D. Seyferth, G.H. Wiseman, and C. Prud'Homme, "A Liquid Silazane Precursor to Silicon Nitride," *J. Am. Ceram. Soc.*, **66** [1] C13-14 (1983).
17. W.R. Schmidt, L.V. Interrante, R.H. Doremus, T.K. Trout, P.S. Marchetti, and G.E. Maciel, "Pyrolysis Chemistry of an Organometallic Precursor to Silicon Carbide," *Chem. Mater.*, **3**, 257-267 (1991).
18. B.A. Bishop, M.S. Spotz, W.E. Rhine, H.K. Bowen, and J.R. Fox, "Sintering of Silicon Carbide Prepared from a Polymeric Precursor"; pp. 856-63 in Ceramic Powder Science II, Ceramic Transactions, Vol. 1B. Edited by G.L. Messing, E.R. Fuller, Jr., and H. Hausner. American Ceramic Society, Westerville, OH, 1988.
19. Y. Hasegawa, M. Imura, and S. Yajima, "Synthesis

of Continuous Silicon Carbide Fibre, Part 2 Conversion of Polycarbosilane Fibre into Silicon Carbide Fibres" *J. Mater. Sci.*, **15** 720-28 (1980).

20. Y. Hasegawa nd K. Okamura, "Synthesis of Continuous Silicon Carbide Fibre, Part 3 Pyrolysis Process of Polycarbosilane and Structure of the Products," *J. Mat. Sci.*, **18** 3633-3648 (1983).
21. P. Calvert and M.J. Cima, "Theoretical Models for Binder Burnout," *J. Am. Ceram. Soc.*, **73** [3] 575-79 (1990).
22. B.G. Streetman, Solid State Electronic Devices. Prentice-Hall, Inc., Englewood, NJ, 1980.
23. A. Lee Smith, "Infrared Spectra-Structure Correlations for Organosilicon Compounds," *Spectrochimica Acta*, **16** 87 (1960).
24. L.J. Bellamy, "The Infra-red Spectra of Complex Molecules," 2nd Edition, John Wiley & Sons, 1964, Chapters 3 and 20
25. C. Dong and H.K. Bowen, "Hot-stage Study of Bubble Formation During Binder Burnout," *J. Am. Ceram. Soc.*, **72** [6] 1082-87 (1989).
26. A.L. Smith and N.C. Angelotti, "Correlation of the SiH Stretching Frequency with Molecular Structure," *Spectrochimica Acta*, **15**, 412 (1959).
27. B.E. Walker, Jr., R.W. Rice, P.F. Becher, B.A. Bender, and W.S. Coblenz, "Preparation and Properties of Monolithic and Composite Ceramics Produced by Polymer Pyrolysis," *Am. Ceram. Soc. Bull.*, **62** [8] 916-23 (1983).

SECTION 26

PRECERAMIC BINDERS IN CERAMIC POWDER PROCESSING

Mark S. Spotz

ABSTRACT

The behavior of preceramic polymers as binders was investigated for a polycarbosilane and a vinylic polysilane using submicrometer β-SiC powders. Ceramic packing density and uniformity are influenced by compaction behavior, the ceramic yield of the polymer, and pyrolysis shrinkage. Compaction of polymer/powder mixtures follows typical semilogarithmic density-pressure relationships, with polymer rheology the primary variable determining the packing density and uniformity. The pyrolyses of both organosilicon polymers are sensitive to two types of extrinsic factors encountered in powder processing: mass transport factors and contamination from oxygen and H_2O. Incremental shrinkage measurements show that pyrolysis shrinkage is caused by the large volume contraction of the binder during conversion, although capillary forces may play a minor role for liquid binder systems.

INTRODUCTION

Certain families of inorganic and metalorganic polymers convert to ceramic materials under appropriate pyrolytic conditions, and for this reason they have been termed preceramic polymers [1]. Rather than decomposing fully into volatile pyrolysis products, they crosslink to form stable intermediates which complete the transformation to ceramic at higher temperatures. Preceramic polymers are useful in the production of a variety of ceramic shapes, with the polymer acting as either the sole starting material or as a binder for particulate bodies. In a particulate body, the pyrolysis products form a ceramic matrix phase intermingled with the particulate phase.

The presence of this matrix phase leads to several unique effects. First, it acts as a high temperature binder that strengthens the compact throughout the pyrolysis process [2, 3]. This feature is of particular importance in fabricating large and/or delicate structures, such as fibers. Second, the binder pyrolysis product contributes to ceramic packing density [4]. Third, the polymer can be a source of dispersed phases [5] or of dopants, as in the case of polyphenylene, which is used as a carbon source in sintering of SiC [6]. These effects are usually enhanced when the preceramic polymer has a high pyrolytic yield of ceramic.

This paper addresses several issues concerning how a preceramic binder can influence the various stages of ceramic processing. The study focused on three aspects of the process: (1) consolidation or compaction during forming; (2) the ceramic yield of the polymer; and (3) shrinkage during pyrolysis. In compaction studies with conventional organic binders, polymer rheology has been identified as a key variable [7, 8]. Nonoptimal rheology leads to packing defects which reduce packing densities and mechanical strengths. In the second case, the ceramic yield of the polymer is determined by its molecular structure and pyrolysis chemistry. Within a compact this chemistry may differ from that of pure polymer because conversion reactions are frequently sensitive to mass transport factors [9] and to chemical contaminants which may be present on the powder surface. In the third case, the degree of shrinkage during pyrolysis can be significant [3]. The preceramic binder experiences a severe reduction in volume during pyrolytic conversion; it is unclear whether this contraction is solely responsible for compact shrinkage or whether capillary forces play a contributing role. Capillary forces are important in binder removal processes [10], as well as in the related phenomenon of liquid phase sintering [11].

For each of these aspects, polymer properties play an important role in determining mean ceramic packing density and/or packing uniformity, two process characteristics which have a fundamental impact on process performance and microstructure quality. The goal was to further understand how the preceramic binder functions, how the polymer is affected by processing operations, and how its properties might be adjusted to improve process performance and ceramic quality.

EXPERIMENTAL PROCEDURE

The polymers used for this research were a polycarbosilane (PCS, Nicalon™ X9-6348, Dow Corning Corp., Midland, MI) and a vinylic polysilane (PVS, Y-12044, Union Carbide Corp., Specialty Chemical Div., Tarrytown, NY). These polymers were characterized by proton magnetic resonance (^{1}H-NMR, Model WM-250, Bruker Spectrometer, 250 MHz, $CDCl_3$ diluent), Fourier transform infrared spectroscopy (FTIR, PC/IR-44, Nicolet Instrument Corp., Madison, WI), and elemental analyses. Molecular weights were determined cryoscopically in benzene. The silicon carbide powders used were a submicrometer β-SiC powder (Betarundum Ultrafine, Ibiden Co., Ltd., Ogaki, Japan) and an α-SiC powder (Lonza Carbogran™ UF-15, Swiss Aluminum, Ltd., Neuhausen, Switzerland).

Polymer/powder batches were prepared in a nitrogen-filled glove box to protect the polymers from possible oxidation or hydrolysis. The PVS was initially degassed at 80°C for 2 h under vacuum, and the powders were dried at 180°C for 24 h under vacuum. Appropriate quantities of the polymers were dissolved in 40 mL of toluene previously distilled over Na-benzophenone. Then 20 g of β-SiC was added and the mixture was stirred magnetically. The batches were sealed in round-bottom flasks, removed from the glove box, and ultrasonicated for 10 min. The toluene was extracted by vacuum at 40-50°C while stirring vigorously. The batches were then returned to the glove box, granulated with a mortar and pestle, and stored. Batch formulations were prepared with PCS at concentrations of 10 wt% and 20 wt% and PVS at 8.5 wt% and 17.3 wt%, in both cases equivalent to volume concentrations of 24.2 vol% and 41.7 vol%.

Dry compaction was selected over other forming methods because of its tolerance for wide variations in binder content. Uniaxial compaction tests were performed under dry nitrogen, except for the tests on pure powders which took place in ambient air (otherwise these pellets cracked upon die removal). Cylindrical pellets were pressed in a 16-mm diameter floating die set with applied pressure in the range 18-200 MPa. Since the β-SiC gave the higher packing densities of the two pure powders, it was used predominantly. The volume fractions for powder, polymer, and porosity were calculated using the batch composition, phase densities, and pellet weights and dimensions. Compacts were fractured and examined with a scanning electron microscope (SEM, Model S-530, Hitachi, Ltd., Tokyo, Japan) in the as-pressed condition and also after heating to 300°C in argon to cure the liquid PVS. This inspection was effective in detecting granule artifacts and intergranular porosity. Compact porosities and pore size distributions were measured by mercury porosimetry (Autopore II 9220, Micromeritics Corp., Norcross, GA) to a maximum intrusion pressure of 205 MPa.

Pyrolysis of the pure polymers was observed for use as a standard to which pyrolysis within compacts could be compared. Bulk polymer was analyzed as-received and after pyrolysis at 1000°C in gettered argon. Silicon content determined by atomic emission spectroscopy using an inductively coupled plasma (ICP, Model 5500, Perkin-Elmer ICP, Galbraith Laboratories, Inc., Knoxville, TN) emission source. Carbon (Model CR-12, Leco Corp., performed at Galbraith Laboratories, Inc) and hydrogen (Model 800 CHN Analyzer, Leco Corp., Galbraith Laboratories, Inc) contents were determined by oxidation, and oxygen content was measured by fast-neutron activation (IRT Corp., San Diego, CA.). Process variables examined included sample mass for pure polymer samples; heating rate from 10-600°C/h; oxidation; and exposure to the hydroxylated β-SiC powder, in compacts or as loose granules.

Weight loss data were obtained on 5-10 mg samples using thermogravimetric analysis (TGA, Model TGA 7, Perkin-Elmer, Norwalk, CT). The TGA procedure consisted of initially purging the system with argon (UHP grade) at 300-400 cm^3/min for 50 min, followed by heating at 600°C/h to 1000°C at a flow rate of 100 cm^3/min. Measurements with a ZrO_2/Pt sensor showed that this procedure yielded oxygen partial pressures [($P(O_2)$)] of ~10 ppm. Larger samples were pyrolyzed in a tube furnace which was equipped with a silica tube, an evacuation pump, and a gettering system (Model 2A-100-SS, Centorr Associates, Inc., Suncook, NH; copper element) to remove oxygen from the inert gas stream. With this system $P(O_2)$ levels were typically 10^{-9}–10^{-12} atm.

The compacts used to measure binder ceramic yield and pyrolysis shrinkage were heated in the tube furnace (silica tube) to the following upper temperatures: 80°C, 300°C, 700°C, or 1000°C. The following heating schedule was used: 120°C/h to 80°C; 60°C/h to 250°C; 20°C/h to 700°C; then 60°C/h to 1000°C. The compacts heated only to 80°C or to 300°C were held there for 4 h to give capillary forces a chance to act within the respective fluid ranges of PVS and PCS. After heat treatment the compact weights and dimensions were measured, and incremental weight loss and shrinkage were calculated. Mercury porosimetry was used to determine open porosity and pore size distributions for selected compacts. The wetting criterion for capillary action was verified by observing the

Table 1. Preceramic Polymer Characteristics.

Polymer	Density (g/cm^3)	M_n[a]	Viscosity, 25°C	1000°C Ceramic Yield[b] (Pa·s)	1000°C Equivalent SiC Purity[c] (wt%)	1000°C Impurity Oxygen[d] (wt%)
PCS	1.12	1580	solid	56	83	0.85
PVS	0.939	1040	7.9	59	76	1.49

[a] Number-average molecular weight by cryoscopic method in benzene.
[b] Non-oxidative pyrolysis; 41.7 vol% concentration in ~1-g compacts with β-SiC powder.
[c] Based on elemental analysis of polymer pyrolysis products.
[d] Neutron Activation, IRT Corp., San Diego, CA.

Table 2. Powder Characteristics.

Powder	Density (g/cm^3)	Surface Area (m^2/g)	Particle Size (μm)	Morphology	Impurities (wt%)
β-SiC[a]	3.21	18.3	0.05-2.0	equiaxed	0.59[c]
α-SiC[b]	3.19	16.8	0.05-3.0	angular	0.81[d]

[a] Betarundum Ultrafine, Ibiden Co., Ltd., Ogaki, Japan.
[b] Lonza Carbogran™ UF-15, Swiss Aluminum, Ltd., Neuhausen, Switzerland.
[c] Neutron Activation, IRT Corp., San Diego, CA.
[d] Vacuum Fusion, Swiss Aluminum, Ltd., Neuhausen, Switzerland.

state of wetting for PCS and PVS on α-SiC substrates (Hexoloy™ SA, Carborundum Company, Niagara Falls, NY) heated slowly (120°C/h to 400°C; 60°C/h to 510°C) in gettered argon. The substrates had a relative density of ~97 vol% and a flat, as-sintered surface.

RESULTS AND DISCUSSION

Materials

The silicon carbide system was investigated using submicrometer powders and two organosilicon polymers. The polymers were a polycarbosilane (PCS) and a vinylic polysilane (PVS). Some characteristics of PCS and PVS are given in Table 1. The results of proton magnetic resonance (^{1}H-NMR), Fourier transform infrared spectroscopy (FTIR), and chemical analyses of these polymers indicate their structures are essentially the same as those reported in the literature [12-14]. PCS softens near 200°C and is fluid to >500°C in the absence of oxygen. PVS is a viscous liquid below 100°C; it cures to a solid in the range 150-250°C without requiring oxygen. Both polymers pyrolyze non-oxidatively to products consisting of SiC and excess carbon, with similar pyrolysis yields and SiC contents. Composites of these polymers were prepared using a submicrometer β-SiC powder or an α-SiC powder. The characteristics of these powders are given in Table 2.

Compaction

Powder packing densities for both the as-received powders and the polymer/powder mixtures followed semilogarithmic relationships with applied pressure, as shown in Figure 1. This behavior is characteristic of agglomerated, fine powders. Frey and Halloran [8] expressed the following empirical relationship for compaction of spray-dried alumina:

$$V_S - V_{SY} = m \ln(P/P_Y) \tag{1}$$

with V_{SY} as the packing density at the applied pressure, P_Y, and V_S as packing density at pressure $P > P_Y$. The apparent yield pressure, P_Y, is defined by a slope transition frequently seen in the range 0.1-1 MPa and associated with the onset of granule deformation. The slope m has been termed the compaction efficiency [15]. Compaction efficiencies corresponding to these data are given in Table 3.

As expected, polymer rheology and concentration were both important in determining how the polymer affected the compaction process. With PVS, powder packing densities were almost unchanged from those of pure β-SiC powder, except for the highest binder content and pressure (41.7 vol% at 280 MPa). Compaction efficiently forced liquid polymer into pores without affecting the baseline packing density, even at high polymer concentrations. It is notable that a liquid binder system can be "dry"-pressed at these high concentrations without tackiness or handling problems. In contrast, the presence of PCS resulted in low mean packing densities, an effect which intensified with PVS concentration, and in increased values of m, an effect dependent of concentration.

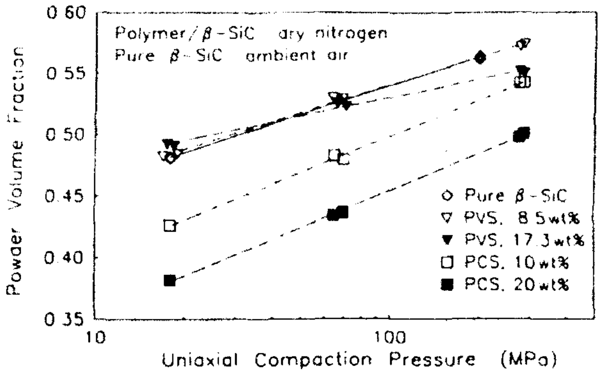

Fig. 1. Powder packing densities for polymer/β-SiC granules pressed in dry nitrogen and pure β-SiC powder pressed in air.

Table 3. Compaction Efficiency.

Material	Slope (Powder vol%/decade[a])
Pure β-SiC	7.97
8.5 wt% PVS	7.57
17.3 wt% PVS	4.99
10.0 wt% PCS	9.74
20.0 wt% PCS	9.88

[a]Theoretical density, 3.21 g/cm^3.

Calculated total porosities reflect these powder packing relationships and further demonstrate the greater ease in eliminating porosity with the PVS/β-SiC system. Calculated values given in Figure 2 are in agreement with mercury intrusion measurements on selected compacts, indicating that for those cases essentially all porosity was open and accessible. For the sample containing 41.7 vol% PVS compacted at 280 MPa, however, a calculated porosity of 5 ± 2 vol% suggested a significant amount of closed pore space.

Mean packing density is determined primarily by granule deformation behavior which has been correlated with the glass transition temperature, T_g, of the binder [16]. In the case of PVS, $T_g << 25°C$, while for PCS, $T_g >> 25°C$. The deformation behavior of PVS and PCS is clearly different in the micrographs of fracture surfaces of cured compacts in Figures 3 and 4. In PVS-containing compacts, granules deformed easily to eliminate intergranular porosity and produce highly uniform packing. With PCS, granular artifacts and associated intergranular porosity were prevalent. Mercury intrusion measurements showed a much broader pore size distribution in the PCS/β-SiC compacts, as indicated by the cumulative intrusion volumes in Figure 5.

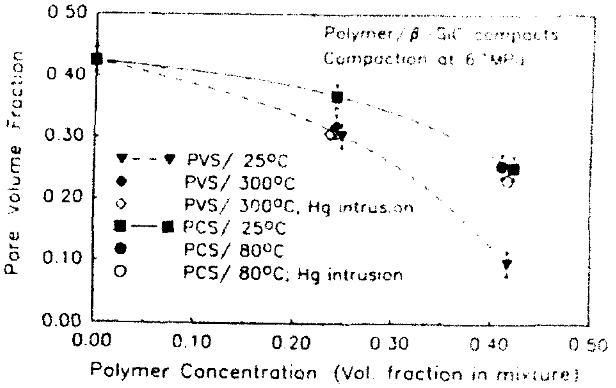

Fig. 2. Calculated total porosity versus polymer concentration for green compacts pressed at 67 MPa; mercury intrusion data included.

Pyrolysis Chemistry

Elemental analyses before and after pyrolysis (Table 4) can be used to calculate the retention of elements and equivalent (rule-of-mixtures) phases [17] after pyrolysis (Table 5). In calculating the phases present, oxygen is first assigned as SiO_2, all remaining silicon as SiC, and then any remaining carbon as "excess" carbon. This method provides a nominal phase composition and is not intended to describe the actual assemblage. Several details can be noted. First, although silicon retention is higher for PVS, its pyrolyzed SiC content (76 wt%) is lower than that of PCS (83 wt%) because of its initially lower silicon level. Correspondingly, the excess carbon in PVS is higher: 19.6 wt% versus 14.4 wt% for PCS. Finally, considering the pyrolyzed yields and elemental analyses, the effective SiC yields for these polymers are very similar: 46.5 wt% for PCS and 44.8 wt% for PVS.

The thermogravimetric analysis of PCS indicates it is most similar to Hasegawa and Okamura's PC-470 [12]. Since the pyrolysis yield at 1000°C was 52 ± 1 wt% for small quantities (5-10 mg) in both the TGA system and the gettered tube furnace, this value was taken to represent the yield of ceramic at 1 atm under an inert gas. Pyrolysis yield can be reduced significantly under vacuum [9] and increased in a closed system under pressure [18]. The TGA of PVS [25] is similar to the one obtained for PCS. In PVS a small amount of material is lost below 165°C due to the presence of low molecular weight fractions. Most of the volatile materials can be removed by degassing the PVS under vacuum prior to thermal treatment.

The effects of process variables on ceramic yield can be classified as either due to mass transport factors or due to chemical reactions with oxygen or H_2O in the atmosphere or at the powder surface. For example, the ceramic

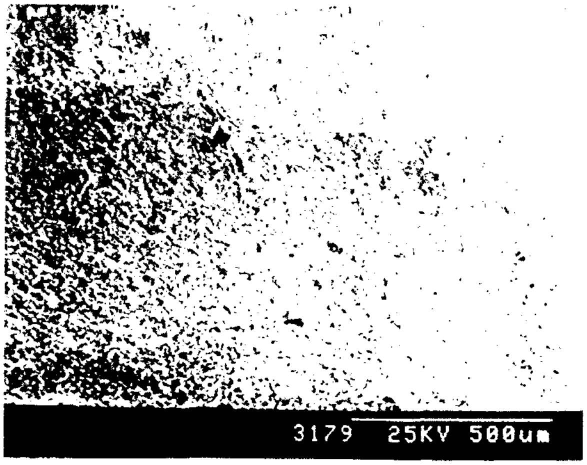

Fig. 3. Scanning electron micrograph of 17.3 wt% PVS/β-SiC compact pressed at 67 MPa and cured at 300°C.

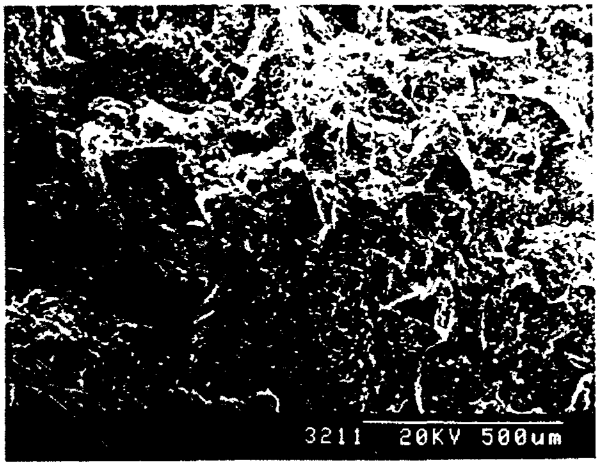

Fig. 4. Scanning electron micrograph of 20 wt% PCS/β-SiC compact pressed at 67 MPa and heated to 300°C.

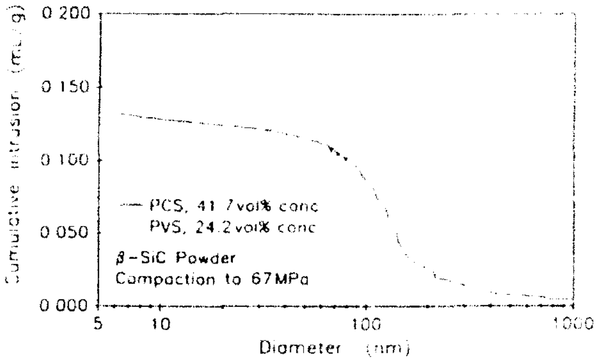

Fig. 5. Cumulative intrusion versus pore size for 20 wt% PCS (green) and 8.5 wt% PVS (cured at 300°C) samples compacted to 67 MPa.

yield is sensitive to initial polymer mass and heating rate, indicating mass transport effects influence the ceramic yield. Slow heating rates increase the ceramic yield and, at the slow heating rate of 10°C/h, the ceramic yield increased 3-4% relative to yields obtained at 60°C/h, as shown in Figure 6. Analysis of the oxygen content of the pyrolyzed polymer showed no oxygen gain at these slow heating rates; therefore, the increase in yield must be a mass transport effect. Figure 6 also shows that the ceramic yield increased as the mass of initial polymer increased. These results indicate the efficiency of retaining and incorporating low molecular weight materials by secondary reactions increases as the initial mass increases and as the heating rate decreases.

Poupeau et al. [18] and Hasegawa et al. [19] have previously established that during pyrolysis of PCS, oxygen can be incorporated into the structure. Incorporation of oxygen involves thermolytic oxidation of Si-H and Si-CH_3 groups, with subsequent crosslinking to form Si-O-Si and Si-O-C bridges. These bridges help stabilize the structure, resulting in higher ceramic yield but also higher oxygen content. TGA analyses of PCS at two heating rates under an nitrogen atmosphere containing trace amounts of oxygen [$P(O_2) = \sim 10$ ppm] are shown in Figure 7. At a heating rate of 600°C/h, the ceramic yield was identical to that obtained under gettered argon (52 ± 1 wt%). At 120°C/h, the ceramic yield increased to 62 ± 1 wt%, indicating an increased yield due to the reaction with trace amounts of oxygen.

Pyrolysis of organosilicon polymers in polymer/powder mixtures depends on a combination of polymer chemistry and processing conditions. Figure 8 contains weight loss data for composites prepared with various amounts of preceramic polymer. The binder pyrolysis yield at a given temperature is defined by the residual polymer mass and calculated as a percent of initial polymer mass. Pyrolysis of PCS and PVS in polymer/powder mixtures proceeded in the same fashion as for the pure polymer, with two exceptions. First, a greater incremental loss from mixtures occurred in one or more decomposition stages. A granulated mixture is more finely divided than a sample of pure polymer, and the retention of volatiles through secondary reactions is less efficient due to increased rates of volatile transport through the porosity of the mixture. The second effect due to the SiC powder is that low initial polymer concentrations produced higher binder pyrolysis yields at 700°C and 1000°C (Fig. 8). This concentration dependence is the reverse of

Table 4. Chemical Analysis Before and After 1000°C Pyrolysis.

	Polycarbosilane		Vinylic Polysilane	
Element, wt%	Uncured	1000°C	Degassed	1000°C
silicon[a]	49.14	57.15	41.55	54.56
carbon[b]	41.73	37.97	45.91	42.22
hydrogen[c]	7.83	0.88	8.99	1.02
oxygen[d]	0.71	0.85	1.13	1.49
total	99.41	96.85	97.58	99.29

[a] Inductively coupled plasma (ICP).

[b] Organic and inorganic oxidation.

[c] Organic oxidation.

[d] Fast-neutron activation.

Table 5. Chemical Analysis: Element Retention and Equivalent (Rule-of-Mixtures) Phases After 1000°C Pyrolysis.[a]

Retention (wt% Retained)			Equilibrium Phases, wt%		
Element	PCS[b]	PVS[c]	Phase	PCS	PVS
silicon	67.4	78.8	SiC	83.1	76.0
carbon	52.8	55.2	carbon	14.3	19.6
hydrogen	6.5	6.8	hydrogen	0.9	1.0
oxygen	69.0	79.1	SiO_2	1.7	2.8
			total	100.0	100.0

[a] Calculated from Table 2 data using rule-of-mixtures method.

[b] Based on pyrolysis product yield of 58 wt% for analyzed sample.

[c] Based on 60 wt% pyrolysis product yield.

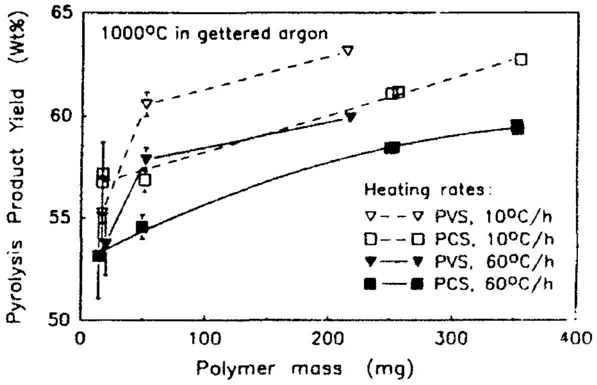

Fig. 6. Pyrolysis product yield in gettered argon for pure polymer versus initial polymer mass and heating rate.

that expected based on transport considerations and, therefore, indicates pyrolysis was influenced by powder surface chemistry.

One likely reaction scheme is hydrolysis of the Si-H groups present in both polymers by H_2O which adsorbed during the transfer of pellets between the glove box and pyrolysis furnace. Thermolytic hydrolysis of organosilicon hydrides may be catalyzed by the slightly acidic SiC surface [20, 21]. However, there are other possible reactions involving the hydroxylated SiC surface [14]. Summarizing, the pyrolysis of these polymers can be modified in the polymer/powder compact both by mass transport and by surface chemical factors.

Pyrolysis Shrinkage

The magnitude of pyrolysis shrinkage in a compact is concentration-dependent and becomes significant (>10%) when the volume percent polymer (e.g., >40 vol%) is higher than the pore volume. Rogers et al. [3] reported similar shrinkage behavior for a series of polysilazane/SiC formulations. Shrinkage for PCS/β-SiC compacts occurred at temperatures coincident with conversion to ceramic, as shown by the shrinkage versus temperature data in Figure 9 for initial polymer concentrations of 24.2 and 41.7 vol%. No shrinkage was observed for PVS/β-SiC after a 4 h hold at 80°C, a

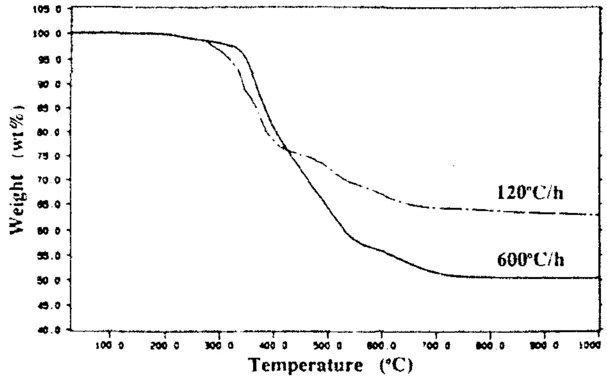

Fig. 7. TGA of polycarbosilane in argon: the effect of heating rate on the degree of oxidation at ~10 ppm oxygen.

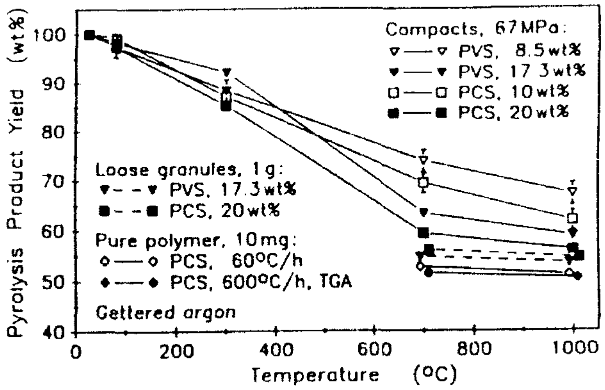

Fig. 8. Polymer pyrolysis yield versus temperature for compacts (67 MPa), loose granules, and pure PCS.

temperature estimated to be near the point of minimum viscosity, since PVS cures slowly above ~100°C. In the case of PVS, shrinkage is clearly caused by contraction of the solid binder phase as it loses mass and densifies. The contribution of capillary forces cannot be ruled out for PCS, however, with its extended range of fluidity (to >500°C).

Estimates of the capillary driving force for particle rearrangement can be made using expressions developed for equivalent external pressure [11, 22]. Heady and Cahn defined an equivalent external pressure P_x, where γ_{LV} is the liquid/vapor surface energy, as follows [22]:

$$P_x = \frac{2\sqrt{2}\,\pi\,\gamma_{LV}\cos\theta}{R} \qquad (2)$$

where R is the particle radius and θ is the liquid/particle contact angle, here assumed to be ~0. For polymers, γ_{LV} ≈ 20-50 mN/m, so P_x ≈ 0.8 MPa (~120 psi) for particles of 0.5 μm in diameter. The driving force for particle

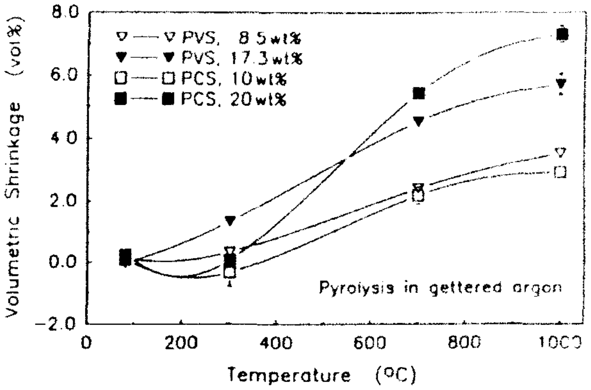

Fig. 9. Cumulative volumetric shrinkage to 1000°C.

rearrangement with liquid polymers is thus 1-2 orders of magnitude lower than for liquid metals and oxides, and the contribution of capillary-driven rearrangement during pyrolysis shrinkage is expected to be minor.

Contributions to Packing Density

Schwartz and Rowcliffe [4] accounted for the contributions of the preceramic binder to ceramic packing density with a fixed-packing model which assumed that compaction and pyrolysis produced negligible changes to the baseline packing density of the pure ceramic powder. This method can be modified to account for non-ideal compaction and pyrolysis shrinkage. In Figure 10, the total ceramic packing densities after compaction and after pyrolysis are plotted against polymer volume fraction, V_B, after compaction. For this calculation the polymer fraction is replaced by its equivalent ceramic product regardless of whether the compact has been pyrolyzed. Using the ceramic yield and SiC purity factors from Table 1, the equivalent SiC yields for PCS and PVS were calculated as 46.5 wt% and 44.8 wt%, respectively. Although based on pyrolysis to 1000°C, these values are also good estimates of the SiC yields at ~2000°C [23]. The empirical data are compared to the fixed-packing model with a powder volume fraction, V_S, of 0.57. For fixed powder packing, the total packing density increases until all pore space is filled at $V_B = 0.43$; further additions of polymer must then be accompanied by reductions in powder content, resulting in the negative slope in Figure 10.

For the PVS system, slightly higher total packing densities were obtained relative to the fixed-packing case, due to the combination of nearly ideal compaction and moderate pyrolysis shrinkage. Also plotted is the theoretical behavior for a hypothetical binder with rheology and shrinkage like that of PVS but with a SiC yield of 85 wt% (as opposed to 45 wt% for SiC). Even for a ceramic yield

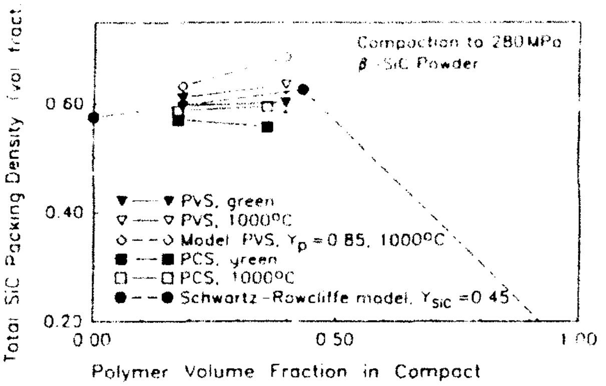

Fig. 10. Total SiC packing density versus organosilicon polymer volume fraction, including contributions of compaction, ceramic yield, and pyrolysis shrinkage; comparison with Schwartz-Rowcliffe fixed packing model [4].

of 100%, total packing density is limited by the ratio of binder density to ceramic density, ρ_{B1}/ρ_{B2}. The importance of this ratio was recognized by Rice [24].

SUMMARY AND CONCLUSIONS

As with conventional binders, the application of preceramic polymers as binder systems requires an understanding of and control over the various steps in particulate processing. The compaction process, conversion of the binder to ceramic, and shrinkage during pyrolysis are three important phenomena which control a number of characteristics of the compact microstructure including packing density, packing uniformity, and pore size distribution. These phenomena were investigated for the SiC system in an effort to optimize preceramic binder properties.

Compaction behavior of polymer/powder mixtures is determined by the nature of the powder as well as by polymer rheology. In the present case, compaction of granulated mixtures followed the common semilogarithmic density-pressure relationship. Results were in agreement with previous correlations between granule deformation and the polymer glass temperature, T_g. The granules containing liquid PVS deformed easily to eliminate intergranular porosity and produce dense, highly uniform packing.

While the pyrolysis product yield and ceramic composition are largely determined by polymer chemistry, pyrolysis of the binder is also influenced by the processing variables. Mass transport effects are important since the conversion reactions are sensitive to the amount of volatile materials. Also, since the polymers can undergo thermolytic oxidation and hydrolysis, contamination can be a serious problem, especially since the SiC powder surface attracts moisture.

Binder pyrolysis represents the final opportunity to influence the characteristics of the pre-sintered ceramic microstructure. Although the state of packing is largely determined in the initial preparation and forming operations, conceivably packing uniformity could be influenced during pyrolysis of liquid binders through the action of capillary forces. While surface tension of fluid polymers is high enough to produce migration of the polymer itself [10], it is apparently insufficient to cause much rearrangement of submicrometer ceramic particles. The shrinkages observed for PVS/β-SiC and PCS/β-SiC can be explained by volume contraction of the binder phase. While useful for increasing mean packing density, this mechanism is not expected to result in a significant correction of packing inhomogeneities. Preceramic binders contribute to ceramic packing density, but the effect is ultimately limited by the polymer/ceramic density ratio. The conditions to achieve the maximum benefit from preceramic binders are the following: low ceramic density, as with BN; polymer $T_g < 25°C$; high pyrolysis product yield and ceramic purity; and a degree of pyrolysis shrinkage, probably enhanced by a region of fluidity during pyrolysis. Overall, the unique properties of preceramic polymers make them useful as high temperature binder systems, particularly for increasing the processability of delicate structures, and to create unique ceramic phase mixtures and microstructures.

ACKNOWLEDGMENTS

The authors are grateful to Prof. P. Calvert, Dr. W. Coblenz, and Prof. D. Seyferth for their advice and encouragement.

REFERENCES

1. Schwartz, K.B., Rowcliffe, D.J., and Blum, Y.D., "Microstructural Development in Si_3N_4/Polysilazane Bodies During Heating," *Adv. Ceram. Mater.*, 3 [4] 320-3 (1988).
2. S. Yajima, T. Shishido, and K. Okamura, "SiC Bodies Sintered with Three-Dimensional Cross-Linked Polycarbosilane," *Am. Ceram. Soc. Bull.*, **56** [12] 1060-63 (1977).
3. J.J. Rogers, J. Semen, and D.Y.-F. Yu, "Silicon Carbide and Silicon Nitride Structural Ceramics Derived from a Preceramic Polymer Binder," *Ceram. Eng. Sci. Proc.*, **10** [7-8] 833-36 (1989).

4. K.B. Schwartz and D.J. Rowcliffe, "Modeling Density Contributions in Preceramic Polymer/Ceramic Powder Systems," *J. Am. Ceram. Soc.*, **69** [5] C106-C108 (1986).

5. M. Bougoin and F. Thevenot, "Pressureless Sintering of Boron Carbide with an Addition of Polycarbosilane," *J. Mater. Sci.*, **22** 109-14 (1987).

6. S. Prochazka, "Sintering of Silicon Carbide," pp. 421-31 in Mass Transport Phenomena in Ceramics, Materials Science Research, Vol. 9. Edited by A.R. Cooper and A.H. Heuer. Plenum Press, New York, 1975.

7. R.A. DiMilia and J.S. Reed, "Effect of Humidity on the Pressing Characteristics of Spray-Dried Alumina"; pp. 38-46 in Forming of Ceramics, Advances in Ceramics, Vol. 9. Edited by J.A. Mangels and G.L. Messing. American Ceramic Society, Columbus, OH, 1984.

8. R.G. Frey and J.W. Halloran, "Compaction Behavior of Spray-Dried Alumina," *J. Am. Ceram. Soc.*, **67** [3] 199-203 (1984).

9. S.L. Madorsky, Thermal Degradation of Organic Polymers. John Wiley & Sons, New York, 1964.

10. M.J. Cima, J.A. Lewis, and A.D. Devoe, "Binder Distribution in Ceramic Greenware During Thermolysis," *J. Am. Ceram. Soc.*, **72** [7] 1192-99 (1989).

11. W.D. Kingery, "Densfication During Sintering in the Presence of a Liquid Phase. I. Theory," *J. Appl. Phys.*, **30** [3] 301-306 (1959).

12. Y. Hasegawa and K. Okamura, "Synthesis of Silicon Carbide Fibre; Part 3, Pyrolysis Process of Polycarbosilane and Structure of the Products," *J. Mater. Sci.*, **18**, 3633-48 (1983).

13. C.L. Schilling, Jr., "Polymeric Routes to Silicon Carbide," *Br. Polym. Jour.*, **18** [6] 355-58 (1986).

14. M.S. Spotz, "Organosilicon Polymers as Preceramic Binders for Silicon Carbide"; PhD Thesis. Dept. Mat. Sci. Eng., MIT, 1990.

15. J. Zheng and J.S. Reed, "Particle and Granule Parameters Affecting Compaction Efficiency in Dry Pressing," *J. Am. Ceram. Soc.*, **71** [11] C456-C458 (1988).

16. C.W. Nies and G.L. Messing, "Binder Hardness and Plasticity in Granule Compaction"; pp. 58-66 in Forming of Ceramics, *Advances in Ceramics*, Vol. 9. Edited by J.A. Mangels and G.L. Messing. The American Ceramic Society, Columbus, OH, 1984.

17. J. Lipowitz, H.A. Freeman, R.T. Chen, and E.R. Prack, "Composition and Structure of Ceramic Fibers Prepared from Polymer Precursors," *Adv. Ceram. Mater.*, **2** [2] 121-28 (1987).

18. J.J. Poupeau, D. Abbe, and J. Jamet, "Gas Analysis during the Pyrolysis of Carbosilane"; pp. 287-97 in Emergent Process Methods for High-Technology Ceramics, Materials Science Research, Vol. 17. Edited by R.F. Davis, H. Palmour III, and R.L. Porter. Plenum Press, New York, 1984.

19. Y. Hasegawa, M. Iimura, and S. Yajima, "Synthesis of Continuous Silicon Carbide Fibre; Part 2, Conversion of Polycarbosilane Fibre into Silicon Carbide Fibres," *J. Mater. Sci.*, **15**, 720-28 (1980).

20. C. Eaborn, Organosilicon Compounds; pp. 194-218. Academic Press, New York, 1960.

21. M. Okuyama, G.J. Garvey, T.A. Ring, and J.S. Haggerty, "Dispersion of Silicon Carbide Powders in Nonaqueous Solvents," *J. Am. Ceram. Soc.*, **72** [10] 1918-24 (1989).

22. R.B. Heady and J.W. Cahn, "An Analysis of the Capillary Forces in Liquid-Phase Sintering of Spherical Particles," *Met. Trans.*, **1**, 185-89 (1970).

23. B.A. Bishop, M.S. Spotz, W.E. Rhine, H.K. Bowen, and J.R. Fox, "Sintering of Silicon Carbide Prepared from a Polymeric Precursor"; pp. 856-63 in Ceramic Powder Science II, Ceramic Transactions, Vol. 1, Part B. Edited by G.L. Messing, E.R. Fuller, Jr., and H. Hausner. The American Ceramic Society, Westerville, OH, 1988.

24. R.W. Rice, "Ceramics from Polymer Pyrolysis, Opportunities and Needs - A Materials Perspective," *Am. Ceram. Soc. Bull.*, **62** [8] 889-92 (1983).

25. W.R. Schmidt, L.V. Interrante, R.H. Doremus, T.K. Trout, P.S. Marchetti, and G.E. Maciel, "Pyrolysis Chemistry of an Organometallic Precursor to Silicon Carbide," *Chem. Mater.*, **2**, 257 (1991).

SECTION 27

PREPARATION OF SiC-CORDIERITE COMPOSITES

Anne B. Hardy, Peter W. Jacobs and Wendell E. Rhine

Published in Chemical Processing of Advanced Materials, p 791, Eds. L.L. hench and J. West, John Wiley and Sons, NY, 1992.

INTRODUCTION

Whisker-reinforced ceramic-ceramic composites are of interest because of their improved mechanical properties but, unfortunately, addition of whiskers often inhibits densification. Hot pressing can be used to prepare dense composites, but this process has limited commercial application because of the difficulty in creating complex shapes. A number of researchers [e.g., 1-5] have investigated the use of pressureless sintering to obtain high density SiC-reinforced ceramic composites. This research has shown the difficulty of obtaining high density composites particularly at high whisker loadings; however, optimization of starting materials and processing conditions has been shown to increase the composite densities.

This paper describes a two-step process for forming a ceramic-ceramic composite. In the first step, an amorphous matrix powder is combined with SiC and then densified by viscous sintering to obtain a glass-ceramic composite. In the second step, the amorphous matrix is crystallized to obtain a thermally stable ceramic-ceramic composite. Cordierite was selected as the ceramic matrix because it belongs to a class of materials which densify by viscous sintering and because it has several commercially interesting properties, including a low thermal expansion coefficient and relatively high thermal stability (mp = 1471°C [6]). As with many ceramic materials, improving the mechanical properties of cordierite through addition of a reinforcing phase could extend its uses. By using a matrix which densifies by viscous sintering we may be able to overcome some of the difficulties of densifying a ceramic matrix around fully dense inclusions. This paper discusses the effect of SiC whiskers and powders on the densification of amorphous cordierite powders.

EXPERIMENTAL PROCEDURE

Cordierite powders were prepared by adding aqueous HCl to a tetraethylorthosilicate (TEOS; Aldrich Chemical Co., Milwaukee, WI) in ethanol solution and then heating the solution to 60-70°C for 1 h. Sufficient water was added so that the water-to-TEOS molar ratio was 1 to 4. Aluminum sec-butoxide (Aldrich Chemical Co., Milwaukee, WI) dissolved in isopropanol (dried over 3A molecular sieves) was added to the solution and refluxing was continued for 3 h. The solution was cooled to room temperature. Magnesium nitrate (Mallinckrodt Inc., Paris, KY) dissolved in a minimum amount of water and diluted in an ethanol/isopropanol solution was added to the cooled aluminum silicate solution and the solution was stirred for 1 h. After the addition of the magnesium solution, a hazy, bluish precipitate sometimes formed. The alkoxide-salt solution was slowly dripped into vigorously stirred ammonia-saturated water, and a white precipitate formed immediately. The dispersion was stirred overnight, and the precipitate was then isolated by vacuum filtration. The precipitate was washed with isopropanol, dried, and then calcined at 775°C for 2 h.

The powders were dispersed in an isopropanol solution containing hydroxypropyl cellulose (Aldrich Chem. Co., Milwaukee, WI) as a dispersant and ballmilled for 12 h. SiC was then added either as whiskers (Arco Metals Co., Greer, SC or American Matrix Inc., Knoxville, TN) or as a powder (Betarundum Ultrafine, Ibiden Co. Ltd., Ogaki, Japan). Whiskers were used as-received or, in some cases, Arco whiskers were ballmilled for 68 h and then classified to reduce the whisker aspect ratio as described previously [5]. The cordierite and SiC were mixed by ballmilling for 2 h. These dispersions were then added to rapidly stirred hexane. The powder and whiskers flocced rapidly upon addition to hexane. The flocced powder-whisker mixture was recovered by vacuum filtration and then dried. Compacts were prepared by uniaxially dry pressing at 20.4 ksi followed by isostatic pressing at 40 ksi. Samples were heated to 1000°C under gettered ultra-high purity argon to densify the composites.

Differential thermal analysis (DTA), thermal gravimetric analysis (TGA), and dilatometric measurements (Netzsch, Inc., Exton, PA) were done at a heating rate of 10°C/min. Powder densities were measured using a helium pycnometer and surface areas were measured by nitrogen absorption (Quantasorb Quantachrome, Syosset, NY). Particle size was measured using a centrifugal particle size analyzer (Horiba CAPA 500, Irvine, CA). Densities were measured by the Archimedes method.

RESULTS AND DISCUSSION

Glass ceramic materials, including cordierite and lithium aluminum silicates, have been investigated as matrix materials for composites, and it has been shown that mechanical properties can be improved by the addition of reinforcing whiskers [see, for example, 7-9]. However, previous investigations have concentrated on forming composites by hot pressing, typically using commercially available glass powders. We developed a method for preparing chemically derived cordierite powder to produce a high purity, highly reactive amorphous powder and then investigated the effect of different processing conditions on the density of the pressureless sintered composite.

Cordierite powders were prepared using modifications of methods presented in the literature [10, 11]. Chemical analysis of the powders showed that the cation composition was in good agreement (within 1-2%) of the calculated composition of the sol. BET surface areas measured after calcination and ballmilling were ~200-250 m^2/g. Particle size measurement showed that the average agglomerate size after calcination and ballmilling was ~0.9 μm. Thermal analysis of the cordierite powders showed that most of the weight loss occurred below 600°C; powders were calcined at 775°C to remove residual organics and to convert the powders to the oxide form. The calcined powder density was 2.3 g/cm^3 (theoretical density = 2.51 g/cm^3 [6]). DTA showed two exothermic peaks: one centered around 985°C and another peak at 1040°C. These peaks are in agreement with crystallization peaks reported by Zelinski et al. [12], who attributed the 985°C peak to the transformation of an amorphous structure to a crystalline beta-stuffed quartz structure and the 1040°C peak to the crystallization to cordierite. Dilatometric measurements showed that the composites sintered rapidly between 850°C and 950°C.

SiC was added to the cordierite by codispersing the cordierite powder and the SiC and then rapidly flocculating the dispersion in hexane. Hexane was a nonsolvent for the polymeric dispersant (hydroxypropyl cellulose), and SiC and cordierite could not be dispersed in hexane without a dispersant. By using this two-step process, we hoped to form flocs that maintained the homogeneity of the dispersion. Similar techniques involving dispersing the powder followed by flocculation have been shown to increase the homogeneity of mixed component systems [13]. Although the whiskers were presumably randomly oriented in the flocs, after dry pressing they appeared to align in a direction perpendicular to the pressing direction, as indicated by scanning electron microscopy (SEM) observation of fracture surfaces and by the nonuniform shrinkage of the composites (the composites shrank more in the z-direction than in the radial direction). SEM observation of the composite fracture surfaces showed that the whiskers were dispersed evenly across the cross section of the sample.

The effect of green density on the sintered density was observed by comparing isostatically pressed samples with samples that were only uniaxially pressed. Figure 1 shows the green densities and the corresponding sintered densities. The low green densities were due partly to the incomplete densification of the calcined powder. Pure amorphous cordierite powder sintered to about the same density regardless of the green density. However, with addition of whiskers, the sintered density became very dependent on the green density, particularly at higher whisker loadings. For example, at 30 vol% SiC the sintered composite density dropped from 64% for isostatically pressed samples to 53% for uniaxially pressed samples.

Composites were also formed using as-received Arco whiskers, Arco whiskers ballmilled for 68 h, American

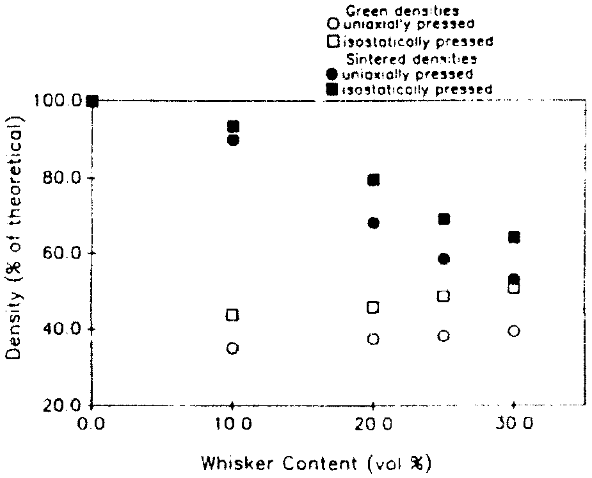

Fig. 1. Sintered composite density compared for dry pressed and isostatically pressed composites.

Table 1 SiC Characteristics.

SiC Type	Form	Avg. Diameter (mm)	Avg. Length (mm)	Aspect Ratio
Arco as-received	whisker	0.6	>20	>30
Arco ballmilled 68 h	whisker	0.6	5	8
American Matrix	whisker	1.5	15	10
Betarundum Ultrafine	powder	0.05-2.0	–	1

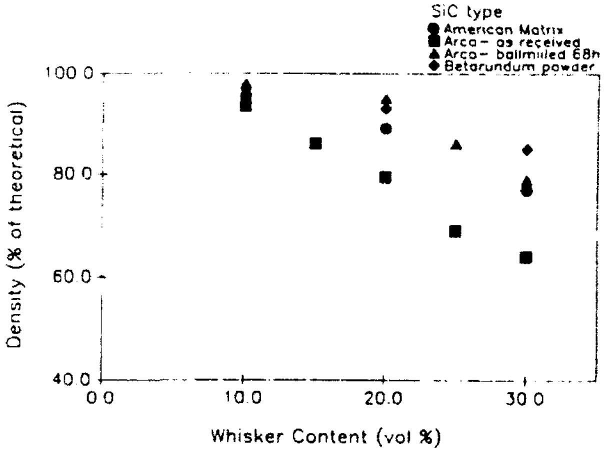

Fig. 2. Sintered composite density as a function of SiC source and concentration.

Matrix whiskers, or Betarundum Ultrafine powders. Table 1 summarizes some of the SiC characteristics, including the aspect ratio. The different silicon carbide sources were used to compare the effect of the whisker aspect ratio on the sintered density. Figure 2 shows the sintered composite density as a function of SiC concentration for the different SiC sources. At all SiC concentrations the composite density showed some dependence on the aspect ratio, but the dependence increased at higher whisker loadings. Composites formed with American Matrix whiskers and composites formed with Arco whiskers ballmilled for 68 h (whiskers which have similar aspect ratios) had comparable densities, indicating aspect ratio was more important than whisker size in determining the composite density.

Fracture surfaces clearly show the differences in densification between composites formed with as-received Arco whiskers and Arco whiskers ballmilled for 68 h as shown in Figure 3. At 10 vol% the microstructures appear to be fairly similar, but at 30 vol% composites formed from the as-received whiskers have extensive remaining porosity, particularly in the region of longer whiskers.

Addition of the SiC hinders densification in two ways. For the composite to densify, the cordierite matrix must be able to shrink around fully dense SiC inclusions. In addition, as the SiC concentration is increased, at some critical concentration it will form a continuous, nonshrinking network. It has been shown both theoretically [14] and experimentally [1, 5] that as the whisker aspect ratio is decreased, more whiskers can be added before the network-forming concentration is reached. Shorter aspect ratio whiskers also appear to pack more uniformly to give higher green densities [15]. We attributed the decrease in sintered density at higher Betarundum powder concentrations primarily to the difficulty of sintering around dense inclusions. The differences between the sintered densities of composites formed with SiC powder and whiskers reflected the difficulty of packing whiskers and also the formation of continuous, nonshrinking SiC networks.

CONCLUSIONS

Composites were formed by viscous sintering using chemically derived cordierite powders and SiC loadings ranging from 0 to 30 vol%. We found that sintered composite densities were dependent on the initial green density and on the aspect ratio of the whiskers, particularly at higher whisker loadings. We were able to sinter composites containing 20 vol% SiC to 93-95% of theoretical density using both powders and whiskers with aspect ratios less than 10.

REFERENCES

1. T.N. Tiegs and P.F Becher, "Sintered Al_2O_3-SiC-Whisker Composites," *Am. Ceram. Soc. Bull.*, **66** [2] 339-42 (1987).

2. M.D. Sacks, H.W. Lee, and O.E. Rojas, "Pressureless Sintering of SiC Whisker-Reinforced Composites," *Ceram. Eng. Sci. Proc.*, **9** [7-8] 741-54 (1988).

3. H.W. Lee and M.D. Sacks, "Pressureless Sintering of Al_2O_3/SiC Whisker Composites," *Ceram. Eng Sci. Proc.*, **10** [7-8] 720-29 (1989).

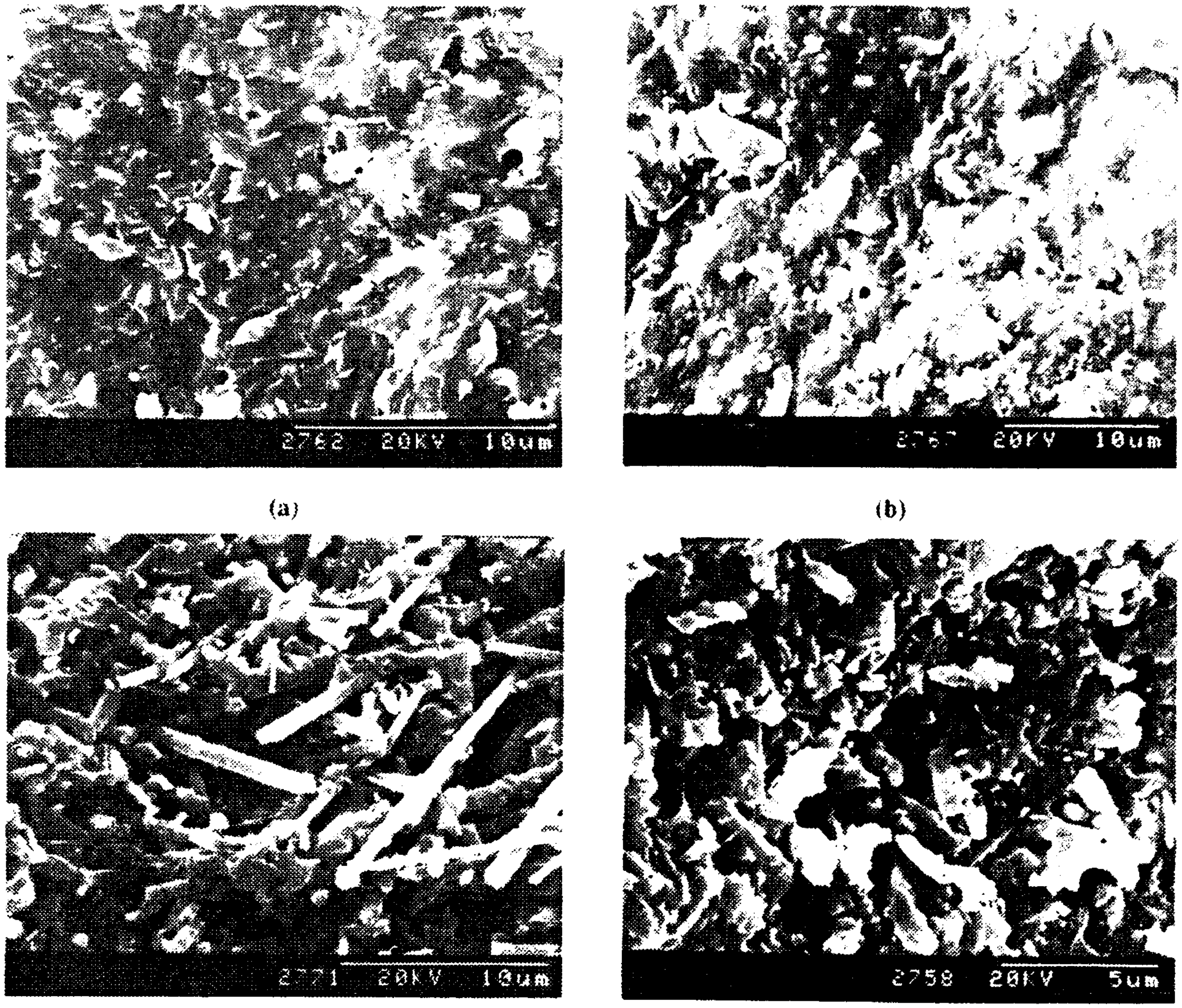

(a) (b)

(c) (d)

Fig. 3. Fracture surfaces of composites formed with (a) 10 vol% as-received Arco whiskers, (b) 10 vol% Arco whiskers ballmilled 68 h, (c) 30 vol% Arco whiskers as-received, and (d) 30 vol% Arco whiskers ballmilled 68 h.

4. M.D. Sacks, H-W. Lee, and O.E. Rojas, "Suspension Processing of Al_2O_3/SiC Whisker Composites," *J. Am. Ceram. Soc.*, **71** [5] 370-79 (1988).

5. T. Ishii and H.K. Bowen, "Dispersion and Pressureless Sintering of Al_2O_3-SiC Whisker Composites": pp. 452-59 in Ceramic Powders Science II. Edited by G.L. Messing, E.R. Fuller, and H. Hausner. American Ceramic Society, Westerville, OH, 1987.

6. C.T. Lynch, editor, Handbook of Materials Science, Vol 2; pp. 374-75. CRC Press, Boca Raton, FL, 1974.

7. J.J. Brennan and K.M. Prewo, "Silicon Carbide Fibre Reinforced Glass-Ceramic Matrix Composites Exhibiting High Strength and Toughness," *J. Mater. Sci.*, **17**, 2371-83 (1982).

8. K.M. Prewo "Tension and Flexural Strength of Silicon Carbide Fibre-Reinforced Glass Ceramics," *J. Mater. Sci.*, **21**, 3590-3600 (1986).

9. R. Chaim, D.G. Brandon, and L. Baum, "Mechanical Properties and Microstructural Characterization of SiC-Fiber-Reinforced Cordierite Glass-Ceramics," *Ceram. Eng. Sci. Proc.*, **9** [7-8] 695-703 (1988).

10. H. Vesteghem, A.R. DiGiampaolo, and A. Dauger, "Low-Temperature Cordierite Glass from Autoclave-Prepared Gel," *J. Mater. Sci. Lett.*, **6**, 1187-89 (1987).

11. C. Gensse and U. Chowdry, "Non-Conventional Route to Glass-Ceramic for Electronic Packaging"; pp. 693-703 in Better Ceramics Through Chemistry II. Mat. Res. Soc. Symp. Proc., Vol. 73. Edited by C.J. Brinker, D.E. Clark, and D.R. Ulrich. Elsevier Science Publishers, New York, NY, 1986.

12. B.J.J. Zelinski, B.D. Fabes, and D.R. Uhlman, "Crystallization Behavior of Sol-Gel Derived Glasses," *J. Non-Cryst. Solids*, **82**, 307-13 (1986).

13. W.C. Moffatt, P. White, and H.K. Bowen, "Production of Alumina-Zirconia Composite Ceramics by Nonsolvent Flocculation of Polymer-Containing Powder Dispersions"; pp. 645-53 in Ceramic Powder Science II. Edited by G.L. Messing, E.R. Fuller, and H. Hausner. American Ceramic Society, Westerville, OH, 1987.

14. E.A. Holm, "A Percolation Model for the Zero Shrinkage Whisker Fraction Ceramic Matrix-Ceramic Whisker Composite"; MS Thesis. Dept. of Mat. Sci. Eng., MIT, February, 1989.

15. J.V. Milewski, "Efficient Use of Whiskers in the Reinforcement of Ceramics," *Adv. Ceram. Mater.*, **1** [1] 36-41 (1986).

SECTION 28

PREPARATION OF SIC/CORDIERITE COMPOSITES BY PRESSURELESS VISCOUS SINTERING

Anne Bagley Harady and Wendell E. Rhine
Ceramics Processing Research Laboratory
Massachusetts Institute of Technology
Cambridge, MA 02139

ABSTRACT

Parameters which influenced the densification of cordierite-SiC composites were studied. It was found that cordierite and SiC composites with high green and sintered densities could be formed by floccing ultrasonicated dispersions and then dry pressing the filtered powders. Calcination of the sol-gel derived powder significantly decreased the sinterability of the composites. Green densities were shown to have a strong effect on the sintered density. Other parameters, such as heating rate, had only a moderate effect on the densification. Using uncalcined sol-gel synthesized powder, composites with densities greater than 95% could be formed using SiC whiskers and SiC powder.

INTRODUCTION

Because of reported improvements in mechanical properties, there has been considerable interest in preparing ceramics reinforced with whiskers or fibers. Fabricating composites using whiskers as the reinforcement phase has the advantage that conventional powder processing techniques can be used. However, it has been shown that addition of nonsintering, nonshrinking inclusions, such as whiskers, inhibits densification.[e.g.,1,2,3.] To achieve high densities, composites are often prepared by hot pressing, but this limits the product to simple shapes or introduces expensive machining costs. Researchers have shown that composites can be densified by pressureless sintering; however, optimization of starting materials and processing conditions are necessary to achieve high sintered densities.[3,4,5,6,7,8,9.]

The effect of various processing parameters on the densification of crystalline matrix composites has been reported in detail.[1-8] It is also known that glass-ceramic composites can be more easily prepared. Recently, Sachs *et al.*[8] have reported that when the matrix material densifies by viscous sintering rather than a diffusion mechanism as in a crystalline material) the inhibiting effect of non-sinterable inclusions on densification is reduced. This fact has particular relevance for materials prepared by sol-gel techniques because a variety of sol-gel derived materials have been shown to densify in the amorphous state by viscous sintering. Further heating converts the amorphous matrix to a crystalline ceramic.[1,8]

A sol-gel derived material which densifies by a vicous sintering mechanism is cordierite.[14] Techniques for preparing cordierite powders by sol-gel methods have been widely described[e.g.,10,11,12,13.] and cordierite prepared by sol-gel methods has been shown to densify by viscous sintering.[14.] In the present work, the fabrication of SiC/cordierite composites by pressureless sintering of sol-gel derived cordierite powders is described. The effect of the properties of the cordierite powder and the SiC whiskers, consolidation methods, and sintering conditions on densification were investigated to determine their effect on the densification of SiC/cordierite composites. A preliminary account of this research has been published elsewhere.[15.]

EXPERIMENTAL PROCEDURE

(1) Materials

Cordierite was prepared by a sol-gel method adapted from the literature.[10-13] The TEOS was partially hydrolyzed by adding an aqueous HCl solution to TEOS (Aldrich Chemical Co. Milwaukee, WI) in ethanol (Water:TEOS = 1:4) and heating the solution to 60-70 °C for 1 h. Alumunium *sec*-butoxide dissolved in isopropanol was added to the TEOS solution and refluxed for 3 h. The solution was cooled to room temperature and dried magnesium nitrate hexahydrate (Mallinckrodt, Paris, KY) dissolved in a minimum amount of water and diuluted with ethanol-isopropanol solution was added and the solution stirred for 1 h. After addition of the nagnesium nitrate solution, a hazy, bluish precipitate sometimes formed. This solution of tetraethylorthosilicate, aluminum *sec*-butoxide, and magnesium nitrate in isopropanol was added slowly into a vigourously stirred NH_3 saturated water. A white precipitate formed immediately which was recovered by filtration and air dried. Both calcined and uncalcined powders were investigated. When calcined powders were used they were heated at 600 °C for 20 min (heating rate of 10°C/min). The powder, as prepared, had a surface area of 175 m^2/g which decreased to 150 m^2/g after calcination at 600 °C. Particle size measurement of the calcined powder showed an average diameter of 0.6 µm.

SiC whiskers were used both as received and after ballmilling for 68 h followed by a classification step. The as received SiC whiskers had an average diameter of 0.6 µm and an average aspect ratio of > 30. After ballmilling for 68 h and classifying to remove the largest aspect ratio whiskers, the aspect ratio decreased to ~8. The β-SiC powder (Betarundum, Ibeden) was used as received

(2) Preparation of composites

The cordierite powder was dispersed in isopropanol and ballmilled for 12 h. SiC and cordierite powders were mixed by vibratory milling in isopropanol for 2 h (alumina milling media). The SiC-cordierite dispersions were sonicated for 1 min and then while sonicating hexane (2:1 vol ratio hexane:dispersion) was added. The dispersion rapidly flocced and the powder was recovered by filtration. Compacts were uniaxially pressed at 10 ksi and then isostatically pressed at 40 ksi. This differs from our previous work in which the composites were calcined before isostatic pressing.[15] In some cases composites were isopressed directly (no uniaxial pressing) using rubber molds. The composites were sintered in ultrahigh purity argon 1000°C for 20 min. Heating rates ranged from 0.1°C to 100°C/min.

(3) Characterization

The cordierite's composition was measured by inductively coupled plasma emission (ICP). Powder surface areas were measured by single point BET and powder densities were measured by a helium pycnometer. Green densities were calculated from the weight and measured volume of the composite. In addition, green density and pore diameters were measured by Hg porosimetry. Sintered densities were measured by the Archimedes method. Crystallization temperatures were measured by differential thermal analysis (DTA) and shrinkage as a function of temperature was measured by a dilatometer.

RESULTS AND DISCUSSION

(1) Powder characteristics

Cordierite powders have been prepared from alkoxides and reductions in sintering and crystallization temperatures have been observed. In this effort, the cordierite powder was precipitated by adding an isopropanol solution of $Mg(NO_3)_2$, $Al(O\text{-}sec\text{-}Bu)_3$, and TEOS to an aqueous solution of ammonium hydroxide. The composition was within ~2% of the theoretical for cordierite as shown in Table 1. Thermogravimetric analysis indicated that most of the weight loss occurred below 600°C. DTA results indicated that the powder behaved as a typical sol-gel derived cordierite[16] and crystallized first to μ-cordierite at about 985 °C and then to α-cordierite at 1040 °C. Dilatometric measurements showed that the cordierite powders sintered rapidly between 850 and 950°C in agreement with previous investigators who have shown that amorphous cordierite begins to densify *via* a viscous sintering mechanism at 850-900 °C before crystallization begins.

Table 1. Composition of synthesized cordierite

Component	wt%
Al_2O_3	35.42 (34.9)
MgO	13.5 (13.8)
SiO_2	51.1 (51.4)

* numbers in parentheses are for stoichiometric cordierite

(2) Powder Flocculation

To obtain high densities and optimum mechanical properties the whiskers must be uniformly distributed in the composite. This uniform distribution of whiskers is often accomplished by dispersing the powder and whiskers in a solvent and then trying to prevent segregation as the composite mixture is recovered from the dispersion. Lange[17] and Moffatt[18] have shown that flocculating the dispersion locks in the homogeneous distribution obtained in the dispersed state and is one of the best approaches for obtaining uniformly mixed composites. Lange *et al.* adjusted the pH to cause flocculation and Moffatt used coacervation of a polymer to cause flocculation. In our case, flocculation was accomplished by sonicating these cordierite-SiC dispersions and then, while sonicating, rapidly floccing the dispersions by adding hexane (a solvent with a low dielectric constant). The flocced

Table 2. Effect of consolidation method on green density (composites contained 20 vol% as received Arco whiskers).

powder	consolidation method	green density based on sintered sintered density	green density based on powder density
calcined powder	isopressed	54.1	
uncalcined powder	uniaxial pressed	37.1	46.2
	isopressed once	55.0	64.0
	isopressed twice	57.0	71.0

powders were then filtered, air dried (or calcined), and then were consolidated. An advantage of using dried, flocced powders was that it was possible to form the compact by directly isopressing the powders.

To determine the effect of the powder isolation method, green and sintered densities were compared for compacts formed from whisker/powder mixtures which were isolated after flocculating the dispersion during sonication and for whisker/powder mixtures which were isolated by filtering the dispersion. Differences in whisker homogeneity could not be observed by SEM and the green densities were comparable. However, after sintering, composites formed from the flocculated whisker/powder mixtures had average densities that were 3-5% greater than for composites formed from powders recovered by filtatration. Evidently the powders isolated after flocculating the dispersions during sonication are more compressible.

(3) Powder Consolidation

When powders are consolidated using uniaxial pressing (or filter casting) the whiskers tend to align in a direction perpendicular to the pressing direction. Orientation of the whiskers can lead to composites with anisotropic properties. To measure the degree of whisker orientation, shrinkage in both the direction perpendicular to the pressing direction and in the radial direction (sample shape was a disk) were measured. Alignment of the whiskers caused the composites to shrink less in the radial direction and more in the pressing direction.

Figure 1 compares the shrinkage results for composites formed by isopressing and for composites formed by uniaxial pressing followed by isopressing to shrinkages for pure cordierite. Uniaxial pressed (sample b) composites showed a strong orientation of the whiskers as evidenced by the considerably larger ratio of shrinkage in the pressing direction to the shrinkage in the radial direction. However, for composites formed solely by isostatic pressing (sample c) the shrinkage ratio was similar to pure cordierite. Isopressing can be used to minimize whisker orientation which leads to composites with more isotropic properties. Although the directional shrinkage was very different for the two forming methods, the composites sintered to the same final densities. As expected, isopressing reduced the orientation of the whiskers and gave composites with more isotropic porperties.

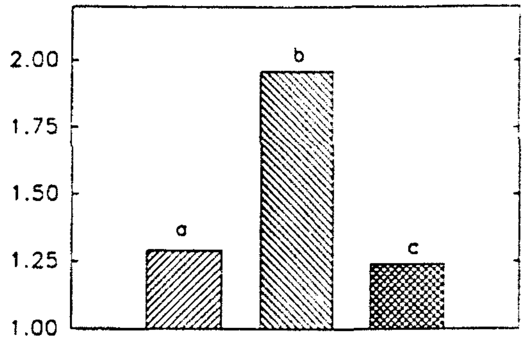

Figure 1. Comparison of the ratio of shrinkage in the pressing direction to the radial direction/for (a) pure cordierite and composites formed with 20 vol% as received Arco whiskers consolidated by (b) uniaxial pressing (10 ksi) followed by isopressing (40 ksi) and (c) isopressing (40 ksi).

(4) Effect of Calcination

Chemically derived powders often are calcined before forming the ceramic to reduce the weight loss and shrinkage that occurs as the powders are heated. However, calcination can lead to larger particles and agglomeration which reduces the sinterability of the powder. We compared the formation of composites using both calcined and uncalcined powders.

To determine the effects of calcination on the powders processability, calcined and uncalcined powders containing 20 vol% as received Arco whiskers were consolidated. Table 2 lists the consolidation methods and the resulting green and sintered densities. Isopressing the composites increased the green density substantially, e.g., by over 50%. Green densities were referenced both to the theoretical density of the sintered composite and to the theoretical density of a fully dense green compact based on measured powder density. (The uncalcined powders had a density of ~2.0 compared to a calcined density of 2.3 g/cm^3.) Relative densities based on sintered theoretical sintered density were similar for both the calcined and uncalcined powders (57-58%). However when the relative densities were compared based on the actual powder density, it can be seen that the composites formed with uncalcined powders reached very high densities (> 70%).

There are several reasons why the uncalcined powders were more sinterable. Calcination reduced the surface area from 175 m^2/g to 150 m^2/g. Although, we observed that the calcination product retained a high surface area and had an average agglomerate size less than 1 μm, sintering rates were significantly reduced when the cordierite powders were calcined first. Therefore, the uncalcined powders were more sinterable than the calcined powders.

An additional effect could be the efficiency of packing based on the relative size of the powders compared to the whiskers. Milewski has shown that whiskers pack more efficiently with powders that have a much smaller size than the whisker diameter.[19] After calcination the powders average agglomerate size was comparably to the whisker diameter, but the surface area measured for these powders suggested that the particle sizes are much smaller than the diameter of the whiskers.

Another possibility is that the uncalcined powders are more compressable. In general, sol-gel derived powders do compress or deform under pressure, and Rahaman *et al.* have observed that sol-gel powders exhibit some pseudo plasticity.[20] Calcination apparently causes hard agglomerates to form so that calcined powders deform less under pressure. Therefore, the higher green densities of composites formed with uncalcined powder was attributed to the ability of the soft flocs present in the uncalcined powders to deform under high pressures to give very dense green bodies. It is well known that, high green densities reduce the amount of material transport that must occur on densification and increases the sinterability of a compact.

To confirm that the uncalcined powders pack more efficiently than the calcined powders, the pore size distributions in the green compacts were determined. Figure 2 compares the pore size distribution of isostatically pressed composites formed with uncalcined powder to isostatically pressed composites formed with calcined powder. The median pore diameter for composites (20 vol% as received Arco whiskers) formed with uncalcined powder was 10 nm while the median pore diameter for composites formed with calcined powder was 33 nm. Therefore, composites formed with uncalcined powders formed compacts with a high green densities, very uniform packing of powders, and a very small pore size. (and small pore size distribution).

SEM micrographs (Figure 3) of fracture surfaces of green compacts confirmed the Hg porosimetry data by showing that in composites formed with uncalcined powder the cordierite powder are uniformly packed around the whiskers with few voids while composites formed with calcined powder have a much more open structure with large voids between particles.

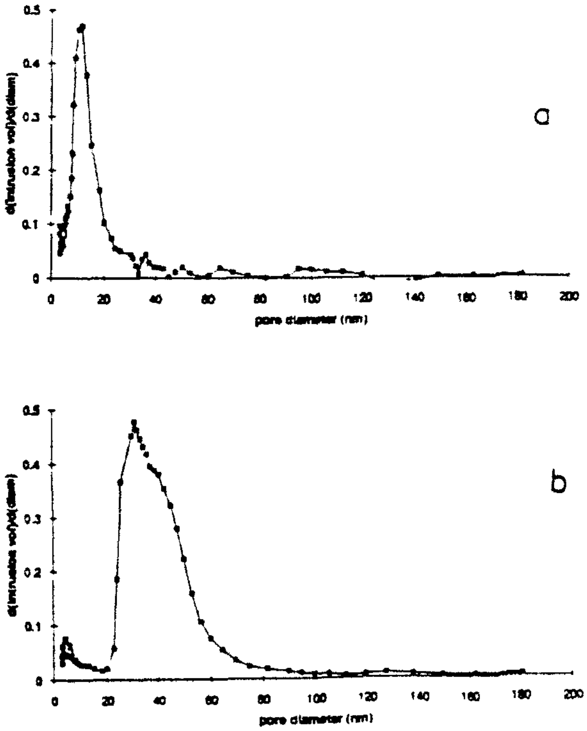

Figure 2. Pore size distributions for composites containing 20 vol% as received Arco whiskers and (a) uncalcined cordierite powder and (b) calcined (600°C) cordierite powder.

Figure 4 shows the sintered density as a function of green density (using uncalcined powders and 20 vol% whiskers). Different green densities were generated by using different pressing conditions. The sintered densities showed a strong dependence on the green density indicating that even with highly sinterable, high surface area powders that viscous sinter, high green densities are necessary to obtain high density sintered composites.

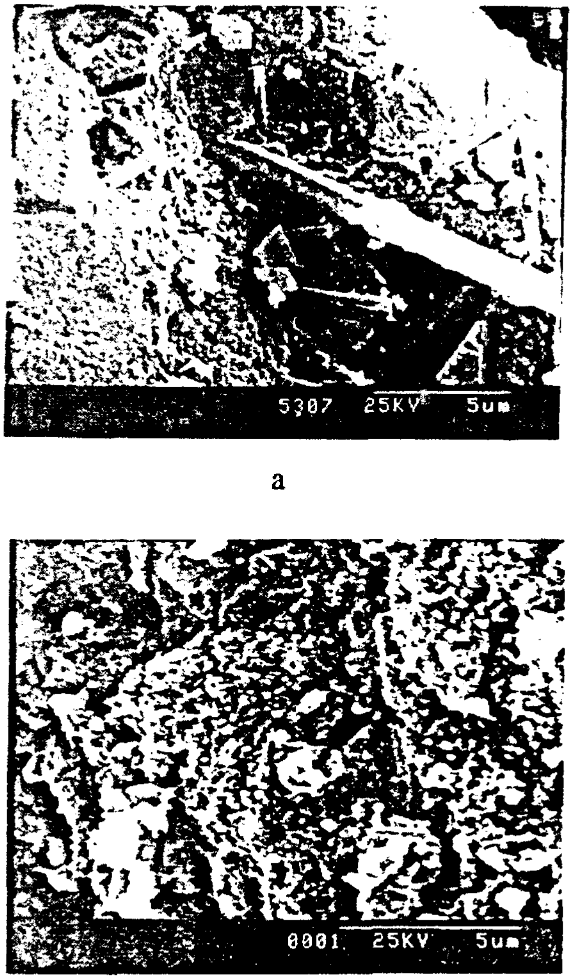

a

b

Figure 3. Fracture surface of unsintered composites containing 20 vol% whiskers formed with (a) uncalcined powder and (b) calcined powder

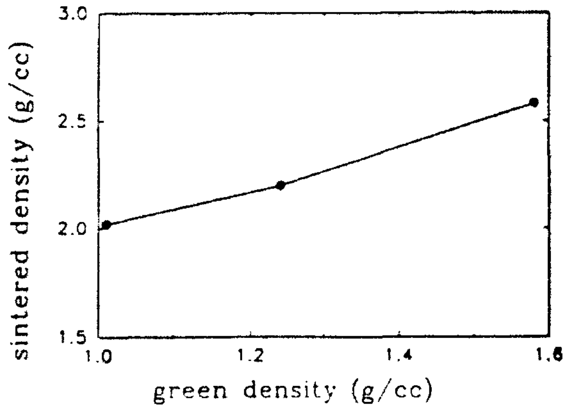

Figure 4. Sintered density as a function of green density for composites formed with uncalcined powder and 20 vol% as received Arco whiskers.

Figure 5 shows the sintered density for composites formed with both calcined and uncalcined powder as a function of SiC concentration (Arco as received). With no whiskers the calcined and uncalcined powders sintered to close to theoretical density. However, the SiC/cordierite composites formed with uncalcined cordierite powder consistently sintered to higher densities than composite formed with calcined powders.

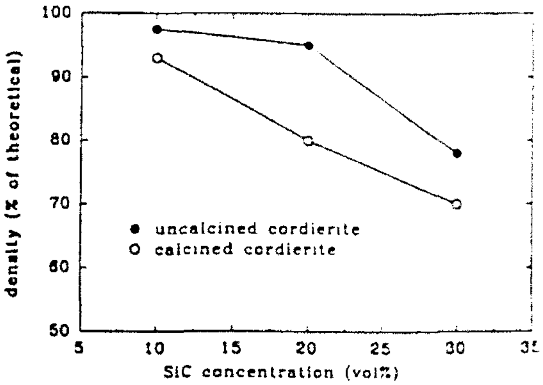

Figure 5. Sintered densities for composites formed with either uncalcined or calcined powder as a function of SiC_w concentration (Arco as received).

(3) Effect of heating rate

Dilatometry measurement of composites formed from uncalcined powders showed two regimes in which shrinkage occurred. The first region occurred between 50°C and 850°C. Shrinkage in this region represented ~40% of the overall linear shrinkage (in the pressing direction) and was attributed to densification of the uncalcined powder. The second densification regime began above 800°C and represented densification due to viscous sintering of the cordierite matrix. Composites formed with calcined powders showed no densification below 800°C.

Figure 6 shows the crystallization temperature range as a function of temperature. The lower boundary represents the start of crystallization and the upper boundary represents the completion of crystallization as measured by DTA. Crystallization temperatures, as expected, showed a dependence on heating rate: slower heating rates lowered the crystallization temperature range. Superimposed on Figure 6 are the temperature at which densification started and the temperature at which densification was completed as measured by dilatometry. Figure 6 shows that, within the accuracy of the measurement of the DTA curves and the dilatometer, the end of densification coincided with the completion of crystallization. Sintering stopped as crystallization of the cordierite was completed; for cordierite to viscous sinter, densification must be complete before the cordierite fully crystallizes.

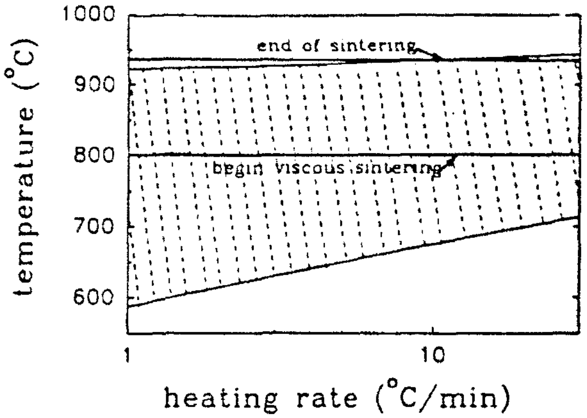

Figure 6. Crystallization regions as a function of heating rate. The lower boundary represents the temperature at which crystallization begins. The upper boundary represents the temperatureat which crystallization ends.

Composite densities (calcined powder, 20 vol% as received whiskers) were measured as a function of heating rate. Figure 7 shows that the sintered densities were dependent on heating rate and that an densities could be optimized using a heating rate of 20-30°C/min. At faster heating rates the sintered samples had many surface cracks and the resulting densities were therefore lower. At low heating rates, the dependence of the sintered density on heating rate was assumed to be a result of the competition between crystallization and densification. Because densification and crystallization occur simultaneously over a fairly narrow temperature range, small changes in the crystallization temperature range could affect the densification. Increasing the heating rate increased the crystallization temperature and allowed the composite to densify to higher temperatures.

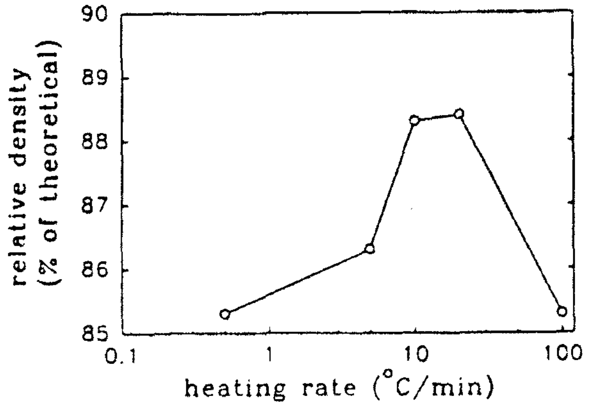

Figure 7. Composite densities as a function of heating rate.

(4) Effect of inclusion aspect ratio.

Figure 8 shows the density of composites formed with 3 SiC sources: Betarundum Ultrafine SiC powder (aspect ratio = 1), as received Arco whiskers (aspect ratio >30) and classified Arco whiskers that were ballmilled and classified to remove the largest aspect ratio whiskers (aspect ratio = 8). At low volume fractions the inclusions had only a moderate effect on the sintered density: densities were still 95% or greater. However in the region above 20 vol% SiC, the aspect ratio had a strong effect on the density. At 30 vol%, for example, there is a 15 vol% difference in the sintered density between composites formed with Betarundum ultrafine and those formed with as received whiskers.

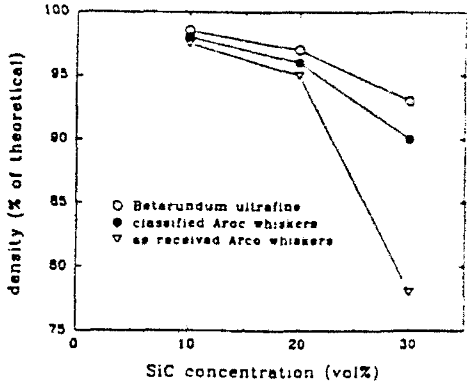

Figure 8. Effect of SiC aspect ratio on the sintered composite densities.

Inclusions limit the sintering in two ways: addition of a second, nonsintering phase can cause differential sintering rates which can lead to transient stresses within the composites.[1] In addition, when the volume fraction of the inclusions exceed the percolation threshold, nonshrinking networks are formed which can severely limit the densification. The percolation threshold has been shown to be a strong function of the inclusion aspect ratio.[2] For powders (aspect ratio ~ 1) the percolation threshold is predicted to be ~ 40 vol% whereas for whiskers with aspect ratios >30 the percolation threshold is predicted to be at about 16 vol%. (These results are predicted from computer models for two dimensional arrays.) Because the whiskers tend to align during pressing, the whiskers can be treated as two dimensional arrays. At low volume fractions, decreases in composite densities were attributed to stresses caused by differential sintering rates. The larger differences in sintered densities at higher volume fractions of SiC were attribute to the formation of nonsintering SiC networks.

CONCLUSIONS

We found that homogeneous mixtures of SiC and cordierite could be prepared by floccing the dispersions during sonication. Composites formed with uncalcined powders had higher green densities and smaller pore diameters than composites formed with uncalcined powders and sintered to higher densities than composites formed with uncalcined powders. Using uncalcined sol-gel derived cordierite powders, composites could be sintered to > 95% relative density using both SiC whiskers (as-received and classified) and SiC powders.

REFERENCES

1. L.C. DeJonghe, M.N. Rahaman and C.H. Hsueh, "Transient Stresses in Bimodal Compacts During Sintering," *Acta metall.* 34 [7] 1467-71 (1986)

2. M.N. Rahaman, L.C. DeJonghe, "Effect of Rigid Inclusions on the Sintering of Glass Powder Compacts," *J. Am. Ceram. Soc.* 70 [12] C-348- C-352 (1987)

3. F.F. Lange, Constrained Network Model for Predicting Densification Behavior of Composite Powders," *J. Mater. Res.* 2 [1] 59-65 (1987)

4. T.N. Tiegs and P.F. Becher, "Sintered Al_2O_3-SiC-Whisker Composites," *Am. Ceram. Soc. Bull.* 66[2] 339-42 (1987)

5. M.D. Sacks, H.W. Lee and O.E. Rojas, "Suspension Processing of Al_2O_3/SiC Whisker Composites," *J. Am. Ceram. Soc.* 71 [5] 370-70 (1988)

6. H.W. Lee and M. E. Sacks, "Pressureless Sintering of Al_2O_3/SiC Whisker Composites," *Ceram. Eng. Sci. Proc.* 10 [7-8] 720-29 (1989)

7. H.W. Lee and M.D. Sacks, "Pressureless Sintering of SiC-Whisker-Reinforced Al_2O_3 Composites: I. Effect of Matrix Powder Surface Area," *J. Am. Ceram. Soc.*, 73 [7] 1884-93 (1990) and II. Effects of Sintering Additives and Green Body Infiltration," *J. Am. Ceram. Soc.*, [7] 1894-1900 (1990)

8. M.D. Sacks, N. Bozkurt, and G.W. Scheiffele, "Fabrication of Mullite and Mullite Matrix Composites by Transient Viscous Sintering of Composite Powders," *J. Am. Ceram. Soc.*, 74 [10] 2428-37 (1991)

9. C. Olagnon, E. Bullock, and G. Fantozzi, "Processing of High Density Sintered SiC Whisker Reinforced Si_3N_4 Composites," *Ceram. International* 17 53-60 (1991)

10. H. Vesteghem, A.R. DiGiampaolo, and A. Dauger, "Low-Temperature Cordierite Glass form Autoclave-prepared Gel," *J. Mater. Sci. Lett.* 1187-1189 (1987)

11. C. Gensse and U. Chowdry, "Nonconventional Route to Glass-Ceramic for Electronic Packaging," *Mater. Res. Soc. Symp. Proc.*, 73 693-703 (1986)

12. M. Okuyama, T. Fukui and C. Skaurai, "Effect of Solvent and Alkoxy Group on Powder Precipitation of Cordierite by Complex-Alkoxide Hydrolysis," *J. Non-Cryst. Solids*, 143, 112 (1992)

13. M. Okuyama, T. Fukui and C. Skaurai, "Effect Complex Precursors on Alkoxide- Derived Cordierite Powder," *J. Am. Ceram. Soc.*, 75, 153 (1992).

14. M. Nogami, S. Ogawa, and K. Nagasaka, "Preparation of Cordierite Glass by the Sol-Gel *J. Mater. Sci.* 4339-4342 (1989)

15. A.B. Hardy and W.E. Rhine, "Preparation of SiC-Cordierite Composites," p 791 in Chemical Processing of Advanced Materials, Eds. L.L. Hench and J.K. West, John Wiley and Sons, NY (1992).

16. B.J.J. Zelinski, B.D. Fabes, and D.R. Uhlman, "Crystallization Behavior of Sol-GEl Derived Glasses," *J. Non-Cryst. Solids*, 82, 307 (1986)

17. F.F. Lange, B.I. Davis, and E. Wright, "Processing-Related Fracture Origins: IV, Elimination of Voids Produced by Organic Inclusions," *J. Am. Ceram. Soc.* **69** 66-69 (1986).

18. W.C. Moffat, P. White and H.K. Bowen, "Production of Alumina-Zirconia Composite Ceramics by Nonsolvent Flocculation of Polymer-Containing Powder Dispersions," pp 645-653 Ceramic Transactions, Ceramic Powder Science, vol 1. Edited by G.L. Messing, E.R. Fuller, and H. Hausner, American Ceramic Society, Westerville, OH (1987)

19. J.V. Milewski, "Efficient Use of Whiskers in the Reinforcement of Ceramics, *Adv. Ceram. Mater.* 1 [1] 36-41 (1986)

20. M. N. Rahaman, L.C. DeJonghe, S. L. Shinde and P.H. Tewari, "Sintering and Microstructure of Mullite Aerogels," *J. Am. Ceram. Soc.* 71 [7] C-338-C-341 (1988)

21. E.A. Holm and M.J. Cima, "Two-Dimensional Whisker Percolation in Ceramic Matrix Ceramic Whisker Composites," *J. Am. Ceram. Soc.* 72 [2] 303-305 (1989)